

**Design of functional metal-organic  
frameworks for catalytic conversion of CO<sub>2</sub>  
to value-added chemicals**

**Doctoral Thesis**

by

**Rajesh Das**

**(2018CYZ0002)**



**DEPARTMENT OF CHEMISTRY  
INDIAN INSTITUTE OF TECHNOLOGY ROPAR**

**April 2023**

**Design of functional metal-organic  
frameworks for catalytic conversion of CO<sub>2</sub>  
to value-added chemicals**

A Thesis Submitted  
In Partial Fulfillment of the Requirements  
for the Degree of  
**DOCTOR OF PHILOSOPHY**

by

**Rajesh Das**

**(2018CYZ0002)**



**DEPARTMENT OF CHEMISTRY  
INDIAN INSTITUTE OF TECHNOLOGY ROPAR**

**April 2023**

**Rajesh Das**  
**© Indian Institute of Technology Ropar-2023**  
**All rights reserved**

*Dedicated to my parent*



## **Declaration of originality**

I hereby declare that the work which is being presented in the thesis entitled “Design of functional metal-organic frameworks for catalytic conversion of CO<sub>2</sub> to value-added chemicals” has been authored by me. It presents the result of my own independent investigation/research conducted during the time period from July 2018 to April 2023 under the supervision of Dr. C. M. Nagaraja, Associate Professor, Department of Chemistry. To the best of my knowledge, it is an original work, both in terms of research content and narrative, and has not been submitted or accepted elsewhere, in part or in full, for the award of any degree, diploma, fellowship, associateship, or similar title of any university or institution. Further, due credit has been attributed to the relevant state-of-the-art and collaborations with appropriate citations and acknowledgments, in line with established ethical norms and practices. I also declare that any idea/data/fact/source stated in my thesis has not been fabricated/ falsified/ misrepresented. All the principles of academic honesty and integrity have been followed. I fully understand that if the thesis is found to be unoriginal, fabricated, or plagiarized, the Institute reserves the right to withdraw the thesis from its archive and revoke the associated Degree conferred. Additionally, the Institute also reserves the right to appraise all concerned sections of society of the matter for their information and necessary action. If accepted, I hereby consent for my thesis to be available online in the Institute’s Open Access repository, inter-library loan, and the title & abstract to be made available to outside organizations.

*R. Das*

Name: Rajesh Das

Entry Number: 2018CZY0002

Program: Ph. D

Department: Chemistry

Indian Institute of Technology Ropar

Rupnagar, Punjab 140001

Date: 26-04-2023



## Certificate

This is to certify that the thesis entitled “Design of functional metal-organic frameworks for catalytic conversion of CO<sub>2</sub> to value-added chemicals” submitted by Rajesh Das, (2018CYZ0002) for the award of the degree of Doctor of Philosophy of Indian Institute of Technology Ropar, is a record of bonafide research work carried out under my guidance and supervision. To the best of my knowledge and belief, the work presented in this thesis is original and has not been submitted, either in part or full, for the award of any other degree, diploma, fellowship, associateship, or similar title of any university or institution. In my opinion, the thesis has reached the standard of fulfilling the requirements of the regulations relating to the degree.



Name: Dr. C. M. Nagaraja

Department: Chemistry

Indian Institute of Technology Ropar

Rupnagar, Punjab 140001

Date: 26-04-2023



## Acknowledgements

First and foremost, I would like to express my heartfelt and deepest gratitude to my research supervisor, Dr. C. M. Nagaraja, for seeing my potential and taking a chance on me. I also thank him for his patience, motivation, timely advice, steady guidance, support, and encouragement throughout my Ph.D tenure. I am also very much thankful to him for introducing me to an interesting world of carbon capture and utilization (CCU) and Metal-Organic Frameworks. It would not have been possible without you, allowing me to explore new scientific areas with both autonomy and excitement. Because of his enormous support, I could maintain a balance between my professional and personal life towards the end of the program.

I would like to thank my doctoral committee (DC) members Dr. T. J. Dhillip Kumar, Dr. Rajendra Srivastava, Dr. Indranil Chatterjee, and Dr. L Vijay Anand for their research assistance, beneficial suggestions, insightful comments, and continuous encouragement over the past years of my Ph.D. Also, for their time-to-time evaluation of the work. I thank the director, IIT Ropar for providing infrastructure and all the technical facilities for doing research. I also thank the institute for providing financial support to attend national and international conferences.

My special thanks to my older brother Bilash Mohanty with whom I shared my professional and personal life. His advice and guidance motivate me to go ahead in every moment of my life. I thank my friends Dr. Ashish, Rajib, Gopal, Dr. Arjun, Manas, Priti, Raju and Swadhin for their time and support in the hour of need, who made my life cheerful.

I am grateful to have such friendly and cooperative labmates, and I thank them all (Dr. Bharat, Dr. Sandeep, Dr. Rekha, Dr. Nayush, Dr. Suman, Gulshan, Amit Nagar, Vaibhav, Ram, Shubham, Paltu, Sudipta, Srijan, Sakshi, Sahil, Mehek, Aniket, and Beekesh) for creating such a cheerful and lively environment in the lab. They were very supportive, collaborative, and helpful during my entire stay at IIT Ropar. It's great to have such a diverse group with so many different areas of expertise. We have created quite an interesting family, one that will be difficult to achieve ever again. I have learned a great deal from all of you, not only about science but also about living and working together.

I offer sincere regards to my teachers (Pani Sir, Tubula Sir, Khirod Sir, Barada nana, Sushil Sir, Nari Sir, Pramila mam) who have inspired me directly or indirectly in my research career. My stay at IIT-Ropar has been pleased with the relationship of all the research scholars. I am thankful to Dr. Anil, Dr. Sandeep Kumar, Dr. Suman, Nahida, Debarshi, Majid, Moumita,

Prasoon, Manisha, Gautam, Daisy, Divyani, Alankar, Diksha, Himanshu, Ganesh, Navpreet. I thank chemistry department staff Poonam mam, Mr. Sushil, Mr. Nagendra, Mrs. Samita, Ms. Hanspreet, Mr. Manish and Mr. Gurwinder for their help thought-out my Ph. D journey.

I would like to thank my parents (Bapa, Bou, Cuttack Bapa, Mummy, Dada, Khudi) for backing me throughout this study and supporting me in all the phases. I know it was a challenge from time to time, but their open-ended belief in me has allowed me to reach the ultimate goal. None of my achievements in life would be imaginable without their selfless unconditional love and dedication. I owe everything to them. Dedicating this thesis to them is a minor recognition of their precious support and encouragement. Thank you to my brother and my sisters, Rajashree, Rashmi, Itishree, Minu, Rakesh, Mukesh, Tapan Bhai, and Smruti Bhai for their support and encouragement.

My greatest regards to the almighty for bestowing upon me the courage to face the complexities of life and complete this degree successfully, and for inculcating my dedication.

**Rajesh Das**

## Lay summary

Over the past two decades, the concentration of atmospheric carbon dioxide is increasing exponentially and it has exceeded 410 ppm, currently. This rapid increase in the atmospheric CO<sub>2</sub> content has been attributed to various human activities leading to the increased combustion of fossil fuels. This unprecedented rise in carbon dioxide emissions has resulted in the most serious environmental issues such as global warming, unpredictable weather patterns, ocean acidification, and so on. To mitigate this growing carbon dioxide concentration, carbon capture and sequestration (CCS) has been followed. However, an alternative and value-added route is carbon capture and utilization (CCU) as a C1 source by converting it into high-value chemicals and fuels. Among the various catalytic transformations of carbon dioxide, into value-added chemicals and fuels, the cycloaddition of CO<sub>2</sub> with epoxides to produce cyclic carbonates is one of the most studied processes due to its absolute atom economy. Besides, the synthesis of oxazolidinone, an important building block of antibiotics by a one-pot three-component cyclization of carbon dioxide, propargylic alcohol, and primary amine is also of significant interest. Further, the catalytic reduction of CO<sub>2</sub> into fuels such as CH<sub>4</sub>, CH<sub>3</sub>OH, HCOOH, and syngas (CO + H<sub>2</sub>) is of potential significance and is being investigated by researchers worldwide. However, the majority of the catalytic systems reported for fixation of carbon dioxide require either high temperature and/or high pressure of carbon dioxide and often additional co-catalysts are employed. However, towards green and sustainable utilization of carbon dioxide, it is highly desirable to carry out the catalysis under co-catalyst-free mild conditions. To achieve this, the catalyst should exhibit high carbon dioxide affinity as well as superior catalytic activity to capture and activate CO<sub>2</sub> at ambient conditions. Besides, the catalyst should be highly stable and recyclable for multiple cycles of reuse. In this context, metal-organic framework (MOF)-based catalysts have shown unique advantages over other conventional porous materials due to their tunable pore size and functionality along with high surface areas. The modular nature of these materials facilitates rational design by incorporating a high density of CO<sub>2</sub>-philic and catalytic functionalities for simultaneous capture and catalytic conversion of carbon dioxide to fine chemicals. In this direction, the objectives of this thesis work were to strategically construct functionalized MOF-based materials and their exploration as recyclable catalysts for the chemical fixation of carbon dioxide into high-value chemicals under environment-friendly mild conditions.

With the aforementioned motivation for the capture and utilization of CO<sub>2</sub> as C1-feedstock to generate various high-value chemicals, we rationally designed MOF-based heterogeneous catalysts for effective CCU under mild green conditions. The thesis has been divided into six chapters as summarized below.

Chapter 1: This chapter includes a comprehensive introduction to the topic. The importance of CCU and the various ways of chemical fixation of CO<sub>2</sub> into high-value chemicals. The introduction to MOF-based porous materials and their catalytic applications for CCU.

Chapter 2: This chapter is divided into two parts, in chapter 2a, the rational design of a novel 3D, microporous, bifunctional Zn(II)-organic framework, Zn-DAT, {[Zn<sub>2</sub>(TDC)<sub>2</sub>(DATRZ)]·(3H<sub>2</sub>O)·(DMF)}<sub>n</sub> (where TDC = 2,5-thiophene dicarboxylate ion and DATRZ = 3,5-diamino-1,2,4-triazole) using a mixed ligand strategy is reported. Here, the presence of basic -NH<sub>2</sub> functionalized pores rendered selective adsorption property for CO<sub>2</sub> with a high heat of adsorption (Q<sub>st</sub>) of 39.5 kJ mol<sup>-1</sup> which is further supported by a theoretically computed binding energy (BE) of 40.9 kJ mol<sup>-1</sup>. Further, the role of -NH<sub>2</sub> group in enhancing the catalytic fixation of CO<sub>2</sub> was studied by preparing an analogous MOF {[Zn<sub>2</sub>(TDC)(TRZ)<sub>2</sub>]·(DMA)·(MeOH)}<sub>n</sub> (Zn-TAZ) containing 1,2,4-triazole (TAZ) linker, which lacks -NH<sub>2</sub> group. Notably, Zn-DAT MOF exhibited efficient catalytic activity for chemical fixation of CO<sub>2</sub> to cyclic carbonates under mild conditions of RT.

In chapter 2b, the strategic design of a hydrogen-bonded 3D framework, HbMOF1, {[Zn(hfipbba)(MA)]·3DMF}<sub>n</sub> (hfipbba=4,4'-(hexafluoroisopropylene)bis(benzoic acid), MA = Melamine) by incorporating basic -NH<sub>2</sub> and polar -CF<sub>3</sub> groups is reported. The HbMOF1 possesses two types of 1D channels decorated with CO<sub>2</sub>-philic (-NH<sub>2</sub> and -CF<sub>3</sub>) groups affording highly selective CO<sub>2</sub> capture property to the framework. Further, the synergistic effect of both Lewis acidic and basic sites exposed in the confined 1D channels afforded high catalytic activity for efficient fixation of CO<sub>2</sub> with terminal/internal epoxides at RT and 1 bar of CO<sub>2</sub>. This work demonstrates the rational design of porous MOFs incorporating multiple functional sites for enhanced fixation of CO<sub>2</sub> with terminal/internal epoxides at mild conditions.

Chapter 3: In this chapter, we strategically constructed 3D MOF, {Mg<sub>3</sub>(TATAB)<sub>2</sub>(HCO<sub>2</sub>)(DMA)}<sub>n</sub> (where, TATAB = 4,4',4''-s-triazine-1,3,5-triyltri-p-aminobenzoate) by utilizing CO<sub>2</sub>-philic Mg(II) and nitrogen-rich tripodal linker (TATAB). The MOF possesses a high BET surface area of 2606.13 m<sup>2</sup> g<sup>-1</sup> and highly polar 1D channels

decorated with a high density of CO<sub>2</sub>-philic sites which promoted remarkably high CO<sub>2</sub> uptake of 50.2 wt% at 273 K with a high heat of adsorption of 55.13 kJ mol<sup>-1</sup>. The high CO<sub>2</sub> affinity combined with the presence of a high density of Lewis acidic sites conferred efficient catalytic properties to the Mg-MOF for chemical fixation of CO<sub>2</sub> from direct air under ambient conditions. The remarkable performance of Mg-MOF for the fixation of CO<sub>2</sub> from direct air was further supported by in-depth theoretical calculations. This work represents a rare demonstration of carbon capture and utilization (CCU) from direct air under eco-friendly mild conditions.

Chapter 4: In this chapter, the application of Mg-centered porphyrin MOF (PCN-224(Mg)) having relevance to chlorophyll in green plants as a visible light-promoted recyclable catalyst for effective fixation of CO<sub>2</sub> to cyclic carbonates is reported. The Mg-centered porphyrin MOF showed good CO<sub>2</sub> capture ability with high interaction energy of 44.5 kJ/mol and superior catalytic activity under visible light irradiation over thermal-driven conditions. The excellent light-promoted catalytic activity of Mg-porphyrin MOF has been attributed to facile ligand-to-metal charge transfer (LMCT) transition from photo-excited Mg-porphyrin unit (SBU) to Zr6 cluster which intern activates CO<sub>2</sub> thereby lowering the activation barrier for its cycloaddition with epoxides. The in-depth theoretical studies further unveiled the detailed mechanistic path of the light-promoted conversion of CO<sub>2</sub> into value-added cyclic carbonates.

Chapter 5: In this chapter, the chemical fixation of CO<sub>2</sub> to propargylic alcohols/primary amines to generate oxazolidinones, an important building blocks for antibiotics is reported. In chapter 5a, the rational construction of Ag(I)-anchored sulfonate-functionalized MOF, named MOF-SO<sub>3</sub>Ag composed of CO<sub>2</sub>-philic sulfonate and catalytically active alkynophilic Ag(I) sites for chemical fixation of carbon dioxide is discussed. The MOF-SO<sub>3</sub>Ag acts as an efficient heterogeneous catalyst for cyclic carboxylation of propargylic alcohols to generate  $\alpha$ -alkylidene cyclic carbonates in >99% yield at mild conditions of RT and 1 bar CO<sub>2</sub>. More importantly, one-pot synthesis of oxazolidinones by a three-component reaction between CO<sub>2</sub>, propargylic alcohol, and primary amine has also been achieved using MOF-SO<sub>3</sub>Ag catalyst under mild conditions. Moreover, the MOF is highly recyclable and retains its superior catalytic activity even after several cycles.

In chapter 5b, the development of noble metal-free Cu(I) anchored N-heterocyclic carbene (NHC)-based MOF for one-step synthesis of oxazolidinones by coupling of CO<sub>2</sub> with propargylic alcohols and primary amines is reported. The presence of a high density of CO<sub>2</sub>-

philic NHC and catalytic Cu(I) sites in the 1D channels of the MOF rendered efficient catalytic activity for the conversion of CO<sub>2</sub> to oxazolidinones at RT and atmospheric pressure conditions. Notably, Cu(I)@NHC-MOF showed excellent recyclability for up to 10 cycles of regeneration with retention of catalytic activity as well as chemical stability. To the best of our knowledge, Cu(I)@NHC-MOF represents the first example of a noble metal-free MOF-based heterogeneous catalyst for the transformation of CO<sub>2</sub> to oxazolidinones under mild conditions.

Chapter 6: In this chapter, the application of Co(II)-centered porphyrin-based porous organic framework, Co-POF for photocatalytic reduction of CO<sub>2</sub> to syngas (CO & H<sub>2</sub>) is reported. Notably, the Co-POF showed a selective reduction of CO<sub>2</sub> to CO with a rate of 1347  $\mu\text{mol g}^{-1}\text{h}^{-1}$  under visible-light irradiation. Further, the role of single Co(II) sites towards high photocatalytic activity was studied by preparing an analogous Zn(II)-framework. Interestingly, Zn-POF showed negligible activity for the photocatalytic CO<sub>2</sub> reduction under the same optimized conditions highlighting the importance of Co(II) for the CO<sub>2</sub> reduction reaction. Furthermore, the in-sight mechanistic details of the photocatalytic process were revealed from theoretical studies.

## Abstract

The immense amount of carbon dioxide (CO<sub>2</sub>) emissions has resulted in the most serious environmental issues like ocean acidification, extreme weather, species extinction, and global warming. Consequently, the utilization of carbon dioxide as C1-feedstock offers the dual advantages of mitigating the increasing atmospheric CO<sub>2</sub> concentration and production of valuable chemicals. However, the inertness of carbon dioxide puts a significant challenge to its functionalization at ambient conditions. Thus, the majority of the catalytic systems reported for fixation of carbon dioxide require either high temperature and/or high pressure of CO<sub>2</sub> and often additional co-catalysts are employed. However, towards green and sustainable utilization of carbon dioxide, it is highly desirable to carry out the transformation under co-catalyst-free mild conditions. In this context, metal-organic framework (MOF)-based catalysts have shown unique advantages over other conventional porous materials due to their tunable pore size and functionality along with high surface areas. The thesis work has been divided into six chapters. The Chapter 1 includes introduction to framework materials and importance of carbon capture/utilization and various strategies employed for chemical fixation of CO<sub>2</sub> to high-value chemicals and fuels under environment-friendly mild conditions. Further, with the aforementioned motivation for capture and utilization of CO<sub>2</sub> as C1-feedstock to generate various high-value chemicals, we rationally designed MOF-based heterogeneous catalysts for effective conversion of carbon dioxide under eco-friendly conditions. In this regard, the work carried out in Chapter 2 includes rational design of catalytic MOFs based on Lewis acidic Zn(II) and organic linker composed of basic sites suitable for effective fixation of CO<sub>2</sub> to value-added cyclic carbonates at mild conditions.

Notably, the utilization of carbon dioxide from direct air has attracted tremendous attention as this process enables carbon capture from any place independent of emission sources. In this context, by utilizing reticular synthesis, we strategically designed a Mg-based highly MOF with pores functionalized with CO<sub>2</sub>-philic sites for chemical fixation of CO<sub>2</sub> from air into high-value cyclic carbonates at mild conditions which will be presented in Chapter 3. Besides, the sunlight-driven fixation of CO<sub>2</sub> into valuable chemicals constitutes a promising approach toward a sustainable generation of valuable chemicals over the traditional thermal-driven process. In this regard, in Chapter 4, Mg-centered porphyrin MOF having relevance to chlorophyll in green plants was developed and its application for visible light promoted effective

fixation of CO<sub>2</sub> was investigated. Encouraged by the unique advantages of MOFs towards the stabilization of catalytically active metal ions, the post-synthetic functionalization of NHC-based MOFs with catalytically active Ag(I)/Cu(I) species and their catalytic activity for CO<sub>2</sub> fixation is presented in Chapter 5. These Ag(I)/Cu(I) anchored NHC-MOFs were utilized as recyclable catalysts for the transformation of carbon dioxide to  $\alpha$ -alkylidene cyclic carbonates and oxazolidinone, an important building block for antibiotics under mild conditions. Further, towards photocatalytic reduction of CO<sub>2</sub> to valuable chemicals and fuels, in Chapter 6, design of 2D Co-based porphyrin network and its photocatalytic performance for carbon dioxide reduction is reported. Overall, the work carried out in the thesis involving the strategic design of framework materials and their catalytic investigation for chemical fixation of CO<sub>2</sub> to high-value chemicals.

## List of publications out of thesis

- (1) **Das, R.;** Dhankhar, S. S.; Nagaraja, C. M. Construction of a bifunctional Zn(II)-organic framework containing basic amine functionality for selective capture and room temperature fixation of CO<sub>2</sub>. *Inorg. Chem. Front.* **2020**, *7*, 72-81 (Featured on the front cover of the issue).
- (2) **Das, R.;** Muthukumar, D.; Pillai, R. S.; Nagaraja, C. M. Rational design of a Zn(II)-MOF with multiple functional sites for highly efficient fixation of CO<sub>2</sub> at mild conditions: combined experimental and theoretical investigation. *Chem. Eur. J.* **2020**, *26*, 17445-17454.
- (3) **Das, R.;** Ezhil, T.; Palakkal, A. S.; Muthukumar, D.; Pillai, R. S.; Nagaraja, C. M. Efficient chemical fixation of CO<sub>2</sub> from direct air under environment-friendly co-catalyst and solvent-free ambient conditions. *J. Mater. Chem. A* **2021**, *9*, 23127-23139.
- (4) **Das R.;** Nagaraja, C. M. Highly Efficient Fixation of Carbon Dioxide at RT and Atmospheric Pressure Conditions: Influence of Polar Functionality on Selective Capture and Conversion of CO<sub>2</sub>. *Inorg. Chem.* **2020**, *59*, 9765-9773 (A unique CAS number has been registered for the compound reported in this work).
- (5) **Das R.;** Nagaraja, C. M. Noble metal-free Cu(I)-anchored NHC-based MOF for highly recyclable fixation of CO<sub>2</sub> under RT and atmospheric pressure conditions. *Green Chem.* **2021**, *23*, 5195-5204.
- (6) **Das, R.;** Manna, S. S.; Pathak, B.; Nagaraja, C. M. Strategic Design of Mg-Centered Porphyrin MOF for Efficient Visible Light-Promoted Fixation of CO<sub>2</sub> at Ambient Conditions: Combined Experimental and Theoretical Investigation. *ACS Appl. Mater. Interfaces* **2022**, *14*, 33285-33296.
- (7) **Das, R.;** Parihar, V.; Nagaraja, C. M. Strategic design of a bifunctional Ag(I)-grafted NHC-MOF for efficient chemical fixation of CO<sub>2</sub> from dilute gas at ambient conditions. *Inorg. Chem. Front.* **2022**, *9*, 2583-2593.
- (8) **Das, R.;** C. M. Nagaraja, Rational design of 2D Co(II)-porphyrin framework for efficient Visible light-promoted reduction of CO<sub>2</sub> from dilute gas: combined experimental and theoretical investigation (Manuscript submitted).

## Oral/Poster presentations at conferences

- (1) Presented poster at International Conference on Modern Trends in Inorganic Chemistry (MTIC-XVII), organized by the Department of Chemistry, IITG December-2019.
- (2) Presented poster at CRIKC Chemistry symposium (CCS-2019) organized by the Department of Chemistry, IISER Mohali, 2019 (Won a best poster award).
- (3) Presented poster at International Conference on Main-group molecules to material-II (MMM), organized by the Department of Chemistry, NISER, BBSR 2021 (Won ACS catalysis best poster award).
- (4) Presented oral at 58th International Conference on Recent Trends in Chemical Sciences-Environmental Chemistry” (RTCS-ENV 2021) hosted by the Department of Chemistry, IIT Ropar.
- (5) Presented poster at ‘Conference on Advances in Catalysis for Energy and Environment (CACEE-2022)’, & CO<sub>2</sub> India Network 1st Annual Meet, TIFR, Mumbai, India.
- (6) Presented poster at Chemical Research Society of India (CRSI) national symposium in Chemistry organized by Department of Chemistry, IISER Mohali, 2022.
- (7) Presented poster in MOF-2022 8th International Conference on Metal-Organic Frameworks and Open Framework Compounds held at the international congress center Dresden, Germany.
- (8) Presented oral at Chem Fest-2023, Department of Chemistry, IIT Ropar.

## Table of contents

Chapters	Page
<b>Chapter 1. Introduction</b>	1
1.1 Carbon dioxide (CO <sub>2</sub> ) a greenhouse gas	3
1.2 Carbon capture and utilization (CCU)	4
1.3 Framework-based materials	5
1.3.1. Metal-organic frameworks (MOFs)	5
1.3.2. Historical aspects of MOFs	6
1.3.2. Porous organic frameworks (POFs)	7
1.4. Applications of MOFs	8
1.5. MOFs for CCU	8
1.5.1. MOFs for CO <sub>2</sub> capture	8
1.5.2. MOF materials for CO <sub>2</sub> utilization	10
1.5.2.1. Opportunistic catalysis with metal nodes	10
1.5.2.2. Designed catalysis with functionalized linkers	10
1.5.2.3. Incorporation of the catalytic active site by PSM of MOF	11
1.5.3. Various ways of CO <sub>2</sub> fixation by utilizing frameworks as catalysts	12
1.5.3.1. CO <sub>2</sub> fixation via C-O bond formation	12
1.5.2.2. CO <sub>2</sub> fixation via C-N bond formation	15
1.5.2.3. CO <sub>2</sub> utilization via C-C bond formation	17
1.5.2.4. CO <sub>2</sub> utilization via reduction	18
1.6. Summary	20
1.7. References	20
<b>Chapter 2a. Construction of a bifunctional Zn(II)-organic framework containing basic amine functionality for selective capture and room temperature fixation of CO<sub>2</sub></b>	33
2a.1. Introduction	35
2a.2. Experimental section	36
2a.2.1. Materials	36
2a.2.2. Physicochemical characterization	36

2a.2.3. Synthesis	36
2a.2.3.1. Synthesis of $\{[\text{Zn}_2(\text{TDC})_2(\text{DATRZ})].(3\text{H}_2\text{O}).(\text{DMF})\}_n$ (Zn-DAT)	36
2a.2.3.2. Synthesis of $\{[\text{Zn}_2(\text{TDC})(\text{TRZ})_2].(\text{DMA}).(\text{MeOH})\}_n$ , (Zn-TAZ)	37
2a.2.4. Catalytic cycloaddition reactions of $\text{CO}_2$ with epoxides	37
2a.2.5. X-ray crystallography	38
2a.2.6. Gas adsorption measurements	38
2a.2.7. Theoretical calculations	40
2a.3. Results and discussion	40
2a.3.1. Synthesis and structural description	40
2a.3.2. Thermogravimetric analysis of Zn-DAT MOF	43
2a.3.3. Gas adsorption studies	44
2a.3.4. Theoretical study	45
2a.3.5. Catalytic cycloaddition reaction of $\text{CO}_2$	46
2a.3.6. Recyclability test	49
2a.3.7. Plausible mechanism	49
2a.4. Conclusion	51
2a.5. References	51
<b>Chapter 2b: Rational design of a Zn(II)-MOF with multiple functional sites for highly efficient fixation of <math>\text{CO}_2</math> at mild conditions: A combined experimental and theoretical investigation</b>	57
2b.1. Introduction	59
2b.2. Experimental section	60
2b.2.1. Physicochemical characterization	60
2b.2.2. Synthesis of HbMOF1	60
2b.2.3. Adsorption measurements	61
2b.2.4. Catalytic cycloaddition reactions of $\text{CO}_2$ with epoxides	61
2b.2.5. X-ray crystallography	62
2b.2.6. Computational methods	62
2b.2.6.1. Microscopic models for the host framework	62
2b.2.6.2. DFT optimization on HbMOF1 loaded with epoxides	63

2b.2.6.3. Computational methods for the catalytic mechanism	65
2b.3. Results and discussion	66
2b.3.1. Synthesis and structural description	66
2b.3.2 Gas adsorption studies of HbMOF1	68
2b.3.3. Thermal and chemical stability of HbMOF1	70
2b.3.4. Catalytic cycloaddition reaction of CO <sub>2</sub> with terminal/internal epoxides	71
2b.3.5. Plausible mechanism of cycloaddition reaction	75
2b.3.6. Recyclability	78
2b.4. Conclusion	78
2b.5. References	79
<b>Chapter 3. Efficient chemical fixation of CO<sub>2</sub> from direct air under environment-friendly co-catalyst and solvent-free ambient conditions</b>	85
3.1. Introduction	87
3.2. Experimental section	88
3.2.1. Materials	88
3.2.2. Physicochemical characterization	88
3.2.3. Synthesis	89
3.2.3.1. Synthesis of 4,4',4''-s-triazine-1,3,5-triyltri-p-aminobenzoic acid (H <sub>3</sub> TATAB) ligand	89
3.2.3.2. Synthesis of Mg-MOF	89
3.2.4. Catalytic cycloaddition reactions of CO <sub>2</sub> with epoxides	90
3.2.5 Computational studies	90
3.3. Results and discussion	91
3.3.1. Synthesis and structural studies	91
3.3.2. Thermal and chemical stability of Mg-MOF	94
3.3.3. Gas adsorption study of Mg-MOF	94
3.3.4. Solvent and co-catalyst-free fixation of CO <sub>2</sub> under mild conditions	97
3.3.5. Solvent and co-catalyst-free fixation of CO <sub>2</sub> from direct air	100
3.3.6. Theoretical insight for higher CO <sub>2</sub> selectivity from direct air	102

3.3.7. Catalyst leaching and recyclability test	102
3.3.8. Plausible mechanism for solvent and co-catalyst-free fixation of CO <sub>2</sub>	103
3.4. Conclusions	105
3.5. References	106
<b>Chapter 4: Visible light-promoted efficient fixation of CO<sub>2</sub> at ambient conditions using Mg-porphyrin based MOF as highly recyclable photocatalyst</b>	115
4.1. Introduction	117
4.2. Experimental section	118
4.2.1. Materials	118
4.2.1. Physicochemical characterization	118
4.2.2. Synthesis	119
4.2.2.1. Synthesis of 5, 10, 15, 20-Tetrakis (4-methoxycarbonylphenyl) porphyrin (TPPCOOMe)	119
4.2.2.2. Synthesis of 5, 10, 15, 20-Tetrakis (4-methoxycarbonylphenyl) Mg(II) porphyrin (Mg(II)TPPCOOMe)	119
4.2.2.3. Synthesis of [5, 10, 15, 20-Tetrakis (4-carboxyphenyl) porphyrin] (H <sub>4</sub> TCPP(H <sub>2</sub> ))	119
4.2.2.4. Synthesis of [5, 10, 15, 20-Tetrakis (4-carboxyphenyl) Mg(II) porphyrin] (H <sub>4</sub> TCPP(Mg))	120
4.2.2.5. Synthesis of PCN-224 and PCN-224(Mg)	121
4.2.3. Gas adsorption measurements	121
4.2.4. Catalytic cycloaddition reactions of CO <sub>2</sub> with epoxides	121
4.2.5. Theoretical section	122
4.3. Results and discussion	123
4.3.1. Synthesis and characterization	123
4.3.2. X-ray photoelectron spectroscopy (XPS) analysis	125
4.3.3. Gas adsorption study	126
4.3.4. Photocatalytic fixation of CO <sub>2</sub>	127
4.3.5. Photocatalytic fixation of CO <sub>2</sub> from direct air	132
4.3.6. Mechanistic investigation	132

4.3.7. Theoretical insight for the LMCT transition	134
4.3.8. Mechanistic investigation of photocatalytic CO <sub>2</sub> fixation	136
4.3.9. Catalyst recyclability and leaching test	138
4.4. Conclusion	139
4.5. References	140
<b>Chapter 5a. Highly efficient fixation of carbon dioxide at RT and atmospheric pressure conditions: Influence of polar functionality on selective capture and conversion of CO<sub>2</sub></b>	147
5a.1. Introduction	149
5a.2. Experimental section	150
5a.2.1. Materials	150
5a.2.2. Physicochemical characterization	150
5a.2.3. Synthesis	151
5a.2.3.1. Synthesis of MOF-SO <sub>3</sub> H	151
5a.2.3.2. Synthesis of MOF-SO <sub>3</sub> Ag	151
5a.2.3.3. Synthesis of Ag(I)@UiO-66	152
5a.2.4. Catalytic cycloaddition reactions of CO <sub>2</sub> with propargylic alcohols	152
5a.3. Results and discussion	153
5a.3.1. Synthesis and characterization	153
5a.3.2. Gas adsorption studies	155
5a.3.3. Catalytic carboxylation of propargylic alcohols with CO <sub>2</sub>	157
5a.3.4. The three-component reaction of CO <sub>2</sub> with propargylic alcohol and primary amines	158
5a.3.5. Recyclability test	161
5a.3.6. Plausible mechanism	161
5a.4. Conclusion	163
5a.5. References	164
<b>Chapter 5b. Noble metal-free Cu(I)-anchored NHC-based MOF for highly efficient fixation of CO<sub>2</sub> under RT and atmospheric pressure conditions</b>	171
5b.1. Introduction	173

5b.2. Experimental section	174
2a.2.1. Materials	174
5b.2.2. Physicochemical characterization	174
5b.2.3. Synthesis	175
5b.2.3.1. Synthesis of 1,3-bis(4-carboxyphenyl)imidazolium chloride (H <sub>2</sub> L <sup>+</sup> Cl <sup>-</sup> )	175
5b.2.3.2. Synthesis of NHC-MOF	176
5b.2.3.3. Synthesis of Cu(I)@NHC-MOF	176
5b.2.4. Catalytic cycloaddition reactions of CO <sub>2</sub> with propargylic alcohols	176
5b.3. Results and discussion	177
5b.3.1. Synthesis and characterization	177
5b.3.2. Gas adsorption studies	179
5b.3.3. Catalytic fixation of CO <sub>2</sub> with propargylic alcohols	180
5b.3.4. Recyclability and catalyst leaching test	182
5b.3.5. Proposed mechanism	184
5b.4. Conclusion	185
5b.5. References	186
<b>Chapter 6. Rational design of 2D Co(II)-porphyrin framework for efficient visible light-promoted reduction of CO<sub>2</sub> from dilute gas: Combined experimental and theoretical investigation</b>	193
6.2. Experimental section	196
6.2.1. Materials	196
6.2.2. Physicochemical characterization	196
6.2.3. Synthesis	196
6.2.3.1. Synthesis of 5, 10, 15, 20-tetrakis (4-bromophenyl) porphyrin (TBPP(H <sub>2</sub> ))	196
6.2.3.2. Synthesis of 5, 10, 15, 20-tetrakis (4-bromophenyl) Zn/Co(II) porphyrin (TBPP(Zn/Co))	197
6.2.3.3. Synthesis of POF(Zn/Co)	198
6.1. Introduction	195

6.2.4. Gas adsorption measurements	198
6.2.5. Photocatalytic CO <sub>2</sub> reduction studies	198
6.2.6. Theoretical investigation	199
6.3. Results and discussion	200
6.3.1. Synthesis and characterization	200
6.3.1. X-ray photoelectron spectroscopy (XPS) analysis	200
6.3.2. Gas adsorption studies	201
6.3.3. Photocatalytic CO <sub>2</sub> reduction	201
6.3.4. Mechanistic investigation	205
6.4. Conclusion	208
6.5. References	208
7. Annexure	213

## Notations and abbreviations

1D = 1-Dimensional

2D = 2-Dimensional

3D = 3-Dimensional

$\lambda$  = Wavelength

Å = Angstrom

a. u. = Arbitrary unit

BDC = Benzene-1,4-dicarboxylic acid

BE = Binding energy

BET = Brunauer Emmett Teller

4,4'-bipy = 4,4'-Bipyridine

°C = Degree Celsius

Calc. wt % = Calculated weight percentage

CCDC = Cambridge Crystallographic Database Center

CCS = CO<sub>2</sub> capture and storage

CCU = CO<sub>2</sub> capture and utilization

CO<sub>2</sub> = Carbon dioxide

COFs = Covalent organic frameworks

DMA = N,N'-Dimethylacetamide

DMF = N,N'-Dimethylformamide

ECH = Epichlorohydrin

eV = Electron volt

EDS = Energy dispersive X-ray spectroscopy

FE-SEM = Field emission scanning electron microscopy

FTIR = Fourier transform infra-red spectroscopy

gL<sup>-1</sup> = Gram per litre

h $\nu$  = Photon energy

<sup>1</sup>H NMR = Proton nuclear magnetic resonance

HKUST = Hong Kong University of Science and Technology

H<sub>2</sub>hfipbba = 4,4'-(Hexafluoroisopropylene)bis-(benzoic acid)

H<sub>3</sub>TATAB = 4,4',4''-s-Triazine-1,3,5- triyl-tri-p-aminobenzoic acid

HOMO = Highest occupied molecular orbital  
IRMOF = Isoreticular metal-organic framework  
IUPAC = International Union of Pure and Applied Chemistry  
K = Kelvin  
LUMO = Lowest unoccupied molecular orbital  
MA = Melamine  
MeOH = Methanol  
mg = milligram  
mmol = millimole  
mL = millilitre  
MPa = Megapascal  
mTorr = millitorr  
MIL = Material Institut Lavoisier  
MOFs = Metal-organic frameworks  
PCN = Porous coordination network  
PO = Propylene oxide  
P/P<sub>o</sub> = Relative pressure  
PXRD = Powder X-ray diffraction  
Q<sub>st</sub> = Isosteric heat of adsorption  
RT = Room temperature  
SO = Styrene oxide  
STP = Standard temperature and pressure  
TBAB = Tetra-n-butylammonium bromide  
TGA = Thermogravimetric analysis  
TON = Turn over number  
μL = Microlitre  
UiO = University of Oslo  
UV-vis = Ultra-violet visible spectroscopy  
v/v = Volume by volume  
wt% = Weight percentage  
XRD = X-Ray Diffraction

# Chapter 1

## Introduction



### 1.1. Carbon dioxide (CO<sub>2</sub>) a greenhouse gas

The current energy demand for human activities is encountered by the combustion of petroleum, natural gas, and coal which are releasing large amounts of Greenhouse gases like Carbon dioxide (CO<sub>2</sub>), Nitrous oxide, Fluorinated gases, etc<sup>1</sup> (Figure 1a). As a result, CO<sub>2</sub> concentration in the atmosphere is increasing with time, from 280 ppm in the early 1800s to 420 ppm, currently and it continues to increase.<sup>2,3</sup> Figure 2b represents global greenhouse gas emissions by economic sector. The maximum amount of CO<sub>2</sub> is released from electricity and heat production followed by agriculture process, industrial process, transport process, and other energy-related processes.<sup>4</sup> This rapid growth of CO<sub>2</sub> concentration in the atmosphere has resulted in various undesirable environmental issues like climate change, ocean acidification, global warming, and so on.<sup>5</sup> Thus, finding the best solution that can meet energy demands with the decrease of environmental issues is urgently needed. In this direction, sequestration of carbon dioxide from fossil-fuel-based power plants which are major contributors (~45%) to total CO<sub>2</sub> emissions is of utmost importance.<sup>6-10</sup> However, the present tracked CCS technology requires high energy for the processes of separation, purification, compression, transportation, and storage.<sup>11-13</sup> Therefore, carbon capture and utilization (CCU) as C1 feedstock is a value-added alternative to CCS.<sup>14-17</sup>

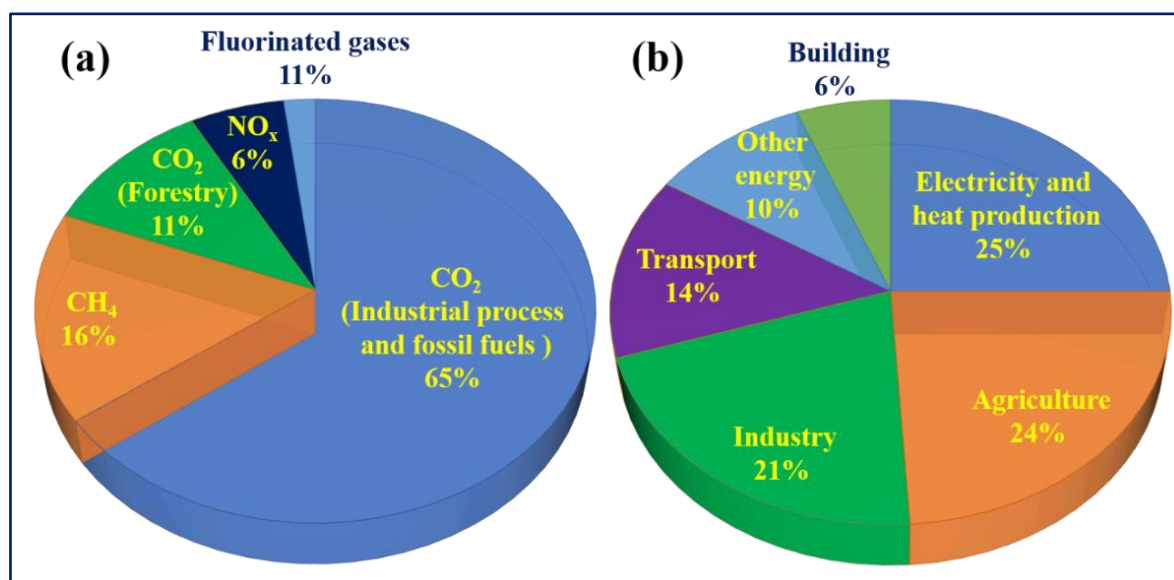


**Figure 1.** (a) Global greenhouse gases emission from various processes, and (b) global greenhouse gas emission by economic sector.

## 1.2. Carbon capture and utilization (CCU)

The utilization of carbon dioxide as C1-feedstock offers the dual advantages of mitigating the atmospheric CO<sub>2</sub> content and production of valuable chemicals (Figure 2).<sup>18-20</sup> However, the inertness of carbon dioxide offers a significant challenge to its functionalization at ambient conditions.<sup>21,22</sup> Especially, selective carbon dioxide capture and utilization from direct air has attracted tremendous attention as this process enables carbon capture from any place independent of emission sources. In this context, extensive research efforts are being carried out by researchers worldwide for the development of high-performance catalytic systems for effective CCU from direct air to prepare valuable chemicals and fuels. To achieve this, the catalyst employed should exhibit high CO<sub>2</sub> affinity and superior catalytic activity to capture carbon dioxide at a very low concentration of 0.03% in air. Besides, the catalyst should be highly stable towards moisture and other contaminants in the air. The literature study revealed that the number of examples of recyclable catalysts known for CCU from direct air is sparse. Considering the unique advantages of MOF-based materials, their high carbon dioxide capture property has been exploited to rationally develop an effective recyclable catalyst for the simultaneous capture and functionalization of CO<sub>2</sub> from air into value-added chemicals at mild conditions.

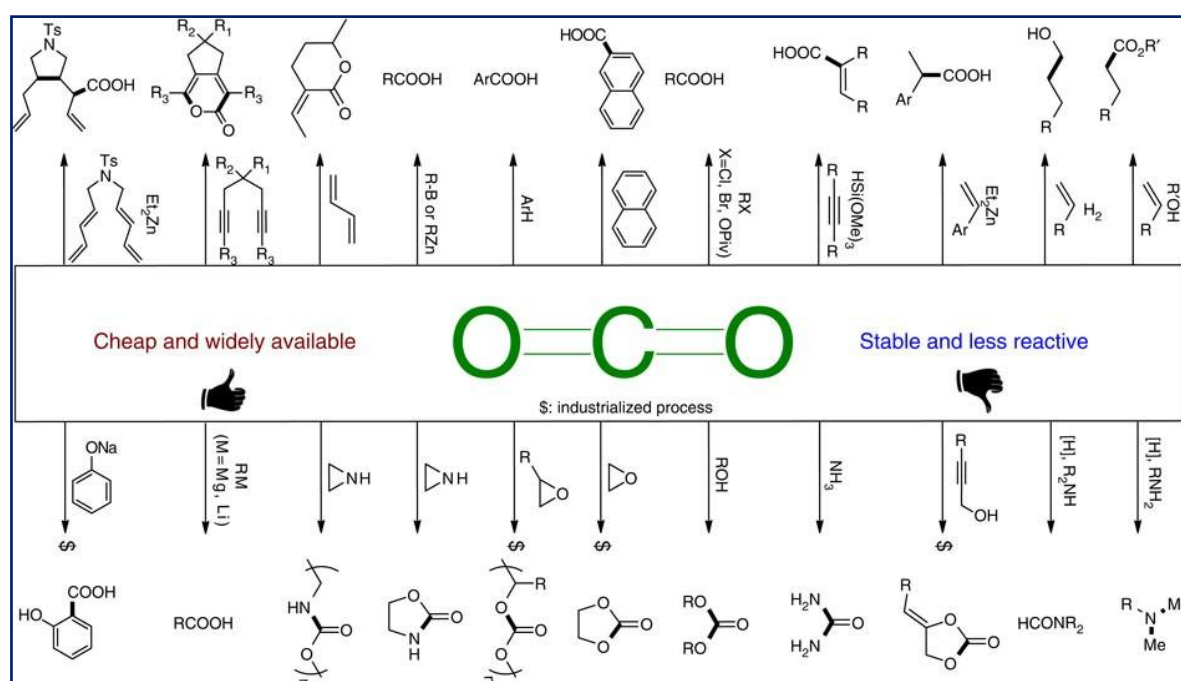


**Figure 2.** Representative examples of CO<sub>2</sub> utilization processes as C1-feedstock. Reproduced with permission from reference 18.

### 1.3. Framework-based materials

#### 1.3.1. Metal-organic frameworks (MOFs)

The past two decades have witnessed an explosive growth of a new class of inorganic-organic hybrid porous materials known as metal-organic frameworks (MOFs) or porous coordination polymers (PCPs). Having the merits of both inorganic and organic building blocks, MOFs or PCPs exhibit unique properties like high surface area, tunable pore size, and functionality, which makes them ideal candidate materials for various applications such as selective gas storage, separation, catalysis, sensing, drug delivery and so on.<sup>23</sup> MOFs are constructed by connecting metal ions (nodes) or clusters (SBUs) with multidentate organic spacers (linkers or struts) to obtain frameworks with diverse structural architectures. The network topology and functionality can be tuned by a judicious choice of organic linkers to obtain MOFs/coordination polymers with infinite 1D, 2D, or 3D network structures (Figure 3).<sup>24</sup> According to the International Union of Pure and Applied Chemistry (IUPAC) nomenclature, MOFs are defined as “*Coordination compounds continuously extending in one-, two- or three- dimensions through coordination bonds with an open framework containing potential voids*”.

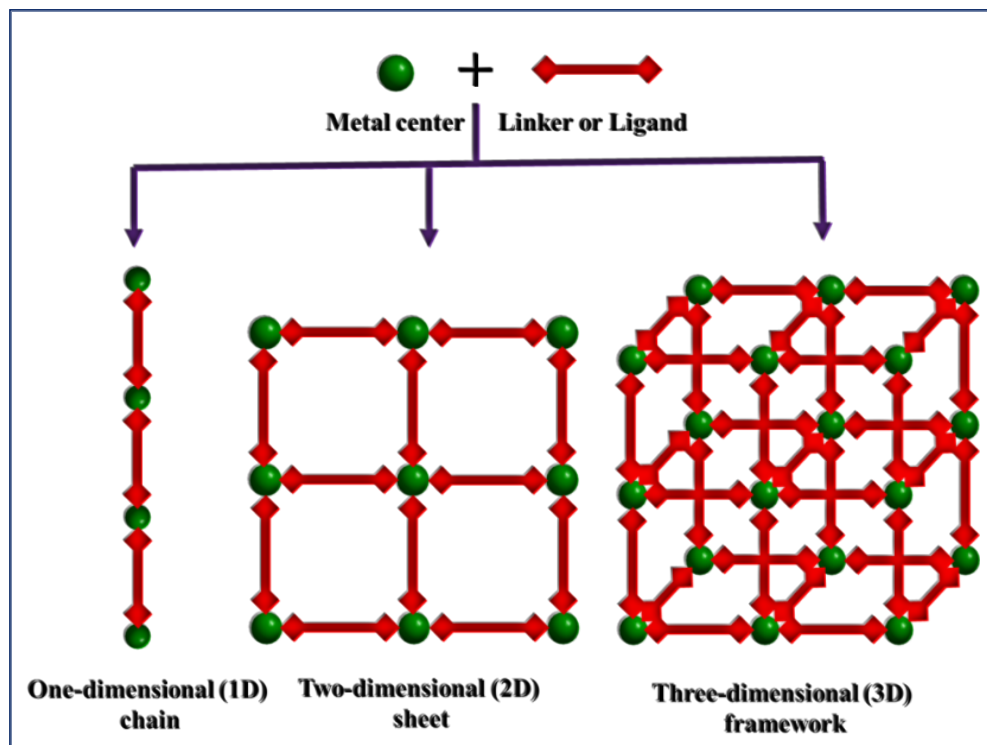


**Figure 3.** Schematic representation of the construction of 1D-chain, 2D-sheet, and 3D-frameworks by utilizing metal nodes and organic linkers/ligands as building blocks.

### 1.3.1.1. Historical aspects of MOFs

In 1704, a Berlin color-maker named Diesbach accidentally created the first synthetic blue pigment, Prussian Blue<sup>25</sup> which was identified 273 years later as the first coordination polymer. The crystal structure of Prussian Blue remained unknown until 1977.<sup>26</sup> Further, in 1959, Saito co-worker reported the structure of bis(alkylnitrilo)copper(I) composed of tetrahedral  $\text{Cu}(\text{CN})_4$  units (Figure 4).<sup>27-29</sup> At the end of 60s, Powell and Rayner determined the structure of Hofmann clathrate,  $\{[\text{Ni}(\text{NH}_3)_2(\text{Ni}(\text{CN})_4)] \cdot 2\text{C}_6\text{H}_6\}$  and its structural description was reported a few years later by Ywamoto and coworkers (Figure 4). The interest in coordination polymers took off at the end of 70's when Prof. A. F. Wells published a revolutionary paper in the journal *monographs in crystallography*<sup>30</sup> in 1977 which introduced the concept that inorganic crystal structures can be seen as networks by reducing them to well-defined nodes and connections. With this understanding, a hallmark discovery was made by Robson and coworkers in 1989 in which the first example of a Cu(I) coordination network was discovered while analyzing the X-ray crystal structure of  $[\text{Cu}(\text{C}(\text{C}_6\text{H}_4\text{-CN})_4)]\text{BF}_4 \cdot x\text{C}_6\text{H}_5\text{NO}_2$  ( $x \geq 7.7$ ).<sup>31</sup> Here, they reported the X-ray single crystal structures of  $\text{Zn}(\text{CN})_2$  and  $\text{Cd}(\text{CN})_2$  as diamond-based frameworks with M-CN-M rods connecting the tetrahedral metal centers.<sup>32</sup>

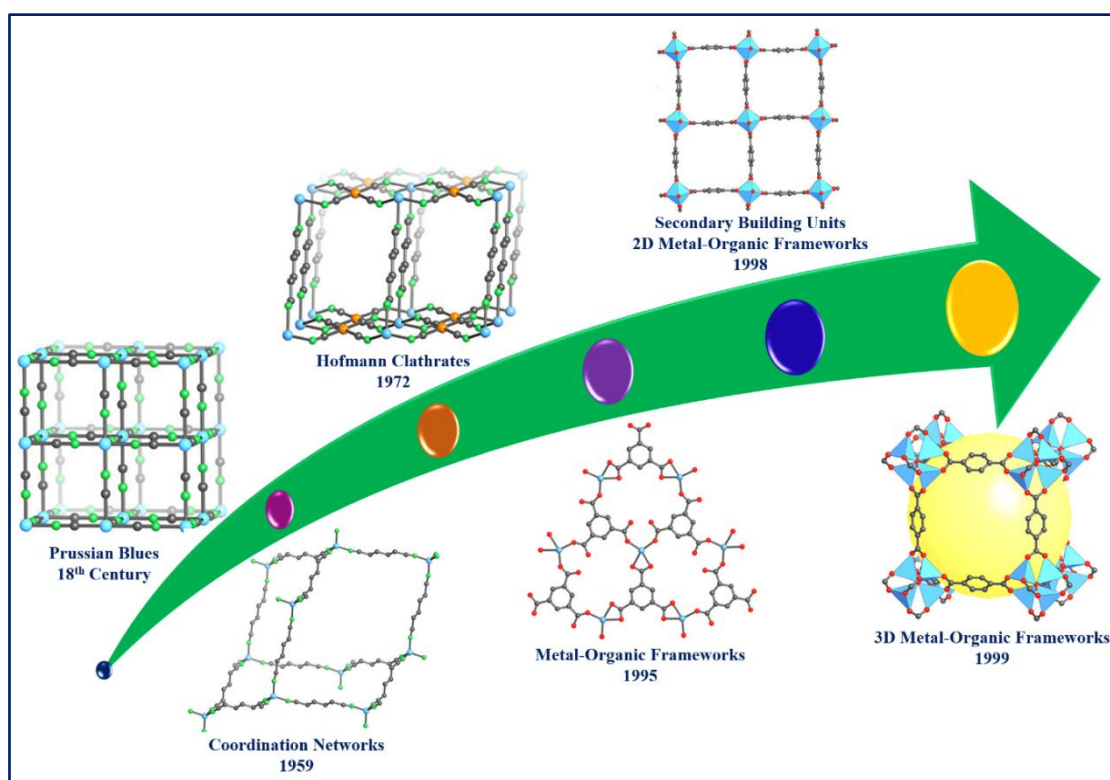


**Figure 4.** Advancement in the field of coordination chemistry of extended structures.

Furthermore, the use of pyridine-based bifunctional linkers was reported in 1994 by Fujita and co-workers (Figure 4).<sup>33</sup> Interestingly, the term “MOF” was not coined until 1995 when Yaghi and co-workers described the structure of  $[\text{Co}(\text{C}_6\text{H}_3)(\text{CO}_2\text{H}_{1/3})_3 \cdot (\text{NC}_5\text{H}_5)_2]$  as the metal-organic framework.<sup>34</sup> The first three-dimensional (3D), Zn(II)-organic framework commonly known as MOF-5,  $[\text{Zn}_4\text{O}(\text{BDC})_3]$  was reported by the group of Yaghi shortly after they discovered a 2D MOF structure.<sup>35</sup> The MOF-5, constructed from octahedral  $\text{Zn}_4\text{O}(\text{COO})_6$  SBUs and BDC linkers exhibited the highest reported surface area for any structure known at that time. The enormous popularity of this structure inspired researchers towards the rapid development of MOF chemistry.<sup>36,37</sup> Followed by the report of IRMOFs by Yaghi and coworkers, several other important MOFs have been developed by various research groups worldwide. For example, the synthesis of  $[\text{Cu}_3(\text{TMA})_2 \cdot (\text{H}_2\text{O})_3]$  (HKUST: Hong Kong University of Science and Technology), was reported by Williams and co-workers in 1999.<sup>38</sup> On the other hand, Ferey and co-workers reported the synthesis of MIL-101 (Material Institute Lavoisier-101) in 2005<sup>39</sup> by changing the SBU from  $\text{Zn}_4\text{O}$  (in MOF5) to  $\text{Cr}_3\text{O}$  and obtained a framework with a completely different pore structure and topology compared to MOF-5.<sup>11</sup> Further, in 2008, Lillerud and co-worker, reported the synthesis of a yet another MOF, UiO-66 (University of Oslo-66)<sup>40</sup> constituted by a more complicated SBU based on octahedral Zr-centers,  $(\text{Zr}_6\text{O}_4(\text{OH})_{10}(\text{H}_2\text{O})_6(\text{COO})_6)$  and BDC. In 2013, Zhou and co-worker synthesized a series of porphyrin-based MOF named PCN-222 (porous coordination network) which are highly rigid and photoactive.<sup>41</sup> This process of modulation of pores with polar functionalities is beneficial to introduce selective gas adsorption and catalytic properties to the frameworks.<sup>42</sup>

### 1.3.2. Porous organic frameworks (POFs)

Porous organic frameworks (POFs) are a new class of organic polymers having permanent porosity and high crystallinity with highly ordered structures. Similar to the MOFs, POFs are structurally pre-designable, synthetically controllable, and functionally manageable.<sup>43</sup> Further, POFs possess tunable chemical and physical properties, which provided a suitable platform for various applications, such as gas storage, separation, photoelectricity, and catalysis especially  $\text{CO}_2$  capture and conversion.<sup>44</sup> An efficient COFs/POFs for  $\text{CO}_2$  capture and conversion at milder conditions should possess a high density of  $\text{CO}_2$ -philic basic sites such as azo ( $\text{N}=\text{N}$ ), azine ( $\text{C}-\text{N}-\text{N}-\text{C}$ ), imine ( $\text{C}=\text{N}$ ), and triazine linkers along with Lewis acidic catalytic sites.<sup>45,46</sup> Thus, the novel structural properties of

framework-based materials provided a suitable platform for potential application in various fields.

#### 1.4. Applications of MOFs

The unique properties of high surface areas, tunable pore size, functionality, and high rigidity of MOF-based materials offer diverse applications in the area of heterogeneous catalysis, gas storage/separation, drug delivery, CCU, and so on (Figure 5).<sup>47-49</sup> These novel properties of MOF-based materials motivated us, to develop effective framework materials for the simultaneous capture and functionalization of CO<sub>2</sub> into value-added chemicals at mild conditions.

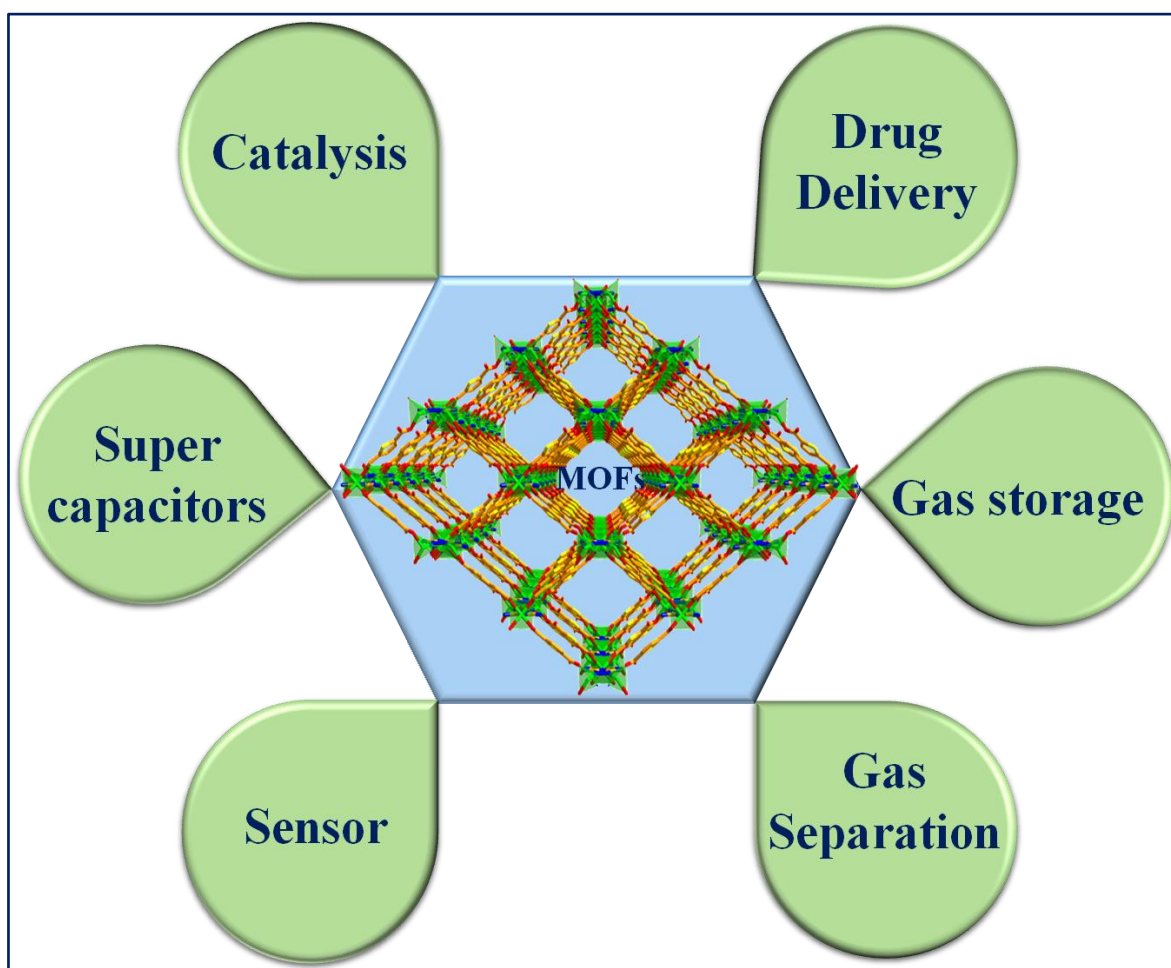


**Figure 5.** Schematic representation showing various applications of metal-organic frameworks.

## 1.5. MOFs for CO<sub>2</sub> capture and utilization (CCU)

### 1.5.1. MOFs for CO<sub>2</sub> capture

The current state-of-art technique applied for CO<sub>2</sub> capture from flue gas (composition: N<sub>2</sub> : 76-77%, CO<sub>2</sub> : 12.5-12.8%, H<sub>2</sub>O: 6.2%, O<sub>2</sub> : 4.4%, SO<sub>2</sub> : 420 ppm, NO<sub>x</sub> : 60-70 ppm, CO : 50 ppm)<sup>50</sup> is mainly by using liquid amines as adsorbent where the aqueous solutions of monoethanolamine (MEA), methyldiethanolamine (MDEA) and diethanolamine (DEA) are used for the capture of CO<sub>2</sub> on large scale. It was estimated in the IPCC report 2014-2015 that the global average surface temperature change for the end of 21<sup>st</sup> century (2081-2100) relative to 1986-2005 will likely to increase from 2.6 to 4.8 °C.<sup>51</sup>

The literature study revealed that MOFs offer potential scope for CO<sub>2</sub> capture and storage (CCS) applications owing to their tunable pore size, generation of unsaturated metal centers, and incorporation of Lewis basic sites *via* functionalization of the ligand.<sup>52</sup> Some of the representative examples of MOFs reported for high wt% storage of CO<sub>2</sub> at 298 K temperature and 1 bar pressure along with the Q<sub>st</sub> values are listed in Table 3. It has been shown that, incorporation of ethylenediamine (en) into the H<sub>3</sub>[Cu<sub>4</sub>(Cl)<sub>3</sub>(BTTri)<sub>8</sub>] (where H<sub>3</sub>BTTri = 1,3,5-tri(1H-1,2,3-triazol-4-yl)benzene) MOF has resulted CO<sub>2</sub> uptake of 3.24 mmol/g (14.3 wt%) at 1 bar and 298K with high Q<sub>st</sub> value of 90 kJ/mol which has been attributed to the stronger interaction of CO<sub>2</sub> with the basic amine groups present in the framework. Further, the incorporation of N, N'-dimethylenediamine (mmem) into the same framework has resulted in CO<sub>2</sub> uptake capacity of 2.38 mmol/g (9.5 wt%) with high isosteric heat of adsorption value of 96 kJ/mol. Here the adsorption of CO<sub>2</sub> with the framework has been attributed to a chemisorptive-type process. Whereas, Cu<sub>3</sub>(BTC)<sub>2</sub>(H<sub>2</sub>O)<sub>1.5</sub> (HKUST-1) MOF shows Q<sub>st</sub> value of 30 kJ/mol and CO<sub>2</sub> adsorption capacity of 27 wt%<sup>53</sup> Further, MOF-74 (M = Co, Ni, Fe, Zn, Mn, and Mg) containing open metal centers (OMCs) are reported to show high CO<sub>2</sub> storage capacity (27 wt%) with Q<sub>st</sub> value of 47 kJ/mol in case of Mg-MOF-74 at ambient temperature and pressure conditions.<sup>54</sup> Recently, Vaidhyanathan and co-worker designed an ultra-microporous MOF, Ni-4PyC, [Ni<sub>9</sub>(m-H<sub>2</sub>O)<sub>4</sub>(H<sub>2</sub>O)<sub>2</sub>(C<sub>6</sub>NH<sub>4</sub>O<sub>2</sub>)<sub>18</sub>.solvent] (where 4PyC = pyridine-4-carboxylic acid) which shows high CO<sub>2</sub> storage capacity of 8.2 mmol/g (36 wt%) at 10 bar and 298 K with estimated Q<sub>st</sub> value of 32.8 kJ/mol.<sup>55</sup> Further, Maji and co-workers reported ultra-small HKUST-1 MOF nanoparticles on a 2D aminoclay template (CuBTC@AC-2) which has shown a CO<sub>2</sub> uptake capacity of 5.35 mmol/g (23.5 wt%) at 1 bar and 298 K which is 46% higher than that of pristine MOF.<sup>56</sup> Thus, the

development of MOFs as efficient absorbent materials for high wt% storage of CO<sub>2</sub> at ambient pressure and temperature conditions is being investigated worldwide (Table 1).

**Table 1.** Representative examples of MOFs with their CO<sub>2</sub> uptake capacities and Q<sub>st</sub> values.

Sl. No.	MOF	Functionality type	wt% *	-Q <sub>st</sub> (kJ/mol)	References
01.	H <sub>3</sub> [(Cu <sub>4</sub> Cl) <sub>3</sub> (BTTri) <sub>8</sub> (en) <sub>3.75</sub> ]	Amines	14.3	90	57
02.	H <sub>3</sub> [(Cu <sub>4</sub> Cl) <sub>3</sub> (BTTri) <sub>8</sub> (mmen) <sub>12</sub> ]	Amines	9.5 <sup>a</sup>	96	58
03.	MIL-101(Cr)	UMC	4.2	44	59
04.	NH <sub>2</sub> -BDC-MIL-53 (Al)	Amines	12	38.4	60
05.	Mg-MOF-74	Amines	27.5	47	61
06.	Bio-MOF-11	Amines	15.2	45	62
07.	Ni-MOF-74	UMC	23.9	42	63
08.	HKUST-1	UMC	18.4	35	64
09.	MIL-53 (Al)	-	10.6	35	65
10.	HKUST-1	-	27	30	66
11.	IRMOF-3	Amines	5.1	19	67
12.	MOF-5	-	15.2	17	68

\*isotherms reported at temperature 298 K and 1 bar pressure, <sup>a</sup>isotherm reported at 0.15 bar CO<sub>2</sub>/ 0.75 bar N<sub>2</sub> mixture and 298 K temperature.

### 1.5.2. MOF materials for CO<sub>2</sub> utilization

The presence of both inorganic and organic building blocks along with the possibility to tune the pore size and functionality makes MOFs suitable candidate materials for CCU under mild conditions. The various strategies employed for the utilization of MOFs as recyclable catalysts for CCU (Figure 6) are discussed below.

**1.5.2.1. Opportunistic catalysis with metal nodes:** The unsaturated reactive metal nodes generated by the removal of coordinated solvent molecules by activation (Figure 6) act as Lewis acidic catalytic sites for CO<sub>2</sub> transformations. For example, Lewis acidic metal sites polarize the epoxides during the cycloaddition of CO<sub>2</sub> to generate cyclic carbonates.<sup>69</sup>

**1.5.2.2. Designed catalysis with functionalized linkers:** The presence of functionalized organic linkers with various functional groups such as azo  $-(N=N-)$ , azine  $(-C=N-)$ , and amine  $(-NH_2)$  are known to act as  $CO_2$ -philic sites (Figure 7). These sites increase  $CO_2$  density around the active sites and thus enhance the catalytic activity of the framework for effective CCU.

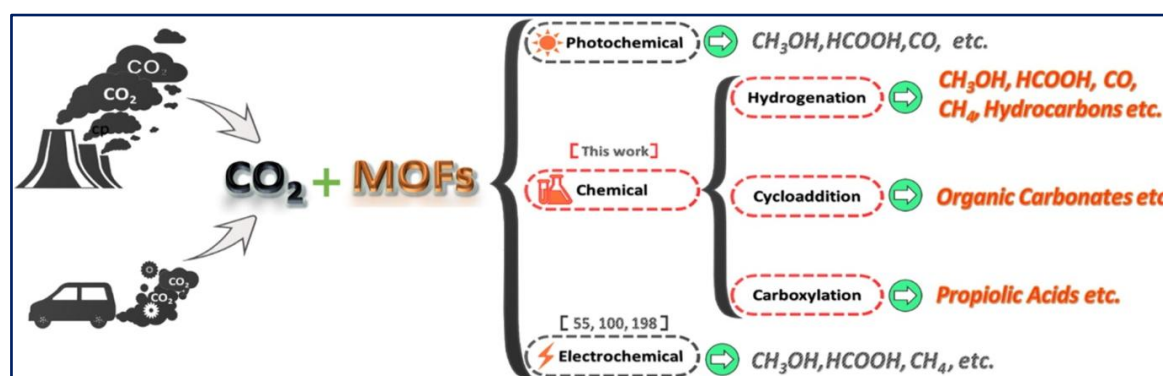


**Figure 6.** The main source of  $CO_2$  and the transformation paths over the MOF catalysts. Reproduced with permission from reference number 70.

### 1.5.2.3. Incorporation of the catalytic active site by PSM

The post-synthetic modification (PSM) approach was first conceptualized in an extended network where pores are modified by Hoskins and Robson in 1990.<sup>47</sup> Later, in 1999 and 2000, Lee,<sup>71</sup> Kim,<sup>72</sup> and Williams<sup>55</sup> utilized this approach for modifying the pores in porous materials. The term PSM was coined by Wang and Cohen in 2007.<sup>73</sup> In literature, the PSM approach was also employed for other porous organic networks,<sup>74</sup> coordination oligomers,<sup>75</sup> and mesoporous silica.<sup>76</sup> The PSM approach in Frameworks can be carried out by non-covalent modification, by covalent bond modification, by doping, or by coordinative interactions (Figure 7).<sup>77</sup> The covalent transformation of the organic linker was the most common type of PSM in MOFs. The first example where a ligand having amine was converted into amide in IRMOF-3 by Cohen and Wang in 2007.<sup>9</sup> Followed by this report, many literature examples on PSM of frameworks for the utilization of  $CO_2$  and catalysis have been reported.<sup>78</sup> The PSM phenomena provided a new direction to stabilize catalytically active sites in the functionalized pore of the framework to generate a hybrid material for the fixation of  $CO_2$ .

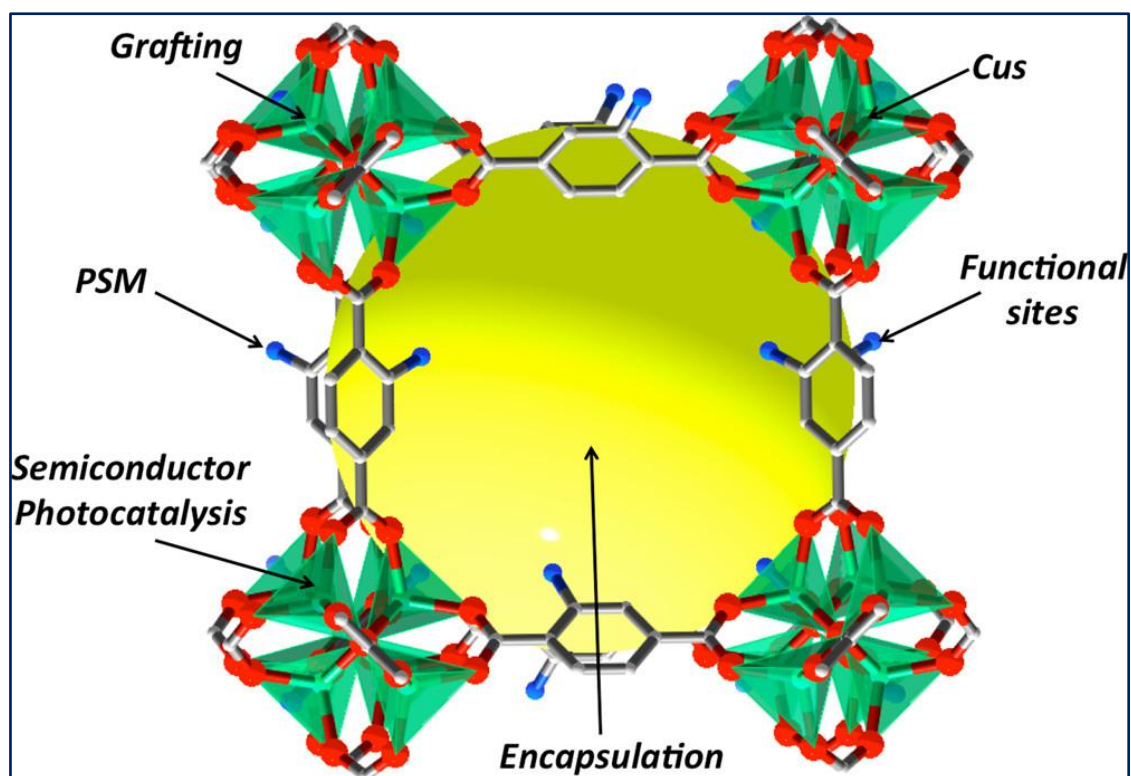


**Figure 7.** Different strategies for the inclusion of catalytic moieties into a MOF scaffold. Reproduced with permission from reference number 79.

### 1.5.3. Various ways of CO<sub>2</sub> fixation via C-X (X = O, N, and C) bond formation

The modular nature of framework-based materials facilitates rational design by incorporating a high density of CO<sub>2</sub>-philic and catalytic functionalities for simultaneous capture and catalytic conversion of carbon dioxide to fine chemicals. Thus, rationally designed framework-based catalysts for CCU offers the dual advantages of mitigating the increasing atmospheric CO<sub>2</sub> concentration and production of valuable chemicals. Further, a large number of value-added chemicals and fuels have been produced by the fixation of CO<sub>2</sub> via C-X (X = O, N, and C) bond formation between CO<sub>2</sub> and substrate molecules (Figure 8). Thus intensive research efforts have been made on the rational design of frameworks for the chemical fixation of CO<sub>2</sub> into value-added chemicals or fuels as summarized below.

#### 1.5.3.1. CO<sub>2</sub> fixation via C-O bond formation

The CO<sub>2</sub> fixation with epoxides via C-O bond formation has been employed to generate various cyclic carbonates and polycarbonates.<sup>80</sup> Especially, the cycloaddition of CO<sub>2</sub> with epoxides has been studied extensively due to its atom efficiency yielding carbonates with 100% selectivity.<sup>81,82</sup> Further, cyclic carbonates offer widespread

applications in a variety of fields, i. e. as precursors for polymeric materials, electrolytes in lithium-ion batteries, pharmaceuticals, intermediates for the synthesis of ethylene glycol, beta-keto carboxylic acids, and so on.<sup>83,84</sup>

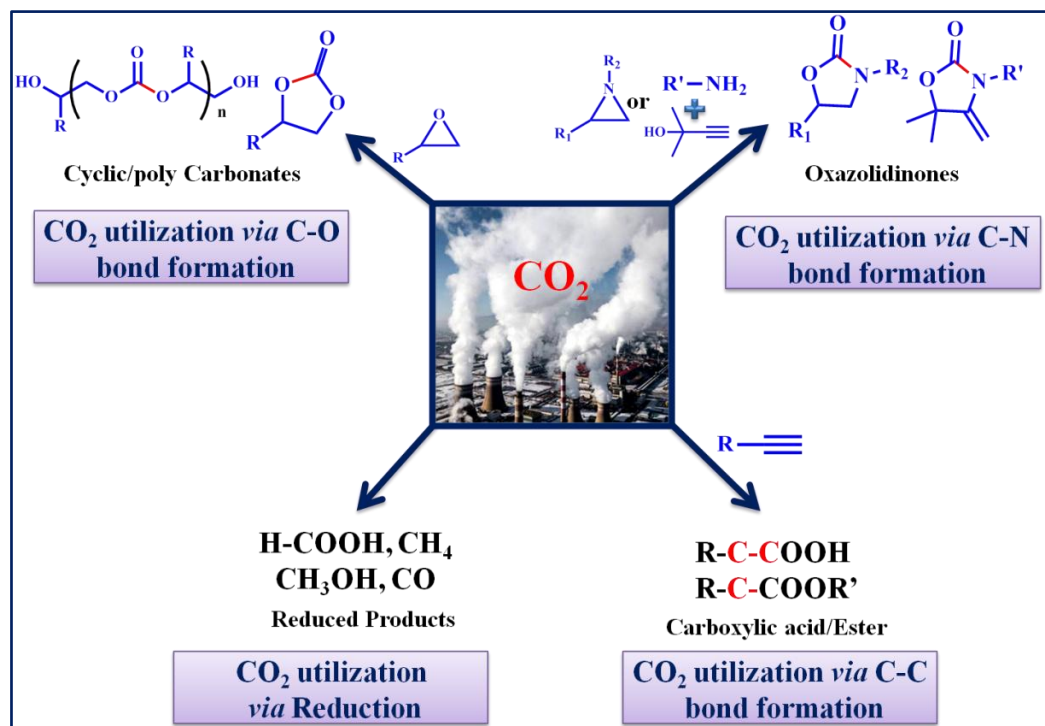
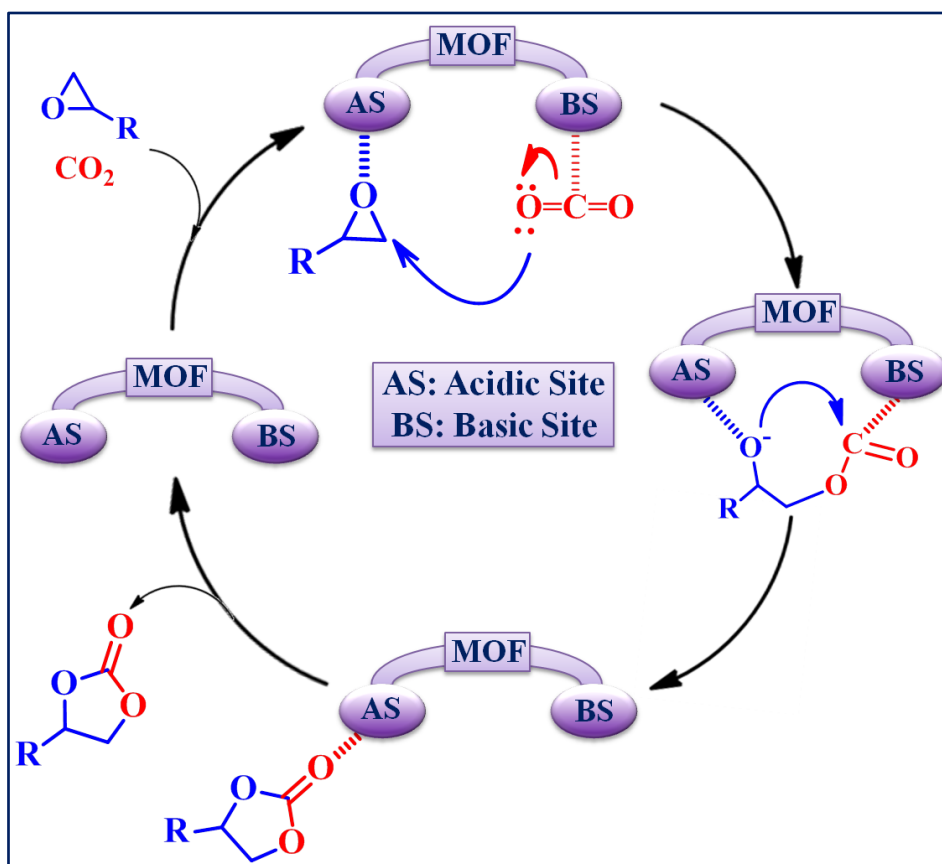


**Figure 8.** Schematic representation of CO<sub>2</sub> fixation *via* C-X bond formation.

To date, various homogeneous catalysts including, transition metal complexes,<sup>85</sup> organocatalysts,<sup>86</sup> and quaternary ammonium salts,<sup>87</sup> and imidazolium-based ionic liquids<sup>88</sup> have been employed for the catalytic transformation of CO<sub>2</sub> to cyclic carbonates. However, to achieve facile separation of the products and recycling of catalysts, heterogeneous catalysts like metal oxides, zeolites, carbon-based materials, functional polymers, covalent-organic frameworks (COFs), metal-organic frameworks (MOFs), etc have been employed for the functionalization of CO<sub>2</sub> with epoxides.<sup>89,90</sup> Among these, MOFs offer unique advantageous due to their well-defined pore channels, facilitating diffusion of the reactants and products along with tunable pore size and functionality. However, most of the MOFs reported so far require high temperature and pressure conditions for the cycloaddition reaction. But, Green and sustainable chemistry practices require the catalysis to be done under environmentally friendly mild conditions of room temperature and atmospheric pressure. In this regard, the rational design of the MOFs by incorporating a high density of CO<sub>2</sub>-philic as well as catalytic

sites for the utilization of CO<sub>2</sub> under RT and atmospheric pressure conditions offers potential benefits.

The general mechanism for CO<sub>2</sub> cycloaddition reaction via C-O bond formation is shown in Scheme 1. It involves a binary catalytic system composed of a Lewis acid catalytic site and a nucleophilic co-catalyst (TBAB) for the ring-opening of epoxide. The first step involves polarization of the epoxide at the Lewis acidic site which is followed by nucleophilic attack of Br<sup>-</sup> anion of TBAB leading to ring opening of the epoxide and formation of metal-coordinated bromo-alkoxide. Subsequent insertion of CO<sub>2</sub> to metal alkoxide generates metal carbonate species which undergoes an intramolecular ring-closure reaction to form the cyclic carbonate and its elimination from the metal center leads to regeneration of the active catalyst. Overall, for the high-yield generation of cyclic carbonates by coupling CO<sub>2</sub> with epoxides, a bifunctional catalyst composed of Lewis acidic and nucleophilic sites is essential. In Table 2, various MOFs reported for the cycloaddition of CO<sub>2</sub> to cyclic carbonates are summarized.



**Scheme 1.** A plausible mechanism for CO<sub>2</sub> fixation to cyclic carbonates via C-O bond formation.

**Table 2.** Representative examples of MOFs reported for cycloaddition of CO<sub>2</sub> with epichlorohydrin.

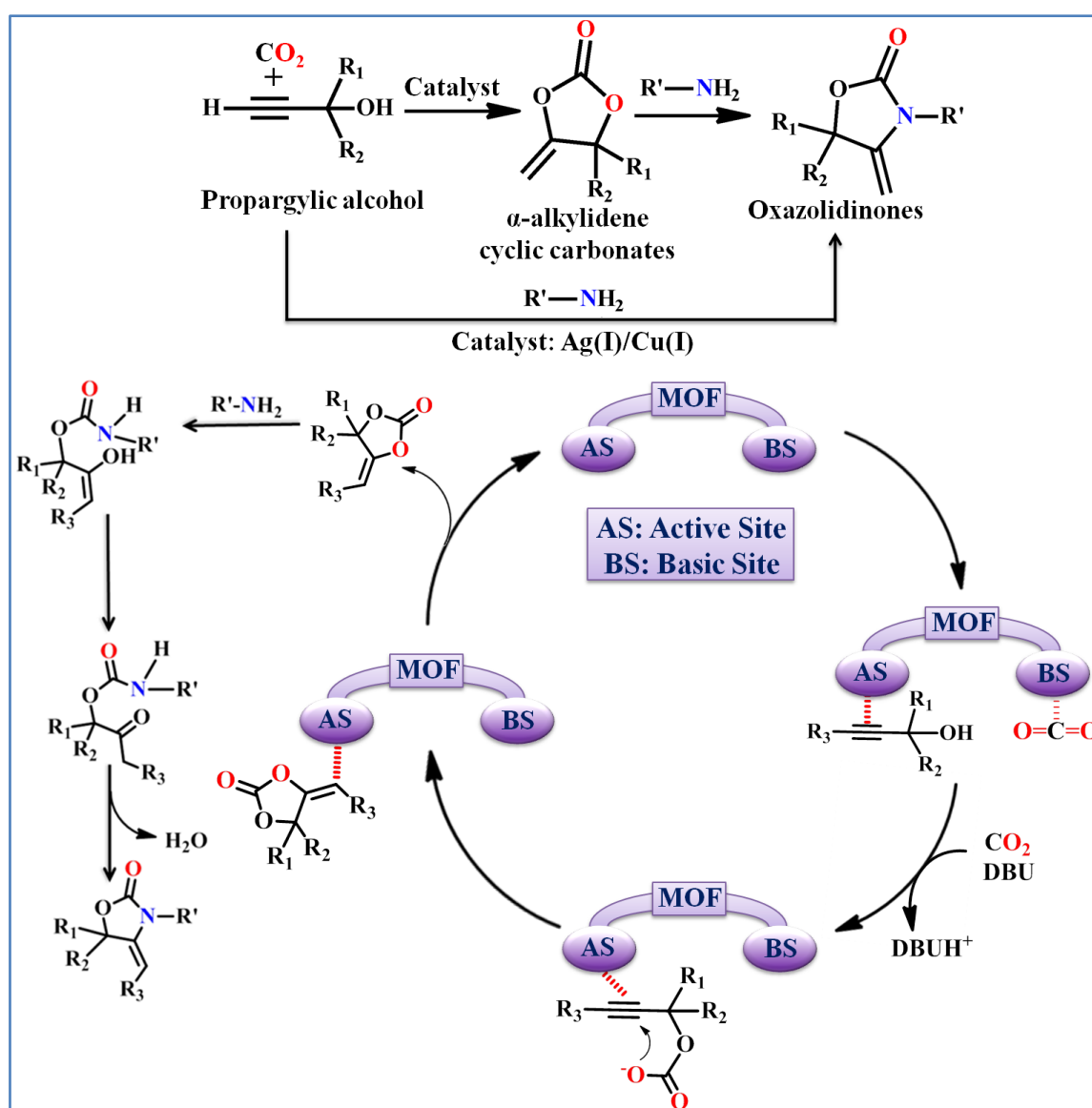
Sl. No.	Catalyst	Co-catalyst	Temperature (°C)	Pressure (bar)	Yield (%)	Reference
01	MOF-5	TBAB	50	60	93	91
02	ZIF-8	-	80	7	73	92
03	HKUST	-	100	7	33	93
04	MOF-53	DMAP	100	16	80	94
05	UiO-66	TBAB	60	12	67	95
06	Cu-MOF	TBAB	100	10	95.2	96
07	MOF-Zn-1	TBAB	100	10	97	97
08	UMCM-1-NH <sub>2</sub>	TBAB	RT	12	78	98
09	Meim-UiO-66	-	120	1	93	99
10	UiO-67-IL	-	90	1	95	100
11	F-ZIF-90	-	120	11.7	94	101
12	Zn-TATAB	-	100	1	95	102
13	IL@MIL-101-SO <sub>3</sub> Na		90	1	88	103
14	Co-MOF1	-	80	1	93	104
15	Zn-DAT	TBAB	RT	08	99	105
16	Hb-MOF	TBAB	RT	1	99	106
17	Mg-MOF	-	60	1	99	107
18	PCN-224(Mg)	-	RT	1	99	108

### 1.5.3.2. CO<sub>2</sub> fixation via C-N bond formation

The CO<sub>2</sub> fixation via C-N bond formation offers the dual advantages of mitigating the CO<sub>2</sub> concentration and production of valuable chemicals such as oxazolidinones.<sup>109</sup> Inspired by natural enzymatic reactions, various research groups designed amine-functionalized MOFs for CO<sub>2</sub> fixation to carbamic acid via C-N bond formation under co-catalysts-free conditions.<sup>88,110</sup> Further, the carbamic acid can be transformed into ammonium carbamate under humid conditions.<sup>111</sup> Besides, cycloaddition reactions of aziridines/propargylic amines with CO<sub>2</sub> are well-studied CO<sub>2</sub> utilization processes via C-N bond formation.<sup>112,113</sup> On the other hand, generation of oxazolidinones, valuable commodity chemicals for the synthesis of

antibiotics via a cascade reaction of CO<sub>2</sub> with propargylic alcohol and primary amines, represents a green and sustainable approach for the conversion of greenhouse gas into bio-relevant products.<sup>114</sup> The literature study revealed that Ag(I), AgNPs, and Cu(I) ions are active catalysts for this conversion.<sup>115-117</sup> Thus, the incorporation of these active metal sites in porous frameworks by post-synthetic modification (PSM) renders effective catalytic systems for fixation of CO<sub>2</sub> via C-N bond formation.<sup>118</sup>

A plausible mechanism for the chemical fixation of CO<sub>2</sub> via C-N bond formation to produce oxazolidinones is shown in Scheme 2.



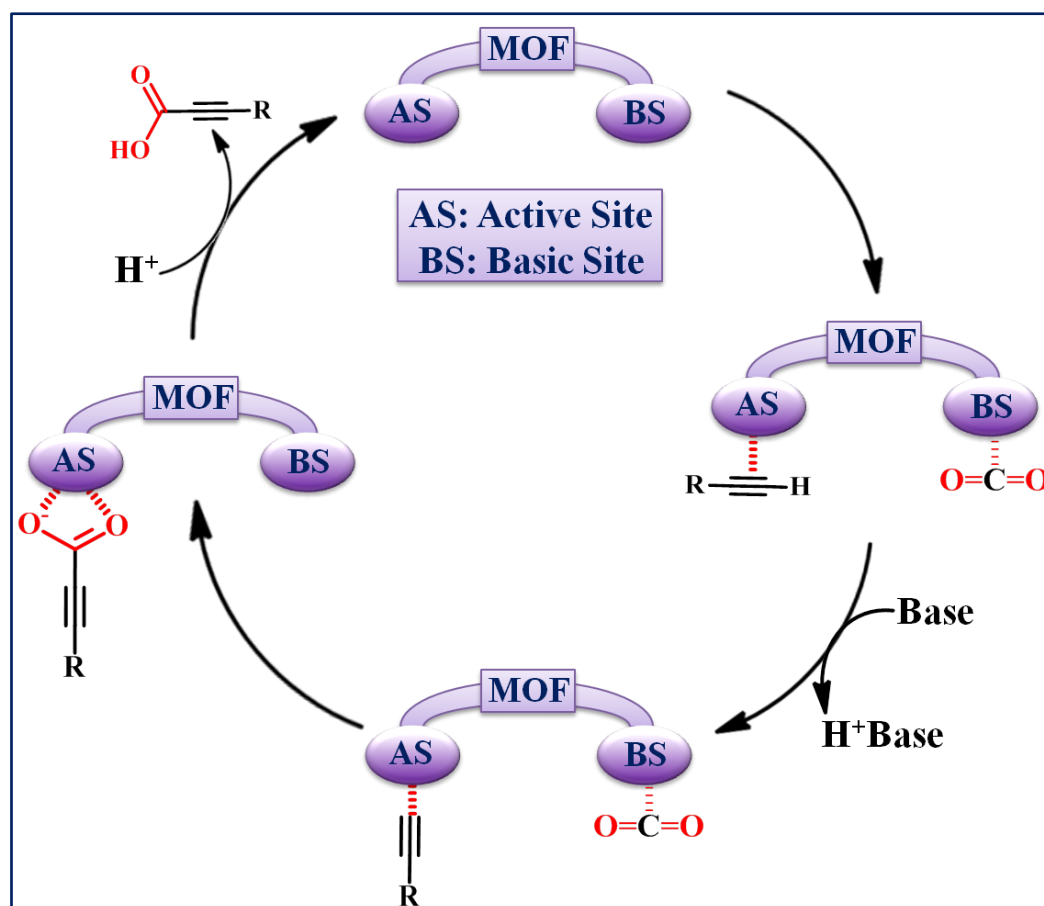
**Scheme 2.** A plausible mechanism for CO<sub>2</sub> fixation to oxazolidinone via a three-component reaction of CO<sub>2</sub> with propargylic alcohol and primary amines.

The first step involves the polarization of the  $C\equiv C$  bond by coordination with the catalytic active site (AS) such as Cu(I) or Ag(0/I). At the same time, polarization of  $CO_2$  takes place at the  $CO_2$ -philic basic sites followed by deprotonation of propargylic alcohol in the presence of a base (DBU/ $PPh_3$ / $Et_3N$ , etc). Then subsequent  $CO_2$  insertion and ring-closure reaction lead to the formation of  $\alpha$ -alkylidene cyclic carbonates and its elimination regenerates the active catalyst and the cycle continues. Notably, in the presence of the primary amine, the  $\alpha$ -alkylidene cyclic carbonate undergoes aminolysis resulting in the generation of oxazolidinone. Overall, for high-yield generation of oxazolidinone by a three-component reaction of  $CO_2$  with propargylic alcohol and primary amines, a bifunctional catalyst composed of catalytic site (Ag(I)/Cu(I)) and nucleophilic site is essential.

### 1.5.3.3. $CO_2$ fixation via C-C bond formation

The fixation of  $CO_2$  via C-C bond formation is one of the emerging strategies to generate value-added carboxylic acid and ester derivatives.<sup>119</sup> The literature study revealed that catalysts based on Cu(I)/Ag(I)/Ag(0) are active for the fixation of  $CO_2$  via C-C bond formation.<sup>120</sup> In this regard, various efforts have been reported by researchers in anchoring Ag(I)/Cu(I) ions in MOFs and utilized as heterogeneous catalysts for the fixation of  $CO_2$  via C-C bond formation.<sup>121</sup> In this direction, Cheng and co-worker<sup>122</sup> developed Ag@MIL-101 by a simple liquid impregnation method and utilized it for carboxylative cyclization of terminal alkynes with  $CO_2$  under atmospheric pressure conditions. Later, the same research group<sup>123</sup> designed Ag@MIL-100(Fe) for carboxylation of 1-ethynylbenzene with  $CO_2$  at 50 °C and 1 atm pressure conditions. In similar efforts, Zhang and co-worker<sup>124</sup> and Wei and co-worker<sup>125</sup> embedded AgNPs in covalent triazine framework (CTF) and ZIF-8, respectively for carboxylation of various terminal alkenes via direct  $CO_2$  insertion reaction. However, the application of noble-metal free catalysts for the carboxylative cyclization of terminal alkynes is relatively less studied. Hence there is significant scope for the design of noble-metal-free catalysts for the fixation of  $CO_2$  to value-added acids/esters through C-C bond formation.

The plausible mechanism for the fixation of  $CO_2$  via carboxylation of terminal alkynes into corresponding alkynyl carboxylic acid is shown in Scheme 3. The reaction proceeds with the polarization of  $C\equiv C$  bond at the catalytic active site (AS), then deprotonation of alkynes takes place in the presence of bases like  $Cs_2CO_3$ / $K_2CO_3$ / $PPh_3$  followed by  $CO_2$  insertion reaction to generate an intermediate which is further hydrolyzed to get carboxylic acid and the catalytic cycle continues.



**Scheme 3.** A plausible mechanism for fixation of CO<sub>2</sub> to alkynyl carboxylic acid via C-C bond formation.

#### 1.5.3.4. CO<sub>2</sub> utilization via reduction

Solar-driven CO<sub>2</sub> reduction to energy-rich fuels/chemicals represents a promising approach for addressing the energy crisis and reducing atmospheric CO<sub>2</sub> levels.<sup>126,127</sup> To date, a variety of inorganic semiconductors have been explored for efficient photo-reduction of CO<sub>2</sub>, but their indistinct active sites and imprecise microenvironments with complicated structures have impeded the mechanistic insights of CO<sub>2</sub> reduction process.<sup>128,129</sup> Further, the majority of the photo-catalysts possess a wide band gap and are active mainly in the UV region of the solar spectrum which constitutes only about 4% of sunlight reaching earth. Consequently, development of photocatalysts with broad absorption of sunlight including visible light has gained significant interest since natural sunlight contains about 40% of visible light.<sup>130,131</sup> For an effective photocatalytic fixation of CO<sub>2</sub> to fine chemicals, the catalyst should possess good visible light absorption, high surface area along with a high density of CO<sub>2</sub>-philic and catalytic sites.<sup>132,133</sup> In this regard, porphyrin-based frameworks have gained special interest

because they serve as excellent light-harvesting or resonance energy transfer functional struts and facilitate efficient photocatalytic CO<sub>2</sub> reduction activity.<sup>134</sup> Further, the band gap of porphyrin-based frameworks can be tuned by introducing substituents on the porphyrin ring and by incorporating suitable red-ox metal ion in the porphyrin core to obtain frameworks with optimal band edge potentials suitable for CO<sub>2</sub> reduction to fine chemicals.<sup>135</sup> The optimum redox potentials required for effective photoreduction of CO<sub>2</sub> to various fine chemicals is shown in Figure 8.<sup>136</sup>

In addition, syngas (a mixture of CO and H<sub>2</sub>) is an important raw material for the synthesis of methanol, ammonia, and hydrocarbon-based fuels that can be generated by photoreduction of CO<sub>2</sub>.<sup>137</sup> However, in the traditional method, syngas is synthesized by a water gas shift reaction which requires high energy and produces a large amount of CO<sub>2</sub>.<sup>138</sup> Thus, it is highly desirable to develop efficient catalysts that can produce syngas under environmentally friendly mild conditions.<sup>139,140</sup> This can be achieved by a simultaneous reaction of CO<sub>2</sub> reduction reaction (CO<sub>2</sub>RR) coupled with hydrogen evolution reaction (HER).<sup>141,142</sup>

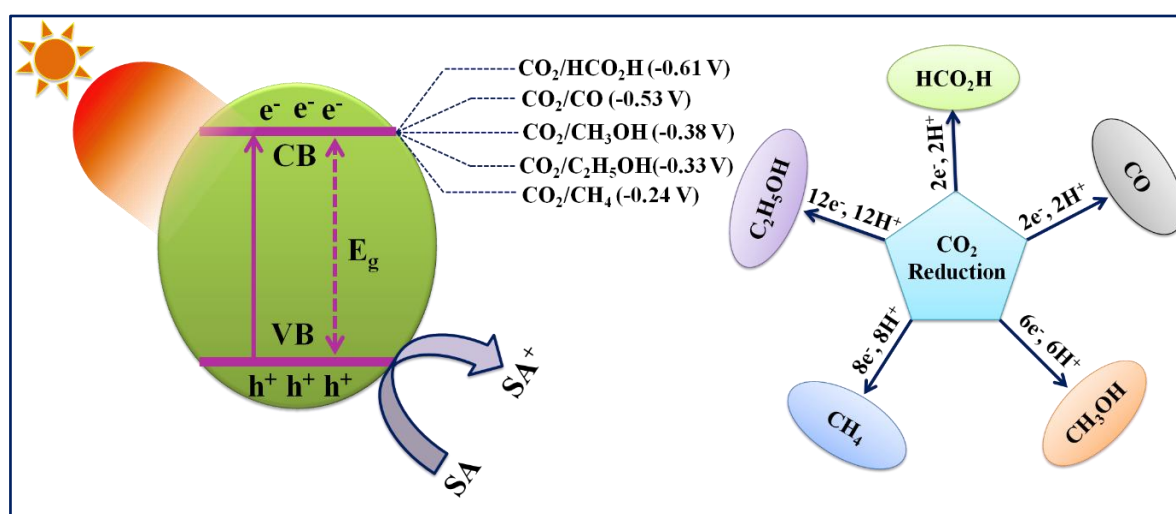


**Figure 8.** General representation of photocatalytic reduction of CO<sub>2</sub> and redox potentials required for conversion of CO<sub>2</sub> to various fine chemicals.

With the aforementioned motivation for the capture and utilization of CO<sub>2</sub> as C1-feedstock to generate various high-value chemicals, we rationally designed MOF-based heterogeneous catalysts for effective CCU into value-added chemicals/fuels especially cyclic carbonates,  $\alpha$ -alkylidene cyclic carbonates, oxazolidinones, and syngas generation under environment-friendly mild conditions which are discussed in the subsequent chapters.

## 1.6. Summary

In this chapter, we presented a brief introduction to MOFs, the history of MOFs, and their application for CO<sub>2</sub> uptake and subsequent conversion. Besides, the various ways of CO<sub>2</sub> fixation to generate value-added chemicals through C-X (X = O, N, and C) bond formation along with reduction are discussed.

## 1.7. References

- (1) Meinshausen, M.; Meinshausen, N.; Hare, W.; Raper, S. C. B.; Frieler, K.; Knutti, R.; Frame, D. J.; Allen, M. R. Greenhouse-gas emission targets for limiting global warming to 2 °C. *Nature* **2009**, *458*, 1158.
- (2) Glikson, A. The lungs of the Earth: Review of the carbon cycle and mass extinction of species. *Energy Procedia* 2018, *146*, 3-11.
- (3) IPCC Fifth Assessment Report, Intergovernmental Panel on Climate Change (IPCC). **2014**; [https://www.ipcc.ch/site/assets/uploads/2018/02/ipcc\\_wg3\\_ar5\\_full.pdf](https://www.ipcc.ch/site/assets/uploads/2018/02/ipcc_wg3_ar5_full.pdf).
- (4) Hernández, S.; Farkhondehfal, M. A.; Sastre, F.; Makkee, M.; Saracco, G.; Russo, N. Syngas production from electrochemical reduction of CO<sub>2</sub>: current status and prospective implementation. *Green Chem.* **2017**, *19*, 2326-2346.
- (5) Jacobson, M. Z. Review of solutions to global warming, air pollution, and energy security. *Energy Environ. Sci.* **2009**, *2*, 148-173.
- (6) Pires, J. C. M.; Martins, F. G.; Alvim-Ferraz, M. C. M.; Simoes, M.; Recent developments on carbon capture and storage: An overview. *Chem. Eng. Res. Des.* **2011**, *89*, 1446-1460.
- (7) Szulczewski, M. L.; MacMinn, C. W.; Herzog, H. J.; Juanes, R. Lifetime of carbon capture and storage as a climate-change mitigation technology. *Proc. Natl. Acad. Sci. U.S.A.* **2012**, *109*, 5185-5189.
- (8) Haszeldine, R. S. Carbon Capture and Storage: How Green Can Black Be? *Science* **2009**, *325*, 1647-1652.
- (9) Cormos, C. -C. Integrated assessment of IGCC power generation technology with carbon capture and storage (CCS). *Energy* **2012**, *42*, 434-445.
- (10) Sgouridis, S.; -Dale, M. C.; Csala, D.; Chiesa, M.; Bardi, U. Comparative net energy analysis of renewable electricity and carbon capture and storage. *Nature Energy* **2019**, *4*, 456-465.

- (11) Kolster, C.; Mechleri, E.; Krevor, S.; Dowell, N. M. The role of CO<sub>2</sub> purification and transport networks in carbon capture and storage cost reduction. *Int. J. Greenhouse Gas Contr.* **2017**, *58*, 127-141.
- (12) Wawrzyńczak, D.; Panowski, M.; Majchrzak-Kubęba, I. Possibilities of CO<sub>2</sub> purification coming from oxy-combustion for enhanced oil recovery and storage purposes by adsorption method on activated carbon. *Energy* **2019**, *180*, 787-796.
- (13) Santori, G.; Charalambous, C.; Ferrari, M.-C.; Brandani, S. Adsorption artificial tree for atmospheric carbon dioxide capture, purification and compression. *Energy* **2018**, *162*, 1158-1168.
- (14) Omae, I. Recent developments in carbon dioxide utilization for the production of organic chemicals. *Coord. Chem. Rev.* **2012**, *256*, 1384-1405.
- (15) North, M.; Pasquale, R.; Young, C. Synthesis of cyclic carbonates from epoxides and CO<sub>2</sub>. *Green Chem.* **2010**, *12*, 1514-1539.
- (16) Li, Y. N.; Ma, R.; He, L. N.; Diao, Z. F. Homogeneous hydrogenation of carbon dioxide to methanol. *Catal. Sci. Technol.* **2014**, *4*, 1498-1512.
- (17) Yu, B.; He, L.-N. Upgrading Carbon Dioxide by Incorporation into Heterocycles. *ChemSusChem* **2015**, *8*, 52-62.
- (18) Liu, Q., Wu, L., Jackstell, R.; Beller, M. Using carbon dioxide as a building block in organic synthesis. *Nat. Commun.* **2015**, *6*, 5933.
- (19) Sneddon, G.; Greenaway, A.; Yiu, H. H. P. The Potential Applications of Nanoporous Materials for the Adsorption, Separation, and Catalytic Conversion of Carbon Dioxide. *Adv. Energy Mater.* **2014**, *4*, 1301873.
- (20) Yaashika, P. R.; Kumar, P. S.; Varjani, S. J.; Saravanan, A. A review on photochemical, biochemical and electrochemical transformation of CO<sub>2</sub> into value-added products. *J. CO<sub>2</sub> Util.* **2019**, *33*, 131-147.
- (21) Cui, W.-G.; Zhang, G.-Y.; Hu, T.-L.; Bu, X.-H. Metal-organic framework-based heterogeneous catalysts for the conversion of C1 chemistry: CO, CO<sub>2</sub> and CH<sub>4</sub>. *Coord. Chem. Rev.* **2019**, *387*, 79-120.
- (22) Jin, F.; Huo, Z.; Zeng, X.; Enomoto, H. Advances in CO<sub>2</sub> Conversion and Utilization. **2010**, *1056*, 31-53.
- (23) Ma, L. Q.; Abney, C.; Lin, W. B. Enantioselective catalysis with homochiral metal-organic frameworks. *Chem. Soc. Rev.* **2009**, *38*, 1248-1256.

- (24) S. Wang, Q. Wang, X. Feng, B. Wang, L. Yang, Explosives in the Cage: Metal-Organic Frameworks for High-Energy Materials Sensing and Desensitization. *Adv. Mater.* **2017**, *29*, 1701898.
- (25) Kraft, A. ON THE DISCOVERY AND HISTORY OF PRUSSIAN BLUE. *Bull. Hist. Chem.* **2008**, *33*, 61-67.
- (26) Buser, H. J.; Schwarzenbach, D.; Petter, W.; Ludi, A. The crystal structure of Prussian blue:  $\text{Fe}_4[\text{Fe}(\text{CN})_6]_3 \cdot x\text{H}_2\text{O}$ . *Inorg. Chem.* **1977**, *16*, 2704-2710.
- (27) Kinoshita, Y.; Matsubara, I.; Saito, Y. The crystal structure of bis (succinonitrilo) copper (I) nitrate. *Bull. Chem. Soc. Jap.* **1959**, *32*, 741-747.
- (28) Kinoshita, Y.; Matsubara, I.; Saito, Y. The crystal structure of bis(glutaronitrilo)-copper(I) nitrate. *Bull. Chem. Soc. Jap.* **1959**, *32*, 1216-1221.
- (29) Kinoshita, Y.; Matsubara, I.; Higuchi, T.; Saito, Y. The crystal structure of bis (adiponitrilo) copper (I) nitrate. *Bull. Chem. Soc. Jap.* **1959**, *32*, 1221-1226.
- (30) Wells, A. F. Three-Dimensional Nets and Polyhedra. Wiley. New York **1977**.
- (31) Hoskins, B. F.; Robson, R. Infinite polymeric frameworks consisting of three dimensionally linked rod-like segments. *J. Am. Chem. Soc.* **1989**, *111*, 5962-5964.
- (32) Hoskins, B. F.; Robson, R. Design and construction of a new class of scaffolding-like materials comprising infinite polymeric frameworks of 3D-linked molecular rods. A reappraisal of the zinc cyanide and cadmium cyanide structures and the synthesis and structure of the diamond-related frameworks  $[\text{N}(\text{CH}_3)_4][\text{Cu}^{\text{I}}\text{Zn}^{\text{II}}(\text{CN})_4]$  and  $\text{CuI}[4,4',4'',4'''$ -tetracyanotetraphenylmethane  $\text{BF}_4 \cdot x\text{C}_6\text{H}_5\text{NO}_2$ . *J. Am. Chem. Soc.* **1990**, *112*, 1546-1554.
- (33) Fujita, M.; Kwon, Y. J.; Washizu, S.; Ogura, K. Preparation, clathration ability, and catalysis of a two-dimensional square network material composed of cadmium(II) and 4, 4'-bipyridine. *J. Am. Chem. Soc.* **1994**, *116*, 1151-1152.
- (34) Yaghi, O. M.; Li, G.; Li, H. Selective binding and removal of guests in a microporous metal-organic framework. *Nature* **1995**, *378*, 703-706.
- (35) Li, H.; Eddaoudi, M.; O'Keeffe, M.; Yaghi, O. M. Design and synthesis of an exceptionally stable and highly porous metal-organic framework. *Nature* **1999**, *402*, 276-279.
- (36) Yaghi, O. M.; O'Keeffe, M.; Ockwig, N. W.; Chae, H. K.; Eddaoudi, M.; Kim, J. Reticular synthesis and the design of new materials. *Nature* **2003**, *423*, 705-714.
- (37) Furukawa, H.; Cordova, K. E.; O'Keeffe, M.; Yaghi, O. M. The Chemistry and Applications of Metal-Organic Frameworks. *Science* **2013**, *341*, 1230444.

- (38) Chui, S. S. Y.; Los, S. M. F.; Charmant, J. P. H.; Open, A. G.; Williams, I. D. A Chemically Functionalizable Nanoporous Material  $[\text{Cu}_3(\text{TMA})_2(\text{H}_2\text{O})_3]_n$ . *Science* **1999**, *283*, 1148-1150.
- (39) Ferey, G.; Mellot-Draznikens, C.; Serre, C.; Millange, F.; Dutour, J.; Serble, S.; Margiolaki, I. A Chromium Terephthalate-Based Solid with Unusually Large Pore Volumes and Surface Area. *Science* **2005**, *309*, 2040-2042.
- (40) Cavka, J. H.; Jakobsen, S.; Olsbye, U.; Guillou, N.; Lamberti, C.; Bordiga, S.; Lillerud, K. P. A New Zirconium Inorganic Building Brick Forming Metal Organic Frameworks with Exceptional Stability. *J. Am. Chem. Soc.* **2008**, *130*, 13850-13851.
- (41) Feng, D.; Chung, W.-C.; Wei, Z.; Gu, Z.-Y.; Jiang, H.-L.; Chen, Y.-P.; Darenbourg, D. J.; Zhou, H.-C. Construction of Ultrastable Porphyrin Zr Metal-Organic Frameworks through Linker Elimination. *J. Am. Chem. Soc.* **2013**, *135*, 17105-17110.
- (42) Ding, M.; Flaig, R. W.; Jiang, H.-L.; Yaghi, O. M. Carbon capture and conversion using metal-organic frameworks and MOF-based materials. *Chem. Soc. Rev.* **2019**, *48*, 2783-2828.
- (43) Geng, K.; He, T.; Liu, R.; Tan, K. T.; Li, Z.; Tao, S.; Gong, Y.; Jiang, Q.; Jiang, D. Covalent organic frameworks: design, synthesis, and functions. *Chem. Rev.* **2020**, *120*, 16, 8814-8933.
- (44) Ding, S.-Y.; Wang, W. Covalent organic frameworks (COFs): from design to applications. *Chem. Soc. Rev.* **2013**, *42*, 548-568.
- (45) Li, Z.; Feng, X.; Zou, Y.; Zhang, Y.; Xia, H.; Liu, X. A 2D azine-linked covalent organic framework for gas storage applications. *Chem. Commun.* **2014**, *50*, 13825-13828.
- (46) Huang, N.; Chen, X.; Krishna, R.; Jiang, D. Two-dimensional covalent organic frameworks for carbon dioxide capture through channel-wall functionalization. *Angew. Chem. Int. Ed.* **2015**, *54*, 2986-2990.
- (47) Zou, C.; Zhang, Z.; Xu, X.; Gong, Q.; Li, J.; Wu, C. D. A Multifunctional Organic-Inorganic Hybrid Structure Based on  $\text{Mn}^{\text{III}}$ -Porphyrin and Polyoxometalate as a Highly Effective Dye Scavenger and Heterogenous Catalyst. *J. Am. Chem. Soc.* **2012**, *134*, 87-90.
- (48) Kreno, L. E.; Leong, K.; Farha, O. K.; Allendorf, M.; Van Duyne, R. P.; Hupp, J. T. Metal-organic framework materials as chemical sensors. *Chem. Rev.* **2012**, *112*, 1105-1125.
- (49) Herm, Z. R.; Wiers, B. M.; Mason, J. A.; van Baten, J. M.; Hudson, M. R.; Zajdel, P.; Brown, C. M.; Masciocchi, N.; Krishna, R.; Long, J. R. Separation of hexane isomers in a metal-organic framework with triangular channels. *Science* **2013**, *360*, 960-964.

- (50) Xu, X.; Song, C.; Wincek, R.; Andrése, J. M.; Miller, B. G.; Scaroni, A. W. Separation of CO<sub>2</sub> from power plant flue gas using a novel CO<sub>2</sub> "molecular basket" adsorbent. *Fuel Chem. Div. Prepr.* **2003**, *48*, 162-163.
- (51) IPCC. Climate Change 2013: The Physical Science Basis. Contribution of Working Group I to the Fifth Assessment Report of the Intergovernmental Panel on Climate Change; Stocker, T. F.; Qin, D.; Plattner, G.-K.; Tignor, M.; Allen, S. K.; Boschung, J.; Nauels, A.; Xia, Y.; Bex, V.; Midgley, P. M. Eds.; Cambridge University Press: Cambridge, U. K., and New York, **2013**.
- (52) Ding, M.; Flaig, R. W.; Jiang, H.-L.; Yaghi, O. M. Carbon capture and conversion using metal-organic frameworks and MOF-based materials. *Chem. Soc. Rev.* **2019**, *48*, 2783-2828.
- (53) Yazaydin, A. O.; Benin, A. I.; Faheem, S. A.; Jakubczak, P.; Low, J. J.; Willis, R. R.; Snurr, R. Q. Enhanced CO<sub>2</sub> Adsorption in Metal-Organic Frameworks via Occupation of Open-Metal Sites by Coordinated Water Molecules. *Chem. Mater.* **2009**, *21*, 1425-1430.
- (54) Shekhah, O.; Belmabkhout, Y.; Adil, K.; Cairns, A. J.; Bhatt, P.; Eddaoudi, M. A facile solvent-free synthesis route for the assembly of a highly CO<sub>2</sub> selective and H<sub>2</sub>S tolerant NiSIFSIX metal-organic framework. *Chem. Commun.* **2015**, *51*, 13595-13598.
- (55) Nandi, S.; Luna, P. D.; Daff, T. D.; Rother, J.; Liu, M.; Buchanan, W.; Hawari, A. I.; Woo, T. K.; Vaidhyanathan, R. A single-ligand ultra-microporous MOF for precombustion CO<sub>2</sub> capture and hydrogen purification. *Sci. Adv.* **2015**, *1*, e1500421.
- (56) Chakarborty, A.; Achari, A.; Eswaramoorthy, M.; Maji, T. K. MOF-aminoclay composites for superior CO<sub>2</sub> capture, separation and enhanced catalytic activity in chemical fixation of CO<sub>2</sub>. *Chem. Commun.* **2016**, *52*, 11378-11381.
- (57) Demessence, A.; D'Alessandro, D. M.; Foo, M. L.; Long, J. R. Strong CO<sub>2</sub> Binding in a Water-Stable, Triazolate-Bridged Metal-Organic Framework Functionalized with Ethylenediamine. *J. Am. Chem. Soc.* **2009**, *131*, 8784-8786.
- (58) McDonald, T. M.; D'Alessandro, D. M.; Krishna, R.; Long, J. R. Enhanced carbon dioxide capture upon incorporation of N, N'-dimethylethylenediamine in the metal-organic framework CuBTTri. *Chem. Sci.* **2011**, *2*, 2022-2028.
- (59) Llewellyn, P. L.; Bourrelly, S.; Serre, C.; Vimont, A.; Daturi, M.; Hamon, L.; Weileld, G. D.; Chang, J.-S.; Hong, D.-Y.; Hwang, Y. K.; Jung, S. H.; Férey, G. High Uptakes of CO<sub>2</sub> and CH<sub>4</sub> in Mesoporous Metal-Organic Frameworks MIL-100 and MIL-101. *Langmuir* **2008**, *24*, 7245-7250.

- (60) Couck, S.; Denayer, J. F. M.; Baron, G. V.; Rémy, T.; Gascon, J.; Kaptejin, F. An Amine-Functionalized MIL-53 Metal–Organic Framework with Large Separation Power for CO<sub>2</sub> and CH<sub>4</sub>. *J. Am. Chem. Soc.* **2009**, *131*, 6326-6327.
- (61) Caskey, S. R.; Wong-Foy, A. G.; Matzer, A. J. N-enriched ACF from coal-based pitch blended with urea-based resin for CO<sub>2</sub> capture. *J. Am. Chem. Soc.* **2009**, *130*, 10870-10871.
- (62) An, J.; Geib, S. J.; Rosi, N. L. High and Selective CO<sub>2</sub> Uptake in a Cobalt Adeninate Metal-Organic Framework Exhibiting Pyrimidine- and Amino-Decorated Pores. *J. Am. Chem. Soc.* **2009**, *132*, 38-39.
- (63) Dietzel, P. D.; Besikiotis, V.; Blom, R. Application of metal-organic frameworks with coordinatively unsaturated metal sites in storage and separation of methane and carbon dioxide. *J. Mater. Chem.* **2009**, *19*, 7362-7370.
- (64) Yazaydin, A. O.; Benin, A. I.; Faheem, S. A.; Jakubczak, P.; Low, J. J.; Willis, R. R.; Snurr, R. Q. Enhanced CO<sub>2</sub> Adsorption in Metal-Organic Frameworks via Occupation of Open-Metal Sites by Coordinated Water Molecules. *Chem. Mater.* **2009**, *21*, 1425-1430.
- (65) Bourrelly, S.; Llewellyn, P.L.; Serre, C.; Millange, F.; Loiseau, T.; Férey, G. Different adsorption behaviors of methane and carbon dioxide in the isotypic nanoporous metal terephthalates MIL-53 and MIL-47. *J. Am. Chem. Soc.* **2005**, *127*, 13519-13521.
- (66) Liang, Z.; Marshall, M.; Chaffee, A. L. CO<sub>2</sub> Adsorption-Based Separation by Metal Organic Framework (Cu-BTC) versus Zeolite (13X). *Energy and Fuels* **2009**, *23*, 2785-2789.
- (67) Farrusseng, D.; Daniel, C.; Gaudillère, C.; Ravon, U.; Schuurman, Y.; Mirodatos, C.; Dubbeldam, D.; Frost, H.; Snurr, R. Q. Heats of adsorption for seven gases in three metal–organic frameworks: systematic comparison of experiment and simulation. *Langmuir* **2009**, *25*, 7383-7388.
- (68) Choi, J.-S.; Son, W.-J.; Kim, J.; Ahn, W.-S. Metal-organic framework MOF-5 prepared by microwave heating: Factors to be considered. *Micropor. Mesopor. Mater.* **2008**, *116*, 727-731.
- (69) Ugale, B.; Dhankhar, S. S.; Nagaraja, C. M. Construction of 3-Fold-Interpenetrated Three-Dimensional Metal–Organic Frameworks of Nickel(II) for Highly Efficient Capture and Conversion of Carbon Dioxide. *Inorg. Chem.* **2016**, *55*, 9757-9766.
- (70) Cui, W.-G.; Zhang, G.-Y.; Hu, T.-L.; Bu, X.-H. Metal-organic framework-based heterogeneous catalysts for the conversion of C1 chemistry: CO, CO<sub>2</sub> and CH<sub>4</sub>. *Coord. Chem. Rev.* **2019**, *387*, 79-120.

- (71) Kiang, Y.-H.; Gardner, G. B.; Lee, S.; Xu, Z.; Lobkovsky, E. B. Variable pore size, variable chemical functionality, and an example of reactivity within porous phenylacetylene silver salts. *J. Am. Chem. Soc.* **1999**, *121*, 8204-8215.
- (72) Seo, J. S.; Whang, D.; Lee, H.; Jun, S. I.; Oh, J.; Jeon, Y. J.; Kim, K. A homochiral metal-organic porous material for enantioselective separation and catalysis. *Nature* **2000**, *404*, 982-986.
- (73) Wang, Z.; Cohen, S. M. Postsynthetic covalent modification of a neutral metal-organic framework. *J. Am. Chem. Soc.* **2007**, *129*, 12368-12369.
- (74) Kerneghan, P. A.; Halperin, S. D.; Bryce, D. L.; Maly, K. E. Postsynthetic modification of an imine-based microporous organic network. *Can. J. Chem.* **2011**, *89*, 577-582.
- (75) Wang, M.; Lan, W.-J.; Zheng, Y.-R.; Cook, T. R.; White, H. S.; Stang, P. J. Post-self-assembly covalent chemistry of discrete multicomponent metallosupramolecular hexagonal prisms. *J. Am. Chem. Soc.* **2011**, *133*, 10752-10755.
- (76) Mehdi, A.; Reye, C.; Corriu, R. From molecular chemistry to hybrid nanomaterials. Design and functionalization. *Chem. Soc. Rev.* **2011**, *40*, 563-574.
- (77) Qin, Y.; Hao, M.; Wang, D.; Li, Z. Post-synthetic modifications (PSM) on metal-organic frameworks (MOFs) for visible-light-initiated photocatalysis, *Dalton Trans.* **2021**, *50*, 13201-13215.
- (78) Yin, Z.; Wan, S.; Yang, J.; Kurmoo, M.; Zeng, M.-H. Recent advances in post-synthetic modification of metal-organic frameworks: New types and tandem reactions. *Coord. Chem. Rev.* **2019**, *378*, 500-512.
- (79) Gascon, J.; Corma, A.; Kapteijn, F.; Xamena, F. X. L. Metal Organic Framework Catalysis: Quo vadis? *ACS Catal.* **2014**, *4*, 361-378.
- (80) Hou, S.-L.; Dong, J.; Zhao, B. Formation of C-X Bonds in CO<sub>2</sub> Chemical Fixation Catalyzed by Metal-Organic Frameworks. *Adv. Mater.* **2020**, *32*, 1806163.
- (81) Liang, J.; Huang, Y.-B.; Cao, R. Metal-organic frameworks and porous organic polymers for sustainable fixation of carbon dioxide into cyclic carbonates. *Coord. Chem. Rev.* **2019**, *378*, 32-65.
- (82) Pal, T. K.; De, D.; Bhardwaj, P. K. Metal-organic frameworks for the chemical fixation of CO<sub>2</sub> into cyclic carbonates. *Coord. Chem. Rev.* **2020**, *408*, 213173.
- (83) Ninokata, R.; Yamahira, T.; Onodera, G.; Kimura, M. Nickel-Catalyzed CO<sub>2</sub> Rearrangement of Enol Metal Carbonates for the Efficient Synthesis of  $\beta$ -Ketocarboxylic Acids. *Angew. Chem. Int. Ed.* **2017**, *56*, 208-211.

- (84) Fukuoka, S.; Kawamura, M.; Komiya, K.; Tojo, M.; Hachiya, H.; Hasegawa, K.; Aminaka, M.; Okamoto, H.; Fukawa, I.; Konno, S. A novel non-phosgene polycarbonate production process using by-product CO<sub>2</sub> as starting material. *Green Chem.* **2003**, *5*, 497-507.
- (85) Ma, R.; He, L. N.; Zhou, Y. B. An efficient and recyclable tetraoxo-coordinated zinc catalyst for the cycloaddition of epoxides with carbon dioxide at atmospheric pressure. *Green Chem.* **2016**, *18*, 226-231.
- (86) Wilhelm, M. E.; Anthofer, M. H.; Cokoja, M.; Markovits, I. I. E.; Herrmann, W. A.; Kühn, F. E. Cycloaddition of carbon dioxide and epoxides using pentaerythritol and halides as dual catalyst system. *ChemSusChem* **2014**, *7*, 1357-1360.
- (87) Langanke, J.; Greiner, L.; Leitner, W. Substrate dependent synergetic and antagonistic interaction of ammonium halide and polyoxometalate catalysts in the synthesis of cyclic carbonates from oleochemical epoxides and CO<sub>2</sub>. *Green Chem.* **2013**, *15*, 1173-1182.
- (88) Yang, Z. Z.; Zhao, Y. N.; He, J.; Gao, Z. S. Yin, Highly efficient conversion of carbon dioxide catalyzed by polyethylene glycol-functionalized basic ionic liquids. *Green Chem.* **2012**, *14*, 519-527.
- (89) Li, J.; Jia, D.; Guo, Z.; Liu, Y.; Lyu, Y.; Zhou, Y.; Wang, J. Imidazolium based porous hypercrosslinked ionic polymers for efficient CO<sub>2</sub> capture and fixation with epoxides. *Green Chem.* **2017**, *19*, 2675-2686.
- (90) Geng, K.; He, T.; Liu, R.; Tan, K. T.; Li, Z.; Tao, S.; Gong, Y.; Jiang, Q.; Jiang, D. Covalent organic frameworks: design, synthesis, and functions. *Chem. Rev.* **2020**, *120*, 16, 8814-8933.
- (91) Song, Ji.; Zhang, Z.; Hu, S.; Wu, T.; Jiang, T.; Han, B. MOF-5/n-Bu<sub>4</sub>NBr: an efficient catalyst system for the synthesis of cyclic carbonates from epoxides and CO<sub>2</sub> under mild conditions. *Green Chem.* **2009**, *11*, 1031-1036.
- (92) Miralda, C. M.; Macias, E. E.; Zhu, M.; Ratnasamy, P.; Carreon, M. A. Zeolitic Imidazole Framework-8 Catalysts in the Conversion of CO<sub>2</sub> to Chloropropene Carbonate. *ACS Catal.* **2012**, *2*, 180-183.
- (93) Macias, E. E.; Ratnasamy, P.; Carreon, M. A. Catalytic activity of metal organic framework Cu<sub>3</sub>(BTC)<sub>2</sub> in the cycloaddition of CO<sub>2</sub> to epichlorohydrin reaction. *Catal. Today* **2012**, *198*, 215-218.

- (94) Demir, S.; Usta, S.; Tamar, H.; Ulusoy, M. Solvent free utilization and selective coupling of epichlorohydrin with carbon dioxide over zirconium metal-organic frameworks. *Micropor. Mesopor. Mater.* **2017**, *244*, 251-257.
- (95) Kurisingal, J. F.; Rachuri, Y.; Gu, Y.; Kim, G.-H.; Park, D.-W. Binary metal-organic frameworks: Catalysts for the efficient solvent-free CO<sub>2</sub> fixation reaction via cyclic carbonates synthesis. *Appl. Catal. A: Gen.* **2019**, *571*, 1-11.
- (96) Gao, C.-Y.; Tian, H.-R.; Ai, J.; Li, L.-J.; Dang, S.; Land, Y.-Q.; Sun, Z.-M. A microporous Cu-MOF with optimized open metal sites and pore spaces for high gas storage and active chemical fixation of CO<sub>2</sub>. *Chem. Commun.* **2016**, *52*, 11147-11150.
- (97) Lan, J.; Liu, M.; Lu, X.; Zhang, X.; Sun, J. Novel 3D Nitrogen Rich Metal Organic Framework for Highly Efficient CO<sub>2</sub> Adsorption and Catalytic Conversion to Cyclic Carbonates under Ambient Temperature. *ACS Sustainable Chem. Eng.* **2018**, *6*, 8727-8735.
- (98) Babu, R.; Kathalikkattil, A. C.; Roshan, R.; Tharun, J.; Kim, D.-W.; Park, D.-W. Dual-porous metal organic framework for room temperature CO<sub>2</sub> fixation via cyclic carbonate synthesis. *Green Chem.* **2016**, *18*, 232-242.
- (99) Liang, J.; Chen, R. P.; Wang, X. Y.; Liu, T. T.; Wang, X. S.; Huang, Y. B.; Cao, R. Postsynthetic ionization of an imidazole-containing metal-organic framework for the cycloaddition of carbon dioxide and epoxides. *Chem. Sci.* **2017**, *8*, 1570-1575.
- (100) Ding, L. G.; Yao, B. J.; Jiang, W. L.; Li, J. T.; Fu, Q. J.; Li, Y. A.; Liu, Z. H.; Ma, J. P.; Dong, Y. B. Bifunctional imidazolium-based ionic liquid decorated UiO-67 type MOF for selective CO<sub>2</sub> adsorption and catalytic property for CO<sub>2</sub> cycloaddition with epoxides. *Inorg. Chem.* **2017**, *56*, 2337-2344.
- (101) Jose, T.; Hwang, Y.; Kim, D. W.; Kim, M. I.; Park, D. W. Functionalized zeolitic imidazolate framework F-ZIF-90 as efficient catalyst for the cycloaddition of carbon dioxide to allyl glycidyl ether. *Catal. Today* **2015**, *245*, 61-69.
- (102) Han, Y. H.; Zhou, Z. Y.; Tian, C. B.; Du, S. W. A dual-walled cage MOF as an efficient heterogeneous catalyst for the conversion of CO<sub>2</sub> under mild and co-catalyst free conditions. *Green Chem.* **2016**, *18*, 4086-4091.
- (103) Sun, Y.; Huang, H.; Vardhan, H.; Aguila, B.; Zhong, C.; Perman, J. A.; Al-Enizi, A. M.; Nafady, A.; Ma, S. Facile approach to graft ionic liquid into MOF for improving the efficiency of CO<sub>2</sub> chemical fixation. *ACS Appl. Mater. Interfaces* **2018**, *10*, 27124-27130.
- (104) Ugale, B.; Kumar, S.; Kumar, T. J. D.; Nagaraja, C. M. Environmentally Friendly, Co-catalyst-Free Chemical Fixation of CO<sub>2</sub> at Mild Conditions Using Dual-Walled Nitrogen-

Rich Three-Dimensional Porous Metal-Organic Frameworks. *Inorg. Chem.* **2019**, *58*, 3925-3936.

(105) Das, R.; Dhankhar, S. S.; Nagaraja, C. M. Construction of a bifunctional Zn(II)-organic framework containing basic amine functionality for selective capture and room temperature fixation of CO<sub>2</sub>. *Inorg. Chem. Front.* **2020**, *7*, 72-81.

(106) Das, R.; Muthukumar, D.; Pillai, R. S.; Nagaraja, C. M. Rational design of a Zn(II)-MOF with multiple functional sites for highly efficient fixation of CO<sub>2</sub> at mild conditions: combined experimental and theoretical investigation. *Chem. Eur. J.* **2020**, *26*, 17445-17454.

(107) Das, R.; Ezhil, T.; Palakkal, A. S.; Muthukumar, D.; Pillai, R. S.; Nagaraja, C. M. Efficient chemical fixation of CO<sub>2</sub> from direct air under environment-friendly co-catalyst and solvent-free ambient conditions. *J. Mater. Chem. A* **2021**, *9*, 23127-23139.

(108) Das, R.; Manna, S. S.; Pathak, B.; Nagaraja, C. M. Strategic Design of Mg-Centered Porphyrin MOF for Efficient Visible Light-Promoted Fixation of CO<sub>2</sub> at Ambient Conditions: Combined Experimental and Theoretical Investigation. *ACS Appl. Mater. Interfaces* **2022**, *14*, 33285-33296.

(109) Flaig, R. W.; Popp, T. M. O.; Fracaroli, A. M.; Kapustin, E. A.; Kalmutzki, M. J.; Altamimi, R. M.; Fathieh, F.; Reimer, J. A.; Yaghi, O. M. The Chemistry of CO<sub>2</sub> Capture in an Amine-Functionalized Metal-Organic Framework under Dry and Humid Conditions. *J. Am. Chem. Soc.* **2017**, *139*, 12125.

(110) Zhao, D.; Liu, X.; Zhu, C.; Kang, Y.; Wang, P.; Shi, Z.; Lu, Y.; Sun, W. Efficient and reusable metal-organic framework catalysts for carboxylative cyclization of propargylamines with carbon dioxide. *ChemCatChem* **2017**, *9*, 4598.

(111) Zhao, Y.; Xia, W. Recent advances in radical-based C-N bond formation via photo-/electrochemistry. *Chem. Soc. Rev.* **2018**, *47*, 2591.

(112) Xu, H.; Liu, X.; Cao, C.; Zhao, B.; Cheng, P.; He, L. A Porous Metal-Organic Framework Assembled by [Cu<sub>30</sub>] Nanocages: Serving as Recyclable Catalysts for CO<sub>2</sub> Fixation with Aziridines. *Adv. Sci.* **2016**, *3*, 1600048.

(113) Wang, X.; Gao, W.; Niu, Z.; Wojtas, L.; Perman, J. A.; Chen, Y.; Li, Z.; Aguila, B.; Ma, S. A metal-metalloporphyrin framework based on an octatopic porphyrin ligand for chemical fixation of CO<sub>2</sub> with aziridines. *Chem. Commun.* **2018**, *54*, 1170.

(114) Das, R.; Nagaraja, C. M. Highly Efficient Fixation of Carbon Dioxide at RT and Atmospheric Pressure Conditions: Influence of Polar Functionality on Selective Capture and Conversion of CO<sub>2</sub>. *Inorg. Chem.* **2020**, *59*, 9765-9773.

- (115) Song, Q.-W.; Yu, B.; Li, X.-D.; Ma, R.; Diao, Z.-F.; Li, R.-G.; Li, W.; He, L.-N. Efficient chemical fixation of CO<sub>2</sub> promoted by a bifunctional Ag<sub>2</sub>WO<sub>4</sub>/Ph<sub>3</sub>P system. *Green Chem.* **2014**, *16*, 1633-1638.
- (116) Kayaki, Y.; Yamamoto, M.; Ikariya, T. Stereoselective Formation of  $\alpha$ -Alkylidene Cyclic Carbonates via Carboxylative Cyclization of Propargyl Alcohols in Supercritical Carbon Dioxide. *J. Org. Chem.* **2007**, *72*, 647-649.
- (117) Karmakar, R.; Lee, D. Reactions of arynes promoted by silver ions. *Chem. Soc. Rev.* **2016**, *45*, 4459-4470.
- (118) Das, R.; Nagaraja, C. M. Noble metal-free Cu(I)-anchored NHC-based MOF for highly recyclable fixation of CO<sub>2</sub> under RT and atmospheric pressure conditions. *Green Chem.* **2021**, *23*, 5195-5204.
- (119) Liu, X.-H.; Ma, J.-G.; Niu, Z.; Yang, G.-M.; Cheng, P. An efficient nanoscale heterogeneous catalyst for the capture and conversion of carbon dioxide at ambient pressure. *Angew. Chem. Int. Ed.* **2015**, *54*, 988-991.
- (120) Dang, Q.-Q.; Liu, C.-Y.; Wang, X.-M.; Zhang, X.-M. Novel Covalent Triazine Framework for High-Performance CO<sub>2</sub> Capture and Alkyne Carboxylation Reaction. *ACS Appl. Mater. Interfaces* **2018**, *10*, 27972-27978.
- (121) Shi, J.; Zhang, L.; Sun, N.; Hu, D.; Shen, Q.; Mao, F.; Gao, Q.; Wei, W. Facile and Rapid Preparation of Ag@ZIF-8 for Carboxylation of Terminal Alkynes with CO<sub>2</sub> in Mild Conditions. *ACS Appl. Mater. Interfaces* **2019**, *11*, 28858-28867.
- (122) Liu, X.-H.; Ma, J.-G.; Niu, Z.; Yang, G.-M.; Cheng, P. An efficient nanoscale heterogeneous catalyst for the capture and conversion of carbon dioxide at ambient pressure. *Angew. Chem. Int. Ed.* **2015**, *54*, 988-991.
- (123) Zhu, N.-N.; Liu, X.-H.; Li, T.; Ma, J.-G.; Cheng, P.; Yang, G.-M. Composite system of Ag nanoparticles and metal-organic frameworks for the capture and conversion of carbon dioxide under mild conditions. *Inorg. Chem.* **2017**, *56*, 3414-3420.
- (124) Dang, Q.-Q.; Liu, C.-Y.; Wang, X.-M.; Zhang, X.-M. Novel Covalent Triazine Framework for High-Performance CO<sub>2</sub> Capture and Alkyne Carboxylation Reaction. *ACS Appl. Mater. Interfaces* **2018**, *10*, 27972-27978.
- (125) Shi, J.; Zhang, L.; Sun, N.; Hu, D.; Shen, Q.; Mao, F.; Gao, Q.; Wei, W. Facile and Rapid Preparation of Ag@ZIF-8 for Carboxylation of Terminal Alkynes with CO<sub>2</sub> in Mild Conditions. *ACS Appl. Mater. Interfaces* **2019**, *11*, 28858-28867.

- (126) Jiang, Z.; Xu, X.; Ma, Y.; Cho, H. S.; Ding, D.; Wang, C.; Wu, J.; Oleynikov, P.; Jia, M.; Cheng, J.; Zhou, Y.; Terasaki, O.; Peng, T.; Zan, L.; Deng, H. Filling metal-organic framework mesopores with TiO<sub>2</sub> for CO<sub>2</sub> photoreduction. *Nature* **2020**, *586*, 549-554.
- (127) Li, R.; Zhang, W.; Zhou, K. Metal-organic-framework-based catalysts for photoreduction of CO<sub>2</sub>. *Adv. Mater.* **2018**, *30*, 1705512.
- (128) Li, A.; Cao, Q.; Zhou, G. Y.; Schmidt, B. V. K. J.; Zhu, W. J.; Yuan, X. T.; Huo, H. L.; Gong, J. L.; Antonietti, M. Three-phase photocatalysis for the enhanced selectivity and activity of CO<sub>2</sub> reduction on a hydrophobic surface. *Angew. Chem., Int. Ed.* **2019**, *58*, 14549-14555.
- (129) Wang, L.; Duan, S. H.; Jin, P. X.; She, H. D.; Huang, J. W.; Lei, Z. Q.; Zhang, T. R.; Wang, Q. Z. Anchored Cu(II) tetra(4-carboxylphenyl)porphyrin to P<sub>25</sub>(TiO<sub>2</sub>) for efficient photocatalytic ability in CO<sub>2</sub> reduction. *Appl. Catal. B* **2018**, *239*, 599-608.
- (130) Zhai, G.; Liu, Y.; Lei, L.; Wang, J.; Wang, Z.; Zheng, Z.; Wang, P.; Cheng, H.; Dai, Y.; Huang, B. Light-Promoted CO<sub>2</sub> Conversion from Epoxides to Cyclic Carbonates at Ambient Conditions over a Bi-Based Metal Organic Framework. *ACS Catal.* **2021**, *11*, 1988-1994.
- (131) Karmakar, S.; Barman, S.; Rahimi, F. A.; Maji, T. K. Covalent grafting of molecular photosensitizer and catalyst on MOF-808: effect of pore confinement toward visible light-driven CO<sub>2</sub> reduction in water. *Energy Environ. Sci.* **2021**, *14*, 2429-2440.
- (132) Sheng, J.; He, Y.; Huang, M.; Yuan, C.; Wang, S.; Dong, F. Frustrated Lewis Pair Sites Boosting CO<sub>2</sub> Photoreduction on Cs<sub>2</sub>CuBr<sub>4</sub> Perovskite Quantum Dots. *ACS Catal.* **2022**, *12*, 2915-2926.
- (133) Shi, X.; Dong, X.; He, Y.; Yan, P.; Zhang, S.; Dong, F. Photoswitchable Chlorine Vacancies in Ultrathin Bi<sub>4</sub>O<sub>5</sub>Cl<sub>2</sub> for Selective CO<sub>2</sub> Photoreduction. *ACS Catal.* **2022**, *12*, 3965-3973.
- (134) Nikoloudakis, E.; Lo'pez-Duarte, I.; Charalambidis, G.; Ladomenou, K.; Ince, M.; Coutsolelos, A. G. Porphyrins and phthalocyanines as biomimetic tools for photocatalytic H<sub>2</sub> production and CO<sub>2</sub> reduction. *Chem. Soc. Rev.* **2022**, *51*, 6965-7045.
- (135) Asselin, P.; Harvey, P. D. Visible-Light-Driven Production of Solar Fuels Catalyzed by Nanosized Porphyrin-Based Metal–Organic Frameworks and Covalent–Organic Frameworks: A Review. *ACS Appl. Nano Mater.* **2022**, *5*, 6055-6082.
- (136) Li, D.; Kassymova, M.; Cai, X.; Zang, S. Q.; Jiang, H. L. Photocatalytic CO<sub>2</sub> reduction over metal-organic framework-based materials. *Coord. Chem. Rev.* **2020**, *412*, 213262.

(137) Underwood, A. J. V. Industrial Synthesis of Hydrocarbons from Hydrogen and Carbon Monoxide. *Ind. Eng. Chem.* **1940**, *32*, 449-454.

(138) Huang, Y.; Xin, Z.; He, L.-N. Water activated main element-based syngas surrogates for safe functionalization of unsaturated chemicals. *Sci. Bull.* **2021**, *66*, 865-867.

(139) Zhang, J.; An, B.; Li, Z.; Cao, Y.; Dai, Y.; Wang, W.; Zeng, L.; Lin, W.; Wang, C. Neighboring Zn-Zr Sites in a Metal-Organic Framework for CO<sub>2</sub> Hydrogenation. *J. Am. Chem. Soc.* **2021**, *143*, 8829-8837.

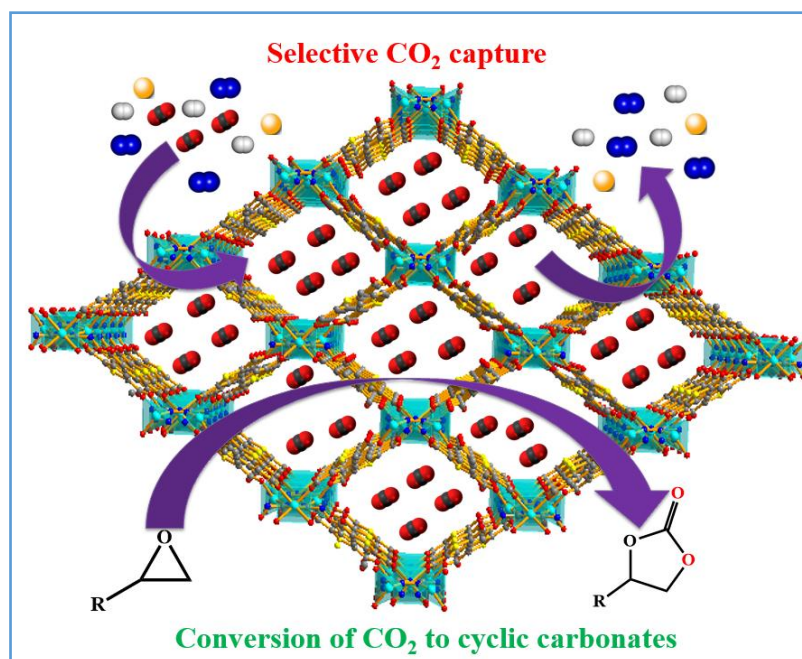
(140) Li, Y.; Zhang, S. L.; Cheng, W.; Chen, Y.; Luan, D.; Gao, S.; Lou, X. W. Loading Single-Ni Atoms on Assembled Hollow N-Rich Carbon Plates for Efficient CO<sub>2</sub> Electroreduction. *Adv. Mater.* **2022**, *34*, 2105204.

(141) Stanley, P. M.; Su, A. Y.; Ramm, V.; Fink, P.; Kimna, C.; Lieleg, O.; Elsner, M.; Lercher, J. A.; Rieger, B.; Warnan, J.; Fischer, R. A. Photocatalytic CO<sub>2</sub>-to-syngas Evolution with Molecular Catalyst Metal-organic Framework Nanozymes. *Adv. Mater.* **2023**, *35*, 2207380.

(142) Yao, X.; Chen, K.; Qiu, L.-Q.; Yang, Z.-W.; He, L.-N. Ferric Porphyrin-Based Porous Organic Polymers for CO<sub>2</sub> Photocatalytic Reduction to Syngas with Selectivity Control. *Chem. Mater.* **2021**, *33*, 8863-8872.

# Chapter 2a

**Construction of a bifunctional Zn(II)-  
organic framework containing basic amine  
functionality for selective capture and room  
temperature fixation of CO<sub>2</sub>**





### 2a.1. Introduction

The carbon dioxide (CO<sub>2</sub>) capture and utilization (CCU) as an abundant, non-toxic, C1 feedstock for the synthesis of valuable chemicals or fuels is one of the most promising solutions to mitigate the growing CO<sub>2</sub> concentration in the atmosphere.<sup>1,2</sup> To achieve this goal, several approaches have been developed for the functionalization of CO<sub>2</sub> into valuable chemicals like polycarbonates, cyclic carbonates, and others by forming C-C, C-N, and C-O bonds.<sup>3-14</sup> However, the kinetic inertness and thermodynamic stability of CO<sub>2</sub> puts limitations on its conversion under mild conditions.<sup>15</sup> Hence, the large-scale synthesis of cyclic carbonates is generally carried out at high temperature and pressure conditions.<sup>16-21</sup> Therefore, it is essential to develop efficient catalytic systems for selective capture and utilization of carbon dioxide under mild conditions of room temperature (RT). To date, various homogeneous catalysts have been developed for the conversion of CO<sub>2</sub> into cyclic carbonates owing to its 100% atom efficiency in generating cyclic carbonates with high yield and selectivity.<sup>22</sup> On the other hand, several heterogeneous catalysts including porous MOFs have been developed for the catalytic conversion of CO<sub>2</sub>.<sup>23-26</sup> Particularly, MOFs have attracted considerable attention due to their high surface area and modular nature which facilitates the introduction of a high density of Lewis acidic and basic functionalities.<sup>27</sup> However, there are limited number of MOFs reported for efficient carbon dioxide conversion at mild conditions of RT.<sup>28,29</sup> In this direction, we intend to synthesize porous MOFs composed of a high density of Lewis acidic metal ions and basic functionalities suitable for selective capture and utilization of CO<sub>2</sub>.<sup>30</sup> In this chapter, we report the synthesis of a novel 3D porous MOF, {[Zn<sub>2</sub>(TDC)<sub>2</sub>(DATRZ)].(3H<sub>2</sub>O).(DMF)}<sub>n</sub>, (Zn-DAT) constructed by utilizing a rigid ligand, 2,5-thiophene dicarboxylic acid (H<sub>2</sub>TDC), and an organic linker, 3,5-diamino-1,2,4-triazole (DATRZ) containing basic -NH<sub>2</sub> groups. The Zn-DAT MOF possesses a 3D microporous framework structure with two types of 1D channels of dimension 12.5 X 8.7 Å<sup>2</sup> and 7.0 X 4.8 Å<sup>2</sup> along the crystallographic *c*- and *b*-axis, respectively. Further, the presence of basic -NH<sub>2</sub> groups induce selective adsorption property for CO<sub>2</sub> with high heat of adsorption (Q<sub>st</sub>) value of 39.5 kJ/mol which was further supported by theoretically computed BE of 40.9 kJ/mol. More interestingly, the Q<sub>st</sub> value observed for Zn-DAT is about 8 kJ/mol higher than that of the analogs MOF, {[Zn<sub>2</sub>(TDC)(TRZ)<sub>2</sub>].(DMA).(MeOH)}<sub>n</sub>, (Zn-TAZ) containing 1,2,4-triazole (TAZ) linker, which further supports the critical role of -NH<sub>2</sub> groups in enhancing the interaction of CO<sub>2</sub> with the framework. Furthermore, the presence of Lewis acidic Zn(II) and basic -NH<sub>2</sub> groups make Zn-DAT MOF an excellent recyclable catalyst for the chemical fixation of CO<sub>2</sub> to cyclic carbonates under solvent-free mild conditions of RT.

In this chapter, the design and synthesis of a rare example of porous Zn(II)-MOF exhibiting efficient fixation of CO<sub>2</sub> at RT and the influence of -NH<sub>2</sub> groups on the BE of CO<sub>2</sub> and catalytic activity is demonstrated.

## 2a.2. Experimental section

### 2a.2.1. Materials

All the reagents used in this work were commercially available and used as received without any further purification. Zn(NO<sub>3</sub>)<sub>2</sub>·6H<sub>2</sub>O, 2,5-thiophene dicarboxylic acid, 3,5-diamino-1,2,4-triazole, and 1,2,4-triazole were purchased from Sigma Aldrich Chemical Co. The N, N'-dimethylformamide (DMF), N, N'-dimethylacetamide (DMA), and methanol (MeOH) were obtained from S. D. Fine Chem. Limited. All the epoxides and the internal standard used for catalytic reactions were purchased from TCI chemicals and used without further purification.

### 2a.2.2. Physicochemical characterization

The phase purity of the as-synthesized samples was confirmed by powder XRD analysis using Rigaku Miniflex 600 with Cu K $\alpha$  radiation ( $\lambda = 0.154$  nm). UV-Vis (Diffuse Reflectance) spectra were recorded on the Shimadzu spectrophotometer using BaSO<sub>4</sub> as a reference. Thermogravimetric analysis (TGA) of the compounds was carried out on Metler Toledo Thermogravimetric analyzer in an inert (N<sub>2</sub>) atmosphere with a flow rate of 30 mL/min in the temperature range of 30–600 °C and a heating rate of 5 °C/min. FTIR (Fourier transform infrared) spectra of the samples were recorded from 400 to 4000 cm<sup>-1</sup> on a Perkin Elmer ATR-FTIR spectrometer. Gas adsorption studies were carried out on Quantachrome QUADRASORB-SI automatic volumetric instrument. Thermo Fischer Flash 2000 Elemental Analyzer was used for elemental analysis (CHN) of the samples. The catalytic conversions were analyzed by recording <sup>1</sup>H-NMR spectra of the products on a JEOL JNM-ECS-400 spectrometer operating at a frequency of 400 MHz using 1,1',2,2'-tetrachloroethane as an internal standard.

### 2a.2.3. Synthesis

#### 2a.2.3.1. Synthesis of {[Zn<sub>2</sub>(TDC)<sub>2</sub>(DATRZ)].(3H<sub>2</sub>O).(DMF)}<sub>n</sub> (Zn-DAT)

The Zn-DAT MOF was synthesized as follows: 2,5-thiophene dicarboxylic acid (34.4 mg, 0.2 mmol) and 3,5-diamino-1,2,4-triazole (9.9 mg, 0.1 mmol) were mixed in DMF (4

mL) in a 30 mL glass vial. The mixture was sonicated for 15 min and to which DMF (2 mL) solution of  $\text{Zn}(\text{NO}_3)_2 \cdot 6\text{H}_2\text{O}$  (59.5 mg, 0.2 mmol) was added with stirring. The glass vial was sealed with Teflon and parafilm and heated at 120 °C for 72 h. Then the vial was cooled down to room temperature slowly to obtain colorless crystals of Zn-DAT which were collected by filtration and washed by DMF thoroughly. Yield: 75%. The phase purity of the as-synthesized sample was confirmed by powder XRD analysis (Figure A1). Elemental analysis calculated (%) for  $\{[\text{Zn}_2(\text{TDC})_2(\text{DATRZ})] \cdot (3\text{H}_2\text{O}) \cdot (\text{DMF})\}_n$  ( $\text{C}_{17}\text{H}_{21}\text{N}_6\text{O}_{15}\text{S}_2\text{Zn}_2$ ): C: 27.43; H: 2.84; N: 11.29; S: 8.62. Found: C: 28.03; H: 2.93; N: 11.91; S: 9.10. FT-IR (KBr,  $\text{cm}^{-1}$ ): 3441(w), 3330 (w), 3211 (w), 1586(s), 1518(s), 1463(w), 1355(s), 1103(m), 1015(m), 845(w), 804(m), 763(s), 674(m) (Figure A2).

#### 2a.2.3.2. Synthesis of $\{[\text{Zn}_2(\text{TDC})(\text{TRZ})_2] \cdot (\text{DMA}) \cdot (\text{MeOH})\}_n$ , (Zn-TAZ)

The analogues MOF,  $\{[\text{Zn}_2(\text{TDC})(\text{TRZ})_2] \cdot (\text{DMA}) \cdot (\text{MeOH})\}_n$ , (Zn-TAZ) was synthesized by following the previously reported procedure.<sup>31</sup> Briefly,  $\text{Zn}(\text{NO}_3)_2 \cdot 6\text{H}_2\text{O}$  (0.2 mmol, 60 mg), 2,5-thiophene dicarboxylic acid ( $\text{H}_2\text{tda}$ ) (14 mg, 0.1 mmol), and 1,2,4-triazole (TRZ) (0.2 mmol, 14 mg) were dissolved by 3 mL of DMA and 3 mL MeOH. The resulting mixture was transferred into a Teflon-lined stainless-steel vessel (23 mL) and heated at 100 °C for 72 h under autogenous pressure. Colourless crystals resulted were washed with DMA, MeOH, and dried at 120 °C under vacuum. The phase purity of the as-synthesized MOF was confirmed by powder XRD analysis (Figure A3).

#### 2a.2.4. Catalytic cycloaddition reactions of $\text{CO}_2$ with epoxides

The cycloaddition reaction of  $\text{CO}_2$  with various epoxides was carried out in a glass reactor (50 mL) under RT and 0.1/0.8 MPa pressure of  $\text{CO}_2$ . Before starting catalytic reactions, the Zn-DAT and Zn-TAZ were activated at 373K for 12 h under vacuum to remove guest solvent molecules. The reactants were taken in the reactor at room temperature and it was flushed with  $\text{CO}_2$  twice, and the required pressure (0.1/0.8 MPa) of  $\text{CO}_2$  was introduced and the contents were allowed to stir at RT. After 24 h, the excess  $\text{CO}_2$  was released slowly and the Zn-DAT catalyst was separated from the reaction mixture by filtration and centrifugation. The catalytic conversions were determined by  $^1\text{H}$  NMR spectra of the filtrate. The recovered catalyst was washed with methanol three times and activated at 373 K under vacuum for 12 h and reused for the subsequent catalytic cycles.

### 2a.2.5. X-ray crystallography

Single crystal X-ray structural data of Zn-DAT was collected on a CMOS-based Bruker D8 Venture PHOTON 100 diffractometer equipped with an INCOATEC micro-focus source with graphite monochromated Mo K $\alpha$  radiation ( $\lambda = 0.71073 \text{ \AA}$ ) operating at 50 kV and 30 mA. The SAINT<sup>32</sup> program was used for the integration of diffraction profiles and absorption correction was made with SADABS program.<sup>33</sup> The structures were solved by SIR 92<sup>34</sup> and refined by full-matrix least square method using SHELXL-2013<sup>35</sup> and WinGX system, Ver 2013.3.<sup>36</sup> The non-hydrogen atoms in all the structures were located from the difference Fourier map and refined anisotropically. All the hydrogen atoms were fixed by HFIX and placed in ideal positions and included in the refinement process using riding model with isotropic thermal parameters. The disordered guest solvent molecules were treated with the SQUEEZE option of PLATON<sup>37</sup> multipurpose software. Therefore, the formula of Zn-DAT was confirmed based on the elemental analyses and TGA. The potential solvent accessible area or void space was calculated using the PLATON software. All the crystallographic and structure refinement data of the Zn-DAT are summarized in Table 1. Selected bond lengths and angles are given in Table A1 and selected hydrogen bond details of the Zn-DAT are summarized in Table A2. The crystallographic information file is deposited with the CCDC number: 1918936.

### 2a.2.6. Gas adsorption measurements

N<sub>2</sub> adsorption-desorption studies were carried out at 77 and 273K, while CO<sub>2</sub> adsorption-desorption measurements were carried out at 273, 298, and 195K using QUANTACHROME Quadrasorb SI automated surface area and pore size analyzer instrument. For H<sub>2</sub> and Ar, the measurements were carried out at 273K. Ultrapure (99.995%) N<sub>2</sub>, He, H<sub>2</sub>, Ar, and CO<sub>2</sub> gases were used for the adsorption-desorption measurements. Prior to adsorption measurements, the sample (~0.150g) was evacuated at 373K under vacuum (20 mTorr) for 20 h on QUANTACHROME Flovac degasser and further purged with ultrapure N<sub>2</sub> (99.995%) gas on cooling. PXRD patterns of the activated samples revealed the retaining of the original framework structure after activation (Figures A1 and A3). The BET surface area of the MOFs was estimated from N<sub>2</sub> and CO<sub>2</sub> sorption isotherms carried out at 77 and 273K, respectively. The gas selectivity experiments were carried out at 273K. The dead volume of the sample cell was measured using Helium gas (99.995%).

**Table 1.** Crystal data and structure refinement parameters for Zn-DAT.

Parameters	Zn-DAT
Empirical formula	C <sub>14</sub> H <sub>8</sub> N <sub>5</sub> O <sub>8</sub> S <sub>2</sub> Zn <sub>2</sub>
Formula mass	569.17
Crystal system	Monoclinic
Space group	<i>C2/m</i>
<i>a</i> / Å	18.054(4)
<i>b</i> / Å	20.290(4)
<i>c</i> / Å	12.812(3)
$\alpha$ (degree)	90
$\beta$ (degree)	128(5)
$\gamma$ (degree)	90
<i>V</i> (Å <sup>3</sup> )	3688.7(14)
<i>Z</i>	4
<i>M</i> (mm <sup>-1</sup> )	1.443
<i>F</i> (000)	1132
<i>T</i> (K)	298
$\lambda$ (Mo K $\alpha$ ) (Å)	0.71073
$\theta_{\min}$ (deg)	2.3
$\theta_{\max}$ (deg)	26.8
total data	18973
unique data	3940
<i>R</i> <sub>int</sub>	0.042
Data [ <i>I</i> > 2 $\sigma$ ( <i>I</i> )]	2817
<sup>a</sup> <i>R</i> <sub>1</sub>	0.0787
<i>wR</i> <sub>2</sub>	0.2664
<i>S</i>	1.23
CCDC	1918936

$${}^aR_1 = \sum \|F_0\| - \|F_c\| / \sum \|F_0\|, \quad wR_2 = [\sum w(F_0^2 - F_c^2)^2 / \sum w(F_0^2)]^{1/2}$$

### 2a.2.7. Theoretical calculations

The CO<sub>2</sub> interaction with Zn-DAT was studied by density functional theory (DFT) calculations. All the calculations were performed with the DMOL3 package.<sup>38,39</sup> Generalized gradient approximations (GGA) along with Perdew, Bruke, and Ernzerhof (PBE) exchange-correlation functional was used. Double numeric polarization (DNP) basis set with the DFT-D Grimme function has been used to accurately demonstrate the weak van der Waals interactions.

The average CO<sub>2</sub> interaction energy ( $E_{Int}$ ) with Zn-DAT was determined using the following relation,

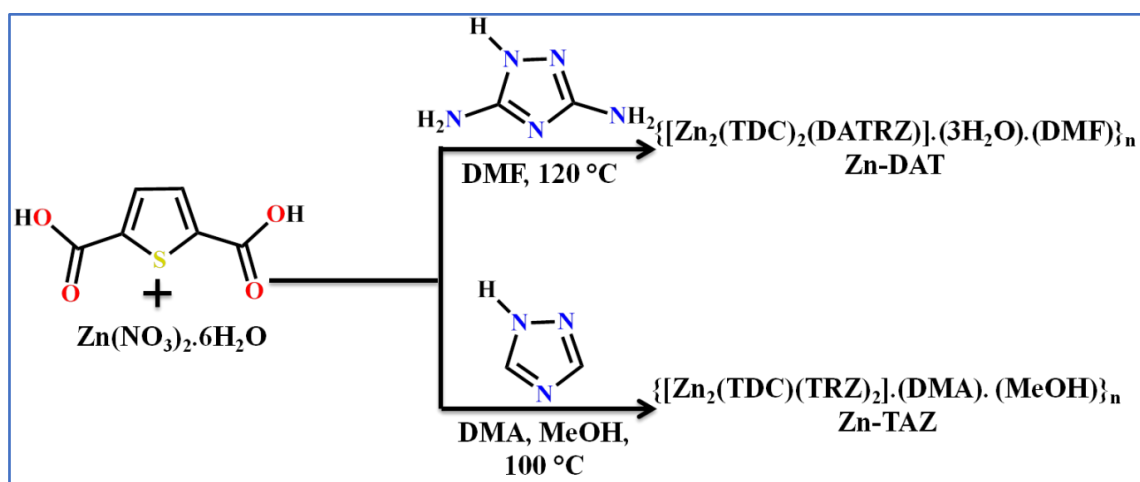
$$E_{Int} = \frac{1}{2} [E(MOF - DAT + 2CO_2) - E(MOF - DAT) - 2E(CO_2)]$$

Here,  $E(MOF - DAT + 2CO_2)$  is the total energy of two molecules of CO<sub>2</sub> interacting with Zn-DAT,  $E(MOF - DAT)$  and  $2E(CO_2)$  are the energy of Zn-DAT and the energy of CO<sub>2</sub> molecules, respectively.

## 2a.3. Results and discussion

### 2a.3.1. Synthesis and structural description

The reaction of Zn(NO<sub>3</sub>)<sub>2</sub>·6H<sub>2</sub>O with a 2,5-thiophene dicarboxylic acid (H<sub>2</sub>TDC) and 3,5-diamino-1,2,4-triazole (DATRZ) in DMF at 120 °C for three days afforded colorless crystals of Zn-DAT (Scheme 1). X-ray single-crystal structural determination revealed that the compound crystallizes in the monoclinic crystal system with the *C2/m* space group (Table 1). The asymmetric unit consists of two distinct binuclear Zn(II) units, two 2,5-thiophene dicarboxylates (TDC) anions, and one 3,5-diamino-1,2,4-triazole (DATRZ) linker (Figure 1).



**Scheme 1.** The synthesis scheme of Zn-DAT and Zn-TAZ MOFs.

The Zn-O and Zn-N bond lengths are in the range of 1.955-2.031 Å and 1.972-1.993 Å, respectively (Table A1). The structure shows N-H...O hydrogen bonding interactions between the -NH<sub>2</sub> groups of the DATRZ ligand and the carboxylate oxygens of the TDC ion (Table A2). The coordination environment at Zn1 in the [Zn1N1O1]<sub>2</sub> binuclear unit is satisfied by two carboxylate oxygen (O1 and O1a,  $a = 1-x, y, -z$ ) atoms of TDC ion and two nitrogen (N1 and N1a,  $a = 1-x, y, -z$ ) atoms of DATRZ linker. Whereas, the coordination at Zn2 in the Zn<sub>2</sub>(COO)<sub>4</sub> paddle-wheel secondary building unit (SBU) is satisfied by four carboxylate oxygen (O3, O3b, O4, and O4b,  $b = x, 2-y, z$ ) atoms of two TDC ligands.

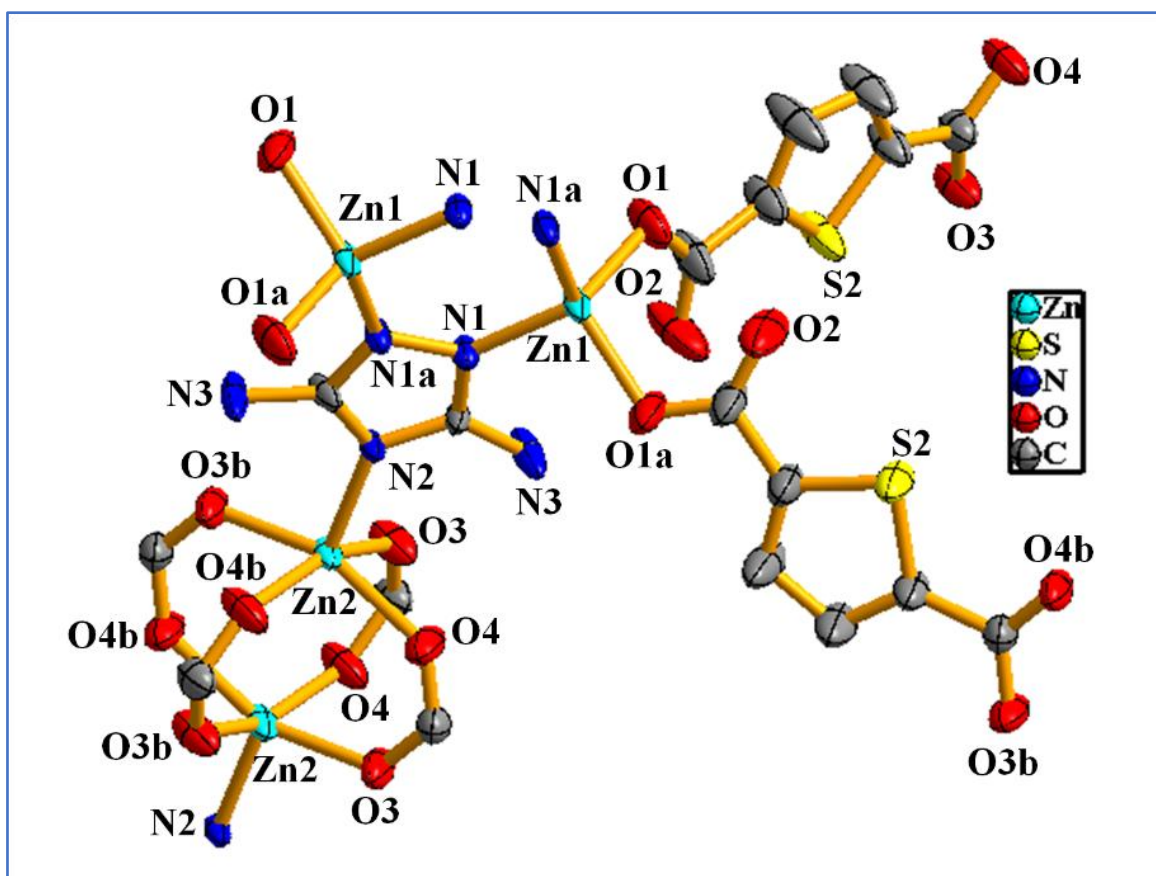


**Figure 1.** The asymmetric unit of Zn-DAT MOF showing the coordination environment at the Zn(II) sites (hydrogens and guest solvent molecules are omitted for clarity, symmetry operations:  $a = 1-x, y, -z$  and  $b = x, 2-y, z$ ).

As shown in Figure 2, the Zn(II) ions are bridged by the nitrogens of the DATRZ linker and the carboxylate groups of TDC ions forming a three-dimensional (3D) microporous framework with two types of 1D channels of dimension 12.5 X 8.7 Å<sup>2</sup> and 7.0 X 4.8 Å<sup>2</sup> along the crystallographic *c*- and *b*-axis, respectively (Figure 2 and A4). Further, the -NH<sub>2</sub> groups of the DATRZ linker are free and exposed in the 1D channels of the framework

(Figure 2c). Topological analysis by TOPOS<sup>40</sup> suggests that the framework has 6-connected uni-nodal *pcu*-net topology with vertex symbol of  $\{4^6\}$  (Figure 2d and A5). Further, the effective solvent-accessible void was estimated to be 57.0% (3688.7 Å<sup>3</sup>) per unit cell calculated using PLATON<sup>41</sup> software after the removal of guest solvent molecules.

In order to get more insight into the critical role of basic -NH<sub>2</sub> groups on the high heat of adsorption value (39.5 kJ/mol) for CO<sub>2</sub>, we synthesized an analogues MOF,  $\{[\text{Zn}_2(\text{TDC})(\text{TRZ})_2]\cdot(\text{DMA})\cdot(\text{MeOH})\}_n$ , (Zn-TAZ) containing 1, 2, 4-triazole ligand which lacks basic -NH<sub>2</sub> groups. As shown in Figure 3, the crystal structure of Zn-TAZ reported before shows the presence of a 1D channel along the crystallographic *a*- and *c*-axis free from -NH<sub>2</sub> groups.

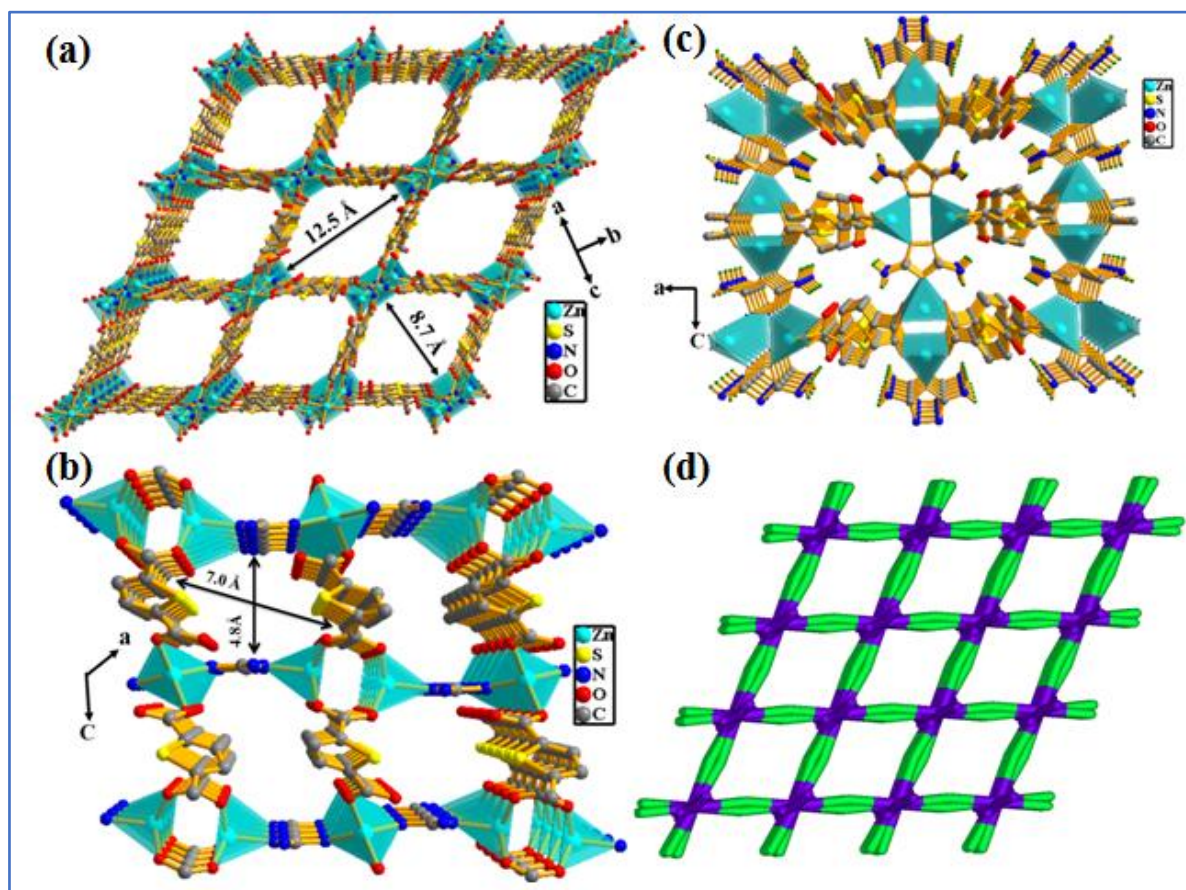


**Figure 2.** (a) View of the 3D framework of Zn-DAT MOF showing the presence of rectangular 1D channels of dimension 12.5 X 8.7 Å<sup>2</sup> along the crystallographic *c*-axis and (b) 1D channels of dimension 7.0 X 4.8 Å<sup>2</sup> along *b*-axis (c) the presence of free -NH<sub>2</sub> groups of DATRZ in the 1D channels and (d) TOPOS picture of the MOF.

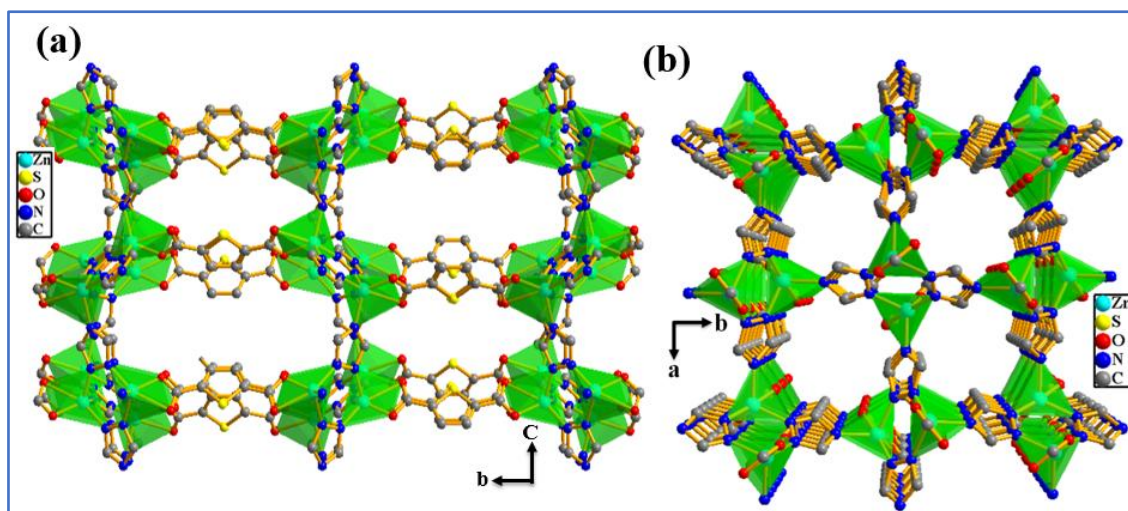


**Figure 3.** View of the 3D framework of Zn-TAZ MOF showing the presence of 1D channel (a) along the crystallographic *a*-axis (b) along the crystallographic *c*-axis.

### 2a.3.2. Thermogravimetric analysis of Zn-DAT MOF

Thermogravimetric analysis of as-synthesized Zn-DAT MOF shows a weight loss of ~8% (calc wt% 7.7) around RT-120 °C corresponding to the loss of three guest water molecules. The second weight loss of ~11.5% (calc wt% 11.38) around 120-200 °C corresponds to the loss of a guest DMF molecule. Whereas, the third weight loss of ~47% (calc wt% 47.6) around 220-380 °C is due to the combined loss of TDC and DATRZ linker. On the other hand, the activated sample of Zn-DAT MOF does not show any weight loss up to 200 °C, indicating the absence of guest solvent molecules (Figure 4).

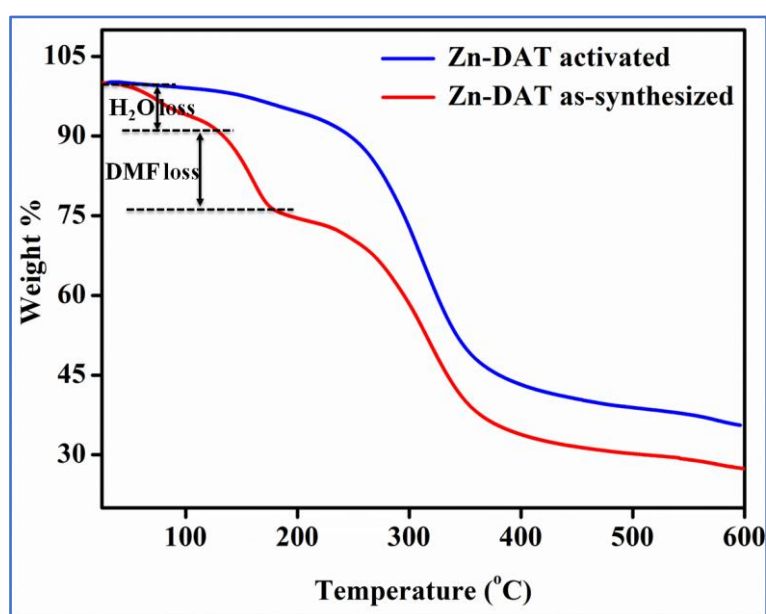


**Figure 4.** Thermogravimetric analysis of Zn-DAT MOF.

### 2a.3.3. Gas adsorption studies

As discussed before, Zn-DAT MOF is microporous with two types of 1D channels of dimension  $12.5 \times 8.7 \text{ \AA}^2$  and  $7.0 \times 4.8 \text{ \AA}^2$  along the crystallographic *c*- and *b*-axis, respectively. To determine the permanent porosity of the sample, N<sub>2</sub> adsorption-desorption measurements were carried out. Before starting the adsorption measurements, the as-synthesized sample was activated at an elevated temperature of 373 K under vacuum (18 mTorr) for 15 h to obtain solvent-free MOF. The powder X-ray diffraction (PXRD) pattern of the activated MOF confirmed the retention of its original framework structure (Figure A1). Further, the N<sub>2</sub> adsorption isotherm of Zn-DAT MOF shows a type-I profile supporting the microporous nature of the MOF and the estimated Brunauer-Emmett-Teller (BET) surface area was found to be  $51.6 \text{ m}^2/\text{g}$  (Figure A6). Furthermore, CO<sub>2</sub> adsorption isotherms follow a typical type-I behaviour with the uptake of 59.54, 27.07 and 17.64 cc/g carried out at 195, 273, and 298 K, respectively (Figure 5a, 6a). Moreover, the adsorption isotherms of CO<sub>2</sub> were analyzed with the Langmuir-Freundlich equation<sup>42</sup> (Figure A7 and A8) to get the exact prediction of CO<sub>2</sub> gas adsorbed at saturation. The calculated value of heat of adsorption ( $Q_{st}$ ) for CO<sub>2</sub> was found to be 39.5 kJ/mol following the Clausius-Clayperon equation<sup>43</sup> (Figure A9). The moderately high value of  $Q_{st}$  indicates stronger interaction of CO<sub>2</sub> gas with the basic -NH<sub>2</sub> groups present in the 1D channel of Zn-DAT MOF.<sup>44</sup> To get further support on the role of -NH<sub>2</sub> groups on the high value of  $Q_{st}$ , gas adsorption studies of the analogous MOF, Zn-TAZ containing 1,2,4-triazole (TAZ) ligand instead of 3,5-diaminotriazole was carried out. The estimated Brunauer-Emmett-Teller (BET) surface area of Zn-TAZ MOF was found to be  $46.76 \text{ m}^2/\text{g}$  based on the N<sub>2</sub> adsorption isotherm carried out at 77 K (Figure A6). Moreover, the CO<sub>2</sub> adsorption isotherms carried out at 273 and 298 K (Figure 7) were analyzed with the Langmuir-Freundlich equation (Figure A8) to get the exact prediction of CO<sub>2</sub> gas adsorbed at saturation and the calculated value of heat of adsorption was found to be 31.7 kJ/mol (Figure A9) which was about 8 kJ/mol lower than that of Zn-DAT (39.5 kJ/mol) MOF. These results highlight the role of basic -NH<sub>2</sub> groups in enhancing the interaction energy of CO<sub>2</sub> with Zn-DAT MOF. Furthermore, CO<sub>2</sub> selectivity studies of Zn-DAT MOF with other gases like N<sub>2</sub>, Ar, and H<sub>2</sub> revealed negligible uptake of 1.85, 2.16, and 1.91 cc/g for N<sub>2</sub>, Ar, and H<sub>2</sub>, respectively (Figure 5b). Thus, the observed selective uptake of CO<sub>2</sub> by Zn-DAT MOF can be attributed to the presence of basic -NH<sub>2</sub> functionalized 1D channels.<sup>45</sup> The estimated gas selectivity constants following Henry's law for CO<sub>2</sub>/H<sub>2</sub>, CO<sub>2</sub>/Ar, and CO<sub>2</sub>/N<sub>2</sub> were found to be 40, 38, and 34, respectively (Figure A10 and A11). The relatively high value of the gas

selectivity constant for CO<sub>2</sub> over other gases indicates the potential scope of Zn-DAT MOF for selective capture of CO<sub>2</sub> from other gases like N<sub>2</sub>, Ar, and H<sub>2</sub>.

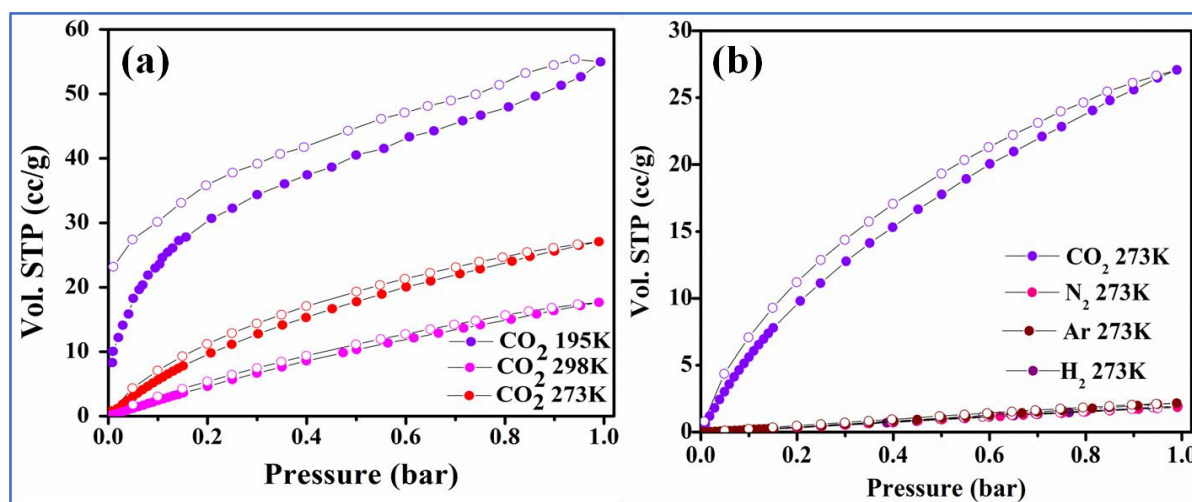


**Figure 5.** (a) CO<sub>2</sub> adsorption-desorption isotherms of Zn-DAT MOF carried out at 195, 273, and 298 K, (b) Selectivity study for CO<sub>2</sub> over other (H<sub>2</sub>, Ar, and N<sub>2</sub>) gases carried out at 273 K.

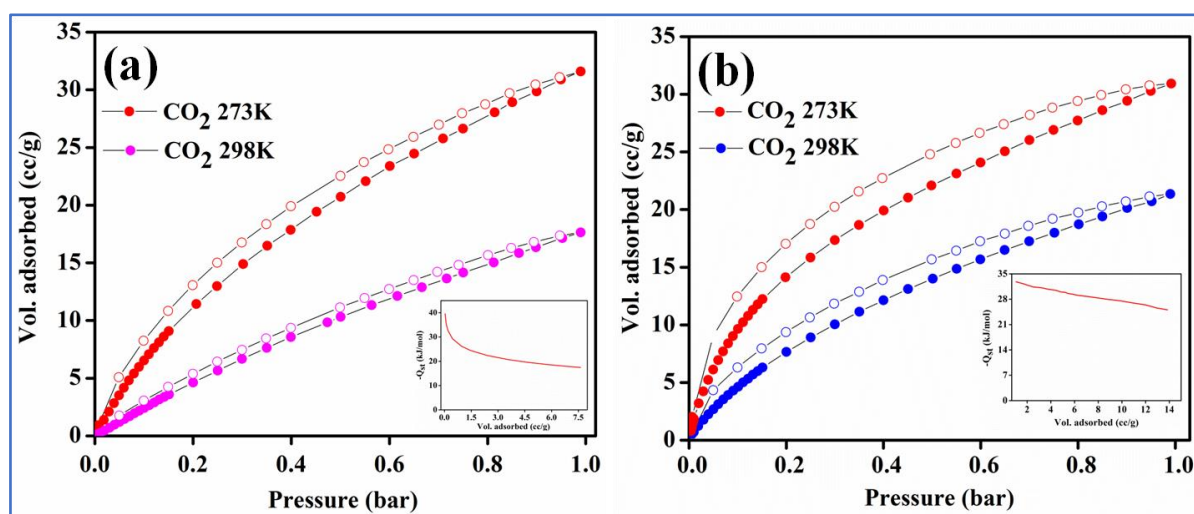


**Figure 6.** CO<sub>2</sub> adsorption-desorption isotherms of MOFs carried out at 273 and 298 K, (a) Zn-DAT MOF and (b) Zn-TAZ MOF (insets show enthalpy of CO<sub>2</sub> adsorption).

#### 2a.3.4. Theoretical study

To further establish the interaction of CO<sub>2</sub> with the -NH<sub>2</sub> groups of DATRZ linker exposed in the 1D channels of Zn-DAT MOF, theoretical calculations were performed considering a single 1D pore of MOF as shown in Figure 7a. Further, two CO<sub>2</sub> molecules were placed in the pore space of Zn-DAT MOF and the resulting structures were optimized.

As shown in Figure 7b, the CO<sub>2</sub> molecules are interacting with the -NH<sub>2</sub> groups present in the 1D channels through HN-H...OCO and H-N-H...OCO...H-N-H) interactions with the bond distances ranging from 2.785 to 3.781 Å indicated as type-I and type-II, respectively. The computed average CO<sub>2</sub> binding energy (BE) was found to be 40.9 kJmol<sup>-1</sup> which is very close to the experimentally determined heat of adsorption value of 39.5 kJ/mol. Moreover, the bond angle of CO<sub>2</sub> molecules deviates from 180° to 177.5° and 178.2° in the case of type-I and II, respectively supporting the interaction of CO<sub>2</sub> molecules with the -NH<sub>2</sub> groups of DATRZ linker.

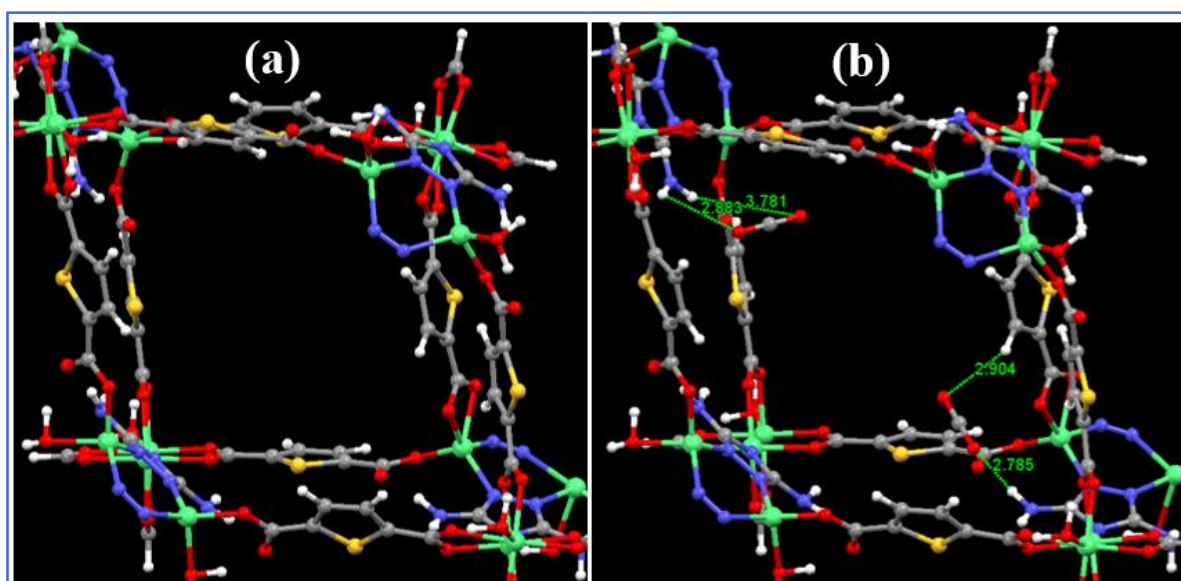


**Figure 7.** (a) Optimized structure of Zn-DAT MOF showing the 1D pore and (b) with two CO<sub>2</sub> molecules interacting with the -NH<sub>2</sub> groups of DATRZ linker.

### 2a.3.5. Catalytic cycloaddition reaction of CO<sub>2</sub>

The selective CO<sub>2</sub> adsorption property and the presence of both Lewis acidic Zn(II) sites and basic -NH<sub>2</sub> groups motivated us to study the catalytic activity of Zn-DAT MOF for the cycloaddition of CO<sub>2</sub> to cyclic carbonates. Initially, the catalytic activity was tested at the mild conditions of 0.1 MPa (1 bar) and RT (25 °C) for the cycloaddition of CO<sub>2</sub> with 1, 2-epoxypropane (PO) as a model substrate in the presence of tetrabutylammonium bromide (TBAB) as cocatalyst. Remarkably, about 51% of PO was converted to the corresponding cyclic carbonate within 24 h (Table 2). Comparison of the catalytic activity with the literature-reported MOFs revealed the higher activity of Zn-DAT for catalytic cycloaddition of CO<sub>2</sub> to PO under mild conditions of 1 bar and RT (Table 3) highlighting the excellent catalytic activity of Zn-DAT MOF for chemical fixation of CO<sub>2</sub>. Further, upon increasing the

pressure of CO<sub>2</sub> from 1 bar to 8 bar (0.8 MPa) resulted in almost complete conversion (> 99%) of PO to the corresponding cyclic carbonate (Table 2). Encouraged by the high catalytic activity of Zn-DAT MOF, the cycloaddition reaction of CO<sub>2</sub> was extended to other epoxides with increasing alkyl chain length and the results are shown in Table 2. Interestingly, the cycloaddition reaction of smaller epoxides like epichlorohydrin (ECH) and 1,2-epoxybutane (BO) with CO<sub>2</sub> yielded the corresponding cyclic carbonate with > 99% conversion (Table 2). This observation can be attributed to the presence of a large 1D channel in Zn-DAT (12.5 X 8.7 Å<sup>2</sup>) MOF which is a good fit for the epoxides to diffuse in and react with the catalytic Zn(II) sites (Table A3). While, the relatively lower conversion of longer epoxides, such as 1,2-epoxyhexane, allyl glycidyl ether, butyl glycidyl ether, and 1,2-epoxydecane compared to that of ECH can be attributed to the restricted diffusion of the epoxides in the 1D channels (Table 2). Whereas, considerably lower conversion of 1,2-epoxydecane can be attributed to the bigger size of the epoxide (~13.32 X 3.39 Å<sup>2</sup>) compared to the pore size of Zn-DAT MOF. Furthermore, no formation of side products was observed and the selectivity for the cyclic carbonates was 100%. Further, the catalytic activity of Zn-TAZ was investigated under similar optimized conditions for cycloaddition of ECH and BO, interestingly about 89% and 87% conversion of the epoxides to corresponding cyclic carbonates was observed, respectively in 24 h (Table 2) which are slightly lower than the conversions observed for the Zn-DAT MOF. The relatively higher catalytic activity of Zn-DAT MOF over Zn-TAZ can be attributed to the CO<sub>2</sub>-philic nature of the former MOF owing to the presence of basic -NH<sub>2</sub> groups in the 1D channel. Hence, from this discussion, it is clear that Zn-DAT acts as an efficient catalyst for the cycloaddition of CO<sub>2</sub> with various epoxides under mild conditions of RT. Controlled experiments carried out in the absence of Zn-DAT under similar reaction conditions showed the conversion of only 44% of ECH to the corresponding cyclic carbonate. Further, there is no conversion of ECH was observed in the absence of TBA. Therefore, from the above-mentioned discussion, it is clear that synergistic cooperation between the MOF catalyst and TBAB is essential for the high-yield generation of cyclic carbonate by efficient cycloaddition of CO<sub>2</sub> with epoxides at mild conditions of RT.

**Table 2.** Catalytic performance of Zn-DAT for cycloaddition reaction of CO<sub>2</sub> with various epoxides carried out at RT.<sup>a</sup>

Entry No.	Substrate (R)	Product	Catalyst	Conversion <sup>c</sup> (%)
1			Zn-DAT	51 <sup>b</sup>
2			Zn-DAT	>99
3			Zn-DAT	>99
4			Zn-TAZ	89
5			Zn-DAT	>99
6			Zn-TAZ	87
7			Zn-DAT	78
8			Zn-DAT	40
9			Zn-DAT	66
10			Zn-DAT	60

<sup>a</sup>Reaction conditions: epoxide (20 mmol), catalyst (0.4 mol %), cocatalyst: TBAB (4 mol%), RT (25 °C), pressure 0.8 MPa, and time: 24 h. <sup>b</sup> Time is 12 h and other conditions are same.

<sup>c</sup>The catalytic conversions of epoxides were determined by <sup>1</sup>H NMR analysis.

**Table 3.** Comparison of catalytic activity of Zn-DAT for cycloaddition of CO<sub>2</sub> to PO with various MOFs reported in the literature.<sup>a</sup>

Catalyst (mol%)	Time (h)	Temperature (°C)	Pressure (MPa)	Yield (%)	Ref.
Cu(tactmb)	48	RT	0.1	47.5	13a
HKUST-1	48	RT	0.1	49	
MOF-505	48	RT	0.1	48	13b
MMPF-9	48	RT	0.1	87.4	46
<b>Zn-DAT</b>	<b>24</b>	<b>RT</b>	<b>0.1</b>	<b>51</b>	<b>This work</b>
ZnGlu	24	RT	1.0	65	13c
Cr-MIL-101	24	RT	0.8	82	13e
Fe-MIL-101	24	RT	0.8	87	
UMCM-1	24	RT	1.2	85	47
UMCM-1NH <sub>2</sub>	24	RT	1.2	90	
MOF-Zn-1	24	RT	1.0	98	47
<b>Zn-DAT</b>	<b>24</b>	<b>RT</b>	<b>0.8</b>	<b>&gt;99</b>	<b>This work</b>

<sup>a</sup>Reaction condition: propylene oxide (PO), TBAB as co-catalyst, RT = room temperature.

### 2a.3.6. Recyclability test

To test the recyclability, Zn-DAT MOF was separated from the reaction mixture by centrifugation followed by washing with methanol and activation at 373 K and it was reused for subsequent catalytic cycles for cycloaddition of ECH with CO<sub>2</sub> under the optimized conditions of RT and 0.8 MPa. Interestingly, no significant decrease in the catalytic activity was observed even after five cycles (Figure 8). Further, the PXRD pattern of the recycled sample after five cycles matches well with the parent MOF suggesting retention of the original framework structure after catalysis (Figure A1).

### 2a.3.7. Plausible mechanism

A plausible mechanism for the catalytic cycloaddition reaction of CO<sub>2</sub> with epoxides catalyzed by Zn-DAT MOF is shown in Scheme 2 it involves a binary catalytic system composed of a Lewis acidic Zn(II) site and a TBAB co-catalyst which is essential for ring-opening of the epoxides.<sup>49</sup> As proposed in Scheme 2, the first step involves the coordination of the epoxide to the Lewis acidic Zn(II) site followed by the polarization of CO<sub>2</sub> molecule

through interaction with the basic  $\text{-NH}_2$  groups of DATRZ linker which were further supported by the theoretical calculations discussed before.<sup>50</sup> Then, ring-opening of the epoxide takes place by nucleophilic attack of  $\text{Br}^-$  anion of TBAB at the less hindered  $\beta$ -carbon atom of the epoxide. The subsequent intramolecular ring-closure reaction by a nucleophilic attack of the oxyanion with  $\text{CO}_2$  generates cyclic carbonate which undergoes reductive elimination to regenerate the catalyst and the catalytic cycle continues.

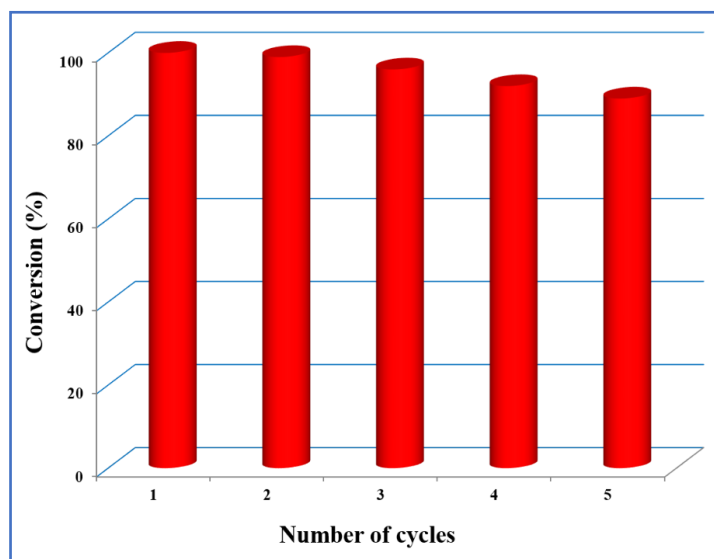
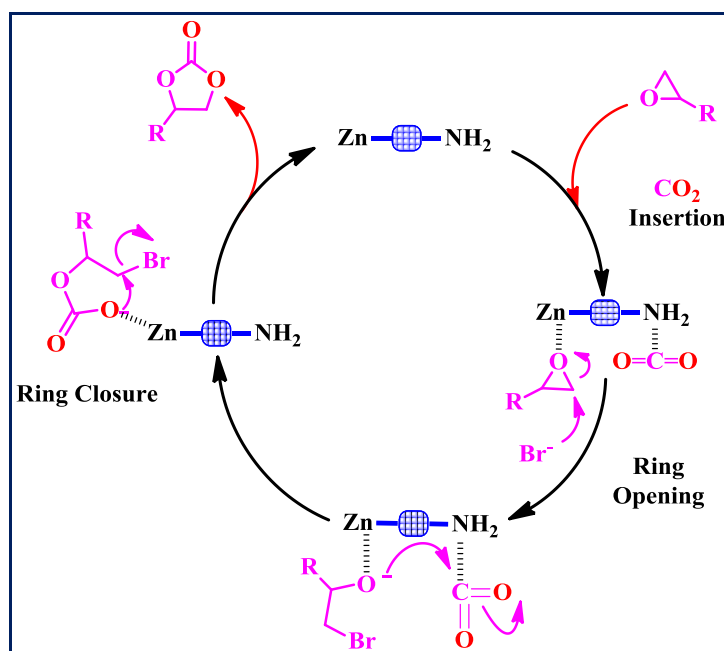


**Figure 8.** Recyclability of Zn-DAT for five consecutive cycles.



**Scheme 2.** Proposed mechanism for the catalytic cycloaddition of epoxides to  $\text{CO}_2$  catalyzed by Zn-DAT MOF.

#### 2a.4. Conclusion

In summary, this work demonstrates the synthesis of a novel 3D, microporous, bifunctional MOF,  $\{[\text{Zn}_2(\text{TDC})_2(\text{DATRZ})].(3\text{H}_2\text{O}).(\text{DMF})\}_n$  (Zn-DAT) by solvothermal route using mixed ligand strategy. Further, the MOF features a 3D framework structure with two types of 1D channels of dimension  $12.5 \times 8.7 \text{ \AA}^2$  and  $7.0 \times 4.8 \text{ \AA}^2$  along the crystallographic *c*- and *b*-axis, respectively. Due to the presence of basic  $-\text{NH}_2$  functionalized pores, Zn-DAT MOF shows selective adsorption of  $\text{CO}_2$  with a high heat of adsorption ( $Q_{\text{st}}$ ) value of 39.5 kJ/mol which is further confirmed by the theoretical BE of 40.9 kJ/mol. Interestingly, the  $Q_{\text{st}}$  value observed for Zn-DAT is about 8 kJ/mol higher than the analogues MOF,  $\{[\text{Zn}_2(\text{TDC})(\text{TRZ})_2].(\text{DMA}).(\text{MeOH})\}_n$ , (Zn-TAZ) containing 1,2,4-triazole (TAZ) linker, which supports the critical role of the  $-\text{NH}_2$  group for  $\text{CO}_2$  capture. The significantly high value of  $Q_{\text{st}}$  indicates stronger interaction of Lewis acidic  $\text{CO}_2$  molecules with the basic  $-\text{NH}_2$  groups present in the 1D channels of Zn-DAT. Furthermore, the Zn-DAT MOF acts as a bifunctional heterogeneous catalyst for the conversion of  $\text{CO}_2$  into cyclic carbonates under solvent-free mild conditions of RT. This work demonstrates the influence of basic  $-\text{NH}_2$  groups on the selective capture and conversion of  $\text{CO}_2$  into cyclic carbonates at mild conditions.

#### 2a.5. References

- (1) Jacobson, M. Z. Review of solutions to global warming, air pollution, and energy security. *Energy Environ. Sci.* **2009**, 2, 148-173.
- (2) Chu, S. Carbon Capture and Sequestration. *Science* **2009**, 325, 1599.
- (3) Li, Y. N.; Ma, R.; He, L. N.; Diao, Z. F. Homogeneous hydrogenation of carbon dioxide to methanol. *Catal. Sci. Technol.* **2014**, 4, 1498-1512.
- (4) Sakakura, T.; Choi, J. C.; Yasuda, H. Transformation of Carbon Dioxide. *Chem. Rev.* **2007**, 107, 2365-2387.
- (5) Duval, A.; Avérous, L. Cyclic Carbonates as Safe and Versatile Etherifying Reagents for the Functionalization of Lignins and Tannins. *ACS Sustainable Chem. Eng.* **2017**, 5, 7334-7343.
- (6) Das, R.; Ezhil, T.; Palakkal, A. S.; Muthukumar, D.; Pillai, R. S.; Nagaraja, C. M. Efficient chemical fixation of  $\text{CO}_2$  from direct air under environment-friendly co-catalyst and solvent-free ambient conditions. *J. Mater. Chem. A* **2021**, 9, 23127-23139.
- (7) Jones, W. D. Carbon Capture and Conversion. *J. Am. Chem. Soc.* **2020**, 142, 4955-4957.

- (8) Das, R.; Nagaraja, C. M. Noble metal-free Cu(I)-anchored NHC-based MOF for highly recyclable fixation of CO<sub>2</sub> under RT and atmospheric pressure conditions. *Green Chem.* **2021**, *23*, 5195-5204.
- (9) Katelhon, A.; Meys, R.; Deutz, S.; Suh, S.; Bardow, A. Climate change mitigation potential of carbon capture and utilization in the chemical industry. *Proc. Natl. Acad. Sci. U. S. A.* **2019**, *116*, 11187-11194.
- (10) Sharma, N.; Dhankhar, S. S.; Kumar, S.; Kumar, T. J. D.; Nagaraja, C. M. Rational Design of a 3D Mn<sup>II</sup>-Metal-Organic Framework Based on a Nonmetallated Porphyrin Linker for Selective Capture of CO<sub>2</sub> and One-Pot Synthesis of Styrene Carbonates. *Chem. Eur. J.* **2018**, *24*, 16662-16669.
- (11) Liu, Q.; Wu, L.; Jackstell, R.; Beller, M. Using carbon dioxide as a building block in organic synthesis. *Nat. Commun.* **2015**, *6*, 5933.
- (12) Sakakura, T.; Choi, J. C.; Yasuda, H. Transformation of Carbon Dioxide. *Chem. Rev.* **2007**, *107*, 2365-2387.
- (13) Das, R.; Dhankhar, S. S.; Nagaraja, C. M. Construction of a bifunctional Zn(II)-organic framework containing basic amine functionality for selective capture and room temperature fixation of CO<sub>2</sub>. *Inorg. Chem. Front.* **2020**, *7*, 72-81.
- (14) Peter, S. C. Reduction of CO<sub>2</sub> to Chemicals and Fuels: A Solution to Global Warming and Energy Crisis. *ACS Energy Lett.* **2018**, *3*, 1557-1561.
- (15) Yun, D.; Park, D. S.; Lee, K. R.; Yun, Y. S.; Kim, T. Y.; Park, H.; Lee, H.; Yi, J. A New Energy-Saving Catalytic System: Carbon Dioxide Activation by a Metal/Carbon Catalyst. *ChemSusChem* **2017**, *10*, 3671-3678.
- (16) Liu, Q.; Wu, L.; Jackstell, R.; Beller, M. Using carbon dioxide as a building block in organic synthesis. *Nat. Commun.* **2015**, *6*, 5933.
- (17) Yuan, Y.; Li, J.; Sun, X.; Li, G.; Liu, Y.; Verma, G.; Ma, S. Indium-Organic Frameworks Based on Dual Secondary Building Units Featuring Halogen-Decorated Channels for Highly Effective CO<sub>2</sub> Fixation. *Chem. Mater.* **2019**, *31*, 1084-1091.
- (18) Ugale, B.; Dhankhar, S. S.; Nagaraja, C. M. Construction of 3-Fold-Interpenetrated Three-Dimensional Metal-Organic Frameworks of Nickel(II) for Highly Efficient Capture and Conversion of Carbon Dioxide. *Inorg. Chem.* **2016**, *55*, 9757-9766.
- (19) Wu, P.; Li, Y.; Zheng, J.-J.; Hosono, N.; Otake, K.; Wang, J.; Liu, Y.; Xia, L.; Jiang, M.; Sakaki, S.; Kitagawa, S. Carbon dioxide capture and efficient fixation in a dynamic porous coordination polymer. *Nat. Commun.* **2019**, *10*, 4362.

- (20) Das, R.; Muthukumar, D.; Pillai, R. S.; Nagaraja, C. M. Rational design of a Zn(II)-MOF with multiple functional sites for highly efficient fixation of CO<sub>2</sub> at mild conditions: combined experimental and theoretical investigation. *Chem. Eur. J.* **2020**, *26*, 17445-17454.
- (21) Baalbaki, H. A.; Roshandel, H.; Hein, J. E.; Mehrkhodavandi, P. Conversion of dilute CO<sub>2</sub> to cyclic carbonates at sub-atmospheric pressures by a simple indium catalyst. *Catal. Sci. Technol.* **2021**, *11*, 2119-2129.
- (22) Liu, M.; Gao, K.; Liang, L.; Sun, J.; Sheng, L.; Arai, Experimental and theoretical insights into binary Zn-SBA-15/KI catalysts for the selective coupling of CO<sub>2</sub> and epoxides into cyclic carbonates under mild condition. *Catal. Sci. Technol.* **2016**, *6*, 6406-6416.
- (23) Liang, J.; Huang, Y.-B.; Cao, R. Metal-organic frameworks and porous organic polymers for sustainable fixation of carbon dioxide into cyclic carbonates. *Coord. Chem. Rev.* **2019**, *378*, 32-65.
- (24) Ding, M.; Flaig, R. W.; Jiang, H.-L.; Yaghi, O. M. Carbon capture and conversion using metal-organic frameworks and MOF-based materials. *Chem. Soc. Rev.* **2019**, *48*, 2783-2828.
- (25) Dhankhar, S. S.; Ugale, B.; Nagaraja, C. M. Co-Catalyst-Free Chemical Fixation of CO<sub>2</sub> into Cyclic Carbonates by using Metal-Organic Frameworks as Efficient Heterogeneous Catalysts. *Chem Asian J.* **2020**, *15*, 2403-2427.
- (26) Pal, T. K.; De, D.; Bhardwaj, P. K. Metal-organic frameworks for the chemical fixation of CO<sub>2</sub> into cyclic carbonates. *Coord. Chem. Rev.* **2020**, *408*, 213173.
- (27) Vaidhyanathan, R.; Iremonger, S. S.; Shimizu, G. K. H.; Boyd, P. G.; Alavi, S.; Woo, T. K. Direct Observation and Quantification of CO<sub>2</sub> Binding Within an Amine-Functionalized Nanoporous Solid, *Science* **2010**, *330*, 650-653.
- (28) Gao, W. Y.; Chen, Y.; Niu, Y.; Williams, K.; Cash, L.; Perez, P. J.; Wojtas, L.; Cai, J.; Chen, Y. S.; Ma, S. Crystal Engineering of an nbo Topology Metal-Organic Framework for Chemical Fixation of CO<sub>2</sub> under Ambient Conditions. *Angew. Chem. Int. Ed.* **2014**, *53*, 2615-2619.
- (29) Kathalikkattil, A. C.; Roshan, R.; Tharun, J.; Babu, R.; Jeong, G. S.; Kim, D. W.; Cho, S. J.; Park, D. W. A sustainable protocol for the facile synthesis of zinc-glutamate MOF: an efficient catalyst for room temperature CO<sub>2</sub> fixation reactions under wet conditions. *Chem. Commun.* **2016**, *52*, 280-283.
- (30) Ugale, B.; Kumar, S.; Kumar, T. J. D.; Nagaraja, C. M. Environmentally Friendly, Co-catalyst-Free Chemical Fixation of CO<sub>2</sub> at Mild Conditions Using Dual-Walled Nitrogen-Rich Three-Dimensional Porous Metal-Organic Frameworks, *Inorg. Chem.* **2019**, *58*, 3925-3936.

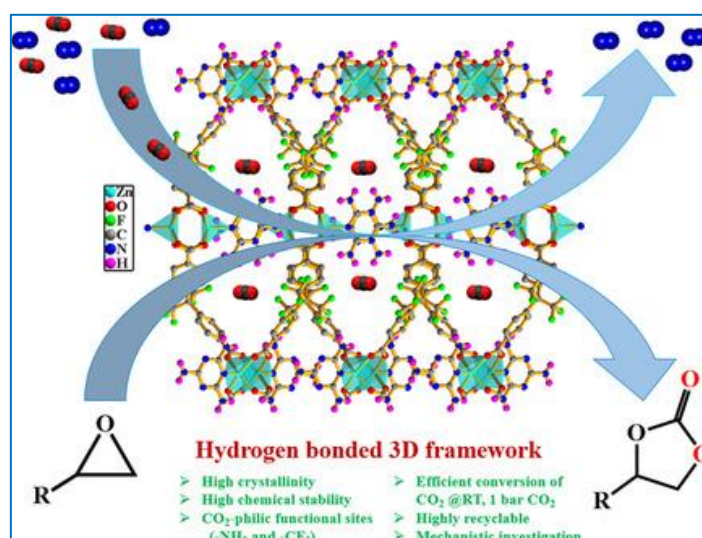
- (31) Liu, F.-H.; Qin, C.; Ding, Y.; Wu, H.; Shaoa, K.-Z.; Su, Z.-M. Pillared metal organic frameworks for the luminescence sensing of small molecules and metal ions in aqueous solutions. *Dalton Trans.* **2015**, *44*, 1754-1760.
- (32) SMART (V 5.628), SAINT (V 6.45a), XPREP, SHELXTL; Bruker AXS Inc., Madison, Wisconsin, USA, **2004**.
- (33) Sheldrick, G. M. *Siemens Area Detector Absorption Correction Program*, University of Göttingen, Göttingen, Germany, **2004**.
- (34) Altomare, A.; Cascarano, G.; Giacovazzo, C.; Guagliardi, A. Completion and refinement of crystal structures with SIR92. *J. Appl. Cryst.* **1993**, *26*, 343-350.
- (35) Sheldrick, G. M. SHELXL-2014, *Program for Crystal Structure Solution and Refinement*; University of Göttingen, Göttingen, Germany, **2014**.
- (36) Farrugia, L. J. WinGX-A Windows Program for Crystal Structure Analysis. *J. Appl. Cryst.* **2001**, *45*, 849-854.
- (37) Spek, A. L. Single-crystal structure validation with the program PLATON. *J. Appl. Crystallogr.* **2003**, *36*, 7-13.
- (38) Delley, B. An all electron numerical method for solving the local density functional for polyatomic molecules. *J. Chem. Phys.* **1990**, *92*, 508-517.
- (39) Delley, B. From molecules to solids with the DMol3 approach. *J. Chem. Phys.* **2000**, *113*, 7756-7764.
- (40) Blatov, V. A.; Shevchenko, A. P.; Proserpio, D. M. Applied Topological Analysis of Crystal Structures with the Program Package ToposPro. *Cryst. Growth Des.* **2014**, *14*, 3576-3586.
- (41) Spek, A. L. Single-crystal structure validation with the program PLATON. *J. Appl. Crystallogr.* **2003**, *36*, 7-13.
- (42) Yang, R. T. *Gas Separation by Adsorption Processes*, Butterworth, Boston, **1997**.
- (43) Pan, H.; Ritter, J. A.; Balbuena, P. B. Examination of the approximations used in determining the isosteric heat of adsorption from the Clausius-Clapeyron equation. *Langmuir* **1998**, *14*, 6323-6327.
- (44) Couck, S.; Denayer, J. F. M.; Baron, G. V.; Rémy, T.; Gascon, J.; Kapteijn, F. An Amine-Functionalized MIL-53 Metal-Organic Framework with Large Separation Power for CO<sub>2</sub> and CH<sub>4</sub>. *J. Am. Chem. Soc.* **2009**, *131*, 6326-6327.
- (45) Yang, H.-Y.; Li, Y.-Z.; Shi, W.-J.; Hou, L.; Wang, Y.-Y.; Zhu, Z. A new layer-stacked porous framework showing sorption selectivity for CO<sub>2</sub> and luminescence. *Dalton Trans.* **2017**, *46*, 11722-11727.

- (46) Gao, W. Y.; Wojtas, L.; Ma, S. A porous metal-metalloporphyrin framework featuring high-density active sites for chemical fixation of CO<sub>2</sub> under ambient conditions. *Chem. Commun.* **2014**, *50*, 5316-5318.
- (47) Babu, R.; Kathalikkattil, A. C.; Roshan, R.; Tharun, J.; Kimb, D. W.; Park, D. W. Dual-porous metal organic framework for room temperature CO<sub>2</sub> fixation *via* cyclic carbonate synthesis. *Green Chem.* **2016**, *18*, 232-242.
- (48) Lan, J.; Liu, M.; Lu, X.; Zhang, X.; Sun, J. Novel 3D Nitrogen-Rich Metal Organic Framework for Highly Efficient CO<sub>2</sub> Adsorption and Catalytic Conversion to Cyclic Carbonates under Ambient Temperature. *ACS Sustain. Chem. Eng.* **2018**, *6*, 8727-8735.
- (49) Liang, J.; Xie, Y. Q.; Wang, X. S.; Wang, Q.; Liu, T. T.; Huang, Y. B.; Cao, R. An imidazolium-functionalized mesoporous cationic metal-organic framework for cooperative CO<sub>2</sub> fixation into cyclic carbonate. *Chem. Commun.* **2018**, *54*, 342-345.
- (50) Sumida, K.; Rogow, D. L.; Mason, J. A.; McDonald, T. M.; Bloch, E. D.; Herm, Z. R.; Bae, T.-H.; Long, J. R. Carbon Dioxide Capture in Metal–Organic Frameworks. *Chem. Rev.* **2012**, *112*, 724-78.



# Chapter 2b

**Rational design of a Zn(II)-MOF with multiple functional sites for highly efficient fixation of CO<sub>2</sub> at mild conditions: A combined experimental and theoretical investigation**





### 2b.1. Introduction

The growing concentration of atmospheric carbon dioxide (CO<sub>2</sub>) caused by the extensive use of fossil fuels has resulted in serious environmental issues like extreme weather, ocean acidification, global warming, and so on.<sup>1</sup> These undesirable environmental issues can be resolved by selective capture and subsequent utilization of CO<sub>2</sub> as a sustainable C1 feedstock to synthesize high-value chemicals and fuels.<sup>2,3</sup> In this regard, several strategies have been employed for the conversion of CO<sub>2</sub> to various value-added chemicals such as cyclic carbonates, polycarbonates, and other fine chemicals.<sup>3</sup> Among them, the cycloaddition reaction of CO<sub>2</sub> to epoxides has gained significant interest of researchers as one of the most atom economic processes to obtain cyclic carbonates in high yield and selectivity.<sup>4</sup> Further, cyclic carbonates possess various advantages as electrolytes, in the production of polymers, fuel additives, and so on.<sup>5</sup> However, the high thermodynamic stability (bond enthalpy of + 805 kJ/mol) and kinetic inertness of CO<sub>2</sub> impose limitations on its chemical fixation into cyclic carbonates under mild conditions.<sup>6</sup> Therefore, catalysts are essential to achieve efficient functionalization of CO<sub>2</sub> into high-value chemicals at mild conditions. To date, several homogeneous catalysts<sup>7-10</sup> exhibiting efficient conversion of CO<sub>2</sub> to cyclic carbonates are reported. However, to achieve facile separation of the products and recycling of catalysts, several heterogeneous catalysts including metal-organic frameworks (MOFs) have been employed for the functionalization of CO<sub>2</sub> with epoxides.<sup>11</sup> Especially, the modular nature of MOFs facilitating the incorporation of multiple functional groups has facilitated the rational design of MOF-based heterogeneous catalysts<sup>12</sup> for the chemical fixation of CO<sub>2</sub> into value-added chemicals.<sup>13</sup> However, most of the MOF-based catalysts reported so far require drastic reaction conditions of high pressure of CO<sub>2</sub> and/or high temperature.<sup>14,15</sup> An ideal catalyst for CO<sub>2</sub> fixation at milder conditions should possess a high density of CO<sub>2</sub>-philic sites such as -NH<sub>2</sub>, -NH, -F, -N=N, etc<sup>16,17</sup> along with Lewis/Bronsted acidic catalytic sites for combined selective capture and conversion. This chapter includes, the synthesis of a novel hydrogen-bonded 3D framework by incorporating multiple functional sites, i.e. Zn(II) center, polar (-CF<sub>3</sub>) group from dicarboxylate ligand (hfipbba), and basic amine (-NH<sub>2</sub>) groups from melamine (MA) co-ligand (Scheme 1). Owing to the presence of high density of -NH<sub>2</sub> and fluorinated (-CF<sub>3</sub>) groups exposed in the 1D pores, HbMOF1 exhibited highly selective as well as recyclable uptake of CO<sub>2</sub> with experimentally determined Q<sub>st</sub> value of 36.7 kJ/mol which is further supported by the theoretically computed value of 36.0 kJ/mol. The high density of Lewis basic/acidic sites combined with high thermal/chemical stability rendered HbMOF1 an ideal catalytic material for carrying out heterogeneous cycloaddition of CO<sub>2</sub>

with epoxides at mild conditions. Indeed, HbMOF1 exhibited exceptional catalytic activity for the fixation of CO<sub>2</sub> with various terminal as well as internal epoxides affording the cyclic carbonates at RT and 1bar CO<sub>2</sub>. The high catalytic performance of HbMOF1 could be attributed to the synergistic effect of the Zn(II) center with CO<sub>2</sub>-philic (-NH<sub>2</sub> and -CF<sub>3</sub>) groups projected in the 1D pores supported by an in-depth theoretical study. A detailed mechanistic investigation of the cycloaddition reaction has been carried out through periodic Density Functional Theory (DFT) calculations. In this chapter 2b, we present the design of a rare example of porous MOF composed of multiple functional sites suitable for coupling CO<sub>2</sub> with epoxides to obtain value-added cyclic carbonates at RT combined with an insight mechanistic investigation of the catalytic process.

## 2b.2. Experimental section

### 2b.2.1. Physicochemical characterization

The phase purity of the as-synthesized samples was confirmed by powder XRD analysis using Rigaku Miniflex 600 with Cu K $\alpha$  radiation ( $\lambda = 0.154$  nm). UV-Vis (Diffuse Reflectance) spectra were recorded on the Shimadzu spectrophotometer using BaSO<sub>4</sub> as a reference. Thermogravimetric analysis (TGA) of the compounds was carried out on Mettler Toledo Thermogravimetric analyzer in an inert (N<sub>2</sub>) atmosphere with a flow rate of 30 mL/min in the temperature range of 30-600 °C and a heating rate of 5 °C/min. FTIR (Fourier transform infrared) spectra of the samples were recorded from 400 to 4000 cm<sup>-1</sup> on a Perkin Elmer ATR-FTIR spectrometer. Adsorption analyses were carried out by Quantachrome QUADRASORB-SI automatic volumetric instrument. Thermo Fischer Flash 2000 Elemental Analyzer was used for elemental analyses (CHN) of the samples. The metal content in the MOF was determined by Agilent's microwave-plasma atomic emission spectrometer (MP-AES). The catalytic conversions were determined by recording <sup>1</sup>H-NMR spectra of the products on a JEOL JNM-ECS-400 spectrometer operating at a frequency of 400 MHz using 1,1',2,2'-tetrachloroethane as an internal standard.

### 2b.2.2. Synthesis of HbMOF1

HbMOF1 was synthesized following a mixed ligand strategy at 100 °C using the procedure as follows. A mixture containing H<sub>2</sub>hfipbba (0.2 mmol) and MA (0.2 mmol) was dissolved in 2 mL of N, N-dimethylformamide (DMF) in a 30 ml glass vial. In another vial, Zn(NO<sub>3</sub>)<sub>2</sub>.6H<sub>2</sub>O (0.2 mmol) was dissolved in DMF (2 mL). Then both solutions were mixed

in a glass vial, stirred for 10 minutes, sealed with Teflon and parafilm, and heated at 100 °C in preheated oven. After 5 days the vial was cooled down to room temperature slowly. The colorless rod-like crystals of HbMOF1 obtained were collected by filtration and washed with DMF and methanol thoroughly. Yield: 75%. The synthesized sample was exchanged with acetone for three days followed by activation at room temperature under a vacuum (18 mTorr) for 24 h. The phase purity of the as-synthesized sample was confirmed by powder X-ray diffraction analysis (Figure A12). The elemental analysis of activated HbMOF1: calculated (%) for  $[\text{Zn}(\text{hfipbba})(\text{MA})]_n$  C: 41.29; H: 2.43; N: 14.45 and found: C: 40.89; H: 2.12; N: 13.98. FT-IR ( $\text{cm}^{-1}$ ): 3435 (w), 3386 (m), 3234 (w), 1672 (m), 1634 (m), 1606 (m), 1537 (s), 1404 (s), 1254 (s), 1206 (s), 1164 (s), 1084 (m), 1020 (w), 779 (s), 723 (s) (Figure A13).

### 2b.2.3. Adsorption measurements

$\text{N}_2$  adsorption isotherm measurements were performed at 77 and 273K, while  $\text{H}_2$  and Ar adsorption-desorption measurements were conducted at 273K.  $\text{CO}_2$  adsorption-desorption measurements were carried out at 273 and 298K on a Quantachrome QUADRASORB SI automatic volumetric instrument. Ultrapure (99.995%)  $\text{H}_2$ , Ar,  $\text{N}_2$ , and  $\text{CO}_2$  gases were used for the isotherm measurements. Before starting the isotherm measurements, the HbMOF1 sample (0.10 g) was exchanged with acetone for 3 d and further outgassed at RT under vacuum (18 mTorr) for 24 h, then the activated sample was connected to a surface area analyzer and all the operations were computer-controlled. The 273 and 298K temperatures were achieved by using water and ethylene glycol mixture (1:1 v/v mixture) using a chiller. Whereas, 77K was achieved by using liquid nitrogen. The dead volume of the sample cell was determined using He gas (99.995%).

### 2b.2.4. Catalytic cycloaddition reactions of $\text{CO}_2$ with epoxides

The cycloaddition reactions of  $\text{CO}_2$  with various epoxides were carried out in a glass reactor (50 mL) under RT and 1 bar  $\text{CO}_2$ . Before catalytic reactions, the HbMOF1 sample was exchanged with acetone for 72h and further outgassed at RT under vacuum (18 mTorr) for 24h to remove guest solvent molecules. In a typical reaction, the epoxide, co-catalyst (tetra-n-butyl ammonium bromide, TBAB), and the activated catalyst (HbMOF1) were taken in the glass reactor at room temperature and the reactor was flushed with  $\text{CO}_2$  twice and the required pressure (1 bar) was maintained and then the contents were allowed stir at RT. After 24h, the  $\text{CO}_2$  gas was released and the catalyst was separated from the reaction mixture by

filtration. The catalytic conversions were determined by  $^1\text{H}$  NMR analysis of the filtrate. The recovered catalyst was washed with methanol thoroughly for the complete removal of epoxides and their corresponding cyclic carbonates from the pores of HbMOF1 followed by activated at 353K under vacuum for 12h and reused for subsequent catalytic cycles.

### 2b.2.5. X-ray crystallography

Single crystal X-ray structural data of HbMOF1 was collected on a CMOS-based Bruker D8 Venture PHOTON 100 diffractometer equipped with an INCOATEC micro-focus source with graphite monochromated Mo  $K\alpha$  radiation ( $\lambda = 0.71073 \text{ \AA}$ ) operating at 50 kV and 30 mA. The SAINT<sup>18</sup> program was used for the integration of diffraction profiles and the absorption correction was made with the SADABS program.<sup>19</sup> The structures were solved by SIR 92<sup>20</sup> and refined by full-matrix least square method using SHELXL-2018<sup>21</sup> and WinGX system, Ver 2013.3.<sup>22</sup> The non-hydrogen atoms in all the structures were located from the difference Fourier map and refined anisotropically. All the hydrogen atoms were fixed by HFIX and placed in ideal positions and included in the refinement process using a riding model with isotropic thermal parameters. The disordered guest DMF molecules were treated with the SQUEEZE option of PLATON<sup>23</sup> software. Hence the formula of HbMOF1 was established based on the elemental analyses and TGA. The potential solvent accessible area or void space was calculated using the PLATON software. All the crystallographic and structure refinement data of the HbMOF1 are summarized in Table 1. Selected hydrogen bond details of HbMOF1 are given in Table A4 and in Table A5 selected bond lengths and angles are summarized. The crystallographic information file is deposited with CCDC number 1948861.

### 2b.2.6. Computational Methods

#### 2b.2.6.1. Microscopic models for the host framework

The crystal structure of HbMOF1 obtained from SCXRD was geometry optimized at the Density Functional Theory (DFT) level using the CP2K package.<sup>24</sup> In these simulations, the positions of the atoms of the framework were relaxed while the unit cell parameters were kept fixed at the values determined experimentally. All the structural optimizations were done using Perdew-Burke-Ernzerhof (PBE)<sup>25</sup> functional along with a combined Gaussian basis set and pseudopotential. For Carbon, Nitrogen, Oxygen, Fluorine, and Hydrogen, a triple zeta (TZVP-MOLOPT) basis set was considered, while a double zeta (DZVP-

MOLOPT) was applied for Zinc.<sup>26</sup> The pseudopotentials used for all of the atoms were those derived by Goedecker, Teter, and Hutter.<sup>27</sup>

**Table 1.** Crystal data and structure refinement parameters for HbMOF1.

Parameters	HbMOF1
Empirical formula	C <sub>20</sub> H <sub>14</sub> F <sub>6</sub> N <sub>6</sub> O <sub>4</sub> Zn
Formula mass	581.76
Crystal system	Monoclinic
Space group	<i>P21/n</i>
a/ Å	13.2013(10)
b/ Å	11.2188(7)
c/ Å	21.4217(14)
α (degree)	90
β (degree)	92.9(3)
γ (degree)	90
V (Å <sup>3</sup> )	3168.4(4)
Z	4
M (mm <sup>-1</sup> )	0.840
F (000)	1168
T (K)	298
λ (Mo Kα) (Å)	0.71073
θ <sub>min</sub> (deg)	2.5
θ <sub>max</sub> (deg)	26.4
total data	79486
unique data	6453
R <sub>int</sub>	0.028
Data [I > 2σ(I)]	5985
R <sub>1</sub>	0.0416
wR <sub>2</sub> [I > 2σ(I)] <sup>a</sup>	0.1559
S	1.17
CCDC	1948861

$${}^a R_1 = \frac{\sum \|F_o\| - \|F_c\|}{\sum \|F_o\|}, {}^b wR_2 = [\frac{\sum w(F_o^2 - F_c^2)^2}{\sum w(F_o^2)^2}]^{1/2}$$

The Van der Waals interactions were taken into account via the use of semi-empirical dispersion corrections as implemented in the DFT-D3 method.<sup>28</sup> Three hypothetical mixed ligand HbMOF1 topology structure models which consist of a composition of (i) melamine/4,4'-(propane-2,2-diyl)bisbenzoic acid, (ii) 1,3,5-triazine/4,4'-hexafluoroisopropylene bisbenzoic acid (hfipbba) and (iii) 1,3,5-triazine/4,4'-(propane-2,2-diyl)bisbenzoic acid, were generated by a ligand replacement strategy starting with the melamine/4,4'-hexafluoroisopropylene bisbenzoic acid analog structure, i.e. HbMOF1. These structure models labeled as HbMOF1-hypo-1, HbMOF1-hypo-2, and HbMOF1-hypo-3 were further geometry optimized allowing the relaxation of both the atomic positions and the unit cell parameters. The atomic point charges for all framework atoms of HbMOF1 and three hypothetical HbMOF1 were obtained using the REPEAT method proposed by Campana *et al.*,<sup>29</sup> which was implemented into the CP2K code based on a restrained electrostatic potential framework.<sup>30-39</sup>

#### 2b.2.6.2. DFT optimization on HbMOF1 loaded with epoxides

To identify the molecular as well as energetic interaction of various internal/terminal epoxides, geometry optimizations of epoxides such as PO, CPO, CHO, and CCO-loaded HbMOF1 were performed with the same level of theory and parameters as used for the optimization of the HbMOF1 by considering one guest molecule per unit cell. Finally, the geometry-optimized epoxide-loaded HbMOF1 was used to explore the single point energy for understanding the binding interaction of the epoxide with HbMOF1. Where the binding energy of epoxide interaction on HbMOF1 was calculated by using the following equation

$$\Delta E_{BE} = E_{\text{HbMOF1+Epoxide}} - E_{\text{HbMOF1}} - E_{\text{Epoxide}}$$

Where  $E_{\text{HbMOF1+Epoxide}}$  corresponds to the energy of the optimized HbMOF1 with epoxide (e.g. PO, CPO, CHO, and CCO) by keeping only one epoxide molecule in its unit cell for extracting the adsorption energy while  $E_{\text{HbMOF1}}$  was calculated in such a way by removing the epoxide from DFT-optimized epoxide-loaded HbMOF1 and  $E_{\text{Epoxide}}$  is the total energy of a single epoxide molecule taken individually by keeping a similar periodic boundary condition to other energy calculations. All these simulations were performed using the CP2K package<sup>[21]</sup> at the PBE level<sup>[11]</sup> and the same basis set<sup>[12]</sup> as used for structural optimization.

### 2b.2.6.3. Computational methods for the catalytic mechanism

Periodic DFT calculations were carried out in the mixed Gaussian plane wave scheme as implemented in the CP2K code package<sup>40</sup> with Grimme's D3 dispersion corrections<sup>14</sup> by keeping the same functional<sup>11</sup> and basis set<sup>12</sup> used as for the geometry optimization of HbMOF1. This basis set and energy cutoff parameters have been considered based on the previous calculation by Ye *et al.*,<sup>41</sup> where they validated that PBE functional with a plane wave cutoff energy of 500 Ry and suggested as the best option for exploring the catalytic mechanism involves MOF. For exploring the reaction mechanism, the unit cell of DFT-optimized HbMOF1 with the incorporation of Br<sup>-</sup> nucleophile was considered. The lattice constants of the optimized unit cell for HbMOF1 are  $a = 13.316$ ,  $b = 11.275$ ,  $c = 21.564$  Å,  $\alpha = 90.00^\circ$ ,  $\beta = 92.97^\circ$ ,  $\gamma = 90.00^\circ$ . The TBAB provides the halide ion (Br<sup>-</sup>) nucleophile for the epoxide ring opening, this simplified Br<sup>-</sup> nucleophile incorporated HbMOF1 catalyst model helps to avoid any complication as blocking TBAB co-catalyst to the pore aperture of HbMOF1 for the substrate and CO<sub>2</sub>. In this work, we examined the case of one Br<sup>-</sup> per HbMOF1 unit cell. We found that fully relaxing the geometry and cell parameters of HbMOF1 gave lattice constants that were almost identical to the relaxed HbMOF1 values. Furthermore, optimizing the structure with chemisorbed propylene oxide or CO<sub>2</sub> in HbMOF1 also perturbed the lattice constants and energies by a very minor amount. Therefore, we held the lattice constants fixed at the ground state HbMOF1 values for most calculations to save computational time. For the calculation, the total relative energy of the Br<sup>-</sup> nucleophile incorporated HbMOF1 (catalyst + nucleophile), CO<sub>2</sub>, and propylene oxide (isolated reactants) was considered to be zero energy, and the optimized structures of reactant complexes are depicted in Scheme 2. In the case of each stage of catalytic reaction (e.g. IC, Int, TS, FC, etc.), the relative energies were computed with respect to the sum of the total energies of the corresponding gas phase molecules as represented in Equation 1.

$$E_{relative} = E_{stage} - (E_{MOF+Br} - E_{CO_2} - E_{PO}) \quad \dots\dots\dots (1)$$

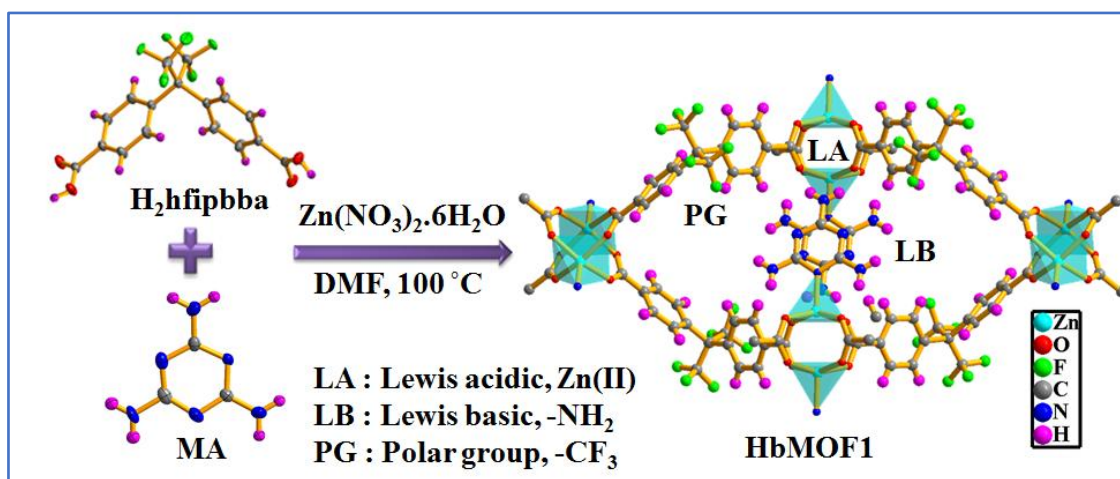
Where  $E_{stage}$ ,  $E_{MOF+Br}$ ,  $E_{CO_2}$  and  $E_{PO}$  represents the total energies of the HbMOF1 + Br<sup>-</sup> with adsorbates at each reaction stage, the empty HbMOF1 + Br<sup>-</sup> catalyst, gas phase CO<sub>2</sub>, and gas phase propylene oxide, respectively. Equation 1 defines negative values as exothermic and positive values as endothermic processes. Transition states along the reaction pathway were determined by using the climbing image nudged elastic band (CI-NEB) method. Transition states were confirmed through frequency analysis, verifying that the transition complex had only one imaginary frequency vibrational mode.

## 2b.3. Results and discussion

### 2b.3.1. Synthesis and structural description

HbMOF1 was synthesized by solvothermal reaction of  $\text{Zn}(\text{NO}_3)_2 \cdot 6\text{H}_2\text{O}$  with  $\text{H}_2\text{hfipbba}$  ligand and MA at 100 °C in DMF (Scheme 1). The powder X-ray diffraction (PXRD) analysis of the as-synthesized sample confirmed the phase purity of the sample (Figure A12). FT-IR spectra of the activated sample showed the characteristic N-H stretching frequency at 3435 and 3386  $\text{cm}^{-1}$  corresponding to  $-\text{NH}_2$  groups of MA (Figure A13).

Single crystal X-ray structural analysis revealed that HbMOF1 crystallizes in monoclinic system with  $P21/n$  space group (Table 1). The asymmetric unit consists of a Zn(II) ion, a  $\text{hfipbba}^{2-}$  ion, and a MA ancillary ligand (Figure 1a). The Zn(II) ion adopts a binuclear paddle-wheel arrangement in which each Zn center is in a distorted square pyramidal geometry with  $\text{ZnO}_4\text{N}$  arrangement fulfilled by four carboxylate oxygens (O1, O2, O3, and O4) of  $\text{hfipbba}^{2-}$  ion forming the square plane and the nitrogen atom of MA occupying the apical position (Figure 1a). These  $[\text{ZnO}_4\text{N}]_2$  paddle-wheel secondary building units (SBUs) are further extended in two directions resulting in a 2D  $[\text{Zn}(\text{hfipbba})(\text{MA})]_n$  network (Figure 1b and 1c). The 2D sheets are further self-assembled via intermolecular  $\text{F} \cdots \text{H}-\text{C}$  (between  $\text{CF}_3$  group and aromatic  $\text{H}-\text{C}$  of  $\text{hfipbba}^{2-}$ ) and also  $\text{N}-\text{H} \cdots \text{O}$  (between the  $-\text{NH}_2$  group of MA and the carboxylate oxygen of  $\text{hfipbba}^{2-}$ ) interactions resulting in the hydrogen-bonded 3D framework (Figure 1d) (Table A4). The 3D framework houses two types of 1D channels of dimension  $6.7 \times 5.1 \text{ \AA}^2$  and  $5.8 \times 4.7 \text{ \AA}^2$  along the crystallographic  $b$ - and  $a$ -axis, respectively (Figure 2a and 2b). The Zn-O bond lengths are in the range of 2.027-2.075 Å and the Zn-N bond length is 2.011 Å (Table A5). TOPOS<sup>42</sup> analysis revealed that the framework has a 4-c uninodal net with a vertex symbol of  $\{4^4.6^2\}$  (Figure 2c and 2d).



Scheme 1. Synthesis scheme for HbMOF1.

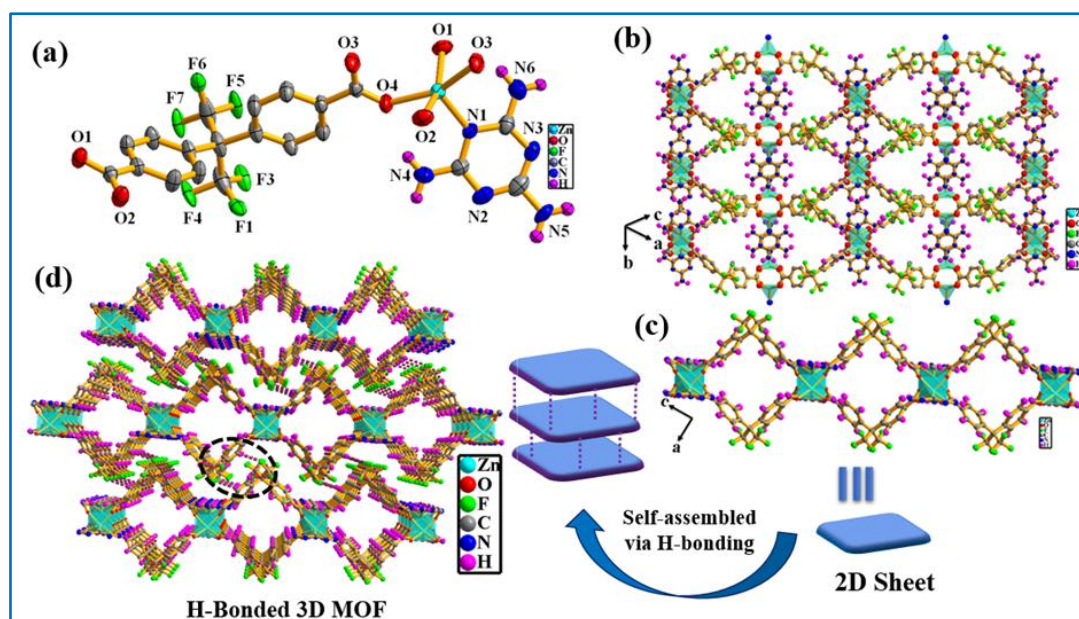


**Figure 1.** (a) Asymmetric unit of HbMOF1 showing the environment around Zn(II) center (b, c) the view of 2D network along *a*- and *b*-axes and (d) the 3D framework formed by hydrogen bonding interaction between the 2D sheets (guest DMF molecules are omitted for clarity).

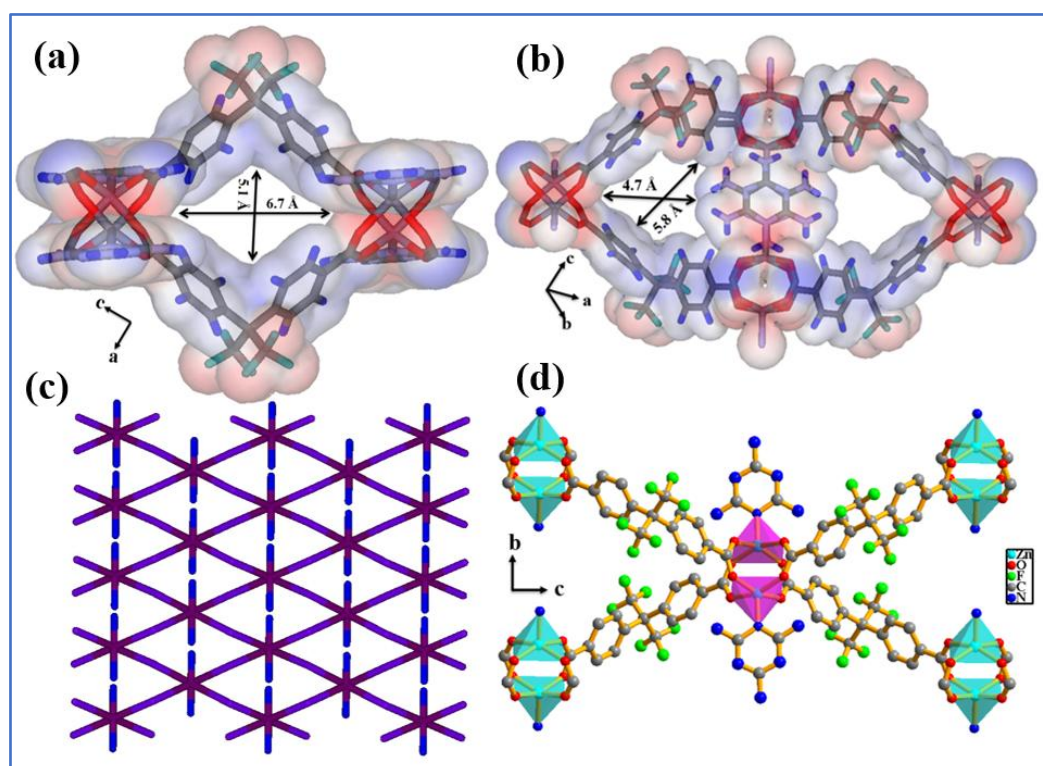


**Figure 2.** (a, b) View of 1D channels of dimension  $6.7 \times 5.1 \text{ \AA}^2$  and  $5.8 \times 4.7 \text{ \AA}^2$  along *b*- and *a*-axis, respectively decorated with free  $-\text{NH}_2$  groups of MA and  $-\text{CF}_3$  groups of hfpbba<sup>2-</sup> (c) TOPOS picture of HbMOF1 and (d) 4-connected view of Zn<sub>2</sub> paddle-wheel dimeric unit.

### 2b.3.2 Gas adsorption studies of HbMOF1

Single-crystal X-ray structure determination of HbMOF1 revealed the presence of two types of 1D microporous channels (Figures 2a and 2b). To further confirm the permanent porosity, N<sub>2</sub> adsorption isotherms were carried out at 77K. Before adsorption measurements, the as-synthesized sample was exchanged with acetone for three days and activated under vacuum (18 mTorr) for 24h at RT to obtain solvent-free MOF. PXRD pattern of the activated sample matched with the simulated pattern supporting the retaining of the original framework structure (Figure A12). Further, the N<sub>2</sub> isotherm follows a typical type-I profile indicative of the microporous nature of the framework, and the estimated Brunauer-Emmett-Teller (BET) and Langmuir surface area were found to be 163 and 319 m<sup>2</sup>/g, respectively (Figure 3a). Further, CO<sub>2</sub> adsorption-desorption isotherms show type-I plots with the uptake of 49.88, and 31.16 cc/g (9.8 and 6.12 wt.%) carried out at 273 and 298K, respectively (Figure 3b). The adsorption isotherms were analyzed following the Langmuir-Freundlich equation<sup>43</sup> (Figure A14 and A15) to get the exact prediction of CO<sub>2</sub> gas adsorbed at saturation.

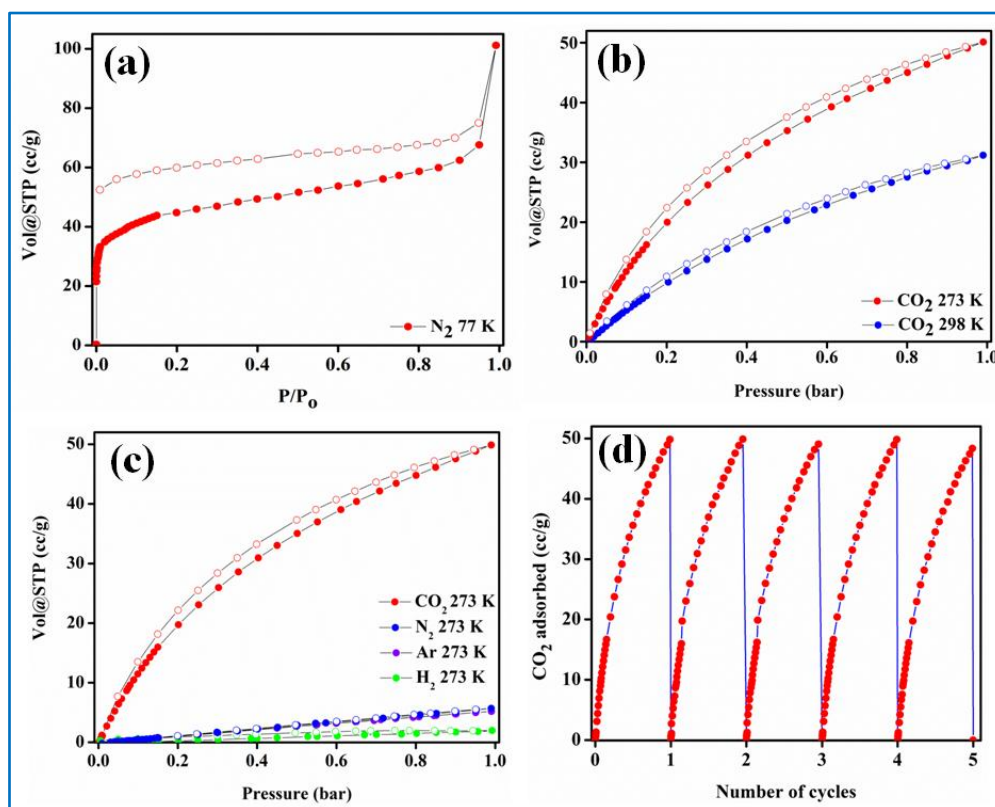


**Figure 3.** (a) N<sub>2</sub> adsorption isotherms of HbMOF1 carried out at 77K; (i) for the activated sample and (ii) the sample recovered after treating with water for three days, (b) CO<sub>2</sub> adsorption isotherms carried out at 273 and 298K, (c) Selective CO<sub>2</sub> adsorption isotherms of HbMOF1 and (d) Recyclability of CO<sub>2</sub> adsorption isotherms carried out at 273K.

The heat of adsorption ( $Q_{st}$ ) value for CO<sub>2</sub> determined following the Clausius-Clayperon equation<sup>44</sup> was found to be 36.7 kJ/mol (Figure A16). Furthermore, gas adsorption studies of HbMOF1 with other gases (N<sub>2</sub>, Ar, and H<sub>2</sub>) revealed negligible uptake of 1.03, 1.73, and 1.49 cc/g, respectively for N<sub>2</sub>, Ar, and H<sub>2</sub>, revealing selective adsorption for CO<sub>2</sub> (Figure 3c). Further, the calculated gas selectivity constants for CO<sub>2</sub>/H<sub>2</sub>, CO<sub>2</sub>/Ar, and CO<sub>2</sub>/N<sub>2</sub> were found to be 68, 45, and 50, respectively (Figure A17). More importantly, HbMOF1 shows highly recyclable CO<sub>2</sub> uptake with retaining the adsorption capacity for up to five cycles (Figure 3d).

To get more insight into details on the preferable adsorption sites for CO<sub>2</sub> gas in HbMOF1, computational adsorption simulations were performed using Grand Canonical Monte Carlo (GCMC) method (see annexure, Figure A18). The simulated CO<sub>2</sub> adsorption isotherms have a similar trend to the experimentally recorded CO<sub>2</sub> adsorption isotherms of HbMOF1 at both temperatures of 273, and 298K, as shown in Figure A19. However, the theoretical (Figure A20) and experimental BET surface area (Figure 3a) values obtained for HbMOF1 are 272 and 163 m<sup>2</sup>/g, respectively. The observed difference of around 109 m<sup>2</sup>/g between the theoretical and experimental surface area could be ascribed to the overestimation (1.5 mmol/g) in the simulated CO<sub>2</sub> adsorption capacities of 3.77 and 2.9 mmol/g when compared to the experimental values of 2.21 and 1.39 mmol/g at 273 and 298K, respectively. The simulated adsorption enthalpy of CO<sub>2</sub> in HbMOF1 is 36.0 kJ/mol (Figure A21) which is in close agreement with the experimental value of 36.7 kJ/mol. Therefore, there exists a strong interaction of CO<sub>2</sub> with the framework and this resulted in a high CO<sub>2</sub> adsorption enthalpy. Detailed analysis of the microscopic adsorption mechanism for CO<sub>2</sub> with HbMOF1 revealed the source of high adsorption capacity and interaction energy. Both the -CF<sub>3</sub> group of hfipbba<sup>2-</sup> and -NH<sub>2</sub> group of MA in the confined 1D channels strongly influence the CO<sub>2</sub> adsorption in HbMOF1 as indicated in Figure 4a. Here, the CO<sub>2</sub> molecules interact with the -CF<sub>3</sub> group of hfipbba<sup>2-</sup> and -NH<sub>2</sub> group of MA with a mean characteristic O(CO<sub>2</sub>)-(CF<sub>3</sub>) and O(CO<sub>2</sub>)-(NH<sub>2</sub>) distances of 2.12 Å and 2.74 Å, respectively (Figure 4a and A22) favoring the adsorption of CO<sub>2</sub> molecules inside the 1D channels of HbMOF1. In addition to the CO<sub>2</sub>-CF<sub>3</sub> and CO<sub>2</sub>-NH<sub>2</sub> interactions, the organic hydrogens of hfipbba<sup>2-</sup> and the nitrogen of MA ligand are also involved in the interaction with CO<sub>2</sub> through H<sub>Organic</sub>-C(CO<sub>2</sub>) and N<sub>Organic</sub>-C(CO<sub>2</sub>) with a mean distance of 3.6 Å and 3.2 Å, respectively (Figure 4a and A22). Figure 4b demonstrates very high CO<sub>2</sub> adsorption density at 1 bar and 298K in the confined 1D channels decorated with -CF<sub>3</sub> groups of hfipbba<sup>2-</sup> and -NH<sub>2</sub> groups of MA. Hence the CO<sub>2</sub>-philic nature of the framework exhibiting enhanced CO<sub>2</sub> uptake property is driven by the

presence of polar functionalized 1D channels constituted by  $-\text{CF}_3$  groups of  $\text{hfipbba}^{2-}$  and  $-\text{NH}_2$  groups of MA which are engaged in various supramolecular interactions. To further validate the influence of polar ( $-\text{CF}_3$ ) and basic ( $-\text{NH}_2$ ) groups on  $\text{CO}_2$  adsorption, we generated three hypothetical structures with the same topology of HbMOF1 via computational methodology. Interestingly, the simulated heat of adsorption value of these models was found to be much lower than that of HbMOF1 (Table A6).

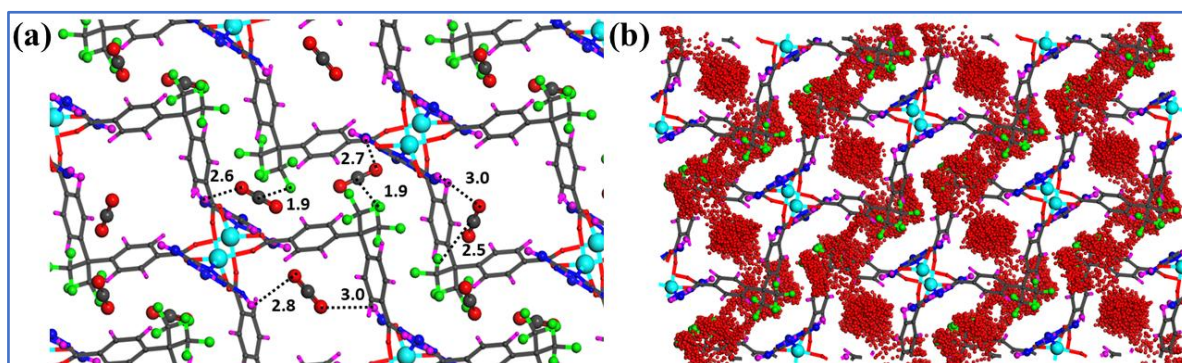


**Figure 4.** (a) Local view for  $\text{CO}_2$  interacting distances ( $\text{\AA}$ ) with functional groups,  $-\text{CF}_3$  and  $-\text{NH}_2$  of HbMOF1 obtained from the GCMC simulations at 298K, and (b) maps of the occupied positions of  $\text{CO}_2$  (red) in 1000 equilibrated frames for a given pressure of 1 bar and at 298K for HbMOF1, color code for the atoms: C (dark grey), N (blue), O (red), F (green), Zn (cyan), H (magenta).

### 2b.3.3. Thermal and chemical stability of HbMOF1

Thermogravimetric analysis of as-synthesized HbMOF1 showed a weight loss of ~26 % (calc. wt.% 26.2) in the temperature range of 120-288 °C corresponding to the loss of three guest DMF molecules. The subsequent weight loss of ~68 % (calc. wt.% 68.1) in the temperature range, 384-500 °C corresponds to the loss of one MA and one hfipbba ligand. Whereas, the activated sample of HbMOF1 after the solvent exchange with acetone did not show any weight loss up to 380 °C indicating the absence of guest solvent molecules (Figure A23). The loss of solvent molecules upon activation was further supported by the elemental analysis of the activated HbMOF1 (annexure). Furthermore, to examine the chemical stability of HbMOF1, the as-synthesized sample was soaked in various solvents of different polarity (MeOH, 1,4-dioxane, acetone, water, DMF, DMA, and isopropanol) with vigorous stirring for 72 h and then the MOF was recovered by filtration and dried. The PXRD pattern of the samples recovered matches well with the simulated pattern indicating that the original framework structure was retained which confirms the solvent stability of the HbMOF1

framework (Figure A24). Moreover, the BET surface area of HbMOF1 recovered after treatment with water for 3 d was found to be 156 m<sup>2</sup>/g (Figure 3a) which is close to the surface area measured for the as-synthesized sample (163 m<sup>2</sup>/g). This supports that the HbMOF1 retains the original framework structure even after treating with water for 72 h.

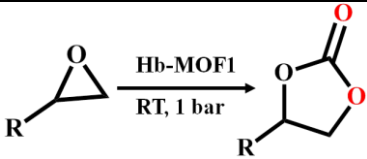
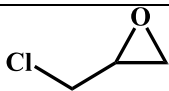
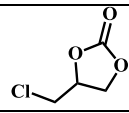
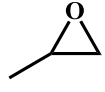
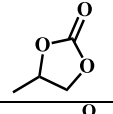
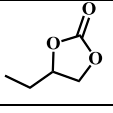
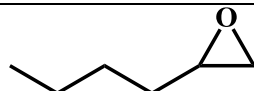
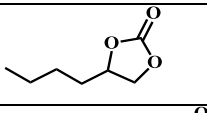
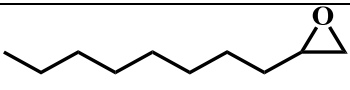
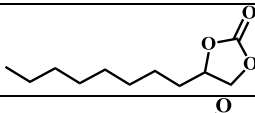
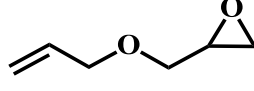
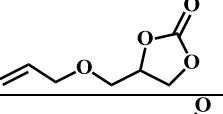
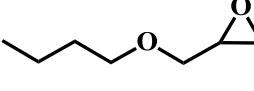
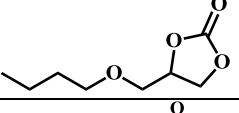
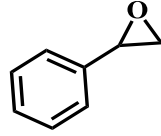
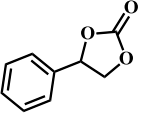
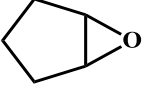
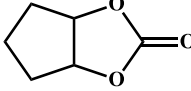
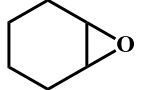
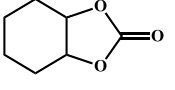
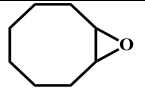
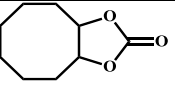
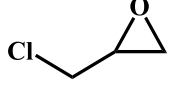
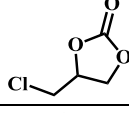
#### 2b.3.4. Catalytic cycloaddition reaction of CO<sub>2</sub> with terminal/internal epoxides

The presence of high density of CO<sub>2</sub>-philic -NH<sub>2</sub> groups of MA and -CF<sub>3</sub> groups of hfpbba<sup>2-</sup> ligand exposed in the 1D pores (Figure 1b) along with Zn(II) center motivated us to study the catalytic activity of HbMOF1 for the cycloaddition of CO<sub>2</sub> with various epoxides to obtain cyclic carbonates at mild conditions. Initial catalytic studies carried out using epichlorohydrin (ECH) as a model substrate showed about 68% conversion of the epoxide to chloropropylene carbonate (CPC) within 12h under the mild reaction conditions of 1 bar of CO<sub>2</sub> and RT with tetrabutylammonium bromide (TBAB) as cocatalyst (Table A7). Further, an increase in the reaction time to 24h led to an almost complete (> 99%) conversion of ECH to CPC with 100% selectivity (Table 2). Whereas, an increase of the reaction temperature to 80 °C resulted in a 97% conversion of ECH to CPC within 4h (Table A7). Furthermore, control experiments carried out in the absence of HbMOF1 catalyst showed only 46% conversion of ECH highlighting the necessity of HbMOF1 catalyst for the high-yield production of cyclic carbonates (Table A7). The excellent catalytic activity of HbMOF1 motivated us to extend the scope of the catalysis for the cycloaddition of CO<sub>2</sub> with various other epoxides. Interestingly, the epoxides, 1,2-epoxypropane (size: 4.35 × 3.41 Å<sup>2</sup>) and 1,2-epoxybutane (size: 6.48 × 3.39 Å<sup>2</sup>) showed complete conversion to the corresponding cyclic carbonates in 99% yield with 100% selectivity under the mild conditions. However, as the alkyl chain length of the epoxides increases, in the case of 1,2-epoxyhexane (size: 8.198 × 3.39 Å<sup>2</sup>) and 1,2-epoxydecane (size: 13.321 × 3.39 Å<sup>2</sup>), the conversion was reduced to 87 and 59%, respectively. This reduced catalytic activity could be ascribed to the restricted diffusion of these longer epoxides in the narrow pore channels owing to their larger size over the pore size (6.7 × 5.1 Å<sup>2</sup>) of HbMOF1 (Table A8). Whereas, a slightly higher catalytic conversion observed for butyl glycidyl ether (BGE) over allyl glycidyl ether (AGE) is due to the electron-donating nature of the former epoxide over the latter one. The catalytic activity of HbMOF1 towards CO<sub>2</sub> cycloaddition was also tested with aromatic epoxide, and styrene oxide (SO) under the same optimized conditions, and the conversion was found to be 78% (Table 1). To test the potential utility of HbMOF1 for practical application, the catalytic activity was tested using N<sub>2</sub>:CO<sub>2</sub> mixture (87:13%), a simulated dry flue gas composition,

and the conversion of ECH was found to be 16% under the same optimized conditions of RT and 1 bar CO<sub>2</sub>. It is worth mentioning that the catalytic efficiency observed for the cycloaddition of CO<sub>2</sub> catalyzed by HbMOF1 was superior in comparison to similar examples of MOFs reported in the literature (Table A10).<sup>45</sup>

The excellent catalytic activity of HbMOF1 for the cycloaddition of various terminal epoxides motivated us to study the catalytic activity for the cycloaddition of internal epoxides which are known to be less reactive than the terminal epoxides.<sup>[15b,46,47]</sup> Therefore, normally higher reaction temperature and/or pressure conditions with prolonged reaction time are employed for the conversion of internal epoxides.<sup>[15b,24-48]</sup> On the contrary, our catalyst HbMOF1 catalyzes the cycloaddition of cyclopentene oxide (CPO) to the corresponding cyclic carbonate with about 70% conversion with a TON of 700 under the optimized mild reaction conditions of 1 bar CO<sub>2</sub> and RT (Table 2). Further, the catalysis was extended to other internal epoxides and the catalytic conversion was found to decrease from cyclopentene oxide (70 %) to cyclohexene oxide (50 %) to cyclooctene oxide (14%) (Table 2). This decrease in the catalytic activity can be attributed to their intrinsic lower reactivity and the bulkiness imparting steric hindrance in approaching the catalytic Zn(II) sites in the confined 1D channels of HbMOF1. Further, periodic DFT-optimized HbMOF1 loaded with various internal epoxide (see SI) revealed the steric hindrance for the approach of internal epoxides to Zn(II) site in the framework as the Zn(II) – O(epoxide) interacting distances are 4.0, 4.7, and 5.4 Å for cyclopentene oxide (CPO), cyclohexene oxide (CHO) and cyclooctene oxide (CCO), respectively (Figure 5), while the prototype terminal epoxide PO exhibits only 3.6 Å. In addition to this, the binding energy observed for the internal epoxides are in the order of -55.2, -20.6, and -14.3 kJ/mol for CPO, CHO, and CCO, respectively. To the best of our knowledge, the catalytic efficiency observed for the conversion of internal epoxides catalyzed by HbMOF1 is the highest amongst the MOF-based heterogeneous catalysts carried out at RT and 1 bar CO<sub>2</sub> (Table 3). It is important to note that the number of examples of MOF-based heterogeneous catalysts known for cycloaddition of internal epoxides are sparse and generally high temperature and/or high-pressure conditions are employed for the conversion. On the contrary, the reaction conditions utilized in our study are relatively milder (Table 3). Hence, the exceptionally higher catalytic activity of HbMOF1 can be attributed to the synergistic effect of CO<sub>2</sub>-philic (-NH<sub>2</sub> and CF<sub>3</sub>) groups and Zn(II) centers which are in close proximity resulting in enhanced catalytic activity affording high yield production of cyclic carbonates with selectivity.

**Table 2.** The catalytic activity of HbMOF1 for cycloaddition of CO<sub>2</sub> with various epoxides under mild conditions.<sup>a</sup>

				
Sl. No.	Substrate	Product	Conversion <sup>c</sup>	TON <sup>d</sup>
1			>99	995
2			>99	992
3			>99	990
4			87	870
5			59	590
6			89	890
7			77	770
8			73	730
9			74	740
10			50	500
11			14	140
12 <sup>b</sup>			16	160

<sup>a</sup>Reaction conditions: epoxide (20 mmol), HbMOF1 catalyst (0.1 mol %), cocatalyst: TBAB (2.5 mol%), RT (30 °C), 1 bar CO<sub>2</sub>, and time: 24h. <sup>b</sup> Pressure (1bar, 13% CO<sub>2</sub>). <sup>c</sup> The conversions determined by <sup>1</sup>H NMR analysis using an internal standard. <sup>d</sup> TON = the number of moles of product formed / number of moles catalyst (HbMOF1) used.

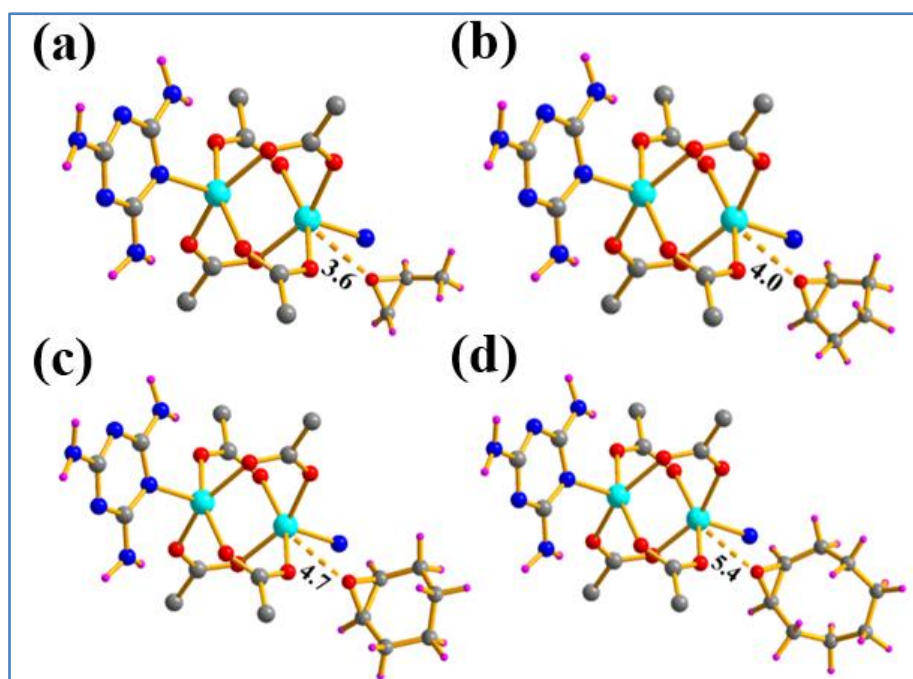


**Figure 5.** Local views of the interacting distance of Zn(II)–O(epoxide) (dashed yellow lines) observed in the periodic DFT optimized HbMOF1 structure loaded with epoxides such as PO (a), CPO (b), CHO (c), and CCO (d). The interacting distances are reported in Å and the color code for the atoms: C (dark grey), N (blue), O (red), F (green), Zn (cyan), and H (magenta).

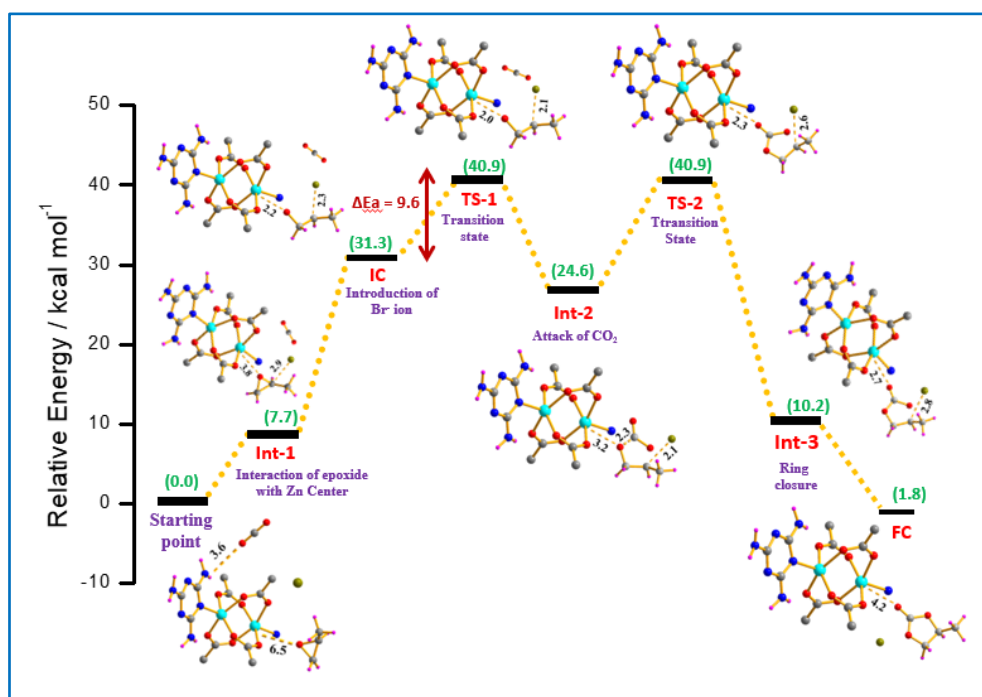
**Table 3.** Comparison of catalytic activity of HbMOF1 with literature reported MOFs for cycloaddition of CO<sub>2</sub> with internal epoxide (cyclohexane oxide) under mild conditions.

Sl. No.	Catalyst (mol%)	Temperature (°C)	Pressure (MPa)	Time (h)	Yield (%)	Ref.
1	Ti-ZIF	100	2.5	8	95	46
2	CoMOF-1	100	3.0	8	99	15b
3	JLU-MOF58	80	0.1	24	92	47
4	1-Urea	RT	0.1	36	19	48
5	UMCM-1-NH <sub>2</sub>	RT	1.2	24	10	49
<b>6</b>	<b>HbMOF1</b>	<b>RT</b>	<b>0.1</b>	<b>24</b>	<b>50</b>	<b>This Work</b>

### 2b.3.5. Plausible mechanism of cycloaddition reaction

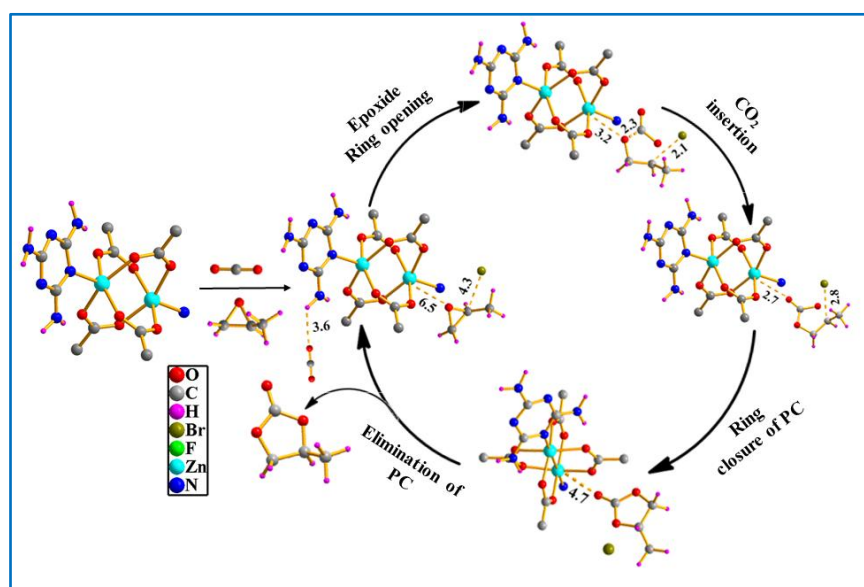
The crystal structure of HbMOF1 discloses the presence of high-density basic  $-NH_2$  and polar  $-CF_3$  groups exposed in the pore channels along with Zn(II) centers on the pore walls promoting the enhanced catalytic activity. Previously reported studies have shown that MOFs constituted by ligands containing  $-amino/amide$  functional sites can act as Lewis basic sites in cycloaddition reactions.<sup>50</sup> The microporous nature of HbMOF1 having fluorinated environment ( $-CF_3$  group of hfpbba<sup>2-</sup>) and amino ( $-NH_2$ ) groups of MA favored strong adsorption of  $CO_2$  and encapsulation of the substrates (epoxides) simultaneously and support synergistic catalytic activity. As discussed before, the GCMC simulated  $CO_2$  adsorption proved that fluorines of  $-CF_3$  and  $-NH_2$  groups of MA in the highly confined 1D channels of HbMOF1 promote strong  $CO_2$  occupancy at the vicinity of Zn(II) centers (Figure 4b). The detailed periodic-DFT calculations guided the molecular-level understanding of the mechanism of the propylene-oxide (PO)– $CO_2$  cycloaddition reaction catalyzed by HbMOF1 in the presence of TBAB co-catalyst. Here, the TBAB delivers the bromide ion ( $Br^-$ ) nucleophile to the pore channels of HbMOF1 and the coordination of the epoxide (PO) to the catalytic site (Zn(II)) along with the loading of  $CO_2$  molecules via interaction with  $-NH_2$  groups of MA initiate the catalytic reaction. The total energy of HbMOF1 with  $Br^-$  nucleophile, PO, and  $CO_2$  was considered to be zero for the calculation of the entire mechanistic pathway of the reaction. Further, Scheme 2 illustrates the relative energies of the optimized structures of the intermediates involving PO and  $CO_2$  with HbMOF1/ $Br^-$ . The initial stages of the reaction are dealt with the ring-opening of the epoxide (PO), where an intermediate (Int-1), incoming complex (IC), and transition state (TS-1) are formed by the simultaneous interaction of the oxygen atom of PO, O(PO), with the zinc metal center, Zn(II), and  $Br^-$  nucleophile to alpha carbon of the PO,  $\alpha-C(PO)$ . The relative energies attained for Int-1, IC and TS-1 are 7.7, 31.3, and 40.9 kcal/mol, respectively. The  $Br^-$  ion interacts with a distance of 2.90 Å to  $\alpha-C(PO)$  in the intermediate stage, Int-1, which increased relative energy. Subsequently, the interacting distance between  $Br^-$  ion and the  $\alpha-C(PO)$  shortens to 2.3 and 2.1 Å in the IC and TS-1 stages, respectively (Figure A25). At the same time, the distances between O(PO) and Zn(II) metal of HbMOF1 in IC and TS-1 are also shortened with a distance of 2.2 and 2.0 Å, respectively. During the ring-opening step, an alkoxide species is formed by the attack of the nucleophile,  $Br^-$  ion at  $\alpha-C(PO)$ , and this is designated as the first transition state (TS-1). The difference between the relative energies of TS-1 and IC as shown in Scheme 2 is 9.6 kcal/mol. Also, this energy barrier for the ring-opening step is treated as the rate-determining step in the  $CO_2$  fixation with PO according to several other

previously reported DFT energy profiles for cycloaddition reaction.<sup>15b,51</sup> Next, the CO<sub>2</sub> insertion to the bromide-substituted alkoxide species in TS-1, occurs with a relative energy value of 24.6 kcal/mol upon progressing the cycloaddition reaction. This intermediate state (Int-2) is formed by the interaction of CO<sub>2</sub> molecule to PO with a distance of 2.3 Å and this guides to the formation of a second transition state (TS-2) by the strong interaction of CO<sub>2</sub> to the negatively charged O(PO) with a relative energy value of 40.9 kcal/mol. At this transition state TS-2, not only the new bond, C(CO<sub>2</sub>)–O(PO), with a bond distance of 2.1 Å is formed but also the alkoxide group interacts strongly with the Zn(II) via Zn–O(CO<sub>2</sub>) with an interacting distance of 2.3 Å. During the ring closure stages of the reaction, a new intermediate, Int-3, is formed with relative energy of 10.2 kcal/mol after the transition state TS-2. The Int-3 consists of a five-membered ring of propylene carbonate (PC) via the insertion of CO<sub>2</sub>, where the inserted CO<sub>2</sub> makes O(CO<sub>2</sub>)–αC(PO) and C(CO<sub>2</sub>)–O(PO) bonds with distances of 1.64 and 1.51 Å, respectively. Altogether, the bond distances of Zn–O(CO<sub>2</sub>) and C(PO)–Br becomes 2.67 and 2.84 Å from 2.3 and 2.56 Å, respectively. In the final stage of ring closure (FC), both the propylene carbonate detachment from the Zn(II) of the HbMOF1 catalyst and regeneration of Br<sup>-</sup> ion occurs at the same time with relative energy of 1.8 kcal/mol. Overall, based on the combined experimental results and periodic-DFT calculations the mechanism depicted in Scheme 3 is proposed for the cycloaddition reaction.



**Scheme 2.** DFT-energy profile for the cycloaddition reaction of CO<sub>2</sub> with PO to produce PC catalyzed by HbMOF1.

In general, the mechanism for cyclic carbonate formation from epoxide and CO<sub>2</sub> takes place through an initial ring-opening of the epoxide, followed by CO<sub>2</sub> insertion, and finally the five-membered cyclic carbonate formation by ring closure step. Scheme 3 represents the catalytic cycle involved in the cycloaddition reaction of CO<sub>2</sub> with PO to produce PC using HbMOF1 catalyst and TBAB co-catalyst. While, the ring-opening of the epoxide proceeds well because the oxygen of the epoxide, O(PO) interacts quickly with the Zn(II) metal site having distorted square pyramidal geometry in the binuclear paddle-wheel arrangement. In a subsequent step, the alkoxide species formed by the attack of the nucleophile, Br<sup>-</sup> ion, at less-hindered carbon atom, is stabilized by supramolecular interactions with -CF<sub>3</sub> and -NH<sub>2</sub> groups. The adsorbed CO<sub>2</sub> interacts with the alkoxide species to form an alkyl carbonate anion and finally, the ring closure of the alkyl carbonate anion leads to the formation of cyclic carbonate and regeneration of HbMOF1 catalyst and Br<sup>-</sup> nucleophile. Also, the functional groups (-CF<sub>3</sub> and -NH<sub>2</sub>) in HbMOF1 support the CO<sub>2</sub> capture with a high adsorption enthalpy as discussed before. Further, the high exothermic CO<sub>2</sub> adsorption at atmospheric pressure and RT due to the confined microporous nature of the HbMOF1 catalyst with the highly active Zn(II) center helped for an efficient formation of cyclic carbonates. Overall, the excellent catalytic activity of HbMOF1 for the CO<sub>2</sub> cycloaddition reactions with epoxides can be mainly ascribed to the synergic effect of the highly active distorted square pyramidal Zn(II) in the binuclear paddle-wheel SBU and multifunctional (-NH<sub>2</sub> and -CF<sub>3</sub>) groups decorated in the pore walls of the microporous 3D framework.



**Scheme 3.** A plausible mechanism for the CO<sub>2</sub> cycloaddition reaction with epoxides catalyzed by HbMOF1.

### 2b.3.6. Recyclability

Recyclability is an important criterion for a heterogeneous catalyst. To test the recyclability, the HbMOF1 catalyst was facilely separated from the reaction mixture by filtration and then washed with methanol and activated at 353K under vacuum for 12h and the sample was reused for subsequent catalytic cycles. Interestingly, there was no substantial reduction in the catalytic conversion of ECH even after five cycles of regeneration (Figures 6a and 25). The PXRD pattern and FT-IR spectra of the recycled sample after five cycles matched well with the as-synthesized sample, which suggests that the original framework structure is retained (Figure A12, A26). Further, the leaching test was carried out in which the catalytic reaction was stopped after 6h and the HbMOF1 catalyst was separated from the reaction mixture, and the filtrate was allowed to stir for an extra period of 18 h.  $^1\text{H}$ NMR analysis of the aliquot taken after 24h showed a negligible increase in activity due to the presence of cocatalyst (TBAB) in the reaction medium which supports the heterogeneous nature of HbMOF1 (Figure 6b).

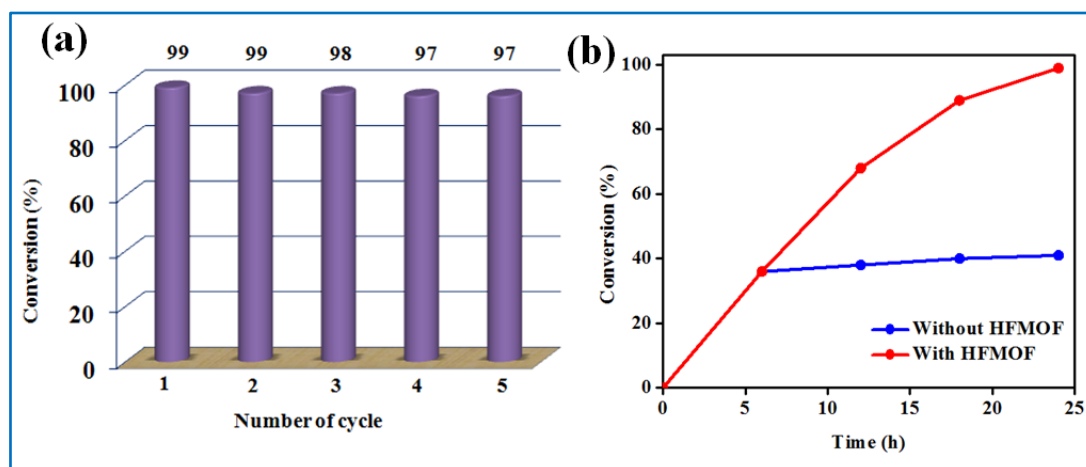


**Figure 6.** Recyclability test and (b) leaching test of HbMOF1.

### 2b.4. Conclusion

In conclusion, the development of a novel, microporous, hydrogen-bonded 3D framework composed of confined 1D channels decorated with  $\text{CO}_2$ -philic ( $-\text{NH}_2$  and  $-\text{CF}_3$ ) groups and Zn(II) centers suitable for efficient utilization of carbon dioxide is achieved. The polar functionalized channels of HbMOF1 promoted selective and highly reproducible adsorption of  $\text{CO}_2$ . The MOF showed excellent catalytic activity for highly efficient fixation of  $\text{CO}_2$  with various terminal/internal epoxides at the mild conditions of 1 bar of  $\text{CO}_2$  and RT. The simulated  $\text{CO}_2$  adsorption on HbMOF1 at 1 bar and RT reinforced that  $-\text{NH}_2$  and  $-\text{CF}_3$

exposure in the pores facilitated selective and high uptake of CO<sub>2</sub> with a high exothermic adsorption enthalpy of 36.0 kJ/mol (sim.) vs 36.7 kJ/mol (exp.). Additionally, a detailed mechanistic investigation of the cycloaddition reaction was studied through periodic Density Functional Theory (DFT) calculations. Indeed, the theoretical studies unveiled the synergistic participation of Zn(II) center and the basic –NH<sub>2</sub> groups in facilitating the efficient coupling of CO<sub>2</sub> with various epoxides affording high-yield generation of cyclic carbonates at mild conditions. This study highlights the rational design of porous MOFs incorporating multiple functional sites for efficient fixation of CO<sub>2</sub> into high-value chemicals under mild conditions.

### 2b.5. References

- (1) (a) Ding, M.; Flaig, R. W.; Jiang, H.-L.; Yaghi, O. M. Carbon capture and conversion using metal-organic frameworks and MOF-based materials. *Chem. Soc. Rev.* **2019**, 48, 2783-2828. (b) Tiba, S. A. Omri, Literature survey on the relationships between energy, environment and economic growth. *Renewable Sustainable Energy Rev.* **2017**, 69, 1129-1146.
- (2) (a) Chu, S. Carbon Capture and Sequestration. *Science* **2009**, 325, 1599. (b) Alessandro, D. M. D.; Smit, B.; Long, J. R. Carbon Dioxide Capture: Prospects for New Materials. *Angew. Chem. Int. Ed.* **2010**, 49, 6058-6082. (c) Jacobson, M. Z. Review of solutions to global warming, air pollution, and energy security. *Energy Environ. Sci.* **2009**, 2, 148-173.
- (3) (a) Liao, J.; Zeng, W.; Zheng, B.; Cao, X.; Wang, Z.; Wang, G.; Yang, Q. Highly efficient CO<sub>2</sub> capture and conversion of a microporous acylamide functionalized *rht*-type metal-organic framework. *Inorg. Chem. Front.* **2020**, 7, 1939-1948. (b) Cui, W.-G.; Zhang, G.-Y.; Hu, T.-L.; Bu, X.-H. Metal-organic framework-based heterogeneous catalysts for the conversion of C1 chemistry: CO, CO<sub>2</sub> and CH<sub>4</sub>. *Coord. Chem. Rev.* **2019**, 387, 79-120.
- (4) (a) Liang, J.; Chen, R. P.; Wang, X. Y.; Liu, T. T.; Wang, X. S.; Huang, Y. B.; Cao, R. Post-synthetic ionization of an imidazole-containing metal-organic framework for the cycloaddition of carbon dioxide and epoxides. *Chem. Sci.* **2017**, 8, 1570-1575. (b) Nguyen, P. T. K.; Nguyen, H. T. D.; Nguyen, H. N.; Trickett, C. A.; Ton, Q. T.; -Puebla, E. G.; Monge, M. A.; Cordova, K. E.; Gandara, F. New Metal-Organic Frameworks for Chemical Fixation of CO<sub>2</sub>. *ACS Appl. Mater. Interfaces* **2018**, 10, 733-744.
- (5) (a) Scrosati, B.; Hassounab, J.; Sun, Y.-K. Lithium-ion batteries. A look into the future. *Energy Environ. Sci.* **2011**, 4, 3287-3295. (b) Fukuoka, S.; Kawamura, M.; Komiyama, K.; Tojo, M.; Hachiya, H.; Hasegawa, K.; Aminaka, M.; Okamoto, H.; Fukawad, I.; Konno, S. A novel

non-phosgene polycarbonate production process using by-product CO<sub>2</sub> as starting material. *Green Chem.* **2003**, *5*, 497-507.

(6) Yun, D.; Park, D. S.; Lee, K. R.; Yun, Y. S.; Kim, T. Y.; Park, H.; Lee, H.; Yi, J. A New Energy-Saving Catalytic System: Carbon Dioxide Activation by a Metal/Carbon Catalyst. *ChemSusChem* **2017**, *10*, 3671-3678.

(7) (a) Ma, R.; He, L. N.; Zhou, Y.-B. An efficient and recyclable tetraoxo-coordinated zinc catalyst for the cycloaddition of epoxides with carbon dioxide at atmospheric pressure. *Green Chem.* **2016**, *18*, 226-231. (b) Ema, T.; Miyazaki, Y.; Shimonishi, J.; Maeda, C.; Hasegawa, J. Y. Bifunctional Porphyrin Catalysts for the Synthesis of Cyclic Carbonates from Epoxides and CO<sub>2</sub>: Structural Optimization and Mechanistic Study. *J. Am. Chem. Soc.* **2014**, *136*, 15270-15279. (c) Liu, M.; Gao, K.; Liang, L.; Sun, J.; Sheng, L.; Arai, M. Experimental and theoretical insights into binary Zn-SBA-15/KI catalysts for the selective coupling of CO<sub>2</sub> and epoxides into cyclic carbonates under mild conditions. *Catal. Sci. Technol.* **2016**, *6*, 6406-6416.

(8) (a) Whiteoak, C. J.; Nova, A.; Maseras, F.; Kleij, A. W. Merging Sustainability with Organocatalysis in the Formation of Organic Carbonates by Using CO<sub>2</sub> as a Feedstock. *ChemSusChem* **2012**, *5*, 2032-2038. (b) Wilhelm, M. E.; Anthofer, M. H.; Cokoja, M.; Markovits, I. I. E.; Herrmann, W. A.; Kühn, F. E. Cycloaddition of Carbon Dioxide and Epoxides using Pentaerythritol and Halides as Dual Catalyst System. *ChemSusChem* **2014**, *7*, 1357-1360.

(9) (a) Monassier, A.; D'Elia, V.; Cokoja, M.; Dong, H.; Pelletier, J. D. A.; Basset, J. M.; Kühn, F. E. Synthesis of Cyclic Carbonates from Epoxides and CO<sub>2</sub> under Mild Conditions Using a Simple, Highly Efficient Niobium-Based Catalyst. *ChemCatChem* **2013**, *5*, 1321-1324. (b) Song, Q. W.; He, L. N.; Wang, J. Q.; Yasuda, H.; Sakakura, T. Catalytic fixation of CO<sub>2</sub> to cyclic carbonates by phosphonium chlorides immobilized on fluororous polymer. *Green Chem.* **2013**, *15*, 110-115.

(10) Yang, Z. Z.; Zhao, Y. N.; He, L. N.; Gao, J.; Yin, Z. S. Highly efficient conversion of carbon dioxide catalyzed by polyethylene glycol-functionalized basic ionic liquids. *Green Chem.* **2012**, *14*, 519-527.

(11) (a) Xie, Y.; Zhang, Z.; Jiang, T.; He, J.; Han, B.; Wu, T.; Ding, K. CO<sub>2</sub> Cycloaddition Reactions Catalyzed by an Ionic Liquid Grafted onto a Highly Cross-Linked Polymer Matrix. *Angew. Chem. Int. Ed.* **2007**, *46*, 7255-7258. (b) Meng, X. L.; Nie, Y.; Sun, J.; Cheng, W. G.; Wang, J. Q.; He, H. Y.; Zhang, S. J. Functionalized dicyandiamide-formaldehyde polymers as efficient heterogeneous catalysts for conversion of CO<sub>2</sub> into organic carbonates. *Green Chem.* **2014**, *16*, 2771-2778;

- (12) Wang, Q.; Astruc, D. State of the Art and Prospects in Metal-Organic Framework (MOF)-Based and MOF-Derived Nanocatalysis. *Chem. Rev.* **2020**, *120*, 1438-1511. (b) Dhankhar, S. S.; Ugale, B.; Nagaraja, C. M. Co-Catalyst-Free Chemical Fixation of CO<sub>2</sub> into Cyclic Carbonates by using Metal-Organic Frameworks as Efficient Heterogeneous Catalysts. *Chem Asian J.* **2020**, *15*, 2403-2427.
- (13) (a) Bavykina, A.; Kolobov, N.; Khan, S.; Bau, J. A.; Ramirez, A.; Gascon, J. Metal-Organic Frameworks in Heterogeneous Catalysis: Recent Progress, New Trends, and Future Perspectives. *Chem. Rev.* **2020**, *120*, 8468-8535. (b) Zhou, H.-C.; Long, J. R.; Yaghi, O. M. Introduction to Metal-Organic Frameworks. *Chem. Rev.* **2012**, *112*, 673-674.
- (14) (a) Kamphuis, A. J.; Picchioni, F.; Pescarmona, P. P. CO<sub>2</sub>-fixation into cyclic and polymeric carbonates: principles and applications. *Green Chem.* **2019**, *21*, 406-448. (b) Sneddon, G.; Greenaway, A.; Yiu, H. H. P. The Potential Applications of Nanoporous Materials for the Adsorption, Separation, and Catalytic Conversion of Carbon Dioxide. *Adv. Energy Mater* **2014**, *4*, 1301873.
- (15) (a) Aguila, B.; Sun, Q.; Wang, X.; Rourke, E. O. Q.; -Enizi, A. M. A.; Nafady, A.; Ma, S. Lower Activation Energy for Catalytic Reactions through Host-Guest Cooperation within Metal-Organic Frameworks. *Angew. Chem. Int. Ed.* **2018**, *57*, 10107-10111. (b) Parmar, B.; Patel, P.; Pillai, R. S.; Kureshy, R. I.; Khan, N. H.; Suresh, E. Efficient catalytic conversion of terminal/internal epoxides to cyclic carbonates by porous Co(II) MOF under ambient conditions: structure-property correlation and computational studies. *J. Mater. Chem. A.* **2019**, *7*, 2884-2894.
- (16) (a) Das, R.; Dhankhar, S. S.; Nagaraja, C. M. Construction of a bifunctional Zn(II)-organic framework containing basic amine functionality for selective capture and room temperature fixation of CO<sub>2</sub>. *Inorg. Chem. Front.* **2020**, *7*, 72-81. (b) Sharma, N.; Dhankhar, S. S.; Kumar, S.; Kumar, T. J. D.; Nagaraja, C. M. Rational Design of a 3D Mn<sup>II</sup>-Metal–Organic Framework Based on a Nonmetallated Porphyrin Linker for Selective Capture of CO<sub>2</sub> and One-Pot Synthesis of Styrene Carbonates. *Chem. Eur. J.* **2018**, *24*, 16662-16669. (c) Liu, Q.; Wu, L.; Jackstell, R.; Beller, M. Using carbon dioxide as a building block in organic synthesis. *Nat. Commun.* **2015**, *6*, 5933. (d) Meng, X. L.; Nie, Y.; Sun, J.; Cheng, W. G.; Wang, J. Q.; He, H. Y.; Zhang, S. J. Superbase/cellulose: an environmentally benign catalyst for chemical fixation of carbon dioxide into cyclic carbonates. *Green Chem.* **2014**, *16*, 2771-2778.
- (17) (a) Comotti, A.; Castiglioni, F.; Bracco, S.; Perego, J.; Pedrini, A.; Negroni, M.; Sozzani, P. Fluorinated porous organic frameworks for improved CO<sub>2</sub> and CH<sub>4</sub> capture. *Chem. Commun.* **2019**, *55*, 8999-9002 (b) Bhatt, P. M.; Belmabkhout, Y.; Cadiau, A.; Adil, K.;

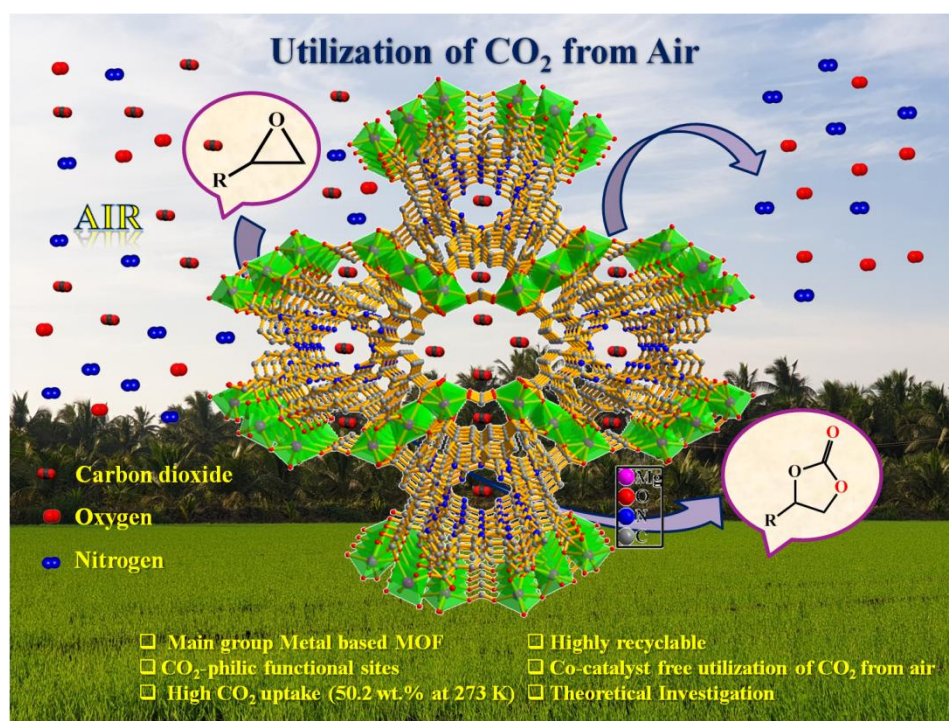
- Shekhah, O.; Shkurenko, A.; Barbour, L. J.; Eddaoudi, M. A Fine-Tuned Fluorinated MOF Addresses the Needs for Trace CO<sub>2</sub> Removal and Air Capture Using Physisorption. *J. Am. Chem. Soc.* **2016**, *138*, 9301-9307. (c) Zhang, G.; Wei, G.; Liu, Z.; Oliver, S. R. J.; Fei, H. A Robust Sulfonate-Based Metal-Organic Framework with Permanent Porosity for Efficient CO<sub>2</sub> Capture and Conversion. *Chem. Mater* **2016**, *28*, 6276-6281. (d) Han, Y.-H.; Zhou, Z.-Y.; Tian, C.-B.; Du, S.-W. A dual-walled cage MOF as an efficient heterogeneous catalyst for the conversion of CO<sub>2</sub> under mild and co-catalyst free conditions. *Green Chem.* **2016**, *18*, 4086-4091. (e) He, H.; Zhu, Q.-Q.; Zhao, J.-N.; Sun, H.; Chen, J.; Li, C.-P.; Du, M. Rational Construction of an Exceptionally Stable MOF Catalyst with Metal-Adeninate Vertices toward CO<sub>2</sub> Cycloaddition under Mild and Cocatalyst-Free Conditions. *Chem. Eur. J.* **2019**, *25*, 11474-11480.
- (18) SMART (V 5.628), SAINT (V 6.45a), XPREP, SHELXTL; Bruker AXS Inc. Madison, Wisconsin, USA, 2004
- (19) Sheldrick, G. M. *Siemens Area Detector Absorption Correction Program*, University of Göttingen, Göttingen, Germany, **2004**.
- (20) Altomare, A.; Casciarano, G.; Giacovazzo, C.; Guagliardi, A. Completion and refinement of crystal structures with SIR92. *J. Appl. Cryst.* **1993**, *26*, 343-350.
- (21) Sheldrick, G. M. SHELXL-2014, *Program for Crystal Structure Solution and Refinement*; University of Göttingen, Göttingen, Germany, **2014**.
- (22) Farrugia, L. J. WinGX-A Windows Program for Crystal Structure Analysis. *J. Appl. Cryst.* **2001**, *45*, 849-854.
- (23) Spek, A. L. Single-crystal structure validation with the program PLATON. *J. Appl. Crystallogr.* **2003**, *36*, 7-13.
- (24) Lippert, G.; Hutter, J.; Parrinello, M. A hybrid Gaussian and plane wave density functional scheme. *Mol. Phys.* **1997**, *92*, 477.
- (25) Perdew, J. P.; Wang, Y. Density-functional approximation for the correlation energy of the inhomogeneous electron gas. *Phys. Rev. B* **1986**, *33*, 8822.
- (26) Vondede, J. V.; Hutter, J. Gaussian basis sets for accurate calculations on molecular systems in gas and condensed phases. *J. Chem. Phys.* **2007**, *127*, 114105.
- (27) Goedecker, S.; Teter, M.; Hutter, J. Separable dual-space Gaussian pseudopotentials. *Phys. Rev. B* **1996**, *54*, 1703.
- (28) Grimme, S.; Antony, J.; Ehrlich, S.; Krieg, H. A consistent and accurate *ab initio* parametrization of density functional dispersion correction (DFT-D) for the 94 elements H-Pu. *J. Chem. Phys.* **2010**, *132*, 154104.

- (29) Campana, C.; Mussard, B.; Woo, T. K. Electrostatic Potential Derived Atomic Charges for Periodic Systems Using a Modified Error Functional. *J. Chem. Theory Comput.* **2009**, *5*, 2866-2878.
- (30) Golze, D.; Hutter, J.; Iannuzzi, M. Wetting of water on hexagonal boron nitride@Rh(111): a QM/MM model based on atomic charges derived for nano-structured substrates. *Phys. Chem. Chem. Phys.* **2015**, *17*, 14307-14316.
- (31) Rappé, A. K.; Casewit, C. J.; Colwell, K. S.; Goddard, W. A.; Skiff, W. M. UFF, a full periodic table force field for molecular mechanics and molecular dynamics simulations. *J. Am. Chem. Soc.* **1992**, *114*, 10024.
- (32) Harris, J. G.; Yung, K. H. Carbon Dioxide's Liquid-Vapor Coexistence Curve and Critical Properties As Predicted by a Simple Molecular Model. *J. Phys. Chem.* **1995**, *99*, 12021.
- (33) Potoff, J. J.; Siepmann, J. I. Vapor-liquid equilibria of mixtures containing alkanes, carbon dioxide, and nitrogen. *Aiche J.* **2001**, *47*, 1676-1682.
- (34) Dubbeldam, D.; Calero, S.; Ellis, D. E.; Snurr, R. Q. RASPA: molecular simulation software for adsorption and diffusion in flexible nanoporous materials. *Mol Simulat.* **2016**, *42*, 81-101.
- (35) Peng, D.-Y.; Robinson, D. B. A New Two-Constant Equation of State. *Ind. Eng. Chem. Fundam.* **1976**, *15*, 59.
- (36) Vlught, T. J. H.; García-Pérez, E.; Dubbeldam, D.; Ban, S.; Calero, S. Computing the Heat of Adsorption using Molecular Simulations: The Effect of Strong Coulombic Interactions. *J. Chem. Theory Comput.* **2008**, *4*, 1107-1118.
- (37) Bae, Y. S.; Yazaydin, A. O.; Snurr, R. Q. Evaluation of the BET Method for Determining Surface Areas of MOFs and Zeolites that Contain Ultra-Micropores. *Langmuir* **2010**, *26*, 5475-5483.
- (38) Rouquerol, F.; Rouquerol, J.; Sing, K. Adsorption by Powders and Porous Solids: Principles, Methodology and Applications. Academic Press: **1999**.
- (39) Duren, T.; Millange, F.; Ferey, G.; Walton, K. S.; Snurr, R. Q. Calculating Geometric Surface Areas as a Characterization Tool for Metal-Organic Frameworks. *J. Phys. Chem. C* **2007**, *111*, 15350-15356.
- (40) VandeVondele, J.; Krack, M.; Mohamed, F.; Parrinello, M.; Chassaing, T.; Hutter, J. QUICKSTEP: Fast and accurate density functional calculations using a mixed Gaussian and plane waves approach. *Comput Phys Commun.* **2005**, *167*, 103.

- (41) Ye, J.; Johnson, J. K. Design of Lewis Pair-Functionalized Metal Organic Frameworks for CO<sub>2</sub> Hydrogenation. *ACS Catal.* **2015**, *5*, 2921-2928.
- (42) Blatov, V. A.; Shevchenko, A. P.; Proserpio, D. M. Applied Topological Analysis of Crystal Structures with the Program Package ToposPro, *Cryst. Growth Des.* **2014**, *14*, 3576-3586.
- (43) Yang, R. T. Gas Separation by Adsorption Processes, Butterworth, Boston, **1997**.
- (44) Pan, H.; Ritter, J. A.; Balbuena, P. B. Examination of the approximations used in determining the isosteric heat of adsorption from the Clausius-Clapeyron equation. *Langmuir* **1998**, *14*, 6323-6327.
- (45) (a) Gao, W. Y.; Chen, Y.; Niu, Y.; Williams, K.; Cash, L.; Perez, P. J.; Wojtas, L.; Cai, J.; Chen, Y. S.; Ma, S. Crystal Engineering of an nbo Topology Metal-Organic Framework for Chemical Fixation of CO<sub>2</sub> under Ambient Conditions. *Angew. Chem. Int. Ed.* **2014**, *53*, 2615-2619. (b) Lan, J.; Liu, M.; Lu, X.; Zhang, X.; Sun, J. Novel 3D Nitrogen-Rich Metal Organic Framework for Highly Efficient CO<sub>2</sub> Adsorption and Catalytic Conversion to Cyclic Carbonates under Ambient Temperature. *ACS Sustainable Chem. Eng.* **2018**, *6*, 8727-8735.
- (46) Verma, S.; Baig, R. B. N.; Nadagouda, M. N.; Varma, R. S. Titanium-based zeolitic imidazolate framework for chemical fixation of carbon dioxide. *Green Chem.* **2016**, *18*, 4855-4858.
- (47) Sun, X.; Gu, J.; Yuan, Y.; Yu, C.; Li, J.; Shan, H.; Li, G.; Liu, Y. A Stable Mesoporous Zr-Based Metal Organic Framework for Highly Efficient CO<sub>2</sub> Conversion. *Inorg. Chem.* **2019**, *58*, 7480-7487.
- (48) Wei, L.-Q.; Ye, B.-H. Efficient Conversion of CO<sub>2</sub> via Grafting Urea Group into a [Cu<sub>2</sub>(COO)<sub>4</sub>]-Based Metal-Organic Framework with Hierarchical Porosity. *Inorg. Chem.* **2019**, *58*, 4385-4393.
- (49) Babu, R.; Kathalikkattil, A. C.; Roshan, R.; Tharun, J.; Kimb, D. W.; Park, D. W. Dual-porous metal organic framework for room temperature CO<sub>2</sub> fixation via cyclic carbonate synthesis. *Green Chem.* **2016**, *18*, 232-242.
- (50) Li, P.-Z.; Wang, X.-J.; Liu, J.; Phang, H. S.; Li, Y.; Zhao, Y. Highly Effective Carbon Fixation via Catalytic Conversion of CO<sub>2</sub> by an Acylamide-Containing Metal-Organic Framework. *Chem. Mater.* **2017**, *29*, 9256-9261.
- (51) Kurisingal, J.; Rachuri, Y.; Palakkal, A. S.; Pillai, R. S.; Gu, Y.; Park, D.-W. Water-Tolerant DUT-Series Metal-Organic Frameworks: A Theoretical-Experimental Study for the Chemical Fixation of CO<sub>2</sub> and Catalytic Transfer Hydrogenation of Ethyl Levulinate to  $\gamma$ -Valerolactone. *ACS Appl. Mater. Interfaces* **2019**, *11*, 41458-41471.

# Chapter 3

## Efficient chemical fixation of CO<sub>2</sub> from direct air under environment-friendly co-catalyst and solvent-free ambient conditions





### 3.1. Introduction

Over the past two decades, the concentration of atmospheric carbon dioxide is increasing exponentially and it has exceeded 400 ppm, currently.<sup>1</sup> This rapid increase in the atmospheric CO<sub>2</sub> content has been attributed to various human activities leading to the increased combustion of fossil fuels.<sup>2</sup> This unprecedented rise in CO<sub>2</sub> emissions has resulted in the most serious environmental issues such as global warming, unpredictable weather patterns, ocean acidification, and so on.<sup>3</sup> To mitigate this growing CO<sub>2</sub> concentration, carbon capture and sequestration (CCS) have been followed.<sup>4-6</sup> However, an alternative, and a value-added route is the utilization of CO<sub>2</sub>, known as carbon capture and utilization (CCU) as a C1 source by converting it into high-value chemicals and fuels.<sup>7-12</sup> Particularly, selective CO<sub>2</sub> capture from direct air has attracted tremendous attention as this process enables carbon capture from any place independent of emission sources.<sup>13-15</sup> In this direction, intensive research efforts are being carried out in devising various strategies for selective carbon capture from direct air and its subsequent conversion to useful chemicals.<sup>16-20</sup> However, the inertness of CO<sub>2</sub> puts up a major synthetic challenge for its conversion under mild conditions. Among the various catalytic transformations of carbon dioxide, the cycloaddition of CO<sub>2</sub> with epoxides to produce cyclic carbonates is considered the most atom economic process.<sup>21-24</sup> Also, cyclic carbonates are valuable as commodity chemicals for the synthesis of pharmaceuticals and polymers.<sup>25-28</sup> The majority of the catalysts employed for the synthesis of cyclic carbonates require either high temperature or high pressure of CO<sub>2</sub> and an additional nucleophilic co-catalyst like tetrabutylammonium bromide (TBAB).<sup>29-32</sup> However, towards green and sustainable utilization of CO<sub>2</sub> from direct air, it is highly desirable to carry out the catalysis under co-catalyst-free mild conditions.<sup>33-35</sup> To achieve this, the catalyst employed should exhibit high carbon dioxide affinity and superior catalytic activity to capture and activate CO<sub>2</sub> at a very low concentration of 0.03% in air. Besides, the catalyst should be highly stable towards moisture and other contaminants in the air. Towards these aforementioned objectives, this chapter represents the rational construction of a bifunctional MOF by utilizing an eco-friendly, Lewis acidic metal ion, Mg(II), and a nitrogen-rich, tripodal organic ligand, TATAB containing nucleophilic basic –NH groups.<sup>36,37</sup> The Mg(II) metal has been known to offer potential advantages over the transition metal ions in selective CO<sub>2</sub> capture.<sup>38-40</sup> Owing to the presence of highly polar 1D channels decorated with a high density of CO<sub>2</sub>-philic basic –NH sites, the Mg-MOF exhibited high CO<sub>2</sub> uptake of 50.2 wt% at 273K with a high heat of adsorption value of 55.13 kJ/mol. The high CO<sub>2</sub> affinity combined with Lewis acidity due to Mg(II) ions, rendered superior catalytic properties for

efficient chemical fixation of CO<sub>2</sub> from direct air under environmentally friendly co-catalyst and solvent-free mild conditions. The remarkable affinity of Mg-MOF for CO<sub>2</sub> over other gases (O<sub>2</sub> and N<sub>2</sub>) in the air was further supported by molecular simulations carried out with the aid of density functional theory (DFT)-derived specific force field. Also, the theoretical simulations on the co-adsorption of wet air with Mg-MOF supplemented the high CO<sub>2</sub> selectivity over other atmospheric gases. To the best of our knowledge, this work represents the first example of co-catalyst-free fixation of CO<sub>2</sub> from direct air under eco-friendly mild conditions.

## 3.2. Experimental section

### 3.2.1. Materials

All the reagents used in this work were commercially available and used as received without any further purification. Mg(NO<sub>3</sub>)<sub>2</sub>·6H<sub>2</sub>O, 4-aminobenzoic acid, and cyanuric chloride were purchased from Sigma Aldrich Chemical Co. N, N'-dimethylformamide (DMF), sodium hydroxide and methanol (MeOH) were obtained from S. D. Fine Chem. Limited. All the epoxides and the internal standard used for catalytic reactions were purchased from TCI chemicals and used without further purification. The 4,4',4''-s-triazine-1,3,5-triyltri-p-aminobenzoic acid (H<sub>3</sub>TATAB) ligand was synthesized by following the previously reported literature procedure with a slight modification.<sup>41</sup>

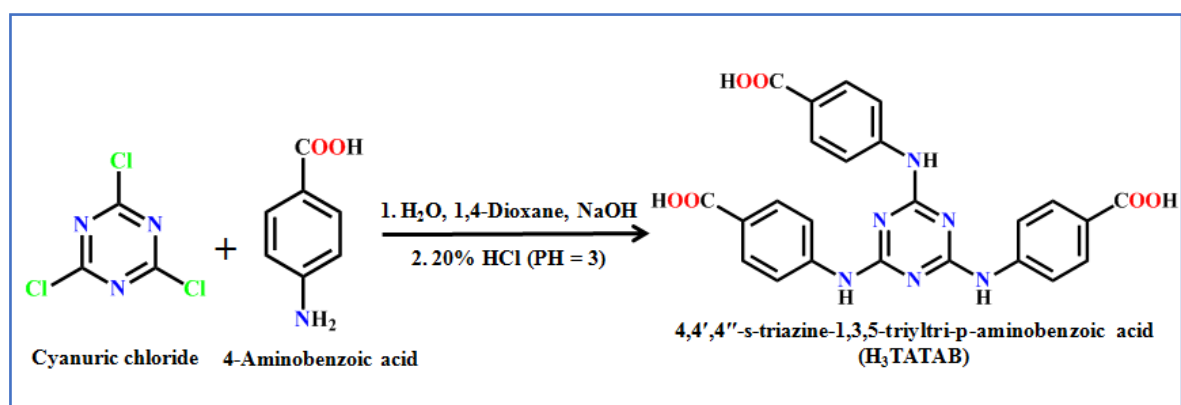
### 3.2.2. Physicochemical characterization

The phase purity of the as-synthesized samples was confirmed by powder XRD analysis using Rigaku Miniflex 600 with Cu K $\alpha$  radiation ( $\lambda = 0.154$  nm). UV-Vis (Diffuse Reflectance) spectra were recorded on the Shimadzu spectrophotometer using BaSO<sub>4</sub> as a reference. FTIR (Fourier transform infrared) spectra of the samples were recorded from 400 to 4000 cm<sup>-1</sup> on a Perkin Elmer ATR-FTIR spectrometer. The metal content of Mg in the framework was determined by Agilent's microwave-plasma atomic emission spectrometer (MP-AES). Thermo Fischer Flash 2000 Elemental Analyzer was used for elemental analyses (CHN) of the samples. The X-ray photoelectron spectroscopy (XPS) analyses were performed on a Thermo Fisher Scientific NEXSA photoemission spectrometer using Al-K $\alpha$  (1486.6 eV) X-ray radiation and analysis of the obtained data was performed using Avantage software. The <sup>1</sup>HNMR spectra were recorded in CDCl<sub>3</sub> on a JEOL JNM-ECS-400 spectrometer operating at a frequency of 400 MHz.

### 3.2.3. Synthesis

#### 3.2.3.1. Synthesis of 4,4',4''-s-triazine-1,3,5-triyltri-p-aminobenzoic acid (H<sub>3</sub>TATAB) ligand.

The 4,4',4''-s-triazine-1,3,5-triyltri-p-aminobenzoic acid (H<sub>3</sub>TATAB) ligand was synthesized by following the previously reported literature procedure with a slight modification (Scheme 1).<sup>41</sup> Briefly, a solution of 4-aminobenzoic acid (1.8 g, 13.3 mmol) in 20 mL of water and 3 mL of 5N sodium hydroxide was charged with sodium bicarbonate (0.9 g, 11.0 mmol). To this solution, cyanuric chloride (0.6 g, 3.3 mmol) in 50 mL of 1,4-Dioxane was added dropwise and stirred for 15 min. The resulting reaction mixture was refluxed overnight then cooled to room temperature and acidified by 20% hydrochloric acid (HCl) to attain pH of 3 (Scheme S1). The resulting precipitate was neutralized by washing with water. <sup>1</sup>H NMR (400 MHz) DMSO-d<sub>6</sub>, δ: 12.55 (s, 3H), 9.84 (s, 3H), 7.97 (d, 2H) and 7.87 (d, 6H).



**Scheme 1.** Synthesis scheme of 4,4',4''-s-triazine-1,3,5-triyltri-p-aminobenzoic acid (H<sub>3</sub>TATAB) ligand.

#### 3.2.3.2. Synthesis of Mg-MOF

The Mg-MOF was synthesized by following the solvothermal route at 120 °C (Scheme 1). The 4,4',4''-s-triazine-1,3,5-triyltri-p-aminobenzoic acid (H<sub>3</sub>TATAB) ligand (0.075 mmol, 36.48 mg) was dissolved in 6 mL of DMF in a glass vial. To this solution, 3mL ethanol solution of Mg(NO<sub>3</sub>)<sub>2</sub>·6H<sub>2</sub>O (0.112 mmol, 30 mg) was added dropwise with stirring. The resulting clear solution was heated in a preheated oven at 120 °C for 4 d. After four days colorless rod-like crystals of Mg-MOF was obtained. The phase purity of the as-synthesized sample was confirmed by powder X-ray diffraction analysis (Figure 1). FTIR (cm<sup>-1</sup>): 3380 (w), 2979 (w), 1592 (m), 1486 (m), 1373 (s), 1238 (m), 1179 (m), 1.97 (m), 853 (w), 784 (m), 702 (w) (Figure A26). The elemental analysis, calculated (%) for as-synthesized

$\{\text{Mg}_3(\text{TATAB})_2(\text{HCOO})(\text{H}_2\text{O})_6(\text{DMF})_3(\text{DMA})\}_n$  ( $\text{C}_{60}\text{H}_{72}\text{N}_{16}\text{O}_{23}\text{Mg}_3$ ) Calculated: C:49.42, H:4.98, N:15.37 and found C:49.21, H:4.82, N:15.19. Activated sample  $\{\text{Mg}_3(\text{TATAB})_2(\text{HCO}_2)(\text{DMA})\}_n$ , ( $\text{C}_{51}\text{H}_{39}\text{N}_{13}\text{O}_{14}\text{Mg}_3$ ) Calculated: C:50.59, H:3.25, N:15.04 and found C:54.01, H:2.98, N:15.23.

### 3.2.4. Catalytic cycloaddition reactions of CO<sub>2</sub> with epoxides

The cycloaddition reactions of CO<sub>2</sub> with various epoxides were carried out in a Schlenk tube. Prior to catalytic reactions, the Mg-MOF was exchanged with acetone and activated at 130 °C for 15 h under vacuum to remove guest solvent molecules. In a typical reaction, the epoxide (20 mmol), and the activated MOF catalyst (0.1 mol%) were taken in the Schlenk tube at room temperature. Then, CO<sub>2</sub> (1 atm) was introduced using a balloon and the reaction mixture was allowed to stir at 60 °C for 24 h. After which time, the mixture was cooled to RT and the catalyst was separated from the reaction mixture by simple centrifugation and the catalytic conversions were determined from <sup>1</sup>H NMR spectra of the filtrate. The recovered catalyst was washed with acetone thoroughly and activated at 130 °C under vacuum for 15 h and reused for subsequent catalytic cycles. A similar procedure was employed for the catalytic reactions carried out with direct air, except that the CO<sub>2</sub> (balloon) was replaced by laboratory air with continuous bubbling.

### 3.2.5. Computational studies

Periodic DFT calculations were carried out in the mixed Gaussian plane wave scheme as implemented in the CP2K package<sup>42-52</sup> with Grimme's D3 dispersion corrections.<sup>53</sup> The PBE functional<sup>54</sup> was used to calculate the exchange-correlation energy. For Carbon, Oxygen, Nitrogen, and Hydrogen, a triple zeta (TZVP-MOLOPT) basis set was considered, while a double zeta (DZVP-MOLOPT) was applied for Magnesium.<sup>55</sup> The pseudopotentials used for all of the atoms were those derived by Goedecker, Teter, and Hutter.<sup>56</sup> This basis set and energy cut-off parameters have been considered based on the previous calculation by Ye *et al.*,<sup>57</sup> where they validated that PBE functional with a plane wave cutoff energy of 500 Ry and suggested as the best option for exploring the catalytic mechanism involves MOF. For constructing the Mg-MOF catalyst model, the unit cell of Mg-MOF was taken from the experimentally elucidated Mg-MOF, however, the calculations were carried out on the primitive cell to save computational time. The lattice constants of the optimized primitive cell are  $a = 34.5309 \text{ \AA}$ ,  $b = 26.5157 \text{ \AA}$ ,  $c = 25.1753 \text{ \AA}$ ,  $\alpha = 83.7869^\circ$ ,  $\beta = 49.7625^\circ$ ,  $\gamma = 46.4507^\circ$  and correspond to the unit cell with  $a = 16.9995 \text{ \AA}$ ,  $b = 47.394 \text{ \AA}$ ,  $c = 50.233 \text{ \AA}$ ,  $\alpha = \beta = \gamma =$

90°. We found that fully relaxing the geometry and cell parameters of Mg-MOF gave lattice constants that were almost identical to the relaxed Mg-MOF values. Furthermore, optimizing the structure with chemisorbed PO and/or CO<sub>2</sub> in Mg-MOF also perturbed the lattice constants and energies by a very minor amount. Therefore, we held the lattice constants fixed at the ground state Mg-MOF values for most calculations to save computational time. For the calculation, the total relative energy of the Mg-MOF (catalyst), CO<sub>2</sub>, and PO (isolated reactants) were considered to be zero energy, and the optimized structures of reactant complexes are depicted in Scheme 2. In the case of each stage of catalytic reaction (e.g. IS, IC, TS, RC, FC, etc.), the relative energies were computed with respect to the sum of the total energies of the corresponding gas-phase molecules as represented in Equation 1.

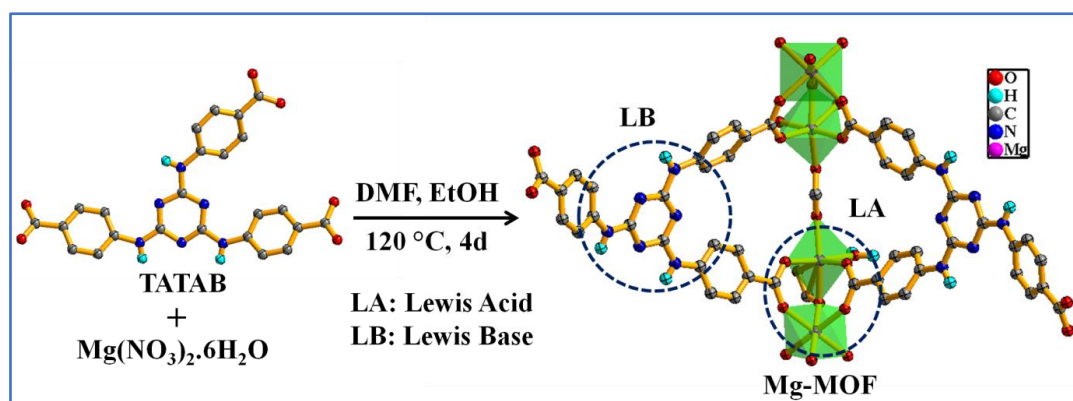
$$E_{relative} = E_{stage} - (E_{MgMOF} - E_{CO_2} - E_{PO}) \quad (1)$$

Where  $E_{stage}$ ,  $E_{MgMOF}$ ,  $E_{CO_2}$  and  $E_{PO}$  represents the total energies of the Mg-MOF with adsorbates at each reaction stage, the empty Mg-MOF, gas-phase CO<sub>2</sub>, and PO, respectively. Equation (1) defines negative values as exothermic and positive values as endothermic processes. Transition states along the reaction pathway were determined by using the climbing image nudged elastic band (CI-NEB) method. Transition states were confirmed through frequency analysis, verifying that the transition complex had only one imaginary frequency vibrational mode.

### 3.3. Results and discussion

#### 3.3.1. Synthesis and structural studies

The Mg-MOF was obtained by a solvothermal reaction of Mg(NO<sub>3</sub>)<sub>2</sub>·6H<sub>2</sub>O with H<sub>3</sub>TATAB ligand at 120 °C in DMF (Scheme 2). Interestingly, formate (HCOO<sup>-</sup>) anion *in situ* formed by the hydrolysis of DMF during the synthesis is involved in bridging the Mg(II) centers. A similar observation of *in situ* generations of HCOOH by hydrolysis of DMF at high temperatures is reported in the literature.<sup>58,59</sup> The powder X-ray diffraction (PXRD) analysis confirmed the phase purity of the as-synthesized sample (Figure 1). FTIR spectra showed the characteristic peaks at 3380 and 2979 cm<sup>-1</sup> corresponding to N-H and C-H stretching frequency originating from H<sub>3</sub>TATAB ligand and HCOO<sup>-</sup>, respectively (Figure A26). The solid-state absorption spectrum of Mg-MOF was found to be similar to that of the TATAB ligand with absorption bands at 267 and 331 nm corresponding to ligand-based  $\Pi \rightarrow \Pi^*$  transitions (Figure A27).



**Scheme 2.** Synthesis scheme for Mg-MOF.

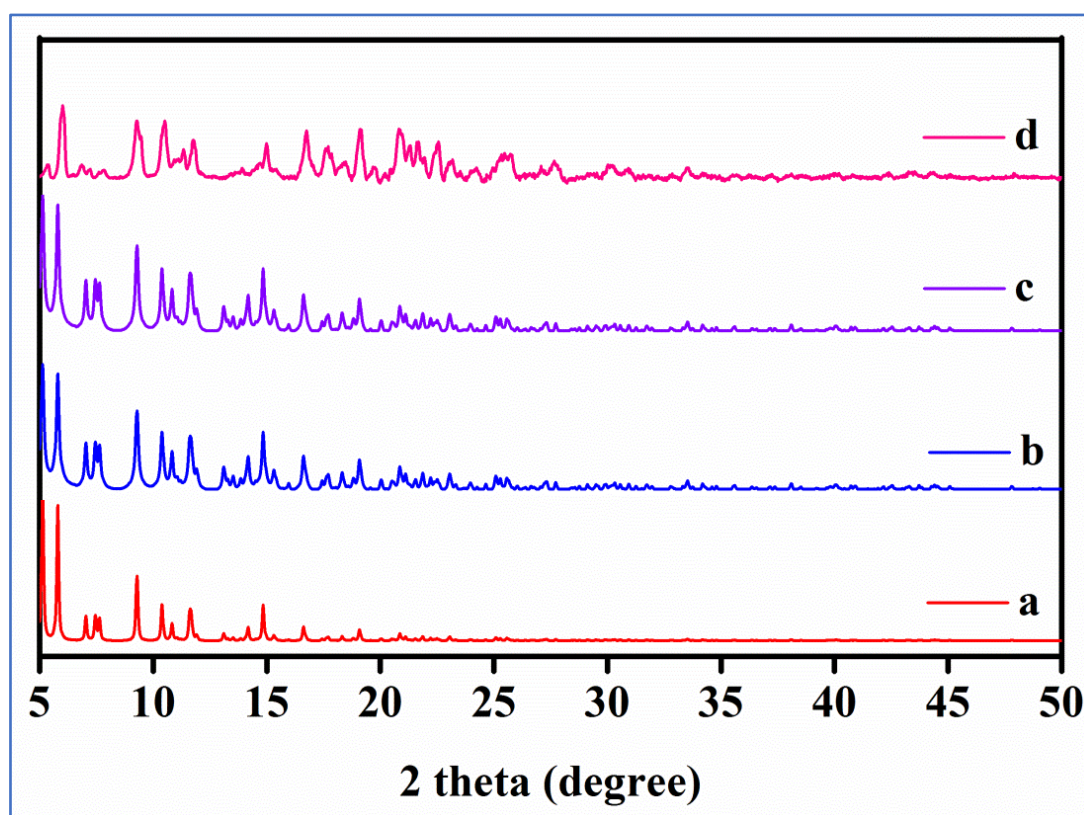


**Figure 1.** PXRD patterns of Mg-MOF (a) simulated pattern from single-crystal X-ray structure, (b) as-synthesized sample, (c) activated sample, and (d) recycled sample after tenth catalytic cycle.

Single-crystal X-ray diffraction study revealed that the 3D Mg-MOF is formed by the bridging of Mg(II) ions by  $\text{TATAB}^{3-}$  and  $\text{HCOO}^-$  anions (Figure 2a). The Mg centers are in a distorted octahedral environment in which the coordination at Mg1 is satisfied by six carboxylate oxygens (O1, O4, O5, O1a, O4a, and O5a, where  $a = 1-x, 1-y, -z$ ) of  $\text{TATAB}^{3-}$  ion, while the co-ordination at Mg2 is satisfied by four carboxylate oxygens (O2, O3, O4, and

O6) of TATAB<sup>3-</sup> ion, formate oxygen (O7) and a coordinated water molecule (O1w) (Figure 2a). The Mg1 and Mg2 nodes are bridged by carboxylate oxygens of TATAB<sup>3-</sup> and HCOO<sup>-</sup> anion forming a [Mg<sub>2</sub>O<sub>11</sub>] secondary building unit (SBU) which is further extended in three dimensions resulting in the 3D framework structure of Mg-MOF as shown in Figure 2b. Interestingly, the Mg-MOF possesses 1D channels along two crystallographic axes in which two types of 1D channels of dimension  $9 \times 5.1 \text{ \AA}^2$  and  $4.4 \times 4.3 \text{ \AA}^2$  are present along the *a*-axis and another type of 1D channel of dimension  $7.3 \times 5.2 \text{ \AA}^2$  along the *b*-axis (Figure 2b and 2c). It is worth noting that, the 1D channels are highly polar and decorated with a high density of basic and Lewis acidic sites (Figure 2c). Topological analysis by TOPOS<sup>60</sup> revealed the presence of a highly connected (3, 8-c), binodal net with  $\{3^{\wedge}27.4^{\wedge}28\}2\{3^{\wedge}54.4^{\wedge}94.5^{\wedge}38.6^{\wedge}4\}$ -net topology (Figure A28 and A29). The crystallographic details and the selected bond lengths and angles are given in Table A11, A12.

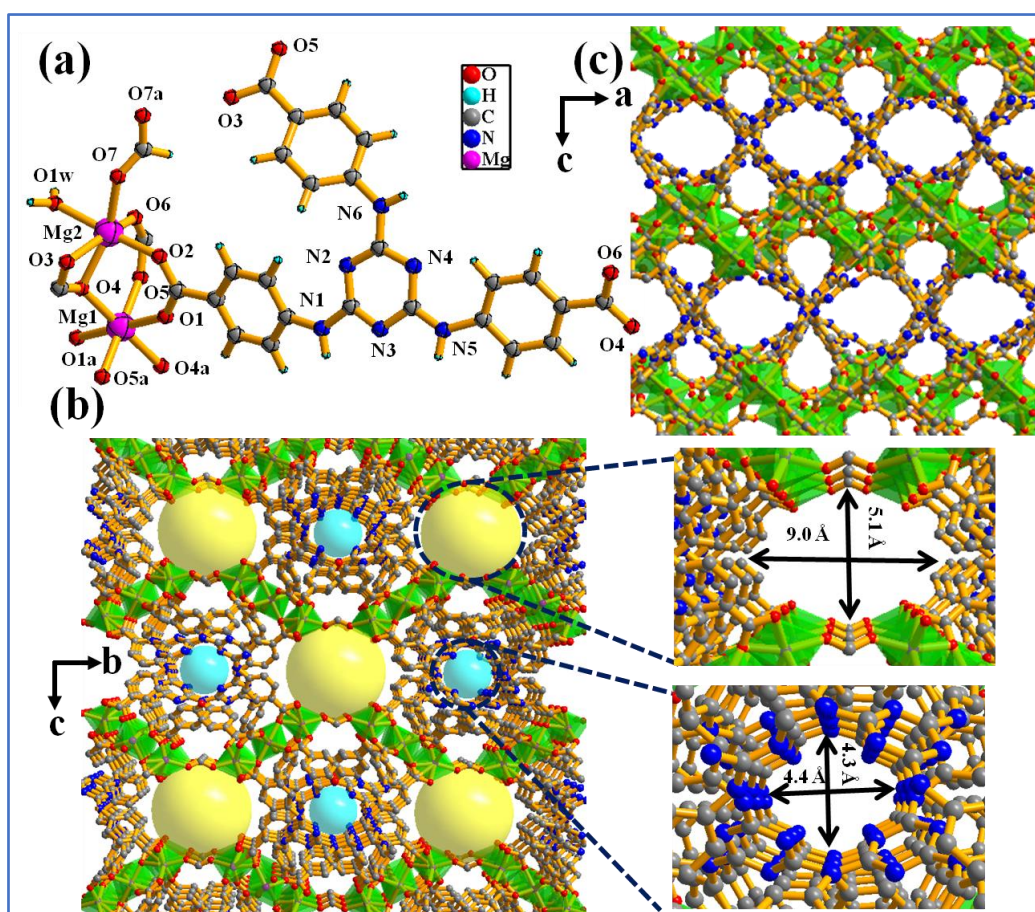


**Figure 2.** (a) The asymmetric unit of Mg-MOF showing coordination around the Mg(II) ions ( $a = 1-x, 1-y, -z$  and  $b = 5/4-x, 5/4-y, z$ ). (b) View of two types of 1D channels with dimensions of  $9.0 \times 5.1 \text{ \AA}^2$  and  $4.4 \times 4.3 \text{ \AA}^2$  along the crystallographic *a*-axis and (c) View of the 1D channel with a dimension of  $7.3 \times 5.2 \text{ \AA}^2$  along crystallographic *b*-axis.

**Table 1.** Crystal data and structure refinement parameters for Mg-MOF.

Parameters	Mg-MOF
Empirical formula	C <sub>60</sub> H <sub>72</sub> Mg <sub>3</sub> N <sub>16</sub> O <sub>23</sub>
Formula mass	1458.22
Crystal system	Orthorhombic
Space group	<i>Fddd</i>
a/ Å	16.950(11)
b/ Å	47.376(3)
c/ Å	50.434(3)
α (degree)	90
β (degree)	90
γ (degree)	90
V (Å <sup>3</sup> )	40500(4)
Z	16
M (mm <sup>-1</sup> )	0.072
F (000)	9360
T (K)	298
λ (Mo Kα) (Å)	0.71073
θ <sub>min</sub> (deg)	2.4
θ <sub>max</sub> (deg)	25.0
total data	183673
unique data	8915
R <sub>int</sub>	0.083
Data [I > 2σ(I)]	6182
R <sub>1</sub>	0.0947
wR <sub>2</sub>	0.3374
S	1.34
CCDC	2036640

$${}^a R_1 = \frac{\sum ||F_o| - |F_c||}{\sum |F_o|}, \quad {}^b wR_2 = [\sum w(F_o^2 - F_c^2)^2 / \sum w(F_o^2)^2]^{1/2}$$

### 3.3.2. Thermal and chemical stability of Mg-MOF

Thermogravimetric analysis (TGA) of as-synthesized Mg-MOF showed a weight loss of ~7.9 % (calc. wt.%: 8.1) in the temperature range of RT to 120 °C corresponding to loss of five guest water molecules (Figure A30). The second weight loss of ~ 24.8 % (calc. wt.%: 25) in the temperature range of 120-238 °C corresponds to the loss of coordinated water and three DMF molecules. A third weight loss of ~3.9 % (calc. wt.%: 4.2) in the temperature range of 250 to 430 °C corresponds to the loss of dimethylamine cation. Further increases in temperature beyond 430 °C led to the loss of framework stability. The acetone exchanged MOF shows a weight loss of ~8.7 % (calc. wt.%: 8.9) in the temperature range of RT to 155 °C corresponding to a loss of guest acetone and a coordinated water molecule. A second weight loss of ~3.9 % (calc. wt.%: 4.2) was observed in the temperature range of 250 to 430 °C corresponding to the loss of dimethylamine cation and then the framework loses its structural rigidity with further increase in temperature. Whereas, the activated MOF does not show any weight loss in the temperature range of RT to 250 °C supporting the absence of guest solvent molecules. A weight loss of ~3.9 % (calc. wt.%: 4.2) in the temperature range of 250 to 430 °C was observed which can be assigned to the loss of dimethylamine cation (Figure A30). Moreover, to test the chemical stability of Mg-MOF, the as-synthesized sample was soaked in various solvents with varying polarity (DMF, water, acetone, ethanol, dichloromethane, and methanol) for four days and the recovered samples were analyzed. The PXRD patterns of the recovered samples matched well with that of the as-synthesized sample confirming the chemical stability of Mg-MOF (Figure A31).

### 3.3.3. Gas adsorption study of Mg-MOF

To determine the permanent porosity of Mg-MOF, N<sub>2</sub> adsorption study was carried out at 77K. Prior to adsorption measurements, the as-synthesized MOF was exchanged with acetone and activated at 130 °C under vacuum for 15 h to obtain solvent-free MOF. As shown in Figure 3a, N<sub>2</sub> adsorption isotherms follow a typical type-I behavior signifying the microporous nature of the framework with a high Brunauer-Emmett-Teller (BET) and Langmuir surface area of 2606.1 and 3098.6 m<sup>2</sup>/g, respectively (Figure 3a). Further, the pore size distribution plot (inset, Figure 3a) of Mg-MOF revealed the presence of micropores with a diameter of 9.4 Å which is found to be in good agreement with the value (9.0 Å) obtained from crystallographic data (structure). Further, CO<sub>2</sub> adsorption isotherms showed type-I plots with a high uptake of 50.2 and 33.1 wt% at 273 and 298K, respectively (Figure 3b). Moreover, the adsorption isotherms were fitted with the Freundlich-Langmuir equation<sup>61</sup>

(Figure A31) and the value of heat of interaction ( $Q_{st}$ ) determined using the Clausius-Clayperon equation<sup>62</sup> was found to be 55.13 kJ/mol which was further supported by the simulated adsorption enthalpy of 59.49 kJ/mol (Figure A33, A34). It is worth highlighting that the  $Q_{st}$  value of  $CO_2$  determined for Mg-MOF was found to be higher in comparison to well-known Mg-based MOFs reported in the literature (Table A13).<sup>63-65</sup> This high value of  $Q_{st}$  indicates stronger interaction of  $CO_2$  with the basic (N and -NH) sites and the unsaturated Mg(II) ions exposed in the 1D channels of the framework.<sup>46,47</sup> Interestingly, the adsorption isotherms of Mg-MOF with  $N_2$  and  $O_2$  showed lower uptake and the calculated experimental values of  $Q_{st}$  were 23.1 and 16.6 kJ/mol, respectively (Figure A35 and A36). The experimentally determined values of heat of adsorption were found to be in good agreement with the simulated adsorption enthalpies (see later). Thus, the gas adsorption studies revealed the selective adsorption property of Mg-MOF for  $CO_2$  over  $N_2$  and  $O_2$  (Figure 3c) with high selectivity value of 86 and 92 for  $CO_2/N_2$  and  $CO_2/O_2$ , respectively calculated based on Henry law (Figure A37). Furthermore, the Mg-MOF exhibits highly recyclable  $CO_2$  adsorption with retaining the adsorption capacity for upto five cycles of regeneration (Figure 3d).

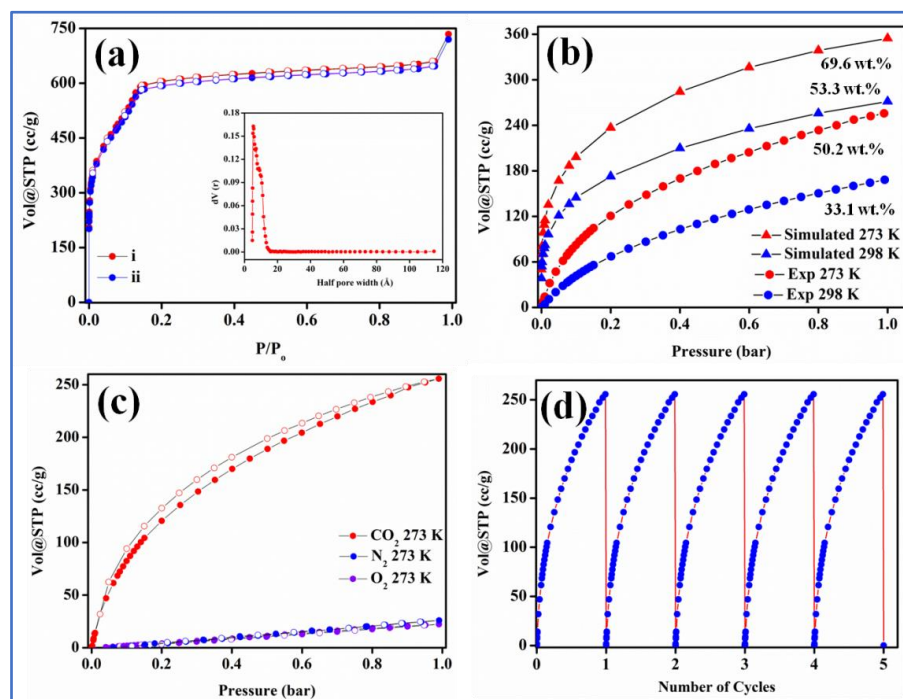


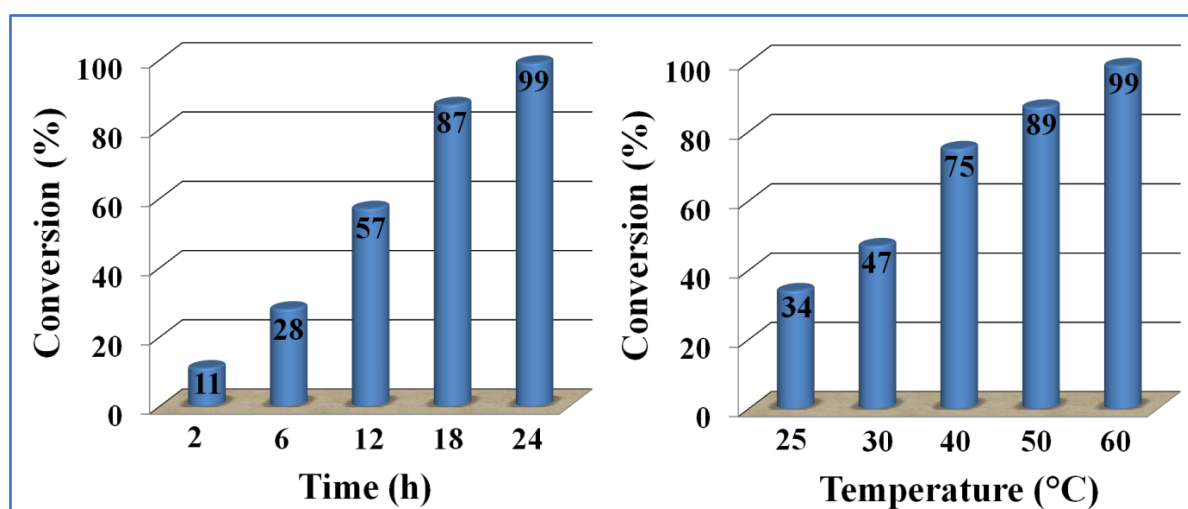
**Figure 3.** (a)  $N_2$  adsorption-desorption isotherms of Mg-MOF, (i) for the pristine sample and (ii) the recycled sample after catalysis carried out at 77K (inset shows pore size distribution plot), (b) Comparison of the experimental and simulated isotherms of  $CO_2$  carried out at 273 and 298K, (c) Selective adsorption of  $CO_2$  over  $N_2$  and  $O_2$ , and (d) Recyclable adsorption of  $CO_2$  carried out at 273K.

To get further insight into the high CO<sub>2</sub> capture performance of Mg-MOF over other atmospheric gases like N<sub>2</sub> and O<sub>2</sub>, molecular simulations were undertaken by employing the Grand Canonical Monte Carlo (GCMC) simulation with a specific force field. As mentioned before, the CO<sub>2</sub> content in the air is significantly lower (0.03 %) in comparison to any other gas streams like flue gas (10-20%). Therefore, the separation/capture of CO<sub>2</sub> from atmospheric air has gained significant attention as it depends on the high CO<sub>2</sub> capture ability of the sorbent with highly specific adsorption sites.<sup>66</sup> As discussed before, the Mg-MOF is composed of the high density of -NH/N sites and coordinatively unsaturated metal sites (CUS) /open metal sites and showed exceptional CO<sub>2</sub> uptake properties. As demonstrated before<sup>67-70</sup> the generic forcefield such as universal forcefield (UFF) and DREIDING are incapable to explain the extra strong interaction between the guest molecule and Mg-MOF having multiple adsorption sites. Therefore, a specific forcefield was derived to explain the guest-host interaction for the Grand Canonical Monte Carlo (GCMC) simulation. Hence, the extra potentials for the interaction of gas molecules with the CUS and the -NH/N adsorption site were derived from Density Functional Theory (DFT) energy profile and further used this energy to represent it in the Buckingham analytical function. The rest of the interactions of gas molecules with all the atoms of the Mg-MOF are represented through Lennard-Jones (LJ) and the potentials are taken from generic forcefield (please see annexure, Figure A38-A46, and Tables A15-A17). As an initial step, single-component adsorption simulation of Mg-MOF for CO<sub>2</sub>, N<sub>2</sub>, and O<sub>2</sub>, i.e. the major components of air, at two temperatures (273 and 298K) was performed by Grand Canonical Monte Carlo (GCMC) simulation, where the interaction between the framework and the gas molecules are explained by specific DFT-derived forcefield. The simulated gas adsorption isotherms follow a type-I behavior as experimentally observed (Figures 3b). The simulated uptake of CO<sub>2</sub>, N<sub>2</sub>, and O<sub>2</sub> by Mg-MOF was found to be slightly higher than those of experimentally determined uptake at 273 and 298K (Figure 3b). This observation can be attributed to the fact that the simulations were carried out with the assumption of a perfectly crystalline solid as compared to the bulk material used for experimental adsorption measurements. It is interesting to note that the simulated adsorption trend at both temperatures was reproduced reasonably well with experimental isotherms for all the atmospheric gases (N<sub>2</sub>, O<sub>2</sub>, and CO<sub>2</sub>). Further, the computed adsorption enthalpy for CO<sub>2</sub>, N<sub>2</sub>, and O<sub>2</sub> with Mg-MOF are 59.49, 27.25, and 18.55 kJ/mol, respectively which are in close agreement with the experimentally determined heat of adsorption (Q<sub>st</sub>) values of 55.1, 23.1, and 16.6 kJ/mol, respectively. Further, the detailed analysis of the adsorption mechanism of CO<sub>2</sub> with Mg-MOF showed that the

presence of polar functionalized 1D pores decorated with nitrogen-rich basic -NH/N sites and coordinatively unsaturated Mg(II) sites promotes high CO<sub>2</sub> adsorption. Here, the CO<sub>2</sub> molecules interact with the CUS, i.e. Mg(II) and -NH groups of the ligand with a mean characteristic Mg...O(CO<sub>2</sub>) and NH...O(CO<sub>2</sub>) distances of 1.61 Å and 2.74 Å, respectively. Whereas, the N<sub>2</sub> molecules interact with the CUS of Mg-MOF with an interatomic distance in the range of 1.7-2.5 Å. The simulated O<sub>2</sub> adsorption on Mg-MOF reflects an Mg-O(O<sub>2</sub>) interacting distance of 1.7 Å. Overall, the simulated adsorption studies support the high CO<sub>2</sub>-affinity of Mg-MOF over other gases (N<sub>2</sub> and O<sub>2</sub>).

### 3.3.4. Solvent and co-catalyst-free fixation of CO<sub>2</sub> under mild conditions

As discussed before, from the structural analysis it was revealed that Mg-MOF is microporous and contains 1D channels decorated with basic (-NH and -N) sites and unsaturated Lewis acidic Mg(II) sites suitable for selective capture and conversion of CO<sub>2</sub>. Considering these novel structural aspects, the catalytic application of the MOF for the chemical fixation of CO<sub>2</sub> into cyclic carbonates, a value-added chemical was investigated under co-catalyst and solvent-free conditions. The catalytic activity was tested using epichlorohydrin (ECH) as a model substrate and the conditions were optimized by varying the time and temperature of the reaction (Figure 4). It was found that an increase in the reaction time and temperature led to an increase in the yield of the cyclic carbonate.

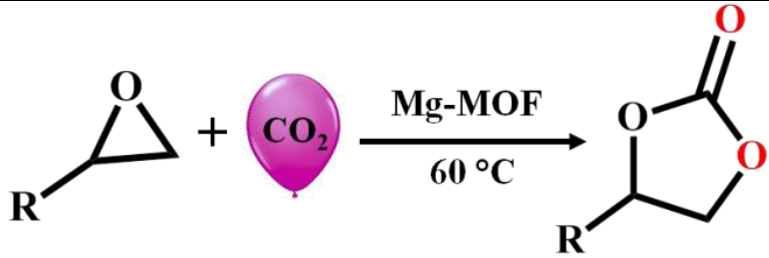
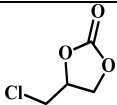
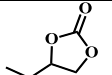
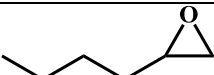
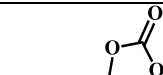
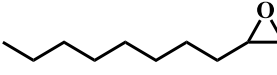
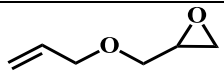
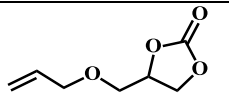
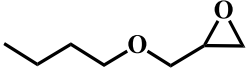
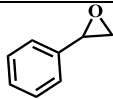
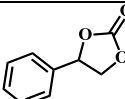
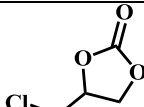


**Figure 4.** The effect of reaction time and temperature on the cycloaddition of ECH with CO<sub>2</sub> (balloon) under solvent and co-catalyst-free conditions.

The catalytic reaction carried out at the optimized conditions of 0.1 mol% of Mg-MOF as a catalyst, ECH (20 mmol), with 1 atm CO<sub>2</sub> (balloon) at 60 °C resulted in more than 99% conversion of ECH into the corresponding cyclic carbonate in 24h with 100% selectivity under solvent and co-catalyst-free conditions (Table 2). Further, control experiments carried out using metal salt, Mg(NO<sub>3</sub>)<sub>2</sub>·6H<sub>2</sub>O, and organic ligand (H<sub>3</sub>TATAB) as catalysts for cycloaddition of ECH at the optimized conditions showed only 10 and 6% yield of cyclic carbonate, respectively. These observations highlight the importance of Mg-MOF to achieve the high catalytic activity. The superior catalytic activity of Mg-MOF can be attributed to synergistic cooperation between the LA Mg(II) and basic (-NH) sites in facilitating the effective capture and conversion of CO<sub>2</sub> into cyclic carbonates.

The excellent catalytic activity of Mg-MOF motivated us to extend the scope of the catalysis to the cycloaddition of CO<sub>2</sub> with various epoxides at optimized conditions. Interestingly, it was found that smaller epoxides like 1,2-epoxypropane and 1,2-epoxybutane undergo 99 and 93% conversion, respectively (Table 2). Whereas, with an increase in the alkyl chain length of the epoxides, the catalytic conversion was found to decrease. For instance, 1,2-epoxyhexane and 1,2-epoxydecane were converted by about 79 and 48%, respectively to the corresponding cyclic carbonates (Table 2). This observation can be attributed to the restricted diffusion of these longer epoxides in the narrow pore channels of the framework.<sup>71</sup> On the other hand, a slight increase in the conversion of butyl glycidyl ether (81%), and allyl glycidyl ether (85%) could be attributed to the electron-donating nature of the epoxides (Table 2).<sup>26,33</sup> Further, the aromatic epoxide (styrene oxide) was also found to undergo conversion to the respective cyclic carbonate (styrene carbonate) in 78% yield under the optimized conditions (Table 2). Moreover, the catalytic activity of Mg-MOF was tested under simulated dry flue gas conditions by using a CO<sub>2</sub>:N<sub>2</sub> (13:87%) mixture. To our delight, about 91% of ECH was converted to the corresponding cyclic carbonate even at the low concentration (13%) of carbon dioxide at the optimized mild conditions. These results highlight the excellent performance of Mg-MOF for high CO<sub>2</sub> capture and conversion to value-added chemicals. It is worth mentioning that the reaction conditions employed in this work are relatively milder and the catalytic activity of Mg-MOF was found to be superior in comparison to the literature-reported MOFs for cycloaddition of CO<sub>2</sub> (Table 3).

**Table 2.** Solvent and co-catalyst-free fixation of CO<sub>2</sub> under mild conditions.<sup>a</sup>

				
Entry No.	Substrate (R)	Product	Conversion <sup>c</sup> (%)	TON <sup>d</sup>
1			99	998
2			99	994
3			93	934
4			79	792
5			48	483
6			85	851
7			81	812
8			78	781
9 <sup>b</sup>			91	911

<sup>a</sup>Reaction conditions: 20 mmol epoxide, 0.1 mol% Mg-MOF, 60 °C, 1 atm CO<sub>2</sub> (balloon), 24h. <sup>b</sup> CO<sub>2</sub>:N<sub>2</sub> (13:87%) mixture (1 atm). <sup>c</sup>Catalytic conversions were determined by <sup>1</sup>H NMR analysis, and <sup>d</sup>TON = number of moles of product formed/number of moles of catalyst used.

**Table 3.** Comparison of catalytic activity of Mg-MOF with literature reported MOFs known for cocatalyst-free cycloaddition of CO<sub>2</sub> with ECH.

Sl. No.	Catalyst	Temp. (°C)	Pressure (bar)	Conversion (%)	TON/TOF	Ref.
1	(I)Meim-UiO-66	120	1	100	188/7.8	72
2	Zn-TATAB	100	1	98	158/9.8	73
3	Co-TATAB	80	1	98	465/31	73
4	MIL-101-IP	50	1	99	335/4.9	74
5	IL-ZIF-90	120	10	94	191/63.6	75
6	UiO-67-IL	90	1	95	63/5.2	76
7	F-ZIF-90	120	1.17	94	97/16.1	77
8	ZnTCPPc(Br-) EtimUiO-66	140	1	86.9	91/6.5	78
9	FJI-C10	120	1	84	494/20.5	79
10	[Zn(II)NMeTPyP ] <sup>4+</sup> [I] <sub>4</sub> @PCN-224	90	8	99	833/4.7	34
11	<b>Mg-MOF</b>	<b>60</b>	<b>1</b>	<b>99</b>	<b>998/41.6</b>	<b>This Work</b>

### 3.3.5. Solvent and co-catalyst-free fixation of CO<sub>2</sub> from direct air

Towards practical implementation of carbon capture and utilization (CCU) for real applications, the catalytic activity of Mg-MOF was investigated for the synthesis of cyclic carbonates by utilizing laboratory air as a source of carbon dioxide. It is worth mentioning that the atmospheric air contains only about 0.03% of CO<sub>2</sub> and hence the catalyst employed should be highly reactive and should possess high CO<sub>2</sub> affinity for its selective capture and conversion at such a low concentration. Interestingly, a test reaction carried out with ECH (20 mmol) as a model substrate and Mg-MOF (0.02 mmol) catalyst, with the bubbling of laboratory air showed about 61% conversion of ECH to the corresponding cyclic carbonate within 24 h under solvent and co-catalyst-free optimized conditions (Table 4). Furthermore, with an increase in the reaction time to 48 h the conversion of ECH was enhanced to 92% with 100% selectivity. Encouraged by this excellent catalytic activity of Mg-MOF, the scope of the catalysis was extended to other epoxides under optimized conditions. The epoxides, 1,2-epoxybutane, 1,2-epoxyhexane, allyl glycidyl ether, butyl glycidyl ether, and styrene

oxide were found to undergo conversion to the corresponding cyclic carbonates with moderate yields and 100% selectivity at the optimized conditions (Table 4). To the best of our knowledge, this is the first report on solvent and co-catalyst-free conversion of CO<sub>2</sub> into value-added cyclic carbonates using direct air under mild conditions.

**Table 4.** Solvent and co-catalyst-free fixation of CO<sub>2</sub> from air catalyzed by Mg-MOF.<sup>a</sup>

Entry No.	Substrate (R)	Product	Conversion <sup>c</sup> (%)	TON <sup>d</sup>
1			61	612
2 <sup>b</sup>			92	921
3			58	579
4			49	493
5			31	311
6			54	540
7			42	421
8			38	384

<sup>a</sup>Reaction conditions: 20 mmol epoxide, 0.1 mol% Mg-MOF, 60 °C, air (1 atm), 24h.

<sup>b</sup>Reaction time, 48 h. <sup>c</sup>Catalytic conversions were determined by <sup>1</sup>H NMR analysis, <sup>d</sup>TON = number of moles of product formed/number of moles of catalyst used.

### 3.3.6. Theoretical insight for higher CO<sub>2</sub> selectivity from direct air

To get further insight into the amazing catalytic activity of Mg-MOF for chemical fixation of CO<sub>2</sub> from direct air, GCMC simulations were performed for co-adsorption of natural air with a composition of N<sub>2</sub>: O<sub>2</sub>: CO<sub>2</sub>: RH (77.41%:20.99%:0.03%:1.57%),<sup>80</sup> (Figure A45) with the help of newly DFT-derived forcefield. For obtaining the CO<sub>2</sub> selectivity over the less adsorbing constituents of air such as N<sub>2</sub> and O<sub>2</sub>, we have considered the adsorption capacity of carbon dioxide over the combination of adsorption capacities of N<sub>2</sub> and O<sub>2</sub>. Interestingly, the CO<sub>2</sub> selectivity observed at the relative humidity of 1.57% in the real composition of air was ~40 at 298K and 1 bar (Figure A46). Thus, the simulated co-adsorption of wet air with the chemical composition of natural air proved that the Mg-MOF is highly CO<sub>2</sub>-selective over the rest of the atmospheric gases. In addition to this, the CO<sub>2</sub> selectivity was also obtained from dry air as well as various pre-humidified compositions of air at 298K and 1 bar (Figure A45 and A46), which is found to be much higher in comparison to most of the porous materials reported in the literature.<sup>81</sup>

### 3.3.7. Catalyst leaching and recyclability test

Recyclability is an important parameter for a heterogeneous catalyst, in this regard, the Mg-MOF was separated from the reaction mixture by simple filtration followed by washing with acetone and activation at 120 °C under vacuum for 12h. The recycled catalyst was used for subsequent catalytic cycles for the cycloaddition of CO<sub>2</sub> with ECH under the optimized conditions of 1 atm of CO<sub>2</sub> and 60 °C. It is interesting to note that the Mg-MOF was recyclable for 10 cycles and the catalytic activity of the MOF was retained without a significant loss (Figure 5a). Furthermore, powder XRD pattern, FTIR spectra, solid-state UV-Vis spectra (Figure 1, A26, A27), and BET surface area (Figure 3a) of the recycled MOF sample after 10 cycles matched well with that of the as-synthesized sample suggesting retention of the original framework structure. Further, to rule out the possibility of leaching of the active catalyst into the homogeneous phase, the reaction was stopped after 6 h and the MOF was separated by filtration and the filtrate was allowed to stir for an additional period of 18 h under the optimized conditions. The <sup>1</sup>H NMR spectroscopic analysis of the filtrate taken after 24 h showed no further conversion of the epoxide into the cyclic carbonate supporting the absence of catalyst leaching (Figure 5b). For further confirmation, MP-AES analysis of the filtrate was carried out and no detectable concentration of Mg(II) was observed confirming the absence of leaching of the active catalyst during the catalysis and also, the absence of unreacted metal salts (Figure A47).

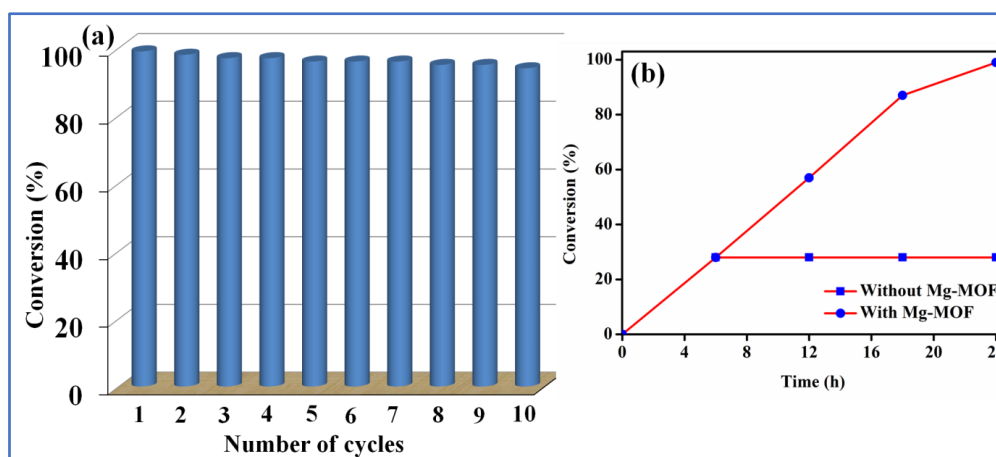
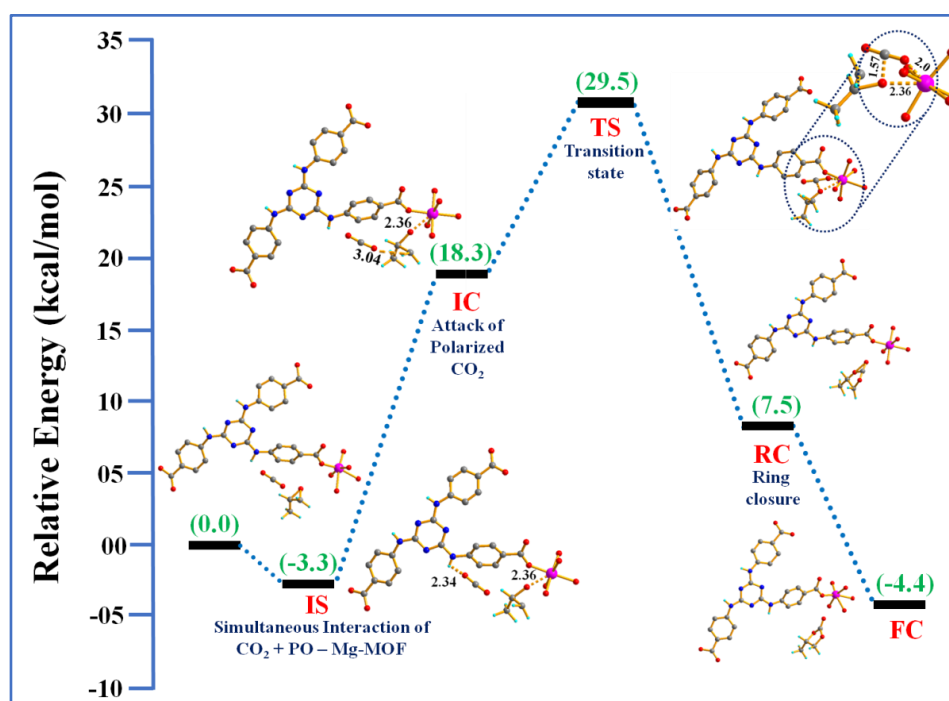


**Figure 6.** Catalyst leaching and recyclability test for Mg-MOF.

### 3.3.8. Plausible mechanism for solvent and co-catalyst-free fixation of CO<sub>2</sub>

For elucidating the reaction mechanism for co-catalyst-free fixation of CO<sub>2</sub> with the novel Mg-MOF catalyst, detailed periodic-DFT calculations were carried out for catalytic cycloaddition of epoxide with Mg-MOF catalyst (Figure A48). On the due course of the catalytic cycloaddition reaction of epoxide, for example, propylene oxide (PO). Initially the epoxide binds to the Mg(II) site of the MOF and simultaneously CO<sub>2</sub> molecule interacts to the basic -NH sites of TATAB<sup>3-</sup> linker. This process is supported by higher binding energy (-63.81 kJ/mol) observed for coordination of PO to LA Mg(II) site when compared to the energy (-59.49 kJ/mol) estimated for binding of CO<sub>2</sub> to Mg(II) site (Table A5). Therefore, the epoxides selectively interact with LA Mg(II) site of Mg-MOF with high binding energy over CO<sub>2</sub> during the catalytic reaction. Based on the aforementioned discussion, the initial step in the catalysis is obtained by simultaneous interaction of the oxygen atom of the epoxide, i.e. O(PO) with LA Mg(II) and CO<sub>2</sub> with the -NH of TATAB<sup>3-</sup> linker. At the initial stage (IS), the polarized CO<sub>2</sub> makes strong interaction with the -NH of TATAB<sup>3-</sup> with a distance of 2.34 Å, in addition to the interaction of PO to Mg(II) with an interacting distance of 2.36 Å (Figure A49 and Scheme 3). Next, an incoming complex (IC) with relative energy of 18.3 kcal mol<sup>-1</sup> is formed by the direct interaction of polarized CO<sub>2</sub> molecules with an interacting distance of 3.04 Å to the beta carbon of the PO, β-C(PO), and this direct to the ring-opening of epoxide (PO) (Figure A49). At the same time, O(PO) makes a strong binding with Mg(II) of MOF with an interacting distance of 2.36 Å, and further an alkoxide species is obtained by the strong interaction of polarized CO<sub>2</sub> to the β-C(PO). This alkoxide complex with a high relative energy value of 29.5 kcal mol<sup>-1</sup> represents the transition state (TS), also as shown in Scheme 3 the difference between the relative energies of TS and IC is as low as 11.2

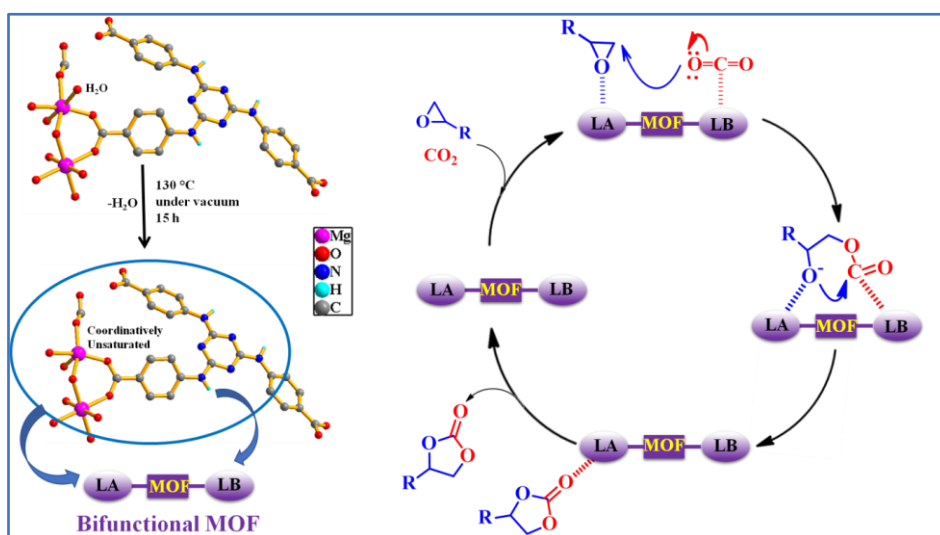
kcal/mol, this is the rate-determining step for the CO<sub>2</sub> fixation with Mg-MOF. While, the transition state, TS, is generated by a new bond, C(CO<sub>2</sub>)-O(PO), with a distance of 1.57 Å, and Mg(II)-O(CO<sub>2</sub>) interacting distance is ~2.0 Å. This TS leads to a ring closure intermediate stage, RC, with relative energy of 7.5 kcal/mol, which is a five-membered ring of propylene carbonate (PCC). In this five-membered ring, the newly formed bonds are C(CO<sub>2</sub>)-O(PO) and O(CO<sub>2</sub>)-β-C(PO) with a bond length of 1.29 and 1.41 Å, respectively. Finally, in the ring closure (FC) stage the Mg-MOF, catalyst is retained with relative energy of -4.4 kcal/mol from the cyclic carbonate. The catalytic pathway based on DFT calculations for the cycloaddition of PO with CO<sub>2</sub> is depicted in Scheme 2, which clearly illustrates that the Mg-MOF contains both Lewis acidic Mg(II) and basic -NH sites suitable for the polarization of epoxides and CO<sub>2</sub>, respectively.



**Scheme 3.** DFT-energy profile for the cycloaddition reaction of CO<sub>2</sub> with PO to produce PCC catalyzed by Mg-MOF.

A proposed mechanism for the catalytic cycloaddition reaction of carbon dioxide with various epoxides catalyzed by Mg-MOF is shown in Scheme 4. As mentioned before, the first step involves the polarization of the epoxide at the coordinately unsaturated Mg(II) center. To get further support on this step, Mg-MOF was treated with ECH for 1 h at room temperature and then recovered by simple filtration followed by washing with methanol thoroughly. FT-IR spectra of the recovered sample showed characteristic peaks at 2995 and 1660 cm<sup>-1</sup>

corresponding to C-H stretching and bending frequency of ECH (Figure A50). This experiment confirmed the interaction of epoxide with Mg-MOF. The subsequent step involves ring-opening of the epoxide by nucleophilic attack at the less hindered  $\beta$ -carbon atom of the epoxide. Then  $\text{CO}_2$  undergoes insertion into metal-alkoxide followed by an intramolecular ring-closure reaction leading to the formation of cyclic carbonate which upon elimination regenerates the catalyst for subsequent cycles (Scheme 4).



**Scheme 4.** A plausible mechanism for the cocatalyst-free conversion of  $\text{CO}_2$  with the epoxide.

### 3.4. Conclusion

In this chapter, the rational design of a novel bifunctional 3D MOF based on an eco-friendly, Lewis acidic metal ion, Mg(II), and the multifunctional nitrogen-rich tripodal ligand is reported. The highly polar functionalized pores with Lewis acidic and basic functionalities facilitated the Mg-MOF with high  $\text{CO}_2$  uptake and efficient catalytic activity for fixation of  $\text{CO}_2$  from direct air into value-added cyclic carbonates under co-catalyst and solvent-free conditions. Theoretical simulations further supported the remarkable affinity of Mg-MOF for  $\text{CO}_2$  over other gases in the air. To the best of our knowledge, the Mg-MOF represents the first example of MOF-based heterogeneous catalyst exhibiting highly efficient fixation of  $\text{CO}_2$  from air under eco-friendly mild conditions. Moreover, the best mechanistic pathway for  $\text{CO}_2$  fixation with Mg-MOF catalyst in the absence of any co-catalyst was identified by thorough periodic-DFT calculations. This chapter paves the way for the design of efficient heterogeneous catalytic systems for the fixation of  $\text{CO}_2$  from direct air into value-added chemicals.

### 3.5. References

- (1) Joos, F.; Plattner, G. -K.; Stocker, T. F.; Marchal, O.; Schmittner, A. Global Warming and Marine Carbon Cycle Feedbacks on Future Atmospheric CO<sub>2</sub>. *Science* **1999**, *284*, 464-467.
- (2) Jacobson, M. Z. Review of solutions to global warming, air pollution, and energy security. *Energy Environ. Sci.* **2009**, *2*, 148-173.
- (3) Matthews, H. D.; Graham, T. L.; Keeverian, S.; Lamontagne, C.; Seto, D.; Smith, T. J. National contributions to observed global warming. *Environ. Res. Lett.* **2014**, *9*, 014010.
- (4) Chu, S. Carbon Capture and Sequestration. *Science* **2009**, *325*, 1599.
- (5) Alessandro, D. M. D.; Smit, B.; Long, J. R. Carbon Dioxide Capture: Prospects for New Materials. *Angew. Chem. Int. Ed.* **2010**, *49*, 6058-6082.
- (6) Wilson, M.; -Palomo, S. N. B.; Stevens, P. C.; Mitchell, N. L.; Oswald, G.; Nagaraja, C. M.; Badyal, J. P. S. Substrate-Independent Epitaxial Growth of the Metal-Organic Framework MOF-508a. *ACS Appl. Mater. Interfaces* **2018**, *10*, 4057-4065.
- (7) Jones, W. D. Carbon Capture and Conversion. *J. Am. Chem. Soc.* **2020**, *142*, 4955-4957.
- (8) Katelhon, A.; Meys, R.; Deutz, S.; Suh, S.; Bardow, A. Climate change mitigation potential of carbon capture and utilization in the chemical industry. *Proc. Natl. Acad. Sci. U. S. A.* **2019**, *116*, 11187-11194.
- (9) Liu, Q.; Wu, L.; Jackstell, R.; Beller, M. Using carbon dioxide as a building block in organic synthesis. *Nat. Commun.* **2015**, *6*, 5933.
- (10) Sakakura, T.; Choi, J. C.; Yasuda, H. Transformation of Carbon Dioxide. *Chem. Rev.* **2007**, *107*, 2365-2387.
- (11) Das, R.; Nagaraja, C. M. Noble metal-free Cu(I)-anchored NHC-based MOF for highly recyclable fixation of CO<sub>2</sub> under RT and atmospheric pressure conditions. *Green Chem.* **2021**, *23*, 5195-5204.
- (12) Peter, S. C.; Reduction of CO<sub>2</sub> to Chemicals and Fuels: A Solution to Global Warming and Energy Crisis. *ACS Energy Lett.* **2018**, *3*, 1557-1561.
- (13) Sanz-Perez, E. S.; Murdock, C. R.; Didas, S. A.; Jones, C. W. Direct Capture of CO<sub>2</sub> from Ambient Air. *Chem. Rev.* **2016**, *161*, 11840-11876.
- (14) Bhatt, P. M.; Belmabkhout, Y.; Cadiau, A.; Adil, K.; Shekhah, O.; Shkurenko, A.; Barbour, L. J.; Eddaoudi, M. A Fine-Tuned Fluorinated MOF Addresses the Needs for Trace CO<sub>2</sub> Removal and Air Capture Using Physisorption. *J. Am. Chem. Soc.* **2016**, *138*, 9301-9307.

- (15) McDonald, T. M.; Lee, W. R.; Mason, J. A.; Wiers, B. M.; Hong, C. S.; Long, J. R. Capture of Carbon Dioxide from Air and Flue Gas in the Alkylamine Appended Metal-Organic Framework mmen-Mg<sub>2</sub>(dobpdc). *J. Am. Chem. Soc.* **2012**, *134*, 7056-7065.
- (16) Rawool, S. A.; Belgamwar, R.; Jana, R.; Maity, A.; Bhumla, A.; Yigit, N.; Datta, A.; Rupprechter, G.; Polshettiwar, V. Direct CO<sub>2</sub> capture and conversion to fuels on magnesium nanoparticles under ambient conditions simply using water. *Chem. Sci.* **2021**, *12*, 5774.
- (17) Sen, R.; Goepfert, A.; Kar, S.; Prakash, G. K. S. Hydroxide Based Integrated CO<sub>2</sub> Capture from Air and Conversion to Methanol. *J. Am. Chem. Soc.* **2020**, *142*, 4544-4549.
- (18) Hanusch, J. M.; Kerschgens, I. P.; Huber, F.; Neuburger, M.; Gademann, K. Pyrrolizidines for direct air capture and CO<sub>2</sub> conversion. *Chem. Commun.* **2019**, *55*, 949-952.
- (19) Wu, X.; Li, Y.; Zhang, G.; Chen, H.; Li, J.; Wang, K.; Pan, Y.; Zhao, Y.; Sun, Y.; Xie, Y. Photocatalytic CO<sub>2</sub> Conversion of M<sub>0.33</sub>WO<sub>3</sub> Directly from the Air with High Selectivity: Insight into Full Spectrum-Induced Reaction Mechanism. *J. Am. Chem. Soc.* **2019**, *141*, 5267-5274.
- (20) Sharma, V.; De, D.; Saha, R.; Das, R.; Chattaraj, P. K.; Bharadwaj, P. K. A Cu(II)-MOF capable of fixing CO<sub>2</sub> from air and showing high capacity H<sub>2</sub> and CO<sub>2</sub> adsorption. *Chem. Commun.* **2017**, *53*, 13371-13374.
- (21) Liang, J.; Huang, Y. -B.; Cao, R. Metal-organic frameworks and porous organic polymers for sustainable fixation of carbon dioxide into cyclic carbonates. *Coord. Chem. Rev.* **2019**, *378*, 32-65.
- (22) Ding, M.; Flaig, R. W.; Jiang, H.-L.; Yaghi, O. M. Carbon capture and conversion using metal-organic frameworks and MOF-based materials. *Chem. Soc. Rev.* **2019**, *48*, 2783-2828.
- (23) Dhankhar, S. S.; Ugale, B.; Nagaraja, C. M. Co-Catalyst-Free Chemical Fixation of CO<sub>2</sub> into Cyclic Carbonates by using Metal-Organic Frameworks as Efficient Heterogeneous Catalysts. *Chem Asian J.* **2020**, *15*, 2403-2427.
- (24) Pal, T. K., De, D.; Bhardwaj, P. K. Metal-organic frameworks for the chemical fixation of CO<sub>2</sub> into cyclic carbonates. *Coord. Chem. Rev.* **2020**, *408*, 213173.
- (25) Scrosati, B.; Hassounab, J.; Sun, Y.-K. Lithium-ion batteries. A look into the future. *Energy Environ. Sci.* **2011**, *4*, 3287-3295.
- (26) Grignard, B.; Gennen, S.; Je'rome, C.; Kleij, A. W.; Detrembleur, C. Advances in the use of CO<sub>2</sub> as a renewable feedstock for the synthesis of polymers. *Chem. Soc. Rev.* **2019**, *48*, 4466-4514.
- (27) Liu, H.; Lin, S.; Feng, Y.; Theato, P. CO<sub>2</sub>-Responsive polymer materials. *Polym. Chem.* **2017**, *8*, 12-23.

- (28) Fukuoka, S.; Kawamura, M.; Komiya, K.; Tojo, M.; Hachiya, H.; Hasegawa, K.; Aminaka, M.; Okamoto, H.; Fukawad, I.; Konno, S. A novel non-phosgene polycarbonate production process using by-product CO<sub>2</sub> as starting material. *Green Chem.* **2003**, *5*, 497-507.
- (29) Das, R.; Muthukumar, D.; Pillai, R. S.; Nagaraja, C. M. Rational design of a Zn(II)-MOF with multiple functional sites for highly efficient fixation of CO<sub>2</sub> at mild conditions: combined experimental and theoretical investigation. *Chem. Eur. J.* **2020**, *26*, 17445-17454.
- (30) Meng, X. L.; Nie, Y.; Sun, J.; Cheng, W. G.; Wang, J. Q.; He, H. Y.; Zhang, S. J. Functionalized dicyandiamide–formaldehyde polymers as efficient heterogeneous catalysts for conversion of CO<sub>2</sub> into organic carbonates. *Green Chem.* **2014**, *16*, 2771-2778.
- (31) Sharma, N.; Dhankhar, S. S.; Kumar, S.; Kumar, T. J. D.; Nagaraja, C. M. Rational Design of a 3D Mn<sup>II</sup>-Metal-Organic Framework Based on a Nonmetallated Porphyrin Linker for Selective Capture of CO<sub>2</sub> and One-Pot Synthesis of Styrene Carbonates. *Chem. Eur. J.* **2018**, *24*, 16662-16669.
- (32) Li, J.; Jia, D.; Guo, Z.; Liu, Y.; Lyu, Y.; Zhou, Y.; Wang, J. Imidazolium based porous hyper cross linked ionic polymers for efficient CO<sub>2</sub> capture and fixation with epoxides. *Green Chem.* **2017**, *19*, 2675-2686.
- (33) Sun, Y.; Huang, H.; Vardhan, H.; Aguila, B.; Zhong, C.; Perman, J. A.; Enizi, A. M. A.; Nafady, A.; Ma, S. Facile Approach to Graft Ionic Liquid into MOF for Improving the Efficiency of CO<sub>2</sub> Chemical Fixation. *ACS Appl. Mater. Interfaces* **2018**, *10*, 27124-27130.
- (34) Sharma, N.; Dhankhar S. S.; Nagaraja, C. M. Environment-friendly, co-catalyst- and solventfree fixation of CO<sub>2</sub> using an ionic zinc(II)-porphyrin complex immobilized in porous metal-organic frameworks. *Sustain. Energy Fuels* **2019**, *3*, 2977-2982.
- (35) Das, R.; Nagaraja, C. M. Highly Efficient Fixation of Carbon Dioxide at RT and Atmospheric Pressure Conditions: Influence of Polar Functionality on Selective Capture and Conversion of CO<sub>2</sub>. *Inorg. Chem.* **2020**, *59*, 9765-9773.
- (36) Dhankhar, S. S.; Das, R.; Ugale, B.; Pillai, R. S.; Nagaraja, C. M. Chemical Fixation of CO<sub>2</sub> Under Solvent and Co-Catalyst-free Conditions Using a Highly Porous Two-fold Interpenetrated Cu(II)-Metal–Organic Framework, *Cryst. Growth Des.* **2021**, *21*, 1233-1241.
- (37) Dhankhar, S. S., Sharma, N., Kumar, S., Kumar, T. J. D.; Nagaraja, C. M. Rational Design of a Bifunctional, Two-Fold Interpenetrated Zn<sup>II</sup>-Metal–Organic Framework for Selective Adsorption of CO<sub>2</sub> and Efficient Aqueous Phase Sensing of 2,4,6-Trinitrophenol, *Chem. Eur. J.* **2017**, *23*, 16204-16212.

- (38) Remy, T.; Peter, S. A.; Perre, S. V.; Valvekens, P.; Vos, D. E. D.; Baron, G. V.; Denayer, J. F. M. Selective Dynamic CO<sub>2</sub> Separations on Mg-MOF-74 at Low Pressures: A Detailed Comparison with 13X, *J. Phys. Chem. C* **2013**, *117*, 9301-9310.
- (39) Kong, X.; Scott, E.; Ding, W.; Mason, J. A.; Long, J. R.; Reimer, J. A. CO<sub>2</sub> Dynamics in a Metal-Organic Framework with Open Metal Sites. *J. Am. Chem. Soc.* **2012**, *134*, 14341-14344.
- (40) Yang, D.-A.; Cho, H.-Y.; Kim, J.; Yang, S.-T.; Ahn, W.-S. CO<sub>2</sub> capture and conversion using Mg-MOF-74 prepared by a sonochemical method. *Energy Environ. Sci.* **2012**, *5*, 6465-6473.
- (41) Karuehanon, W.; Fanfuenha, W.; Rujiwatra, A.; Pattarawarapan, M. Microwave-assisted SNAr reaction of 2,4,6-trichloro-1,3,5-triazine for therapid synthesis of C<sub>3</sub>-symmetrical polycarboxylate ligands. *Tetrahedron Lett.* **2012**, *53*, 3486-3489.
- (42) Kühne, T. D.; Iannuzzi, M.; Ben, M. D.; Rybkin, V. V.; Seewald, P.; Stein, F.; Laino, T.; Khaliullin, R. Z.; Schütt, O.; Schiffmann, F.; Golze, D.; Wilhelm, J.; Chulkov, S.; BaniHashemian, M. H.; Weber, V.; Borstnik, U.; Taillefumier, M.; Jakobovits, A. S.; Lazzaro, A.; Pabst, H.; Müller, T.; Schade, R.; Guidon, M.; Andermatt, S.; Holmberg, N.; Schenter, G. K.; Hehn, A.; Bussy, A.; Belleflamme, F.; Tabacchi, G.; Glöß, A.; Lass, M.; Bethune, I.; Mundy, C. J.; Plessl, C.; Watkins, M.; VandeVondele, J.; Krack, M.; Hutter, J. CP2K: An electronic structure and molecular dynamics software package - Quickstep: Efficient and accurate electronic structure calculations. *J. Chem. Phys.* **2020**, *152*, 194103-194150.
- (43) Perdew, J. P. Density-functional approximation for the correlation energy of the inhomogeneous electron gas. *Phys. Rev. B* **1986**, *33*, 8822-8824.
- (44) Perdew, J. P.; Burke, K.; Ernzerhof, M. Generalized Gradient Approximation Made Simple. *Phys. Rev. Lett.* **1996**, *77*, 3865-3868.
- (45) VandeVondele, J.; Hutter, J. Gaussian basis sets for accurate calculations on molecular systems in gas and condensed phases. *J. Chem. Phys.* **2007**, *127*, 114105.
- (46) Goedecker, S.; Teter, M.; Hutter, J. Separable dual-space Gaussian pseudopotentials, *Phys. Rev. B*, **1996**, *54*, 1703.
- (47) Grimme, S.; Antony, J.; Ehrlich, S.; Krieg, H. A consistent and accurate *ab initio* parametrization of density functional dispersion correction (DFT-D) for the 94 elements H-Pu. *J. Chem. Phys.* **2010**, *132*, 154104.

- (48) Campana, C.; Mussard, B.; Woo, T. K. J. Electrostatic Potential Derived Atomic Charges for Periodic Systems Using a Modified Error Functional. *Chem. Theory Comput.* **2009**, *5*, 2866-2878.
- (49) Golze, D.; Hutter, J.; Iannuzzi, M. Wetting of water on hexagonal boron nitride@Rh(111): a QM/MM model based on atomic charges derived for nano-structured substrates. *Phys. Chem. Chem. Phys.* **2015**, *17*, 14307-14316.
- (50) Dubbeldam, D.; Calero, S.; Ellis, D. E.; Snurr, R. Q. RASPA: molecular simulation software for adsorption and diffusion in flexible nanoporous materials. *Mol Simulat.* **2016**, *42*, 81-101.
- (51) Peng D.-Y.; Robinson, D. B. A New Two-Constant Equation of State. *Ind. Eng. Chem. Fundam.* **1976**, *15*, 59.
- (52) Vlugt, T. J. H.; García-Pérez, E.; Dubbeldam, D.; Ban, S.; Calero, S. Computing the Heat of Adsorption Using Molecular Simulations: The Effect of Strong Coulombic Interactions, *J. Chem. Theory Comput.* **2008**, *4*, 1107-1118.
- (53) S. Grimme, J. Antony, S. Ehrlich and H. J. Krieng, A consistent and accurate *ab initio* parametrization of density functional dispersion correction (DFT-D) for the 94 elements H-Pu, *Chem. Phys.* **2010**, *132*, 154104.
- (54) Perdew, J. P. Density-functional approximation for the correlation energy of the in homogeneous electron gas. *Phys. Rev. B* **1986**, *33*, 8822.
- (55) VandeVondele J.; Hutter, J. Gaussian basis sets for accurate calculations on molecular systems in gas and condensed phases. *J. Chem. Phys.* **2007**, *127*, 114105.
- (56) Goedecker, S.; Teter, M.; Hutter, J. Separable dual-space Gaussian pseudopotentials. *Phys. Rev. B.* **1996**, *54*, 1703.
- (57) Ye, J.; Johnson, J. K. Design of Lewis Pair-Functionalized Metal Organic Frameworks for CO<sub>2</sub> Hydrogenation. *ACS Catal.* **2015**, *5*, 2921-2928.
- (58) Choi, J. I.; Chun, H.; Lah, M. S. Zirconium-Formate Macrocycles and Supercage: Molecular Packing versus MOF-like Network for Water Vapor Sorption. *J. Am. Chem. Soc.* **2018**, *140*, 10915-10920.
- (59) Dong, B.-X.; Gu, X.-J.; Xu, Q. Solvent effect on the construction of two microporous yttrium-organic frameworks with high thermostability *via in situ* ligand hydrolysis. *Dalton Trans.* **2010**, *39*, 5683-5687.
- (60) Blatov, V. A.; Shevchenko, A. P.; Proserpio, D. M. Applied Topological Analysis of Crystal Structures with the Program Package ToposPro. *Cryst. Growth Des.* **2014**, *14*, 3576-3586.

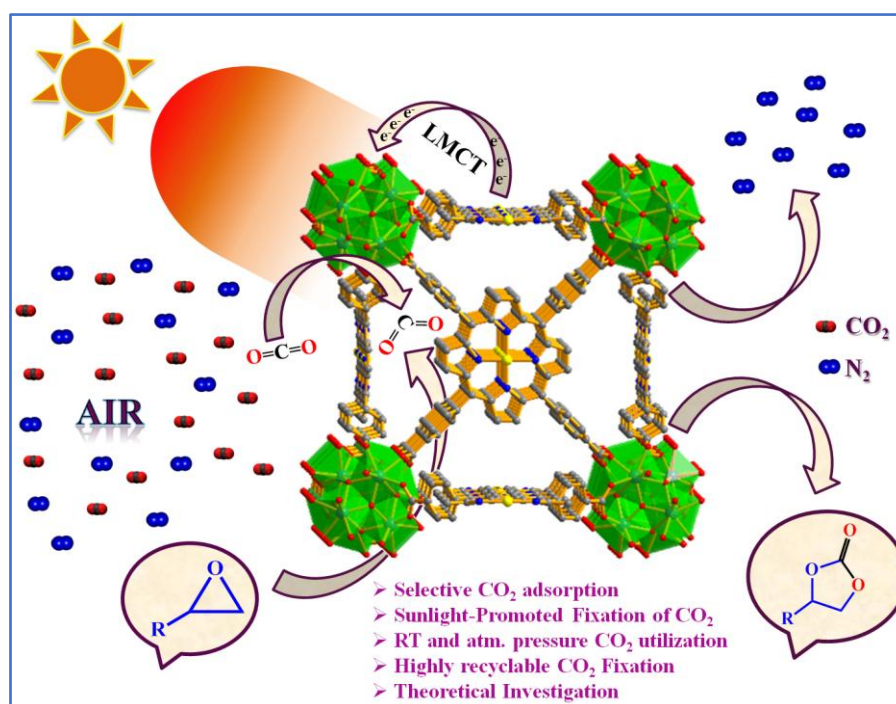
- (61) Yang, R. T. *Gas Separation by Adsorption Processes*, Butterworth, Boston, **1997**.
- (62) Pan, H.; Ritter, J. A.; Balbuena, P. B. Examination of the Approximations Used in Determining the Isothermic Heat of Adsorption from the Clausius-Clapeyron Equation. *Langmuir* **1998**, *14*, 6323-6327.
- (63) Kim, H.; Sohail, M.; Yim, K.; Park, Y. C.; Chun, D. H.; Kim, H. J.; Han, S. O.; Moon, J.-H. Effective CO<sub>2</sub> and CO Separation Using [M<sub>2</sub>(DOBDC)] (M = Mg, Co, Ni) with Unsaturated Metal Sites and Excavation of Their Adsorption Sites. *ACS Appl. Mater. Interfaces* **2019**, *11*, 7014-702.
- (64) Nguyen, P. T. K.; Nguyen, H. T. D.; Pham, H. Q.; Kim, J.; Cordova, K. E.; Furukawa, H. Synthesis and Selective CO<sub>2</sub> Capture Properties of a Series of Hexatopic Linker-Based Metal-Organic Frameworks. *Inorg. Chem.* **2015**, *54*, 10065-10072.
- (65) Dietzel, P. D. C.; Besikiotis, V.; Blom, R. Application of Metal Organic Frameworks with Coordinatively Unsaturated Metal Sites in Storage and Separation of Methane and Carbon Dioxide. *J. Mater. Chem.* **2009**, *19*, 7362-7370.
- (66) Custelcean, R.; Williams, N. J.; Garrabrant, K. A.; Agullo, P.; Brethomé, F. M.; Martin, H. J.; Kidder, M. K. Direct Air Capture of CO<sub>2</sub> with Aqueous Amino Acids and Solid Bisiminoguanidines (BIGs). *Ind. Eng. Chem. Res.* **2019**, *58*, 23338-23346.
- (67) Mercado, R.; Vlasisavljevich, B.; Lin, L.-C.; Lee, K.; Lee, Y.; Mason, J. A.; Xiao, D. J.; Gonzalez, M. I.; Kapelewski, M. T.; Neaton, J. B.; Smit, B. Force Field Development from Periodic Density Functional Theory Calculations for Gas Separation Applications Using Metal-Organic Frameworks. *J. Phys. Chem. C.* **2016**, *120*, 12590-12604.
- (68) Getzschmann, J.; Senkovska, I.; Wallacher, D.; Tovar, M.; Jimenez, D. F.; Düren, T.; Baten, J. M. V.; Krishna, R.; Kaskel, S. Methane storage mechanism in the metal-organic framework Cu<sub>3</sub>(btc)<sub>2</sub>: An in situ neutron diffraction study. *Microporous Mesoporous Mater.* **2010**, *136*, 50-58.
- (69) Wu, H.; Simmons, J. M.; Liu, Y.; Brown, C. M.; Wang, X. -S.; Ma, S.; Peterson, V. K.; Southon, P. D.; Kepert, C. J.; Zhou, H.-C.; Yildirim, T.; Zhou, W. Metal-Organic Frameworks with Exceptionally High Methane Uptake: Where and How is Methane Stored? *Chem. Eur. J.* **2010**, *16*, 5205-5214.
- (70) Mileo, P. G. M.; Cho, K. H.; Park, J.; Vinot, S. D.; Chang, J.-S.; Maurin, G. Unraveling the Water Adsorption Mechanism in the Mesoporous MIL-100(Fe) Metal-Organic Framework. *J. Phys. Chem. C.* **2019**, *123*, 23014-23025.

- (71) Li, Y.; Zhang, X.; Lan, J.; Xu, P.; Sun, J. Porous Zn(Bmic)(AT) MOF with Abundant Amino Groups and Open Metal Sites for Efficient Capture and Transformation of CO<sub>2</sub>. *Inorg. Chem.* **2019**, *58*, 13917-13926.
- (72) Liang, J.; Chen, R.-P.; Wang, X.-Y.; Liu, T.-T.; Wang, X.-S.; Huang, Y. B.; Cao, R. Postsynthetic ionization of an imidazole containing metal-organic framework for the cycloaddition of carbon dioxide and epoxides. *Chem. Sci.* **2017**, *8*, 1570-1575.
- (73) Han, Y.-H.; Zhou, Z.-Y.; Tiana, C.-B.; Du, S.-W. A dual-walled cage MOF as an efficient heterogeneous catalyst for the conversion of CO<sub>2</sub> under mild and co-catalyst free conditions. *Green Chem.* **2016**, *18*, 4086-4091.
- (74) Aguila, B.; Sun, Q.; Wang, X.; O'QRourke, E.; Enizi, A. M. A.; Nafady, A.; Ma, S. Lower Activation Energy for Catalytic Reactions through Host-Guest Cooperation within Metal-Organic Frameworks. *Angew. Chem. Int. Ed.* **2018**, *57*, 10107-10111.
- (75) Tharun, J.; Bhin, K.-M.; Roshan, R.; Kim, D. W.; Kathalikkattil, A. C.; Babu, R.; Ahn, H. Y.; Won, Y. S.; Park, D.-W. Ionic liquid tethered post functionalized ZIF-90 framework for the cycloaddition of propylene oxide and CO<sub>2</sub>. *Green Chem.* **2016**, *18*, 2479-2487.
- (76) Ding, L.-G.; Yao, B. -J.; Jiang, W.-L.; Li, J.-T.; Fu, Q.-J.; Li, Y.-A.; Liu, Z.-H.; Ma, J.-P.; Dong, Y.-B. Bifunctional Imidazolium-Based Ionic Liquid Decorated UiO-67 Type MOF for Selective CO<sub>2</sub> Adsorption and Catalytic Property for CO<sub>2</sub> Cycloaddition with Epoxides. *Inorg. Chem.* **2017**, *56*, 2337-2344.
- (77) Jose, T.; Hwang, Y.; Kim, D.-W.; Kim, M.-I.; Park, D.-W. Functionalized zeolitic imidazolate framework F-ZIF-90 as efficient catalyst for the cycloaddition of carbon dioxide to allyl glycidyl ether. *Catal. Today* **2015**, *245*, 61-67.
- (78) Liang, J.; Xie, Y.-Q.; Wu, Q.; Wang, X.-Y.; Liu, T.-T.; Li, H.-F.; Huang, Y.-B.; Cao, R. Zinc Porphyrin/Imidazolium Integrated Multivariate Zirconium Metal-Organic Frameworks for Transformation of CO<sub>2</sub> into Cyclic Carbonates. *Inorg. Chem.* **2018**, *57*, 2584-2593.
- (79) Liang, J.; Xie, Y.-Q.; Wang, X.-S.; Wang, Q.; Liu, T.-T.; Huang, Y.-B.; Cao, R. An imidazolium-functionalized mesoporous cationic metal-organic framework for cooperative CO<sub>2</sub> fixation into cyclic carbonate. *Chem. Commun.* **2018**, *54*, 342-345.
- (80) Lowry R. K.; Kullberg, R. C. Examining internal gas compositions of a variety of microcircuit package types & ages with a focus on sources of internal moisture, *Proceedings of SPIE - The International Society for Optical Engineering* 7206, **2009**.
- (81) Palakkal A. S.; Pillai, R. S. Fluorinated metal organic frameworks, MFFIVE-Ni-L (M = Fe/Al, L = pyr), with coordinatively unsaturated metal site for CO<sub>2</sub> separation from flue gas in the presence of humidity by computational methods. *Dalton Trans.* **2021**, *50*, 466-471.



# Chapter 4

## Visible light-promoted efficient fixation of CO<sub>2</sub> at ambient conditions using Mg-porphyrin based MOF as highly recyclable photocatalyst





## 4.1. Introduction

The concentration of carbon dioxide in the atmosphere is increasing dramatically over the last two decades exceeding 400 ppm, currently.<sup>1</sup> This significant rise in CO<sub>2</sub> levels in the atmosphere has been ascribed to a variety of human activities that result in greater fossil fuel consumption resulting in major environmental issues.<sup>2,3</sup> In this regard, carbon capture and sequestration (CCS) has been adopted to combat rising CO<sub>2</sub> levels.<sup>4,5</sup> However, owing to the energy-intensive nature of CCS, the application of an alternative and value-added option i. e. carbon capture and utilization (CCU) as a C1 resource for the production of valuable chemicals and fuels has gained potential interest.<sup>6-14</sup> In this context, extensive research efforts are being made by researchers worldwide for the development of high-performance catalytic systems for the effective utilization of CO<sub>2</sub> to prepare valuable compounds.<sup>15-19</sup> Particularly, the fixation of CO<sub>2</sub> from direct air offers potential advantages of carbon capture from any place irrespective of emission sources.<sup>20-22</sup> However, the inertness of CO<sub>2</sub> offers a significant challenge for its functionalization under moderate conditions. Among the several catalytic CO<sub>2</sub> utilization processes known, the cycloaddition of carbon dioxide with epoxides to afford cyclic carbonates is regarded as the most atom-efficient process.<sup>23-26</sup> Furthermore, cyclic carbonates are useful commodity chemicals in the manufacture of polymers and pharmaceuticals.<sup>27-30</sup> However, most of the catalysts known for the production of cyclic carbonates require high CO<sub>2</sub> pressure and/or high-temperature conditions.<sup>31-35</sup> On the contrary, green and sustainable chemistry practices prefer the use of environmental-friendly mild conditions for the fixation of CO<sub>2</sub> into valuable products.<sup>36-38</sup> In this context, photocatalytic fixation of CO<sub>2</sub> by utilizing natural sunlight as a light source for the production of high-value cyclic carbonates offers potential advantages over traditional thermally-driven conversion.<sup>39-41</sup> Therefore, sunlight/visible-light-promoted conversion of CO<sub>2</sub> into value-added chemicals is sought to be a promising step toward green and sustainable development.<sup>42</sup> However, the majority of the photocatalysts possess a wide band gap and are known to be active only in the UV region of the solar spectrum which constitutes only about 4% of sunlight reaching earth. Consequently, the development of visible-light-active photocatalysts has gained significant interest since natural sunlight contains about 40% of visible light.<sup>43-45</sup> However, to accomplish this, the catalyst should possess the properties of good visible light absorption, and a high surface area along with the high density of CO<sub>2</sub>-philic and catalytic sites.<sup>46-49</sup>

On the other hand, in nature green plants utilize sunlight to split water and CO<sub>2</sub> from the air to produce oxygen (O<sub>2</sub>) and reduced sugar in the process of photosynthesis.<sup>50</sup> It is important

to note that the pigment chlorophyll having Mg-centered porphyrin unit is known to be responsible for the absorption of sunlight in facilitating natural photosynthesis.<sup>51,52</sup> Besides, Mg(II) is known for its high CO<sub>2</sub> affinity over other transition metal ions.<sup>53-55</sup> Inspired by this natural photosynthesis, herein we report the application of Mg(II)-porphyrin framework for the utilization of CO<sub>2</sub> to generate cyclic carbonates under light-promoted mild conditions. Indeed, the Mg(II)-incorporated porphyrin framework, PCN-224(Mg) showed good CO<sub>2</sub> capture ability with a high heat of adsorption (44.5 kJ/mol) which is about 7.8 kJ/mol higher than that of Mg-free MOF. Further, PCN-224(Mg) catalyzes efficient functionalization of CO<sub>2</sub> under visible light-assisted, environmental-friendly mild conditions. Indeed, visible light/sunlight was found to play an important role in accelerating the catalytic activity by facilitating ligand-to-metal charge transfer (LMCT) from Mg-porphyrin secondary building unit (SBU) to the Zr site. This charge transfer further activates CO<sub>2</sub> and thereby lowers the energy barrier for its coupling with epoxides to afford CC in high yield and TON. Theoretical studies carried out unveiled the detailed mechanistic path of the light-assisted transformation of CO<sub>2</sub> to cyclic carbonates. Overall, this chapter highlights the environmental-friendly, sunlight-assisted photocatalytic conversion of CO<sub>2</sub> into high-value chemicals.

## 4.2. Experimental section

### 4.2.1. Materials

All the reagents used in this work were commercially available and used as received without any further purification. Mg(NO<sub>3</sub>)<sub>2</sub>·6H<sub>2</sub>O, ZrCl<sub>4</sub>, 4-formylbenzoate, and pyrrole were purchased from Sigma Aldrich Chemical Co. N, N'-dimethylformamide (DMF) and methanol (MeOH) were obtained from S. D. Fine Chem. Ltd. All the epoxides, propionic acid, and the internal standard used for catalytic reactions were purchased from TCI chemicals and used without further purification.

### 4.2.1. Physicochemical characterization

The phase purity of the as-synthesized samples was confirmed by powder XRD analysis using Rigaku Miniflex 600 with Cu K $\alpha$  radiation ( $\lambda = 0.154$  nm). UV-Vis (Diffuse Reflectance) spectra were recorded on the Shimadzu spectrophotometer using BaSO<sub>4</sub> as a reference. Thermogravimetric analysis (TGA) of the compounds was carried out on Mettler Toledo Thermogravimetric analyzer in an inert (N<sub>2</sub>) atmosphere with a flow rate of 30 mL/min in the temperature range of 30–600 °C and a heating rate of 5 °C/min. FTIR (Fourier

transform infrared) spectra of the samples were recorded from 400 to 4000  $\text{cm}^{-1}$  on a Perkin Elmer ATR-FTIR spectrometer. Gas adsorption studies were carried out on Quantachrome QUADRASORB-SI automatic volumetric instrument. Thermo Fischer Flash 2000 Elemental Analyzer was used for elemental analyses (CHN) of the samples. The metal content of Mg in the MOF was determined by Agilent's microwave-plasma atomic emission spectrometer (MP-AES). The catalytic conversions were analyzed by recording  $^1\text{H}$ -NMR spectra of the products on a JEOL JNM-ECS-400 spectrometer operating at a frequency of 400 MHz using an internal standard.

## 4.2.2. Synthesis

### 4.2.2.1. Synthesis of 5, 10, 15, 20-tetrakis (4-methoxycarbonylphenyl) porphyrin (TPPCOOMe)

In a 250-mL round bottom flask, methyl 4-formylbenzoate (6.9 g, 0.042 mol) was added to 100 mL of propionic acid. To this solution, 0.043 mol (3.0 mL) pyrrole was added dropwise and the solution was refluxed at 140 °C for 12h. After the reaction mixture was cooled down to room temperature the solid obtained was filtered and washed with methanol and water and dried under vacuum to obtain a purple solid (1.8 g, 2.12 mmol, 20% yield).  $^1\text{H}$  NMR (400 MHz,  $\text{CDCl}_3$ )  $\delta$ : 8.82 (s, 8H), 8.43 (d, 8H), 8.29 (d, 8H), 4.10 (s, 12H), -2.83 (s, 2H).

### 4.2.2.2. Synthesis of 5, 10, 15, 20-tetrakis (4-methoxycarbonylphenyl) Mg(II) porphyrin (Mg(II)TPPCOOMe)

In a 250-mL round bottom flask, TPPCOOMe (1 mmol, 0.854 mg) and  $\text{MgCl}_2$  (12.8 mmol) were mixed in 100 mL DMF. Then 1 mL triethylamine was added to this solution and stirred at room temperature for 10 min and then refluxed for 24 h. After cooling to room temperature, the solution was poured into 150 mL of water and the solid obtained was filtrated and collected. The obtained solid was dissolved by chloroform and the organic phase was washed with water five times and dried over anhydrous magnesium sulfate. The chloroform was evaporated under reduced pressure and the resulting solid was dried in an oven at 100 °C. The product was characterized by  $^1\text{H}$  NMR analysis.

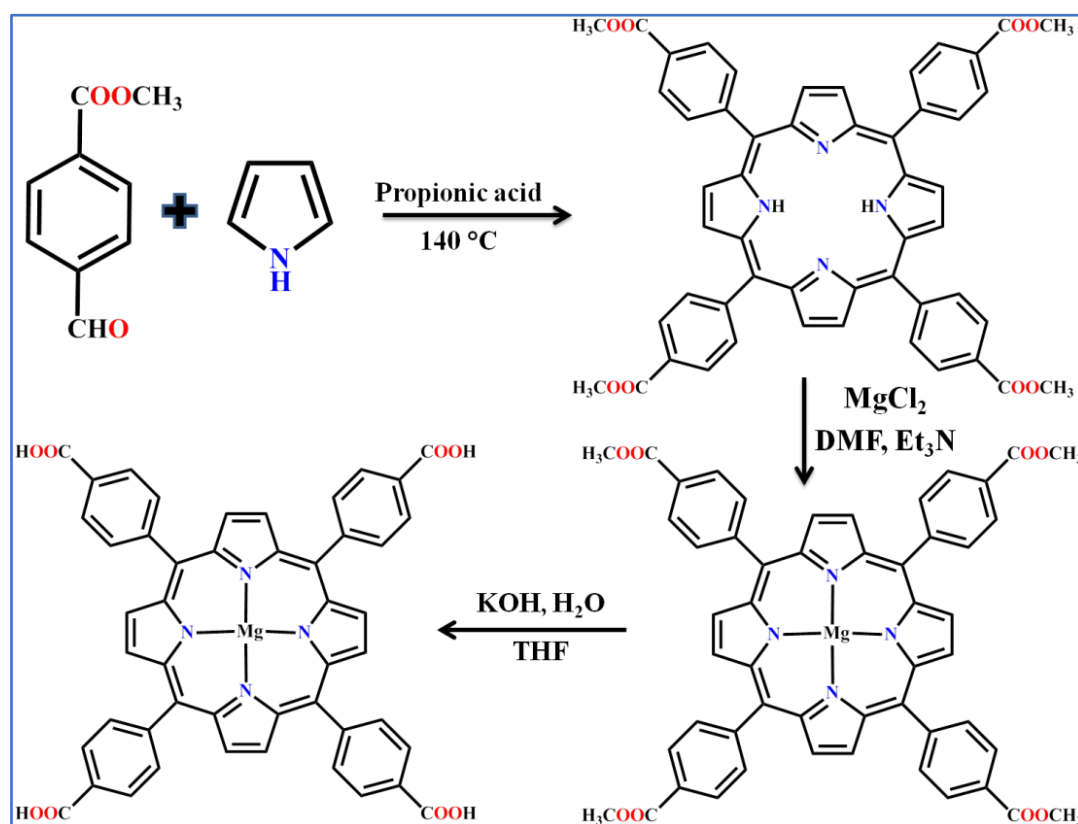
### 4.2.2.3. Synthesis of [5, 10, 15, 20-tetrakis (4-carboxyphenyl) porphyrin] ( $\text{H}_4\text{T CPP}(\text{H}_2)$ )

In a 250-mL round bottom flask, 0.75 g of TPPCOOMe was dissolved in a mixture of 25 mL of THF and 25 mL of MeOH, to which an aqueous solution of 2.63 g KOH (0.0469

mol) in 25 mL H<sub>2</sub>O was added. This mixture was refluxed for 12 h and after being cooled to room temperature the solvent was evaporated. Additional water was added and filtered, the filtrate was acidified with 1M HCl until complete precipitation of purple solid of the ligand which was collected by filtration, washed with water, and dried in vacuum at 60 °C. The product was characterized by <sup>1</sup>H NMR analysis.

#### 4.2.2.4. Synthesis of [5, 10, 15, 20-tetrakis (4-carboxyphenyl) Mg(II) porphyrin] (H<sub>4</sub>TCPP(Mg))

In a 250-mL round bottom flask, 0.75 g of Mg(II)-TPPCOOMe was dissolved in a mixture of 25 mL of THF and 25 mL of MeOH to which an aqueous solution of 2.63 g KOH (0.0469 mol) in 25 mL H<sub>2</sub>O was added. This mixture was refluxed for 12 h and after being cooled to room temperature the solvent was evaporated. Additional water was added and filtered, the filtrate was acidified with 1M HCl until complete precipitation of the purple solid of the ligand which was collected by filtration, washed with water, and dried in vacuum at 60 °C. The product was characterized by <sup>1</sup>H NMR analysis (Figure A51).



**Scheme 1.** The synthesis scheme of [5, 10, 15, 20-Tetrakis (4-carboxyphenyl) Mg(II) porphyrin] (H<sub>4</sub>TCPP(Mg)) ligand.

#### 4.2.2.5. Synthesis of PCN-224 and PCN-224(Mg)

The PCN-224 and PCN-224(Mg) were prepared by following the previously reported procedure with a little modification by using  $H_4TCPP(H_2)$  and  $MgH_4TCPP(Mg)$  ligands, respectively (Scheme 1).<sup>1</sup> Briefly,  $ZrCl_4$  (0.5 mmol, 117 mg), benzoic acid (10 mmol, 1.2 g),  $H_4TCPP(H_2)$  ligand (0.05 mmol, 40 mg), acetic acid (0.5 mL) were mixed in 7.5 mL of DMF and the solution was sonicated for 15 min in a 30 mL glass vial. The vial was sealed by Teflon cap and heated at 120 °C for 24h. For the synthesis of PCN-224(Mg), a similar procedure was used except the use of the  $H_4TCPP(Mg)$  ligand (0.05 mmol, 40 mg) in place of the  $H_4TCPP(H_2)$  ligand.

#### 4.2.3. Gas adsorption measurements

$N_2$  adsorption-desorption studies were carried out at 77 and 273K, while  $CO_2$  adsorption-desorption measurements were carried out at 273, and 298K using QUANTACHROME Quadrasorb SI automated surface area and pore size analyzer instrument. For  $CH_4$  the measurement was carried out at 273K. Ultrapure (99.995%)  $N_2$ , He,  $CH_4$ , and  $CO_2$  gases were used for the adsorption-desorption measurements. Prior to adsorption measurements, the sample (~ 0.10g) was exchanged with methanol and activated at 120 °C for 12 h under vacuum in QUANTACHROME Flovac degasser and further purged with ultrapure  $N_2$  (99.995%) gas on cooling. PXRD patterns of the activated samples revealed the retaining of the original framework structure after activation. The BET surface area of the MOFs was estimated from  $N_2$  sorption isotherms carried out at 77K. The gas selectivity experiments were carried out at 273K. The dead volume of the sample cell was measured using Helium gas (99.995%).

#### 4.2.4. Catalytic cycloaddition reactions of $CO_2$ with epoxides

The cycloaddition reactions of  $CO_2$  with various epoxides were carried out in the Schlenk tube. Before catalytic reactions, the PCN-224(Mg) was exchanged with methanol and activated at 120 °C for 12 h under vacuum to remove guest solvent molecules. In a typical reaction, the epoxide (20 mmol), and the activated MOF catalyst (0.1 mol%) were taken in the Schlenk tube at room temperature. Then,  $CO_2$  (1 atm) (99.99%) was introduced using a balloon and the reaction mixture was allowed to stir under irradiation with LED lights (3 X 30W) for 6 h. After this time, the catalyst was separated from the reaction mixture by simple centrifugation and the catalytic conversions were determined from the  $^1H$  NMR spectra of the filtrate. The recovered catalyst was washed with methanol thoroughly and

activated at 120 °C under vacuum for 12 h and reused for subsequent catalytic cycles. A similar procedure was employed for the catalytic reactions carried out with simulated flue gas ( $N_2:CO_2 = 87:13\%$ ) and by continuous bubbling of laboratory air (for  $CO_2$  conversion from direct air). Further, a similar procedure was followed for the sunlight-driven catalytic reactions in which the catalytic reactions were carried out on the terrace of S. S. Bhatnagar Block, IIT Ropar, Punjab, India, from 10 AM to 4 PM. It is worth mentioning that, during these catalytic reactions, the temperature of the reaction was in the range of 30-35 °C. The photocatalysis was carried out by using white LED light (3 X 30W) possessing maximum emission ( $\lambda_{max}$ ) at 450 nm. The light intensity or the number of photons per unit area received was measured by flux meter and the value was  $3.3 \times 10^{17}$  photons  $s^{-1}$ .

#### 4.2.5. Theoretical section

The geometry optimization of the primitive structure of Mg-MOF unit crystal, HOMO, and LUMO was carried out using density functional theory (DFT) with gradient exchange-correlational functional of B3LYP. The Pople basis of 6-31G\* has been used for all main group elements of H, C, N, O, and the LANL2DZ basis set was implemented for the Zr transition metal.<sup>56</sup> We have included Grimme's dispersion (DFT-D3) correction to account for the effect of all weak interactions.<sup>57</sup> The electronic absorption spectra (ligand to metal charge transfer, LMCT) have been performed by the time-dependent density functional theory (TD-DFT) method, scanning across 300 excited states. All TD-DFT calculations were performed using the PBE functional with the same basis set. All calculations were performed using Gaussian 09 software. The adsorption energy (A.E.) of the gaseous species on the metal center (Mg and Zr) of Mg-MOF was calculated by the following equation.

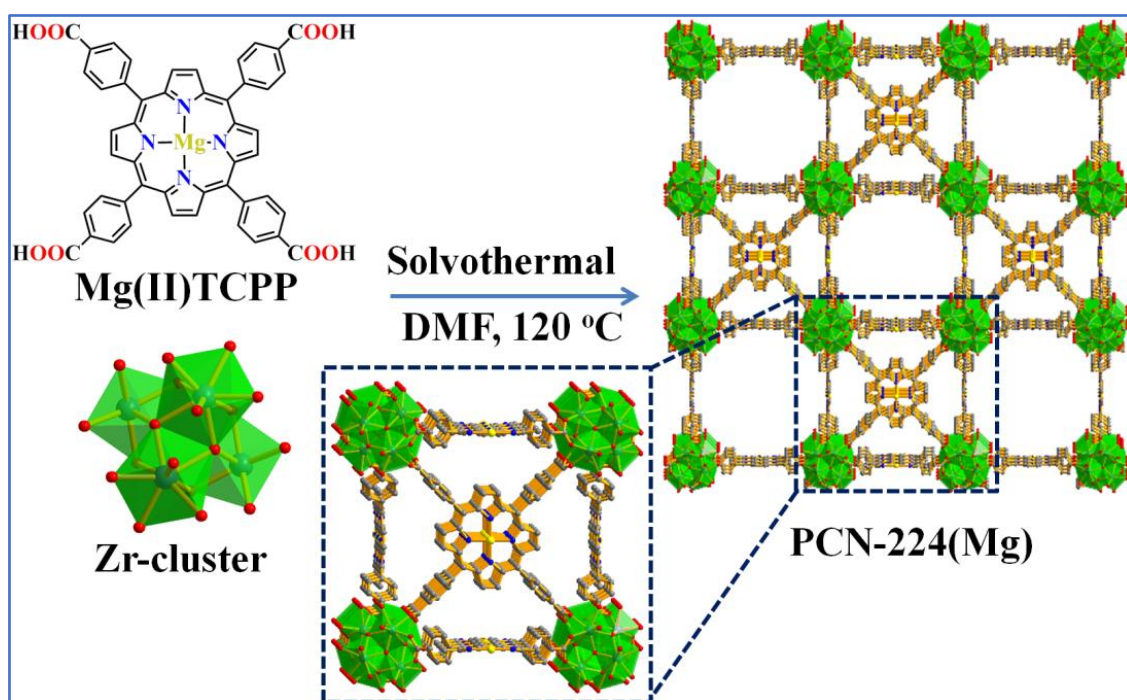
$$A.E. = \{E_{MOF,x} - (E_{MOF} - E_x)\}$$

Where, x denotes the gaseous species such as  $CO_2$ ,  $N_2$ , and  $O_2$ . The  $E_{MOF,x}$ ,  $E_{MOF}$  and  $E_x$  represents the total energy of the gas-adsorbed MOF, free MOF, and individual gas species, respectively. The reaction-free energy changes ( $\Delta G$ ) have been calculated from the reaction-free energy difference between the final and initial intermediates. The Zero-point vibrational energy (ZPVE) and thermal correction have been considered in total electronic energy to obtain the reaction-free energy at 298.15 K temperature and 1 atm pressure. The transition state (TS) has been confirmed in presence of one imaginary frequency along the expected reaction coordinate. The Natural bond orbital (NBO) calculations have also been considered on some intermediates to investigate the natural charges.<sup>58</sup>

### 4.3. Results and discussion

#### 4.3.1. Synthesis and characterization

The  $H_4TCPP(H_2)$  (5, 10, 15, 20-Tetrakis (4-carboxyphenyl) porphyrin) ligand and  $H_4TCPP(Mg)$  metalloligand were synthesized by following the previously reported procedure with a little modification.<sup>59</sup> The PCN-224 and PCN-224(Mg) were prepared by adopting the reported synthetic route with a slight modification by using  $H_4TCPPH_2$  and  $H_4TCPP(Mg)$  ligands, respectively (Scheme 2).<sup>50</sup>



**Scheme 2.** The synthesis scheme of PCN-224(Mg).

The  $^1H$  NMR spectrum of  $H_4TCPP(Mg)$  metalloligand showed the disappearance of pyrrolic N-H peaks indicating the incorporation of Mg(II) ion into the porphyrin ring (Figure A52). Further, FTIR spectra of the MOF established the absence of characteristic peak at  $3320\text{ cm}^{-1}$  corresponding to N-H stretching frequency of the porphyrin ring (Figure A52) supporting the incorporation of Mg(II) ions into the porphyrin ring.<sup>60</sup> Moreover, the UV-Vis absorption spectrum of metal-free porphyrin ligand showed an intense Soret band at 418 nm [ $a_{1u} \rightarrow e_g$ ] with four Q bands [ $a_{2u} \rightarrow e_g$  (forbidden)] at 515, 548, 592, and 648 nm. Notably, upon the incorporation of Mg(II), the soret band was shifted to 428 nm and the number of Q bands was reduced to two (565 and 605 nm) which can be ascribed to a change in the symmetry of the molecule from  $D_{2h}$  to  $D_{4h}$  (Figure A53).<sup>61</sup>

The powder XRD patterns of both the frameworks were well-matched with the simulated pattern indicating the phase purity of the samples and retaining of the original framework structure even after Mg(II) was incorporated. However, a slight broadening of the peaks was observed for PCN-224(Mg) which could be attributed to a partial loss of crystallinity of the framework (Figure 1a). The UV-Vis diffuse reflectance spectra (DRS) of the MOFs showed broad absorption in the visible region (400–700 nm) featuring Soret and Q bands (Figure 1b). The bandgap energy ( $E_g$ ) for PCN-224 and PCN-224(Mg) estimated from the Tauc plot,  $(\alpha h\nu)^2$  vs photon energy ( $h\nu$ ) was found to be 2.64 and 2.70 eV, respectively (Figure A54).

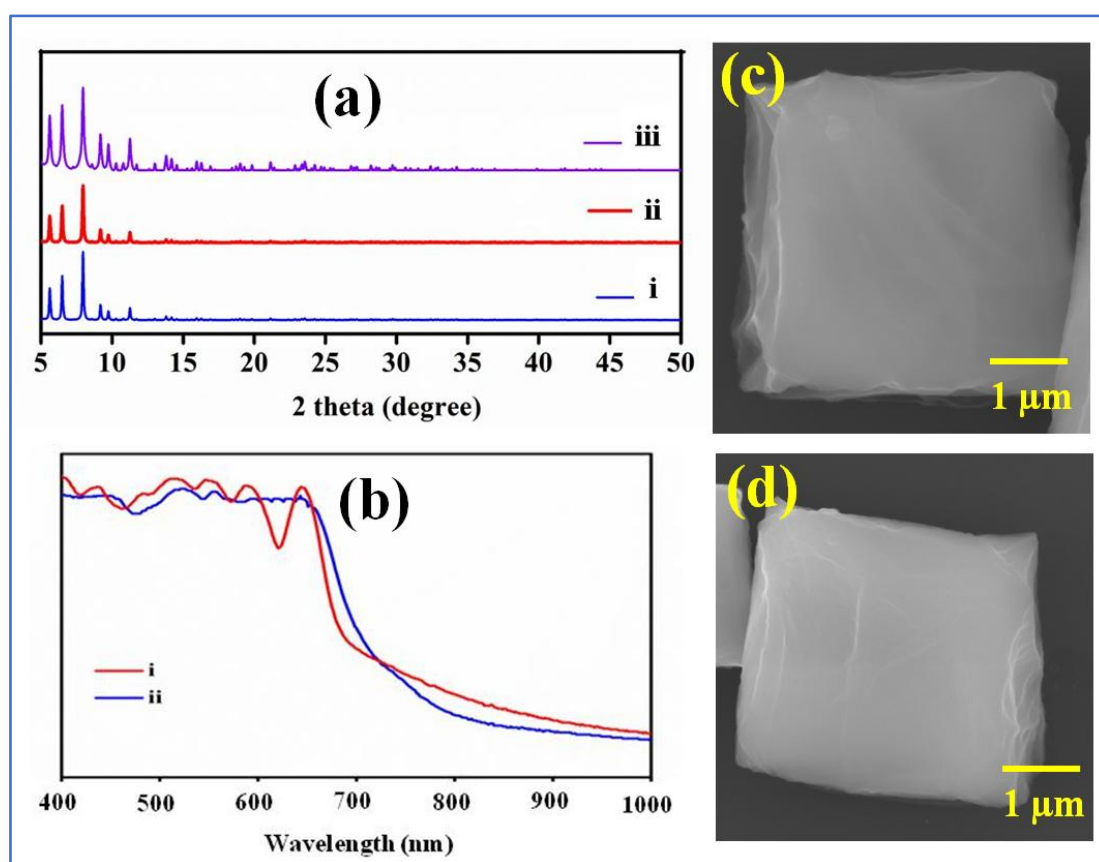


**Figure 1.** (a) PXRD pattern of simulated PCN-224 (i), as-synthesized PCN-224 and PCN-224(Mg) (ii and iii), (b) UV-vis diffuse reflectance spectra (DRS) of PCN-224 (i), PCN-224(Mg) (ii), SEM image of PCN-224 (c), and PCN-224(Mg) (d).

The calculated band gap values highlight the visible light absorption properties of the frameworks. Further, FE-SEM analysis of MOFs revealed that the cubic morphology of PCN-224 was retained even after Mg(II) is incorporated in the porphyrin ring (Figures 1c and 1d). The energy dispersive spectroscopy (EDS) analysis supports the incorporation of Mg(II)

in the framework (Figure A55). Further, thermogravimetric analysis (TGA) of the MOFs revealed that the thermal stability of the pristine MOF was not altered significantly even after Mg(II) was embedded, and both the MOFs exhibited stability up to 430 °C (Figure A56).

### 4.3.2. X-ray photoelectron spectroscopy (XPS) analysis

The XPS survey scan of PCN-224(Mg) showed the presence of Zr, Mg, C, N, and O elements (Figure 2a). Further, the Mg(II) spectra showed a characteristic peak at binding energy (BE) of 1304.7 eV which is well-matched with MgN<sub>4</sub> XPS spectra of Mg(II)-ion in chlorophyll (1304.3 eV)<sup>62</sup> supporting the incorporation of Mg(II) into the porphyrin ring (Figure 2b). Further, the N 1S spectrum (Figure 2c) shows a binding energy peak at 400.0 eV which is in accordance with the reported BE for N in chlorophyll (400.1 eV).<sup>51</sup> The appearance of a single peak for the N 1S can be attributed to the symmetric environment of all the four nitrogen atoms of the porphyrin ring due to metallation (M-N<sub>4</sub>) aided by a change in the symmetry of the molecule from *D*<sub>2h</sub> to *D*<sub>4h</sub>. Similar observations are reported for the N 1S spectra of the metallated porphyrin systems.<sup>59</sup> The Zr(IV) spectra (Figure 2d) show peaks at a binding energy of 182.6 and 184.9 eV assigned to 3d<sub>5/2</sub> and 3d<sub>3/2</sub>, respectively.<sup>63</sup>

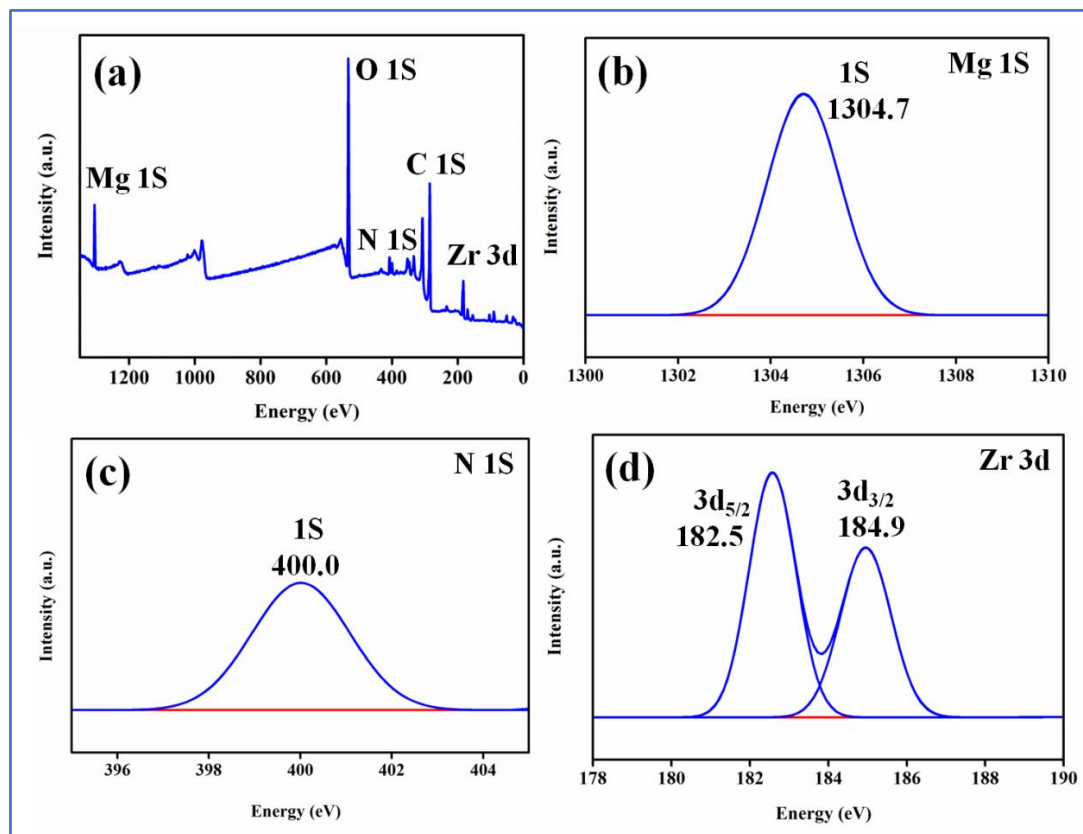


**Figure 2.** XPS spectra of PCN-224(Mg) (a) Survey scan, (b) Mg 1S, (c) N 1S, and (d) Zr 3d.

### 4.3.3. Gas adsorption study

The N<sub>2</sub> adsorption measurements were carried out to estimate the permanent porosity of the MOFs and the estimated Brunauer-Emmett-Teller (BET) surface area for PCN-224, and PCN-224(Mg) were found to be 1611.6 and 1251.1 m<sup>2</sup>/g, respectively (Figure 3a). The reduction in the BET surface area of PCN-224(Mg) framework can be assigned to a partial loss of porosity upon the incorporation of the metal ion in the macrocyclic pyrrole ring of the porphyrin ligand.<sup>62,63</sup> Further, the CO<sub>2</sub> adsorption isotherms of PCN-224 and PCN-224(Mg) showed type-I plots with an uptake of 86.43/43.22 cc/g and 47.64/29.9 cc/g at 273/298K, respectively (Figure 3b). It is worth highlighting that PCN-224(Mg) exhibited exceptionally high CO<sub>2</sub> uptake of 379.86 cc/g (74 wt%) at 195K which is found to be about 1.6 times higher than that of PCN-224 (229.21 cc/g: 45 wt%).

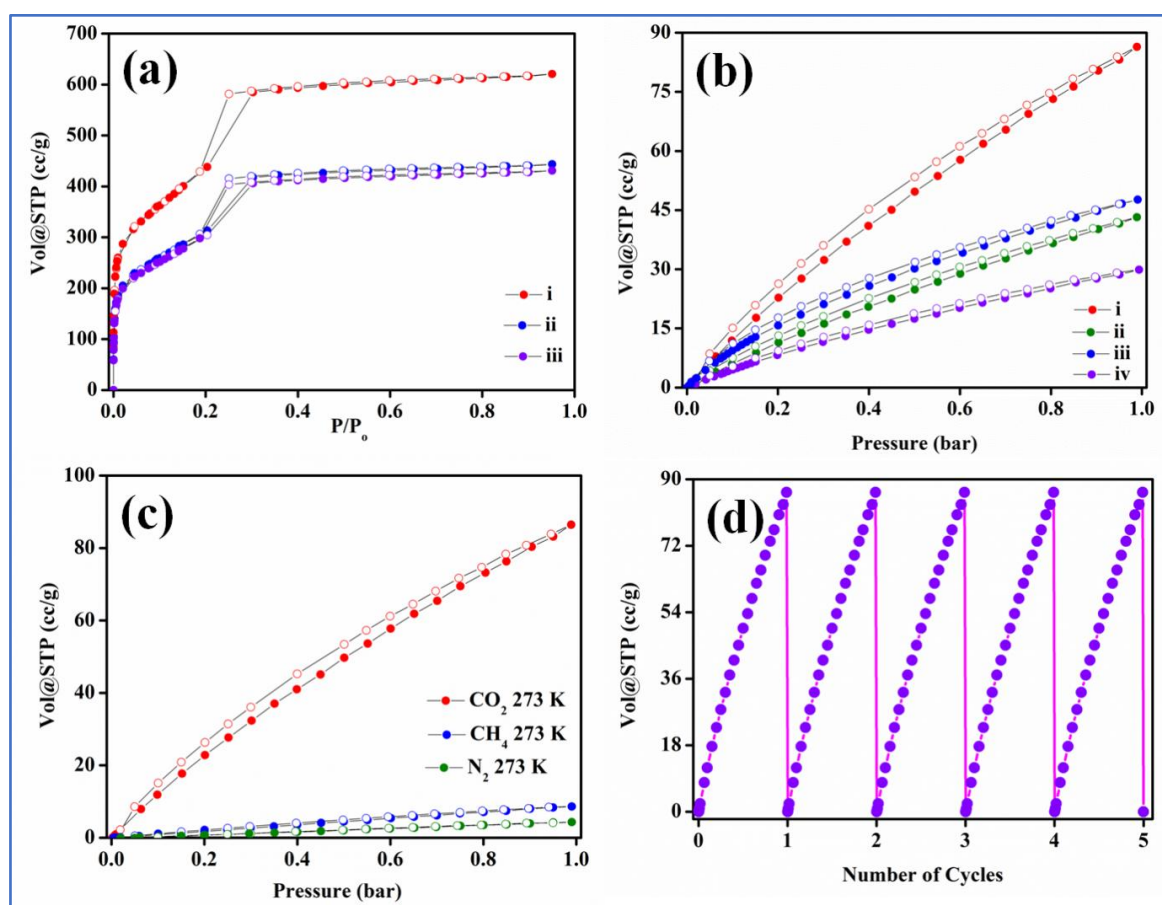


**Figure 3.** (a) N<sub>2</sub> adsorption isotherms for (i) PCN-224, (ii) PCN-224(Mg), (iii) recycled PCN-224(Mg), (b) CO<sub>2</sub> adsorption isotherms of PCN-224(Mg) (i and ii) and PCN-224 (iii and iv) carried out at 273 and 298 K, respectively, (c) selective CO<sub>2</sub> adsorption isotherm of PCN-224(Mg) and (d) recyclable CO<sub>2</sub> adsorption carried out at 273 K.

Further, the isotherms were fitted with the Freundlich-Langmuir equation<sup>64</sup> (Figure A57-A60) to get saturation adsorption values which were incorporated in Clausius-Clayperon equation<sup>65</sup> to compute the heat of adsorption ( $Q_{st}$ ) value (Figure 4). Interestingly, PCN-224(Mg) showed a  $Q_{st}$  value of 44.5 kJ/mol which is about 7.8 kJ/mol higher than that of pristine MOF (36.7 kJ/mol). Further, the experimentally determined value of  $Q_{st}$  was supported by a theoretically calculated value of 44.6 kJ/mol. These studies highlight that incorporation of Mg(II) in MOF enhances its CO<sub>2</sub> uptake and heat of adsorption.<sup>66</sup> Besides, the PCN-224(Mg) showed selective as well as recyclable CO<sub>2</sub> adsorption over other gases like CH<sub>4</sub> and N<sub>2</sub> (Figure 3c and 3d) with Henry selectivity constant of 67.6 and 53.1 for CO<sub>2</sub>/N<sub>2</sub> and CO<sub>2</sub>/CH<sub>4</sub>, respectively (Figure A61).

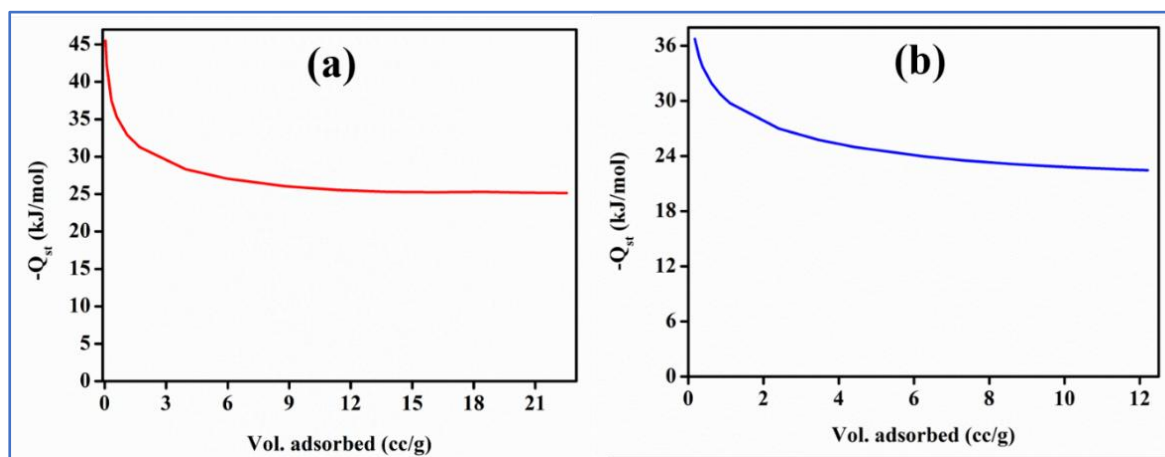


**Figure 4.** The heat of adsorption ( $Q_{st}$ ) plots of carbon dioxide for (a) PCN-224(Mg), and (b) PCN-224(Mg).

#### 4.3.4. Photocatalytic fixation of CO<sub>2</sub>

The broad absorption property of PCN-224(Mg) in the visible region along with its optimal bandgap (2.70 eV) prompted us to test its application for light-assisted fixation of CO<sub>2</sub>. To begin with, the photocatalytic activity was examined for cycloaddition of CO<sub>2</sub> with epichlorohydrin (ECH) as model epoxide by varying the reaction parameters (Table A18, Figure A62). At the optimized conditions of RT and 1 atm (balloon) CO<sub>2</sub>, the use of PCN-224(Mg) as a catalyst and TBAB (tetrabutylammonium bromide) as cocatalyst afforded more than 99 % conversion of ECH to CC within 6 h (Figure 5a) under the irradiation with three 30 W white LED bulbs as a visible light source ( $\lambda = 450$  nm) (Figure A63).<sup>67</sup> Whereas, the use of pristine MOF as a catalyst resulted in only about 47% conversion of ECH to CC at the optimized conditions (Figure 5a). Hence, from the controlled experiments it was revealed that

the Mg-incorporated framework showed about 2.1 times higher catalytic performance in comparison to that of PCN-224. Further, to evaluate the role of light in accelerating the conversion of ECH, the catalysis was carried out under thermal conditions. Notably, the catalytic reaction carried out at RT in dark showed only 18% conversion of ECH to CC (Figure 5b). As the temperature of the reaction was increased, conversion of ECH was also found to increase and complete conversion (> 99%) was reached at 80 °C (Figure 5b). The rate constants for conversion of ECH to CC catalyzed by PCN-224(Mg) were estimated to be 0.03 and 0.54 h<sup>-1</sup> carried out at dark, and white LED light irradiation, respectively (Figure 5c, and A81). The calculated rate constant values suggest about 18 folds enhancement in the rate of the catalytic reaction carried out under LED light over dark conditions (Figure A64). These observations unambiguously support the light-promoted acceleration in catalytic activity for the conversion of ECH to CC at mild conditions of RT and 1 atm (balloon) of CO<sub>2</sub>. Further, to test the role of CO<sub>2</sub> in the formation of CC, the catalytic reaction was carried out in the absence of carbon dioxide using an Ar atmosphere. To our delight, no formation of CC was observed supporting the formation of CC by cycloaddition of CO<sub>2</sub> (Figure 5a). To investigate the role of cocatalyst, the catalytic activity of PCN-224(Mg) was carried out in the absence of TBAB which resulted in no formation of CC (Table A18). Whereas, the use of TBAB alone as a catalyst afforded only about 17% conversion of epoxide at the optimized conditions. These results suggest the requirement of a bifunctional catalytic system involving both MOF and TBAB for efficient conversion of epoxide (Table A18, Figure 5a). Encouraged by the high photocatalytic activity of PCN-224(Mg), the scope of the catalysis was broadened to various epoxides and the results are summarized in Table 1. From the results, it was noticed that smaller epoxides were completely converted into the respective cyclic carbonates, while for the larger epoxides, the conversion decreases with an increase in the alkyl chain length of the epoxides (Table 1). These observations can be assigned to the limited diffusion of bigger epoxides in the narrow voids of the framework. However, a little increase in the catalytic conversion observed for allyl glycidyl ether and butyl glycidyl ether can be rationalized to their electron-donating nature. Besides, the aromatic epoxide, styrene oxide was also converted into styrene carbonate with a 78% yield at the optimized conditions.

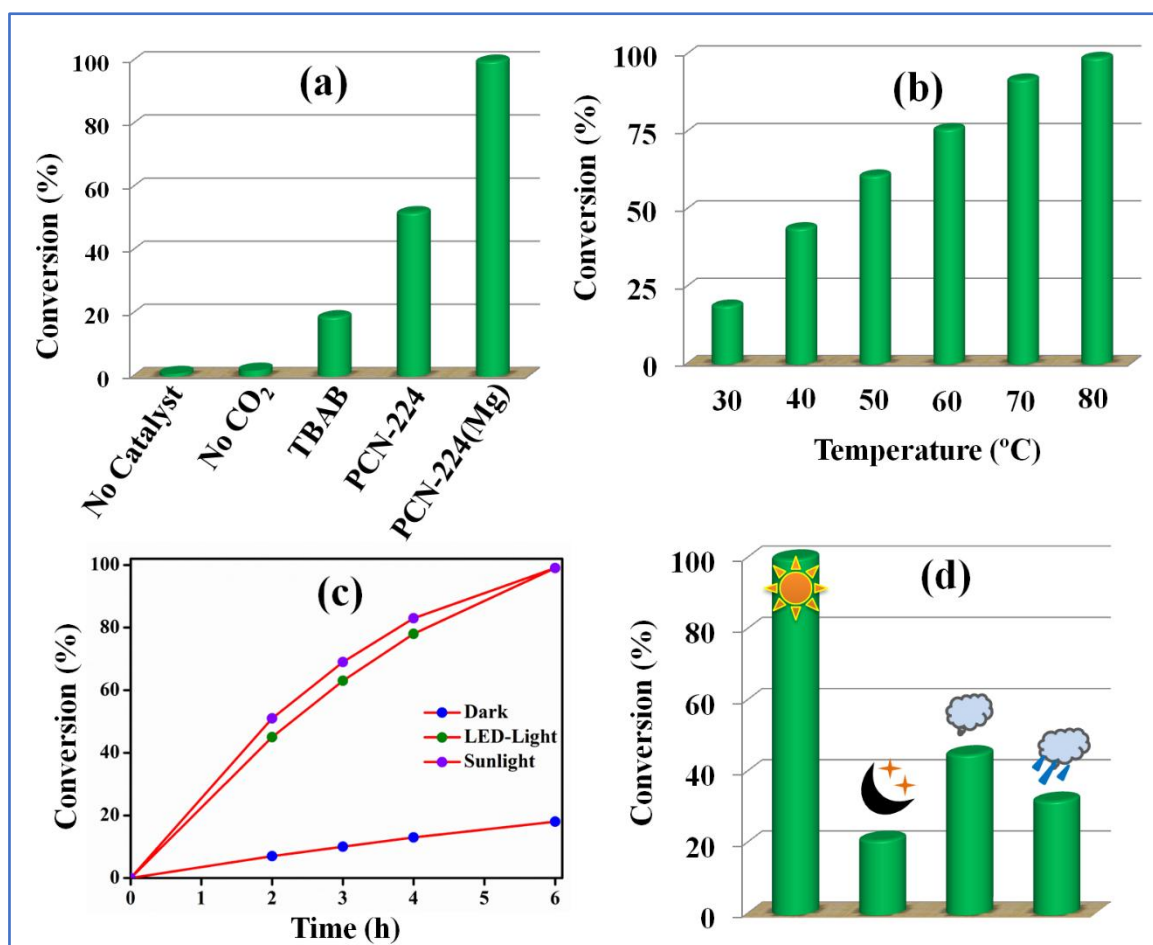


**Figure 5.** Optimization of photocatalytic cycloaddition of CO<sub>2</sub> with ECH by varying (a) catalyst, (b) temperature, (c) catalytic activity in dark and light conditions, and (d) sunlight-dependent photocatalysis.

This visible light-promoted enhanced catalytic activity of PCN-224(Mg) motivated us to test its application for CO<sub>2</sub> fixation under natural sunlight irradiation. At the optimized conditions, almost complete conversion (> 99%) of ECH was observed within 6h and from time-dependent study, the calculated rate constant was 0.66 h<sup>-1</sup>, which is about 1.2 times higher than that of the catalysis carried out under LED light irradiation. This higher catalytic activity of PCN-224(Mg) under natural sunlight irradiation over the LED light could be attributed to the presence of 3-4% UV radiation in sunlight.<sup>68,69</sup> Further, the effect of light intensity on the catalytic activity of the MOF was studied by carrying out the reaction in sunny, dark, rainy, and cloudy conditions (Figure 5d). Interestingly, the catalytic activity was highest for the reaction carried out on a sunny day over the other conditions supporting the sun-light promoted the catalytic activity of PCN-224(Mg).

**Table 1.** Photocatalytic fixation of CO<sub>2</sub> to cyclic carbonates under optimized conditions.<sup>a</sup>

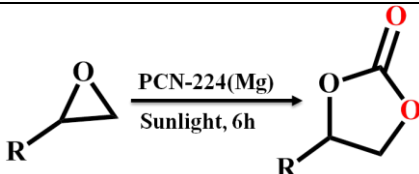
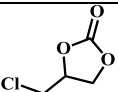
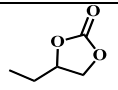
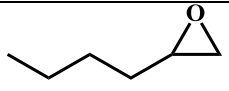
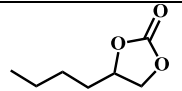
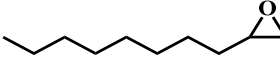
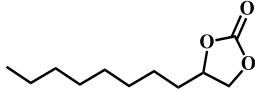
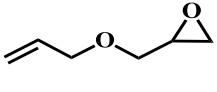
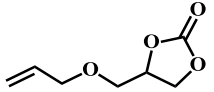
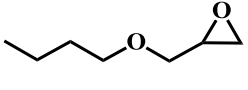
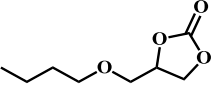
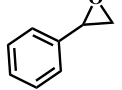
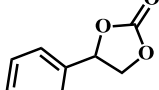
Entry No.	Substrate (R)	Product	Conversion <sup>b</sup> (%)	TON <sup>c</sup>
1			99	3980
2			99	3974
3			94	3768
4			83	3332
5			79	3164
6			89	3568
7			86	3452
8			76	3044

<sup>a</sup>Reaction conditions: catalyst (0.025 mol%), epoxide (20 mmol), TBAB (1 mol%), LED light (3 X 30 W), time (6h), pressure (1 atm), <sup>b</sup>The conversions are based on <sup>1</sup>H NMR analysis by taking 1,1,2,2-tetrachloroethylene as internal standard. <sup>c</sup>TON = number of mol of product formed / number of mol of catalyst used.

The rate constant (0.66 h<sup>-1</sup>) for the catalytic reaction carried out in sunlight was found to be about 21 times higher than that of the dark condition (0.03 h<sup>-1</sup>). It is worth mentioning that, during these catalytic reactions, the temperature of the reaction was in the range of 30-

35 °C, which rules out the influence of temperature on the catalytic rate. These experiments signify the importance of light in accelerating the conversion of CO<sub>2</sub> under mild conditions. Encouraged by the high catalytic activity of PCN-224(Mg) under sunlight irradiation, the catalysis was extended for other epoxides, and the results are shown in Table 2. Notably, most of the epoxides were converted to their respective CCs with high yield and TON at the mild conditions of RT and 1 atm (balloon) conditions under natural sunlight irradiation (Table 2).

**Table 2.** Photocatalytic fixation of CO<sub>2</sub> into cyclic carbonates under natural sunlight irradiation.<sup>a</sup>

				
Entry No.	Substrate (R)	Product	Conversion <sup>b</sup> (%)	TON <sup>c</sup>
1			99	3992
2			95	3779
3			86	3456
4			80	3054
5			94	3760
6			89	3568
7			82	3292

<sup>a</sup>Reaction conditions: epoxide (20 mmol), catalyst (0.025 mol%), TBAB (1 mol%), sunlight, time (6h), and temperature (30-35 °C). <sup>b</sup>The catalytic conversions were determined by <sup>1</sup>H NMR analysis by taking 1,1,2,2-tetrachloroethylene as the internal standard. <sup>c</sup>TON = number of mmol of product formed / number of mmol of catalyst used.

#### 4.3.5. Photocatalytic fixation of CO<sub>2</sub> from direct air

The excellent photocatalytic activity of PCN-224(Mg) with high selectivity (>99%) and TON motivated us to explore its catalytic performance for the conversion of CO<sub>2</sub> from direct air. Towards this direction, the photocatalytic performance of PCN-224(Mg) was studied by the use of laboratory air as a CO<sub>2</sub> source. The reaction conditions were optimized by varying catalyst amount as well as reaction time as shown in Table A19. The catalytic activity carried out using PCN-224(Mg) at RT resulted in about 39% conversion of ECH to CC with continuous bubbling of laboratory air. Further, the yield of CC was enhanced to 68 and 97% upon increasing the reaction time to 24 and 48h, respectively. It is worth noting that atmospheric air comprises of 400 ppm of CO<sub>2</sub> and therefore the catalyst used must be extremely reactive to capture and convert carbon dioxide from such a low concentration.<sup>70-72</sup> This excellent photocatalytic activity of PCN-224(Mg) further prompted us to study the substrate scope by varying epoxides. Interestingly, a series of epoxides (both aliphatic and aromatic) were converted to CCs using direct air as a carbon dioxide source (Table 3). To our knowledge, this work constitutes a unique demonstration of visible light-assisted fixation of CO<sub>2</sub> for high-yield cyclic carbonate synthesis by using MOF-based heterogeneous catalysts under mild conditions.

#### 4.3.6. Mechanistic investigation

To establish the role of photo-generated electrons and holes in the light-assisted CO<sub>2</sub> fixation catalyzed by PCN-224(Mg), controlled reactions were carried out in the presence of Na<sub>2</sub>S<sub>2</sub>O<sub>8</sub> and EDTA (ethylenediaminetetraacetic acid) as electron and hole scavengers, respectively. Interestingly, when the catalysis was carried out in presence of Na<sub>2</sub>S<sub>2</sub>O<sub>8</sub> and EDTA, the conversion of ECH was significantly reduced to 34 and 37%, respectively. Thus the observed reduction in the catalytic conversion of ECH supports the participation of photo-generated electrons and holes in the photocatalytic reaction. Further, to get support for the higher catalytic activity of PCN-224(Mg) over the pristine MOF, transient photocurrent-time (i vs t) measurements were carried out under fitful visible light irradiation. As shown in Figure 6a, the photocurrent density sharply increases under irradiation of light due to the facile separation of charge carriers. Whereas, when the light is turned off, the photocurrent density decays to zero (Figure 6a). Indeed, PCN-224(Mg) showed higher photocurrent density compared to pristine MOF due to the fast separation and migration of charge carriers to the reaction sites.<sup>73</sup> Thus, the higher photocurrent response of PCN-224(Mg) is in accordance with its higher catalytic performance over the pristine MOF.

**Table 3.** Photocatalytic fixation of CO<sub>2</sub> to cyclic carbonates from direct air under optimized conditions.<sup>a</sup>

Entry No.	Substrate (R)	Product	Conversion <sup>b</sup> (%)	TON <sup>c</sup>
1			68	907
2*			97	1293
3			62	826
4			54	720
5			51	680
6			59	786
7			56	746
8			48	640

<sup>a</sup>Reaction conditions: catalyst (0.075 mol%), epoxide (20 mmol), TBAB (1 mol%), LED light (3 X 30 W), 24h, \*time (48h). <sup>b</sup>The catalytic conversions were based on <sup>1</sup>H NMR analysis by taking 1,1,2,2-tetrachloroethylene as an internal standard. <sup>c</sup>TON = number of moles of product formed / number of moles of catalyst used.

This enhanced catalytic activity can be correlated to facile charge transfer from the Mg-porphyrin SBU to the  $Zr_6$ -oxo cluster which further activates  $CO_2$  to lower the energy barrier required for its activation. Further support for the higher catalytic activity of PCN-224(Mg) came from photoluminescence measurements carried out with an excitation wavelength of 440 nm (Figure 6b). As it can be seen from Figure 5b, the MOFs show emission bands around 680 nm and the emission intensity of PCN-224(Mg) was quenched in comparison to non-metallated MOF supporting efficient charge separation which is in line with the photocurrent data. Overall, both photocurrent and fluorescence measurements support the higher catalytic activity of PCN-224(Mg) over the parent MOF.

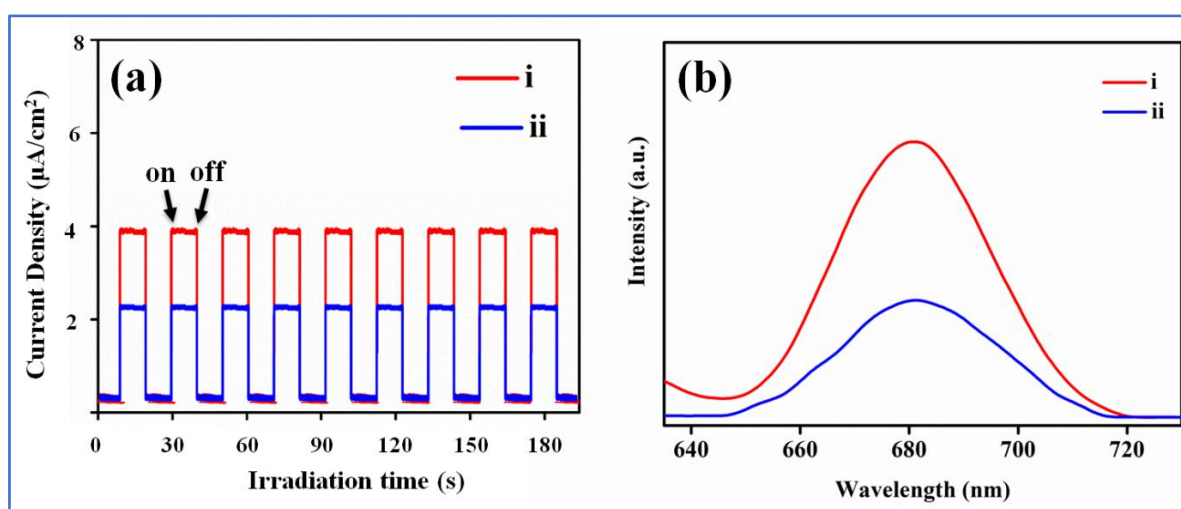


**Figure 6.** (a) Transient photocurrent ( $i$  vs  $t$ ) response of (i) PCN-224(Mg), and (ii) PCN-224. (b) PL spectra of (i) PCN-224, and (ii) PCN-224(Mg).

#### 4.3.7. Theoretical insight for the LMCT transition

To get further insights into the light-assisted charge transfer from Mg-porphyrin SBU to the  $Zr_6$ -oxo cluster, density functional theory (DFT) calculations were performed using the B3LYP functional as implemented in the Gaussian 09.<sup>74,75</sup> The time-dependent density functional theoretical (TD-DFT) calculations were performed on the Mg(II)-porphyrin SBU connected to  $Zr_6$ -oxo cluster (Mg-MOF) as a model system for the PCN-224(Mg) (Figure 6a). We have performed the TD-DFT calculations with and without the addition of epichlorohydrin (ECH) epoxide to understand the charge transfer process between the porphyrin SBU to Zr metal of  $Zr_6$ -oxo cluster. The simulated absorption spectra show that the absorption occurs at 430-530 nm for the Mg-MOF (Figure A65). However, the binding of ECH to the Mg-center resulted in a bathochromic shift (451-562 nm) in the absorption

spectra (Figure A66), which is in good agreement with our experimental solid-state UV-Vis absorption spectra (Figure 1b). Thus, these observations indicate that the ligand-to-metal charge transfer (LMCT) process from Mg-porphyrin SBU to the  $Zr_6$ -oxo cluster is enhanced in the presence of epoxide. To understand further, we have done the molecular orbital analysis, which shows that the high-intensity and low-intensity optical transitions can be characterized as HOMO-1 to LUMO+3 and HOMO to LUMO+2 transitions, respectively (Figure 7).

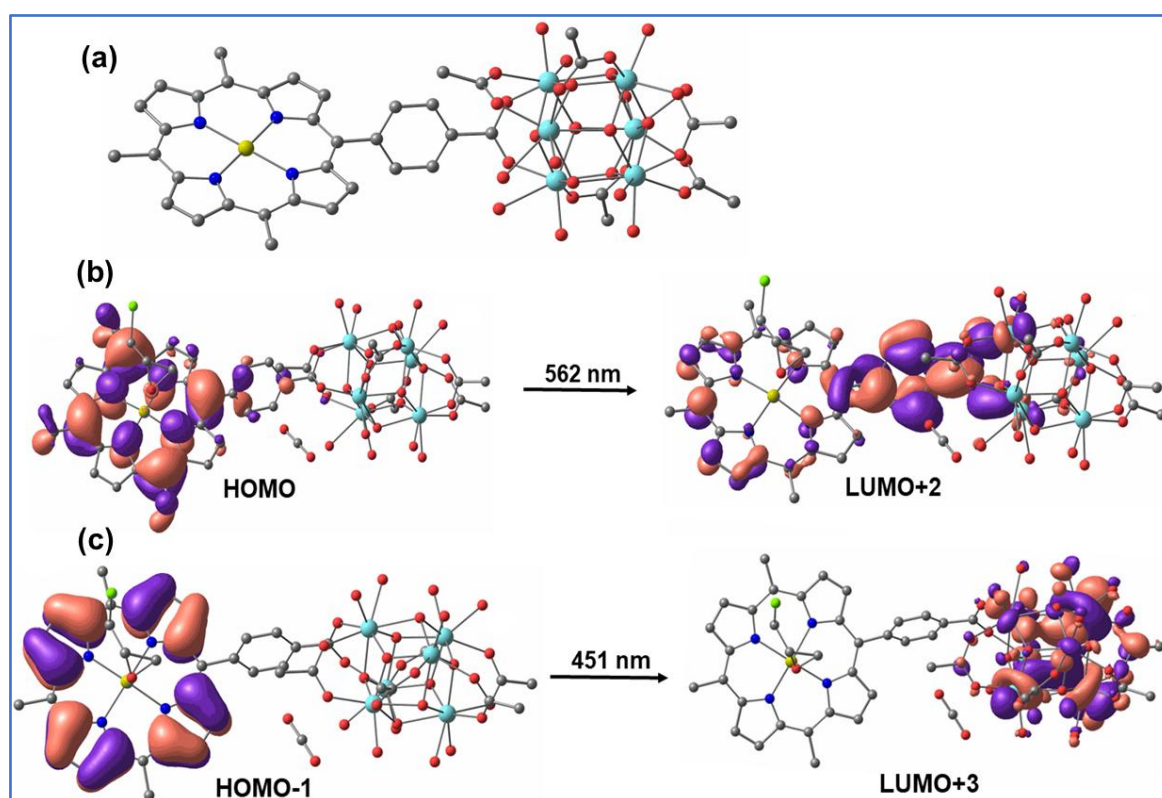


**Figure 7.** (a) Optimized structure of Mg(II)-porphyrin SBU connected to  $Zr_6$ -oxo cluster (Mg-MOF) as a theoretical model system, (b) in presence of epoxide, the frontier molecular orbitals involved in the optical transitions of PCN-224(Mg) are low intensity, and (c) high intense peak. Colour code: Zr, cyan; Cl, green; Mg, yellow; O, red; N, blue; C, grey. For clarity, we have removed the hydrogen atoms.

The low-intense HOMO to LUMO+2 (562 nm) transition is derived mainly from the non-bonding and bonding p-like states of nitrogen and carbon atoms of porphyrin SBU to the antibonding states of Zr 4d and p of the linkers (Figure 7b). Whereas high intense HOMO-1 to LUMO+3 (451 nm) transition is derived mainly from the bonding p-like states of porphyrin SBU to the antibonding 4d states of Zr atom in  $Zr_6$ -oxo cluster (Figure 7c). To get

further support on the LMCT, we have studied the charge transfer process using electron-rich propylene oxide (PO) epoxide, in this case, the wavelength of high and low intense optical transitions have shifted to 468 and 568 nm, respectively. Hence a bathochromic shift in the absorption spectra is observed in the presence of PO epoxide, supporting enhanced LMCT from porphyrin SBU to Zr<sub>6</sub>-oxo cluster (Figure A67). Similarly, we have studied the absorption spectra of Mg-MOF without epoxide, where the high and low intense peaks have been observed around the wavelengths of 438 and 530 nm with the associated transition of HOMO to LUMO+3 and HOMO to LUMO+2, respectively (Figure A67).

Overall, the TD-DFT calculations revealed that the coordination of epoxide to the Mg(II) site led to an enhanced photo-induced charge transfer process owing to the electron-donating nature of epoxides. This phenomenon can be realized by a change in the HOMO/LUMO energies of Mg-MOF with and without epoxide. Upon the addition of epoxide, the LUMO energy of MOF has increased to -2.198 eV from -2.277 eV, supporting the charge-transferring phenomena (Table A20). Moreover, the charge transfer process can also be explained from our natural bond orbital (NBO) charge analysis where the charge on Mg in SBU has decreased to +1.426 |e| from +1.439 |e| in the presence of the epoxide. As a result, the LMCT process is enhanced in the presence of epoxide as previously reported by Huang and co-workers.<sup>45</sup> Therefore, our TD-DFT study confirms the photo-generated charge transfer process from Mg-porphyrin SBU to Zr<sub>6</sub>-O cluster via the LMCT process. Such a charge transfer process facilitates the activation of CO<sub>2</sub>\* (O-C-O bond angle of 171°) resulting in the lowering of the energy barrier for its fixation with the epoxides to yield CC under mild conditions.

#### 4.3.8. Mechanistic investigation of photocatalytic CO<sub>2</sub> fixation

To understand the mechanism of photocatalytic CO<sub>2</sub> cycloaddition by Mg-MOF, we have calculated the stepwise reaction of free energy and activation barrier of the important steps, and the corresponding reaction free energy profile diagram is shown in Figures 8, and A68. Upon the addition of ECH epoxide, the formation of complex **b** takes place with reaction free energy of 6.74 kcal/mol. The reaction is endergonic which could be due to the interaction of epoxide and CO<sub>2</sub>. The O of ECH interacts with Mg(II) at a distance of 2.1 Å as well as molecular CO<sub>2</sub> can interact with the Zr site through C and O atoms, with CO<sub>2</sub>(O)-Zr and CO<sub>2</sub>(C)-Zr distances of 4.0 and 3.8 Å, respectively. Then Br<sup>-</sup> of TBAB interacts with the epoxide for the formation of intermediate **c** with an activation barrier of 0.08 kcal/mol and reaction-free energy of -10.14 kcal/mol. As shown in Figure 8 the TS of

the reaction is placed at higher energy in the reaction free energy profile and therefore, this could be the rate-determining step for this CO<sub>2</sub> cycloaddition reaction. This step (b → c) is highly exergonic (10.14 kcal/mol) which may be due to the strong Lewis acid-base interaction of Mg(II) and O of the epoxide. In the case of intermediate **d**, the activated CO<sub>2</sub>\* (O-C-O bond angle of 171°), formed due to the charge transfer from the Zr<sub>6</sub>-O cluster interacts with ECH through O(ECH)-C(CO<sub>2</sub>\*) interaction, resulting in the formation of alkoxide with a reaction free energy of -0.72 kcal/mol. Furthermore, the ring closer occurs leading to the formation of five-membered cyclic carbonate **f** with C(CO<sub>2</sub>)-O(ECH) and O(CO<sub>2</sub>)-β-C(ECH) bond lengths of 1.34 Å and 1.46 Å, respectively. Our calculated total reaction free energy and activation barrier are -13.1 and 6.82 kcal/mol, respectively which indicate the thermodynamic as well as kinetic favourability of the reaction. Based on the aforementioned discussion, the proposed mechanism for the photocatalytic conversion of CO<sub>2</sub> to CC is given in Scheme 3.

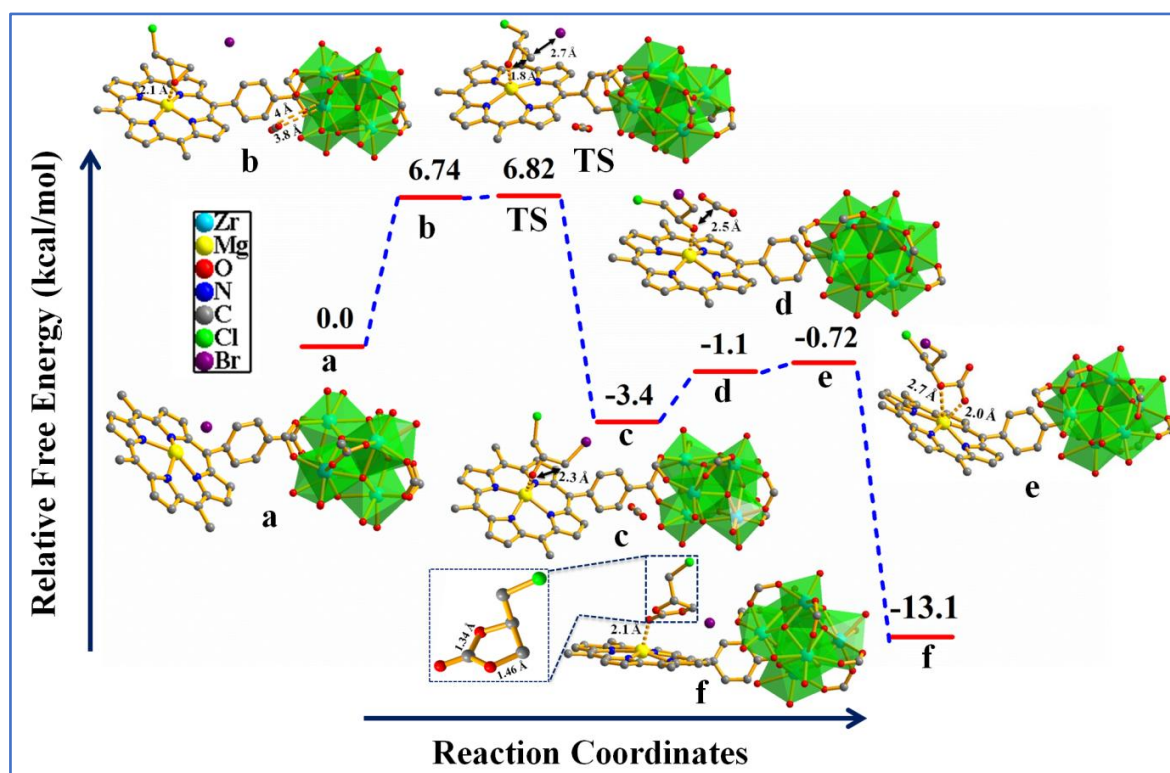
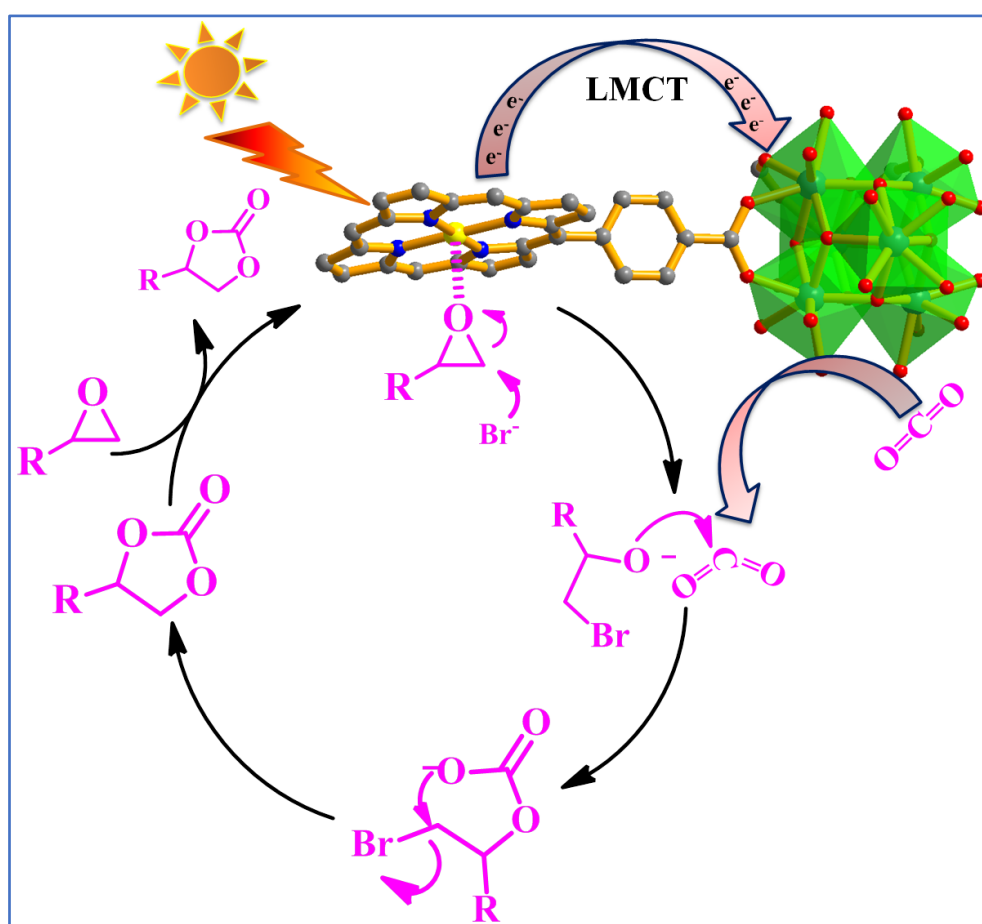


**Figure 8.** Reaction-free energy profile for cycloaddition of CO<sub>2</sub> with epichlorohydrin (ECH) catalyzed by PCN-224(Mg). Color code: Brown, Br; cyan, Zr; green, Cl; yellow, Mg; red, O; blue, N; grey, C; orange, O(CO<sub>2</sub>); magenta, O(ECH); pink, C(ECH); violet, C(CO<sub>2</sub>). For clarity, we have removed the hydrogen atoms.

The photocatalytic reaction proceeds with the polarization of epoxide and CO<sub>2</sub> at the Mg-porphyrin SBU and Zr-node, respectively. To get further support on the polarization of epoxide at Mg(II) site, PCN-224(Mg) was treated with ECH for 2 h and then retrieved, washed with methanol, and dried under vacuum. The FT-IR spectra of the recovered PCN-224(Mg) depicted C-H stretching frequency at 2998 cm<sup>-1</sup> corresponding to ECH (Figure A69). Then the nucleophilic attack of Br<sup>-</sup> of TBAB at the  $\alpha$ -carbon of the epoxide results in the ring-opening of the epoxide leading to Mg-alkoxide formation. Subsequent insertion of activated CO<sub>2</sub> (bent) followed by ring closure leads to CC formation and upon its release regenerates the active catalyst.



**Scheme 3.** The mechanism for the photocatalytic cycloaddition of CO<sub>2</sub> with epoxide.

#### 4.3.9. Catalyst recyclability and leaching test

The recyclability of PCN-224(Mg) was tested by recovering it from the reaction medium and then washing by methanol and drying under vacuum at 120 °C for 12 h. It's worth highlighting that the MOF catalyst was recyclable for ten cycles with no substantial loss in the catalytic activity (Figure 9a). Further, the recycled MOF was characterized by

PXRD, FT-IR, and UV-Vis techniques. The PXRD pattern of the recycled sample matches well with that of the pristine sample, except that a slight broadening of the peaks was observed which could be ascribed to a partial loss of crystallinity of the MOF due to its utilization for ten catalytic cycles with continuous stirring during catalysis (Figure A70). Further, FT-IR and UV-Vis spectra of the recycled sample were found to be similar to that of the as-synthesized sample (Figures A71 and A72). Further, N<sub>2</sub> adsorption studies revealed a slight reduction in the BET surface area of the recycled MOF (1239.7 m<sup>2</sup>/g) in comparison to that of the parent sample (1251.1 m<sup>2</sup>/g) supporting holding of the original framework structure (Figure 3a). To rule out any leaching of active metal, Mg(II)/Zr(IV) into the homogenous phase, the catalytic reaction was stopped after 2 h, and the catalyst was separated by filtration, then the reaction was continued for the remaining time under optimized conditions. Interestingly, no appreciable increase in the catalytic conversion (<5%) was observed affirming the heterogeneous nature of the catalysis (Figure 9b). Furthermore, MP-AES analysis of the reaction filtrate showed the absence of active metals (Zr/Mg) further supporting the absence of leaching of the catalyst during photocatalysis (Figure A73).

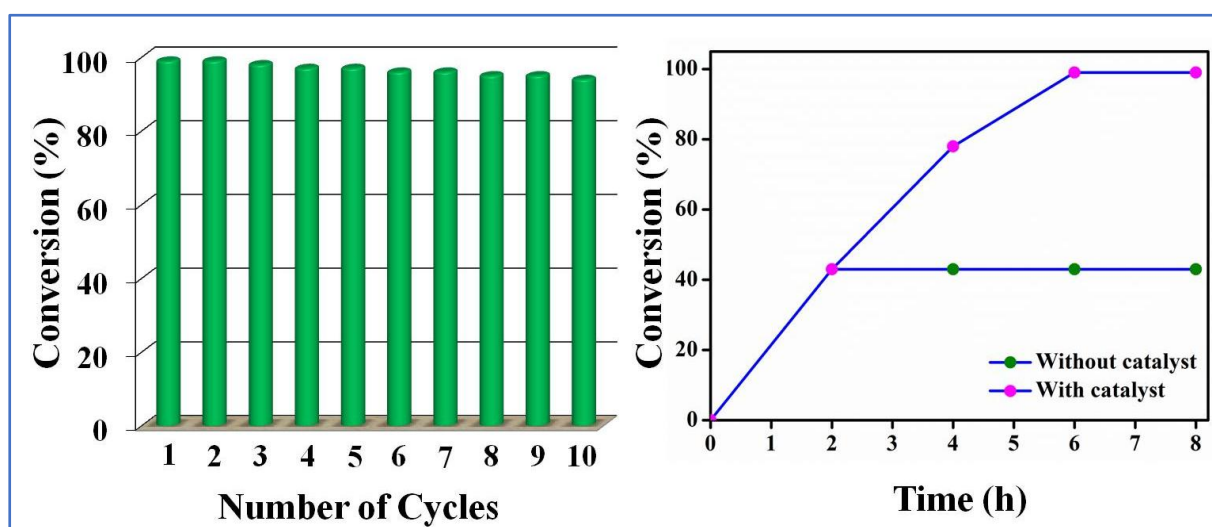


**Figure 9.** Catalyst recyclability (a) and leaching test (b).

#### 4.4. Conclusion

The strategic construction and utilization of Mg(II)-porphyrin MOF having relevance to chlorophyll in green plants is demonstrated for visible light-assisted effective fixation of CO<sub>2</sub> into value-added cyclic carbonates at ambient conditions. Indeed, PCN-224(Mg) showed superior catalytic activity under visible light irradiation over the thermally-driven condition. The excellent light-driven activity has been attributed to facile ligand-to-metal charge transfer

(LMCT) transition from photo-excited Mg-porphyrin unit to Zr<sub>6</sub>-oxo cluster which intern activates CO<sub>2</sub> thereby lowering the activation barrier for cycloaddition reaction. The mechanistic path for the light-driven catalytic fixation of CO<sub>2</sub> was unveiled from the in-depth theoretical studies. Overall, this study represents a rare demonstration of sunlight-promoted fixation of CO<sub>2</sub> from direct air and paves a way for green and sustainable utilization of greenhouse gas for the generation of value-added chemicals.

#### 4.5. References

- (1) Joos, F.; Plattner, G.-K.; Stocker, T. F.; Marchal, O.; Schmittner, A. Global Warming and Marine Carbon Cycle Feedbacks on Future Atmospheric CO<sub>2</sub>. *Science* **1999**, *284*, 464-467.
- (2) Jacobson, M. Z. Review of solutions to global warming, air pollution, and energy security. *Energy Environ. Sci.* **2009**, *2*, 148-173.
- (3) Matthews, H. D.; Graham, T. L.; Keeverian, S.; Lamontagne, C.; Seto, D.; Smith, T. J. National contributions to observed global warming. *Environ. Res. Lett.* **2014**, *9*, 014010.
- (4) Chu, S. Carbon Capture and Sequestration. *Science* **2009**, *325*, 1599.
- (5) Alessandro, D. M. D.; Smit, B.; Long, J. R. Carbon Dioxide Capture: Prospects for New Materials. *Angew. Chem. Int. Ed.* **2010**, *49*, 6058-6082.
- (6) Das, R.; Ezhil, T.; Palakkal, A. S.; Muthukumar, D.; Pillai, R. S.; Nagaraja, C. M. Efficient chemical fixation of CO<sub>2</sub> from direct air under environment-friendly co-catalyst and solvent-free ambient conditions. *J. Mater. Chem. A*, **2021**, *9*, 23127-23139.
- (7) Jones, W. D. Carbon Capture and Conversion. *J. Am. Chem. Soc.* **2020**, *142*, 4955-4957.
- (8) Das, R.; Nagaraja, C. M. Noble metal-free Cu(I)-anchored NHC-based MOF for highly recyclable fixation of CO<sub>2</sub> under RT and atmospheric pressure conditions. *Green Chem.* **2021**, *23*, 5195-5204.
- (9) Katelhon, A.; Meys, R.; Deutz, S.; Suh, S.; Bardow, A. Climate change mitigation potential of carbon capture and utilization in the chemical industry. *Proc. Natl. Acad. Sci. U. S. A.* **2019**, *116*, 11187-11194.
- (10) Sharma, N.; Dhankhar, S. S.; Kumar, S.; Kumar, T. J. D.; Nagaraja, C. M. Rational Design of a 3D Mn<sup>II</sup>-Metal–Organic Framework Based on a Nonmetallated Porphyrin Linker for Selective Capture of CO<sub>2</sub> and One-Pot Synthesis of Styrene Carbonates. *Chem. Eur. J.* **2018**, *24*, 16662-16669.
- (11) Liu, Q.; Wu, L.; Jackstell, R.; Beller, M. Using carbon dioxide as a building block in organic synthesis. *Nat. Commun.* **2015**, *6*, 5933.

- (12) Sakakura, T.; Choi, J. C.; Yasuda, H. Transformation of Carbon Dioxide. *Chem. Rev.* **2007**, *107*, 2365-2387.
- (13) Das, R.; Dhankhar, S. S.; Nagaraja, C. M. Construction of a bifunctional Zn(II)-organic framework containing basic amine functionality for selective capture and room temperature fixation of CO<sub>2</sub>. *Inorg. Chem. Front.* **2020**, *7*, 72-81.
- (14) Peter, S. C. Reduction of CO<sub>2</sub> to Chemicals and Fuels: A Solution to Global Warming and Energy Crisis. *ACS Energy Lett.* **2018**, *3*, 1557-1561.
- (15) Meng, X. L.; Nie, Y.; Sun, J.; Cheng, W. G.; Wang, J. Q.; He, H. Y.; Zhang, S. J. Superbase/cellulose: an environmentally benign catalyst for chemical fixation of carbon dioxide into cyclic carbonates. *Green Chem.* **2014**, *16*, 2771-2778.
- (16) Sharma, N.; Dhankhar, S. S.; Nagaraja, C. M. Environment-friendly, co-catalyst- and solventfree fixation of CO<sub>2</sub> using an ionic zinc(II)-porphyrin complex immobilized in porous metal-organic frameworks. *Sustain. Energy Fuels* **2019**, *3*, 2977-2982.
- (17) Mitsuka, Y.; Ogiwara, N.; Mukoyoshi, M.; Kitagawa, H.; Yamamoto, T.; Toriyama, T.; Matsumura, S.; Haneda, M.; Kawaguchi, S.; Kubota, Y.; Kobayashi, H. Fabrication of Integrated Copper-Based Nanoparticles/Amorphous Metal-Organic Framework by a Facile Spray-Drying Method: Highly Enhanced CO<sub>2</sub> Hydrogenation Activity for Methanol Synthesis. *Angew. Chem. Int. Ed.* **2021**, *60*, 22283-22288.
- (18) SK, M.; Barman, S.; Paul, S.; De, R.; Sreejith, S. S.; Reinsch, H.; Grzywa, M.; Stock, N.; Volkmer, D.; Biswas, S.; Roy, S. An Anthracene-Based Metal-Organic Framework for Selective Photo-Reduction of Carbon Dioxide to Formic Acid Coupled with Water Oxidation. *Chem. Eur. J.* **2021**, *27*, 4098-4107.
- (19) Gu, Y.; Tamura, M.; Nakagawa, Y.; Nakao, K.; Suzukic, K.; Tomishige, K. Direct synthesis of polycarbonate diols from atmospheric flow CO<sub>2</sub> and diols without using dehydrating agents. *Green Chem.* **2021**, *23*, 5786-5796.
- (20) Sanz-Perez, E. S.; Murdock, C. R.; Didas, S. A.; Jones, C. W. Direct Capture of CO<sub>2</sub> from Ambient Air. *Chem. Rev.* **2016**, *116*, 11840-11876.
- (21) Bhatt, P. M.; Belmabkhout, Y.; Cadiau, A.; Adil, K.; Shekhah, O.; Shkurenko, A.; Barbour, L. J.; Eddaoudi, M. A Fine-Tuned Fluorinated MOF Addresses the Needs for Trace CO<sub>2</sub> Removal and Air Capture Using Physisorption. *J. Am. Chem. Soc.* **2016**, *138*, 9301-9307.
- (22) Rawool, S. A.; Belgamwar, R.; Jana, R.; Maity, A.; Bhumla, A.; Yigit, N.; Datta, A.; Rupprechter, G.; Polshettiwar, V. Direct CO<sub>2</sub> capture and conversion to fuels on magnesium nanoparticles under ambient conditions simply using water. *Chem. Sci.* **2021**, *12*, 5774-5786.

- (23) Liang, J.; Huang, Y.-B.; Cao, R. Metal–organic frameworks and porous organic polymers for sustainable fixation of carbon dioxide into cyclic carbonates. *Coord. Chem. Rev.* **2019**, *378*, 32-65.
- (24) Ding, M.; Flaig, R. W.; Jiang, H.-L.; Yaghi, O. M. Carbon capture and conversion using metal–organic frameworks and MOF-based materials. *Chem. Soc. Rev.* **2019**, *48*, 2783-2828.
- (25) Dhankhar, S. S.; Ugale, B.; Nagaraja, C. M. Co-Catalyst-Free Chemical Fixation of CO<sub>2</sub> into Cyclic Carbonates by using Metal-Organic Frameworks as Efficient Heterogeneous Catalysts. *Chem Asian J.* **2020**, *15*, 2403-2427.
- (26) Pal, T. K.; De, D.; Bhardwaj, P. K. Metal–organic frameworks for the chemical fixation of CO<sub>2</sub> into cyclic carbonates. *Coord. Chem. Rev.* **2020**, *408*, 213173.
- (27) Scrosati, B.; Hassounab, J.; Sun, Y.-K. Lithium-ion batteries. A look into the future. *Energy Environ. Sci.* **2011**, *4*, 3287-3295.
- (28) Grignard, B.; Gennen, S.; Jérôme, C.; Kleij, A. W.; Detrembleur, C. Advances in the use of CO<sub>2</sub> as a renewable feedstock for the synthesis of polymers. *Chem. Soc. Rev.* **2019**, *48*, 4466-4514.
- (29) Liu, H.; Lin, S.; Feng, Y.; Theato, P. CO<sub>2</sub>-Responsive polymer materials. *Polym. Chem.* **2017**, *8*, 12-23.
- (30) Fukuoka, S.; Kawamura, M.; Komiya, K.; Tojo, M.; Hachiya, H.; Hasegawa, K.; Aminaka, M.; Okamoto, H.; Fukawad, I.; Konno, S. A novel non-phosgene polycarbonate production process using by-product CO<sub>2</sub> as starting material. *Green Chem.* **2003**, *5*, 497-507.
- (31) Yuan, Y.; Li, J.; Sun, X.; Li, G.; Liu, Y.; Verma, G.; Ma, S. Indium-Organic Frameworks Based on Dual Secondary Building Units Featuring Halogen-Decorated Channels for Highly Effective CO<sub>2</sub> Fixation. *Chem. Mater.* **2019**, *31*, 1084-1091.
- (32) Ugale, B.; Dhankhar, S. S.; Nagaraja, C. M. Construction of 3-Fold-Interpenetrated Three-Dimensional Metal-Organic Frameworks of Nickel(II) for Highly Efficient Capture and Conversion of Carbon Dioxide. *Inorg. Chem.* **2016**, *55*, 9757–9766.
- (33) Wu, P.; Li, Y.; Zheng, J.-J.; Hosono, N.; Otake, K.; Wang, J.; Liu, Y.; Xia, L.; Jiang, M.; Sakaki, S.; Kitagawa, S. Carbon dioxide capture and efficient fixation in a dynamic porous coordination polymer. *Nat. Commun.* **2019**, *10*, 4362.
- (34) Das, R.; Muthukumar, D.; Pillai, R. S.; Nagaraja, C. M. Rational design of a Zn(II)-MOF with multiple functional sites for highly efficient fixation of CO<sub>2</sub> at mild conditions: combined experimental and theoretical investigation. *Chem. Eur. J.* **2020**, *26*, 17445-17454.

- (35) Baalbaki, H. A.; Roshandel, H.; Hein, J. E.; Mehrkhodavandi, P. Conversion of dilute CO<sub>2</sub> to cyclic carbonates at sub-atmospheric pressures by a simple indium catalyst. *Catal. Sci. Technol.* **2021**, *11*, 2119-2129.
- (36) Das, R.; Nagaraja, C. M. Highly Efficient Fixation of Carbon Dioxide at RT and Atmospheric Pressure Conditions: Influence of Polar Functionality on Selective Capture and Conversion of CO<sub>2</sub>. *Inorg. Chem.* **2020**, *59*, 9765-9773.
- (37) Das, R.; Ezhil, T.; Nagaraja, C. M. Design of Bifunctional Zinc(II)-Organic Framework for Efficient Coupling of CO<sub>2</sub> with Terminal/Internal Epoxides under Mild Conditions. *Cryst. Growth Des.* **2022**, *22*, 598-607.
- (38) Das, R.; Parihar, V.; Nagaraja, C. M. Strategic design of a bifunctional Ag(I)-grafted NHC-MOF for efficient chemical fixation of CO<sub>2</sub> from a dilute gas under ambient conditions. *Inorg. Chem. Front.* **2022**, *9*, 2583-2593.
- (39) Yang, Q.; Peng, H.; Zhang, Q.; Qian, X.; Chen, X.; Tang, X.; Dai, S.; Zhao, J.; Jiang, K.; Yang, Q.; Sun, J.; Zhang, L.; Zhang, N.; Gao, H.; Lu, Z.; Chen, L. Atomically Dispersed High-Density Al-N<sub>4</sub> Sites in Porous Carbon for Efficient Photodriven CO<sub>2</sub> Cycloaddition. *Adv. Mater.* **2021**, *33*, 2103186.
- (40) Zhai, G.; Liu, Y.; Mao, Y.; Zhang, H.; Lin, L.; Li, Y.; Wang, Z.; Cheng, H.; Wang, P.; Zheng, Z.; Dai, Y.; Huang, B. Improved photocatalytic CO<sub>2</sub> and epoxides cycloaddition via the synergistic effect of Lewis acidity and charge separation over Zn modified UiO-bpydc. *Appl. Catal. B: Environ.* **2022**, *301*, 120793.
- (41) Gong, L.; Sun, J.; Liu, Y.; Yang, G. Photoinduced synergistic catalysis on Zn single-atom-loaded hierarchical porous carbon for highly efficient CO<sub>2</sub> cycloaddition conversion. *J. Mater. Chem. A* **2021**, *9*, 21689-21694.
- (42) Wang, S.; Han, X.; Zhang, Y.; Tian, N.; Ma, T.; Huang, H. Inside-and-Out Semiconductor Engineering for CO<sub>2</sub> Photoreduction: From Recent Advances to New Trends. *Small Struct.* **2021**, *2*, 2000061.
- (43) Zhai, G.; Liu, Y.; Lei, L.; Wang, J.; Wang, Z.; Zheng, Z.; Wang, P.; Cheng, H.; Dai, Y.; Huang, B. Light-Promoted CO<sub>2</sub> Conversion from Epoxides to Cyclic Carbonates at Ambient Conditions over a Bi-Based Metal Organic Framework. *ACS Catal.* **2021**, *11*, 1988-1994.
- (44) Karmakar, S.; Barman, S.; Rahimi, F. A.; Maji, T. K. Covalent grafting of molecular photosensitizer and catalyst on MOF-808: effect of pore confinement toward visible light-driven CO<sub>2</sub> reduction in water. *Energy Environ. Sci.* **2021**, *14*, 2429-2440.
- (45) Li, L.; Wang, X.; Liu, T.; Ye, J. Titanium-Based MOF Materials: From Crystal Engineering to Photocatalysis. *Small Methods* 10.1002/smt.202000486.

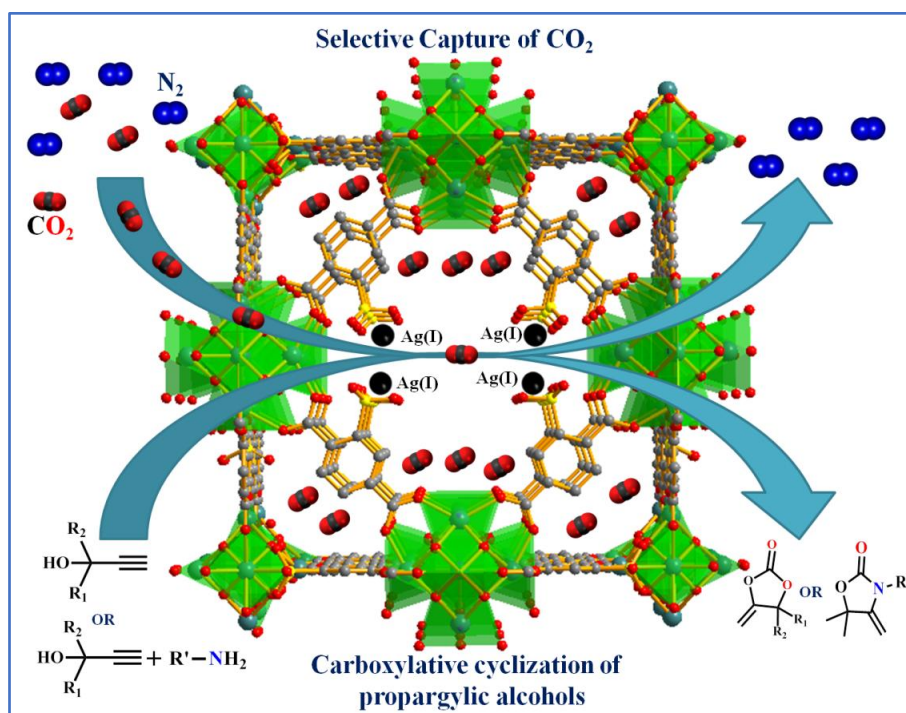
- (46) Xiong, X.; Zhao, Y.; Shi, R.; Yin, W.; Zhao, Y.; Waterhouse, G. I. N.; Zhang, T. Selective photocatalytic CO<sub>2</sub> reduction over Zn-based layered double hydroxides containing tri or tetravalent metals. *Sci. Bull.* **2020**, *65*, 987-994
- (47) Sheng, J.; He, Y.; Huang, M.; Yuan, C.; Wang, S.; Dong, F. Frustrated Lewis Pair Sites Boosting CO<sub>2</sub> Photoreduction on Cs<sub>2</sub>CuBr<sub>4</sub> Perovskite Quantum Dots. *ACS Catal.* **2022**, *12*, 2915-2926.
- (48) Shi, X.; Dong, X.; He, Y.; Yan, P.; Zhang, S.; Dong, F. Photoswitchable Chlorine Vacancies in Ultrathin Bi<sub>4</sub>O<sub>5</sub>Cl<sub>2</sub> for Selective CO<sub>2</sub> Photoreduction. *ACS Catal.* **2022**, *12*, 3965-3973.
- (49) Yu, Y.; Dong, X.; Chen, P.; Geng, Q.; Wang, H.; Li, Ji.; Zhou, Y.; Dong, F. Synergistic Effect of Cu Single Atoms and Au-Cu Alloy Nanoparticles on TiO<sub>2</sub> for Efficient CO<sub>2</sub> Photoreduction. *ACS Nano* **2021**, *15*, 14453-14464.
- (50) Zhang, S.; Heyes, D. J.; Feng, L.; Sun, W.; Johannissen, L. O.; Liu, H.; Levy, C. W.; Li, X.; Yang, J.; Yu, X.; Lin, M.; Hardman, S. J. O.; Hoeven, R.; Sakuma, M.; Hay, S.; Leys, D.; Rao, Z.; Zhou, A.; Cheng, Q.; Scrutton, N. S. Structural basis for enzymatic photocatalysis in chlorophyll biosynthesis. *Nature* **2019**, *574*, 722-725.
- (51) Borah, K. D.; Bhuyan, J. Magnesium porphyrins with relevance to chlorophylls. *Dalton Trans.* 2017, *46*, 6497-6509.
- (52) Bhuyan, J.; Sarkar, R.; Sarkar, S. A Magnesium Porphyrin Bicarbonate Complex with CO<sub>2</sub>-Modulated Photosystem I Action. *Angew. Chem.* **2011**, *123*, 10791-10795.
- (53) Remy, T.; Peter, S. A.; Perre, S. V.; Valvekens, P.; Vos, D. E. D.; Baron, G. V.; Denayer, J. F. M. Selective Dynamic CO<sub>2</sub> Separations on Mg-MOF-74 at Low Pressures: A Detailed Comparison with 13X. *J. Phys. Chem. C* **2013**, *117*, 9301-9310.
- (54) Kong, X.; Scott, E.; Ding, W.; Mason, J. A.; Long, J. R.; Reimer, J. A. CO<sub>2</sub> Dynamics in a Metal-Organic Framework with Open Metal Sites. *J. Am. Chem. Soc.* **2012**, *134*, 14341-14344.
- (55) Yang, D.-A.; Cho, H.-Y.; Kim, J.; Yang, S.-T.; Ahn, W.-S. CO<sub>2</sub> capture and conversion using Mg-MOF-74 prepared by a sonochemical method. *Energy Environ. Sci.* **2012**, *5*, 6465-6473.
- (56) Frisch, M. J.; Pople, J. A.; Binkley, J. S. Self-consistent molecular orbital methods 25. Supplementary functions for Gaussian basis sets. *J. Chem. Phys.* **1984**, *80*, 3265-3269.
- (57) Reed, A. E.; Curtiss, L. A.; Weinhold, F. Intermolecular Interactions from a Natural Bond Orbital, Donor-Acceptor Viewpoint. *Chem. Rev.* **1988**, *88*, 899.

- (58) Grimme, S.; Antony, J.; Ehrlich, S.; Krieg, H. A Consistent and Accurate ab initio Parametrization of Density Functional Dispersion Correction (DFT-D) for the 94 Elements H-Pu. *J. Chem. Phys.* **2010**, *132*, 154104-154119.
- (59) Feng, D.; Chung, W.-C.; Wei, Z.; Gu, Z.-Y.; Jiang, H.-L.; Chen, Y.-P.; Darensbourg, D. J.; Zhou, H.-C. Construction of Ultrastable Porphyrin Zr Metal-Organic Frameworks through Linker Elimination. *J. Am. Chem. Soc.* **2013**, *135*, 17105-17110.
- (60) Qi, S.; Yang, Z.; Zhu, R.; Lu, X.; Xue, D.; Liu, X.; Sun, L. The cascade catalysis of the porphyrinic zirconium metal-organic framework PCN-224-Cu for CO<sub>2</sub> conversion to alcohols. *J. Mater. Chem. A*, **2021**, *9*, 24510–24516.
- (61) Zhang, H.; Wei, J.; Dong, J.; Liu, G.; Shi, L.; An, P.; Zhao, G.; Kong, J.; Wang, X.; Meng, X.; Zhang, J.; Ye, J. Efficient Visible Light-Driven Carbon Dioxide Reduction by a Single-Atom Implanted Metal-Organic Framework. *Angew. Chem. Int. Ed.* **2016**, *55*, 14310 - 14314.
- (62) Zhu, B.; Liu, B.; Qu, C.; Zhang, H.; Guo, W.; Liang, Z.; Chen, F.; Zou, R. Tailoring biomass-derived carbon for high performance super capacitors from controllably cultivated algae microspheres. *J. Mater. Chem. A* **2018**, *6*, 1523-1530.
- (63) He, J.; Zhang, Y.; He, J.; Zeng, X.; Hou, X.; Long, Z. Enhancement of photoredox catalytic properties of porphyrinic metal-organic frameworks based on titanium incorporation via post-synthetic modification. *Chem. Commun.* **2018**, *54*, 8610-8613.
- (64) Yang, R. T. Gas Separation by Adsorption Processes, Butterworth, Boston, **1997**.
- (65) Pan, H.; Ritter, J. A.; Balbuena, P. B. Examination of the Approximations Used in Determining the Isothermic Heat of Adsorption from the Clausius-Clapeyron Equation. *Langmuir* **1998**, *14*, 6323-6327.
- (66) Ugale, B.; Kumar, S.; Kumar, T. J. D.; Nagaraja, C. M. Environmentally Friendly, Co-catalyst-Free Chemical Fixation of CO<sub>2</sub> at Mild Conditions Using Dual-Walled Nitrogen-Rich Three-Dimensional Porous Metal-Organic Frameworks. *Inorg. Chem.* **2019**, *58*, 3925-3936.
- (67) Gligoric, N.; Krco, S.; Hakola, L.; Vehmas, K.; De, S.; Moessner, K.; Jansson, K.; Polenz, I.; Kranenburg, R. SmartTags: IoT Product Passport for Circular Economy Based on Printed Sensors and Unique Item-Level Identifiers. *Sensors* **2019**, *19*, 586.
- (68) Hajimohammadi, M.; Safari, N.; Mofakham, H.; Deyhimi, F. Highly selective, economical and efficient oxidation of alcohols to aldehydes and ketones by air and sunlight or visible light in the presence of porphyrins sensitizers. *Green Chem.* **2011**, *13*, 991-997.

- (69) Ghaleno, M. R.; Ghaffari-Moghaddam, M.; Khajeh, M.; Oveisi, A. R.; Bohlooli, M. Iron species supported on a mesoporous zirconium metal-organic framework for visible light driven synthesis of quinazolin-4(3*H*)-ones through one-pot three-step tandem reaction. *J. Colloid Interface Sci.* **2019**, *535*, 214-226.
- (70) Sanz-Perez, E. S.; Murdock, C. R.; Didas, S. A.; Jones, C. W. Direct Capture of CO<sub>2</sub> from Ambient Air. *Chem. Rev.* **2016**, *116*, 11840-11876.
- (71) Bhatt, P. M.; Belmabkhout, Y.; Cadiau, A.; Adil, K.; Shekhah, O.; Shkurenko, A.; Barbour, L. J.; Eddaoudi, M. A Fine-Tuned Fluorinated MOF Addresses the Needs for Trace CO<sub>2</sub> Removal and Air Capture Using Physisorption. *J. Am. Chem. Soc.* **2016**, *138*, 9301-9307.
- (72) McDonald, T. M.; Lee, W. R.; Mason, J. A.; Wiers, B. M.; Hong, C. S.; Long, J. R. Capture of Carbon Dioxide from Air and Flue Gas in the Alkylamine Appended Metal–Organic Framework mmen-Mg<sub>2</sub>(dobpdc). *J. Am. Chem. Soc.* **2012**, *134*, 7056-7065.
- (73) Sharma, N.; Dey, A. K.; Sathe, R. Y.; Kumar, A.; Krishnan, V.; Kumar, T. J. D.; Nagaraja, C. M. Highly efficient visible-light-driven reduction of Cr(VI) from water by porphyrin-based metal–organic frameworks: effect of band gap engineering on the photocatalytic activity. *Catal. Sci. Technol.* **2020**, *10*, 7724-7733.
- (74) Frisch, M. J.; Trucks, G. W.; Schlegel, H. B.; Scuseria, G. E.; Robb, M. A.; Cheeseman, J. R.; Scalmani, G.; Barone, V.; Mennucci, B.; Petersson, G. A.; Nakatsuji, H.; Caricato, M.; Li, X.; Hratchian, H. P.; Izmaylov, A. F.; Bloino, J.; Zheng, G.; Sonnenberg, J. L.; Hada, M.; Ehara, M.; Toyota, K.; Fukuda, R.; Hasegawa, J.; Ishida, M.; Nakajima, T.; Honda, Y.; Kitao, O.; Nakai, H.; Vreven, T.; Montgomery, J. A.; Peralta, J. E.; Ogliaro, F.; Bearpark, M.; Heyd, J. J.; Brothers, E.; Kudin, K. N.; Staroverov, V. N.; Keith, T.; Kobayashi, R.; Normand, J.; Raghavachari, K.; Rendell, A.; Burant, J. C.; Iyengar, S. S.; Tomasi, J.; Cossi, M.; Rega, N.; Millam, J. M.; Klene, M.; Knox, J. E.; Cross, J. B.; Bakken, V.; Adamo, C.; Jaramillo, J.; Gomperts, R.; Stratmann, R. E.; Yazyev, O.; Austin, A. J.; Cammi, R.; Pomelli, C.; Ochterski, J. W.; Martin, R. L.; Morokuma, K.; Zakrzewski, V. G.; Voth, G. A.; Salvador, P.; Dannenberg, J. J.; Dapprich, S.; Daniels, A. D.; Farkas, O.; Foresman, J. B.; Ortiz, J. V.; Cioslowski, J.; Fox, D. J. Gaussian 09; Gaussian, Inc.: Wallingford, CT, **2013**.
- (75) Becke, A. D. Density-functional Thermochemistry. III. The Role of Exact Exchange, *J. Chem. Phys.* **1993**, *98*, 5648-5652.

# Chapter 5a

**Highly efficient fixation of carbon dioxide  
at RT and atmospheric pressure conditions:  
Influence of polar functionality on selective  
capture and conversion of CO<sub>2</sub>**





### 5a.1. Introduction

The immense amount of carbon dioxide (CO<sub>2</sub>) emissions has resulted in the most serious environmental issues like global warming, ocean acidification, extreme weather, and so on.<sup>1</sup> Hence, extensive research efforts are being made worldwide to mitigate the increasing concentration of CO<sub>2</sub> through selective capture and subsequent conversion to value-added chemicals or fuels.<sup>2-4</sup> However, the carbon dioxide being thermodynamically stable (bond enthalpy of +805 kJ/mol) and kinetically inert, requires high temperature and pressure conditions for its activation.<sup>5-7</sup> In this regard, it is highly desirable to develop efficient catalysts that can selectively capture and convert CO<sub>2</sub> into value-added chemicals under mild conditions. Towards this direction, several strategies have been developed for the conversion of CO<sub>2</sub> into various high-value chemicals.<sup>8-11</sup> Among them, the cyclic carboxylation of propargylic alcohols with CO<sub>2</sub> to generate  $\alpha$ -alkylidene cyclic carbonates has attracted significant interest owing to their possible applications in the synthesis of plastics,<sup>12</sup> natural products, and polymers,<sup>13</sup> beta-keto carboxylic acids,<sup>14</sup> polycarbonates and polyurethanes,<sup>15</sup> cyclopentenones<sup>16</sup> and so on. Further, the synthesis of oxazolidinones, an important building block of antibiotics by a tandem reaction between propargylic alcohols, CO<sub>2</sub>, and primary amines has attracted considerable interest of green chemistry researchers.<sup>17</sup> Moreover, the literature survey revealed that most of the catalysts known for carboxylative cyclization of propargylic alcohols with CO<sub>2</sub> require high temperature and pressure conditions.<sup>18,19</sup> Therefore, it is highly desirable to develop efficient catalysts for the fixation of CO<sub>2</sub> into  $\alpha$ -alkylidene cyclic carbonates and oxazolidinones at mild conditions. In this context, metal-organic frameworks (MOFs) have gained special attention due to their unique features like high surface area, tuneable pore size, and functionality.<sup>20-24</sup> MOFs have shown promising applications in the field of gas storage/separation,<sup>25-27</sup> especially for selective CO<sub>2</sub> capture/conversion.<sup>28-34</sup> Significant research efforts have been reported in utilizing MOFs for the conversion of CO<sub>2</sub> to cyclic carbonates.<sup>35-44</sup> On the other hand, the application of MOFs as heterogeneous catalysts for efficient coupling of CO<sub>2</sub> with propargylic alcohols and amines to generate  $\alpha$ -alkylidene cyclic carbonates<sup>45</sup> and oxazolidinones<sup>46</sup> at mild conditions is relatively less explored. Furthermore, literature reports have shown that Ag(I) ions are effective in activating the C $\equiv$ C bonds of alkynes via  $\pi$ -activation.<sup>47,48</sup> Hence the examples of Ag(I) based homogeneous catalysts for efficient carboxylation of propargylic alcohols with CO<sub>2</sub> are reported in the literature.<sup>49-52</sup> However, these reactions possess limitations of catalyst recycling and product separation and hence heterogeneous catalysts are highly desirable. In this regard, we sought to incorporate catalytically active Ag(I) ions in porous CO<sub>2</sub>-philic

MOF to generate bifunctional material suitable for chemical fixation of CO<sub>2</sub> with alkyne molecules (propargylic alcohols) and primary amines to obtain  $\alpha$ -alkylidene cyclic carbonates and oxazolidinones. To achieve this, we selected sulfonate functionalized porous Zr-MOF (UiO-66) and named as MOF-SO<sub>3</sub>H, and was treated with an aqueous solution of AgNO<sub>3</sub> at RT to obtain Ag(I)-embedded MOF, (MOF-SO<sub>3</sub>Ag). Further, the catalytic investigation of MOF-SO<sub>3</sub>Ag for the cyclic carboxylation of alkynes with CO<sub>2</sub> to produce  $\alpha$ -alkylidene cyclic carbonates and oxazolidinones at mild conditions of RT and 1 bar CO<sub>2</sub> was carried out. Further, one-pot synthesis of oxazolidinones by tandem aminolysis of  $\alpha$ -alkylidene cyclic carbonate with primary amines at mild conditions has also been achieved. The high CO<sub>2</sub> affinity and exceptional catalytic activity of MOF-SO<sub>3</sub>Ag can be attributed to the synergetic effect of CO<sub>2</sub>-philic sulfonate functionality and catalytically active Ag(I) sites facilitating efficient capture and conversion of carbon dioxide. This was further confirmed by utilizing analogs MOF, UiO-66 lacking sulfonate group. Indeed, the Ag(I)@UiO-66 showed a lower value of Q<sub>st</sub> (30 kJ/mol) which is found to be about 8 kJ/mol lower than that of MOF-SO<sub>3</sub>Ag and also lower catalytic activity highlighting the role of the sulfonate group in enhancing the chemical fixation of CO<sub>2</sub>. This chapter demonstrates the rational application of a rare example of Ag(I)-embedded sulfonate-based porous Zr-MOF for efficient conversion of CO<sub>2</sub> into high-value chemicals like  $\alpha$ -alkylidene cyclic carbonates and oxazolidinones at environment-friendly mild conditions of RT and 1 bar CO<sub>2</sub>.

## 5a.2. Experimental section

### 5a.2.1. Materials

All the reagents used in this work were commercially available and used as received without any further purification. Ag(NO<sub>3</sub>)<sub>3</sub>, Zirconyl chloride octahydrate, Monosodium 2-sulfoterephthalic acid, and 1, 4-benzenedicarboxylic acid (H<sub>2</sub>BDC) were purchased from Sigma Aldrich Chemical Co. N, N'-dimethylformamide (DMF), N, N'-dimethylacetamide (DMA) and methanol (MeOH) were obtained from S. D. Fine Chem. Limited. All the propargylic alcohols, primary amines, and the internal standard used for catalytic reactions were purchased from TCI chemicals and used without further purification.

### 5a.2.2. Physicochemical characterization

The phase purity of the as-synthesized samples was confirmed by powder XRD analysis using Rigaku Miniflex 600 with Cu K $\alpha$  radiation ( $\lambda = 0.154$  nm). SEM images and

EDAX patterns were recorded on the FEI Nova SEM-450 instrument. UV-Vis (Diffuse Reflectance) spectra were recorded on the Shimadzu spectrophotometer using BaSO<sub>4</sub> as a reference. The metal contents of Zr and Ag in the frameworks were determined by Agilent's microwave-plasma atomic emission spectrometer (MP-AES). The X-ray photoelectron spectroscopy (XPS) analyses were performed on a Thermo Fisher Scientific NEXSA photoemission spectrometer using Al-K<sub>α</sub> (1486.6 eV) X-ray radiation and analysis of the obtained data was performed using Avantage software. <sup>1</sup>H and <sup>13</sup>C NMR spectra were recorded in CDCl<sub>3</sub> on a JEOL JNM-ECS-400 spectrometer operating at a frequency of 400 MHz. Fourier transform infrared (FT-IR) spectra of the samples were recorded on a Perkin Elmer FTIR spectrometer.

### 5a.2.3. Synthesis

#### 5a.2.3.1. Synthesis of MOF-SO<sub>3</sub>H

The MOF-SO<sub>3</sub>H was synthesized by following the previously reported procedure with further modification.<sup>53</sup> Monosodium 2-sulfoterephthalic acid (0.5 mmol) was dissolved in 6 mL of water to which 0.5 mmol of Zirconyl chloride octahydrate and 4 mL of acetic acid were added. The resulting mixture was stirred at room temperature for 15 minutes and then refluxed for 24h. After this time the reaction mixture was centrifuged, washed with water thoroughly, and dried under vacuum. The phase purity of the as-synthesized sample was confirmed by powder XRD analysis. FT-IR (KBr, cm<sup>-1</sup>): 1586 (m), 1488 (w), 3211 (w), 1409 (s), 1277 (m), 1165 (s), 1074 (s), 1018 (m), 767 (w) and 650 (s).

#### 5a.2.3.2. Synthesis of MOF-SO<sub>3</sub>Ag

The activated sample of MOF-SO<sub>3</sub>H (0.02 mmol) was soaked in 10 mL aqueous solution of AgNO<sub>3</sub> (0.3 mmol) and taken in a 30 mL culture tube placed in an ice bath. The tube was placed on a shaker with a shaking rate of 100 rpm for 3h. The solid was filtered out and washed with water thoroughly and dried under vacuum. The activated sample of MOF-SO<sub>3</sub>Ag exhibits a mass growth of 4 % compared with the parent sample MOF-SO<sub>3</sub>H, which was also confirmed by microwave-plasma atomic emission spectroscopy (MP-AES) analysis. FT-IR (KBr, cm<sup>-1</sup>): 1586 (m), 1488 (w), 3211 (w), 1409 (s), 1277 (m), 1180 (s), 1074 (s), 1018 (m), 767 (w) and 650 (s).

### 5a.2.3.3. Synthesis of Ag(I)@UiO-66

The UiO-66 was synthesized by following the previously reported procedure with further modification.<sup>54</sup> In a typical synthesis, a mixture of  $\text{ZrOCl}_2 \cdot 8\text{H}_2\text{O}$  (3.22 g, 10 mmol), 1,4-benzenedicarboxylic acid ( $\text{H}_2\text{BDC}$ ) (1.6 g, 10 mmol), and 50 mL of DMF was taken in a round bottom flask, which was fitted with a reflux condenser. The reaction mixture was stirred for 15 min at ambient conditions and 1.6 mL of concentrated HCl (19.2 mmol) was added to the reaction mixture at ambient conditions. The temperature of the reaction mixture was elevated to 150 °C using an oil bath and the reaction was continued for 24 h under an open-air atmosphere. The resultant white solid was filtered and washed with DMF and dried. The dried product was again taken in 50 mL of DMF and stirred overnight at the ambient condition to remove unreacted  $\text{H}_2\text{BDC}$ . The product was filtered and dried at 100 °C for 2 h. Finally, the obtained product was taken in 25 mL of methanol and stirred overnight at ambient conditions. The product was filtered and again taken in fresh methanol. This methanol treatment process was performed thrice to remove most of the DMF from the product. Finally, the product was dried in an oven at 100 °C for 12 h. The activated sample of UiO-66 (0.02 mmol) was soaked in 10 mL aqueous solution of  $\text{AgNO}_3$  (0.3 mmol) and taken in a 30 mL culture tube placed in an ice bath. The tube was placed on a shaker with a shaking rate of 100 rpm for 3h. The solid was filtered out and washed with water thoroughly and dried under vacuum. The phase purity of the as-synthesized sample was confirmed by powder XRD analysis.

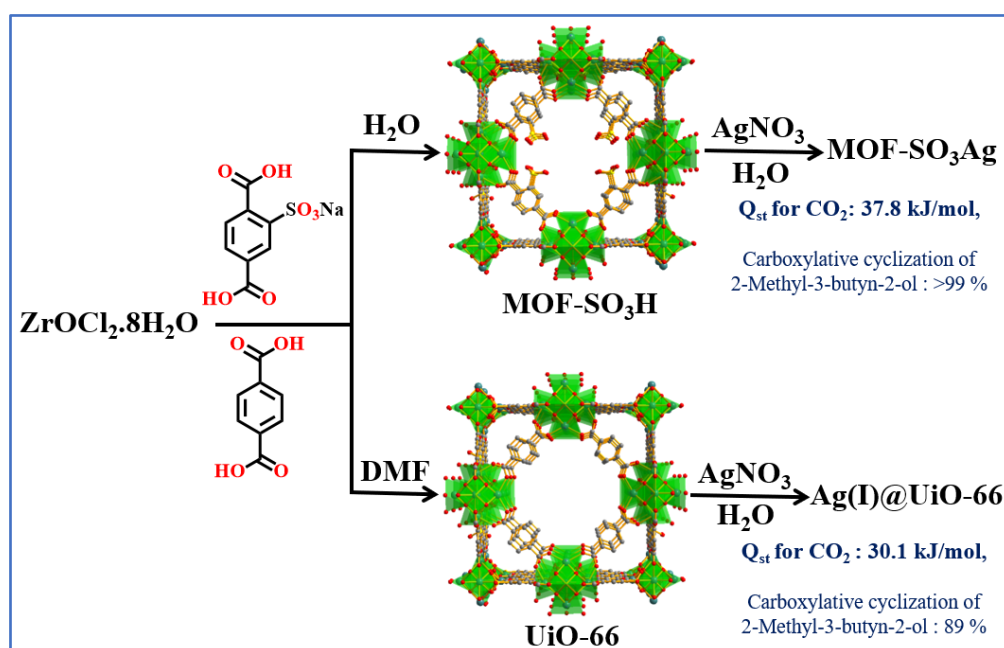
### 5a.2.4. Catalytic cycloaddition reactions of $\text{CO}_2$ with propargylic alcohols

Catalytic cyclic carboxylation reactions of alkyne molecules (propargylic alcohols) with  $\text{CO}_2$  were carried out in a glass reactor (50 mL) under RT and 1 bar  $\text{CO}_2$ . Before catalytic reactions, the catalyst was activated at 323 K for 15 h under vacuum to remove guest solvent molecules. The substrates were taken in the reactor at RT and the reactor was flushed with  $\text{CO}_2$  thrice then 1 bar  $\text{CO}_2$  pressure was maintained and the contents were stirred at RT. After 24 h, the MOF- $\text{SO}_3\text{Ag}$  catalyst was separated from the reaction mixture by filtration and the catalytic conversions were determined by  $^1\text{H}$  NMR spectra of the filtrate using  $\text{CDCl}_3$  solvent. The recovered catalyst was washed with methanol three times and activated at 323 K under vacuum for 15 h and reused for the subsequent catalytic cycles.

### 5a.3. Results and discussion

#### 5a.3.1. Synthesis and characterization

The Ag(I) embedded Zr-sulfonate MOF named as MOF-SO<sub>3</sub>Ag was obtained by treating sulfonate functionalized-UiO-66 MOF with an aqueous solution of AgNO<sub>3</sub> at RT. PXRD pattern (Figure A74) of the MOF-SO<sub>3</sub>Ag sample matches well with the pristine UiO-66-SO<sub>3</sub>H<sup>55</sup> indicating retention of the original crystal structure even after the incorporation of Ag(I) ions in the 1D pore channels of the MOF (Scheme 1).



**Scheme 1.** Synthesis scheme for MOF-SO<sub>3</sub>Ag and Ag(I)@UiO-66.

Further, as shown in Figure A75, FTIR spectra of MOF-SO<sub>3</sub>Ag show the characteristic stretching frequency for the S=O bond at 1165 cm<sup>-1</sup> which is slightly shifted in comparison to that of parent MOF (1180 cm<sup>-1</sup>) indicating anchoring of Ag(I) ions with the sulfonate groups exposed in the 1D channels. Furthermore, the UV-Vis spectrum of MOF-SO<sub>3</sub>Ag matches well with that of parent MOF with absorption bands at 210 and 250 nm which are assigned to ligand-based  $\Pi \rightarrow \Pi^*$  transitions, and no other absorption peaks were observed eliminating the formation of Ag(0) nanoparticles (Figure A76). The atomic percentage of Ag(I), was determined using the microwave-plasma atomic emission spectroscopy (MP-AES) technique which revealed the incorporation of about 4.2% of Ag(I) with Zr:Ag(I) atomic ratio of 5.1:1. To get further support on the state of Ag species embedded in the MOF, X-ray photoelectron spectroscopy (XPS) analysis of MOF-SO<sub>3</sub>Ag was carried out. As shown in Figure 1a, the XPS spectrum shows the presence of characteristic binding energies for Ag(I) at 367.3 and

373.7 eV which is comparable with the spectrum of  $\text{CH}_3\text{SO}_3\text{Ag}$  (368.3 and 374.3 eV), and the peaks are slightly shifted in comparison to the spectrum of  $\text{AgNO}_3$  salt (characteristic peaks at 368.9 and 374.9 eV) indicating the absence free metal salt ( $\text{AgNO}_3$ ).<sup>51</sup> Further, FESEM analysis of the samples revealed the cubic morphology of MOF- $\text{SO}_3\text{H}$ , and the morphology is retained even after the incorporation of Ag(I) ions (Figure 1c and d). Moreover, energy dispersive spectroscopy (EDS) analysis further confirmed the incorporation of Ag(I) in MOF- $\text{SO}_3\text{Ag}$  (Figure A77). In addition, for the sake of comparison, the analog MOF, which lacks the sulfonate group, UiO-66 was utilized to dope Ag(I) (Scheme 1). PXRD pattern (Figure A78) of Ag(I)@UiO-66 matches well with that of the parent UiO-66 MOF indicating the retaining of the original crystal structure even after the incorporation of Ag(I) ions. The atomic percentage of Ag(I) estimated from MP-AES analysis was 3.6% which is slightly lower than that of MOF- $\text{SO}_3\text{Ag}$  (4.2%). Further XPS analysis unveiled the presence of characteristic binding energies for Ag(I) at 367 and 374 eV supporting the presence of Ag(I) and not Ag(0) (Figure 1b). Based on the previous literature reports<sup>56</sup> we speculate that the possible anchoring sites for Ag(I) in UiO-66 MOF are the hydroxide groups of Zr-cluster (Figure A79).

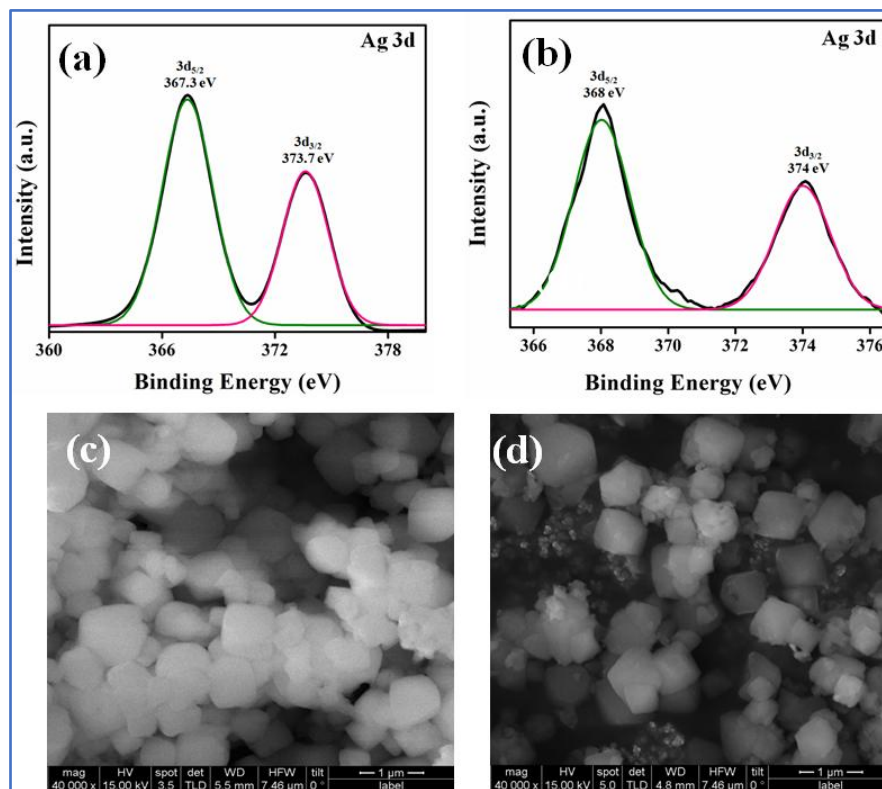


**Figure 1.** XPS spectra of (a) MOF- $\text{SO}_3\text{Ag}$ , (b) Ag(I)@UiO-66 showing the characteristic peaks of Ag(I) and FESEM images for (c) MOF- $\text{SO}_3\text{H}$  and (d) MOF- $\text{SO}_3\text{Ag}$ .

### 5a.3.2. Gas adsorption studies

To determine the permanent porosity of MOF-SO<sub>3</sub>H after incorporation of Ag(I), N<sub>2</sub> adsorption measurements of MOF-SO<sub>3</sub>Ag were carried out at 77K. Before the measurements, the sample was subjected to solvent exchange with acetone for three days and then activated at RT under high vacuum for 20 h to obtain the activated MOF. As shown in Figure 2a, the N<sub>2</sub> adsorption-desorption isotherms follow a typical type-I behaviour, and the estimated value of BET (Brunauer-Emmett-Teller) surface area for MOF-SO<sub>3</sub>H and MOF-SO<sub>3</sub>Ag were found to be 1061 m<sup>2</sup>/g and 825 m<sup>2</sup>/g respectively. The significant reduction in the surface area of MOF-SO<sub>3</sub>Ag over the pristine MOF supports the anchoring of Ag(I) ions on the sulfonate groups projected in the 1D pores of MOF-SO<sub>3</sub>H. Whereas, N<sub>2</sub> adsorption-desorption isotherms of Ag(I)@UiO-66 showed BET surface area of 851 m<sup>2</sup>/g which is lower than the value estimated for pristine MOF (1191 m<sup>2</sup>/g) supporting the loading of Ag(I) ions (Figure A80). The observed surface area of UiO-66 matches well with the previously reported UiO-66 MOF.<sup>57</sup> The CO<sub>2</sub> adsorption isotherms of MOF-SO<sub>3</sub>H and MOF-SO<sub>3</sub>Ag follow a typical type-I behaviour with the uptake of 65.08/40.09 cc/g and 54.28/32.92 cc/g carried out at 273/298K, respectively (Figure 2b and 2c). Further, the CO<sub>2</sub> adsorption isotherms were fitted with the Freundlich-Langmuir equation<sup>58</sup> to get the exact prediction of CO<sub>2</sub> gas adsorbed at saturation (Figure A81-A86). The heat of adsorption value (Q<sub>st</sub>) for CO<sub>2</sub> calculated based on Clausius-Clayperon equation<sup>59</sup> were found to be 30 and 37.8 kJ/mol for MOF-SO<sub>3</sub>H and MOF-SO<sub>3</sub>Ag, respectively (insets of Figure 2b and 2c). On the other hand, CO<sub>2</sub> adsorption-desorption isotherms of Ag(I)@UiO-66 follow a type-I behaviour with the uptake of 55.79 and 35.75 cc/g carried out at 273 and 298K, respectively (Figure 2d). Furthermore, the adsorption isotherms were fitted with the Langmuir-Freundlich equation and the value of Q<sub>st</sub> was estimated to be 30.1 kJ/mol (insets of Figure 2d) which is about 8 kJ/mol lower than that of MOF-SO<sub>3</sub>Ag. Thus, the high CO<sub>2</sub> interaction energy observed for MOF-SO<sub>3</sub>Ag could be ascribed to the stronger interaction of CO<sub>2</sub> with the polar sulfonate groups exposed in the 1D channels of MOF-SO<sub>3</sub>Ag. It is worth mentioning that, the value of Q<sub>st</sub> observed for MOF-SO<sub>3</sub>Ag was found to be the highest among the analogs UiO-66 MOFs with the pore channels decorated with different functional groups (-NH<sub>2</sub>, -Br, -NO<sub>2</sub>, -OMe, and COOH) (Table A1). Further, the gas adsorption measurements of MOF-SO<sub>3</sub>Ag for other gases revealed negligible uptake of 4.9, 3.8, and 1.3 cc/g for N<sub>2</sub>, Ar, and H<sub>2</sub>, respectively suggesting selective adsorption properties of MOF-SO<sub>3</sub>Ag for CO<sub>2</sub> (Figure 3a). Moreover, the calculated Henry gas selectivity constants for CO<sub>2</sub>/H<sub>2</sub>, CO<sub>2</sub>/N<sub>2</sub>, and CO<sub>2</sub>/Ar were found to be 131, 41, and 58, respectively (Figure A87). Hence, we speculate that the selective adsorption property of

MOF-SO<sub>3</sub>Ag for CO<sub>2</sub> may find potential utility in gas separation applications. In addition, MOF-SO<sub>3</sub>Ag shows highly recyclable CO<sub>2</sub> adsorption properties with retaining the CO<sub>2</sub> uptake capacity even after five cycles of adsorption (Figure 3b) along with its crystallinity (Figure A88).

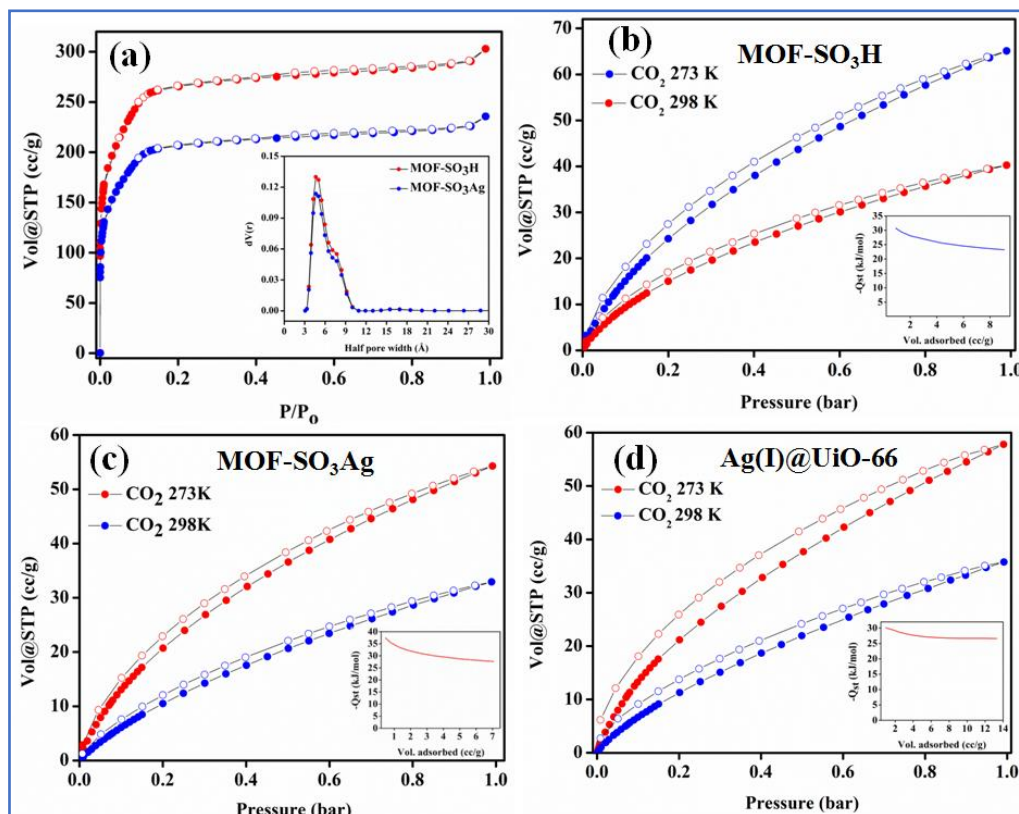


**Figure 2.** (a) N<sub>2</sub> adsorption isotherms for MOF-SO<sub>3</sub>H and MOF-SO<sub>3</sub>Ag carried out at 77K (pore size distribution plots are given as inset) (b) CO<sub>2</sub> adsorption-desorption isotherms of MOF-SO<sub>3</sub>H (c) MOF-SO<sub>3</sub>Ag and (d) Ag(I)@UiO-66 carried out at 273 and 298 K.

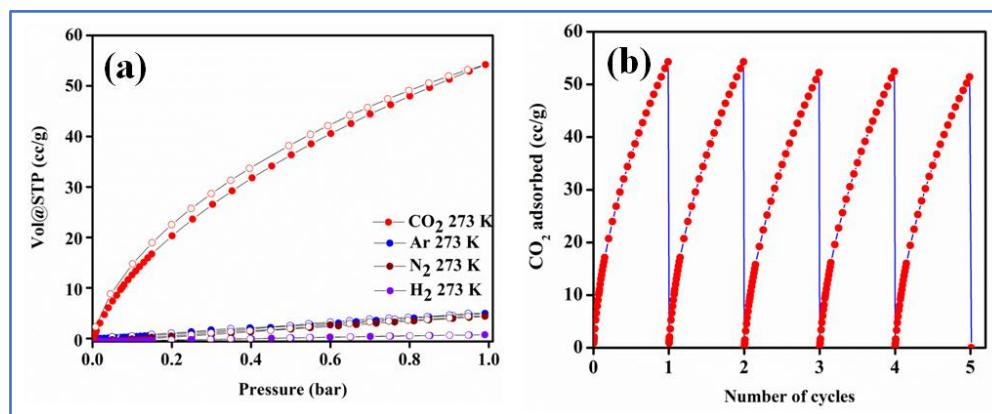


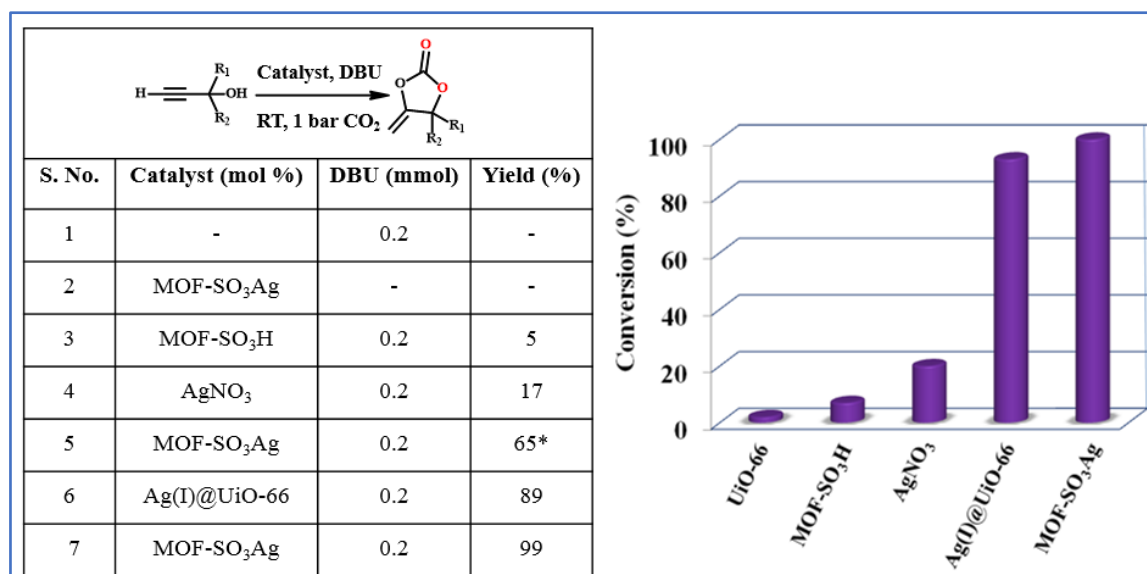
**Figure 3.** (a) Selective CO<sub>2</sub> adsorption isotherms of MOF-SO<sub>3</sub>Ag carried out at 273 K and (b) recyclable CO<sub>2</sub> isotherms of MOF-SO<sub>3</sub>Ag carried out at 273 K.

### 5a.3.3. Catalytic carboxylation of propargylic alcohols with CO<sub>2</sub>

The highly selective CO<sub>2</sub> adsorption property of MOF-SO<sub>3</sub>Ag along with the presence of catalytically active Ag(I) ions in the 1D channels motivated us to study its application for carboxylation of various propargylic alcohols with CO<sub>2</sub> at mild conditions. To start with, the catalytic activity of MOF-SO<sub>3</sub>Ag was tested for cyclic carboxylation of propargylic alcohol, 2-methyl-3-butyn-2-ol with CO<sub>2</sub> in the presence of 1,8-diazabicyclo-[5.4.0]-undec-7-ene (DBU) as a base at RT and 1 bar CO<sub>2</sub> for 12 h. Interestingly, about 65% of 2-Methyl-3-butyn-2-ol was converted to the corresponding  $\alpha$ -alkylidene cyclic carbonate in 12 h (Figure 4). Further increase in the reaction time to 24h led to 99% yield of  $\alpha$ -alkylidene cyclic carbonate with 100% selectivity (Figure 4, A89). Whereas the use of Ag(I)@UiO-66 as catalyst resulted in 89% conversion of 2-methyl-3-butyn-2-ol into the  $\alpha$ -alkylidene cyclic carbonate at the optimized conditions. Interestingly, control experiments carried out using UiO-66, MOF-SO<sub>3</sub>H, and AgNO<sub>3</sub> showed negligible conversion of 2-Methyl-3-butyn-2-ol at the same optimized conditions (Figure 4) highlighting the superior catalytic activity of MOF-SO<sub>3</sub>Ag for high yield generation of  $\alpha$ -alkylidene cyclic carbonates. This high activity can be attributed to the synergistic participation of CO<sub>2</sub>-philic sulfonate group and alkynophilic Ag(I) ions resulting in cooperative catalysis for the capture and conversion of CO<sub>2</sub>. Further, the robust nature of the framework along with highly accessible catalytic Ag(I) sites in the 1D pore channels of the MOF facilitate facile diffusion of the substrates to the catalytically active Ag(I) sites. On the other hand, the lower catalytic activity of the pristine MOF-SO<sub>3</sub>H has been ascribed to the lack of catalytic Ag(I) sites which are essential for the activation of C $\equiv$ C bonds of propargylic alcohols. The higher catalytic activity of MOF-SO<sub>3</sub>Ag over the metal salt (AgNO<sub>3</sub>) could be due to cooperative catalysis promoted by the presence of high local density of the reactants (CO<sub>2</sub> and alcohol) in the confined 1D channel (Figure 4). Similar examples of Ag(I) anchored MOFs exhibiting higher catalytic activity in comparison to that of silver salt are reported in the literature.<sup>51,52</sup> Encouraged by the high catalytic activity of MOF-SO<sub>3</sub>Ag, the catalysis was extended for the carboxylation of various propargylic alcohols with CO<sub>2</sub> under optimized mild conditions. Indeed, the carboxylation reaction of 2-ethyl-3-butyn-2-ol, 3-ethyl-1-pentyn-3-ol, 2-isobutyl-3-butyn-3-ol, and 2-phenyl-butyn-2-ol with CO<sub>2</sub> resulted in the corresponding cyclic carbonates with 92, 88, 83 and 84% yield, respectively (Figure 5). The slight decrease in the yield of  $\alpha$ -alkylidene cyclic carbonates with an increase in the size of the substituent group (-R) on propargylic alcohols can be ascribed to the reduction in the diffusion rate of the alcohols with an increase in the size of -R groups. More importantly, the catalytic activity was tested for CO<sub>2</sub> fixation using simulated

dry flue-gas CO<sub>2</sub>:N<sub>2</sub> (13:87 %). Remarkably, MOF-SO<sub>3</sub>Ag catalyzes about 64% conversion of 2-Methyl-3-butyn-2-ol into  $\alpha$ -alkylidene cyclic carbonate even with a low concentration (13%) of CO<sub>2</sub> carried out at RT and 1 bar CO<sub>2</sub> in 24 h (Figure 5). It is worth mentioning that MOF-SO<sub>3</sub>Ag exhibits superior catalytic activity over the literature-reported heterogeneous catalysts for the carboxylation of 2-Methyl-3-butyn-2-ol with CO<sub>2</sub> under mild conditions (Table 1).

**Figure 4.** Optimization of the reaction conditions for carboxylative cyclization reaction of CO<sub>2</sub> with 2-Methyl-3-butyn-2-ol.



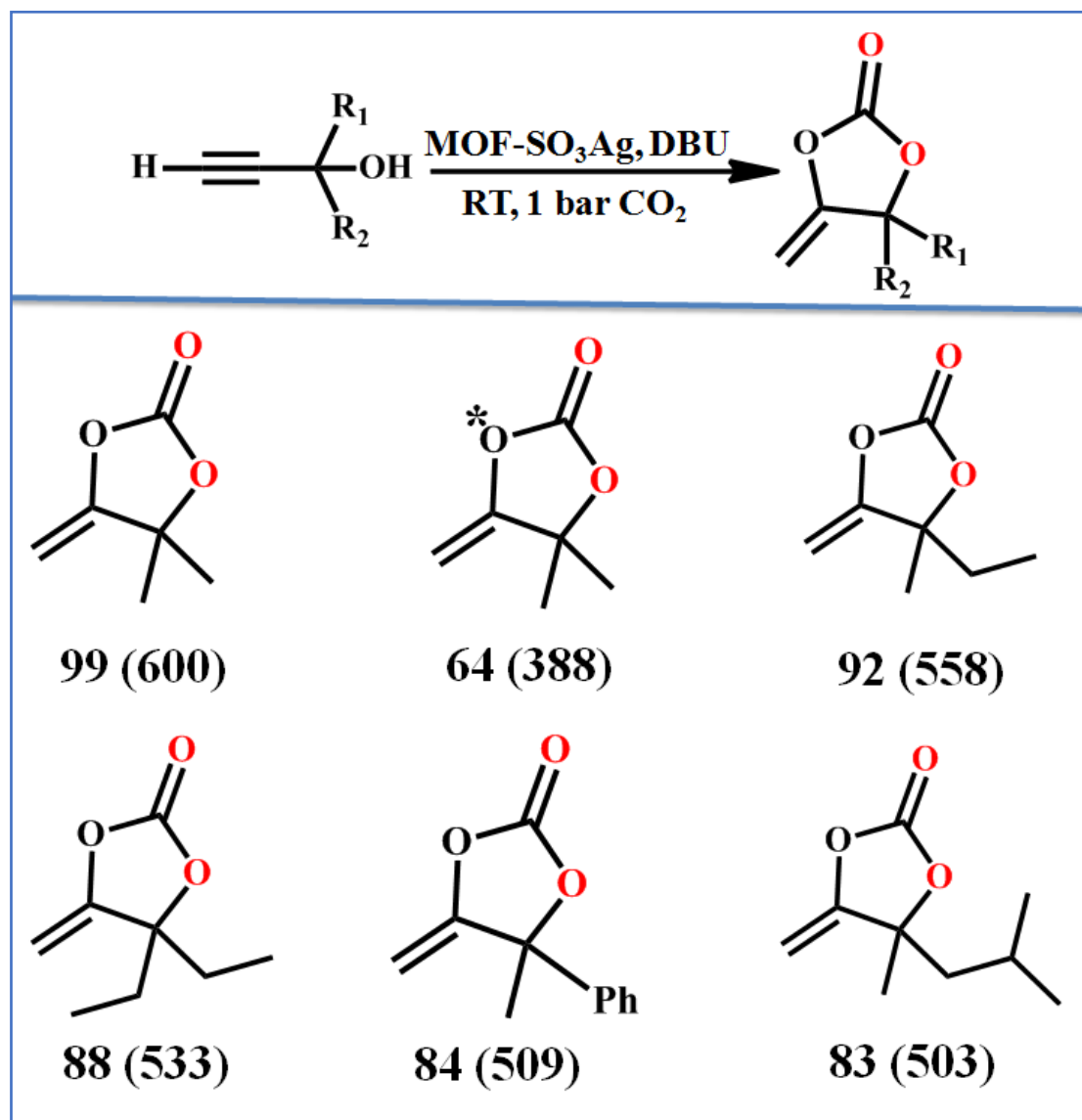
Reaction conditions: 2-Methyl-3-butyn-2-ol (2.0 mmol), catalyst (0.15 mol %), DMF (2 mL), RT (25 °C), 1 atm CO<sub>2</sub> for 24 h. \*Time: 12h. Yields were determined by <sup>1</sup>H NMR with reference to an internal standard (1,1,2,2-tetrachloroethane).

#### 5a.3.4. The three-component reaction of CO<sub>2</sub> with propargylic alcohol and primary amines

Motivated by the high catalytic activity of MOF-SO<sub>3</sub>Ag towards carboxylation of various propargylic alcohols with CO<sub>2</sub>, the scope of the reaction was extended to obtain oxazolidinones by a one-pot reaction of CO<sub>2</sub>, propargylic alcohol, and primary amine (Figure 6). To start with, the catalytic activity was tested for cyclization of 2-methyl-1-butyn-3-ol with CO<sub>2</sub> in the presence of n-butylamine under the optimized conditions of RT and 1 bar CO<sub>2</sub>. Interestingly, more than 99% of the corresponding oxazolidinone was formed in 26 h (Figure A110, A11). To the best of our knowledge, this is the first example of RT synthesis of oxazolidinones by a three-component reaction carried out at mild conditions by using MOF-

based catalyst. Further, the catalysis was extended to aminolysis of  $\alpha$ -alkylidene cyclic carbonates in the presence of different primary amines like cyclohexylamine, iso-butylamine, and n-octylamine. To our delight, all these substrates undergo cyclization resulting in the corresponding oxazolidinones close to 99% yield (Figure 6).

**Figure 5.** Catalytic performance of MOF-SO<sub>3</sub>Ag for carboxylation of various propargylic alcohols with CO<sub>2</sub> at mild conditions.<sup>a</sup>

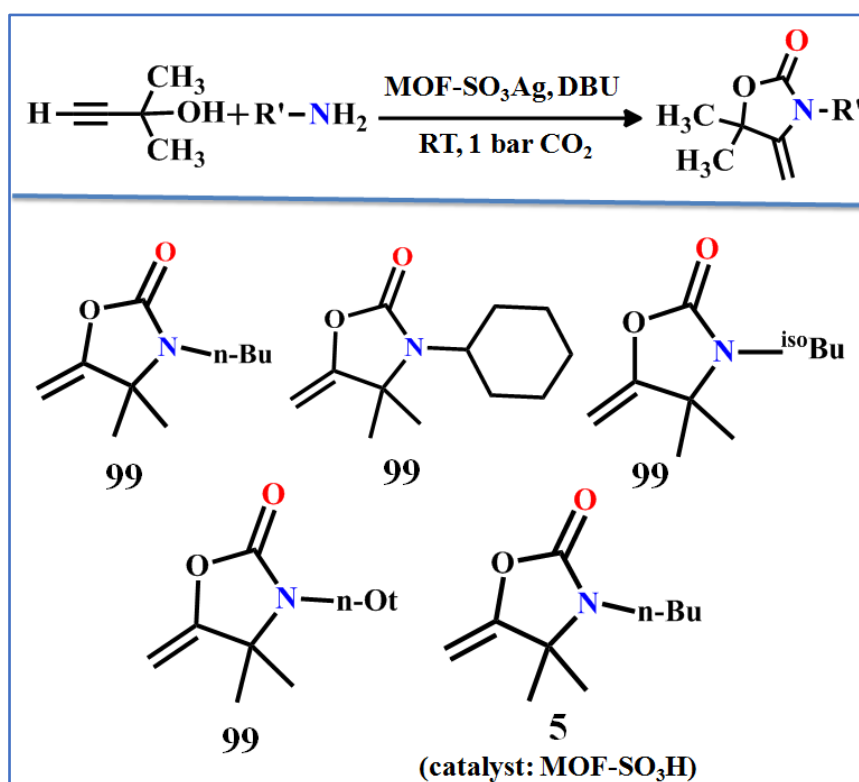


<sup>a</sup>Reaction conditions: propargylic alcohol (2.0 mmol), MOF-SO<sub>3</sub>Ag (0.15 mol %), DBU (0.2 mmol), DMF (2 mL), RT (25 °C), 1 atm CO<sub>2</sub> for 24 h. \*Catalytic conversion by using simulated dry flue-gas, CO<sub>2</sub>:N<sub>2</sub> (13:87 %). Yields were determined by <sup>1</sup>H NMR with reference to an internal standard (1,1,2,2-tetrachloroethane). TON = the number of moles of product formed/moles of catalyst used (given in the parentheses).

**Table 1.** Comparison of the catalytic activity of MOF-SO<sub>3</sub>Ag and Ag(I)@UiO-66 for carboxylation of 2-Methyl-3-butyn-2-ol with CO<sub>2</sub> catalyzed by various heterogeneous catalysts reported in the literature.

Sl. No.	Catalyst	Temperature (°C)	Pressure (bar)	Yield (%)	References
1	Cu-In-MOF	50	5	99	60
2	AgI, IL1	45	1	93	61
3	Ag@RB-POP	30	10	94	62
4	PAzo-POP-Ag	25	10	95	63
5	Dy-Cu MOF	30	1	95	64
6	TMOF-3-Ag	30	1	99	51
7	<b>Ag(I)@UiO-66</b>	<b>25</b>	<b>1</b>	<b>89</b>	<b>This work</b>
8	<b>MOF-SO<sub>3</sub>Ag</b>	<b>25</b>	<b>1</b>	<b>&gt;99</b>	<b>This work</b>

**Figure 6.** Catalytic performance of MOF-SO<sub>3</sub>Ag for one-pot synthesis of oxazolidinones by three-component cyclization of CO<sub>2</sub>, propargylic alcohol and primary amine under mild conditions.<sup>a</sup>



<sup>a</sup>Reaction conditions: propargylic alcohol (2.0 mmol), primary amine (2.0 mmol), MOF-SO<sub>3</sub>Ag (0.15 mol %), DBU (0.2 mmol), DMF (2 mL), RT (25 °C), 1 atm of CO<sub>2</sub> for 26h. Yields were determined by <sup>1</sup>H NMR with reference to 1,1,2,2-tetrachloroethane as an internal standard.

### 5a.3.5. Recyclability test

To check the recyclability of the catalyst, MOF-SO<sub>3</sub>Ag was facilely separated by filtration and then washed with water thoroughly and activated at 353K under vacuum for 15h and reused for subsequent catalytic cycles. It is worth noting that there was no substantial loss of activity with recycling for up to five cycles of regeneration (Figure 7a and A112). Moreover, to eliminate the possibility of leaching of the active catalyst (Ag(I) into the solution), leaching test was carried out. For this, the MOF catalyst was separated from the reaction after 6h and the reaction was extended for another 18 h. The <sup>1</sup>HNMR analysis of the reaction mixture after 24h showed no further conversion supporting the heterogeneous nature of the reaction and no leaching of the active catalyst (Figure 7b). Moreover, MP-AES analysis of the filtrate confirmed the absence of Ag/Zr ions supporting no leaching of the active metal. Hence MOF-SO<sub>3</sub>Ag acts as an excellent recyclable catalyst for the fixation of CO<sub>2</sub> with various propargylic alcohols and amines for high-yield generation of  $\alpha$ -alkylidene cyclic carbonates as well as oxazolidinones at mild reaction conditions. The high catalytic activity could be ascribed to the synergistic effect between the CO<sub>2</sub>-philic sulfonate functionality and the alkynophilic Ag(I) ions responsible for the activation of the C $\equiv$ C bond of propargylic alcohols.

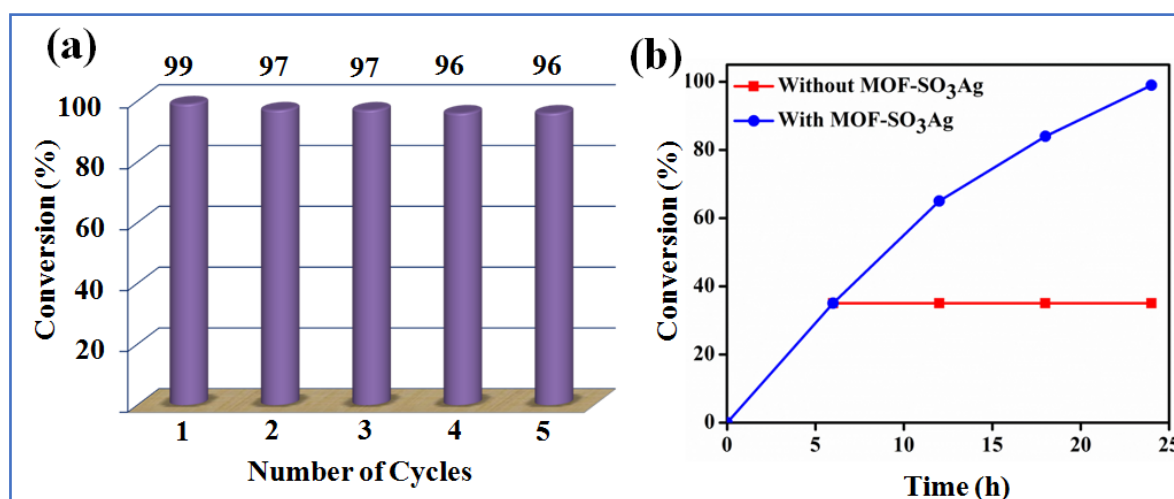


**Figure 7.** (a) Recyclability test of MOF-SO<sub>3</sub>Ag and (b) leaching test of MOF-SO<sub>3</sub>Ag.

### 5a.3.6. Plausible mechanism

A plausible mechanism for the carboxylation of propargylic alcohols with CO<sub>2</sub> catalyzed by MOF-SO<sub>3</sub>Ag is shown in Scheme 2. The reaction begins with the interaction of the propargylic alcohol with the catalytic Ag(I) through C $\equiv$ C bond. To get further support on

this step, control experiments were carried out in which 2-methyl-3-butyn-2-ol was treated with (MOF-SO<sub>3</sub>H and MOF-SO<sub>3</sub>Ag) catalysts for 3h after which time the catalyst was recovered and washed with ethanol thoroughly. FT-IR spectra of the isolated sample showed characteristic peaks at 3350 and 2980 cm<sup>-1</sup> due to O-H and C-H stretching frequency originating from 2-methyl-3-butyn-2-ol supporting the interaction of the alcohol with Ag(I) sites embedded in the framework (Figure 8). The second step involved deprotonation of propargylic alcohol takes place in the presence of DBU (base) followed by CO<sub>2</sub> insertion and subsequent ring-closure reaction leading to the formation of  $\alpha$ -alkylidene cyclic carbonate. Finally, the elimination of the product regenerates the active catalyst and the catalytic cycle continues. On the other hand, when the primary amines are present, the  $\alpha$ -alkylidene cyclic carbonate formed undergoes a tandem aminolysis reaction leading to the formation of oxazolidinones in high yield. Herein, we employed a greener method for one-pot synthesis of oxazolidinones by utilization of CO<sub>2</sub> at mild conditions of RT and 1 bar CO<sub>2</sub>.

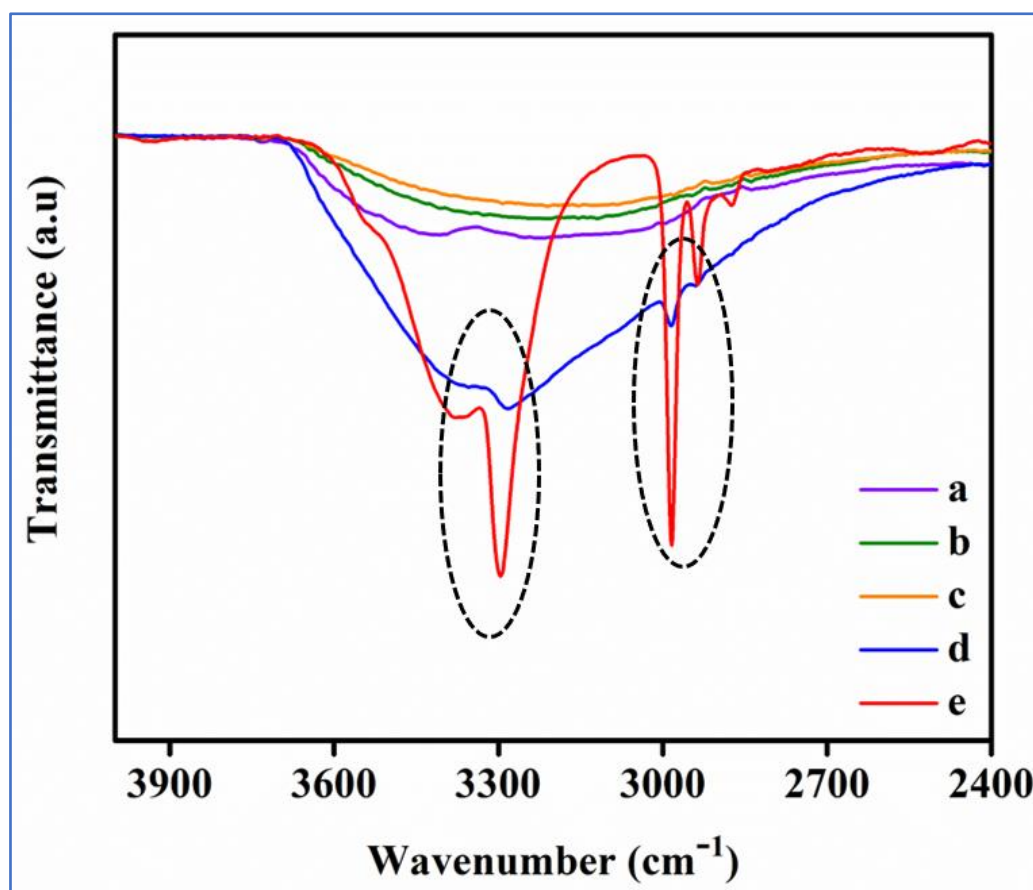
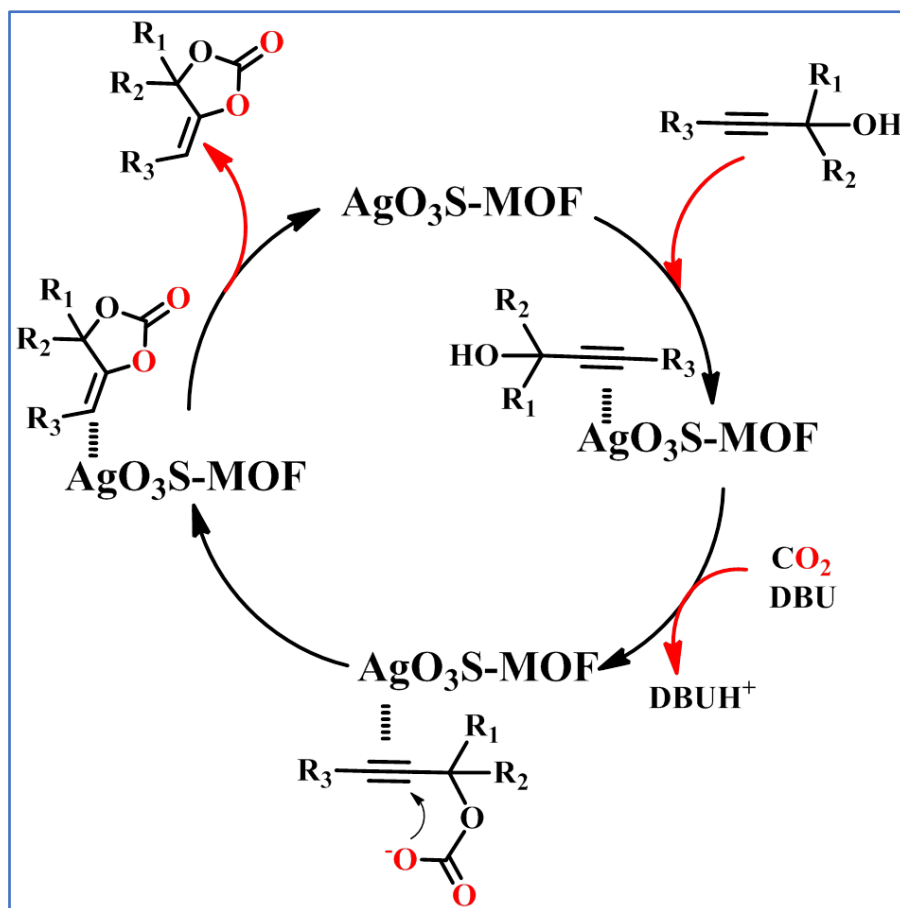


**Figure 8.** FT-IR spectra of a) MOF-SO<sub>3</sub>H, b) MOF-SO<sub>3</sub>Ag, c) 2-methyl-3-butyn-2-ol polarized by MOF-SO<sub>3</sub>H, d) 2-methyl-3-butyn-2-ol polarized by MOF-SO<sub>3</sub>Ag, and e) pure 2-methyl-3-butyn-2-ol.



**Scheme 2.** A plausible mechanism for catalytic carboxylation of propargylic alcohol with  $\text{CO}_2$  catalyzed by  $\text{MOF-SO}_3\text{Ag}$ .

#### 5a.4. Conclusion

In summary, the rational construction of  $\text{Ag(I)}$ -anchored sulfonate-based porous framework,  $\text{MOF-SO}_3\text{Ag}$  incorporated with the advantages of high  $\text{CO}_2$  affinity due to the sulfonate group and catalytic  $\text{Ag(I)}$  sites for alkyne activation, exhibiting efficient carboxylation of propargylic alcohols with  $\text{CO}_2$  is demonstrated. Importantly, the catalysis reported here utilizes green conditions to produce  $\alpha$ -alkylidene cyclic carbonates in high yield at mild conditions of RT and 1 bar  $\text{CO}_2$ . More importantly, high yield generation of oxazolidinones by a three-component catalytic process involving aminolysis of  $\alpha$ -alkylidene cyclic carbonates has also been achieved. To the best of our knowledge,  $\text{MOF-SO}_3\text{Ag}$  is a rare example of  $\text{MOF}$ -supported  $\text{Ag(I)}$  catalyst for the green synthesis of high-value chemicals by chemical fixation of  $\text{CO}_2$  with propargylic alcohols at environment-friendly mild conditions. This work demonstrates the potential application of porous  $\text{MOFs}$  with pores functionalized with polar functionality for selective  $\text{CO}_2$  capture and utilization to synthesize high-value chemicals.

**5a.5. References**

- (1) Jacobson, M. Z. Review of solutions to global warming, air pollution, and energy security. *Energy Environ. Sci.* **2009**, *2*, 148-173.
- (2) Sakakura, T.; Choi, J. C.; Yasuda, H. Transformation of Carbon Dioxide. *Chem. Rev.* **2007**, *107*, 2365-2387.
- (3) He, H.; Perman, J. A.; Zhu G.; Ma, S. Metal-Organic Frameworks for CO<sub>2</sub> Chemical Transformations. *Small* **2016**, *12*, 6309-6324.
- (4) Tiba, S.; Omri, A. Literature survey on the relationships between energy, environment and economic growth. *Renewable Sustainable Energy Rev.* **2017**, *69*, 1129-1146.
- (5) Liu, Q.; Wu, L.; Jackstell, R.; Beller, M. Using carbon dioxide as a building block in organic synthesis. *Nat. Commun.* **2015**, *6*, 5933.
- (6) Song, Q.-W.; Zhou, Z.-H.; He, L.-N. Efficient, selective and sustainable catalysis of carbon dioxide. *Green Chem.* **2017**, *19*, 3707-3728.
- (7) Yun, D.; Park, D. S.; Lee, K. R.; Yun, Y. S.; Kim, T. Y.; Park, H.; Lee, H.; Yi, J. A New Energy-Saving Catalytic System: Carbon Dioxide Activation by a Metal/Carbon Catalyst. *ChemSusChem.* **2017**, *10*, 3671-3678.
- (8) Omae, I. Recent developments in carbon dioxide utilization for the production of organic chemicals. *Coord. Chem. Rev.* **2012**, *256*, 1384-1405.
- (9) Sneddon, G.; Greenaway, A.; Yiu, H. H. P. The Potential Applications of Nanoporous Materials for the Adsorption, Separation, and Catalytic Conversion of Carbon Dioxide. *Adv. Energy Mater.* **2014**, *4*, 1301873.
- (10) Yaashikaa, P. R.; Kumar, P. S.; Varjani S. J.; Saravanan, A. A review on photochemical, biochemical and electrochemical transformation of CO<sub>2</sub> into value-added products. *J. CO<sub>2</sub> Util.* **2019**, *33*, 131-147.
- (11) Dutta, G.; Jana, A. K.; Singh, D. K.; Eswaramoorthy, M.; Natarajan, S. Encapsulation of Ag-nanoparticle in an Amine-Functionalized Porphyrin MOF and its Use as a Heterogeneous Catalyst for CO<sub>2</sub> Fixation under Atmospheric Pressure. *Chem. Asian J.* **2018**, *13*, 2677-2684.
- (12) Fukuoka, S.; Kawamura, M.; Komiya, K.; Tojo, M.; Hachiya, H.; Hasegawa, K., Aminaka, M.; Okamoto, H.; Fukawa, I.; Konno, S. A novel non-phosgene polycarbonate production process using by-product CO<sub>2</sub> as starting material. *Green Chem.* **2003**, *5*, 497-507.
- (13) Ding, X. B.; Furkert, D. P.; Brimble, M. A. General Synthesis of the Nitropyrrolin Family of Natural Products via Regioselective CO<sub>2</sub>-Mediated Alkyne Hydration. *Org. Lett.* **2017**, *19*, 5418-5421.

- (14) Ninokata, R.; Yamahira, T.; Onodera, G.; Kimura, M. Nickel-Catalyzed CO<sub>2</sub> Rearrangement of Enol Metal Carbonates for the Efficient Synthesis of  $\beta$ -Ketocarboxylic Acids. *Angew. Chem. Int. Ed.* **2017**, *56*, 208-211.
- (15) Gennen, S.; Grignard, B.; Tassaing, T.; Jerome C.; Detrembleur, C. CO<sub>2</sub>-Sourced  $\alpha$ -Alkylidene Cyclic Carbonates: A Step Forward in the Quest for Functional Regioregular Poly(urethane)s and Poly(carbonate)s. *Angew. Chem. Int. Ed.* **2017**, *56*, 10394-10398.
- (16) Komatsuki, K.; Sadamitsu, Y.; Sekine, K.; Saito, K.; Yamada, T. Stereospecific Decarboxylative Nazarov Cyclization Mediated by Carbon Dioxide for the Preparation of Highly Substituted 2-Cyclopentenones. *Angew. Chem. Int. Ed.* **2017**, *56*, 11594-11598.
- (17) Diekema, D. J.; Jones, R. N. *Lancet, Oxazolidinone antibiotics.* **2001**, *358*, 1975-1982.
- (18) Song, Q.-W.; Yu, B.; Li, X.-D.; Ma, R.; Diao, Z.-F.; Li, R.-G.; Li, W.; He, L.-N. Efficient chemical fixation of CO<sub>2</sub> promoted by a bifunctional Ag<sub>2</sub>WO<sub>4</sub>/Ph<sub>3</sub>P system. *Green Chem.* **2014**, *16*, 1633-1638.
- (19) Y. Kayaki, M. Yamamoto and T. Ikariya, Stereoselective Formation of  $\alpha$ -Alkylidene Cyclic Carbonates via Carboxylative Cyclization of Propargyl Alcohols in Supercritical Carbon Dioxide. *J. Org. Chem.* **2007**, *72*, 647-649.
- (20) Zhou, H.-C.; Long, J. R.; Yaghi, O. M. Introduction to Metal–Organic Frameworks. *Chem. Rev.* **2012**, *112*, 673- 674.
- (21) Zhou, H.-C.; Kitagawa, S. Metal-Organic Frameworks (MOFs). *Chem. Soc. Rev.* **2014**, *43*, 5415-5418.
- (22) Zhao, Y. Emerging Applications of Metal-Organic Frameworks and Covalent Organic Frameworks, *Chem. Mater.* **2016**, *28*, 8079-8081.
- (23) Liu, J.; Chen, L.; Cui, H.; Zhang, J.; Zhang, L.; Su, C. Y. Applications of metal–organic frameworks in heterogeneous supramolecular catalysis. *Chem. Soc. Rev.* **2014**, *43*, 6011-6061
- (24) Corma, A.; García, H.; Llabrés i Xamena, F. X. Engineering Metal Organic Frameworks for Heterogeneous Catalysis. *Chem. Rev.* **2010**, *110*, 4606-4655.
- (25) Li, J. R.; Sculley, J.; Zhou, H. C. Metal-Organic Frameworks for Separations. *Chem. Rev.* **2012**, *112*, 869-932.
- (26) Wen, H. M.; Wang, H.; Li, B.; Cui, Y.; Wang, H.; Qian, G.; Chen, B. A Microporous Metal-Organic Framework with Lewis Basic Nitrogen Sites for High C<sub>2</sub>H<sub>2</sub> Storage and Significantly Enhanced C<sub>2</sub>H<sub>2</sub>/CO<sub>2</sub> Separation at Ambient Conditions. *Inorg. Chem.* **2016**, *55*, 7214-7218.

- (27) Yu, J.; Xie, L.-H.; Li, J.-R.; Ma, Y.; Seminario, J. M.; Balbuena, P. B. CO<sub>2</sub> Capture and Separations Using MOFs: Computational and Experimental Studies. *Chem. Rev.* **2017**, *117*, 9674-9754.
- (28) Sumida, K.; Rogow, D. L.; Mason, J. A.; Donald, T. M.; Bloch, E. D.; Herm, Z. R.; Bae, T. H.; Long, J. R. Carbon dioxide capture in metal-organic frameworks. *Chem. Rev.* **2012**, *112*, 724-781.
- (29) Liang, J.; Huang, Y.-B.; Cao, R. Metal-organic frameworks and porous organic polymers for sustainable fixation of carbon dioxide into cyclic carbonates. *Coord. Chem. Rev.* **2019**, *378*, 32-65.
- (30) Cui, W. -G.; Zhang, G.-Y.; Hu, T.-L.; Bu, X.-H. Metal-organic framework-based heterogeneous catalysts for the conversion of C1 chemistry: CO, CO<sub>2</sub> and CH<sub>4</sub>. *Coord. Chem. Rev.* **2019**, *387*, 79-120.
- (31) Trickett, C. A.; Helal, A.; Al-Maythaly, B. A.; Yamani, Z. H.; Cordova, K. E.; Yaghi, O. M. The chemistry of metal organic frameworks for CO<sub>2</sub> capture, regeneration and conversion. *Nat. Rev. Mater.* **2017**, *2*, 17045.
- (32) Nagaraja, C. M.; Haldar, R.; Maji, T. K.; Rao, C. N. R. Chiral Porous Metal–Organic Frameworks of Co(II) and Ni(II): Synthesis, Structure, Magnetic Properties, and CO<sub>2</sub> Uptake. *Cryst. Growth. Des.* **2012**, *12*, 975.
- (33) Dhankhar, S. S.; Sharma, N.; S. Kumar; Dhilip Kumar, T. J.; Nagaraja C. M., Rational Design of a Bifunctional, Two-Fold Interpenetrated Zn<sup>II</sup> Metal–Organic Framework for Selective Adsorption of CO<sub>2</sub> and Efficient Aqueous Phase Sensing of 2,4,6-Trinitrophenol. *Chem. Eur. J.* **2017**, *23*, 16204-16212.
- (34) Wilson, M.; Barrientos-Palomo, S. N.; Stevens, P. C.; Mitchell, N. L.; Oswald, G., Nagaraja, C. M.; Badyal, J. P. S. Substrate-Independent Epitaxial Growth of the Metal Organic Framework MOF-508a. *ACS Appl. Mater. Interfaces* **2018**, *10*, 4057-4065.
- (35) Ding, M.; Flaig, R. W.; Jiang, H. -L.; Yaghi, O. M. Carbon capture and conversion using metal-organic frameworks and MOF-based materials. *Chem. Soc. Rev.* **2019**, *48*, 2783-2828.
- (36) Maina, J. W.; -Gonzalo, C. P.; Kong, L.; Schutz, J.; Hillc, M.; Dumeé, L. F. Metal organic framework-based catalysts for CO<sub>2</sub> conversion. *Mater. Horiz.* **2017**, *4*, 345-361.
- (37) Kamphuis, A. J.; Picchioni, F.; Pescarmona, P. P. CO<sub>2</sub>-fixation into cyclic and polymeric carbonates: principles and applications. *Green Chem.* **2019**, *21*, 406-448.
- (38) Das, R.; Dhankhar, S. S.; Nagaraja, C. M. Construction of a bifunctional Zn(II)–organic framework containing a basic amine functionality for selective capture and room temperature fixation of CO<sub>2</sub>. *Inorg. Chem. Front.* **2020**, *7*, 72-81.

- (39) Sharma, N.; Dhankhar, S. S.; Nagaraja, C. M. Environment-friendly, co-catalyst- and solvent-free fixation of CO<sub>2</sub> using an ionic zinc(II)–porphyrin complex immobilized in porous metal–organic frameworks. *Sustain. Energy Fuels*. **2019**, *3*, 2977-2982.
- (40) Aguila, B.; Sun, Q.; Wang, X.; Rourke, E. O. Q.; -Enizi, A. M. A.; Nafady, A.; Ma, S. Lower Activation Energy for Catalytic Reactions through Host-Guest Cooperation within Metal-Organic Frameworks. *Angew. Chem. Int. Ed.* **2018**, *57*, 10107-10111.
- (41) Ugale, B.; Kumar, S.; Dhilip Kumar, T. J.; Nagaraja, C. M. Environmentally Friendly, Co-catalyst-Free Chemical Fixation of CO<sub>2</sub> at Mild Conditions Using Dual-Walled Nitrogen-Rich Three-Dimensional Porous Metal-Organic Frameworks. *Inorg. Chem.* **2019**, *58*, 3925-3936.
- (42) Parmar, B.; Patel, P.; Pillai, R. S.; Kureshy, R. I.; Khan, N. H.; Suresh, E. Efficient catalytic conversion of terminal/internal epoxides to cyclic carbonates by porous Co(II) MOF under ambient conditions: structure-property correlation and computational studies. *J. Mater. Chem. A*. **2019**, *7*, 2884-2894.
- (43) Sharma, N.; Dhankhar, S. S.; Kumar, S.; Dhilip Kumar T. J.; Nagaraja, C. M. Rational design of 3D Mn(II)-metal organic framework based on non-metallated porphyrin linker for selective capture of CO<sub>2</sub> and one-pot synthesis of styrene carbonates. *Chem. Eur. J.* **2018**, *24*, 16662-16669.
- (44) Ugale, B.; Dhankhar, S. S.; Nagaraja, C. M. Construction of 3-Fold-Interpenetrated Three-Dimensional Metal-Organic Frameworks of Nickel(II) for Highly Efficient Capture and Conversion of Carbon Dioxide. *Inorg. Chem.* **2016**, *55*, 9757.
- (45) Zhou, Z.; He, C.; Yang, L.; Wang, Y.; Liu, T.; Duan, C. Alkyne Activation by a Porous Silver Coordination Polymer for Heterogeneous Catalysis of Carbon Dioxide Cycloaddition. *ACS Catal.* **2017**, *7*, 2248-2256.
- (46) Zhang, G.; Yang, H.; Fei, H. Unusual Missing Linkers in an Organosulfonate-Based Primitive-Cubic (pcu)-Type Metal-Organic Framework for CO<sub>2</sub> Capture and Conversion under Ambient Conditions. *ACS Catal.* **2018**, *8*, 2519-2525.
- (47) Letinois, U. H.; Weibel, J. M.; Pale, P. The organic chemistry of silver acetylides. *Chem. Soc. Rev.* **2007**, *36*, 759-769.
- (48) Karmakar, R.; Lee, D. Reactions of arynes promoted by silver ions. *Chem. Soc. Rev.* **2016**, *45*, 4459-4470.
- (49) Kikuchi, S.; Sekine, K.; Ishida, T.; Yamada, T. C-C Bond Formation with Carbon Dioxide Promoted by a Silver Catalyst. *Angew. Chem. Int. Ed.* **2012**, *51*, 6989-6992.

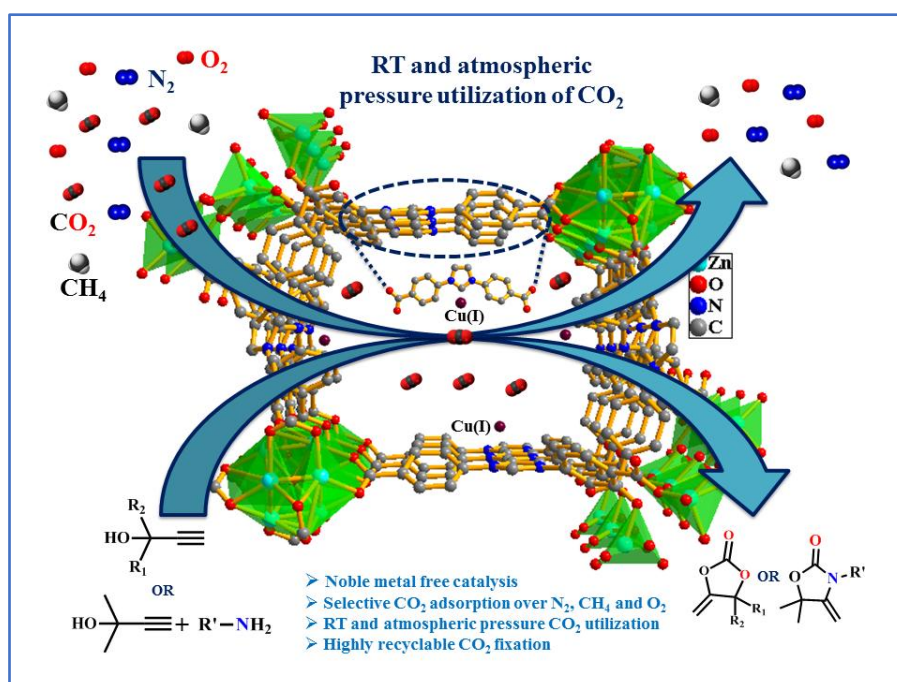
- (50) Song, Q.-W.; Chen, W.-Q.; Ma, R.; Yu, A.; Li, Q.-Y.; Chang, Y.; He, L.-N. Bifunctional Silver(I) Complex-Catalyzed CO<sub>2</sub> Conversion at Ambient Conditions: Synthesis of a Methylene Cyclic Carbonates and Derivatives. *ChemSusChem*. **2015**, *8*, 821-827.
- (51) Song, Q.-W.; He, L.-N. Robust Silver(I) Catalyst for the Carboxylative Cyclization of Propargylic Alcohols with Carbon Dioxide under Ambient Conditions. *Adv. Synth. Catal.* **2016**, *358*, 1251-1258.
- (52) Song, Q.-W.; Zhou, Z.-H.; Yin, H.; He, L.-N. Silver(I)-Catalyzed Synthesis of *b*-Oxopropylcarbamates from Propargylic Alcohols and CO<sub>2</sub> Surrogate: A Gas-Free Process. *ChemSusChem*. **2015**, *8*, 3967-3972.
- (53) Taylor, J. M.; Komatsu, T.; Dekura, S.; Otsubo, K.; Takata, M.; Kitagawa, H. The Role of a Three Dimensionally Ordered Defect Sublattice on the Acidity of a Sulfonated Metal–Organic Framework. *J. Am. Chem. Soc.* **2015**, *137*, 11498-11506.
- (54) Moreira, M. A.; Santos, J. C.; Ferreira, A. F. P.; Loureiro, J. M.; Ragon, F.; Horcajada, P.; Shim, K. E.; Hwang, Y.-K.; Lee, U.-H.; Chang, J.-S.; Serre, C.; Rodrigues, A. E. Reverse Shape Selectivity in the Liquid-Phase Adsorption of Xylene Isomers in Zirconium Terephthalate MOF UiO-66. *Langmuir* **2012**, *28*, 5715-5723.
- (55) Taylor, J. M.; Komatsu, T.; Dekura, S.; Otsubo, K.; Takata M.; Kitagawa, H. The Role of a Three Dimensionally Ordered Defect Sublattice on the Acidity of a Sulfonated Metal–Organic Framework. *J. Am. Chem. Soc.* **2015**, *137*, 11498-11506.
- (56) An, B.; Li, Z.; Song, Y.; Zhang, J.; Zeng, L.; Wang C.; Lin, W. Cooperative CO<sub>2</sub>-to-ethanol conversion via enriched intermediates at molecule–metal catalyst interfaces. *Nature Catalysis* **2019**, *2*, 709-717.
- (57) Yang, Q.; Wiersum, A. D.; Jobic, H.; Guillerm, V.; Serre, C.; Llewellyn, P. L.; Maurin, G. Understanding the Thermodynamic and Kinetic Behavior of the CO<sub>2</sub>/CH<sub>4</sub> Gas Mixture within the Porous Zirconium Terephthalate UiO-66(Zr): A Joint Experimental and Modeling Approach. *J. Phys. Chem. C* **2011**, *115*, 13768-13774.
- (58) Yang, R. T. *Gas Separation by Adsorption Processes*, Butterworth, Boston, **1997**.
- (59) Pan, H.; Ritter, J. A.; Balbuena, P. B. Examination of the Approximations Used in Determining the Isothermic Heat of Adsorption from the Clausius-Clapeyron Equation. *Langmuir* **1998**, *14*, 6323-6327.
- (60) Hou, S.-L.; Dong, J.; Jiang, X.-L.; Jiao, Z.-H.; Zhao, B. A Noble-Metal-Free Metal-Organic Framework (MOF) Catalyst for the Highly Efficient Conversion of CO<sub>2</sub> with Propargylic Alcohols *Angew. Chem. Int. Ed.* **2019**, *58*, 577-581.

- (61) Yuan, Y.; Xie, Y.; Zeng, C.; Song, D.; Chaemchuen, S.; Chen, C.; Verpoort, F. recyclable AgI/OAc<sup>-</sup> catalytic system for the efficient synthesis of  $\alpha$ -alkylidene cyclic carbonates: carbon dioxide conversion at atmospheric pressure. *Green Chem.* **2017**, *19*, 2936-2940.
- (62) Yu, X.; Yang, Z.; Zhang, F.; Liu, Z.; Yang, P.; Zhang, H.; Yu, B.; Zhao, Y.; Liu, Z. A rose bengal-functionalized porous organic polymer for carboxylative cyclization of propargyl alcohols with CO<sub>2</sub>. *Chem. Commun.* **2019**, *55*, 12475-12478.
- (63) Yang, Z.; Yu, B.; Zhang, H.; Zhao, Y.; Chen, Y.; Ma, Z.; Ji, G.; Gao, X.; Han, B.; Liu, Z.; Metalated Mesoporous Poly(triphenylphosphine) with Azo Functionality: Efficient Catalysts for CO<sub>2</sub> Conversion. *ACS Catal.* **2016**, *6*, 1268-1273.
- (64) Wu, Z.; Lan, X.; Zhang, Y.; Lia, M.; Bai, G. Copper(I) iodide cluster-based lanthanide organic frameworks: synthesis and application as efficient catalysts for carboxylative cyclization of propargyl alcohols with CO<sub>2</sub> under mild conditions. *Dalton Trans.* **2019**, *48*, 11063-11069.



# Chapter 5b

## Noble metal-free Cu(I)-anchored NHC-based MOF for highly efficient fixation of CO<sub>2</sub> under RT and atmospheric pressure conditions





### 5b.1. Introduction

The concentration of CO<sub>2</sub> in the atmosphere is rapidly increasing and has exceeded 400 ppm resulting in several environmental issues such as extreme weather, ocean acidification, global warming, and so on.<sup>1</sup> Therefore, it is most important to mitigate this growing concentration of CO<sub>2</sub> by utilizing it as a non-toxic C1 feedstock to synthesize value-added chemicals and fuels.<sup>2-5</sup> However, carbon dioxide is thermally stable and kinetically inert with a high bond strength of 805 kJ/mol. Hence, the development of highly reactive catalytic systems for efficient carbon capture and utilization (CCU) has gained significant interest from researchers worldwide.<sup>6-16</sup> In this direction, extensive research efforts are being carried out for the functionalization of CO<sub>2</sub> into various value-added chemicals and fuels.<sup>17-25</sup> Especially, the production of  $\alpha$ -alkylidene cyclic carbonates from propargylic alcohols and CO<sub>2</sub> has gained a special interest owing to its potential utility for the synthesis of natural products,<sup>26</sup> polymers,<sup>27,28</sup> polyurethanes,<sup>29</sup> and so on.<sup>30</sup> Further, preparation of oxazolidinones, valuable commodity chemicals for the synthesis of antibiotics via a cascade reaction of CO<sub>2</sub> with propargylic alcohol and primary amines represents a green and sustainable approach for the conversion of greenhouse gas into bio-relevant products.<sup>31</sup> The homogeneous catalysts known for this conversion suffer from the limitations of product separation and recyclability.<sup>32-35</sup> Among the heterogeneous catalysts, metal-organic frameworks (MOFs) have shown unique advantages over other conventional porous materials due to their modular nature with tuneable pore size and functionality along with high surface areas.<sup>36-40</sup> Thus over the past few years intensive research efforts are being carried out on the rational design of MOFs incorporating CO<sub>2</sub>-philic basic and acidic functionalities for selective gas storage/separation,<sup>41-44</sup> and catalytic conversion of carbon dioxide.<sup>45-54</sup> Among the various carbon dioxide functionalization reactions studied so far, the conversion of CO<sub>2</sub> into cyclic carbonates has been extensively studied as an atom economic process.<sup>55,56</sup> On the other hand, synthesis of bio-relevant oxazolidinones by a green, environmentally-friendly one-pot reaction involving one-pot coupling of CO<sub>2</sub> with propargylic alcohols and primary amines is rarely studied. Furthermore, recent literature reports have demonstrated the application of silver (Ag)-based catalysts for cyclic carboxylation of alkyne molecules with CO<sub>2</sub> to generate  $\alpha$ -alkylidene cyclic carbonates, and oxazolidinones.<sup>57-64</sup> On the other hand, the application of non-noble metal-based MOFs for catalytic carboxylation of alkyne molecules to generate value-added chemicals is rarely demonstrated. In this regard, Cu(I) based heterogeneous catalysts have attracted significant interest as promising alternatives to expensive noble metal-based catalysts for the production of high-value chemicals by coupling

alkyne molecules with CO<sub>2</sub>. Towards this direction, Cu(I) anchored heterogeneous catalysts have gained significant interest. The literature study revealed that N-heterocyclic carbenes are suitable supports for anchoring Cu(I) ions through coordination with the carbene carbon center.<sup>65-68</sup> Based on these studies, we have chosen a porous MOF composed of N-heterocyclic carbene (NHC) centers in the pore channels, and these NHC sites were utilized to anchor Cu(I) ions to obtain Cu(I)@NHC-MOF. The Cu(I) embedded MOF acts as a highly recyclable heterogeneous catalyst for the fixation of CO<sub>2</sub> into  $\alpha$ -alkylidene cyclic carbonates and oxazolidinones under RT and atmospheric pressure conditions. Besides, the Cu(I)@NHC-MOF exhibits highly selective and recyclable CO<sub>2</sub> uptake properties with a high heat of interaction energy of 43 kJmol<sup>-1</sup>. To the best of our knowledge, this chapter represents the first example of a noble metal-free MOF-based heterogeneous catalyst for carbon capture and utilization (CCU) to generate oxazolidinones valuable chemicals at mild conditions of RT and 1 atm pressure.

## 5b.2. Experimental section

### 2a.2.1. Materials

All the reagents used in this work were commercially available and used as received without any further purification. Zn(NO<sub>3</sub>)<sub>2</sub>·6H<sub>2</sub>O, CuCl, and 4-aminobenzoic acid were purchased from Sigma Aldrich Chemical Co. N, N'-dimethylformamide (DMF), N, N'-dimethylacetamide (DMA) and methanol (MeOH) were obtained from S. D. Fine Chem. Limited. All the epoxides and the internal standard used for catalytic reactions were purchased from TCI chemicals and used without further purification. The 1,3-bis(4-carboxyphenyl)imidazolium chloride (H<sub>2</sub>L<sup>+</sup>Cl<sup>-</sup>) ligand was synthesized by following previous literature with slight modification.<sup>69</sup>

### 5b.2.2. Physicochemical characterization

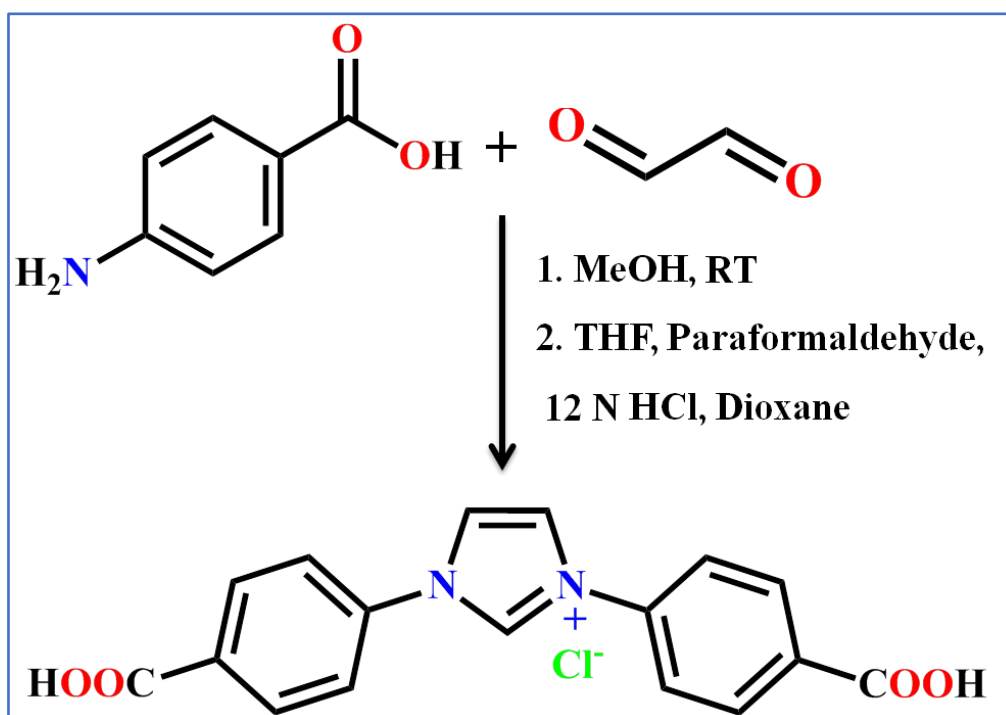
The phase purity of the as-synthesized samples was confirmed by powder XRD analysis using Rigaku Miniflex 600 with Cu K $\alpha$  radiation ( $\lambda = 0.154$  nm). SEM images and EDAX patterns were recorded on the FEI Nova SEM-450 instrument. UV-Vis (Diffuse Reflectance) spectra were recorded on the Shimadzu spectrophotometer using BaSO<sub>4</sub> as a reference. The metal content of Zn and Cu in the hybrid material was determined by Agilent's microwave-plasma atomic emission spectrometer (MP-AES). The X-ray photoelectron spectroscopy (XPS) analyses were performed on a Thermo Fisher Scientific

NEXSA photoemission spectrometer using Al-K $\alpha$  (1486.6 eV) X-ray radiation and analysis of the obtained data was performed using Avantage software.  $^1\text{H}$  and  $^{13}\text{C}$  NMR spectra were recorded in  $\text{CDCl}_3$  on a JEOL JNM-ECS-400 spectrometer operating at a frequency of 400 MHz.

### 5b.2.3. Synthesis

#### 5b.2.3.1. Synthesis of 1,3-bis(4-carboxyphenyl)imidazolium chloride ( $\text{H}_2\text{L}^+\text{Cl}^-$ )

The 1,3-bis(4-carboxyphenyl)imidazolium chloride ( $\text{H}_2\text{L}^+\text{Cl}^-$ ) ligand was synthesized by following previous literature with slight modification (Scheme 1).<sup>69</sup> Briefly, 4-aminobenzoic acid (5 g, 2.0 equiv.) was dissolved in methanol (15 mL) followed by the addition of 2 drops of formic acid and 40% aqueous solution of glyoxal (2.5 mL, 1.0 equiv.) and the solution was stirred at ambient temperature for 24h. The white solid formed was collected by filtration, washed with cold methanol, and dried in air (Compound L1). The compound L1 (1 g), was dissolved in anhydrous THF (10 mL) under an inert atmosphere followed by the addition of a solution of paraformaldehyde (125 mg) in 12 N HCl (400 microlitter) in dioxane (1 mL) at 0 °C. The reaction mixture was stirred at room temperature for 4 h. The light pink precipitate formed was collected by filtration, washed with  $\text{Et}_2\text{O}$ , and dried under vacuum.



**Scheme 1.** Synthesis of 1,3-bis(4-carboxyphenyl)imidazolium chloride ( $\text{H}_2\text{L}^+\text{Cl}^-$ ).

### 5b.2.3.2. Synthesis of NHC-MOF

The NHC-MOF was synthesized by following the procedure reported before with a slight modification.<sup>69</sup> Briefly,  $\text{Zn}(\text{NO}_3)_2 \cdot 6\text{H}_2\text{O}$  (2.0 mmol, 0.5950 g) and  $\text{H}_2\text{L}^+\text{Cl}^-$  (0.5 mmol, 0.1724 g) were dissolved by 3 mL dry DMF solvent in a 50 mL Teflon-lined autoclave. Then it was heated under autogenous pressure to 120 °C for 48 h followed by cooling to ambient temperature slowly. The as-synthesized sample was collected by filtration, washed with DMF, and dried under vacuum at 120 °C overnight. Yield: 42%. The phase purity of NHC-MOF was confirmed by PXRD analysis (Figure 1a). FTIR ( $\text{cm}^{-1}$ ): 3088 (m), 1650 (w), 1608 (s), 1541 (s), 1380 (s). Elemental analysis for NHC-MOF, calculated for  $[\text{Zn}_8(\text{L})_{12}(\text{H}_2\text{O})_{29}(\text{DMF})_{69}(\text{NO}_3)_2]_n$ : C: 49.74, H: 7.08, N:13.41 and found C: 49.02, H: 6.28, N: 12.85.

### 5b.2.3.3. Synthesis of Cu(I)@NHC-MOF

$\text{CuCl}$  (0.05 mmol, 5 mg) was dissolved in 10 mL dry methanol and NHC-MOF (0.01 mmol, 48.8 mg) was added to it. The resulting reaction mixture was stirred at 60 °C for 30 min under an inert atmosphere. Then the mixture was cooled down to room temperature and washed with DMA and methanol thoroughly, dried under vacuum at 80 °C for 12 h. The phase purity of Cu(I)@NHC-MOF was confirmed by PXRD analysis (Figure 1a). FTIR ( $\text{cm}^{-1}$ ): 3085 (w), 1606 (s), 1382 (s), 1257 (m). Elemental analysis for Cu(I)@NHC-MOF, Calculated for  $[\text{Zn}_8\text{Cu}_4(\text{L})_{12}(\text{H}_2\text{O})_{29}(\text{DMF})_{69}\text{Cl}_4]_n$ : C: 49.03, H: 6.94, N: 12.25 and found C: 48.36, H: 6.14, N: 11.97.

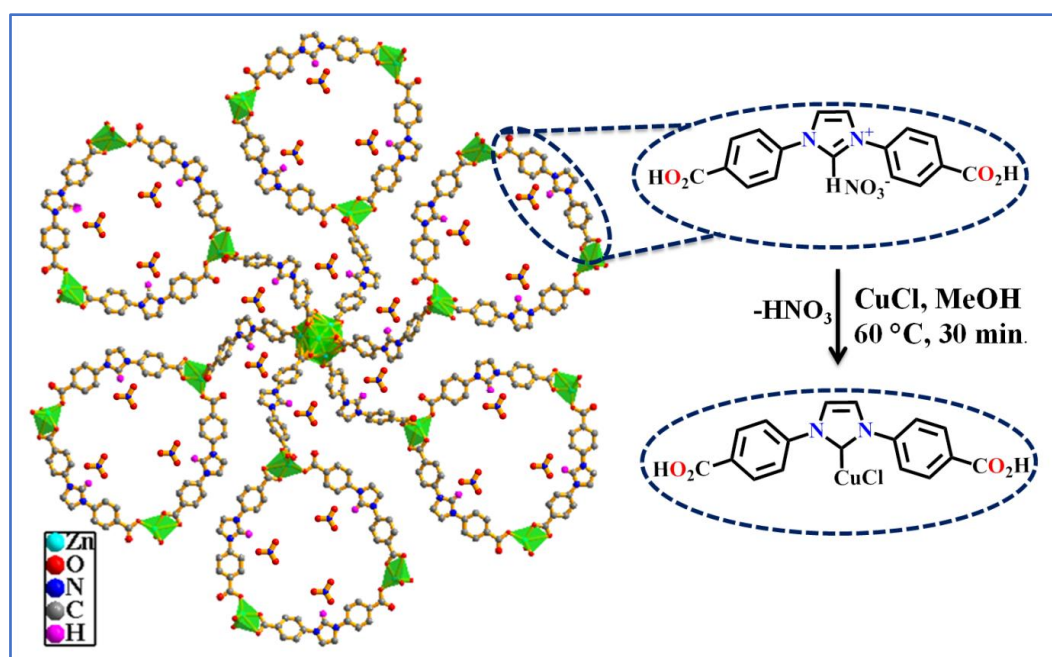
### 5b.2.4. Catalytic cycloaddition reactions of $\text{CO}_2$ with propargylic alcohols

Catalytic cyclic carboxylation reactions of alkyne molecules (propargylic alcohols) and primary amines with  $\text{CO}_2$  were carried out in a Schlenk tube (50 mL) under RT and 1 atm  $\text{CO}_2$  (balloon). Before catalytic reactions, the catalyst was activated at 120 °C under vacuum for 24h to remove guest solvent molecules. The MOF catalyst (0.005 mmol), propargylic alcohol (4 mmol), and DBU (0.05 equiv.) in 2 mL of DMF were taken in the Schlenk tube at RT,  $\text{CO}_2$  was introduced using a balloon and the contents were stirred at RT. After 12 h, the catalyst was separated from the reaction mixture by filtration and the catalytic conversions were determined by  $^1\text{H}$  NMR spectra of the filtrate using  $\text{CDCl}_3$  solvent. The recovered catalyst was washed with methanol thoroughly and activated at 120 °C under vacuum for 24h and reused for subsequent catalytic cycles.

### 5b.3. Results and discussion

#### 5b.3.1. Synthesis and characterization

The NHC-based Zn-MOF was synthesized by following the previously reported procedure (ESI).<sup>69</sup> The phase purity of the as-synthesized MOF was confirmed by powder XRD analysis (Figure 1a). The 3D structure of Zn-MOF possesses large 1D channels which are lined with NHC centers (Figure A90). Thus, the NHC centers exposed in the pores were utilized to anchor Cu(I) ions by treating them with CuCl to obtain Cu(I)@NHC-MOF as depicted in Scheme 2.



**Scheme 2.** View of six-metallomacrocycles connected to {Zn<sub>8</sub>O} SBU in Zn-MOF and generation of Cu(I)@NHC-MOF.

The PXRD pattern of as-synthesized Cu(I)@NHC-MOF is well-matched with the pristine MOF confirming the retention of framework structure even after the incorporation of Cu(I) ions at the carbene sites (Figure 1a). Further, FTIR spectra of Cu(I) incorporated NHC-MOF showed shifting of the characteristic peak due to  $\text{-C=N}^+$  from 1650 to 1257  $\text{cm}^{-1}$  supporting the formation of  $\text{-C-N}$ , upon coordination of Cu(I) (Figure A91). Furthermore, solid-state UV-Vis absorption spectra of Cu(I)@NHC-MOF showed absorption bands at 210 and 260 nm corresponding to ligand-based  $\Pi \rightarrow \Pi^*$  transitions (Figure A92). The percentage loading of Cu(I) in the Zn-MOF was determined from MP-AES (microwave-plasma atomic emission spectroscopy) analysis and was found to be 5.1% (Figure A93). For further

confirmation of the incorporation of Cu(I) in the MOF, X-ray photoelectron spectra (XPS) of Cu(I)@NHC-MOF was recorded. As shown in Figure 1b, survey spectra show the presence of constituent elements, Zn, Cu, C, N, O, and Cl in the sample. The Zn(II) spectrum shows the presence of peaks at binding energies of 1022.3 and 1045.4 eV corresponding to  $2P_{3/2}$  and  $2P_{1/2}$ , respectively (Figure 1c). The Cu(I) spectrum shows characteristic peaks at binding energies of 933.0 and 952.8 eV corresponding to  $2P_{3/2}$  and  $2P_{1/2}$ , respectively (Figure 1d). This observation is in line with the reported examples of Cu(I) complexes. For example, XPS spectra of [1,3-Bis(2,6-diisopropylphenyl)imidazol-2-ylidene]copper(I) chloride [(iPr)CuCl] complex shows peaks at 933.3 and 952.9 eV corresponding to  $2P_{3/2}$  and  $2P_{1/2}$ , of Cu(I), respectively<sup>70</sup> (Figure 1d). Hence, XPS analysis of Cu(I)@NHC-MOF confirmed the incorporation of Cu(I) at the NHC-sites in the MOF. Further, scanning electron microscopy (SEM) analysis of NHC-MOF revealed rod-like morphology, and the morphology was retained even after anchoring of Cu(I) ions (Figure A94). Moreover, energy dispersive spectroscopy (EDS) analysis also supported the loading of Cu(I) in NHC-MOF (Figure A94).

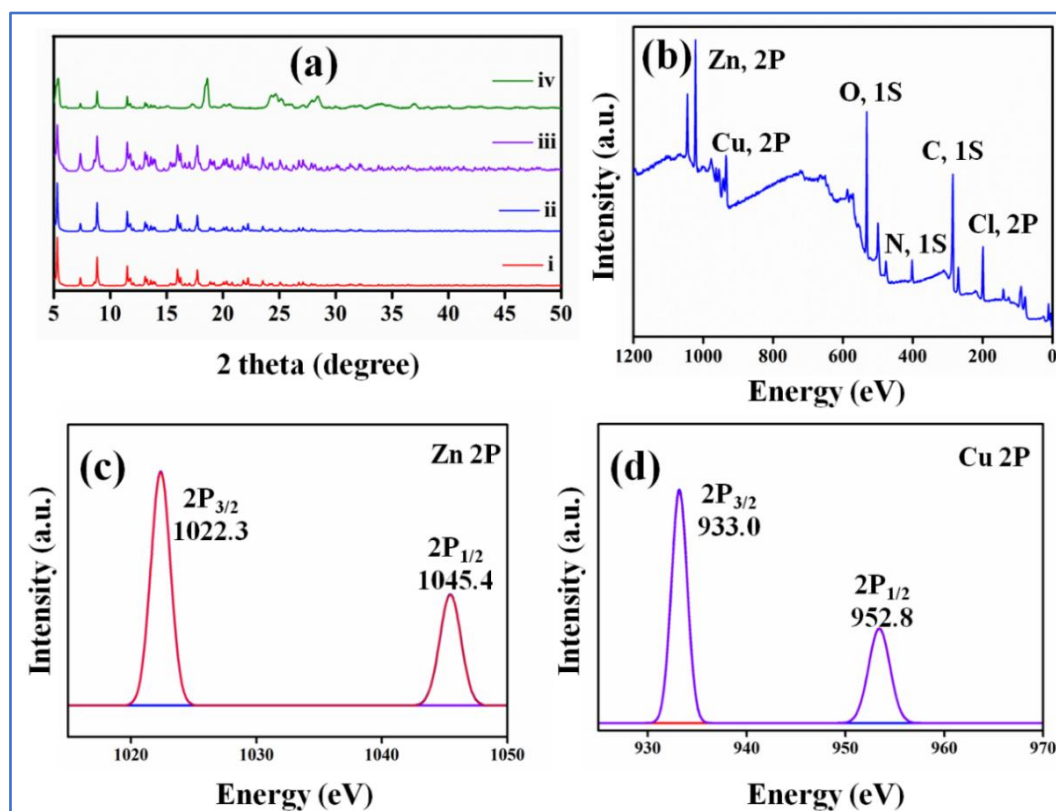


**Figure 1.** (a) PXRD patterns of NHC-MOF (i) simulated pattern, (ii) as-synthesized, (iii) Cu(I)@NHC-MOF, (iv) recycled sample of Cu(I)@NHC-MOF after ten catalytic cycles, X-ray photoelectron spectra for Cu(I)@NHC-MOF, (b) survey spectrum, (c) Zn 2P, and (d) Cu 2p spectrum.

### 5b.3.2. Gas adsorption studies

To determine the permanent porosity of Cu(I) embedded NHC-MOF, N<sub>2</sub> adsorption study was carried out at 77K. The N<sub>2</sub> adsorption-desorption isotherm shown in Figure 2a follows a typical type-I behaviour with an estimated BET surface area of 94 m<sup>2</sup>/g which was found to be about 35 m<sup>2</sup>/g lower than that of pristine NHC-MOF (129 m<sup>2</sup>/g). The reduction in the surface area of Cu(I)@NHC-MOF can be attributed to partial loss of porosity upon anchoring of Cu(I) ions at the NHC sites exposed in the pores of the MOF. Further, CO<sub>2</sub> adsorption isotherms follow a type-I behaviour with the uptake of 66 and 40 ccg<sup>-1</sup> at 273 and 298 K, respectively (Figure 2b), and the accurate prediction of CO<sub>2</sub> uptake at saturation was determined by using the Freundlich-Langmuir equation<sup>71</sup> (Figure A95 and A96). Furthermore, the interaction energy ( $Q_{st}$ ) of Cu(I)@NHC-MOF for CO<sub>2</sub> was further calculated using the Clausius-Clayperon equation<sup>72</sup> and was found to be 43 kJ/mol (Figure A97).

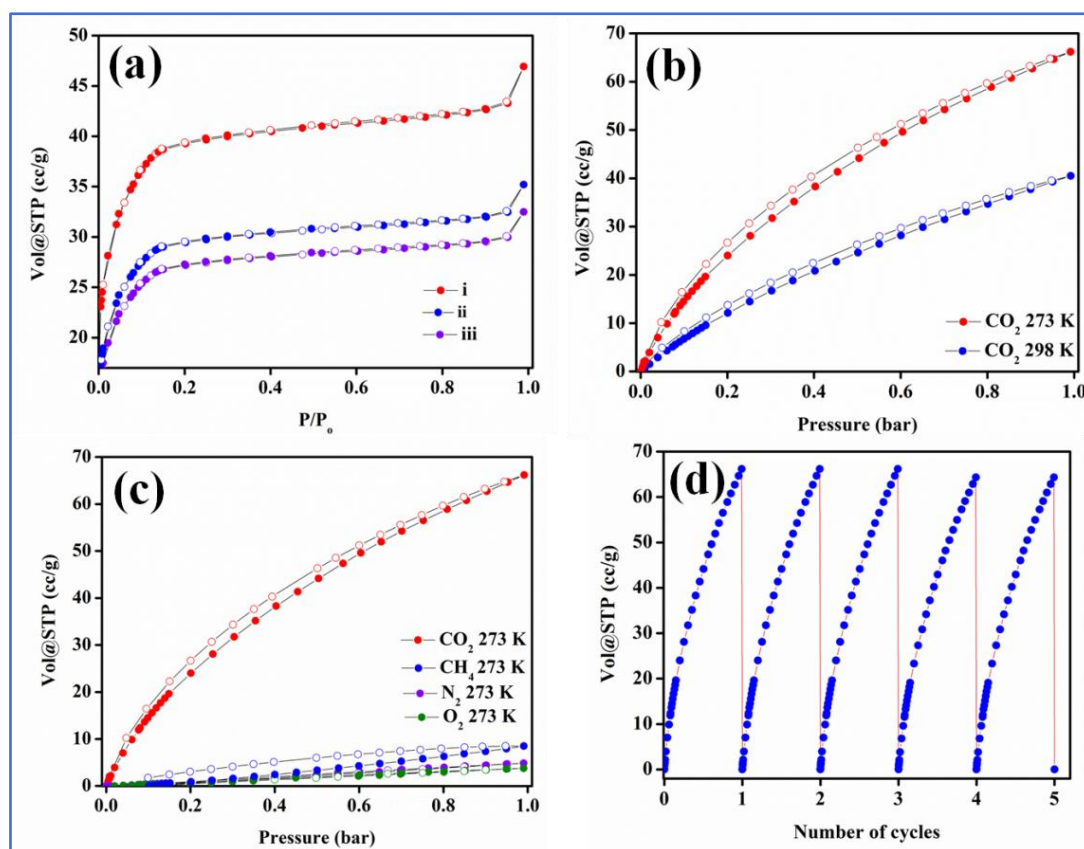


**Figure 2.** N<sub>2</sub> adsorption isotherms for (i) pristine NHC-MOF, (ii) Cu(I)@NHC-MOF, and (iii) Cu(I)@NHC-MOF after ten cycles of regeneration, (b) CO<sub>2</sub> adsorption isotherms of Cu(I)@NHC-MOF, (c) gas selectivity plot for Cu(I)@NHC-MOF, and (d) recyclability of CO<sub>2</sub> adsorption.

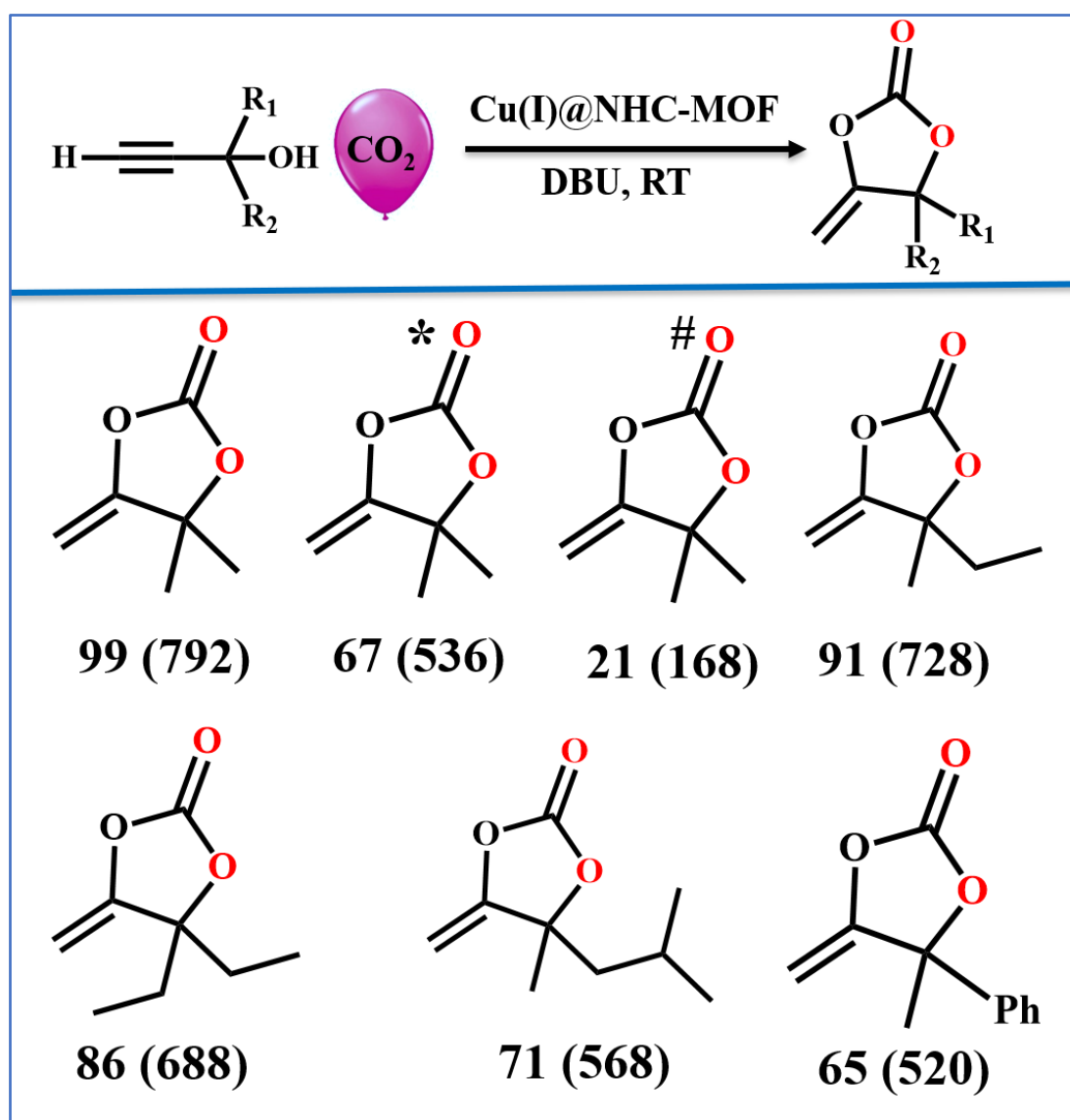
This high heat of interaction energy can be attributed to the stronger interaction of CO<sub>2</sub> with the basic NHC sites exposed in the 1D channels of the framework. Further, selective gas adsorption measurements of Cu(I)@NHC-MOF showed negligible uptake of N<sub>2</sub>, O<sub>2</sub>, and CH<sub>4</sub> (Figure 2C) with Henry gas selectivity constants of 60, 52, and 21 for CO<sub>2</sub>/N<sub>2</sub>, CO<sub>2</sub>/O<sub>2</sub>, and CO<sub>2</sub>/CH<sub>4</sub>, respectively (Figure A98). Notably, Cu(I)@NHC-MOF showed excellent recyclable CO<sub>2</sub> adsorption properties with retention of the adsorption capacity for several cycles (Figure 2d).

### 5b.3.3. Catalytic fixation of CO<sub>2</sub> with propargylic alcohols

The presence of CO<sub>2</sub>-philic NHC sites, as well as alkyno-philic Cu(I) sites in the 1D channels of the MOF, encouraged us to test the catalytic activity of Cu(I)@NHC-MOF for catalytic coupling of propargylic alcohols with CO<sub>2</sub>. To begin with, the catalytic activity was tested under mild conditions of RT and 1 atm (balloon) of CO<sub>2</sub> using 2-methyl-3-butyn-2-ol as a model substrate in presence of DBU (1,8-diazabicyclo-[5.4.0]-undec-7-ene). Interestingly, about 88 % of the alcohol was converted to the corresponding  $\alpha$ -alkylidene cyclic carbonates (4,4'-dimethyl-5-methylene-1,3-dioxolan-2-one) with 100% selectivity within 10h (Table A21). Further, with an increase in the reaction time to 12h, the catalytic conversion was increased to 99% (Table 1) indicating excellent catalytic activity of the Cu(I) anchored MOF. Interestingly, catalytic reactions carried out with pure Cu(NO<sub>3</sub>)<sub>2</sub>·6H<sub>2</sub>O, and NHC-MOF as catalysts did not show conversion of propargylic alcohol (Table A21). This observation demonstrates the necessity of Cu(I)-sites toward carboxylative cyclization of CO<sub>2</sub> with propargylic alcohols. Moreover, the Cu(I)@NHC-MOF showed superior catalytic activity over the homogeneous counterpart, CuCl (78 %) which can be attributed to the synergistic effect of CO<sub>2</sub>-philic NHC and catalytically active Cu(I) sites exposed in the 1D channels (Table A21). To check the practical application of the MOF catalyst, the catalytic activity was tested using simulated dry flue gas (CO<sub>2</sub>:N<sub>2</sub> = 13:87%) as a source of CO<sub>2</sub> and to our delight, the carboxylation of 2-Methyl-3-butyn-2-ol proceeded to yield the corresponding cyclic carbonate in 67% yield (Table A21). Furthermore, the catalytic activity was tested using laboratory air (bubbling) as a source of CO<sub>2</sub>, remarkably about 21% of the alcohol was converted to the corresponding cyclic carbonate under the mild conditions of RT and atmospheric pressure (Table A21). The aforementioned catalytic studies highlight the potential utility of Cu(I)@NHC-MOF for the capture and conversion of CO<sub>2</sub> into high-value chemicals under ambient conditions. Encouraged by the excellent catalytic activity of Cu(I)@NHC-MOF, the scope of the reaction was extended for other propargylic alcohols

under the optimized conditions (Table 1). Thus various propargylic alcohols were converted to the respective carbonates under the optimized mild conditions. Further, the catalytic activity was found to decrease with an increase in the size of the alcohols which can be attributed to restricted diffusion of the larger alcohols in the 1D pores of the MOF. It is worth highlighting that Cu(I)@NHC-MOF displayed superior catalytic activity in comparison to previously reported catalysts known for coupling of propargylic alcohols with CO<sub>2</sub> (Table 2).

**Table 1.** Cyclic carboxylation of propargylic alcohols under optimized conditions.<sup>a</sup>



Reaction conditions: <sup>a</sup>Propargylic alcohol (4 mmol), Cu(I)@NHC-MOF (0.005 mmol), DBU (0.05 equiv.), DMF (2 mL), RT, CO<sub>2</sub> (1 atm, balloon), 12 h. The values given in the parentheses correspond to TON. \*Simulated flue gas (13:87% = CO<sub>2</sub> : N<sub>2</sub>), # air (bubbled), and percentage conversion were determined by <sup>1</sup>H NMR analysis.

**Table 2.** Comparison of catalytic activity of Cu(I)@NHC-MOF for carboxylative cyclization of 2-methyl-3-butyn-2-ol with literature reported catalysts.

SL. No.	Catalyst	Active site	Temp. (°C)	Pressure (bar)	Yield (%)	Ref.
1	AgI, IL1	Ag(I)	45	1	93	73
2	Ag@RB-POP	Ag(0)	30	10	94	74
3	PAzo-POP-Ag	Ag(0)	25	10	95	75
4	TMOF-3-Ag	Ag(I)	30	1	99	76
5	MOF-SO <sub>3</sub> Ag	Ag(I)	25	1	>99	77
6	Cu-In-MOF	Cu(I)	50	5	99	78
7	V-Cu-MOF	Cu(I)	25	4	99	79
8	Dy-Cu MOF	Cu(I)	30	1	95	80
<b>9</b>	<b>Cu(I)@NHC-MOF</b>	<b>Cu(I)</b>	<b>25</b>	<b>1</b>	<b>&gt;99</b>	<b>This Work</b>

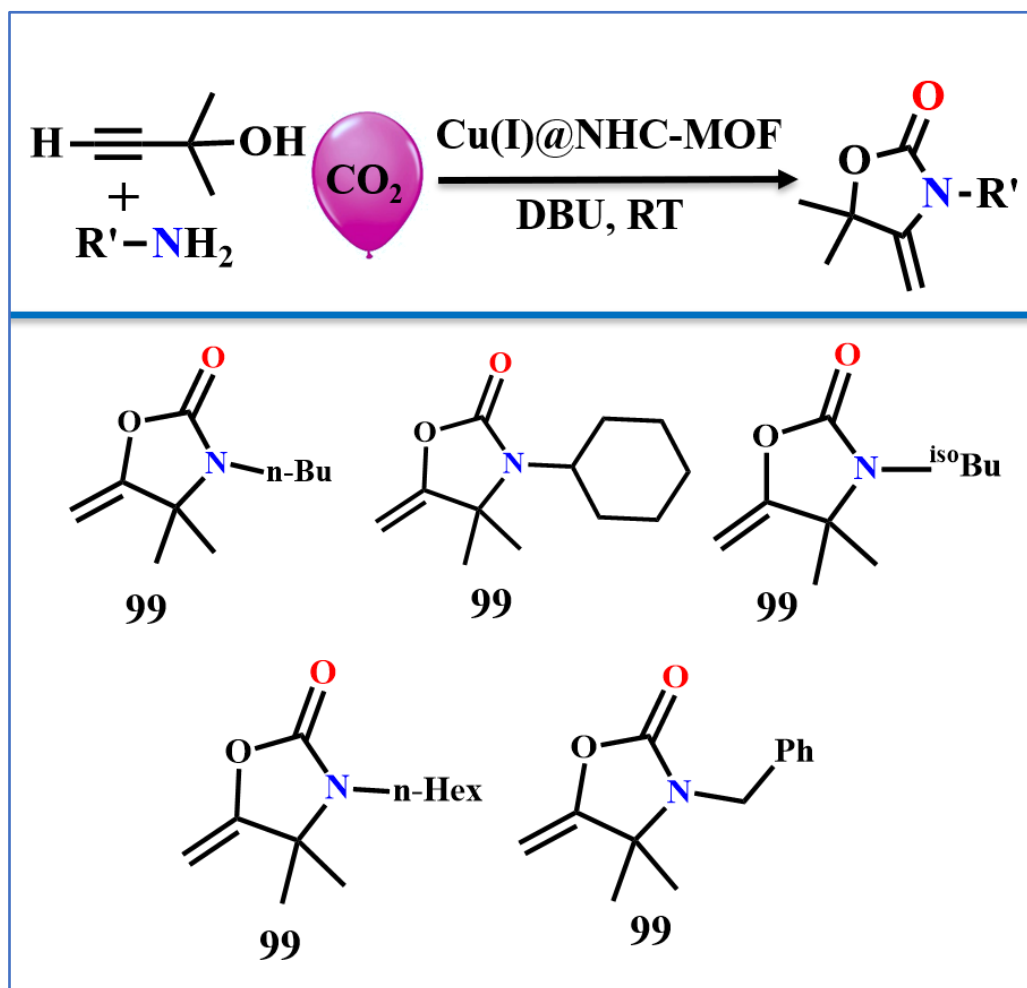
Motivated by the excellent catalytic activity of Cu(I)@NHC-MOF, the scope of the catalysis was further extended for the synthesis of oxazolidinones, important commodity chemicals for antibiotics through a one-pot reaction of CO<sub>2</sub>, primary amines, and propargylic alcohol. The catalytic activity was tested for carboxylation reaction of 2-methyl-1-butyn-3-ol with CO<sub>2</sub> in presence of n-butyl amine as a model substrate for amines under the optimized mild conditions of RT and 1 atm CO<sub>2</sub> (balloon). Interestingly, the reaction yielded the corresponding oxazolidinone in more than 99% yield within 12h. Further, the scope of the reaction was extended using various primary amines such as cyclohexylamine, isobutylamine, n-hexylamine, and benzylamine. All these reactions proceeded to yield the corresponding oxazolidinones with > 99% yield supporting the general scope of the reaction (Table 3). To the best of our knowledge, this work represents the first example of a noble metal-free heterogeneous catalyst known for the synthesis of value-added oxazolidinones under the mild conditions of RT and an atmospheric pressure of CO<sub>2</sub>.

#### 5b.3.4. Recyclability and catalyst leaching test

The catalyst stability and recyclability are important parameters for a heterogeneous catalyst. To test recyclability, Cu(I)@NHC-MOF was separated from the reaction mixture by simple centrifugation followed by washing with methanol and activated at 120 °C for 12 h

and reused for subsequent cycles. Remarkably, Cu(I)@NHC-MOF was recyclable up to ten cycles without significant loss in catalytic activity (Figure 3a). Further, the recycled sample after ten catalytic cycles was analyzed by various techniques to confirm its structural stability and phase purity.

**Table 3.** Three-component reaction of CO<sub>2</sub> with propargylic alcohol and primary amines catalyzed by Cu(I)@NHC-MOF under mild conditions.<sup>a</sup>



Reaction conditions: <sup>a</sup> propargylic alcohol (4 mmol), primary amines (4 mmol), Cu(I)@NHC-MOF (0.005 mmol), DMF (2 mL), DBU (0.05 equiv.), 25 °C, 12 h. The percentage of conversion was determined by <sup>1</sup>H NMR analysis.

The XRD pattern of the recycled sample matches with that of the parent sample supporting the retaining of the original structure even after catalysis. However, a slight broadening of the peaks in the range of 15-35 degrees can be attributed to a partial loss of crystallinity of the MOF catalyst due to its successive usage for ten catalytic cycles. Further,

FTIR and UV-Vis spectra of the recycled sample match with those of the parent sample (Figures A91, and A92). Besides, the N<sub>2</sub> adsorption isotherm of the recycled sample showed a BET surface area of 94 m<sup>2</sup>/g which is close to that of the as-synthesized sample (78 m<sup>2</sup>/g) supporting retention of the porous framework structure even after catalysis (Figure 2a). Further, SEM analysis of the recycled sample revealed that the rod-like morphology of the pristine MOF was almost retained even after ten catalytic cycles (Figure A94). Moreover, MP-AES analysis of filtrate of the catalytic reaction confirmed the absence of Zn(II)/Cu(I) ions which rules out the leaching of the active catalyst during the reaction (Figure A95).

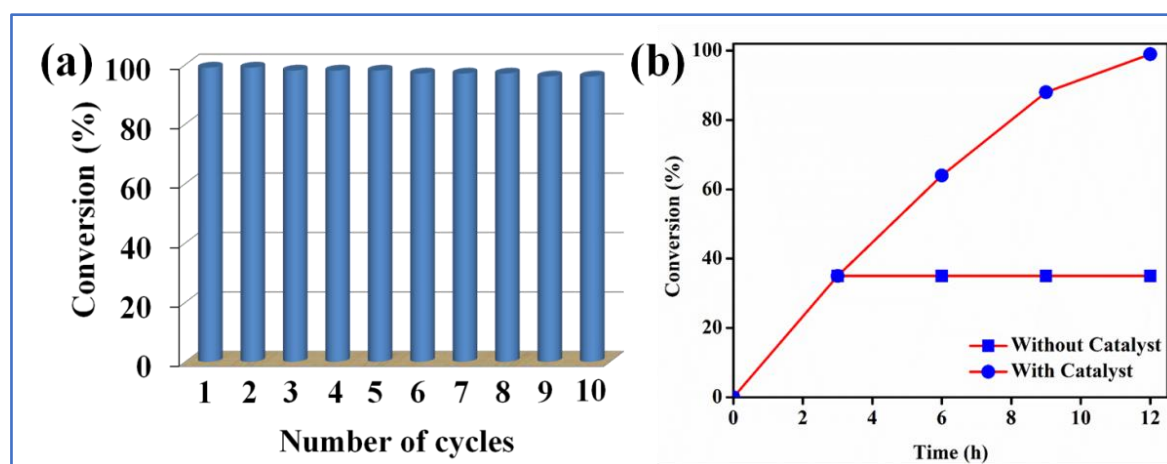
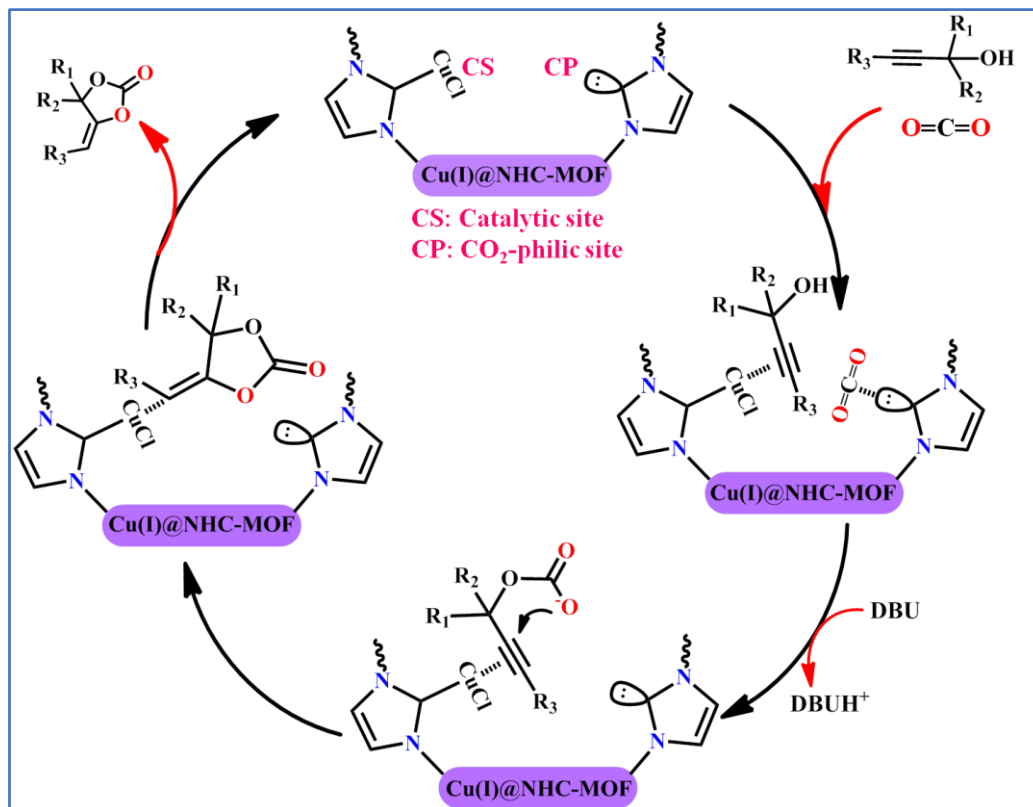


**Figure 3.** (a) Recyclability plot and (b) catalyst leaching test.

### 5b.3.5. Proposed mechanism

A plausible mechanism for the carboxylative cyclization of alkyne molecules catalyzed by Cu(I)@NHC-MOF is shown in Scheme 3. The first step involves the polarization of C≡C bond of alkyne by coordination to the Cu(I) site. To get further support on this step both pristine NHC-MOF and Cu(I)@NHC-MOF were treated with 2-methyl-3-butyn-2-ol for 1h and they were recovered by simple filtration and followed by washing with methanol five times. FT-IR spectra of recovered Cu(I)@NHC-MOF showed a characteristic peak at 2120 cm<sup>-1</sup> due to the C≡C bond of the alcohol coordinating with Cu(I) center. On the contrary, there was no peak corresponding to C≡C bond in the case of pure NHC-MOF, supporting the interaction of propargylic alcohol with the Cu(I) site in the functionalized framework (Figure A99). At the same time, the polarization of CO<sub>2</sub> takes place at the metal-free NHC centers exposed in the 1D channels.<sup>81</sup> Then, deprotonation of propargylic alcohol takes place in the presence of DBU (base) followed by CO<sub>2</sub> insertion and subsequent ring-closure reaction leads to the formation of  $\alpha$ -alkylidene cyclic carbonate. Finally, the

elimination of the product regenerates the active catalyst and the catalytic cycle continues. Whereas in the presence of primary amine added, the  $\alpha$ -alkylidene cyclic carbonate undergoes aminolysis resulting in the generation of oxazolidinone (Scheme A1).



**Scheme 3.** Plausible mechanism for carboxylative cyclization catalyzed by Cu(I)@NHC-MOF.

#### 5b.4. Conclusion

In summary, a rare demonstration of post-synthetic modification of NHC-based Zn(II)-MOF by Cu(I) ions to generate a noble metal-free, bifunctional heterogeneous catalyst exhibiting efficient catalytic activity for fixation of CO<sub>2</sub> to high-value chemicals is presented. The Cu(I)@NHC-MOF showed highly selective and recyclable CO<sub>2</sub> adsorption with high interaction energy. Remarkably, the MOF catalyst exhibits high stability and recyclability up to 10 cycles of regeneration. To the best of our knowledge, this work represents the first example of a noble metal-free MOF-based catalyst known for the highly efficient conversion of CO<sub>2</sub> into value-added chemicals like oxazolidinones under mild conditions. This study paves the way for the design of noble metal-free catalysts for the efficient fixation of CO<sub>2</sub> into high-value chemicals.

**5b.5. References**

- (1) Jacobson, M. Z. Review of solutions to global warming, air pollution, and energy security. *Energy Environ. Sci.* **2009**, *2*, 148-173.
- (2) Sakakura, T.; Choi, J. C.; Yasuda, H. Transformation of Carbon Dioxide. *Chem. Rev.* **2007**, *107*, 2365-2387.
- (3) He, H.; Perman, J. A.; Zhu, G.; Ma, S. Metal-Organic Frameworks for CO<sub>2</sub> Chemical Transformations. *Small*, **2016**, *12*, 6309-6324.
- (4) Tiba S.; Omri, A. Literature survey on the relationships between energy, environment and economic growth. *Renewable Sustainable Energy Rev.* **2017**, *69*, 1129-1146.
- (5) Ugale, B.; Dhankhar, S. S.; Nagaraja, C. M. Construction of 3-Fold-Interpenetrated Three-Dimensional Metal-Organic Frameworks of Nickel(II) for Highly Efficient Capture and Conversion of Carbon Dioxide. *Inorg. Chem.* **2016**, *55*, 9757-9766.
- (6) Liu, Q.; Wu, L.; Jackstell, R.; Beller, M. Using carbon dioxide as a building block in organic synthesis. *Nat. Commun.* **2015**, *6*, 5933.
- (7) Song, Q. -W.; Zhou, Z. -H.; He, L. -N. Efficient, selective and sustainable catalysis of carbon dioxide. *Green Chem.* **2017**, *19*, 3707-3728.
- (8) Yun, D.; Park, D. S.; Lee, K. R.; Yun, Y. S.; Kim, T. Y.; Park, H.; Lee, H.; Yi, J. A New Energy-Saving Catalytic System: Carbon Dioxide Activation by a Metal/Carbon Catalyst. *ChemSusChem* **2017**, *10*, 3671-3678.
- (9) Omae, I. Recent developments in carbon dioxide utilization for the production of organic chemicals. *Coord. Chem. Rev.* **2012**, *256*, 1384-1405.
- (10) Subudhi, S.; Rath, D.; Parida, K. M. A mechanistic approach towards the photocatalytic organic transformations over functionalised metal organic frameworks. *Catal. Sci. Technol.* **2018**, *8*, 679-696.
- (11) Sneddon, G.; Greenaway, A.; Yiu, H. H. P. The Potential Applications of Nanoporous Materials for the Adsorption, Separation, and Catalytic Conversion of Carbon Dioxide. *Adv. Energy Mater.* **2014**, *4*, 1301873.
- (12) Yaashikaa, P. R.; Kumar, P. S.; Varjani, S. J.; Saravanan, A. A review on photochemical, biochemical and electrochemical transformation of CO<sub>2</sub> into value-added products. *J. CO<sub>2</sub> Util.* **2019**, *33*, 131-147.
- (13) Bhanja, P.; Modak, A.; Bhaumik, A. Supported Porous Nanomaterials as Efficient Heterogeneous Catalysts for CO<sub>2</sub> Fixation Reactions. *Chem. Eur. J.* **2018**, *24*, 7278-7297

- (14) Dutta, G.; Jana, A. K.; Singh, D. K.; Eswaramoorthy, M.; Natarajan, S. Encapsulation of Ag-nanoparticle in an Amine-Functionalized Porphyrin MOF and its Use as a Heterogeneous Catalyst for CO<sub>2</sub> Fixation under Atmospheric Pressure. *Chem. Asian J.* **2018**, *13*, 2677-2684.
- (15) Zhang, G.; Wei, G.; Liu, Z.; Oliver, S. R. J.; Fei, H. A Robust Sulfonate-Based Metal Organic Framework with Permanent Porosity for Efficient CO<sub>2</sub> Capture and Conversion. *Chem. Mater.* **2016**, *28*, 17, 6276-6281.
- (16) Yang, H.; Zhang, X.; Zhang, G.; Fei, H. An Alkaline Resistant Ag(I)-Anchored Pyrazolate-Based Metal-Organic Framework for Chemical Fixation of CO<sub>2</sub>. *Chem. Comm.* **2018**, *54*, 4469-4472.
- (17) Dhankhar, S. S.; Ugale, B.; Nagaraja, C. M. Co-Catalyst-Free Chemical Fixation of CO<sub>2</sub> into Cyclic Carbonates by using Metal-Organic Frameworks as Efficient Heterogeneous Catalysts. *Chem. Asian J.* **2020**, *15*, 2403-24.
- (18) Dhankhar, S. S.; Das, R.; Ugale, B.; Pillai, R. S.; Nagaraja, C. M. Chemical Fixation of CO<sub>2</sub> Under Solvent and Co-Catalyst-free Conditions Using a Highly Porous Two-fold Interpenetrated Cu(II)-Metal–Organic Framework. *Cryst. Growth Des.* **2021**, *21*, 1233-1241.
- (19) Sharma, N.; Dhankhar, S. S.; Nagaraja, C. M. Environment-friendly, co-catalyst- and solventfree fixation of CO<sub>2</sub> using an ionic zinc(II)– porphyrin complex immobilized in porous metal– organic frameworks. *Sustain. Energy Fuels* **2019**, *3*, 2977-2982.
- (20) Sharma, N.; Dhankhar, S. S.; Kumar, S.; Kumar, T. J. D.; Nagaraja, C. M. Rational Design of a 3D Mn<sup>II</sup>-Metal–Organic Framework Based on a Nonmetallated Porphyrin Linker for Selective Capture of CO<sub>2</sub> and One-Pot Synthesis of Styrene Carbonates. *Chem. Eur. J.* **2018**, *24*, 16662-16669.
- (21) Jones, W. D. Carbon Capture and Conversion. *J. Am. Chem. Soc.* **2020**, *142*, 4955-4957.
- (22) Sen, R.; Goeppert, A.; Kar, S.; Prakash, G. K. S. Hydroxide Based Integrated CO<sub>2</sub> Capture from Air and Conversion to Methanol. *J. Am. Chem. Soc.* **2020**, *142*, 4544–4549.
- (23) Wu, X.; Li, Y.; Zhang, G.; Chen, H.; Li, J.; Wang, K.; Pan, Y.; Zhao, Y.; Sun, Y.; Xie, Y. Photocatalytic CO<sub>2</sub> Conversion of M<sub>0.33</sub>WO<sub>3</sub> Directly from the Air with High Selectivity: Insight into Full Spectrum-Induced Reaction Mechanism. *J. Am. Chem. Soc.* **2019**, *141*, 5267-5274.
- (24) Dhakshinamoorthy, A.; Garcia, Z.; Li, H. Catalysis and photocatalysis by metal organic frameworks. *Chem. Soc. Rev.* **2018**, *47*, 8134-8172.
- (25) Pal, T. K.; De, D.; Bhardwaj, P. K. Metal-organic frameworks for the chemical fixation of CO<sub>2</sub> into cyclic carbonates. *Coord. Chem. Rev.* **2020**, *408*, 213173.

- (26) Ninokata, R.; Yamahira, T.; Onodera, G.; Kimura, M. Nickel-Catalyzed CO<sub>2</sub> Rearrangement of Enol Metal Carbonates for the Efficient Synthesis of  $\beta$ -Ketocarboxylic Acids. *Angew. Chem. Int. Ed.* **2017**, *56*, 208-211.
- (27) Fukuoka, S.; Kawamura, M.; Komiya, K.; Tojo, M.; Hachiya, H.; Hasegawa, K.; Aminaka, M.; Okamoto, H.; Fukawa, I.; Konno, S. A novel non-phosgene polycarbonate production process using by-product CO<sub>2</sub> as starting material. *Green Chem.* **2003**, *5*, 497-507.
- (28) Ding, X. B.; Furkert, D. P.; Brimble, M. A. General Synthesis of the Nitropyrrolin Family of Natural Products via Regioselective CO<sub>2</sub>-Mediated Alkyne Hydration. *Org. Lett.* **2017**, *19*, 5418-5421.
- (29) Gennen, S.; Grignard, B.; Tassaing, T.; Jerome, C.; Detrembleur, C. CO<sub>2</sub>-Sourced  $\alpha$ -Alkylidene Cyclic Carbonates: A Step Forward in the Quest for Functional Regioregular Poly(urethane)s and Poly(carbonate)s. *Angew. Chem. Int. Ed.* **2017**, *56*, 10394-10398.
- (30) Komatsuki, K.; Sadamitsu, Y.; Sekine, K.; Saito, K.; Yamada, T. Stereospecific Decarboxylative Nazarov Cyclization Mediated by Carbon Dioxide for the Preparation of Highly Substituted 2-Cyclopentenones. *Angew. Chem. Int. Ed.* **2017**, *56*, 11594-11598.
- (31) Diekema, D. J.; Jones, R. N. Lancet, Oxazolidinone antibiotics. **2001**, *358*, 1975-1982.
- (32) Kikuchi, S.; Sekine, K.; Ishida, T.; Yamada, T. C-C Bond Formation with Carbon Dioxide Promoted by a Silver Catalyst. *Angew. Chem. Int. Ed.* **2012**, *51*, 6989-6992.
- (33) Song, Q.-W.; Chen, W.-Q.; Ma, R.; Yu, A.; Li, Q.-Y.; Chang, Y.; He, L.-N. Bifunctional Silver(I) Complex-Catalyzed CO<sub>2</sub> Conversion at Ambient Conditions: Synthesis of a Methylene Cyclic Carbonates and Derivatives. *ChemSusChem* **2015**, *8*, 821-827.
- (34) Song, Q.-W.; He, L.-N. Robust Silver(I) Catalyst for the Carboxylative Cyclization of Propargylic Alcohols with Carbon Dioxide under Ambient Conditions. *Adv. Synth. Catal.* **2016**, *358*, 1251-1258.
- (35) Song, Q.-W.; Zhou, Z.-H.; Yin, H.; He, L.-N. Silver(I)-Catalyzed Synthesis of  $\beta$ -Oxopropylcarbamates from Propargylic Alcohols and CO<sub>2</sub> Surrogate: A Gas-Free Process. *ChemSusChem* **2015**, *8*, 3967-3972.
- (36) Zhou, H.-C.; Long, J. R.; Yaghi, O. M. Introduction to Metal-Organic Frameworks. *Chem. Rev.* **2012**, *112*, 673-674.
- (37) Zhou, H.-C.; Kitagawa, S. Metal-Organic Frameworks (MOFs). *Chem. Soc. Rev.* **2014**, *43*, 5415-5418.
- (38) Zhao, Y. Emerging Applications of Metal-Organic Frameworks and Covalent Organic Frameworks. *Chem. Mater.* **2016**, *28*, 8079-8081.

- (39) Liu, J.; Chen, L.; Cui, H.; Zhang, J.; Zhang, L.; Su, C. Y. Applications of metal–organic frameworks in heterogeneous supramolecular catalysis. *Chem. Soc. Rev.* **2014**, *43*, 6011-6061.
- (40) Corma, A.; García, H.; Xamena, F. X. L. Engineering Metal Organic Frameworks for Heterogeneous Catalysis. *Chem. Rev.* **2010**, *110*, 4606-4655.
- (41) Li, J. R.; Sculley, J.; Zhou, H. C. Metal–Organic Frameworks for Separations. *Chem. Rev.* **2012**, *112*, 869-932.
- (42) Wen, H. M.; Wang, H.; Li, B.; Cui, Y.; Wang, H.; Qian, G.; Chen, B. A Microporous Metal-Organic Framework with Lewis Basic Nitrogen Sites for High C<sub>2</sub>H<sub>2</sub> Storage and Significantly Enhanced C<sub>2</sub>H<sub>2</sub>/CO<sub>2</sub> Separation at Ambient Conditions. *Inorg. Chem.* **2016**, *55*, 7214-7218.
- (43) Yu, J.; Xie, L.-H.; Li, J.-R.; Ma, Y.; Seminario, J. M.; Balbuena, P. B. CO<sub>2</sub> Capture and Separations Using MOFs: Computational and Experimental Studies. *Chem. Rev.* **2017**, *117*, 9674-9754.
- (44) Wilson, M.; Palomo, S. N. B.; Stevens, P. C.; Mitchell, N. L.; Oswald, G.; Nagaraja, C. M.; Badyal, J. P. S. Substrate-Independent Epitaxial Growth of the Metal-Organic Framework MOF-508a. *ACS Appl. Mater. Interfaces* **2018**, *10*, 4057-4065.
- (45) Das, R.; Muthukumar, D.; Pillai, R. S.; Nagaraja, C. M. Rational Design of a Zn<sup>II</sup> MOF with Multiple Functional Sites for Highly Efficient Fixation of CO<sub>2</sub> under Mild Conditions: Combined Experimental and Theoretical Investigation. *Chem. Eur. J.* **2020**, *26*, 17445-17454.
- (46) Liang, J.; Huang, Y. -B.; Cao, R. Metal-organic frameworks and porous organic polymers for sustainable fixation of carbon dioxide into cyclic carbonates. *Coord. Chem. Rev.* **2019**, *378*, 32-65.
- (47) Cui, W.-G.; Zhang, G.-Y.; Hu, T.-L.; Bu, X.-H. Metal-organic framework-based heterogeneous catalysts for the conversion of C1 chemistry: CO, CO<sub>2</sub> and CH<sub>4</sub>. *Coord. Chem. Rev.* **2019**, *387*, 79-120.
- (48) Trickett, C. A.; Helal, A.; Al-Maythaly, B. A.; Yamani, Z. H.; Cordova, K. E.; Yaghi, O. M. The chemistry of metal organic frameworks for CO<sub>2</sub> capture, regeneration and conversion. *Nat. Rev. Mater.* **2017**, *2*, 17045.
- (49) Dhankhar, S. S.; Sharma, N.; Kumar, S.; Kumar, T. J. D.; Nagaraja, C. M. Rational Design of a Bifunctional, Two-Fold Interpenetrated Zn<sup>II</sup>-Metal-Organic Framework for Selective Adsorption of CO<sub>2</sub> and Efficient Aqueous Phase Sensing of 2,4,6-Trinitrophenol. *Chem. Eur. J.* **2017**, *23*, 16204-16212.

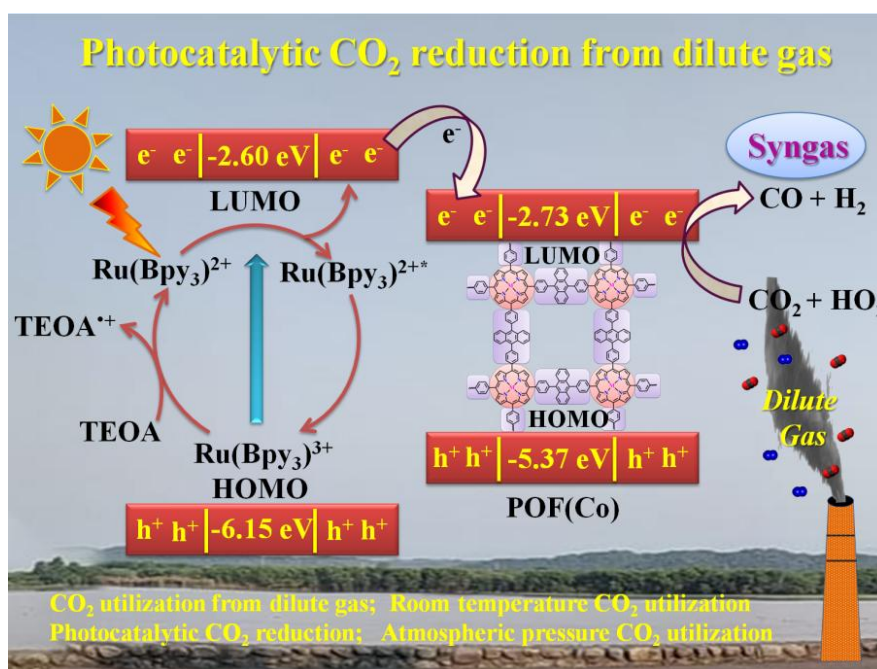
- (50) Ding, M.; Flaig, R. W.; Jiang, H.-L.; Yaghi, O. M. Carbon capture and conversion using metal-organic frameworks and MOF-based materials. *Chem. Soc. Rev.* **2019**, *48*, 2783-2828.
- (51) Kamphuis, A. J.; Picchioni, F.; Pescarmona, P. P. CO<sub>2</sub>-fixation into cyclic and polymeric carbonates: principles and applications. *Green Chem.* **2019**, *21*, 406-448.
- (52) Das, R.; Dhankhar, S. S.; Nagaraja, C. M. Construction of a bifunctional Zn(II)-organic framework containing a basic amine functionality for selective capture and room temperature fixation of CO<sub>2</sub>. *Inorg. Chem. Front.* **2020**, *7*, 72-81.
- (53) Aguila, B.; Sun, Q.; Wang, X.; Rourke, E. O. Q.; Enizi, A. M. A.; Nafady, A.; Ma, S. Lower Activation Energy for Catalytic Reactions through Host-Guest Cooperation within Metal-Organic Frameworks. *Angew. Chem. Int. Ed.* **2018**, *57*, 10107-10111.
- (54) Ugale, B.; Kumar, S.; Kumar, T. J. D.; Nagaraja, C. M. Environmentally Friendly, Co-catalyst-Free Chemical Fixation of CO<sub>2</sub> at Mild Conditions Using Dual-Walled Nitrogen-Rich Three-Dimensional Porous Metal-Organic Frameworks. *Inorg. Chem.* **2019**, *58*, 3925-3936.
- (55) Zhou, Z.; He, C.; Xiu, J.; Yang, L.; Duan, C. Metal-organic polymers containing discrete single-walled nanotube as a heterogeneous catalyst for the cycloaddition of carbon dioxide to epoxides. *J. Am. Chem. Soc.* **2015**, *137*, 15066-15069.
- (56) Nguyen, P. T. K.; Nguyen, H. T. D.; Nguyen, H. N.; Trickett, C. A.; Ton, Q. T.; -Puebla, E. G.; Monge, M. A.; Cordova, K. E.; Gandara, F. New metal-organic frameworks for chemical fixation of CO<sub>2</sub>. *ACS Appl. Mater. Interfaces* **2018**, *10*, 733-744.
- (57) Song, Q.-W.; Yu, B.; Li, X.-D.; Ma, R.; Diao, Z.-F.; Li, R.-G.; Li, W.; He, L.-N. Efficient chemical fixation of CO<sub>2</sub> promoted by a bifunctional Ag<sub>2</sub>WO<sub>4</sub>/Ph<sub>3</sub>P system. *Green Chem.* **2014**, *16*, 1633-1638.
- (58) Kayaki, Y.; Yamamoto, M.; Ikariya, T. Stereoselective Formation of  $\alpha$ -Alkylidene Cyclic Carbonates via Carboxylative Cyclization of Propargyl Alcohols in Supercritical Carbon Dioxide. *J. Org. Chem.* **2007**, *72*, 647-649.
- (59) Letinois, U. H.; Weibel, J. M.; Pale, P. The organic chemistry of silver acetylides. *Chem. Soc. Rev.* **2007**, *36*, 759-769.
- (60) Karmakar, R.; Lee, D. Reactions of arynes promoted by silver ions. *Chem. Soc. Rev.* **2016**, *45*, 4459-4470.
- (61) Kikuchi, S.; Sekine, K.; Ishida, T.; Yamada, T. C-C Bond Formation with Carbon Dioxide Promoted by a Silver Catalyst. *Angew. Chem. Int. Ed.* **2012**, *51*, 6989-6992.

- (62) Song, Q.-W.; Chen, W.-Q.; Ma, R.; Yu, A.; Li, Q.-Y.; Chang, Y.; He, L.-N. Bifunctional Silver(I) Complex-Catalyzed CO<sub>2</sub> Conversion at Ambient Conditions: Synthesis of a Methylene Cyclic Carbonates and Derivatives. *ChemSusChem* **2015**, *8*, 821-827.
- (63) Song, Q.-W.; He, L.-N. Robust Silver(I) Catalyst for the Carboxylative Cyclization of Propargylic Alcohols with Carbon Dioxide under Ambient Conditions. *Adv. Synth. Catal.* **2016**, *358*, 1251-1258.
- (64) Song, Q.-W.; Zhou, Z.-H.; Yin, H.; He, L.-N. Silver(I)-Catalyzed Synthesis of  $\alpha$ -Oxopropylcarbamates from Propargylic Alcohols and CO<sub>2</sub> Surrogate: A Gas-Free Process. *ChemSusChem* **2015**, *8*, 3967-3972.
- (65) Jacquet, O.; Das, C.; Gomes, N.; Ephritikhine, M.; Cantat, T. Recycling of Carbon and Silicon Wastes: Room Temperature Formylation of N-H Bonds Using Carbon Dioxide and Polymethylhydrosiloxane. *J. Am. Chem. Soc.* **2012**, *134*, 2934-2937.
- (66) Das, S.; Bobbink, F. D.; Laurency, G.; Dyson, P. J. Metal-Free Catalyst for the Chemoselective Methylation of Amines Using Carbon Dioxide as a Carbon Source. *Angew. Chem.* **2014**, *53*, 12876-12879.
- (67) Wu, C.; Irshad, F.; Luo, M.; Zhao, Y.; Ma, X.; Wang, S. Ruthenium Complexes Immobilized on an Azolium Based Metal Organic Framework for Highly Efficient Conversion of CO<sub>2</sub> into Formic Acid. *ChemCatChem* **2019**, *11*, 1256-1263.
- (68) Zhanga L.; Hou, Z. N-Heterocyclic carbene (NHC)-copper-catalysed transformations of carbon dioxide. *Chem. Sci.* **2013**, *4*, 3395-3403.
- (69) Sen, S.; Nair, N. N.; Yamada, T.; Kitagawa, H.; Bharadwaj, P. K. High Proton Conductivity by a Metal-Organic Framework Incorporating Zn<sub>8</sub>O Clusters with Aligned Imidazolium Groups Decorating the Channels. *J. Am. Chem. Soc.* **2012**, *134*, 19432-19437.
- (70) Zhang, X.; Jiang, Y.; Fei, H. UiO-type metal-organic frameworks with NHC or metal-NHC functionalities for N-methylation using CO<sub>2</sub> as the carbon source. *Chem. Commun.* **2019**, *55*, 11928-11931.
- (71) Yang, R. T. *Gas Separation by Adsorption Processes*, Butterworth, Boston, **1997**.
- (72) Pan, H.; Ritter, J. A.; Balbuena, P. B. Examination of the Approximations Used in Determining the Isothermic Heat of Adsorption from the Clausius-Clapeyron Equation. *Langmuir* **1998**, *14*, 6323-6327.
- (73) Yuan, Y.; Xie, Y.; Zeng, C.; Song, D.; Chaemchuen, S.; Chen, C.; Verpoort, F. recyclable AgI/OAc- catalytic system for the efficient synthesis of  $\alpha$ -alkylidene cyclic carbonates: carbon dioxide conversion at atmospheric pressure. *Green Chem.* **2017**, *19*, 2936-2940.

- (74) Yu, X.; Yang, Z.; Zhang, F.; Liu, Z.; Yang, P.; Zhang, H.; Yu, B.; Zhao, Y.; Liu, Z. A rose bengal-functionalized porous organic polymer for carboxylative cyclization of propargyl alcohols with CO<sub>2</sub>. *Chem. Commun.* **2019**, 55, 12475-12478.
- (75) Yang, Z.; Yu, B.; Zhang, H.; Zhao, Y.; Chen, Y.; Ma, Z.; Ji, G.; Gao, X.; Han, B.; Liu, Z. Metalated Mesoporous Poly(triphenylphosphine) with Azo Functionality: Efficient Catalysts for CO<sub>2</sub> Conversion. *ACS Catal.* **2016**, 6, 1268-1273.
- (76) Zhang, G.; Yang, H.; Fei, H. Unusual Missing Linkers in an Organosulfonate-Based Primitive- Cubic (pcu)-Type Metal-Organic Framework for CO<sub>2</sub> Capture and Conversion under Ambient Conditions. *ACS Catal.* **2018**, 8, 2519-2525.
- (77) Das, R.; Nagaraja, C. M. Highly Efficient Fixation of Carbon Dioxide at RT and Atmospheric Pressure Conditions: Influence of Polar Functionality on Selective Capture and Conversion of CO<sub>2</sub>. *Inorg. Chem.* **2020**, 59, 9765-9773.
- (78) Hou, S.-L.; Dong, J.; Jiang, X.-L.; Jiao, Z.-H.; Zhao, B. A Noble-Metal-Free Metal-Organic Framework (MOF) Catalyst for the Highly Efficient Conversion of CO<sub>2</sub> with Propargylic Alcohols. *Angew. Chem. Int. Ed.* **2019**, 58, 577-581.
- (79) Tian, H.-R.; Zhang, Z.; Liu, S.-M.; Dang, T.-Y.; Li, Z.; Lu, Y.; Liu, S.-X. A highly stable polyoxovanadate-based Cu(I)-MOF for the carboxylative cyclization of CO<sub>2</sub> with propargylic alcohols at room temperature. *Green Chem.* **2020**, 22, 7513-7520.
- (80) Wu, Z.; Lan, X.; Zhang, Y.; Lia, M.; Bai, G. Copper(I) iodide cluster-based lanthanide organic frameworks: synthesis and application as efficient catalysts for carboxylative cyclization of propargyl alcohols with CO<sub>2</sub> under mild conditions. *Dalton Trans.* **2019**, 48, 11063-11069.
- (81) Yu, D.; Zhang, Y. Copper- and copper-N-heterocyclic carbene-catalyzed C-H activating carboxylation of terminal alkynes with CO<sub>2</sub> at ambient conditions. *PNAS*, **2010**, 107, 20184-20189.

# Chapter 6

## Rational design of 2D Co(II)-porphyrin framework for efficient visible light-promoted reduction of CO<sub>2</sub> from dilute gas: Combined experimental and theoretical investigation





## 6.1. Introduction

The rapid rise in global energy demand has led to increased use of fossil fuel-based resources which are contributing to atmospheric CO<sub>2</sub> emissions.<sup>1</sup> Therefore, it is of urgent need to mitigate this increasing carbon dioxide concentration by capturing and utilizing it as a C1 source for generation of value-added products and fuels.<sup>2-5</sup> Especially, flue gases from power plants and industrial emissions add substantially to the rise of atmospheric CO<sub>2</sub> concentration.<sup>6,7</sup> Thus direct fixation of flue gas/dilute gas (13% CO<sub>2</sub>) into valuable chemicals provides potential benefits. However, fixing carbon dioxide at such low concentrations and in the presence of large amounts of N<sub>2</sub> (87%) necessitates a highly active catalyst having good CO<sub>2</sub>-philicity and catalytic activity.<sup>8</sup> Among the diverse transformations of CO<sub>2</sub>, the generation of syngas (a mixture of CO and H<sub>2</sub>), an important raw material for fuel/methanol production through the Fisher-Tropsch process is of potential significance.<sup>9,10</sup> Thus an integrated approach of CO<sub>2</sub> reduction coupled with H<sub>2</sub> generation by water splitting utilizing visible light/sunlight represents a promising step towards sustainable generation of energy and environmental remediation.<sup>11-14</sup> Moreover, the eco-friendly, photocatalytic route is proven to be advantageous over thermal or electrochemical methods for the controlled generation of syngas.<sup>15-17</sup> However, majority of photocatalytic materials are active in the UV region which makes up only about 4% of sunlight. Hence, the design of efficient photocatalytic materials which are active in visible light facilitates effective sunlight harvesting (~40%).<sup>18,19</sup> In this regard, porphyrins and metalloporphyrins have gained significant interest owing to their photoredox properties along with strong absorption of visible light and high quantum yield.<sup>20,21</sup> Further, transforming the porphyrin monomers into extended 2D/3D frameworks trounces their aggregation-related limitations and renders them highly efficient photocatalytic materials.<sup>22,23</sup> Thus, combining the unique features of porphyrins with suitable red-ox active metal ion with optimum CO<sub>2</sub> reduction and H<sub>2</sub> generation potential render promising photocatalytic materials for effective utilization of carbon dioxide for fine chemicals synthesis.<sup>24-26</sup>

Keeping these points, in this chapter we report construction of porphyrin-based porous, rigid framework, POF(Co) constituted by catalytically active single atom Co<sup>II</sup> sites anchored on CO<sub>2</sub>-philic 2D framework. Indeed, POF(Co) showed excellent photocatalytic activity for reduction of CO<sub>2</sub> to CO with a rate of 7165 μmol/g under visible light irradiation. Besides, the competing water-splitting reaction to hydrogen generation took place at a rate of 26515 μmol/g. Notably, POF(Co) catalyzed the conversion of CO<sub>2</sub> even from dilute gas with a CO generation rate of 1657 μmol/g. Interestingly, the analogues POF(Zn) showed

negligible activity for the generation of syngas with CO/H<sub>2</sub> yield of 18/53 μmol/g highlighting the importance of Co<sup>II</sup> for the combined CO<sub>2</sub> reduction (CO<sub>2</sub>R) and H<sub>2</sub> evolution reaction (HER). The superior performance of POF(Co) has been ascribed to favorable band structure promoting facile transfer of photo-excited electron from [Ru(Bpy)<sub>3</sub>]<sup>2+</sup> sensitizer to Co<sup>II</sup> catalytic site. Whereas, the electron transfer to Zn<sup>II</sup> is hindered due to the higher LUMO energy unveiled from detailed theoretical investigation. Overall, this work showcases a novel demonstration of light-promoted CO<sub>2</sub>R and HER for the controlled generation of syngas under eco-friendly mild conditions.

## 6.2. Experimental section

### 6.2.1. Materials

All the reagents used in this work were commercially available and used as received without any further purification. Co(CH<sub>3</sub>COO)<sub>2</sub>.4H<sub>2</sub>O, Zn(CH<sub>3</sub>COO)<sub>2</sub>.4H<sub>2</sub>O, pyrrole, and 4-bromobenzaldehyde were purchased from Sigma Aldrich Chemical Co. Propionic acid, 9,10-bis(4,4,5,5-tetramethyl-1,3,2-dioxaborolan-2-yl)anthracene, and Pd(PPh<sub>3</sub>)<sub>4</sub> were purchased from TCI chemicals.

### 6.2.2. Physicochemical characterization

The UV-Vis (Diffuse Reflectance) spectra were recorded on the Shimadzu spectrophotometer using BaSO<sub>4</sub> as a reference. Thermogravimetric analysis (TGA) of the compounds was carried out on Metler Toledo Thermogravimetric analyzer in an inert (N<sub>2</sub>) atmosphere with a flow rate of 30 mL/min in the temperature range of 30–600 °C and a heating rate of 5 °C/min. FTIR (Fourier transform infrared) spectra of the samples were recorded from 400 to 4000 cm<sup>-1</sup> on a Perkin Elmer ATR-FTIR spectrometer. Gas adsorption studies were carried out on Quantachrome QUADRASORB-SI automatic volumetric instrument. The CO and H<sub>2</sub> yield was monitored by gas chromatography (Agilent 7890B, Agilent Technologies) equipped with TCD and FID.

### 6.2.3. Synthesis

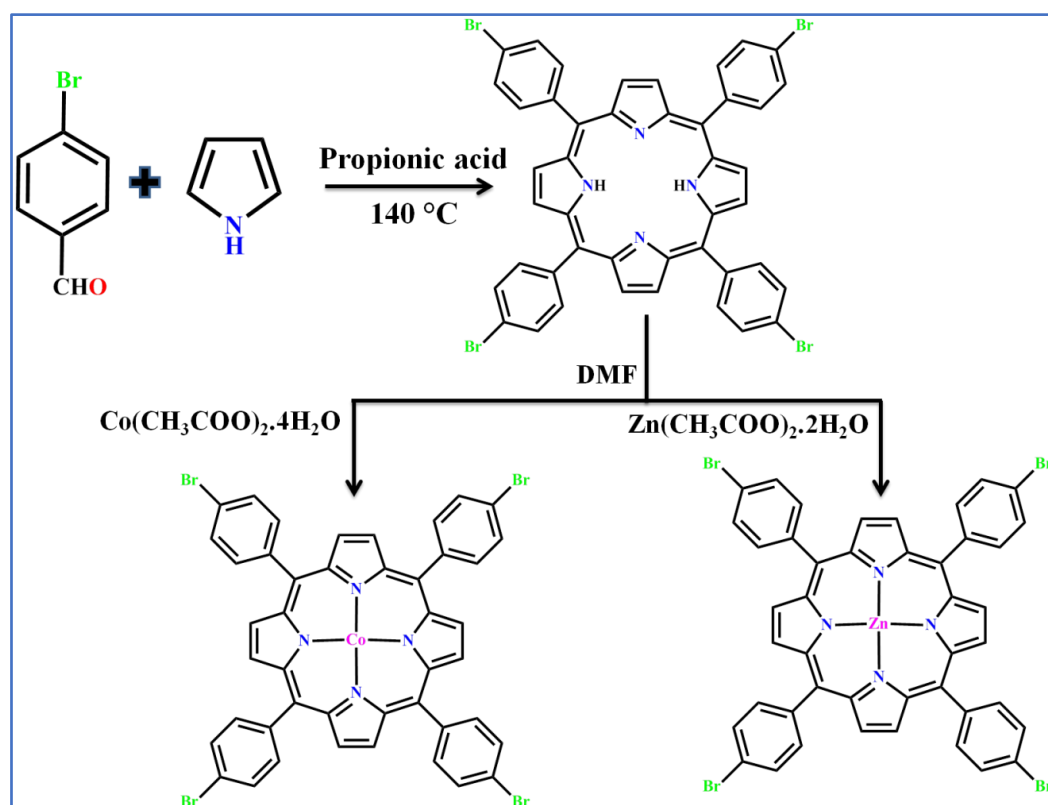
#### 6.2.3.1. Synthesis of 5, 10, 15, 20-tetrakis (4-bromophenyl) porphyrin (TBPP(H<sub>2</sub>))

In a 250-mL round bottom flask, methyl 4-bromobenzaldehyde (5.0 g, 27 mmol) was added to 100 mL of propionic acid. To this solution, 27 mmol (1.867 mL) pyrrole was added dropwise and the solution was refluxed at 140 °C for 12h (Scheme 1). Then the reaction

mixture was cooled down to room temperature and poured into 150 mL methanol, stirred in an ice bath for 30 min. The resulting precipitate was filtered and washed with methanol thoroughly until the filtrate becomes a clear solution. Subsequently, the product was washed with warmed water and methanol and dried at 100 °C under vacuum to obtain a purple solid (32 % yield).  $^1\text{H NMR}$  (400 MHz,  $\text{CDCl}_3$ )  $\delta$ : 8.84 (s, 8H), 8.07 (d, 8H), 7.91 (d, 8H), -2.87 (s, 2H).

### 6.2.3.2. Synthesis of 5, 10, 15, 20-tetrakis (4-bromophenyl) Zn/Co(II) porphyrin (TBPP(Zn/Co))

In a 250-mL round bottom flask, TBPP( $\text{H}_2$ ) (1 mmol) and  $\text{Zn}(\text{CH}_3\text{COO})_2 \cdot 2\text{H}_2\text{O}$  /  $\text{Co}(\text{CH}_3\text{COO})_2 \cdot 4\text{H}_2\text{O}$  (12 mmol) were mixed in 100 mL DMF. The resulting reaction mixture was stirred at room temperature for 15 min and then refluxed for 12 h. After cooling to room temperature, the solution was poured into 100 mL of water and the solid obtained was collected by filtration. Then the solid was dissolved in chloroform and the organic phase was washed with water five times and dried over anhydrous magnesium sulfate. The chloroform was evaporated under reduced pressure and the resulting product was dried under vacuum at 100 °C.  $^1\text{H NMR}$  (400 MHz,  $\text{CDCl}_3$ )  $\delta$ : 8.86 (s, 8H), 8.09 (d, 8H), 7.94 (d, 8H).



Scheme 1. The synthesis scheme of TBPP (Zn/Co).

### 6.2.3.3. Synthesis of POF(Zn/Co)

In a 100 mL two-neck round bottom flask, 0.2 mmol of TBPP(Zn/Co), 9,10-bis(4,4,5,5-tetramethyl-1,3,2-dioxaborolan-2-yl)anthracene (0.4 mmol) were taken under Ar atmosphere. Degassed 1,4-dioxane (16 mL), Pd(PPh<sub>3</sub>)<sub>4</sub> (20 μmol, 23.4 mg), and potassium carbonate (1.6 mmol, 221 mg) in 4 mL water were added under an inert atmosphere (Scheme 2). The resulting reaction mixture was degassed by three cycles of freeze-pump-thaw process and allowed to reflux for 72 h under an Ar atmosphere. After cooling to room temperature the reaction mixture was washed with water, THF, MeOH, and acetone thoroughly. The POF was dried at 120 °C under vacuum for 24h.

### 6.2.4. Gas adsorption measurements

N<sub>2</sub> adsorption-desorption studies were carried out at 77 and 273K, while CO<sub>2</sub> adsorption-desorption measurements were carried out at 273, and 298K using QUANTACHROME Quadrasorb SI automated surface area and pore size analyzer instrument. For CH<sub>4</sub> the measurement was carried out at 273K. Ultrapure (99.995%) N<sub>2</sub>, He, CH<sub>4</sub>, and CO<sub>2</sub> gases were used for the adsorption-desorption measurements. Prior to adsorption measurements, the sample (~ 0.10g) was exchanged with methanol and activated at 120 °C for 12 h under vacuum in QUANTACHROME Flovac degasser and further purged with ultrapure N<sub>2</sub> (99.995%) gas on cooling. PXRD patterns of the activated samples revealed the retaining of the original framework structure after activation. The BET surface area of the POFs was estimated from N<sub>2</sub> sorption isotherms carried out at 77K. The gas selectivity experiments were carried out at 273K. The dead volume of the sample cell was measured using Helium gas (99.995%).

### 6.2.5. Photocatalytic CO<sub>2</sub> reduction studies

The photocatalytic CO<sub>2</sub> reduction reactions were carried out in a 37 mL Quartz photoreactor. Before the catalytic reactions, the POFs were exchanged with acetone and activated at 120 °C for 12 h under vacuum to remove guest solvent molecules. In a typical reaction, acetonitrile (3 mL), water (1 mL), TEOA (2 mL), [Ru(Bpy)<sub>3</sub>]<sup>2+</sup> (3 mg), and the activated POF (5 mg) were taken in a 37 mL Quartz photoreactor. The reactor was sonicated for 10 sec. and sealed with a rubber septum. With the help of a needle, 100mL min<sup>-1</sup> CO<sub>2</sub> gas was bubbled into the photoreactor for 30 min. The reactor was irradiated with UV-IR light using 1000 W Xenon lamp. The output power of the lamp was 1 W/cm<sup>2</sup> at the reactor CO and H<sub>2</sub> yield was monitored by gas chromatography (Agilent 7890B, Agilent Technologies)

equipped with TCD and FID. The recovered catalyst was washed with acetonitrile and acetone thoroughly and activated at 120 °C under vacuum for 12 h and reused for subsequent catalytic cycles.

### 6.2.6. Theoretical investigation

The geometry optimization of the primitive structure of metal-containing POF unit, HOMO, and LUMO energies was carried out using Density Functional Theory (DFT) with gradient exchange-correlational functional of B3LYP (Figure 1). The Pople basis of 6-31G\* has been used for all main group elements of H, C, N, and the LANL2DZ basis set was implemented for the Co and Zn transition metals. Acetonitrile and water mixed solvent is used under the conductor-like polarizable continuum solvation model (CPCM). The electronic absorption spectra (ligand to metal charge transfer, LMCT) have been performed by the time-dependent density functional theory (TD-DFT) method, scanning across 300 excited states. All calculations were performed using Gaussian 09 software. The reaction-free energy change ( $\Delta G$ ) has been calculated from the reaction-free energy difference between the final and initial intermediates. The Zero-point vibrational energy (ZPVE) and thermal correction have been considered in total electronic energy to obtain the reaction-free energy at 298 K temperature and 1 atm pressure. The Natural bond orbital (NBO) calculations have also been considered on some intermediates to investigate the natural charges.

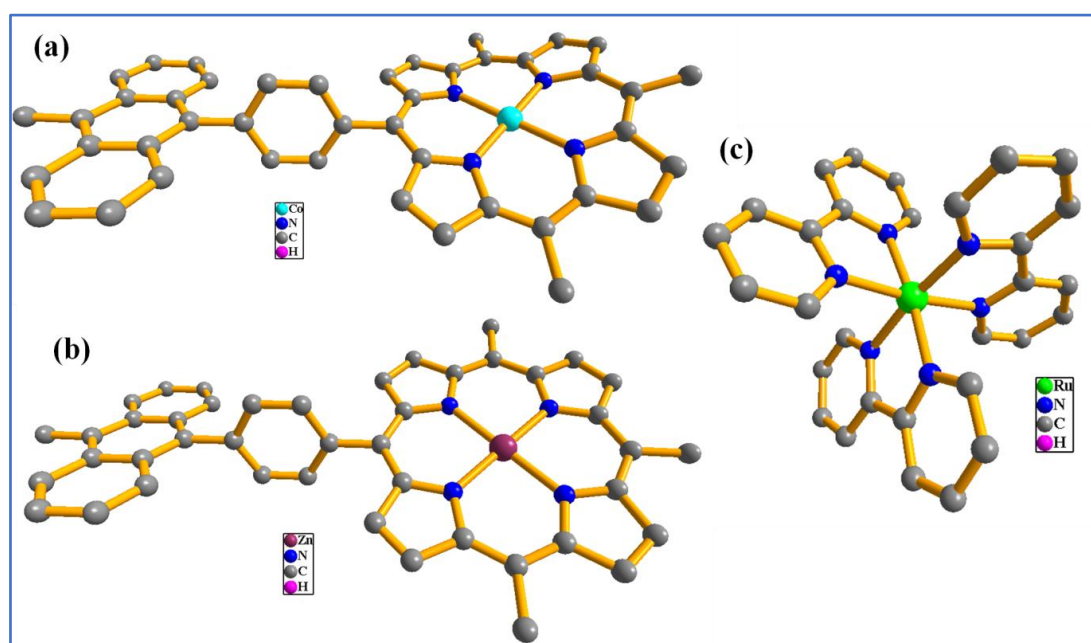
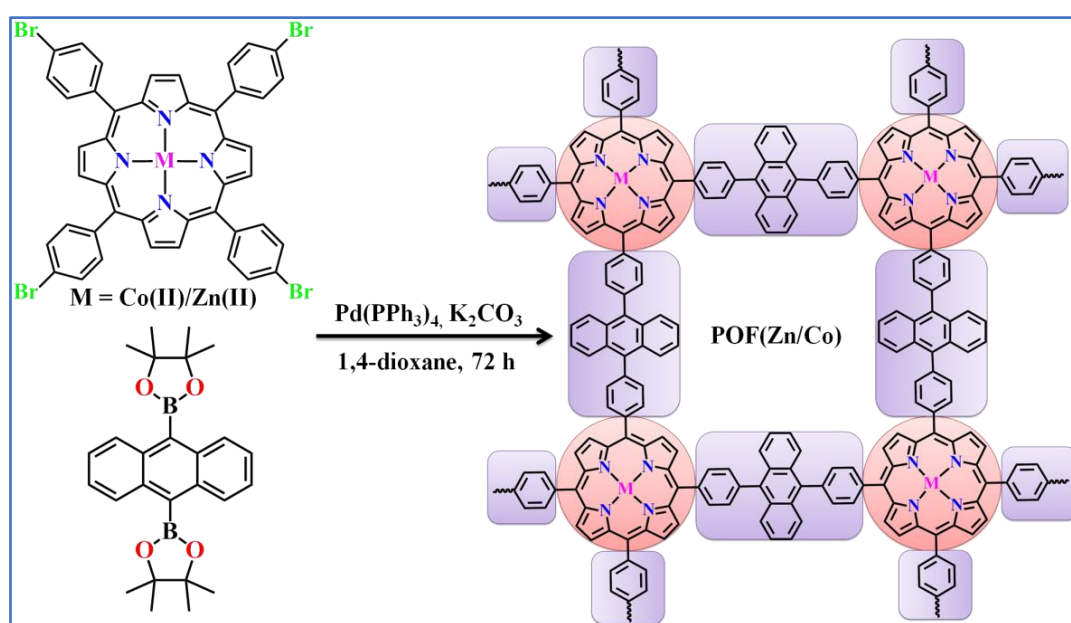


**Figure 1.** Optimized structure of repeating units of (a) POF(Co), (b) POF(Zn), and (c)  $[\text{Ru}(\text{Bpy})_3]^{2+}$  sensitizer.

### 6.3. Results and discussion

#### 6.3.1. Synthesis and characterization

The synthesis of precursors, 5, 10, 15, 20-tetrakis (4-bromophenyl) porphyrin, TBPP(H<sub>2</sub>), and the metallated ligand, TBPP(Zn/Co) was achieved by adopting the reported procedure (Scheme 1).<sup>27</sup> The 2D networks, POF(Zn/Co) were prepared via Suzuki coupling reaction of TBPP(Zn/Co) with 9,10-bis(4,4,5,5-tetramethyl-1,3,2-dioxaborolan-2-yl)anthracene (Scheme 2). The formation of POFs was established by various characterization techniques. The FT-IR spectra showed disappearance of the C-Br stretching frequency of TBPP(M) at 530 cm<sup>-1</sup> supporting the consumption of the porphyrin precursor (Figure A100). Whereas the appearance of a new stretching frequency at 1165 cm<sup>-1</sup> assigned to a new C-C bond formed between the precursors is observed (Figure A100). Further, solid-state <sup>13</sup>C CP-MAS NMR spectra of POF(Zn) showed a characteristic resonance peak at  $\delta$  117 ppm due to the carbon of C-C bond formed between the porphyrin ring and anthracene moiety confirming the framework formation (Figure A101).<sup>16</sup> The PXRD plot of both the POFs showed a broad peak in the 2 $\theta$  range 20-27° due to  $\pi$ - $\pi$  stacking between the porphyrin rings (Figure A102). Thermogravimetric analysis (TGA) revealed that both the POFs exhibit thermal stability up to 410 °C. The UV-vis DRS (diffuse reflectance spectra) of both the POFs showed wide absorption covering the UV-Vis region (200–800 nm) (Figure A103). The band gap energy (E<sub>g</sub>) for POF(Co/Zn) calculated from the Tauc plot was found to be 2.68/2.77 eV, respectively (Figure A104). Further, SEM analysis showed uniform spherical morphology of POFs (Figures 2a and 2b).



**Scheme 2.** The synthesis scheme of POF(Zn/Co).

### 6.3.2. X-ray photoelectron spectroscopy (XPS) analysis

The XPS spectra of POF(Co) depicted the presence of constituent elements, Co, C, and N (Figure A105). The Co<sup>II</sup> spectra (Figure 2c) showed characteristic binding energies (BE) for P<sub>3/2</sub> and P<sub>1/2</sub> at 781.6 and 797.4 eV, respectively, which are in accordance with reported XPS spectra of Co<sup>II</sup> in porphyrin macrocycle (CoN<sub>4</sub>).<sup>27</sup> The N 1s spectra (Figure 2d) showed a BE peak at 400.0 eV which is in line with reported BE for Co<sup>II</sup>-centered porphyrin macrocycle (400.1 eV).<sup>27</sup> The appearance of a single BE peak for N 1s supports the symmetry change from *D*<sub>2h</sub> to *D*<sub>4h</sub> upon Co-metallation.<sup>27</sup>

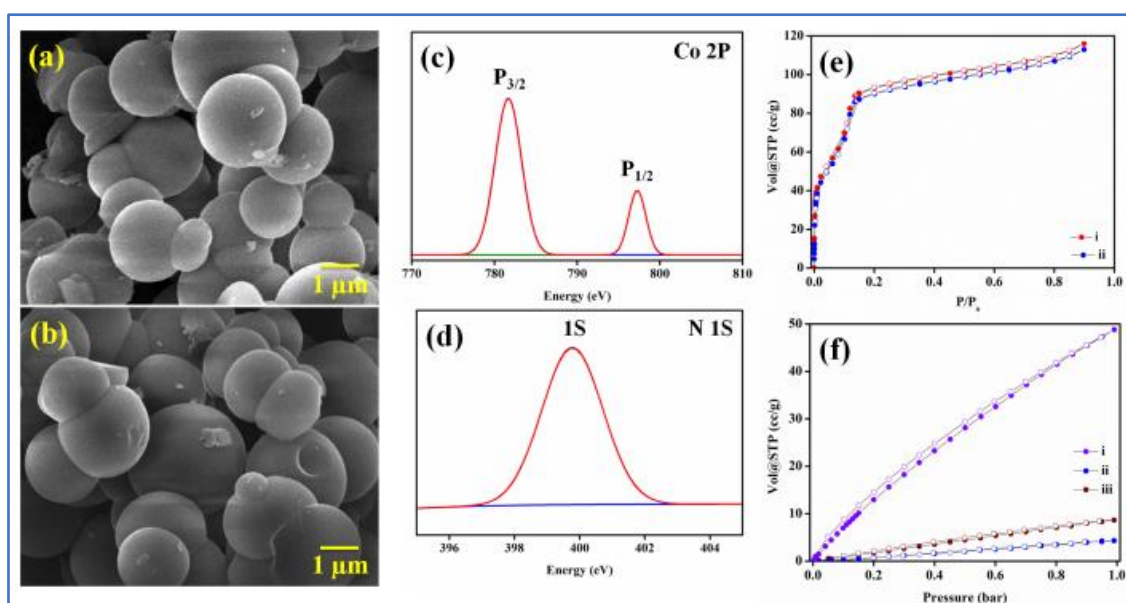


**Figure 2.** SEM images of POF(Co/Zn) (a/b), XPS spectra for Co 2P and N 1S (c/d), (e) N<sub>2</sub> adsorption isotherms for POF(Zn/Co) (i and ii) and (f) selective CO<sub>2</sub> adsorption isotherm (i: CO<sub>2</sub>, ii: CH<sub>4</sub>, iii: N<sub>2</sub>) carried out at 298 K.

### 6.3.3. Gas adsorption studies

The permanent microporosity of the POFs was examined by N<sub>2</sub> adsorption measurements, both POF(Zn/Co) showed similar BET surface areas of 324/301 m<sup>2</sup>g<sup>-1</sup> (Figure 2e). Besides, CO<sub>2</sub> sorption studies showed type-I adsorption profiles with uptake of 61.2/48.9 and 46.6/39.2 cc/g for POF(Co/Zn) at 273 and 298K, respectively (Figure A106). Further, the precise prediction of CO<sub>2</sub> uptake at both temperatures was done following the Freundlich-Langmuir equation<sup>29</sup> (Figure A107-A110) and the CO<sub>2</sub> interaction energy (*Q*<sub>st</sub>) was calculated from the Clausius-Clayperon equation.<sup>30</sup> Interestingly, *Q*<sub>st</sub> for interaction of CO<sub>2</sub> with POF(Co/Zn) was found to be 37.4/34.6 kJmol<sup>-1</sup>, respectively (Figure A111).

Additionally, selective gas adsorption analysis revealed negligible  $N_2$  and  $CH_4$  uptake (Figure 2f) with Henry selectivity constants of 78, and 71 for  $KCO_2/N_2$ , and  $KCO_2/CH_4$ , respectively (Figure A112). The high selectivity constant supports the good affinity of the framework for  $CO_2$  over  $N_2$  and  $CH_4$ .

### 6.3.4. Photocatalytic $CO_2$ reduction studies

The presence of catalytically active single-atom  $Co^{II}$  sites in the porphyrin core, along with the  $CO_2$ -philic rigid framework of  $POF(Co/Zn)$  motivated us to check the photocatalytic  $CO_2$  reduction activity of the frameworks. The optimization of the catalytic reactions was carried out using  $POF(Co)$  as catalyst, along with  $[Ru(Bpy)_3]^{2+}$  as sensitizer and trietanolamine (TEOA) sacrificial agent in presence of white light as a visible light source. The catalysis carried out in pure water as solvent did not show any formation of reduced products (Figure 3). Whereas, the use of pure acetonitrile (MeCN) as solvent resulted in generation of syngas with  $CO$  and  $H_2$  evolution rate of 6015 and 32  $\mu mol/g$ , respectively. Interestingly, when the combination of MeCN :  $H_2O$  (3:1) was employed as solvent afforded the best activity with  $CO$  and  $H_2$  yield of 7165 and 26515  $\mu mol/g$ , respectively (Figure 3b).

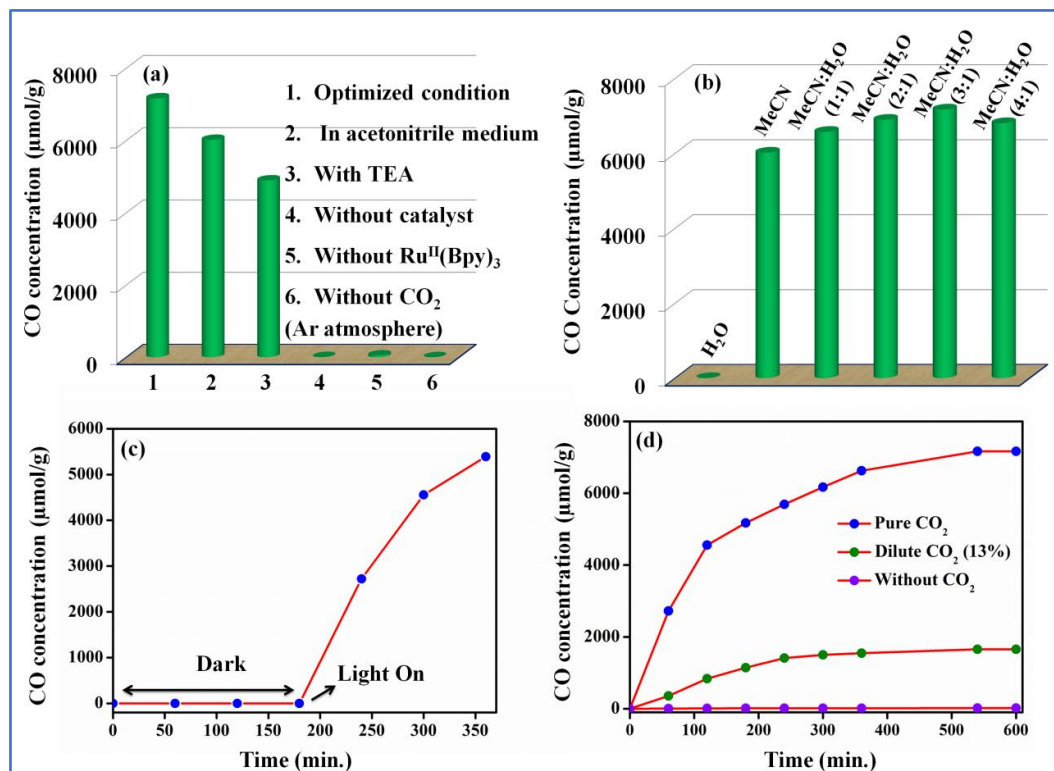


**Figure 3.** (a) Screening of activity in various conditions, (b) varying solvents, (c) effect of light, and (d) photocatalytic production of CO by POF(Co).

The higher activity observed in the mixed solvent can be ascribed to combined effect of good dispersion of Ru-sensitizer and enhanced solubility of CO<sub>2</sub> in the polar aqueous medium (Figure 3).<sup>28</sup> Whereas, the catalysis carried out in the absence of POF(Co), sacrificial agent, sensitizer and visible light yielded no formation of syngas indicating the essential requirement of these components for light-promoted CO<sub>2</sub>R and HER (Figure 3). The control experiment performed under an Ar atmosphere showed the sole formation of H<sub>2</sub> (29710 μmol/g) (Figure 4a). Notably, analysis of the gaseous or liquid products by various techniques confirmed selective formation of CO, and no other CO<sub>2</sub>R products were observed. For further confirmation of CO evolution by CO<sub>2</sub> reduction, the catalysis was carried out using <sup>13</sup>CO<sub>2</sub> gas and to our delight, the GC-MS spectra of the head gas showed a peak at m/z = 29 corresponding to <sup>13</sup>CO formation (Figure 4).

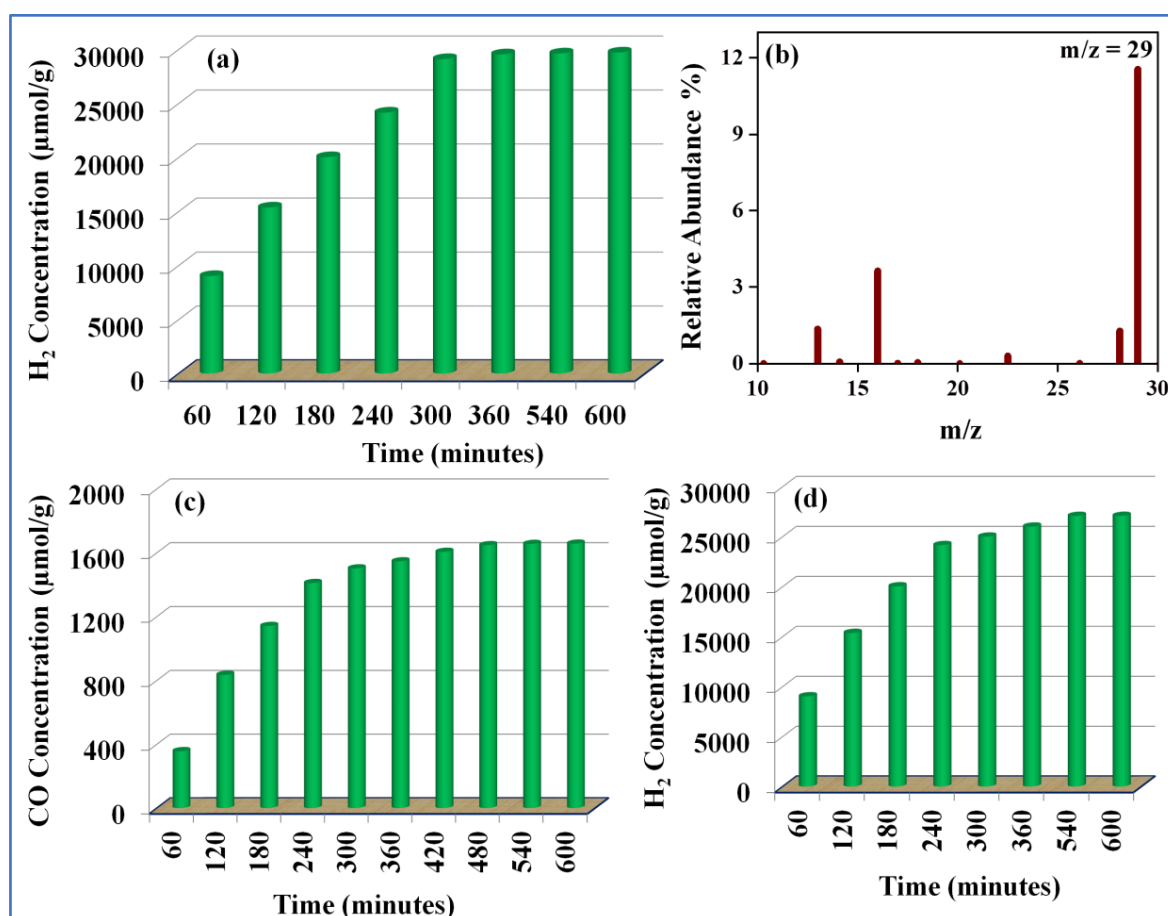


**Figure 4.** (a) Hydrogen evolution by POF(Co) under Ar atmosphere atmosphere, and (b) mass spectra of <sup>13</sup>CO, Photocatalytic production of (c) CO and (d) H<sub>2</sub> from dilute gas (13% CO<sub>2</sub>) catalysed by POF(Co).

This experiment unambiguously confirms CO formation by photocatalytic CO<sub>2</sub>R reaction. To examine the role of Co<sup>II</sup> metal on catalytic CO<sub>2</sub> reduction, the catalysis was repeated using the analogues framework, POF(Zn) as catalyst. Interestingly, a negligible yield of CO/H<sub>2</sub> (18/53 μmol/g) was observed highlighting the critical role of Co<sup>II</sup> in catalyzing CO<sub>2</sub>R and HER process. More importantly, the yield of CO produced catalyzed by POF(Co) was found to be higher than most of the reported photocatalysts (Table 1).<sup>31-36</sup> Motivated by the high catalytic performance of POF(Co), its application for CO<sub>2</sub>R using dilute gas (CO<sub>2</sub>:N<sub>2</sub> = 13:87%) having a similar composition to that of dry flue gas was tested. Indeed, the generation of CO/H<sub>2</sub> in high yield of 1657/27075 μmol/g, respectively was observed highlighting the excellent catalytic performance of POF(Co) (Figure 4).

To examine the reusability and structural stability of the catalyst, the POF(Co) was recovered after the catalysis and reused for consecutive cycles after activation. Notably, the catalytic activity was maintained even after five cycles of reuse with a negligible reduction in the yield of syngas (Figure A113). Further, the characterization of the recycled catalyst by PXRD, FTIR, and SEM analysis confirmed retaining of the original structure and morphology of POF (Figure 5). Moreover, microwave plasma atomic emission spectroscopic (MP-AES) analysis of the filtrate of catalytic reaction did not show presence of Co<sup>II</sup> supporting the absence of leaching of active metal during the reaction and high photo-stability of the framework (Figure A114).

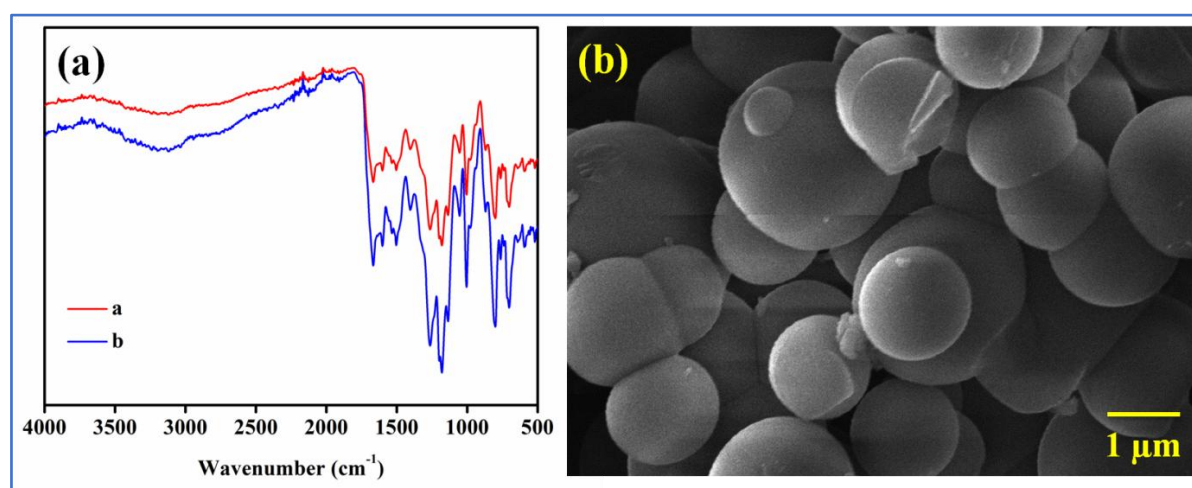


**Figure 5.** (a) FTIR spectra of as-synthesized POF(Co) (i) and recycled POF(Co) (ii), (b) SEM image of recycled POF(Co) after catalysis.

**Table 1.** Comparison of photocatalytic performance of POF(Co) for reduction of CO<sub>2</sub> to CO with literature-reported catalysts.

Sl. No.	Photocatalyst	Hole Scavenger	Rate ( $\mu\text{mol g}^{-1}\text{h}^{-1}$ )	References
<b>01</b>	<b>POF(Co)</b>	<b>TEOA</b>	<b>716.5</b>	<b>Our catalyst</b>
02	PMOF/Re	BIH	535	<i>ACS Appl. Mater. Interfaces</i> <b>2021</b> , <i>13</i> , 2710-2722.
03	NiP-TPE-COF	TEOA	525	<i>Sci. China Chem.</i> <b>2020</b> , <i>63</i> , 1289-1294.
04	Ni-PCD@TD COF, Ru(bpy) <sub>3</sub> Cl <sub>2</sub>	TEOA	478	<i>Adv. Funct. Mater.</i> <b>2020</b> , <i>30</i> , 2002654.
05	COF-367(Co)	TEA	259	<i>J. Am. Chem. Soc.</i> <b>2020</b> , <i>142</i> , 16723-16731.
06	MOF-525(Co)	TEOA	201	<i>Angew. Chem. Int. Ed.</i> <b>2016</b> , <i>55</i> , 14310-14314.
07	In-PMOF	t-AP	144	<i>Inorg. Chem.</i> <b>2020</b> , <i>59</i> , 6301-6307.
08	2D/Zn-MOF	TEOA	117.8	<i>J. Mater. Chem. A</i> <b>2019</b> , <i>7</i> , 11355- 11361.
09	D-TiMOF	TEOA	59.55	<i>J. CO<sub>2</sub> Util.</i> <b>2021</b> , <i>48</i> , 101528.
10	PMOF1/Ru(bpy) <sub>3</sub> Cl <sub>2</sub>	TEOA	56	<i>Dalton Trans.</i> <b>2019</b> , <i>48</i> , 8678-8692.
11	PD-COF-23-Ni	TEOA	40	<i>Dalton Trans.</i> <b>2020</b> , <i>49</i> , 15587-15591.
12	PCN-224(Cu)/TiO <sub>2</sub>	-	37.21	<i>J. Am. Chem. Soc.</i> <b>2019</b> , <i>141</i> , 13841-13848.
13	COF-367(Co), Ru(bpy) <sub>3</sub> Cl <sub>2</sub>	AA	20.2	<i>J. Am. Chem. Soc.</i> <b>2019</b> , <i>141</i> , 17431-17440.
14	g-CNQDs/PMOF	TEOA	16.1	<i>ACS Appl. Mater. Interfaces</i> <b>2019</b> , <i>11</i> , 42243-42249.
15	MAPbI <sub>3</sub> @PCN-221(Fe)	H <sub>2</sub> O	14.16	<i>Angew. Chem. Int. Ed.</i> <b>2019</b> , <i>58</i> , 9491-9495.
16	ZrPP-1(Co)	TEOA	14	<i>Adv. Mater.</i> <b>2018</b> , <i>30</i> , 1704388.
17	Zr-MBA-Re-MOF	TEOA	13.75	<i>Energy Environ. Sci.</i> <b>2021</b> , <i>14</i> , 2429-2440.
18	COF-P	-	4.58	<i>Mater. Chem. Front.</i> <b>2020</b> , <i>4</i> , 2754-2761.

### 6.3.5. Mechanistic investigation

To understand the higher catalytic performance of POF(Co), transient photocurrent and photoluminescence (PL) measurements were conducted with an excitation wavelength of 450 nm (Figure 6). The photocurrent (i) vs time (t) plot (Figure 6a) for POF(Co/Zn) shows a sharp increase in photocurrent density for both the POFs under light irradiation and then it decays to zero when the light is turned off. Notably, POF(Co) showed higher photocurrent density over POF(Zn) due to facile separation/migration of electrons to the reaction sites. This higher photocurrent response of POF(Co) is in line with its superior catalytic performance over its Zn-counterpart.<sup>37</sup> Further, the PL intensity (Figure 6b) of Ru-sensitizer at 610 nm was quenched upon the addition of POF(Co/Zn). Moreover, the emission intensity of POF(Co) was quenched to a higher magnitude than that of POF(Zn). This process signifies that the charge transfer from Ru-sensitizer to Co<sup>II</sup> center is more favored than that of Zn<sup>II</sup> site which is in line with the higher catalytic performance of POF(Co).

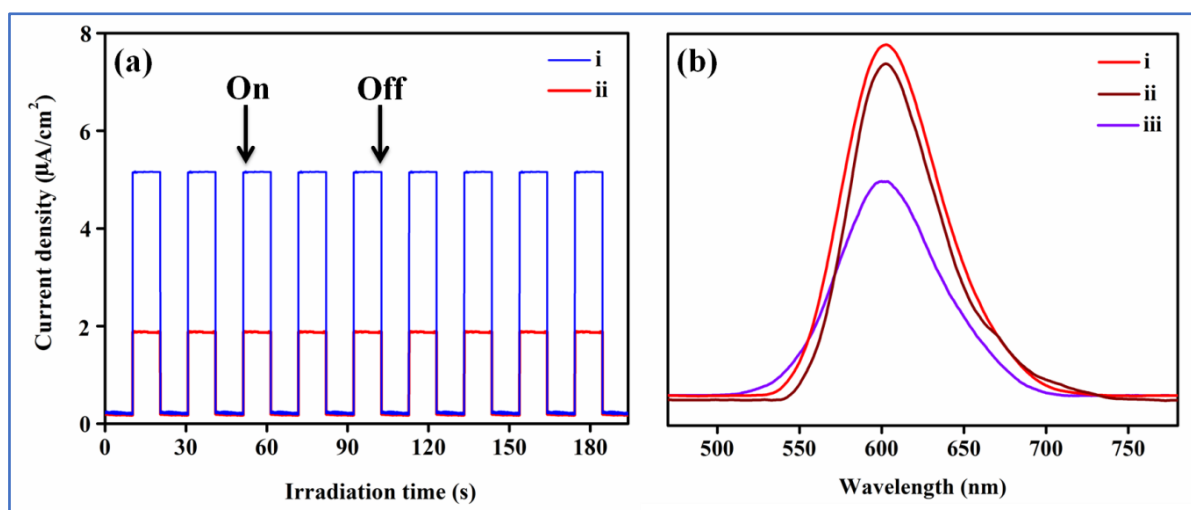
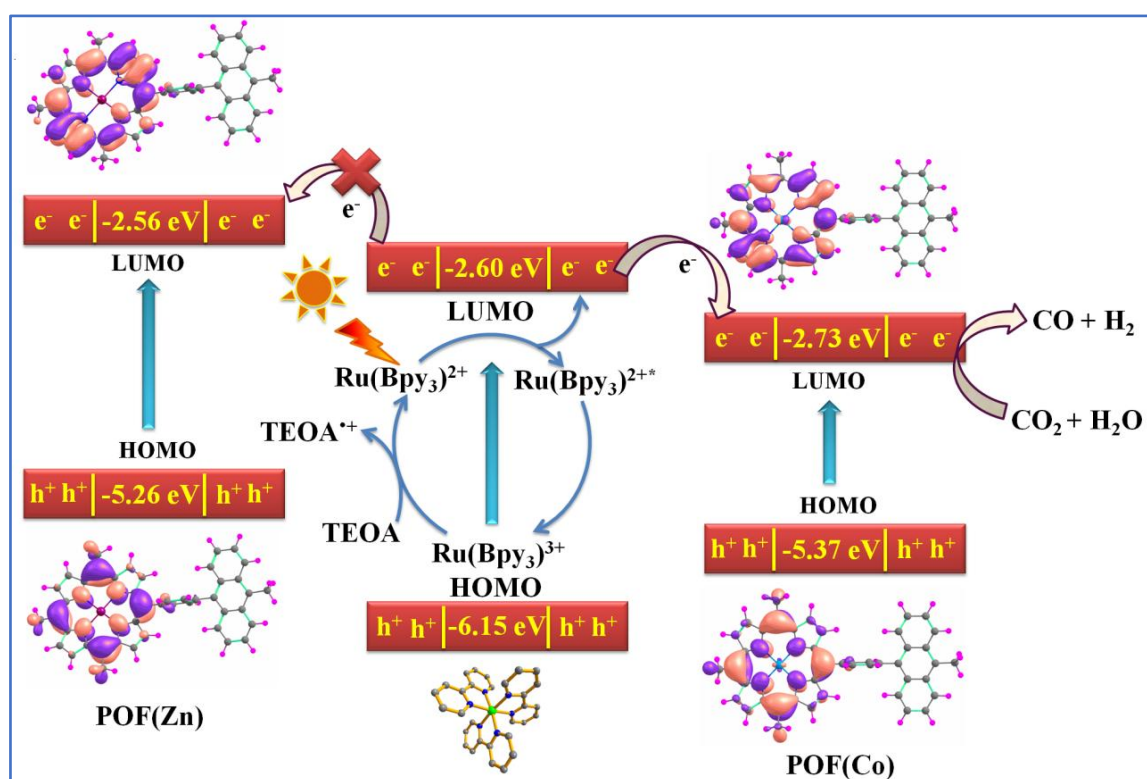


**Figure 6.** (a) Transient photocurrent (i vs t) response for (i) POF(Co) and (ii) POF(Zn), (b) PL spectra of (i)  $[\text{Ru}(\text{Bpy})_3]^{2+}$  solution and after addition of (ii) POF(Zn) and (iii) POF(Co).

Further, to get in-sight mechanistic details of the CO<sub>2</sub>R catalyzed by POF(Co), in-depth theoretical simulations were performed using DFT (see annexure). The TD-DFT calculations were carried out by using B3LYP functional in Gaussian 09 package (more details in the annexure). Our, simulated UV-vis absorption spectra of 450 nm show a  $\pi - \pi^*$  transition occurred from HOMO-1 (filled 2p orbital of carbon anthracene moiety) to LUMO (vacant 2p and 3d orbital of porphyrin ring and Co<sup>II</sup> metal, respectively) (Figure A115). The HOMO-LUMO position of  $[\text{Ru}(\text{Bpy})_3]^{2+}$  and POF(Co/Zn) were calculated to be 6.15-2.60

and 5.27-3.73/5.26-2.56 eV, respectively (Figure A116). It is important to note that the LUMO of Ru-sensitizer lies above that of POF(Co) and below that of POF(Zn). These orbital energies favor facile transfer of photo-induced electrons from the sensitizer to  $\text{Co}^{\text{II}}$  and are utilized for  $\text{CO}_2\text{R}$  and HER processes. On the other hand, the photo-excited electron transfer to  $\text{Zn}^{\text{II}}$  is hindered due to its higher LUMO energy. Furthermore, we have studied the  $\text{CO}_2$  activation on the  $\text{Zn}^{\text{II}}$ -containing POF. Interestingly, the  $\text{CO}_2$  molecule was found to interact strongly with the porphyrin ligand instead of  $\text{Zn}^{\text{II}}$  center. This can be explained by the NBO charge analysis, where  $\text{Zn}^{\text{II}}$  metal possesses a higher positive charge of +1.43 |e| compared to the Co metal of +0.87 |e| and the C atom of  $\text{CO}_2$  possesses +1.06 |e|. <sup>39</sup>



**Scheme 3.** Schematic representation of photocatalytic reduction of  $\text{CO}_2$  and protons for syngas generation.

In the very first step, the  $\text{CO}_2$  molecule experienced a higher repulsive force from  $\text{Zn}^{\text{II}}$  site compared to that of  $\text{Co}^{\text{II}}$  metal and hence allowed to form the stable complex with the porphyrin ligand which is not participating in further reaction. Perhaps this is another reason that Zn-POF is not taking part in the  $\text{CO}_2\text{R}$  to CO experimentally. Based on the above discussion, a plausible mechanism for  $\text{CO}_2\text{R}$  is shown in Scheme 3. Upon irradiation with light, the  $[\text{Ru}(\text{Bpy}_3)_3]^{2+}$  sensitizer undergoes excitation,  $[\text{Ru}(\text{Bpy}_3)_3]^{2+*}$  and the electron is

transferred to  $\text{Co}^{\text{II}}$  site at which  $\text{CO}_2$  to  $\text{CO}$  takes place via a  $2e^-$  reduction process (Figure 7). While the Ru-sensitizer is regenerated by accepting an electron from the sacrificial donor (TEOA). To understand the detailed mechanism, we computed stepwise reaction free energy for POF(Co), and the resulting energy profile is shown in (Scheme 4). Upon treating  $\text{CO}_2$  with framework, the formation of **b** complex with a reaction-free energy of 7.37 Kcal/mol takes place.

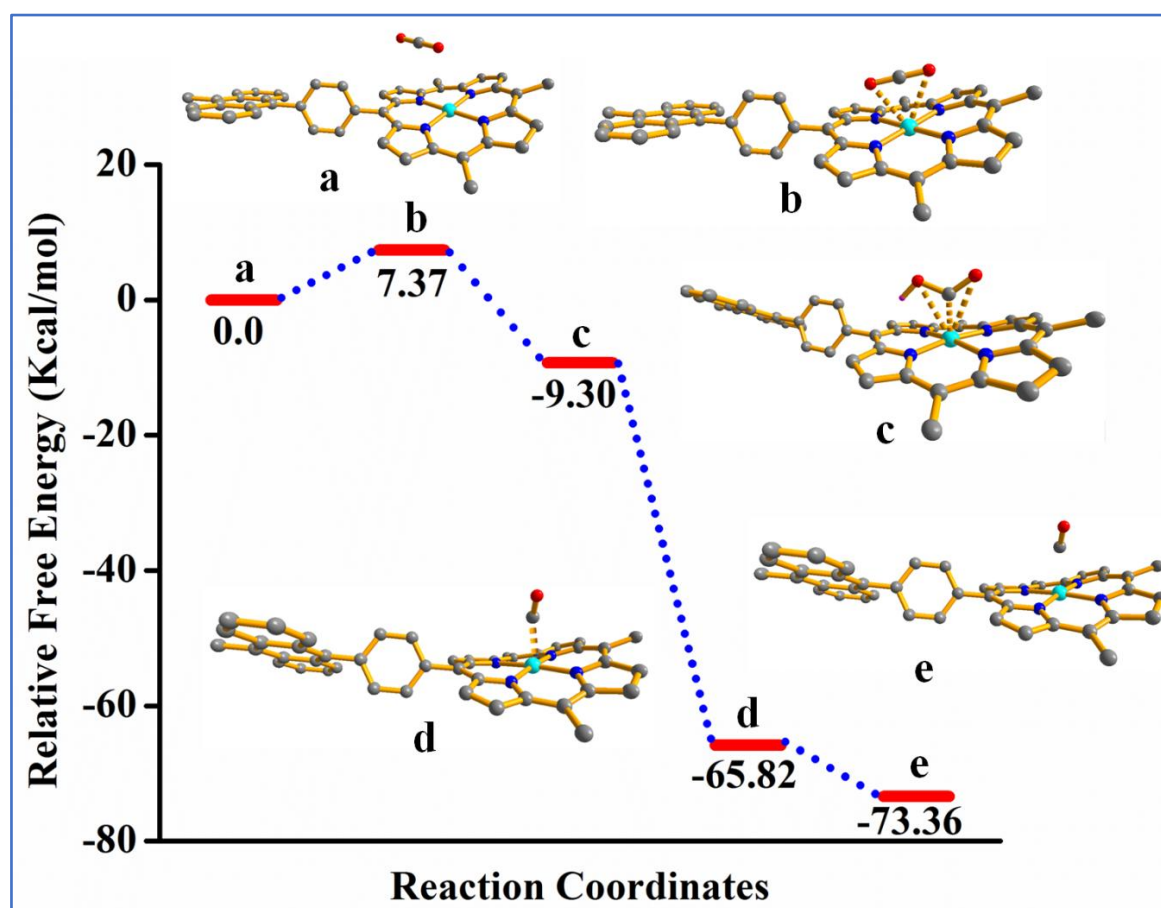


**Figure 7.** Reaction free energy profile for the reduction process.

This step is endergonic due to the interaction of  $\text{CO}_2$  and Co center, through the O of  $\text{CO}_2$  at a distance of 3.5 Å to form an active  $^*\text{CO}_2$  molecule. Further, a proton-electron pair has been transferred to the O of  $^*\text{CO}_2$  producing  $^*\text{COOH}$  complex **c** with exergonic free energy of -16.67 kcal/mol. Then, another proton-electron pair transfer resulted in the transformation of activated  $^*\text{COOH}$  to  $^*\text{CO}$  complex of **d** by release of one  $\text{H}_2\text{O}$  molecule, with a huge exergonic free energy change of -56.52 Kcal/mol. Here the transfer of proton-electron pair drives the formation of water molecule. Finally, the catalyst is regenerated on the removal of the CO molecule with a free energy change of -7.54 Kcal/mol. The overall reaction-free energy change of -73.36 Kcal/mol indicates that the reaction is

thermodynamically favorable. Our calculated reaction-free energy is comparable to other transition metal-based catalysts known for CO<sub>2</sub>R to CO formation.<sup>38,39</sup>

#### 6.4. Conclusion

The strategic construction of 2D porphyrin-based frameworks for efficient visible light-promoted CO<sub>2</sub>R coupled with HER for controlled generation of syngas is achieved. Remarkably, the Co-metallated framework showed superior catalytic performance over the Zn-one owing to the optimum red-ox properties of the metal. The rigid, 2D framework structure with exposed single atom Co<sup>II</sup> sites promoted efficient CO<sub>2</sub>R activity even from dilute gas (13% CO<sub>2</sub>) under visible-light-driven mild conditions. In-sight mechanistic details of CO<sub>2</sub> reduction was unveiled by detailed theoretical investigation. Overall, this work represents a novel demonstration of light-promoted generation of syngas and paves a way for rational construction of recyclable catalysts for effective CO<sub>2</sub>R under eco-friendly mild conditions.

#### 6.5. References

- (1) Meinshausen, M.; Meinshausen, N.; Hare, W.; Raper, S. C. B.; Frieler, K.; Knutti, R.; Frame, D. J.; Allen, M. R. Greenhouse-gas emission targets for limiting global warming to 2 C. *Nature* **2009**, *458*, 1158.
- (2) Jones, W. D. Carbon capture and conversion. *J. Am. Chem. Soc.* **2020**, *142*, 4955-4957.
- (3) Ding, M.; Flaig, R. W.; Jiang, H.-L.; Yaghi, O. M. Carbon capture and conversion using metal-organic frameworks and MOF-based materials. *Chem. Soc. Rev.* **2019**, *48*, 2783-2828.
- (4) Das, R.; Ezhil, T.; Palakkal, A. S.; Muthukumar, D.; Pillai, R. S.; Nagaraja, C. M. Efficient chemical fixation of CO<sub>2</sub> from direct air under environment-friendly co-catalyst and solvent-free ambient conditions. *J. Mater. Chem. A* **2021**, *9*, 23127-23139.
- (5) Rawool, S. A.; Belgamwar, R.; Jana, R.; Maity, A.; Bhumla, A.; Yigit, N.; Datta, A.; Rupprechter, G.; Polshettiwar, V. Direct CO<sub>2</sub> capture and conversion to fuels on magnesium nanoparticles under ambient conditions simply using water. *Chem. Sci.* **2021**, *12*, 5774-5786.
- (6) Khalilpour, R.; Mumford, K.; Zhai, H.; Abbas, A.; Stevens, G.; Rubin, E. S. Membrane-based carbon capture from flue gas: a review. *J. Cleaner Prod.* **2015**, *103*, 286-300.
- (7) Lu, W.; Sculley, J. P.; Yuan, D.; Krishna, R.; Wei, Z.; Zhou, H.-C. Polyamine-tethered porous polymer networks for carbon dioxide capture from flue gas. *Angew. Chem. Int. Ed.* **2012**, *51*, 7480-7484.

- (8) Das, R.; Nagaraja, C. M. Noble metal-free Cu(I)-anchored NHC-based MOF for highly recyclable fixation of CO<sub>2</sub> under RT and atmospheric pressure conditions. *Green Chem.* **2021**, *23*, 5195-5204.
- (9) Underwood, A. J. V. Industrial synthesis of hydrocarbons from hydrogen and carbon monoxide. *Ind. Eng. Chem.* **1940**, *32*, 449.
- (10) Rofer-DePoorter, C. K. A comprehensive mechanism for the Fischer-Tropsch synthesis. *Chem. Rev.* **1981**, *81*, 447.
- (11) Stanley, M.; Su, A. Y.; Ramm, V.; Fink, P.; Kimna, C.; Lieleg, O.; Elsner, M.; Lercher, J. A.; Rieger, B.; Warnan, J.; Fischer, R. A. Photocatalytic CO<sub>2</sub>-to-Syngas Evolution with Molecular Catalyst Metal-organic Framework Nanozymes. *Adv. Mater.* **2022**, 2207380.
- (12) Yang, S.; Sa, R.; Zhong, H.; Lv, H.; Yuan, D.; Wang, R. Microenvironments Enabled by Covalent Organic Framework Linkages for Modulating Active Metal Species in Photocatalytic CO<sub>2</sub> Reduction. *Adv. Funct. Mater.* **2022**, 2110694.
- (13) Fu, Z.; Wang, X.; Gardner, A. M.; Wang, X.; Chong, S. Y.; Neri, G.; Cowan, A. J.; Liu, L.; Li, X.; Vogel, A.; Clowes, R.; Bilton, M.; Chen, L.; Sprick, R. S.; Cooper, A. I. A stable covalent organic framework for photocatalytic carbon dioxide reduction. *Chem. Sci.* **2020**, *11*, 543-550.
- (14) Yao, X.; Chen, K.; Qiu, L.-Q.; Yang, Z.-W.; He, L.-N. Ferric Porphyrin-Based Porous Organic Polymers for CO<sub>2</sub> Photocatalytic Reduction to Syngas with Selectivity Control. *Chem. Mater.* **2021**, *33*, 8863-8872.
- (15) Huang, Y.; Xin, Z.; He, L. -N. Water activated main element-based syngas surrogates for safe functionalization of unsaturated chemicals. *Sci. Bull.* **2021**, *66*, 865-867.
- (16) Dalle, K. E.; Warnan, J.; Leung, J. J.; Reuillard, B.; Karmel, I. S.; Reisner, E. Electro- and solar-driven fuel synthesis with first row transition metal complexes. *Chem. Rev.* **2019**, *119*, 2752.
- (17) Li, Y.; Zhang, S. L.; Cheng, W.; Chen, Y.; Luan, D.; Gao, S.; Lou, X. W. Loading Single-Ni Atoms on Assembled Hollow N-Rich Carbon Plates for Efficient CO<sub>2</sub> Electroreduction. *Adv. Mater.* **2022**, *34*, 2105204.
- (18) Mondal, B.; Sen, P.; Rana, A.; Saha, D.; Das, P.; Dey, A. Reduction of CO<sub>2</sub> to CO by an Iron Porphyrin Catalyst in the Presence of Oxygen. *ACS Catal.* **2019**, *9*, 3895-3899.
- (19) Wu, L.-Y.; Mu, Y.-F.; Guo, X.-X.; Zhang, W.; Zhang, Z.-M. Encapsulating Perovskite Quantum Dots in Iron-Based Metal-Organic Frameworks (MOFs) for Efficient Photocatalytic CO<sub>2</sub> Reduction. *Angew. Chem. Int. Ed.* **2019**, *58*, 9491-9495.

- (20) Asselin, P.; Harvey, P. D. Visible-Light-Driven Production of Solar Fuels Catalyzed by Nanosized Porphyrin-Based Metal–Organic Frameworks and Covalent–Organic Frameworks: A Review. *ACS Appl. Nano Mater.* **2022**, *5*, 6055-6082.
- (21) Nikoloudakis, E.; Lo´pez-Duarte, I.; Charalambidis, G.; Ladomenou, K.; Ince, M.; Coutsolelos, A. G. Porphyrins and phthalocyanines as biomimetic tools for photocatalytic H<sub>2</sub> production and CO<sub>2</sub> reduction. *Chem. Soc. Rev.* **2022**, *51*, 6965-7045.
- (22) Jin, L.; Lv, S.; Miao, Y.; Liu, D.; Song, F. Recent development of porous porphyrin-based nanomaterials for photocatalysis. *ChemCatChem* **2021**, *13*, 140-152.
- (23) Gopalakrishnan, V. N.; Becerra, J.; Pena, E. F.; Sakar, M.; Béland, F.; Do, T. -O. Porphyrin and single atom featured reticular materials: Recent advances and future perspective of solar-driven CO<sub>2</sub> reduction. *Green Chem.* **2021**, *23*, 8332-8360.
- (24) Wang, F. Artificial Photosynthetic Systems for CO<sub>2</sub> Reduction: Progress on Higher Efficiency with Cobalt Complexes as Catalysts. *ChemSusChem* **2017**, *10*, 4393-4402.
- (25) Liao, W.-M.; Zhang, J.-H.; Wang, Z.; Lu, Y.-L.; Yin, S.-Y.; Wang, H.-P.; Fan, Y.-N.; Pan, M.; Su, C.-Y. Semiconductive Amine-Functionalized Co(II)-MOF for Visible-Light-Driven Hydrogen Evolution and CO<sub>2</sub> Reduction. *Inorg. Chem.* **2018**, *57*, 11436-11442.
- (26) Mukherjee, G.; Thote, J.; Aiyappa, H. B.; Kandambeth, S.; Banerjee, S.; Vanka, K.; Banerjee, R. A porous porphyrin organic polymer (PPOP) for visible light triggered hydrogen production. *Chem. Commun.* **2017**, *53*, 4461-4464.
- (27) Richardson, C.; Reed, C. A. Synthesis of meso-Extended Tetraarylporphyrins. *J. Org. Chem.* **2007**, *72*, 4750-4755.
- (28) Zhang, H.; Wei, J.; Dong, J.; Liu, G.; Shi, L.; An, P.; Zhao, G.; Kong, J.; Wang, X.; Meng, X.; Zhang, J.; Ye, J. Efficient visible-light-driven carbon dioxide reduction by a single-atom implanted metal-organic framework. *Angew. Chem. Int. Ed.* **2016**, *55*, 14310-14314.
- (29) Yang, R. T. Gas Separation by Adsorption Processes, Butterworth, Boston, **1997**.
- (30) Pan, H.; Ritter, J. A.; Balbuena, P. B. Examination of the approximations used in determining the isosteric heat of adsorption from the Clausius-Clapeyron equation. *Langmuir*, **1998**, *14*, 6323-6327.
- (31) Chen, E.-X.; Qiu, M.; Zhang, Y.-F.; Zhu, Y.-S.; Liu, L.-Y.; Sun, Y.-Y.; Bu, X.; Zhang, J.; Lin, Q. Acid and Base Resistant Zirconium Polyphenolate-Metalloporphyrin Scaffolds for Efficient CO<sub>2</sub> Photoreduction. *Adv.Mater.* **2018**, *30*, 1704388.

- (32) Zhong, H.; Sa, R.; Lv, H.; Yang, S.; Yuan, D.; Wang, X.; Wang, R. Covalent Organic Framework Hosting Metalloporphyrin-Based Carbon Dots for Visible-Light-Driven Selective CO<sub>2</sub> Reduction. *Adv. Funct. Mater.* **2020**, *30*, 2002654.
- (33) Gong, Y.-N.; Zhong, W.; Li, Y.; Qiu, Y.; Zheng, L.; Jiang, J.; Jiang, H.-L. Regulating photocatalysis by spin-state manipulation of cobalt in covalent organic frameworks. *J. Am. Chem. Soc.* **2020**, *142*, 16723-16731.
- (34) Karmakar, S.; Barman, S.; Rahimi, F. A.; Maji, T. K. Covalent grafting of molecular photosensitizer and catalyst on MOF-808: effect of pore confinement toward visible light-driven CO<sub>2</sub> reduction in water. *Energy Environ. Sci.* **2021**, *14*, 2429-2440.
- (35) Stanley, P. M.; Haimerl, J.; Thomas, C.; Urstoeger, A.; Schuster, M.; Shustova, N. B.; Casini, A.; Rieger, B.; Warnan, J.; Fischer, R. A. Host-Guest Interactions in a Metal-Organic Framework Isorecticular Series for Molecular Photocatalytic CO<sub>2</sub> Reduction. *Angew. Chem. Int. Ed.* **2021**, *60*, 17854-1786.
- (36) Stanley, P. M.; Thomas, C.; Thyraug, E.; Urstoeger, A.; Schuster, M.; Hauer, J.; Rieger, B.; Warnan, J.; Fischer, R. A. Entrapped Molecular Photocatalyst and Photosensitizer in Metal-Organic Framework Nanoreactors for Enhanced Solar CO<sub>2</sub> Reduction. *ACS Catal.* **2021**, *11*, 871-882.
- (37) Das, R.; Manna, S. S.; Pathak, B.; Nagaraja, C. M. Strategic Design of Mg-Centered Porphyrin MOF for Efficient Visible Light-Promoted Fixation of CO<sub>2</sub> at Ambient Conditions: Combined Experimental and Theoretical Investigation. *ACS Appl. Mater. Interfaces* **2022**, *14*, 33285-3329.
- (38) Call, A.; Cibian, M.; Yamamoto, K.; Nakazono, T.; Yamauchi, K.; Sakai, K. Highly Efficient and Selective Photocatalytic CO<sub>2</sub> Reduction to CO in Water by a Cobalt Porphyrin Molecular Catalyst. *ACS Catal.* **2019**, *9*, 4867-4874.
- (39) Grimme, S.; Antony, J.; Ehrlich, S.; Krieg, H. A consistent and accurate ab initio parametrization of density functional dispersion correction (DFT-D) for the 94 elements H-Pu. *J. Chem. Phys.* **2010**, *132*, 154104-154119.

# **Annexure**



Figures/Tables	Pages
<b>Figure A1.</b> PXRD patterns of Zn-DAT (a) simulated pattern from single crystal X-ray diffraction, (b) as-synthesized sample, (c) activated, and (d) recycled sample after five catalytic cycles.	223
<b>Figure A2.</b> FT-IR spectrum of Zn-DAT.	223
<b>Figure A3.</b> PXRD patterns for Zn-TAZ (a') simulated pattern from single crystal X-ray diffraction, (b') as-synthesized sample, (c') activated, and (d') after reaction.	224
<b>Figure A4.</b> 3D view of Zn-DAT showing the pore size along the crystallographic <i>c</i> - and <i>b</i> -axis.	224
<b>Figure A5.</b> (a) 5-connected Zn(II) node (polyhedron shown in different colour) and (b) 8-connected Zn(II) node (polyhedron shown in different colour).	224
<b>Figure A6.</b> N <sub>2</sub> adsorption-desorption isotherm of (a) Zn-DAT (b) Zn-TAZ carried out at 77 K.	225
<b>Table A1.</b> Selected bond length (Å) and angles (°) for Zn-DAT.	225
<b>Table A2.</b> Selected hydrogen bonding geometry (Å) for Zn-DAT.	226
<b>Analysis of gas adsorption isotherms</b>	226
<b>Figure A7.</b> Carbon dioxide adsorption isotherm of Zn-DAT and Zn-TAZ carried out at 273 K.	227
<b>Figure A8.</b> Carbon dioxide adsorption isotherm for Zn-DAT and Zn-TAZ at 298 K.	227
<b>Figure A9.</b> Enthalpy of carbon dioxide for Zn-DAT calculated using the Clausius-Clapeyron equation.	227
<b>Figure A10.</b> Gas selectivity for Zn-DAT calculated following the Henry's law from the CO <sub>2</sub> , N <sub>2</sub> , Ar and H <sub>2</sub> isotherms carried out at 273 K.	228
<b>Figure A11.</b> Linear fitting of CO <sub>2</sub> , Ar, H <sub>2</sub> and N <sub>2</sub> isotherms used for calculation of Henry's selectivity constants.	228
<b>Table A3.</b> Optimized geometries of epoxides using Gaussian09 at b3lyp/6-311g (d,p) level.	229
GCMC Simulations	229
<b>Figure A12.</b> PXRD patterns of HbMOF1 (a) simulated pattern from single-crystal X-ray diffraction and for (b) as-synthesized sample (c) activated and (d) recycled sample after five catalytic cycles.	230
<b>Figure A13.</b> FT-IR spectrum of activated HbMOF1.	231
<b>Table A4.</b> Selected hydrogen bonding geometry for HbMOF1.	231

<b>Table A5.</b> Selected bond length (Å) and angles (°) for HbMOF1.	<b>231</b>
<b>Figure A14.</b> Carbon dioxide adsorption isotherm of HbMOF1 carried out at 273 K. The solid line shows the best fit to the data using the Langmuir-Freundlich Equation.	<b>232</b>
<b>Figure A15.</b> Carbon dioxide adsorption isotherm for HbMOF1 at 298 K.	<b>232</b>
<b>Figure A16.</b> Enthalpy of carbon dioxide for HbMOF1 calculated using the Clausius-Clapeyron equation.	<b>233</b>
<b>Figure A17.</b> Calculation of Henry gas selectivity constants by linear fitting of CO <sub>2</sub> (a), H <sub>2</sub> (b), Ar (c) and N <sub>2</sub> (d) isotherms.	<b>233</b>
<b>Figure A18.</b> The single unit cell (1×1×1 simulation box) considered for the DFT calculations viewed along <i>a</i> -axis for HbMOF1 (a), HbMOF1-hypo-1 (b), HbMOF1-hypo-2 (c) and HbMOF1-hypo-3 (d) where it is slightly twisted for better views of its functional groups (-NH <sub>2</sub> and -CF <sub>3</sub> ) decorated 1D channel.	<b>234</b>
<b>Table A6.</b> LJ potential parameters for the atoms of the HbMOF1.	<b>234</b>
<b>Table A7.</b> Potential parameters and partial charges for the adsorbates	<b>235</b>
<b>Figure A19.</b> Comparison of the single component simulated isotherms for CO <sub>2</sub> (red) with the experimental data (blue) for HbMOF1 at 298 K (a) and 273 K (b).	<b>235</b>
<b>Figure A20.</b> BET surface area calculation for HbMOF1 using simulated N <sub>2</sub> isotherm at 77 K. (a) Plot of $V_{\text{excess}} (1 - P/P_0)$ vs $P/P_0$ for the determination using the first consistency criterion, (b) the selected linear plot that satisfies the second consistency criterion and the corresponding BET surface area from the linear fit.	<b>235</b>
<b>Figure A21.</b> Comparison of the simulated adsorption enthalpy simulated (red) for CO <sub>2</sub> with the experimental data (blue) in HbMOF1.	<b>236</b>
<b>Figure A22.</b> Radial distribution functions (RDF) between CO <sub>2</sub> and the atoms of the MOF framework extracted from the single component adsorption in HbMOF1 at 1 bar and 298 K: Oxygen of CO <sub>2</sub> : O <sub>CO2</sub> (a) and Carbon of CO <sub>2</sub> : C <sub>CO2</sub> (b).	<b>236</b>
<b>Table A8.</b> The simulated CO <sub>2</sub> adsorption enthalpies for HbMOF1 and the hypothetical models having the same topology.	<b>237</b>
<b>Figure A23.</b> Thermogravimetric analysis of HbMOF1.	<b>237</b>
<b>Figure A24.</b> PXRD patterns of HbMOF1 (a) simulated pattern from single-crystal X-ray diffraction, and the sample isolated after treating with various solvents, such as (b) MeOH (c) 1,4-Dioxane (d) Acetone (e) water (f) N, N-dimethylformamide (g) N, N-dimethylacetamide (h) Isopropyl alcohol for 72h.	<b>238</b>
<b>Table A9.</b> Optimization of catalytic cycloaddition reaction of CO <sub>2</sub> with	<b>238</b>

epichlorohydrin (ECH).	
<b>Figure A25.</b> Mechanistic Pathways of the Intermediates and Transition States in the Cycloaddition of Propylene oxide and CO <sub>2</sub> using the HbMOF1 catalyst.	<b>239</b>
<b>Models for the Host Framework Microscopic</b>	<b>239</b>
<b>Table A10.</b> Comparison of catalytic activity of HbMOF1 with literature reported MOFs for cycloaddition of CO <sub>2</sub> with terminal epoxide (PO) under mild conditions.	<b>240</b>
DFT Derived Specific Forcefields.	<b>241</b>
<b>Figure A26.</b> FT-IR spectra of Mg-MOF, (a) activated and (b) recycled sample after tenth catalytic cycle.	<b>242</b>
<b>Figure A27.</b> UV-Vis spectra of (a) H <sub>3</sub> TATAB ligand, (b) activated Mg-MOF, (c) recycled sample after ten catalytic cycles.	<b>242</b>
<b>Figure A28.</b> TOPOS image of Mg-MOF.	<b>243</b>
<b>Figure A29.</b> (a) View of 8-connected Mg1 node and (b) 3-connected Mg2 node.	<b>243</b>
<b>Table A11.</b> Selected bond length (Å) and angles (°) for Mg-MOF.	<b>244</b>
<b>Table 12.</b> Selected hydrogen bonding geometry for Mg-MOF.	<b>244</b>
<b>Figure A30.</b> TGA plots of Mg-MOF (a) as-synthesized, (b) solvent exchanged, and (c) activated MOF.	<b>245</b>
<b>Figure A31.</b> PXRD patterns of Mg-MOF recovered after treating with various solvents (a) simulated pattern and the sample treated with (b) DMF, (c) water, (d) acetone, (e) ethanol, (f), and (g) methanol.	<b>245</b>
<b>Figure A32.</b> Carbon dioxide adsorption isotherm of Mg-MOF carried out at 273 K (a) and 298 K (b). The solid line shows the best fit to the data using the Langmuir-Freundlich equation.	<b>246</b>
<b>Figure A33.</b> The single unit cell (1×1×1 simulation box) of Mg-MOF considered for the DFT calculations viewed along <i>c</i> -direction.	<b>246</b>
<b>Figure A34.</b> Simulated and experimental adsorption enthalpy for CO <sub>2</sub> in Mg-MOF.	<b>247</b>
<b>Table A13.</b> Comparison of interaction energy (Q <sub>st</sub> ) with various reported Mg-based MOF.	<b>247</b>
<b>Figure A35.</b> (a) Comparison of the single component simulated isotherms for N <sub>2</sub> (closed triangle) with the experimental data (closed circle) in Mg-MOF at 273 and 298 K and (b) Simulated and experimental adsorption enthalpy for N <sub>2</sub> in Mg-MOF.	<b>248</b>
<b>Figure A36.</b> (a) Comparison of the single component simulated isotherms for O <sub>2</sub> (closed triangle) with the experimental data (closed circle) in Mg-MOF at 273 and	<b>248</b>

298 K and (b) Simulated and experimental adsorption enthalpy for O <sub>2</sub> in Mg-MOF.	
<b>Figure A37.</b> Calculation of gas selectivity constant for (a) CO <sub>2</sub> and (b) N <sub>2</sub> and (c) O <sub>2</sub> gases using on Henry law.	<b>249</b>
<b>Figure A38.</b> DFT geometry optimization of Mg-MOF cluster model with (a, b) CO <sub>2</sub> , (c) N <sub>2</sub> , (d) O <sub>2</sub> and (e) PO interaction to LA Mg(II) site.	<b>249</b>
<b>Figure A39.</b> The potential energy values are calculated as moving each molecule along the dashed line, (a) C <sub>CO2</sub> , (b) O <sub>CO2</sub> , (c) N <sub>N2</sub> , and (d) O <sub>O2</sub> (comparison of DFT-derived forcefield fitted curve (red circles) on the DFT interaction energy profile (black squares)).	<b>250</b>
<b>Table A14.</b> The DFT based binding energy calculated with PBE functional by Mg-MOF and Guest interaction.	<b>250</b>
<b>Table A15.</b> LJ potential parameters for the atoms of the Mg-MOF.	<b>251</b>
<b>Table A16.</b> Potential parameters and partial charges for the adsorbates.	<b>251</b>
<b>Table A17.</b> Buckingham parameters associated with the Mg-MOF and adsorbates	<b>251</b>
<b>Figure A40.</b> Radial distribution functions (RDF) between CO <sub>2</sub> and the atoms of the MOF framework extracted from the single component adsorption in Mg-MOF in 0.01bar at 273K.	<b>252</b>
<b>Figure A41.</b> Radial distribution functions (RDF) between N <sub>2</sub> and the atoms of the MOF framework extracted from the single-component adsorption in Mg-MOF in 0.01bar at 273K (a) and 298K (b).	<b>252</b>
<b>Figure A42.</b> Radial distribution functions (RDF) between O <sub>2</sub> and the atoms of the MOF framework extracted from the single component adsorption in Mg-MOF in 0.01bar at 298K.	<b>253</b>
<b>Figure A43.</b> Maps of the occupied positions of CO <sub>2</sub> (a), N <sub>2</sub> (b) O <sub>2</sub> (c), and (d) H <sub>2</sub> O in 500 equilibrated frames for a given pressure of 1 bar and at 298 K for Mg-MOF.	<b>253</b>
<b>Figure A44.</b> Selectivity plot of CO <sub>2</sub> /(O <sub>2</sub> + N <sub>2</sub> ) in presence of RH = 1.57% at 298 K.	<b>254</b>
<b>Figure A45.</b> CO <sub>2</sub> adsorption isotherms at various relative humidity of pre-humidified Mg-MOF at 298K.	<b>254</b>
<b>Figure A46.</b> Simulated selectivity of CO <sub>2</sub> /(O <sub>2</sub> + N <sub>2</sub> ) in various pre-humidified air at 1bar..	<b>255</b>
<b>Figure A47.</b> MP-AES calibration curve	<b>255</b>
<b>Figure A48.</b> Unit crystal (left) and primitive (right) structure of Mg-MOF obtained through optimization via DFT method viewed along <i>a</i> vector direction.	<b>255</b>

<b>Figure A49.</b> Mechanistic Pathways of the Intermediates and Transition States in the cycloaddition of propylene oxide and CO <sub>2</sub> using the Mg-MOF catalyst (bond distances are in Å).	<b>256</b>
<b>Figure A50.</b> FT-IR spectra of (a) Mg-MOF, (b) Epichlorohydrin, and (c) Mg-MOF treated with epichlorohydrin.	<b>256</b>
<b>Figure A51.</b> <sup>1</sup> H NMR spectrum of [5, 10, 15, 20-Tetrakis (4-carboxyphenyl) Mg(II) porphyrin] (Mg-TCPPH <sub>4</sub> ) ligand.	<b>257</b>
<b>Figure A52.</b> FT-IR spectra of (a) H <sub>4</sub> TCPP(H <sub>2</sub> ) and (b) Mg-TCPPH <sub>4</sub> complex ligand.	<b>257</b>
<b>Figure A53.</b> UV-Vis absorption spectra of (a) Mg-TCPPH <sub>4</sub> , and (b) H <sub>4</sub> TCPP(H <sub>2</sub> ).	<b>258</b>
<b>Figure A54.</b> Bandgap plots for PCN-224 and PCN-224(Mg) MOF.	<b>258</b>
<b>Figure A55.</b> EDS plot of (a) PCN-224, and (b) PCN-224(Mg) MOF.	<b>258</b>
<b>Figure A56.</b> TGA plot of (a) PCN-224, and (b) PCN-224(Mg) MOF.	<b>259</b>
<b>Figure A57.</b> Carbon dioxide adsorption isotherm of PCN-224(Mg) carried out at 273 K.	<b>259</b>
<b>Figure A58.</b> Carbon dioxide adsorption isotherm of PCN-224(Mg) carried out at 298 K.	<b>259</b>
<b>Figure A59.</b> Carbon dioxide adsorption isotherm of PCN-224 carried out at 273 K.	<b>260</b>
<b>Figure A60.</b> Carbon dioxide adsorption isotherm of PCN-224 carried out at 298 K.	<b>260</b>
<b>Figure S61.</b> Calculation of Henry gas selectivity constants for gases (a) CO <sub>2</sub> , (b) CH <sub>4</sub> , and (c) N <sub>2</sub> .	<b>260</b>
<b>Figure A62.</b> Optimization of photocatalytic cycloaddition of CO <sub>2</sub> with ECH by varying (a) reaction time, and (b) power of LED bulb.	<b>261</b>
<b>Table A18.</b> Catalytic optimization table using ECH as model substrate under mild conditions.	<b>261</b>
<b>Figure A63.</b> Emission spectrum of a commercial white LED light.	<b>262</b>
<b>Figure A64.</b> Kinetics of CO <sub>2</sub> utilization with ECH under sunlight, LED-light, and dark conditions.	<b>262</b>
<b>Table A19.</b> Catalytic optimization table using ECH as model substrate under mild conditions.	<b>262</b>
<b>Figure A65.</b> Simulated absorption spectra of PCN-224(Mg) (a) and with ECH epoxide (b).	<b>263</b>
<b>Figure A66.</b> (a) Simulated absorption spectra of PCN-224(Mg) in PO epoxide. The frontier molecular orbital of high (b) and low (c) intense absorption spectra of PCN-	<b>263</b>

224(Mg) in PO epoxide.	
<b>Figure A67.</b> The frontier molecular orbitals involved in the optical transitions of PCN-224(Mg) without epoxide are low intense (a) and high intense peaks (b).	<b>263</b>
<b>Table A20.</b> HOMO/LUMO energy values of with and without ECH epoxide in PCN-224(Mg).	<b>264</b>
<b>Figure A68.</b> Optimized geometries of intermediates and transition state in the cycloaddition of ECH and CO <sub>2</sub> using the PCN-224(Mg) catalyst.	<b>264</b>
<b>Figure A69.</b> FT-IR spectra of (a) pristine PCN-224(Mg), (b) PCN-224(Mg) treated with epichlorohydrin, and (c) Epichlorohydrin.	<b>265</b>
<b>Figure A70.</b> PXRD pattern of (a) PCN-224(Mg), and (b) recycled PCN-224(Mg).	<b>265</b>
<b>Figure A71.</b> FTIR spectra of (a) PCN-224(Mg), and (b) recycled PCN-224(Mg).	<b>266</b>
<b>Figure A72.</b> UV-Vis diffuse reflectance spectra (DRS) of (a) PCN-224(Mg), and (b) recycled PCN-224(Mg) after catalysis.	<b>266</b>
<b>Figure 73.</b> Calibration curve of MP-AES analysis for (a) Zr-metal, and (b) Mg-metal of PCN-224(Mg).	<b>267</b>
<b>Figure A74.</b> PXRD patterns of MOF-SO <sub>3</sub> H (a) simulated pattern (b) as-synthesized (c) for MOF-SO <sub>3</sub> Ag and (d) recycled sample of MOF-SO <sub>3</sub> Ag after five catalytic cycles.	<b>267</b>
<b>Figure A75.</b> FT-IR spectra of MOF-SO <sub>3</sub> H and MOF-SO <sub>3</sub> Ag.	<b>268</b>
<b>Figure A76.</b> UV-Vis spectra of MOF-SO <sub>3</sub> H and MOF-SO <sub>3</sub> Ag.	<b>268</b>
<b>Figure A77.</b> EDS spectra of (a) MOF-SO <sub>3</sub> H and (b) MOF-SO <sub>3</sub> Ag.	<b>269</b>
<b>Figure A78.</b> PXRD patterns of UiO-66 (a) simulated pattern (b) as-synthesized (c) Ag(I)@UiO-66 and (d) recycled sample of Ag(I)@UiO-66 after reaction.	<b>269</b>
<b>Figure A79.</b> View of Zr-O cluster/SBU of UiO-66 MOF showing the presence of hydroxide groups.	<b>270</b>
<b>Figure A80.</b> N <sub>2</sub> adsorption-desorption isotherms for UiO-66 and Ag(I)@UiO-66 MOF carried out at 77K.	<b>270</b>
<b>Figure A81.</b> Carbon dioxide adsorption isotherm of MOF-SO <sub>3</sub> H carried out at 273 K.	<b>271</b>
<b>Figure A82.</b> Carbon dioxide adsorption isotherm of MOF-SO <sub>3</sub> H carried out at 298 K.	<b>271</b>
<b>Figure A83.</b> Carbon dioxide adsorption isotherm of MOF-SO <sub>3</sub> Ag carried out at 273 K.	<b>272</b>

<b>Figure A84.</b> Carbon dioxide adsorption isotherm of MOF-SO <sub>3</sub> Ag carried out at 298 K.	<b>272</b>
<b>Figure A85.</b> Carbon dioxide adsorption isotherm of Ag(I)@UiO-66 carried out at 273 K.	<b>273</b>
<b>Figure A86.</b> Carbon dioxide adsorption isotherm of Ag(I)@UiO-66 carried out at 298 K.	<b>273</b>
<b>Figure A87.</b> Calculation of Henry gas selectivity constants for gases CO <sub>2</sub> , Ar, H <sub>2</sub> and N <sub>2</sub> .	<b>274</b>
<b>Figure A88.</b> PXRD patterns of MOF-SO <sub>3</sub> Ag (a) simulated pattern, (b) Activated MOF-SO <sub>3</sub> Ag (c) After five cycles of CO <sub>2</sub> adsorption.	<b>274</b>
<b>Figure A89.</b> Reaction progress for cyclic carboxylation of 2-Methyl-3-butyn-2-ol with CO <sub>2</sub> catalysed by MOF-SO <sub>3</sub> Ag.	<b>275</b>
<b>Figure A90.</b> View of one-dimensional pore along <i>b</i> -axis containing NHC sites.	<b>275</b>
<b>Figure A91.</b> FT-IR spectra of (a) NHC-MOF, (b) Cu(I)@NHC-MOF and (c) recycled sample of Cu(I)@NHC-MOF after ten catalytic cycles.	<b>276</b>
<b>Figure A92.</b> UV-Vis absorption spectra of (a) NHC-MOF, (b) Cu(I)@NHC-MOF and (c) recycled sample of Cu(I)@NHC-MOF after ten catalytic cycles.	<b>276</b>
<b>Figure A93.</b> Calibration curve of MP-AES analysis for Cu(I)@NHC-MOF.	<b>277</b>
<b>Figure A94.</b> SEM image of (a) NHC-MOF, (b) Cu(I)@NHC-MOF, (c) recycled sample of Cu(I)@NHC-MOF after ten catalytic cycles, EDS plot of (d) NHC-MOF and (e) Cu(I)@NHC-MOF.	<b>277</b>
<b>Figure A95.</b> Carbon dioxide adsorption isotherm of Cu(I)@NHC-MOF carried out at 273 K.	<b>278</b>
<b>Figure A96.</b> Carbon dioxide adsorption isotherm of Cu(I)@NHC-MOF carried out at 298 K.	<b>278</b>
<b>Figure A97.</b> Enthalpy of carbon dioxide adsorption for Cu(I)@NHC-MOF determined using the Clausius-Clapeyron equation.	<b>279</b>
<b>Figure A98.</b> Calculation of Henry gas selectivity constants for gases (a) CO <sub>2</sub> , (b) N <sub>2</sub> and (c) O <sub>2</sub> .	<b>279</b>
<b>Table A21.</b> Catalyst optimization towards carboxylation of 2-methyl-3-butyn-2-ol.	<b>280</b>
<b>Figure A99.</b> FT-IR spectra of (a) NHC-MOF, (b) Cu(I)@NHC-MOF, (c) 2-methyl-3-butyn-2-ol, (d) NHC-MOF treated with 2-methyl-3-butyn-2-ol, and (e) Cu(I)@NHC-MOF treated with 2-methyl-3-butyn-2-ol.	<b>280</b>

<b>Scheme A1.</b> A plausible mechanism for the three-component reaction between CO <sub>2</sub> , propargylic alcohol and primary amine catalysed by Cu(I)@NHC-MOF.	<b>281</b>
<b>Figure A100.</b> FTIR spectra of (a) TBPP(M), (b) POF(Co), and (c) POF(Zn).	<b>281</b>
<b>Figure A101.</b> <sup>13</sup> C CP-MAS (cross-polarized magic angle spinning) NMR spectra of POF(Zn).	<b>282</b>
<b>Figure A102.</b> PXRD plot of (a) POF(Co), (b) POF(Zn), (c) activated POF(Co), and (d) recycled POF(Co) after catalysis.	<b>282</b>
<b>Figure A103.</b> UV-Vis absorption spectra of (a) POF(Co), and (b) POF(Zn).	<b>283</b>
<b>Figure A104.</b> Bandgap plots for (a) POF(Co), and (b) POF(Zn).	<b>283</b>
<b>Figure A105.</b> XPS survey scan for POF(Co).	<b>284</b>
<b>Figure A106.</b> (a) CO <sub>2</sub> adsorption isotherms of POF(Co) (i and iii ), POF(Zn) (ii and iv) carried out at 273 and 298 K, respectively, and (b) recyclable CO <sub>2</sub> adsorption carried out at 298 K.	<b>284</b>
<b>Figure A107.</b> Carbon dioxide adsorption isotherm of POF(Co) carried out at 273 K.	<b>285</b>
<b>Figure A108.</b> Carbon dioxide adsorption isotherm of POF(Co) carried out at 298 K.	<b>285</b>
<b>Figure A109.</b> Carbon dioxide adsorption isotherm of POF(Zn) carried out at 273 K.	<b>286</b>
<b>Figure A110.</b> Carbon dioxide adsorption isotherm of POF(Zn) carried out at 298 K.	<b>286</b>
<b>Figure A111.</b> Enthalpy of carbon dioxide adsorption for (a) POF(Co), and (b) POF(Zn) determined using the Clausius-Clapeyron equation.	<b>287</b>
<b>Figure A112.</b> Calculation of Henry gas selectivity constants for gases (a) CO <sub>2</sub> , (b) CH <sub>4</sub> , and (c) N <sub>2</sub> .	<b>287</b>
<b>Figure A113.</b> Photocatalytic production of CO (a) and H <sub>2</sub> (b) from dilute gas (13% CO <sub>2</sub> ) catalysed by POF(Co).	<b>287</b>
<b>Figure A114.</b> Recyclability of photocatalytic CO <sub>2</sub> reduction.	<b>288</b>
<b>Figure A115.</b> Calibration curve of MP-AES analysis for detection of Co metal.	<b>288</b>
<b>Theoretical section</b>	<b>288</b>
<b>Figure A116.</b> The frontier molecular orbital and simulated absorption spectra of POF(Co).	<b>289</b>
<b>Figure A117.</b> The frontier HOMO-LUMO molecular orbital of POF(Zn/Co).	<b>289</b>
<b>References</b>	<b>290</b>

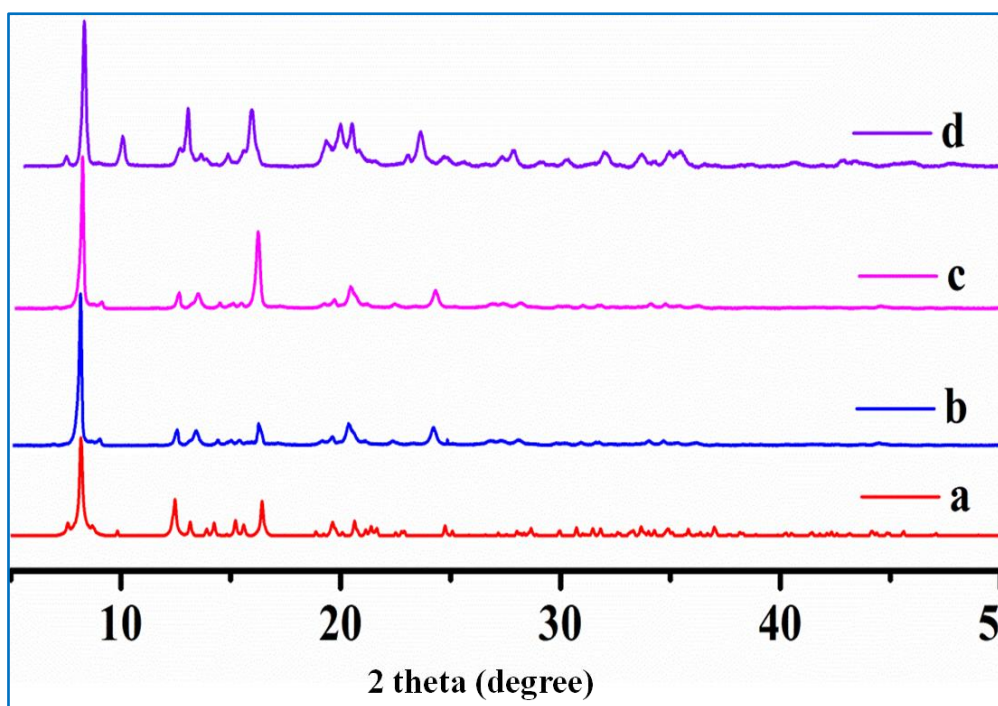


**Figure A1.** PXRD patterns of Zn-DAT (a) simulated pattern from single crystal X-ray diffraction, (b) as-synthesized sample, (c) activated, and (d) recycled sample after five catalytic cycles.

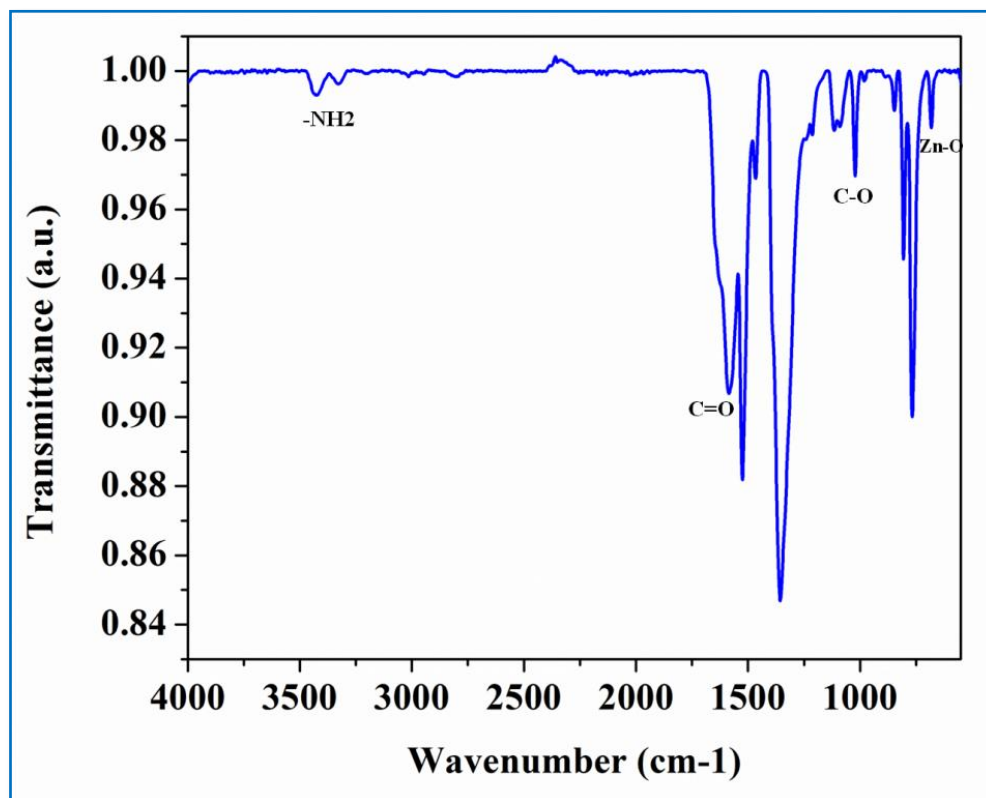


**Figure A2.** FT-IR spectrum of Zn-DAT.

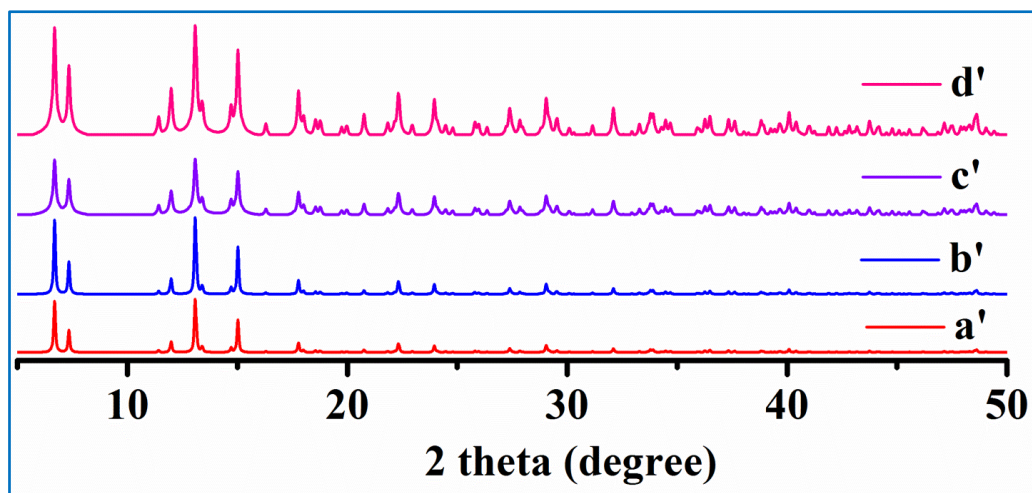


**Figure A3.** PXRD patterns for Zn-TAZ (a') simulated pattern from single crystal X-ray diffraction, (b') as-synthesized sample, (c') activated, and (d') after reaction.

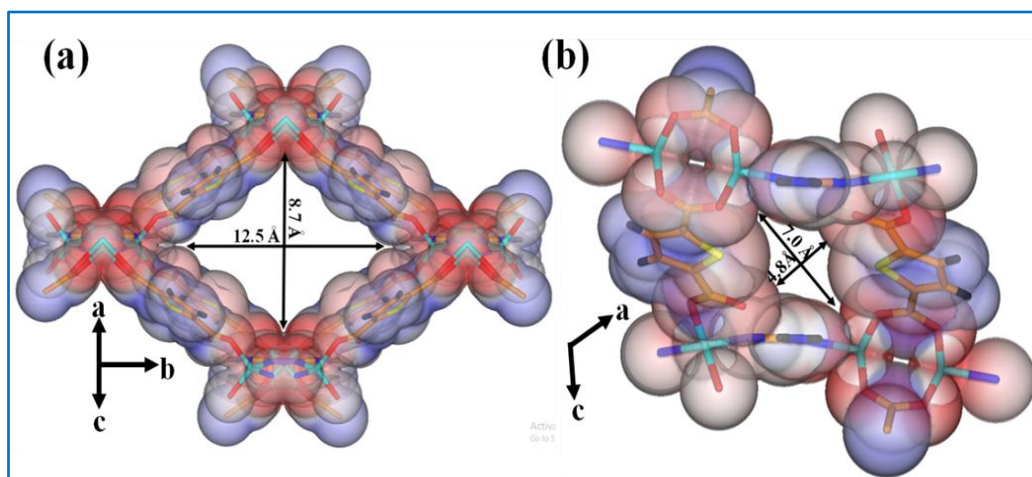


**Figure A4.** 3D view of Zn-DAT showing the pore size along the crystallographic  $c$ - and  $b$ -axis.

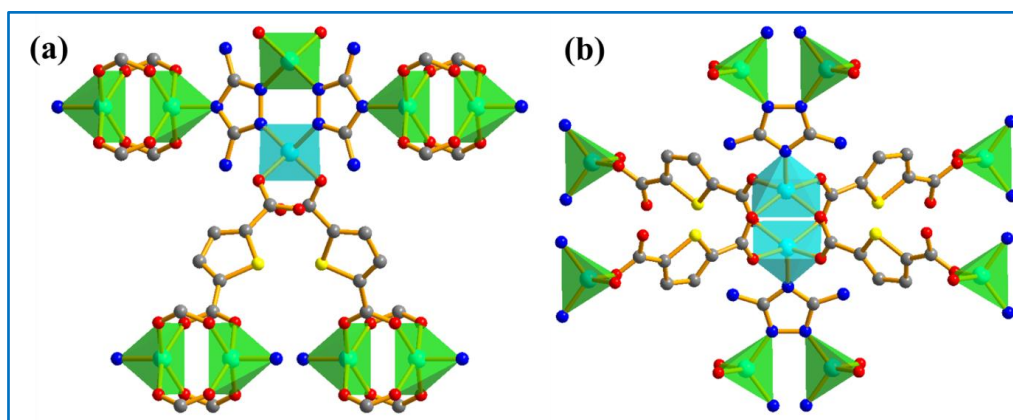


**Figure A5.** (a) 5-connected Zn(II) node (polyhedron shown in different colour) and (b) 8-connected Zn(II) node (polyhedron shown in different colour).

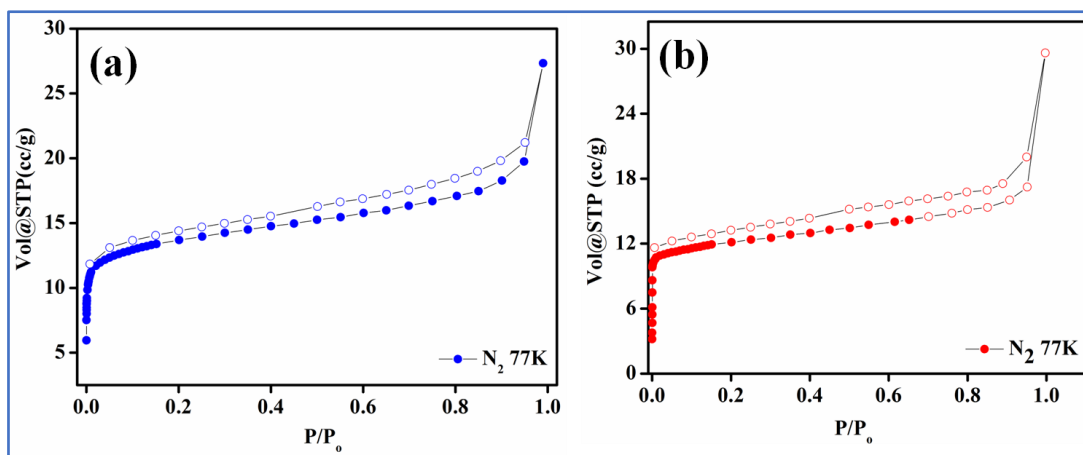


**Figure A6.** N<sub>2</sub> adsorption-desorption isotherm of (a) Zn-DAT (b) Zn-TAZ carried out at 77 K.

**Table A1.** Selected bond length (Å) and angles (°) for Zn-DAT.

Zn1-O1	1.955(4)	O3 <sup>vi</sup> -Zn2-N2	102.29(18)
Zn1-N1	1.972(4)	O4 <sup>viii</sup> -Zn2-N2	101.1(2)
Zn1-O1 <sup>i</sup>	1.955(4)	O3 <sup>vi</sup> -Zn2-O4 <sup>iv</sup>	84.4(2)
Zn1-N1 <sup>i</sup>	1.972(4)	O3 <sup>vi</sup> -Zn2-O4 <sup>iv</sup>	156.6(2)
Zn2-N2	1.993(6)	O4 <sup>iv</sup> -Zn2-O4 <sup>viii</sup>	90.01(18)
Zn2-O4 <sup>iv</sup>	2.031(5)	O3 <sup>vi</sup> -Zn2-O3 <sup>vi</sup>	91.7(2)
Zn2-O3 <sup>vi</sup>	2.020(5)	O3 <sup>vi</sup> -Zn2-O4 <sup>viii</sup>	156.6(2)
Zn2-O3 <sup>vi</sup>	2.020(5)	O3 <sup>vii</sup> -Zn2-O4 <sup>viii</sup>	84.4(2)
Zn2-O4 <sup>viii</sup>	2.031(5)	Zn1-O1-C1	117.4(4)
O1-Zn1-N1	116.8(2)	Zn2 <sup>v</sup> -O3-C6	127.3(4)
O1-Zn1-O1 <sup>i</sup>	108.21(18)	Zn2 <sup>iii</sup> -O4-C6	129.9(5)
O1-Zn1-N1 <sup>i</sup>	102.92(19)	Zn1-N1-C7	128.2(3)
O1 <sup>i</sup> -Zn1-N1	102.92(19)	Zn1-N1-N1 <sup>ii</sup>	125.1(3)
N1-Zn1-N1 <sup>i</sup>	109.83(16)	N1 <sup>ii</sup> -N1-C7	105.7(4)
O1 <sup>i</sup> -Zn1-N1 <sup>i</sup>	116.8(2)	Zn2-N2-C7	127.5(3)
O4 <sup>iv</sup> -Zn2-N2	101.1(2)	Zn2-N2-C7 <sup>ii</sup>	127.5(3)
O3 <sup>vi</sup> -Zn2-N2	102.29(18)		

i = 1-x,y,-z, ii = x,2-y,z, iii = -1/2+x,-1/2+y,-1+z, iv = 1/2+x,1/2+y,1+z, v = 3/2-x,-1/2+y,z, vi = 3/2-x,1/2+y,-z, vii = 3/2-x,3/2-y,-z, viii = 1/2+x,3/2-y,1+z.

**Table A2.** Selected hydrogen bonding geometry (Å) for Zn-DAT.

D–H···A	H···A	D···A	D–H···A
N3-H3A...O2	2.1000	2.874(7)	149.00
N3-H3B...O3	2.5700	3.252(8)	137.00

**Analysis of gas adsorption isotherms**

Clausius-Clapeyron Equation<sup>1</sup> was used to calculate the enthalpies of carbon dioxide adsorption. By using Langmuir Freundlich equation<sup>2</sup> an accurate fit was retrieved which gives a precise prediction of carbon dioxide adsorbed at saturation. A modification of the Clausius-Clapeyron equation is used for calculations.

$$\ln(P_1/P_2) = \Delta H_{\text{ads}}(T_2 - T_1/R \cdot T_1 \cdot T_2) \dots \dots (i)$$

where  $P_1$  and  $P_2$  = Pressures for isotherm at 273K and 298K respectively.

$T_1$  and  $T_2$  = Temperatures for isotherm at 273K and 298K respectively.

$\Delta H_{\text{ads}}$  = Enthalpy of adsorption.

$R$  = Universal gas constant = 8.314 J/K/mol.

The pressure is a function of the amount of gas adsorbed which was determined by using the Langmuir-Freundlich fit.

$$Q/Q_m = B \cdot P^{(1/t)} / (1 + (B \cdot P^{(1/t)})) \dots \dots (ii)$$

Where,  $Q$  = moles of gas adsorbed.

$Q_m$  = moles of gas adsorbed at saturation.

$B$  and  $t$  = constants.

$P$  = Pressure.

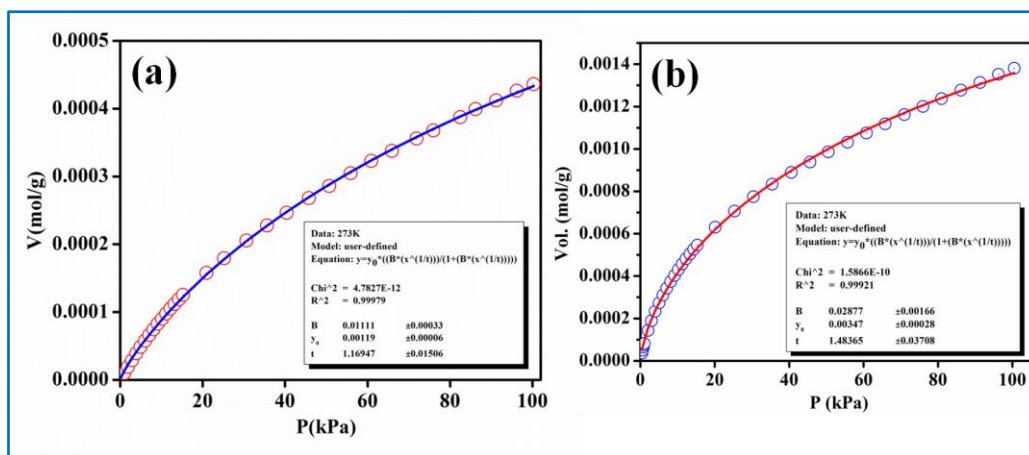
By rearranging equation (ii) we get equation (iii)

$$P = [(Q/Q_m) / \{B - (B \cdot (Q/Q_m))\}]^t \dots \dots (iii)$$

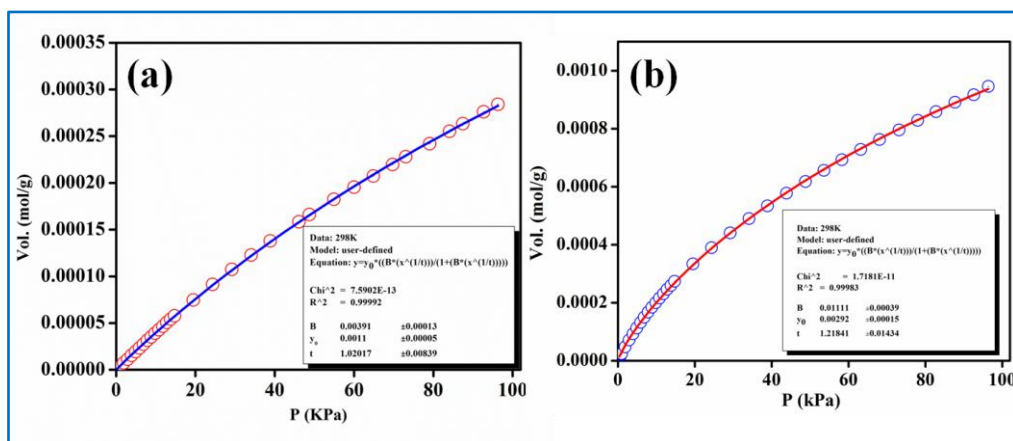
Substituting equation (iii) into equation (i) we get

$$\Delta H_{\text{ads}} = \{R \cdot T_1 \cdot T_2 / (T_2 - T_1)\} \cdot \ln \frac{[(Q/Q_{m1}) / \{B - (B \cdot (Q/Q_{m1}))\}]^{t_1}}{[(Q/Q_{m2}) / \{B - (B \cdot (Q/Q_{m2}))\}]^{t_2}} \dots \dots (iv)$$

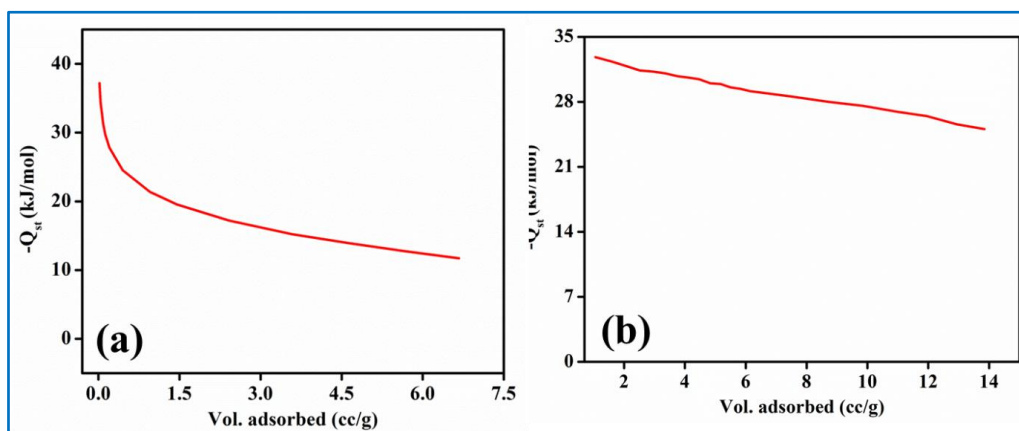
In equation (iv), subscript 1 and 2 are representing data corresponding to 273K and 298K in case of carbon dioxide gas.



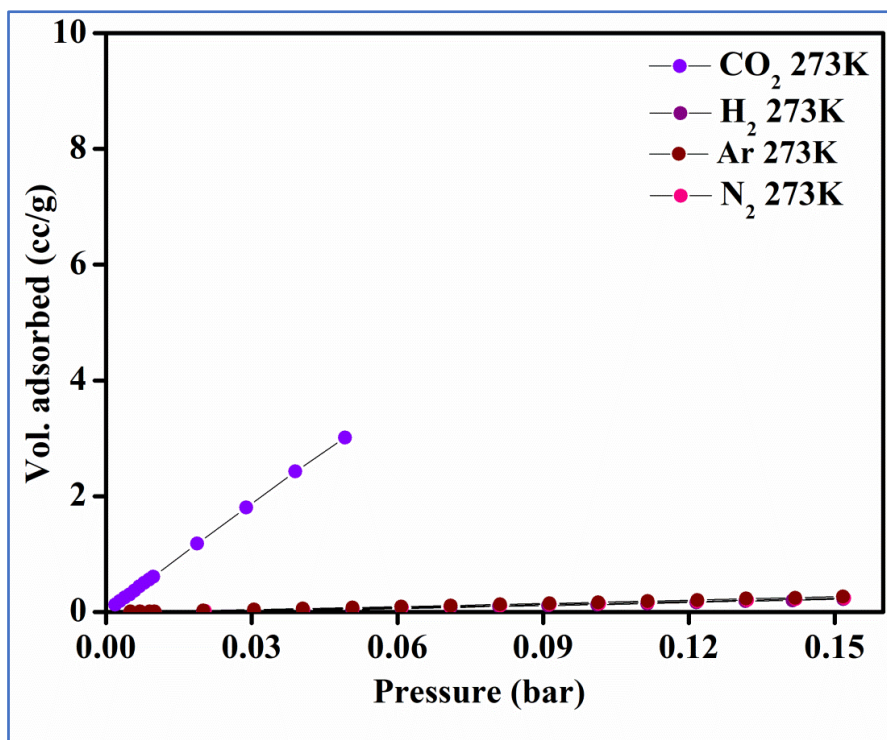
**Figure A7.** Carbon dioxide adsorption isotherm of Zn-DAT and Zn-TAZ carried out at 273 K. The solid line shows the best fit to the data using the Langmuir-Freundlich Equation.



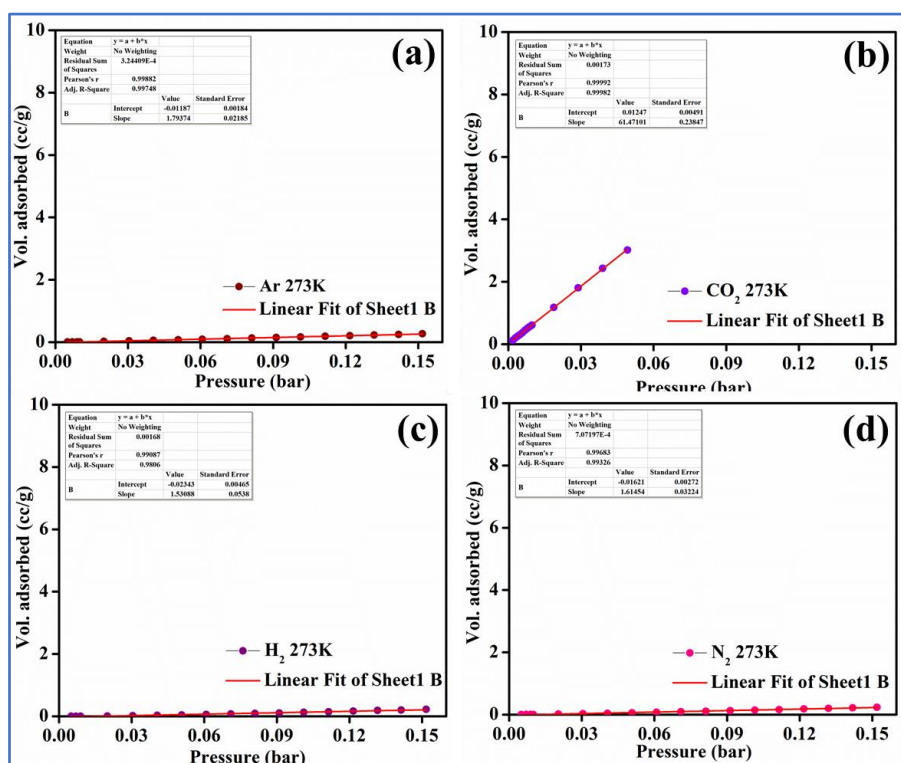
**Figure A8.** Carbon dioxide adsorption isotherm for Zn-DAT and Zn-TAZ at 298 K. The solid line shows the best fit to the data using the Langmuir-Freundlich Equation.



**Figure A9.** Enthalpy of carbon dioxide for Zn-DAT calculated using the Clausius-Clapeyron equation.

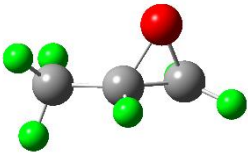
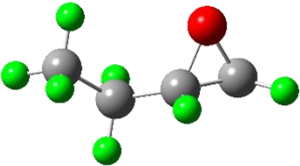
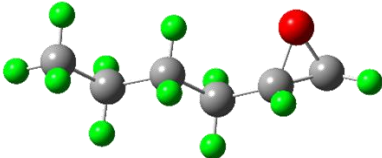
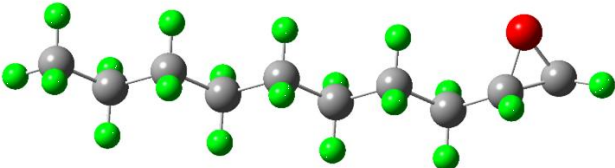
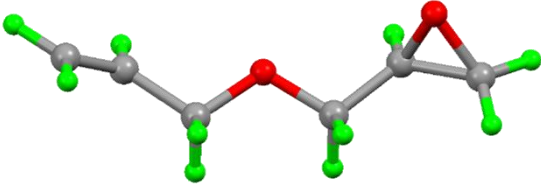
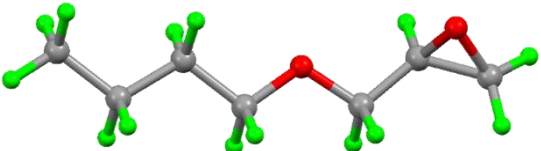


**Figure A10.** Gas selectivity for Zn-DAT calculated following the Henry's law from the CO<sub>2</sub>, N<sub>2</sub>, Ar and H<sub>2</sub> isotherms carried out at 273 K.



**Figure A11.** Linear fitting of CO<sub>2</sub>, Ar, H<sub>2</sub> and N<sub>2</sub> isotherms used for calculation of Henry's selectivity constants.

**Table A3.** Optimized geometries of epoxides using Gaussian09 at b3lyp/6-311g (d,p) level.

Substrates	Optimized structure	Dimensions
1,2-epoxy propane		~4.35 X 3.41 Å <sup>2</sup>
1,2-epoxy butane		~5.648 X 3.39 Å <sup>2</sup>
1,2-epoxy hexane		~8.198 X 3.39 Å <sup>2</sup>
1,2-epoxy decane		~13.321 X 3.39 Å <sup>2</sup>
allyl glycidyl ether		~8.901 X 3.140 Å <sup>2</sup>
butyl glycidyl ether		~ 10.462 X 3.140 Å <sup>2</sup>

### GCMC Simulations

Grand Canonical Monte Carlo (GCMC) simulations were carried out at 298 K for HbMOF1 to predict the single component adsorption of CO<sub>2</sub> at 298 K and N<sub>2</sub> at 77K. These calculations were performed using the RASPA simulation code. The simulation box was

made of 12 (2×3×2) unit cells of HbMOF1. Short-range dispersion forces were truncated at a cutoff radius of 12 Å while the interactions between unlike force field centers  $a$  and  $b$  were treated employing the Lorentz-Berthelot combination rules;  $\varepsilon_{ab} = \sqrt{\varepsilon_a \varepsilon_b}$ ,  $\sigma_{ab} = (\sigma_a + \sigma_b)/2$ , where  $\varepsilon_a$  and  $\sigma_a$  are the LJ parameters for species  $a$ . The long-range electrostatic interactions were handled using the Ewald summation technique. The fugacity for each adsorbed species at a given thermodynamic condition was computed with the Peng-Robinson equation of state (EoS). For each state point,  $5 \times 10^7$  Monte Carlo steps have been used for both equilibration and production runs. Three types of trials were considered for the molecules: (i) translation or rotation, (ii) creation/deletion, and (iii) exchange of molecular identity. The adsorption enthalpy at low coverage ( $\Delta h$ ) for each gas was calculated through configurational-bias Monte Carlo simulations performed in the NVT ensemble using the revised Widom's test particle insertion method. Additionally, to gain insight into the configurational distribution of the adsorbed species in HbMOF1, some additional data were calculated at different pressure including the radial distribution functions (RDF) between the guests and the host.

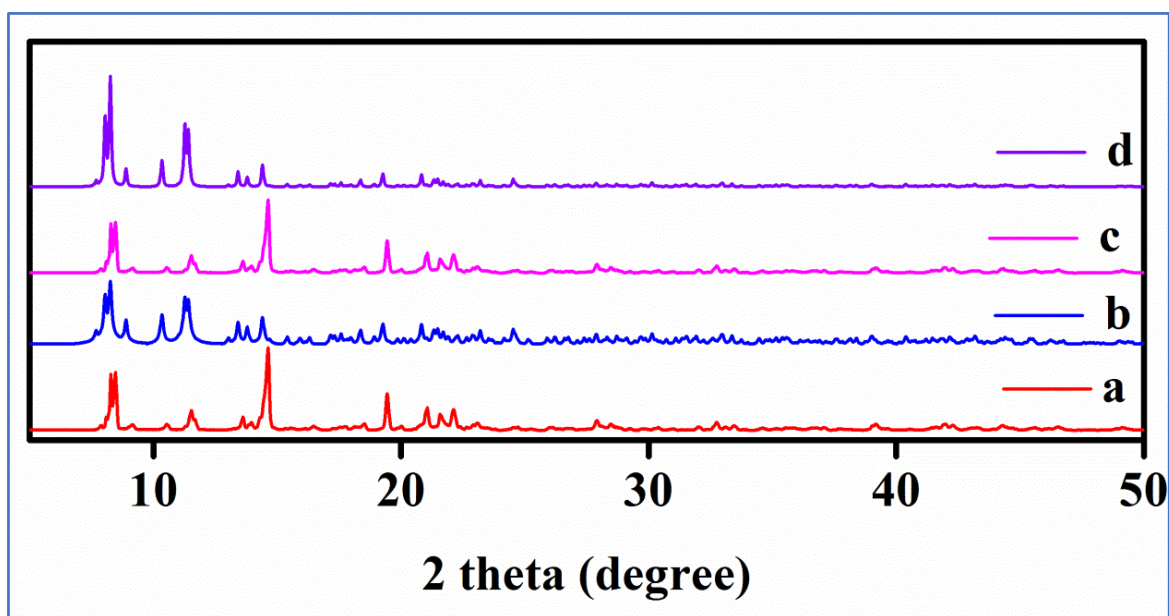


**Figure A12.** PXRD patterns of HbMOF1 (a) simulated pattern from single-crystal X-ray diffraction and for (b) as-synthesized sample (c) activated and (d) recycled sample after five catalytic cycles.

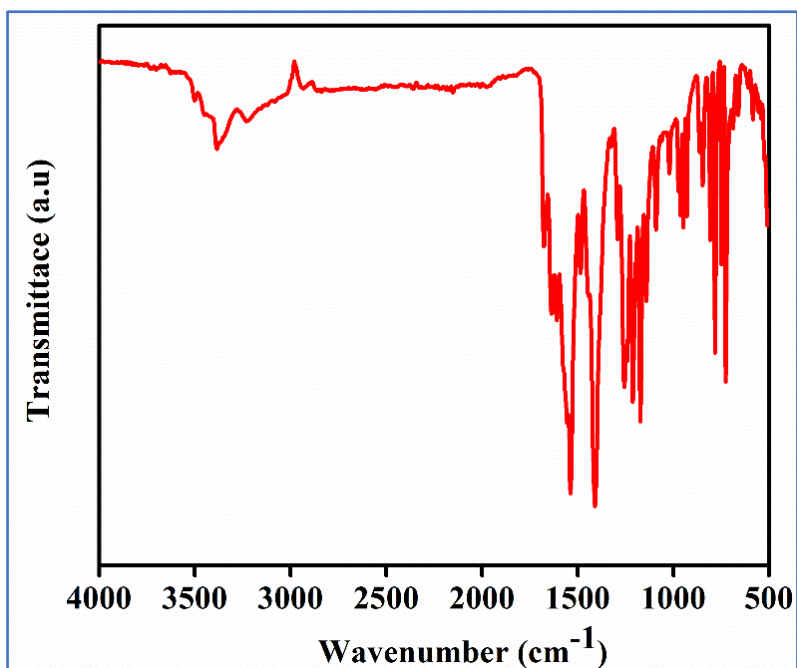


**Figure A13.** FT-IR spectrum of activated HbMOF1.

**Table A4.** Selected hydrogen bonding geometry for HbMOF1.

D-H...A	H...A	D...A	D--H...A
N4-H4B...O4	2.0900	2.906(4)	158.00
N5-H5A...O2	2.3300	3.033(4)	139.00
N5-H5B...O3	2.4200	2.986(4)	124.00
N6-H6B...O1	2.3000	3.088(4)	152.00
C5-H5...F7	2.3800	2.989(4)	123.00
C8-H8...F3	2.34002	2.972(4)	125.00

**Table A5.** Selected bond length (Å) and angles (°) for HbMOF1.

X-Y	Bond length (Å)	X-Y-Z	Bond angle (°)
Zn-O1	2.027(2)	O1-Zn-N1	103.83(9)
Zn-O2	2.063(2)	O2-Zn-O3	85.44(10)
Zn-O3	2.075(2)	O2-Zn-O4	87.86(10)
Zn-O4	2.046(2)	O2-Zn-N1	100.22(9)
Zn-N1	2.011(2)	O3-Zn-O4	155.73(9)
O1-Zn-O2	155.63(9)	O3-Zn-N1	101.41(9)
O1-Zn-O3	86.02(10)	O4-Zn-N1	102.74(9)
O1-Zn-O4	90.64(9)		

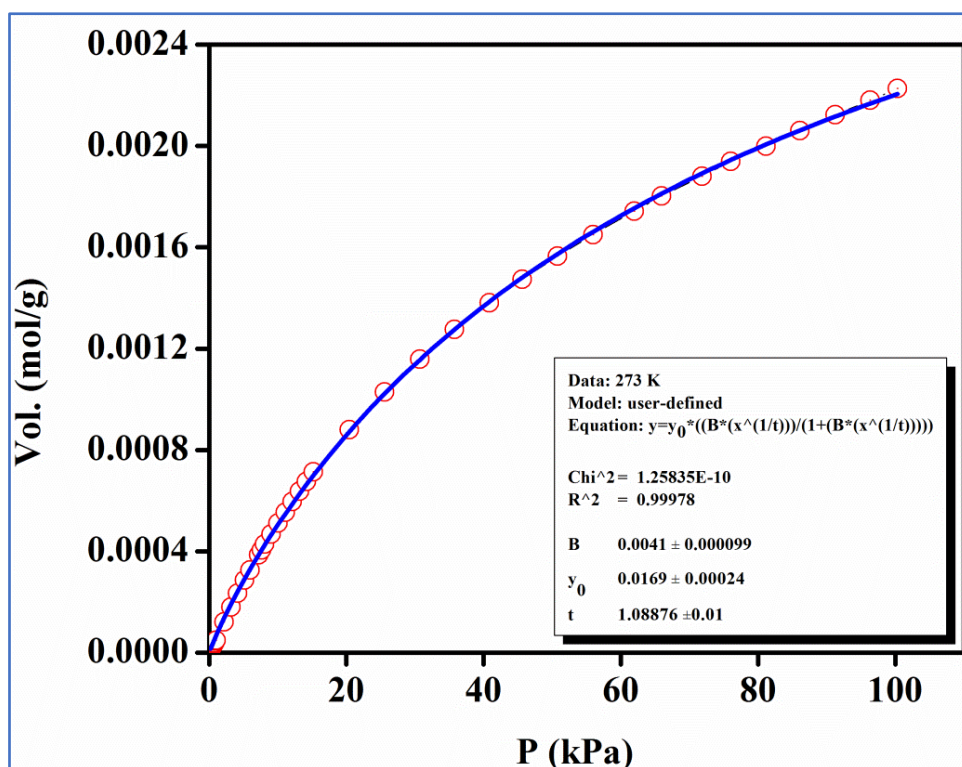


**Figure A14.** Carbon dioxide adsorption isotherm of HbMOF1 carried out at 273 K. The solid line shows the best fit to the data using the Langmuir-Freundlich Equation.

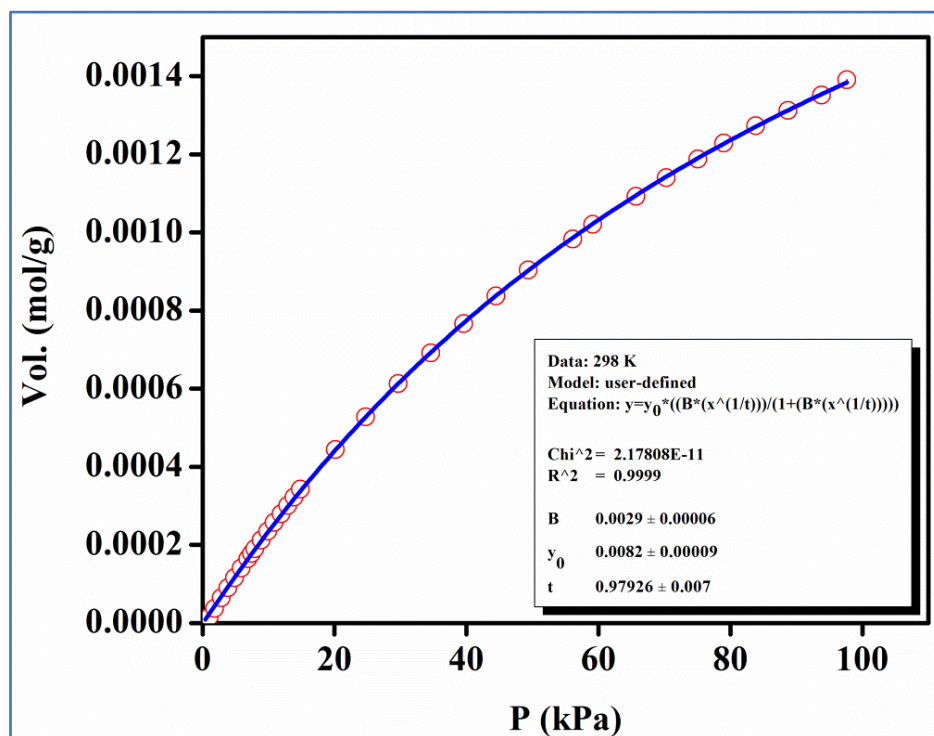


**Figure A15.** Carbon dioxide adsorption isotherm for HbMOF1 at 298 K. The solid line shows the best fit to the data using the Langmuir-Freundlich Equation.

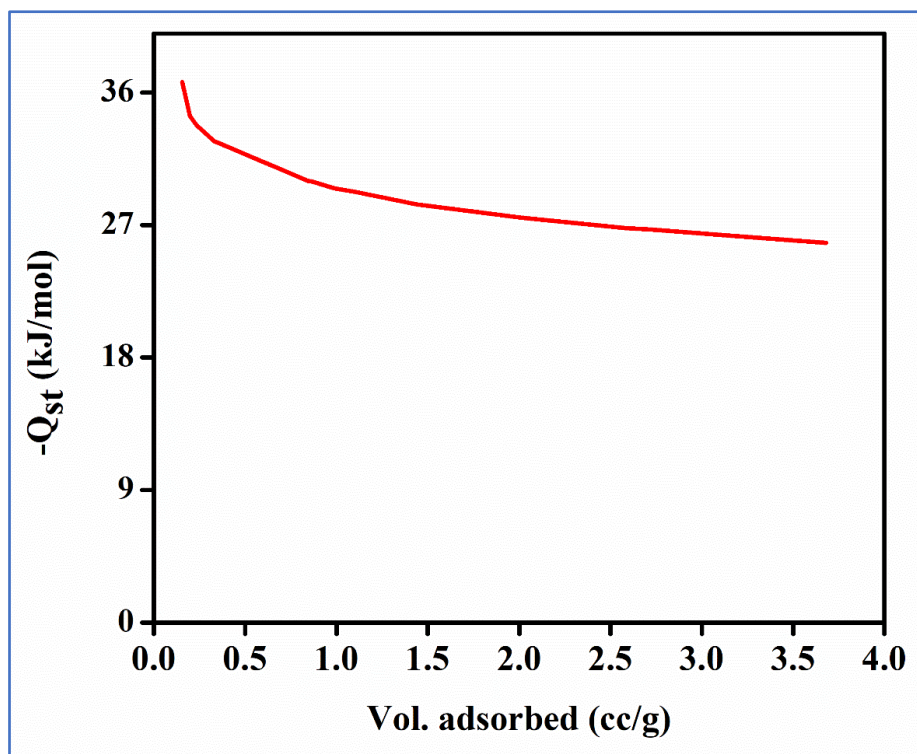


**Figure A16.** Enthalpy of carbon dioxide for HbMOF1 calculated using the Clausius-Clapeyron equation.

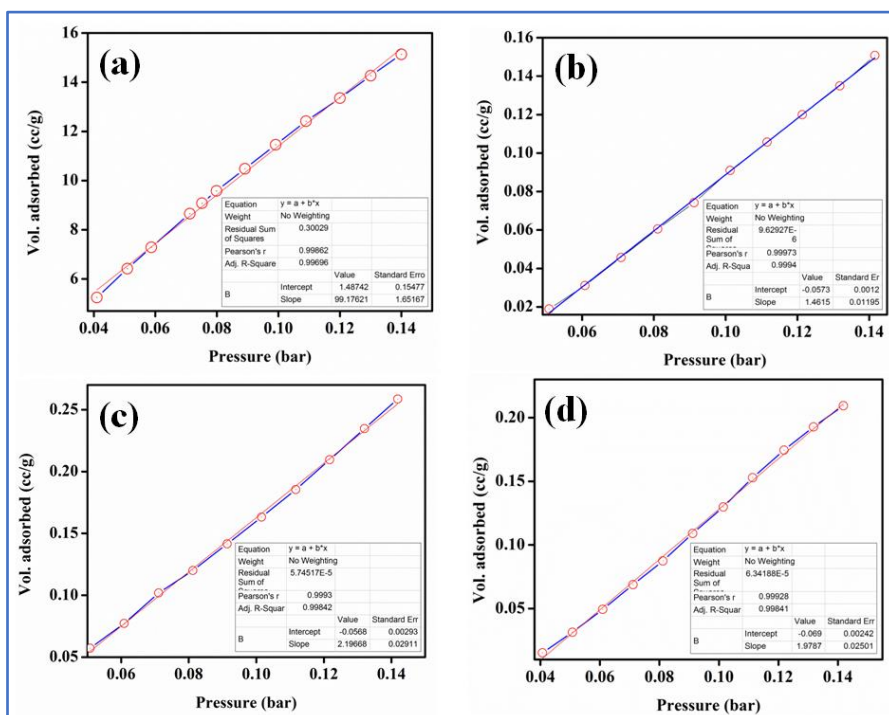


**Figure A17.** Calculation of Henry gas selectivity constants by linear fitting of CO<sub>2</sub> (a), H<sub>2</sub> (b), Ar (c) and N<sub>2</sub> (d) isotherms.

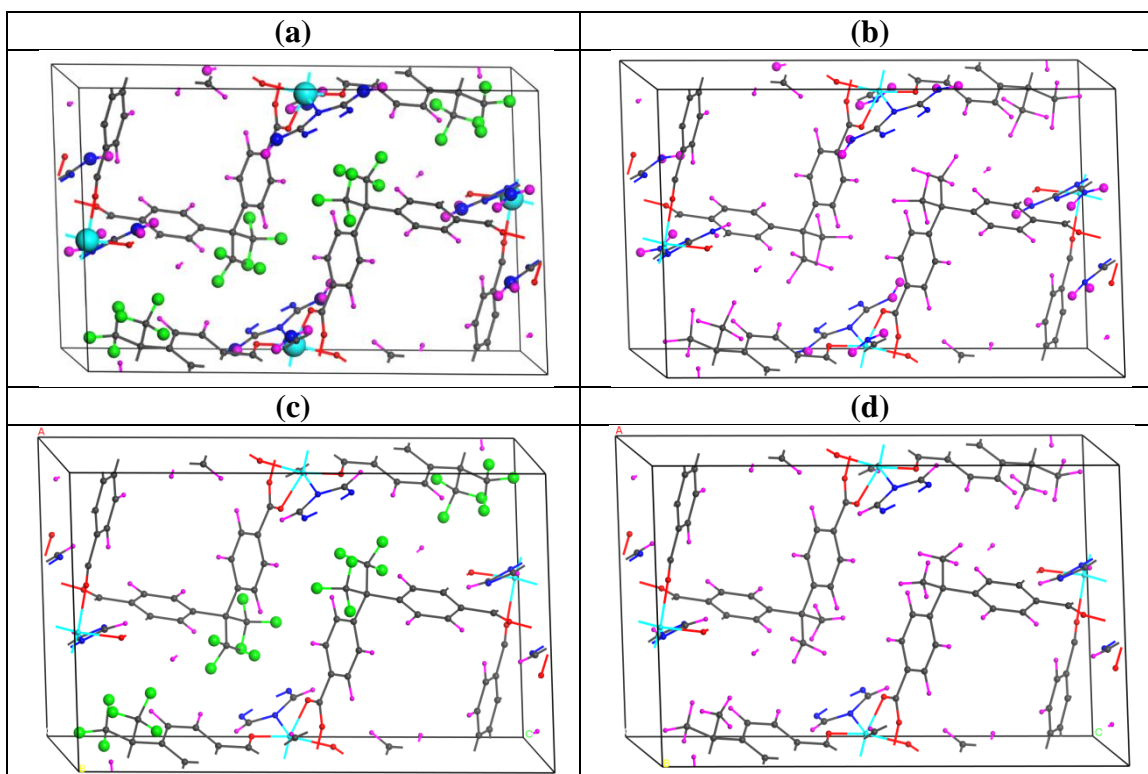


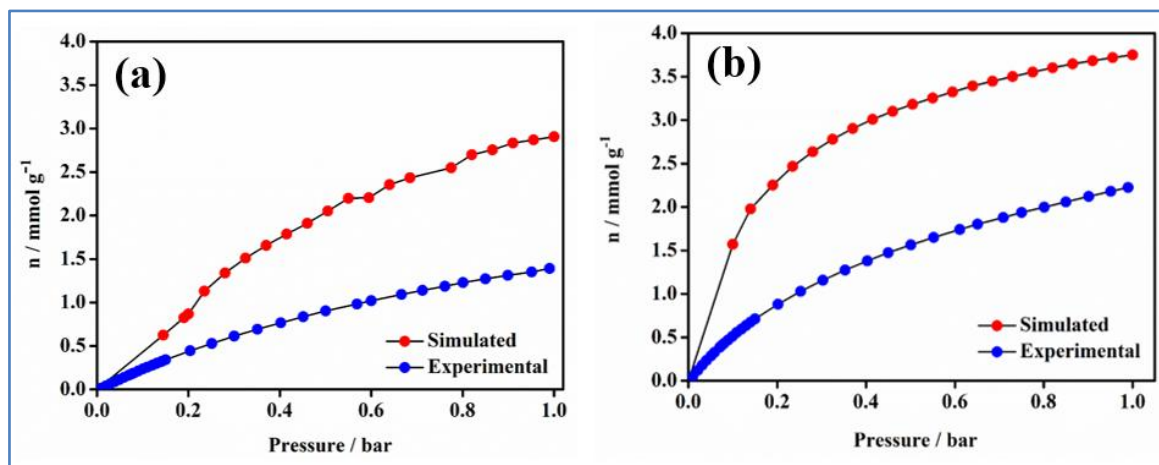
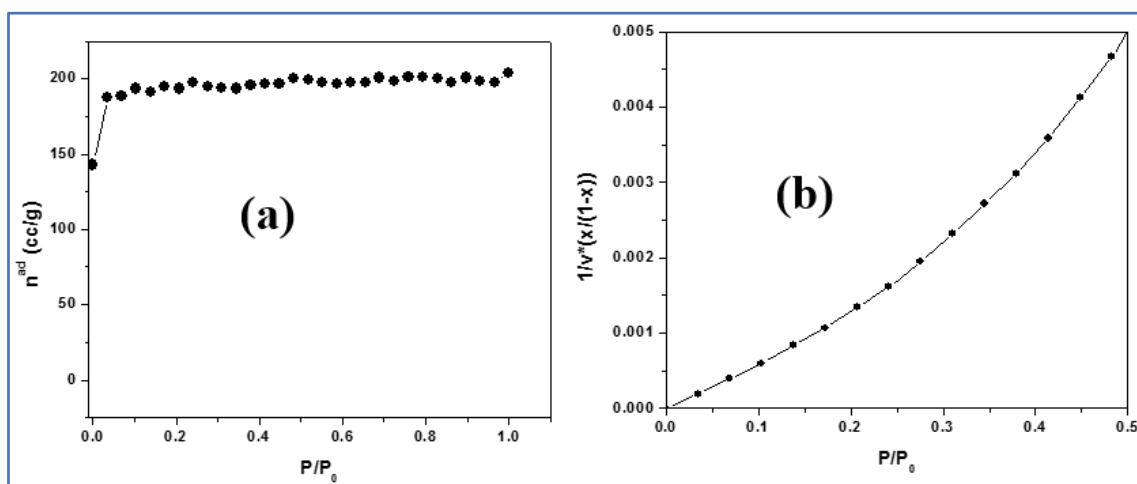
**Figure A18.** The single unit cell ( $1\times 1\times 1$  simulation box) considered for the DFT calculations viewed along  $a$ -axis for HbMOF1 (a), HbMOF1-hypo-1 (b), HbMOF1-hypo-2 (c) and HbMOF1-hypo-3 (d) where it is slightly twisted for better views of its functional groups ( $-\text{NH}_2$  and  $-\text{CF}_3$ ) decorated 1D channel. (Gray, carbon; blue, nitrogen; white, hydrogen; red, oxygen; green, zinc; cyan, fluorine).

**Table A6.** LJ potential parameters for the atoms of the HbMOF1.

Atomic type	UFF	
	$\sigma$ (Å)	$\varepsilon/k_B$ (K)
C	3.851	52.841
H	2.886	22.143
N	3.660	34.724
O	3.500	30.195
Zn	2.763	32.435

**Table A7.** Potential parameters and partial charges for the adsorbates

Atomic type	$\sigma$ (Å)	$\varepsilon/k_B$ (K)	$q$ (e)
CO <sub>2</sub> _C	2.757	28.129	0.6512
CO <sub>2</sub> _O	3.033	80.507	-0.3256
N <sub>2</sub> _N	3.310	36.000	-0.4820
N <sub>2</sub> _COM	0.00	0.00	0.9640

**Figure A19.** Comparison of the single component simulated isotherms for CO<sub>2</sub> (red) with the experimental data (blue) for HbMOF1 at 298 K (a) and 273 K (b).**Figure A20.** BET surface area calculation for HbMOF1 using simulated N<sub>2</sub> isotherm at 77 K. (a) Plot of  $V_{\text{excess}}(1 - P/P_0)$  vs  $P/P_0$  for the determination using the first consistency criterion, (b) the selected linear plot that satisfies the second consistency criterion and the corresponding BET surface area from the linear fit.

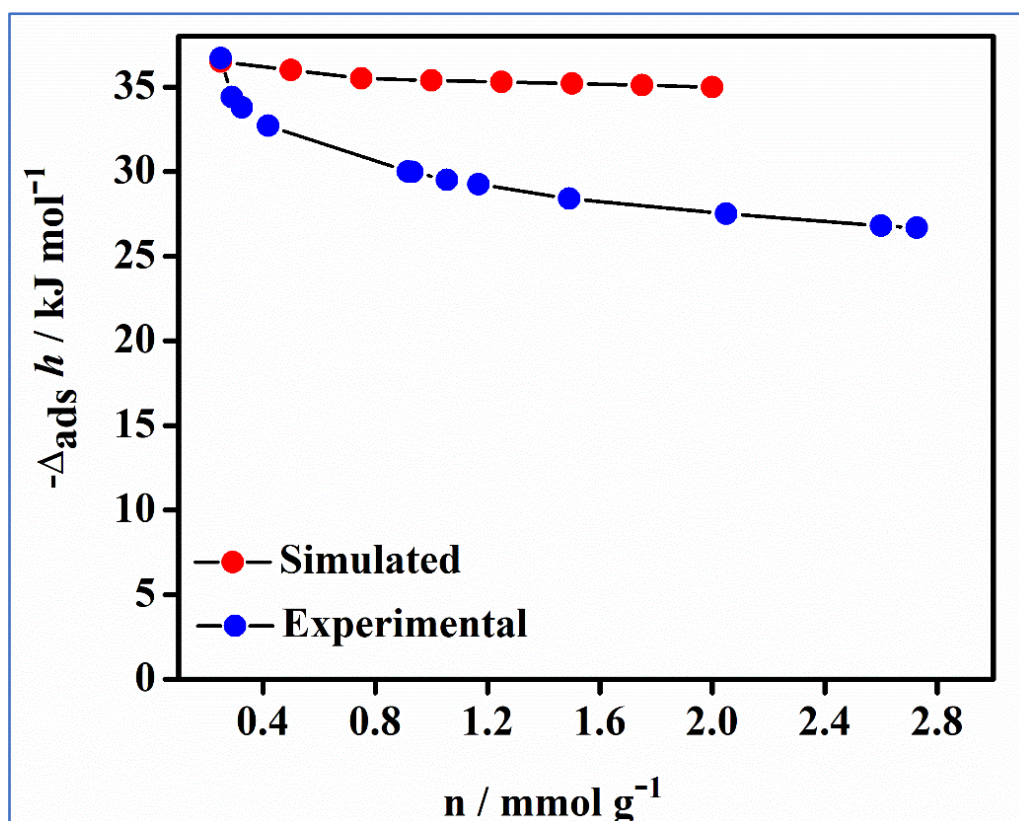


**Figure A21.** Comparison of the simulated adsorption enthalpy simulated (red) for CO<sub>2</sub> with the experimental data (blue) in HbMOF1.

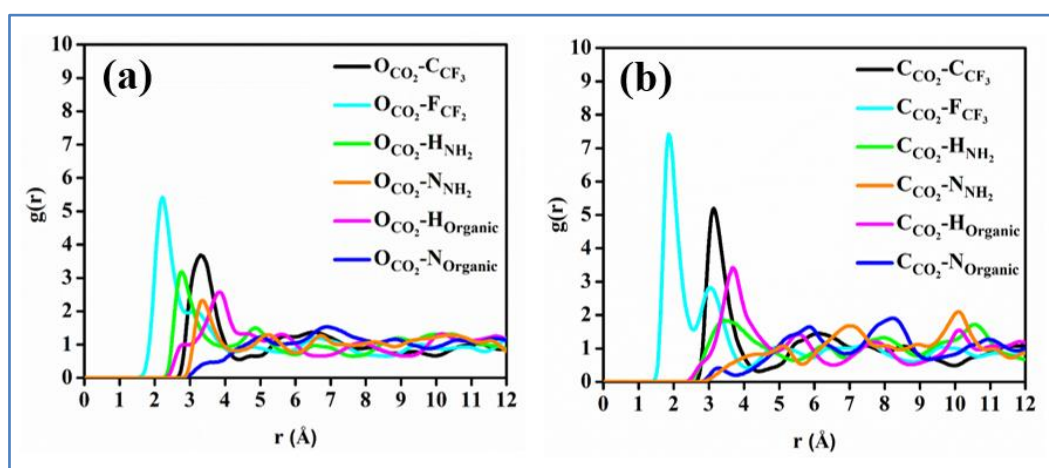


**Figure A22.** Radial distribution functions (RDF) between CO<sub>2</sub> and the atoms of the MOF framework (CF<sub>3</sub> carbon, C<sub>CF3</sub>: black, CF<sub>3</sub> Fluorine, F<sub>CF3</sub>: cyan, NH<sub>2</sub> hydrogen, H<sub>NH2</sub>: green, NH<sub>2</sub> Nitrogen, N<sub>NH2</sub>: orange, Organic Nitrogen, N<sub>Organic</sub>: blue and Organic Hydrogen, H<sub>Organic</sub>: magenta) extracted from the single component adsorption in HbMOF1 at 1 bar and 298 K: Oxygen of CO<sub>2</sub>: O<sub>CO2</sub> (a) and Carbon of CO<sub>2</sub>: C<sub>CO2</sub> (b).

**Table A8.** The simulated CO<sub>2</sub> adsorption enthalpies for HbMOF1 and the hypothetical models having the same topology.

MOF	Enthalpy (kJ/mol)
HbMOF-1	36.0
HbMOF1-hypo-1	29.2
HbMOF1-hypo-2	24.5
HbMOF1-hypo-3	22.7

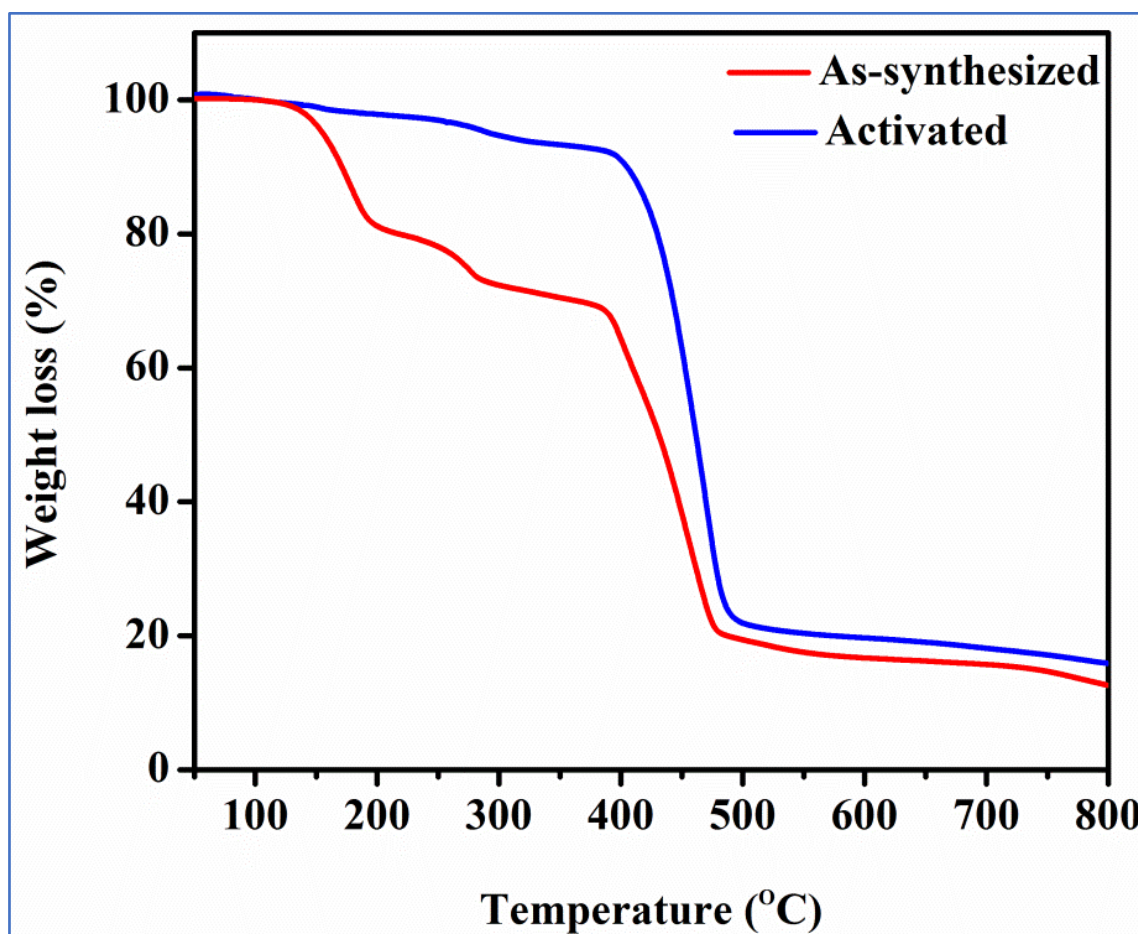


**Figure A23.** Thermogravimetric analysis of HbMOF1.

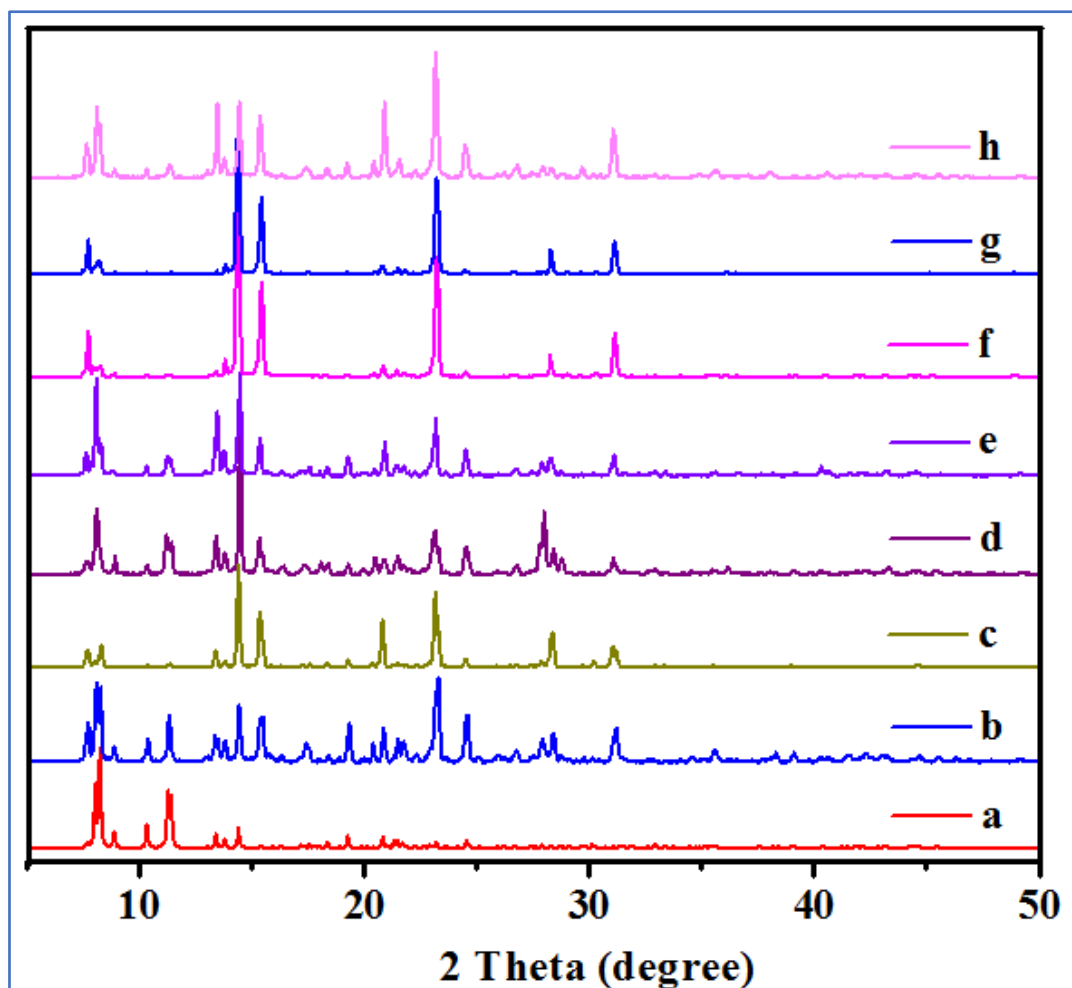


**Figure A24.** PXRD patterns of HbMOF1 (a) simulated pattern from single-crystal X-ray diffraction, and the sample isolated after treating with various solvents, such as (b) MeOH (c) 1,4-Dioxane (d) Acetone (e) water (f) N, N-dimethylformamide (g) N, N-dimethylacetamide (h) Isopropyl alcohol for 72h.

**Table A9.** Optimization of catalytic cycloaddition reaction of CO<sub>2</sub> with epichlorohydrin (ECH).

Entry no.	Catalyst (mol%)	Cocatalyst (mol%)	Temp.	Pressure (MPa)	Time (h)	Yield (%)
1	-	-	RT	0.1	24	-
2	0.1	-	RT	0.1	24	-
3	-	2.5	RT	0.1	24	46
4	0.1	2.5	RT	0.1	12	68
5	0.1	2.5	80	0.1	4	96
6	0.1	2.5	RT	0.1	24	>99

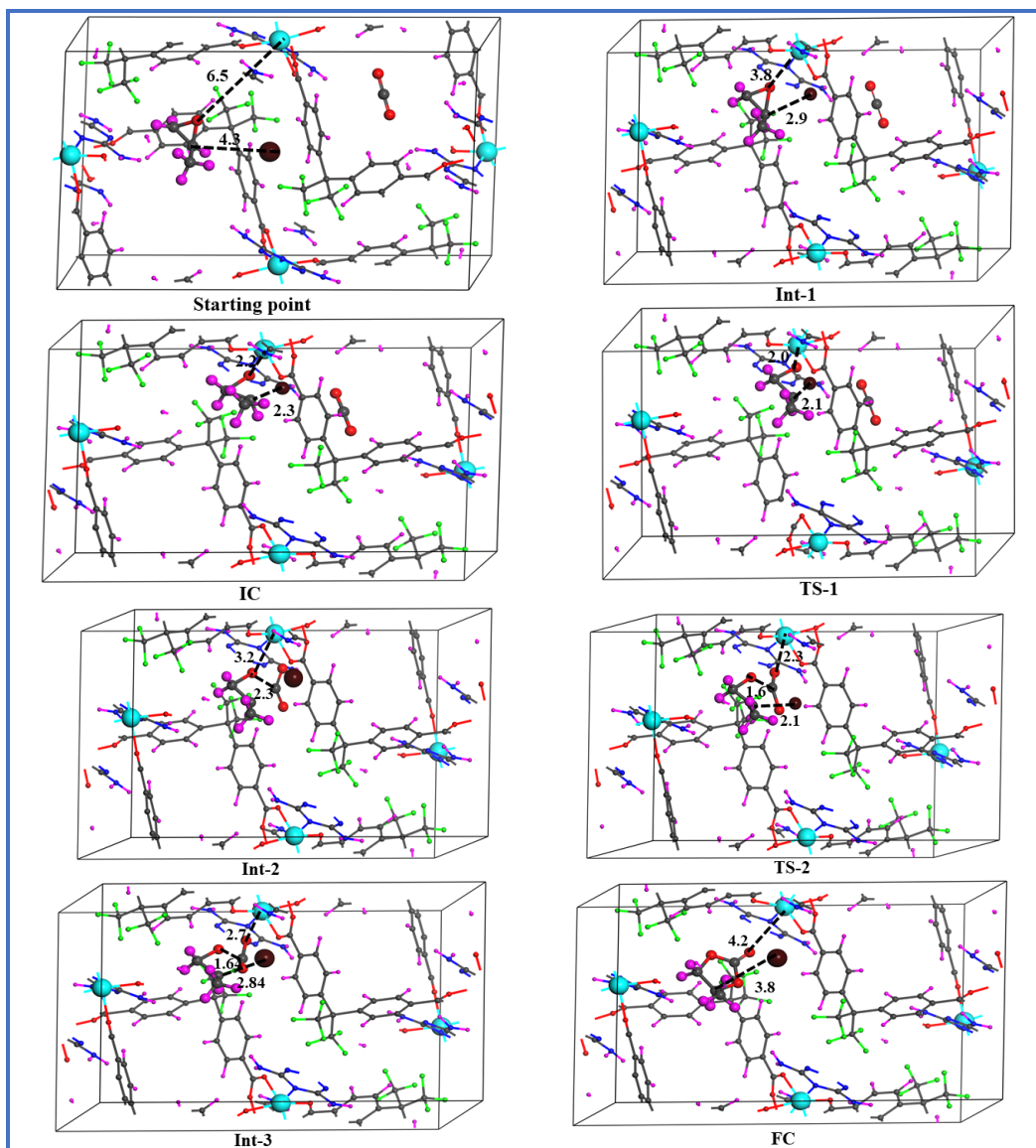


**Figure A25.** Mechanistic Pathways of the Intermediates and Transition States in the Cycloaddition of Propylene oxide and CO<sub>2</sub> using the HbMOF1 catalyst (Bond Distances are in Å)

### Models for the Host Framework Microscopic

The experimentally elucidated structure of Mg-MOF was initially geometry optimized at the Density Functional Theory (DFT) level using the CP2K package. In these simulations, the positions of atoms in the framework were relaxed while the unit cell parameters were kept fixed at the values determined experimentally. All the structural optimizations were done using Perdew-Burke-Ernzerhof (PBE) functional along with a combined Gaussian basis set and pseudopotential. For Carbon, Nitrogen, Oxygen, and Hydrogen, a triple zeta (TZVP-MOLOPT) basis set was considered, while a double zeta (DZVP-MOLOPT) was applied for Magnesium. The pseudopotentials used for all of the atoms were those derived by Goedecker,

Teter, and Hutter. The van der Waals interactions were taken into account via the use of semi-empirical dispersion corrections as implemented in the DFT-D3 method. The atomic point charges for all framework atoms in Mg-MOF were obtained using the REPEAT method proposed by Campana *et al.*, which was implemented into the CP2K code based on a restrained electrostatic potential framework.

**Table A10.** Comparison of catalytic activity of HbMOF1 with literature reported MOFs for cycloaddition of CO<sub>2</sub> with terminal epoxide (PO) under mild conditions.<sup>a</sup>

Sl. No.	Catalyst (mol%)	Temperature (°C)	Pressure (MPa)	Time (h)	Yield (%)	Ref.
1	Cu(tactmb)	RT	0.1	48	47.5	4
2	HKUST-1	RT	0.1	36	35	5
3	1-NH <sub>2</sub>	RT	0.1	36	50	5
4	1-Urea	RT	0.1	36	98	55
5	BPDC-NH <sub>2</sub> -OMe	RT	0.1	48	41	6
6	BPDC-Urea-OMe	RT	0.1	48	37	6
7	MOF-505	RT	0.1	48	48	7
8	ZnGlu	RT	1.0	24	65	8
9	MMPF-9	RT	0.1	48	87.4	9
10	Cr-MIL-101	RT	0.8	24	82	10
11	Fe-MIL-101	RT	0.8	24	87	10
12	UMCM-1	RT	1.2	24	85	11
13	UMCM-1 NH <sub>2</sub>	RT	1.2	24	90	11
14	JLU-MOF58	RT	1	24	95	12
15	MOF-Zn-1	RT	1.0	24	98	13
16	Zn(II)-MOF	RT	0.8	24	>99	14
<b>17</b>	<b>HbMOF1</b>	<b>RT</b>	<b>0.1</b>	<b>24</b>	<b>&gt;99</b>	Chapter-2

<sup>a</sup> Reaction conditions, Epoxide: propylene oxide, Cocatalyst: TBAB.

### DFT Derived Specific Forcefields

The interaction between the guest molecules and Mg-MOF except for coordinatively unsaturated metal center (CUS), i.e. Mg, were explained by using the sum of a 12-6 Lennard-Jones (LJ) contribution and a columbic term. Due to the presence of CUS, we derived a specific forcefield to explain guest to host interactions. Here Buckingham analytic function with the aid of Density Functional Theory (DFT) based energy including Basis Set Superposition Error (BSSE) correction employed to address guest-host interaction (eqn 1).

$$U_{ij} = \underbrace{\sum_{i < j} \frac{1}{4\pi\epsilon_0} \frac{q_i q_j}{r_{ij}}}_{\text{Electrostatic term}} + \underbrace{4\epsilon_{ij} \left[ \left( \frac{\sigma_{ij}}{r_{ij}} \right)^{12} - \left( \frac{\sigma_{ij}}{r_{ij}} \right)^6 \right]}_{\text{Lennard-Jones term}} + \underbrace{\left[ A_{ij} e^{-B_{ij} r_{ij}} - S_g \frac{C_{ij}}{r_{ij}^6} \right]}_{\text{Buckingham term}} \dots\dots\dots 1$$

$\epsilon_{ij}$  and  $\sigma_{ij}$  indicate the interacting pair LJ parameter and the interaction parameters obtained through Lorentz-Berthelot mixing rules (i.e., a geometric combining rule for the energy and an arithmetic one for the atomic size:  $\epsilon_{ij} = (\epsilon_i \epsilon_j)^{1/2}$  and  $\sigma_{ij} = (\sigma_i + \sigma_j)/2$ ). The second term is the Columbic contribution between point charges  $q_i$  and  $q_j$  separated by a distance  $r_{ij}$ . A, B and C are the conventional Buckingham parameters for repulsive and attractive contribution, respectively and  $S_g$  indicates the global scaling factor for the dispersion energies.

For generating Buckingham potentials (A, B, and C parameters) from binding energy profile of guest-host interaction, we performed DFT calculation for the interaction of adsorbate molecules on a symmetric cluster of Mg-MOF framework having an unsaturated metal center which interact directly with the metal center, Mg. The respective symmetric cluster was placed in a tetragonal simulation box having the composition of  $Mg_3C_{50}H_{32}N_{18}O_{14}$  structural unit. Further, the binding energy of cluster to guest results in the potential energy curve and utilize to derive force field. All the energy calculations are performed with the help of DFT-based CP2K Package<sup>16</sup> and followed as same as the principles mentioned above. The binding energy was calculated as follows:

$$E_{B.E} = E_{(symmetrical\ unit + Guest)} - \{ E_{(symmetrical\ unit)} + E_{(Guest)} \}$$

Where  $E_{(symmetrical\ unit + Guest)}$ ,  $E_{(symmetrical\ unit)}$  and  $E_{(Guest)}$  indicate the energy of optimized symmetrical unit with adsorbate molecule, optimized symmetrical unit, and optimized guest molecule, respectively.

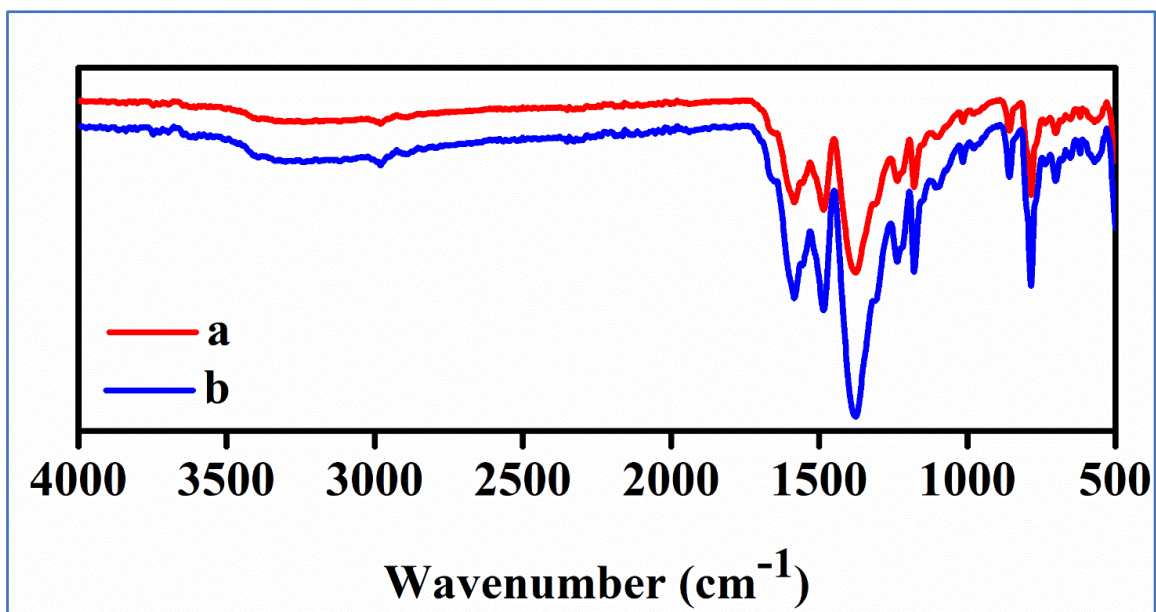


**Figure A26.** FT-IR spectra of Mg-MOF, (a) activated and (b) recycled sample after tenth catalytic cycle.

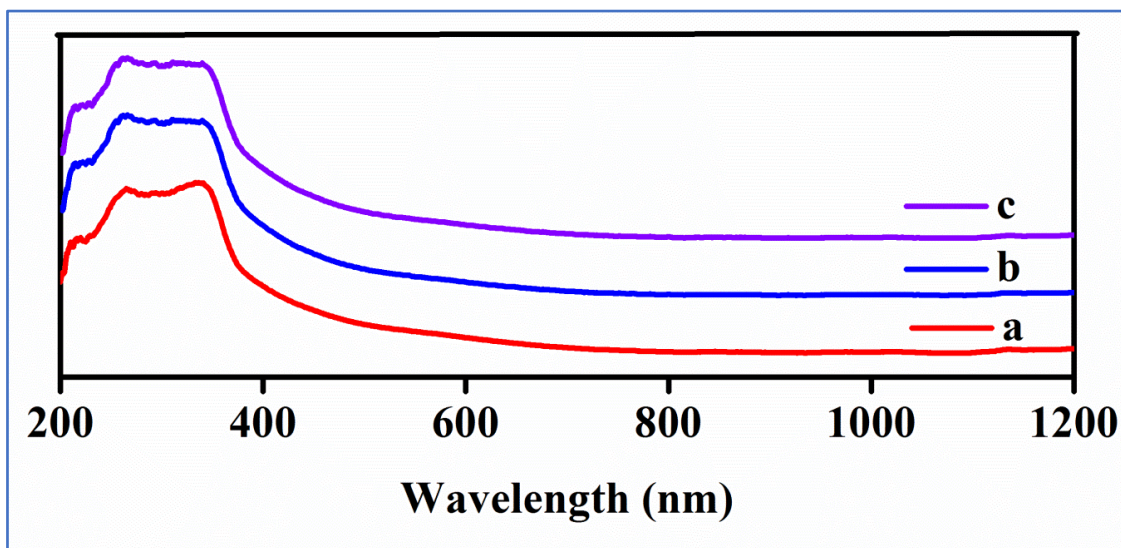


**Figure A27.** UV-Vis spectra of (a) H<sub>3</sub>TATAB ligand, (b) activated Mg-MOF, (c) recycled sample after ten catalytic cycles.

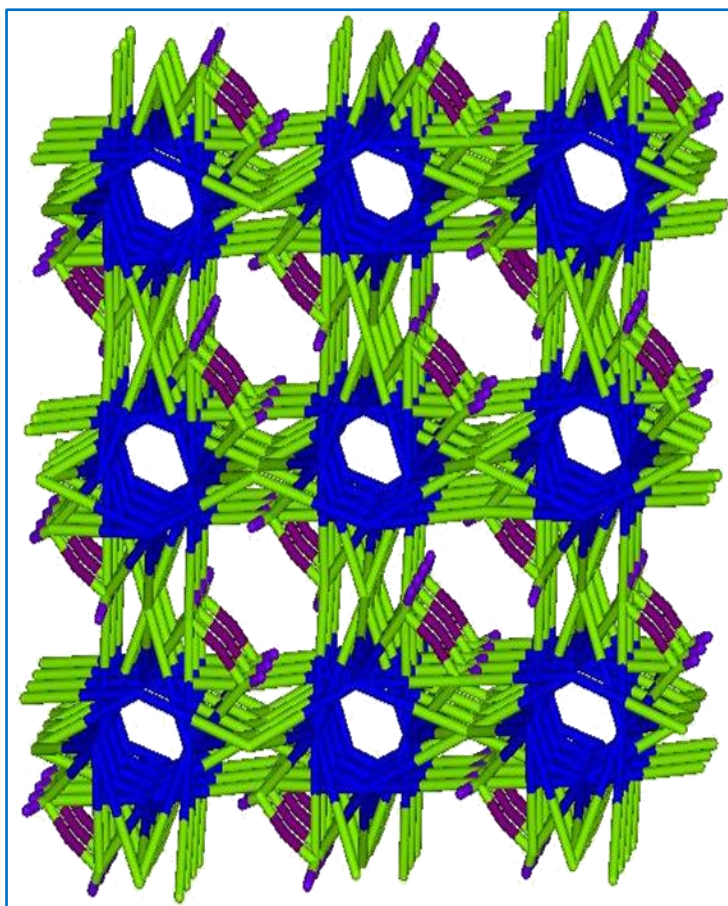


**Figure A28.** TOPOS image of Mg-MOF.

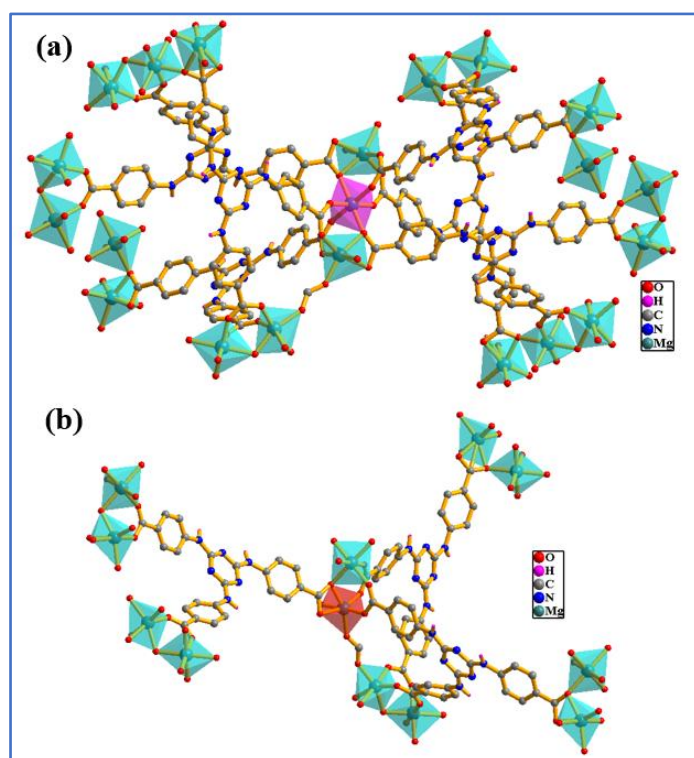


**Figure A29.** (a) View of 8-connected Mg1 node and (b) 3-connected Mg2 node.

**Table A11.** Selected bond length (Å) and angles (°) for Mg-MOF.

<b>X-Y</b>	<b>Bond length (Å)</b>	<b>X-Y-Z</b>	<b>Bond angle (°)</b>
Mg1-O5	2.060(3)	O1-Mg2-O2	94.91(15)
Mg1-O6	2.116(3)	O1-Mg2-O1w	175.45(18)
Mg1-O7	2.061(3)	O1-Mg2-O4	95.74(17)
Mg2-O1	1.999(4)	O1-Mg2-O6	97.17(14)
Mg2-O2	2.178(4)	O1-Mg2-O3	91.10(17)
Mg2-O1w	2.134(5)	O2-Mg2-O3	84.04(18)
Mg2-O4	1.989(4)	O2-Mg2-O4	158.25(18)
Mg2-O6	2.115(3)	O2-Mg2-O6	61.46(13)
Mg2-O3	2.124(5)	O2-Mg2-O3	98.89(17)
		O3-Mg2-O4	86.71(19)
<b>X-Y-Z</b>	<b>Bond angle (°)</b>	O3-Mg2-O6	86.25(16)
O5-Mg1-O6	88.60(11)	O3-Mg2-O3	84.69(19)
O5-Mg1-O7	88.33(12)	O4-Mg2-O6	98.37(16)
O6-Mg1-O7	90.34(11)	O4-Mg2-O3	99.80(19)

**Table 12.** Selected hydrogen bonding geometry for Mg-MOF.

<b>D-H··A</b>	<b>H··A</b>	<b>D··A</b>	<b>D-H··A</b>
N1-H1··N3	2.2000	3.056(5)	174.00
C5-H5··N2	2.3900	2.964(7)	119.00
C11-H11··N4	2.4100	2.974(7)	119.00
C14-H14··O5	2.4700	3.364(6)	161.00
C20-H20··N2	2.4800	2.925(7)	110.00

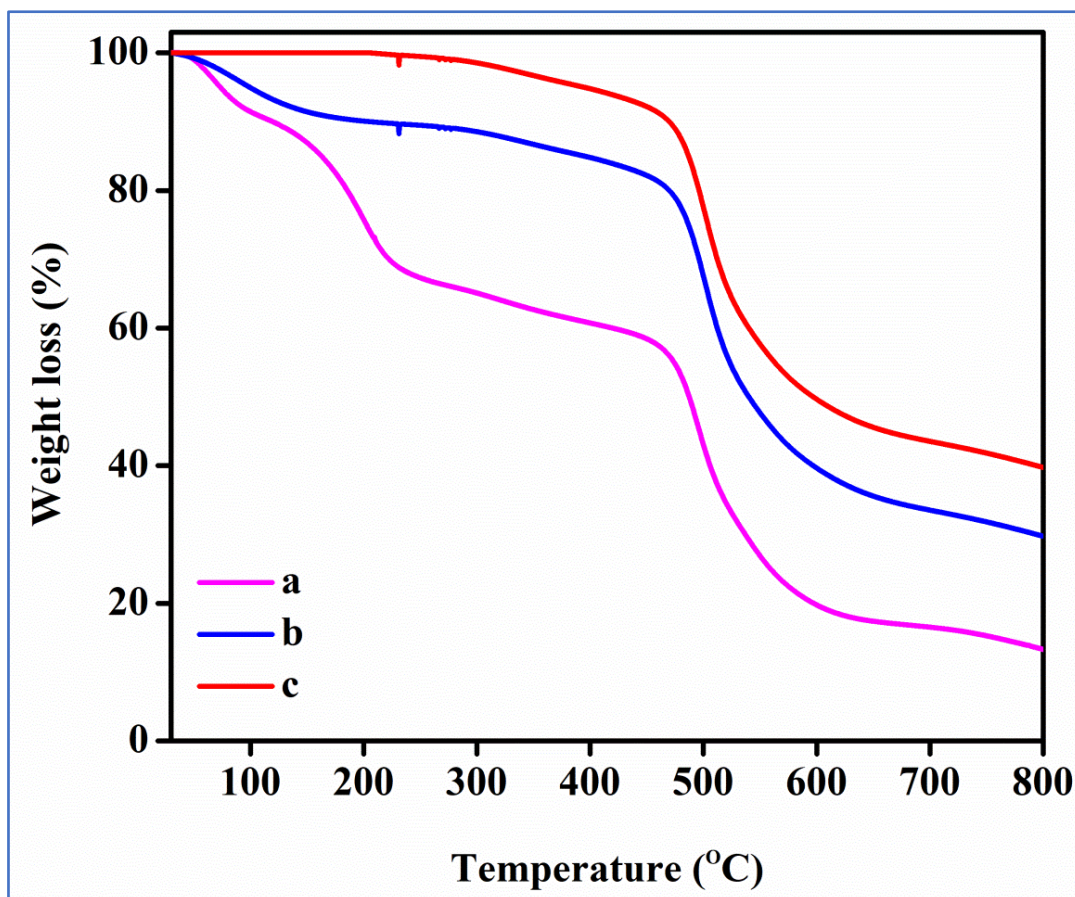


**Figure A30.** TGA plots of Mg-MOF (a) as-synthesized, (b) solvent exchanged, and (c) activated MOF.

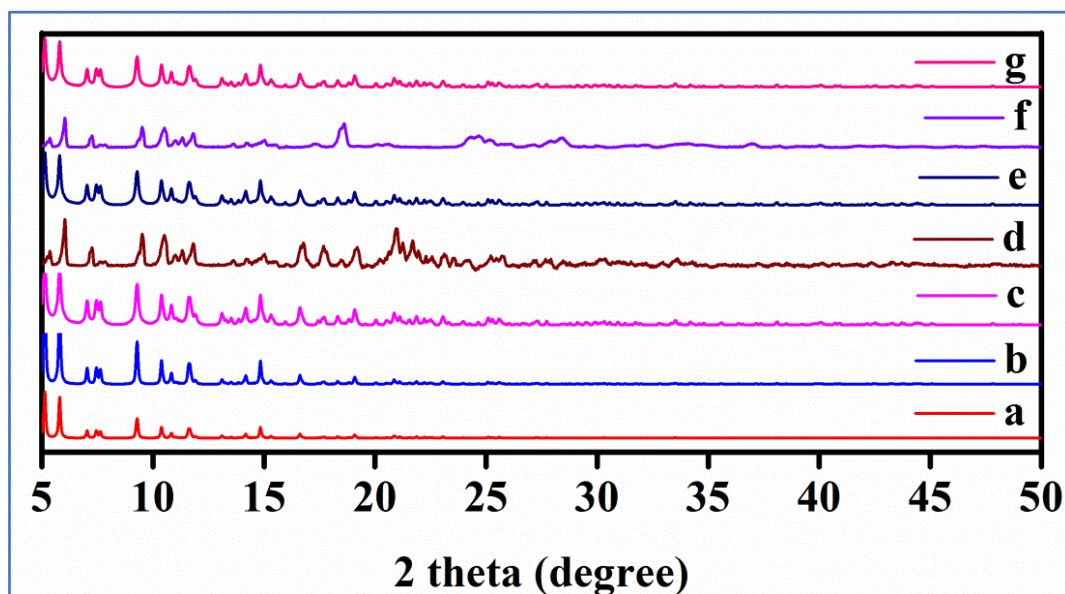


**Figure A31.** PXRD patterns of Mg-MOF recovered after treating with various solvents (a) simulated pattern and the sample treated with (b) DMF, (c) water, (d) acetone, (e) ethanol, (f), and (g) methanol.

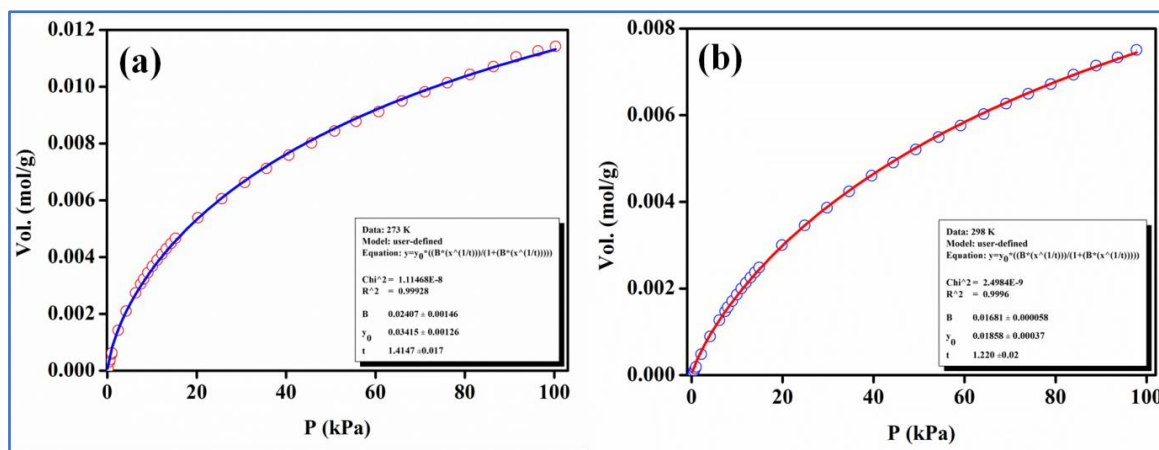


**Figure A32.** Carbon dioxide adsorption isotherm of Mg-MOF carried out at 273 K (a) and 298 K (b). The solid line shows the best fit to the data using the Langmuir-Freundlich equation.

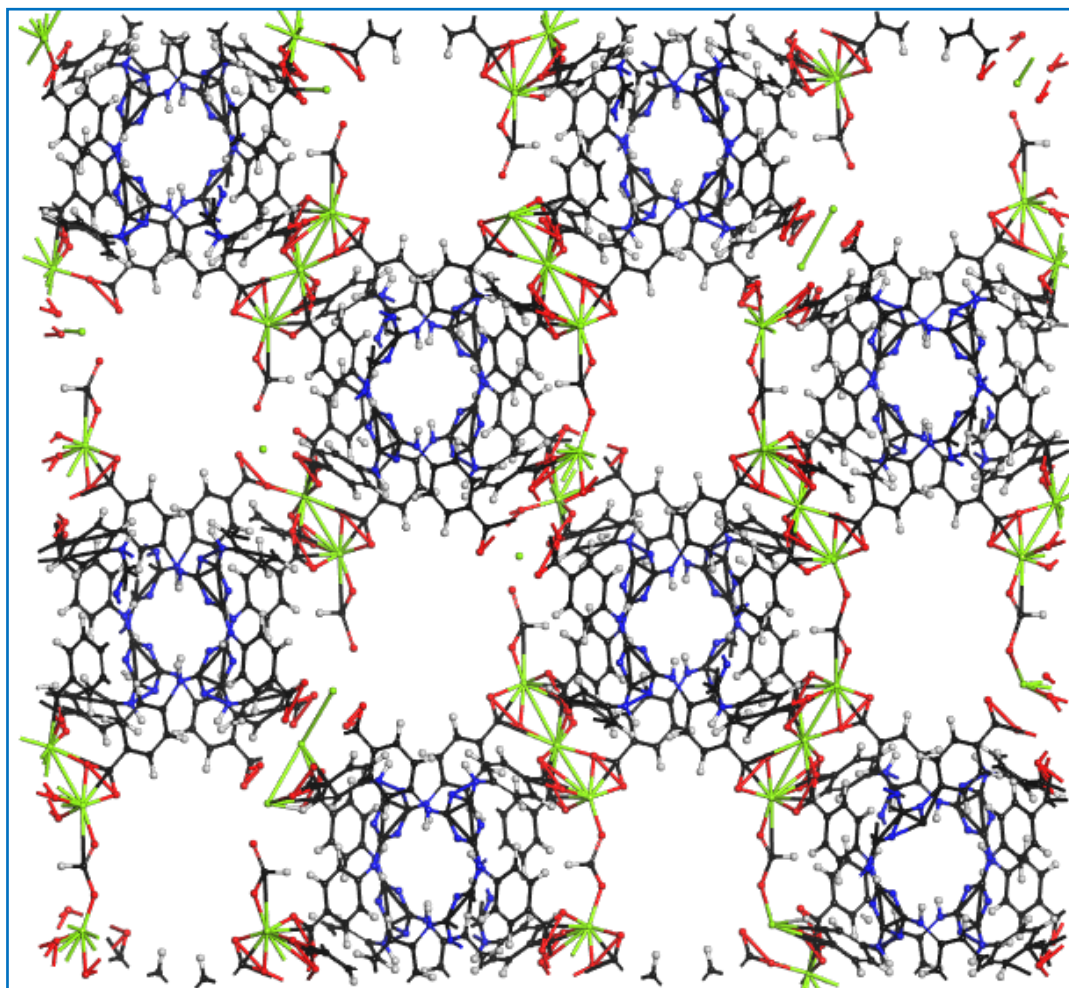


**Figure A33.** The single unit cell (1×1×1 simulation box) of Mg-MOF considered for the DFT calculations viewed along *c*-direction. (black, carbon; grey, hydrogen; red, oxygen; green, Magnesium).

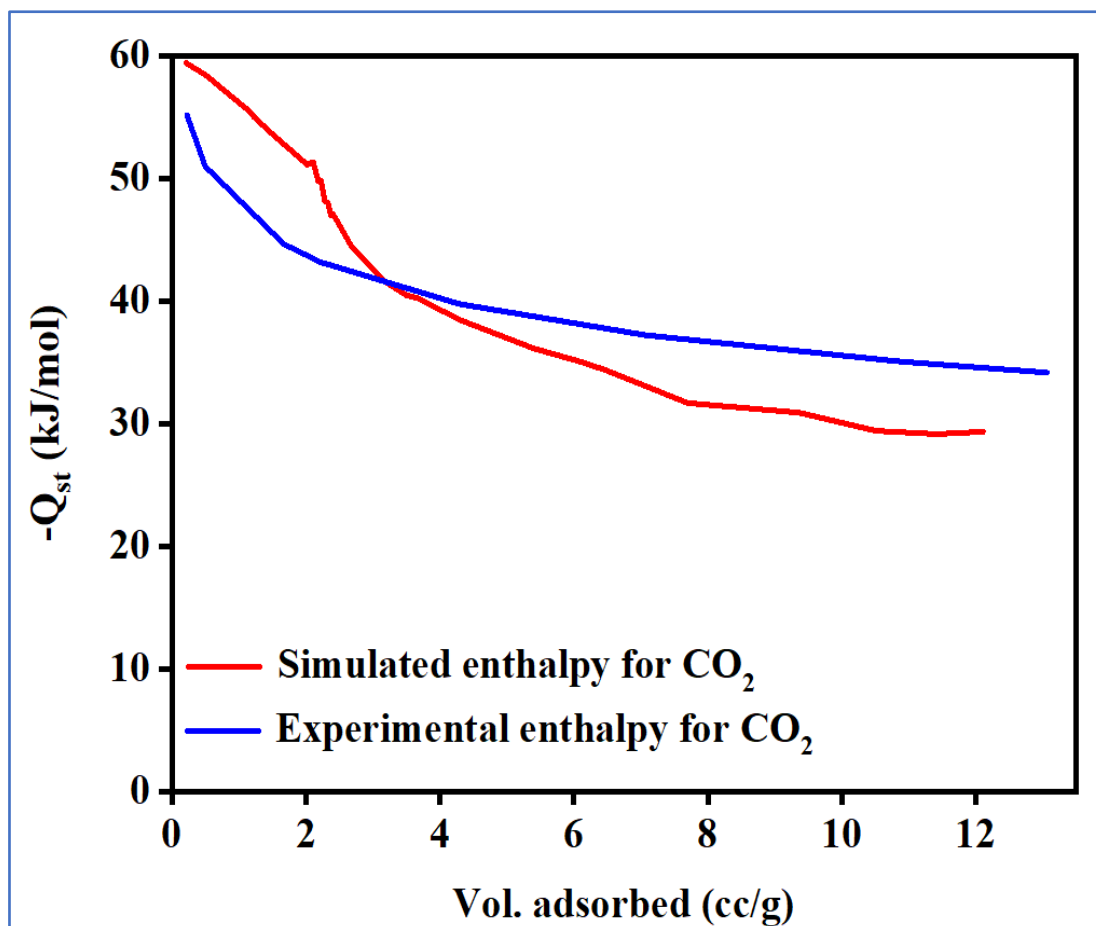


**Figure A34.** Simulated and experimental adsorption enthalpy for CO<sub>2</sub> in Mg-MOF.

**Table A13.** Comparison of interaction energy ( $Q_{st}$ ) with various reported Mg-based MOF.

SL. No	MOF	$Q_{st}$ (kJ/mol)	Reference
1	Mg-MOF-74(S)	42	15
2	Mg-MOF-184	35	16
3	[Mg <sub>2</sub> (DOBDC)]	44	17
4	MOF-889	28	18
5	Mg-MOF-74	41	19
6	Mg-MOF-74 (pellets)	45	20
7	<b>Mg-MOF</b>	<b>55</b>	<b>Chapter-3</b>

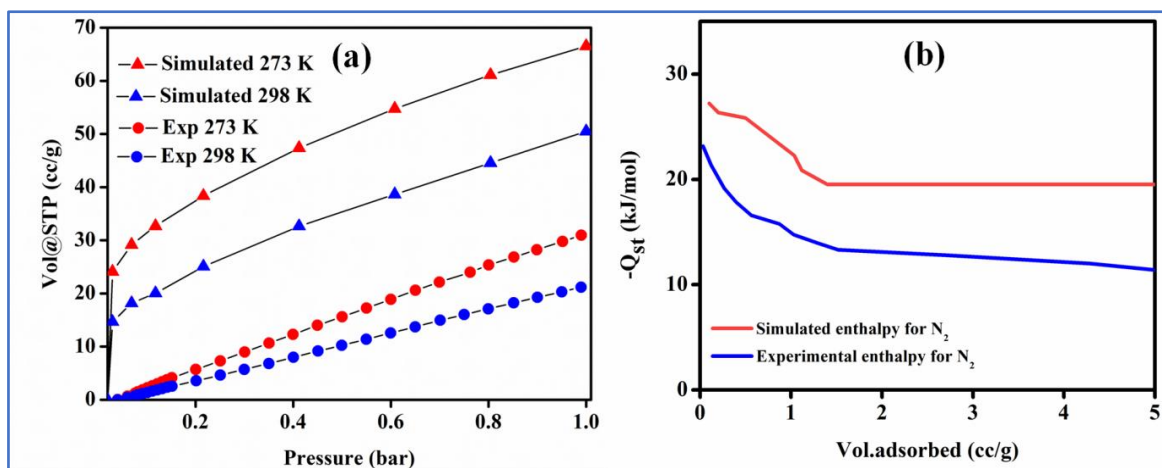


**Figure A35.** (a) Comparison of the single component simulated isotherms for N<sub>2</sub> (closed triangle) with the experimental data (closed circle) in Mg-MOF at 273 and 298 K and (b) Simulated and experimental adsorption enthalpy for N<sub>2</sub> in Mg-MOF.

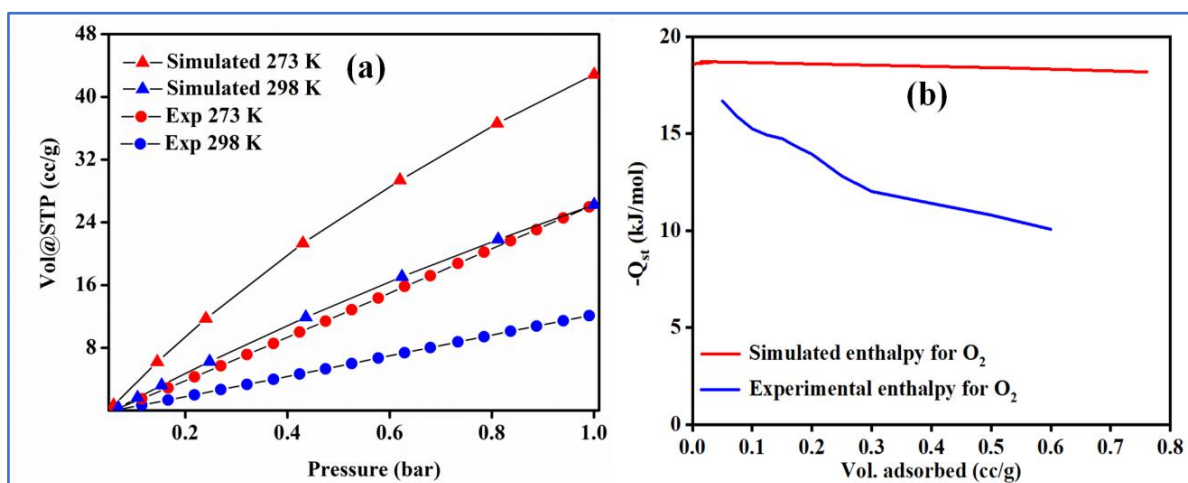


**Figure A36.** (a) Comparison of the single component simulated isotherms for O<sub>2</sub> (closed triangle) with the experimental data (closed circle) in Mg-MOF at 273 and 298 K and (b) Simulated and experimental adsorption enthalpy for O<sub>2</sub> in Mg-MOF.

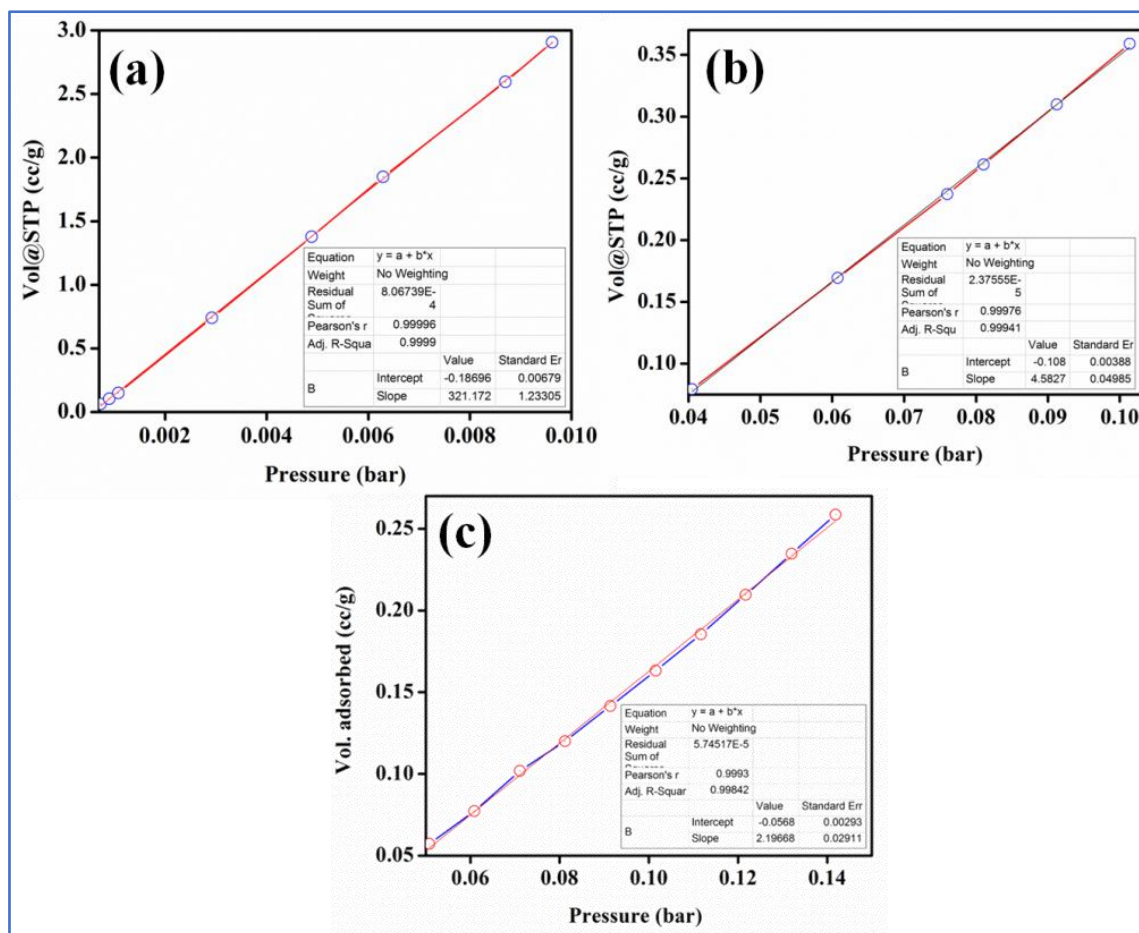


**Figure A37.** Calculation of gas selectivity constant for (a) CO<sub>2</sub> and (b) N<sub>2</sub> and (c) O<sub>2</sub> gases using on Henry law.

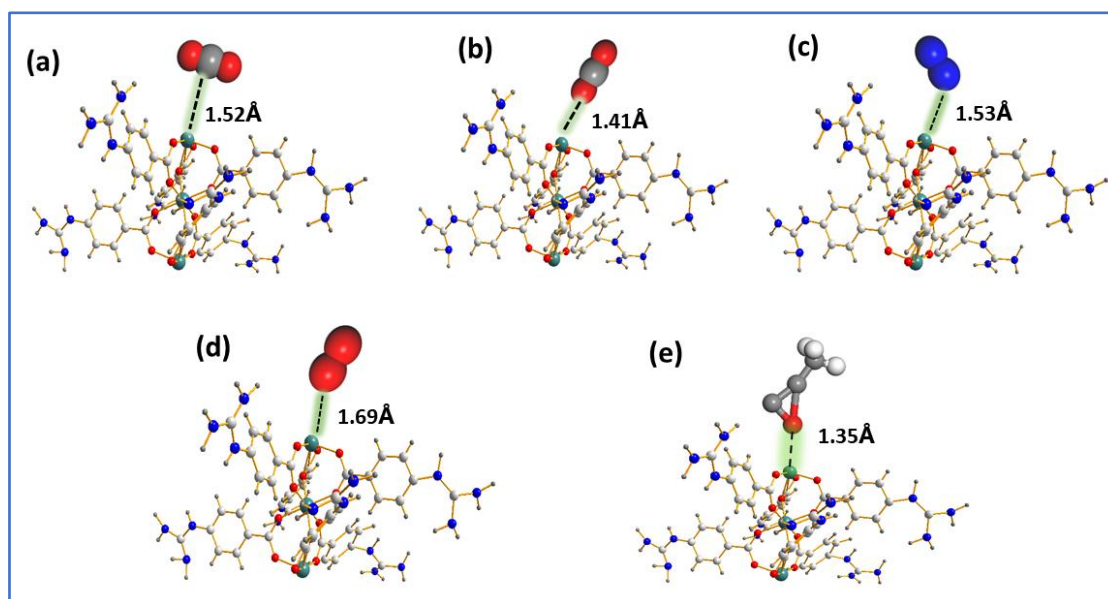


**Figure A38.** DFT geometry optimization of Mg-MOF cluster model with (a, b) CO<sub>2</sub>, (c) N<sub>2</sub>, (d) O<sub>2</sub> and (e) PO interaction to LA Mg(II) site.

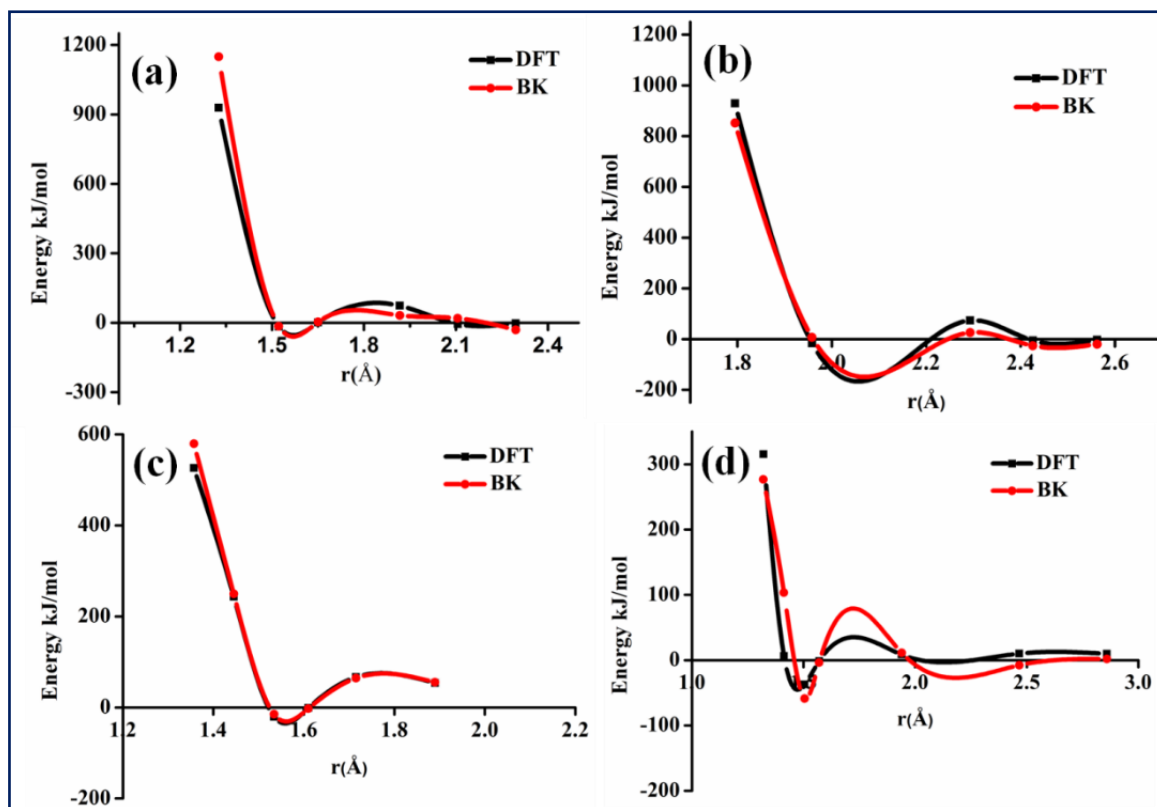


**Figure A39.** The potential energy values are calculated as moving each molecule along the dashed line, (a)  $C_{CO_2}$ , (b)  $O_{CO_2}$ , (c)  $N_{N_2}$ , and (d)  $O_{O_2}$  (comparison of DFT-derived forcefield fitted curve (red circles) on the DFT interaction energy profile (black squares)).

**Table A14.** The DFT based binding energy calculated with PBE functional by Mg-MOF and Guest interaction.

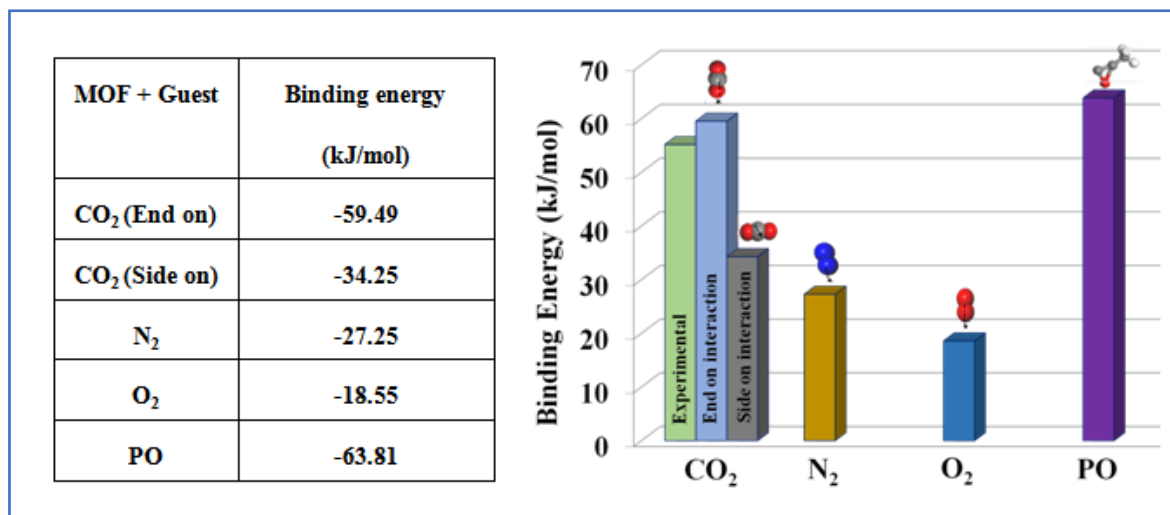


**Table A15.** LJ potential parameters for the atoms of the Mg-MOF

<b>Atomic type</b>	<b>DREIDING</b>	
	$\sigma$ (Å)	$\epsilon / k_B$ (K)
C	3.473	47.860
H	2.844	7.6490
O	3.033	48.158
N	3.662	34.724
Mg	2.6914	55.857

**Table A16.** Potential parameters and partial charges for the adsorbates.

<b>Atomic type</b>	$\sigma$ (Å)	$\epsilon / k_B$ (K)	$q$ (e)
CO <sub>2</sub> _C	2.757	28.129	0.6512
CO <sub>2</sub> _O	3.033	80.507	-0.3256
N <sub>2</sub> _N	3.310	36.000	-0.4820
N <sub>2</sub> _COM	0.000	0.000	0.9640
O <sub>2</sub> _O	3.050	54.400	-0.1120

**Table A17.** Buckingham parameters associated with the Mg-MOF and adsorbates

<b>Atomic type</b>	<b>A</b>	<b>B</b>	<b>C</b>
C <sub>CO2</sub> _Mg	3.5e6	8.5	2186.55
O <sub>CO2</sub> _Mg	3.1e6	4.23	1000
N <sub>N2</sub> _Mg	3.8e5	3.69	1000
O <sub>O2</sub> _Mg	4.3e6	5.89	1000
O <sub>H2O</sub> _Mg	8.9e5	4.09	738.13

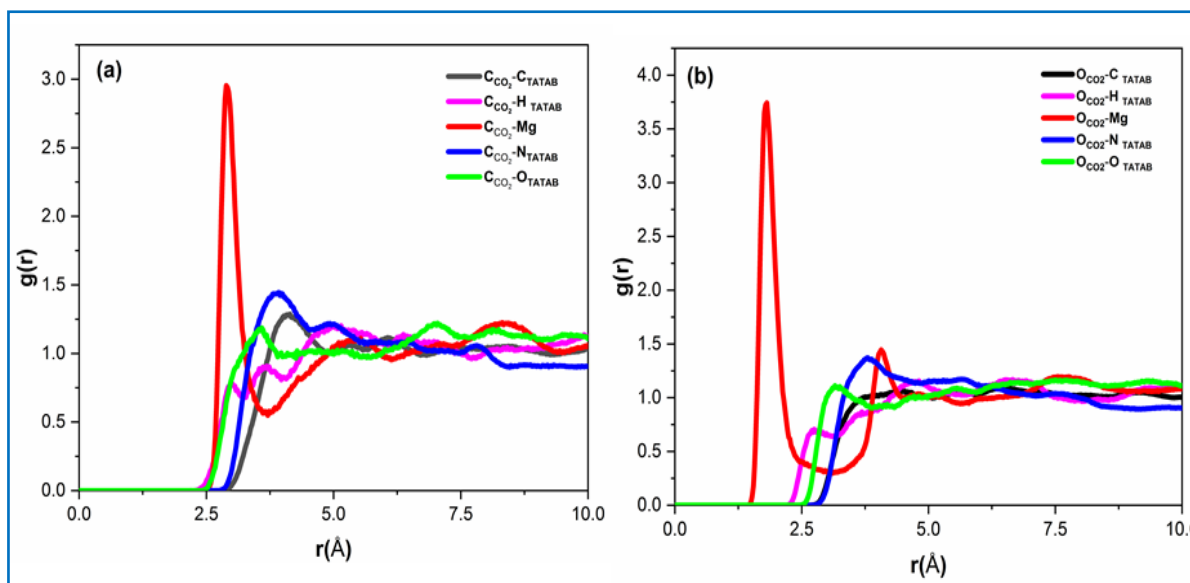


**Figure A40.** Radial distribution functions (RDF) between  $\text{CO}_2$  and the atoms of the MOF framework (Organic nitrogen,  $\text{N}_{\text{TATAB}}$ : blue, Organic hydrogen,  $\text{H}_{\text{TATAB}}$ : Magenta and Organic Oxygen,  $\text{O}_{\text{TATAB}}$ : green, Organic carbon,  $\text{C}_{\text{TATAB}}$ : black, Magnesium, Mg: red) extracted from the single component adsorption in Mg-MOF in 0.01bar at 273K.

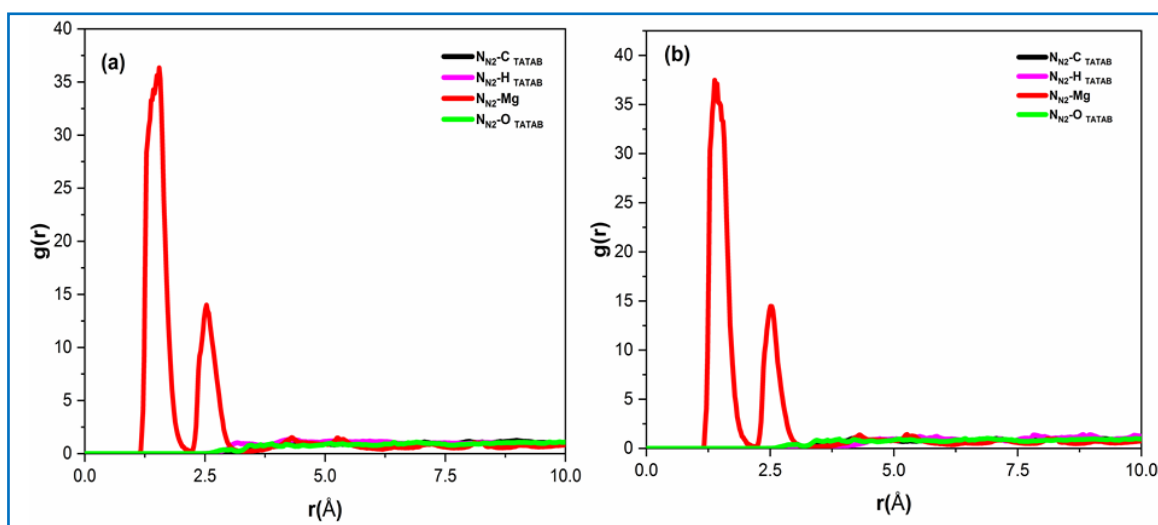


**Figure A41.** Radial distribution functions (RDF) between  $\text{N}_2$  and the atoms of the MOF framework extracted from the single-component adsorption in Mg-MOF in 0.01bar at 273K (a) and 298K (b).

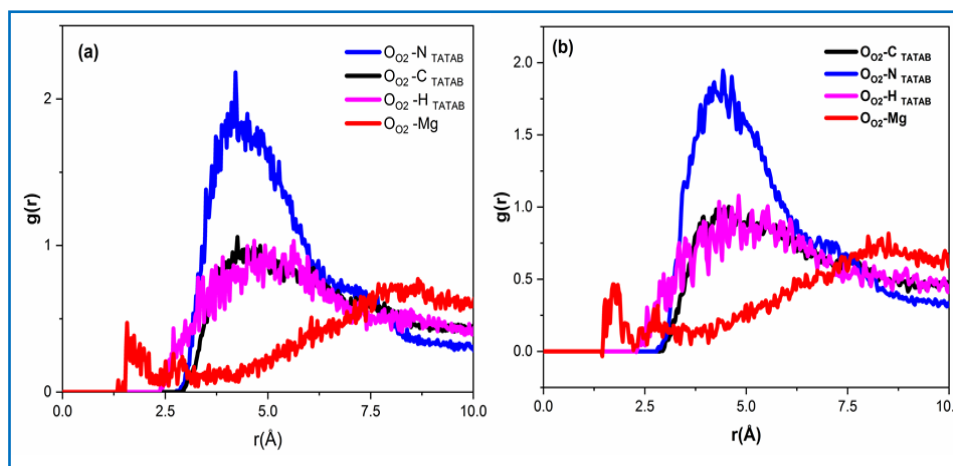


**Figure A42.** Radial distribution functions (RDF) between O<sub>2</sub> and the atoms of the MOF framework (Organic nitrogen, N<sub>TATAB</sub>: blue, Organic hydrogen, H<sub>TATAB</sub>: Magenta and Organic Oxygen, O<sub>TATAB</sub>: green, Organic carbon, C<sub>TATAB</sub>: black, Magnesium, Mg: red) extracted from the single component adsorption in Mg-MOF in 0.01bar at 298K.

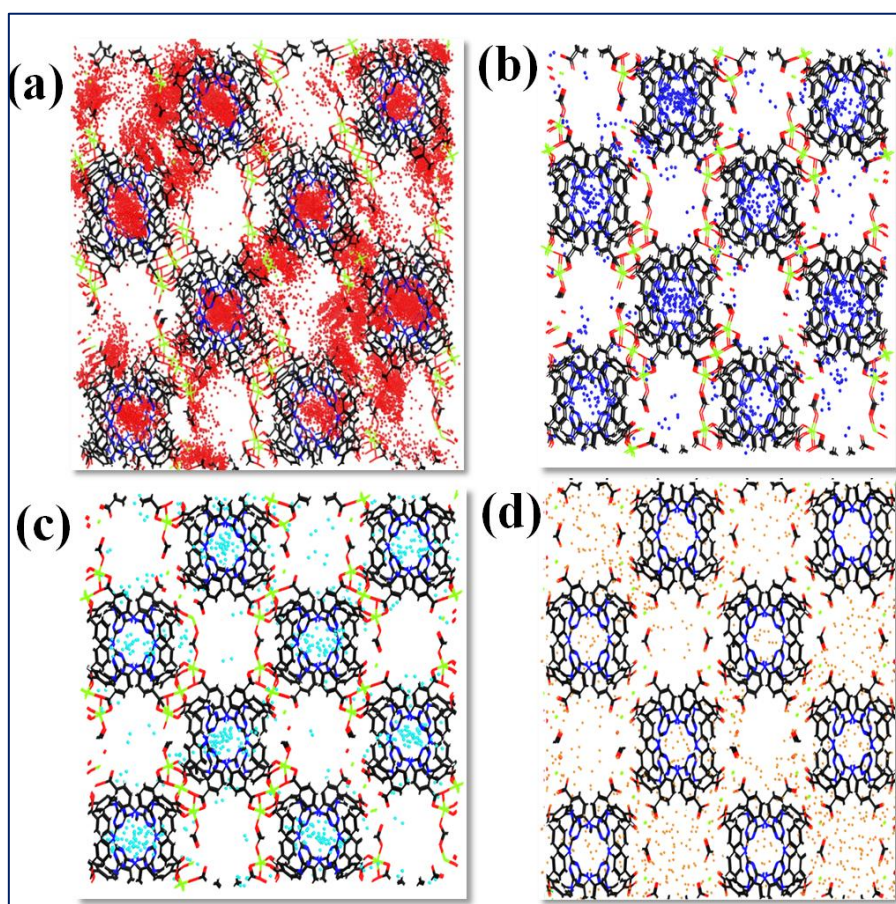


**Figure A43.** Maps of the occupied positions of CO<sub>2</sub> (a), N<sub>2</sub> (b) O<sub>2</sub> (c), and (d) H<sub>2</sub>O in 500 equilibrated frames for a given pressure of 1 bar and at 298 K for Mg-MOF, color code for the atoms: C (black), Mg(green), O (red), H (grey), N(blue).

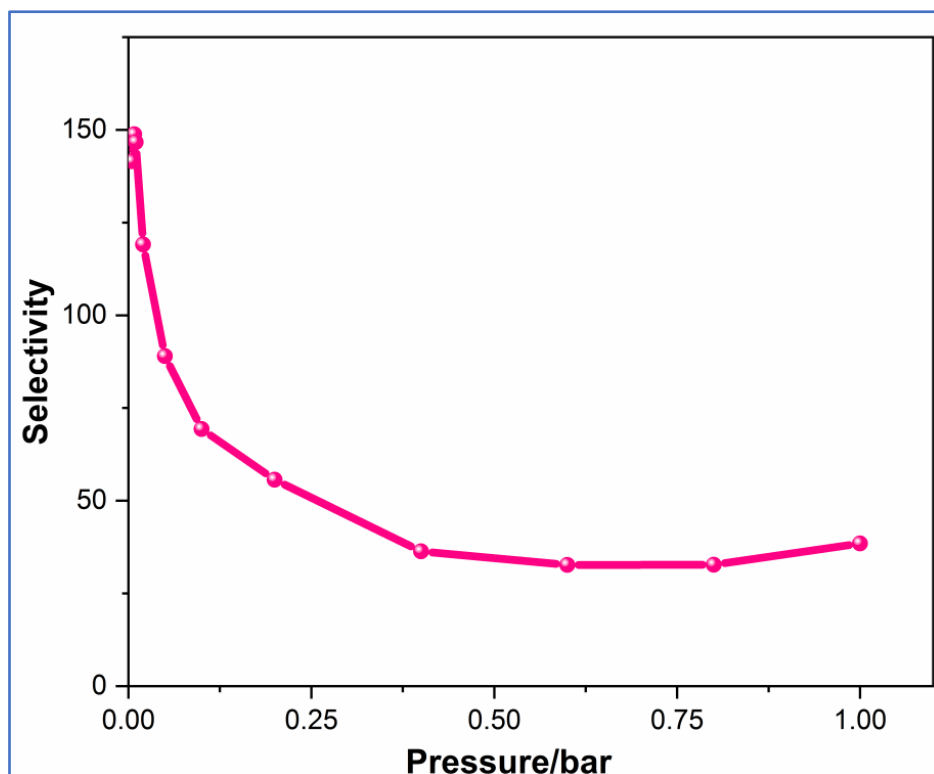


Figure A44. Selectivity plot of  $\text{CO}_2/(\text{O}_2 + \text{N}_2)$  in presence of  $\text{RH} = 1.57\%$  at 298 K.

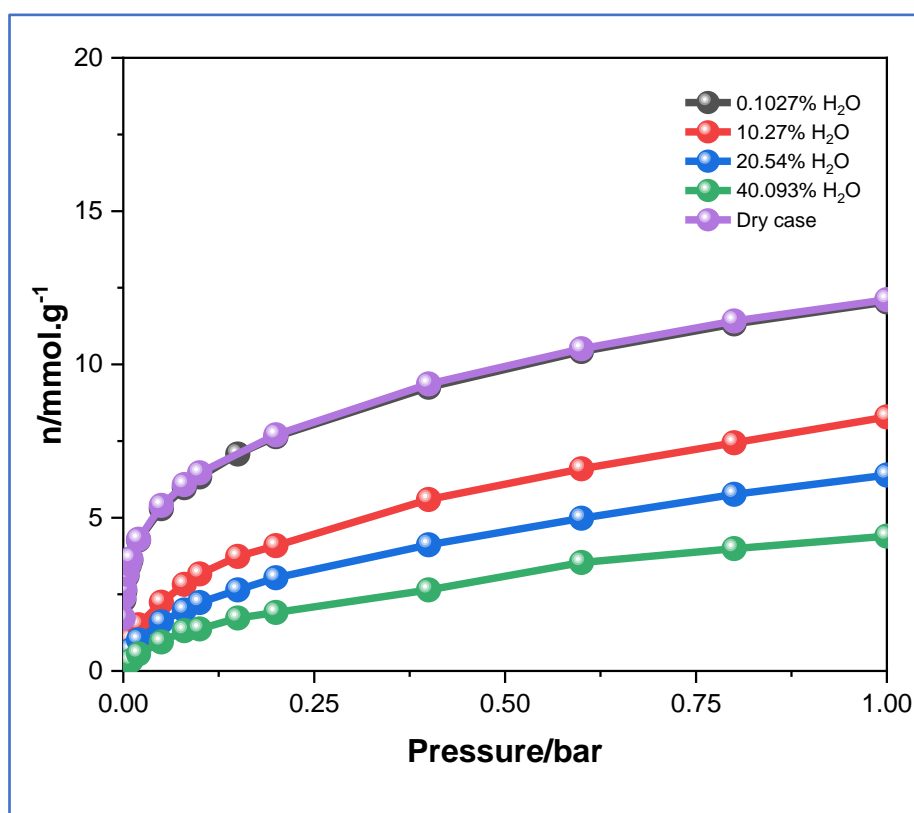
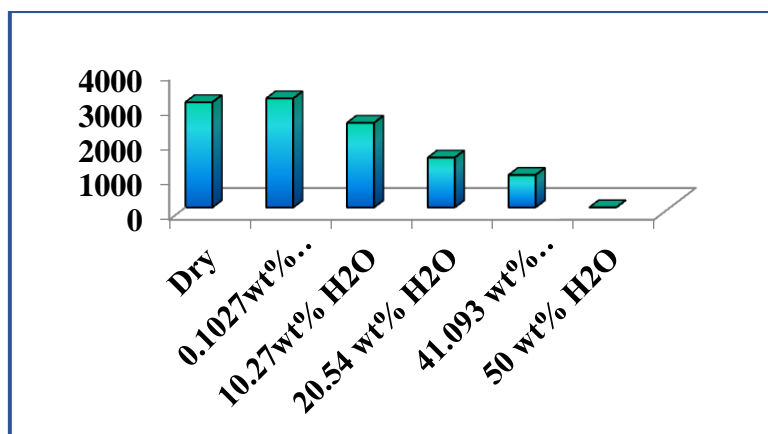
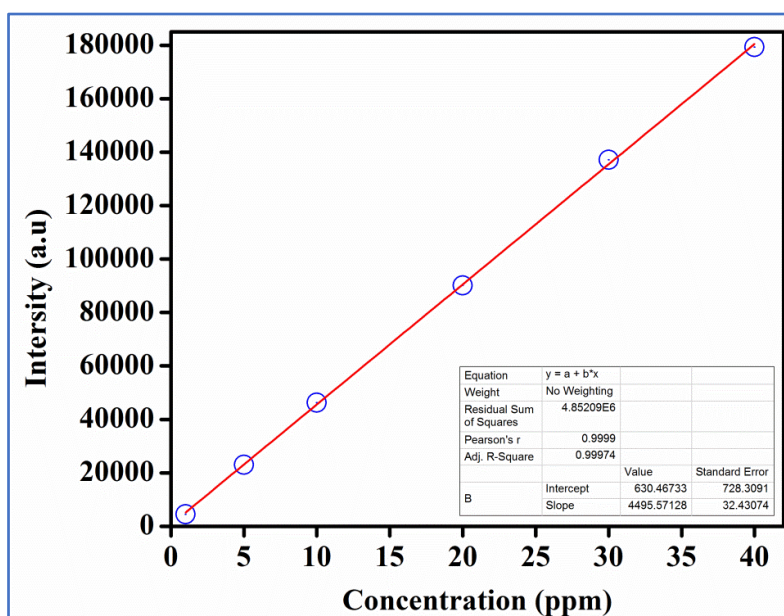


Figure A45.  $\text{CO}_2$  adsorption isotherms at various relative humidity of pre-humidified Mg-MOF at 298K.



**Figure A46.** Simulated selectivity of CO<sub>2</sub>/(O<sub>2</sub> + N<sub>2</sub>) in various pre-humidified air at 1 bar.



**Figure A47.** MP-AES calibration curve.

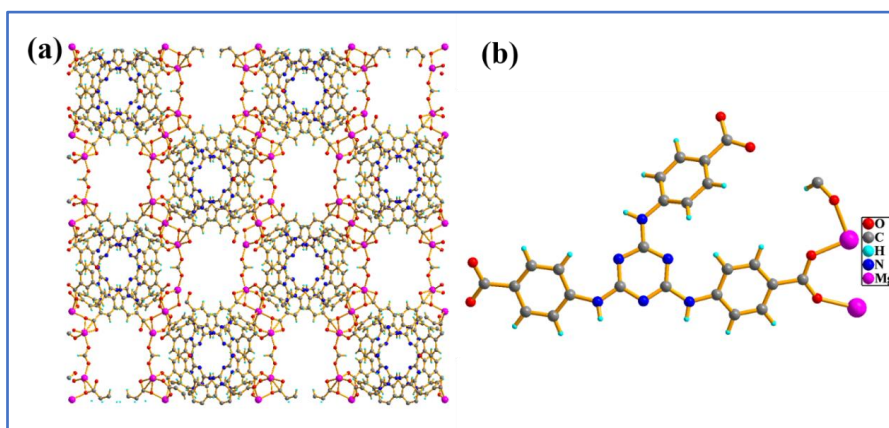


**Figure A48.** Unit crystal (left) and primitive (right) structure of Mg-MOF obtained through optimization via DFT method viewed along *a* vector direction.

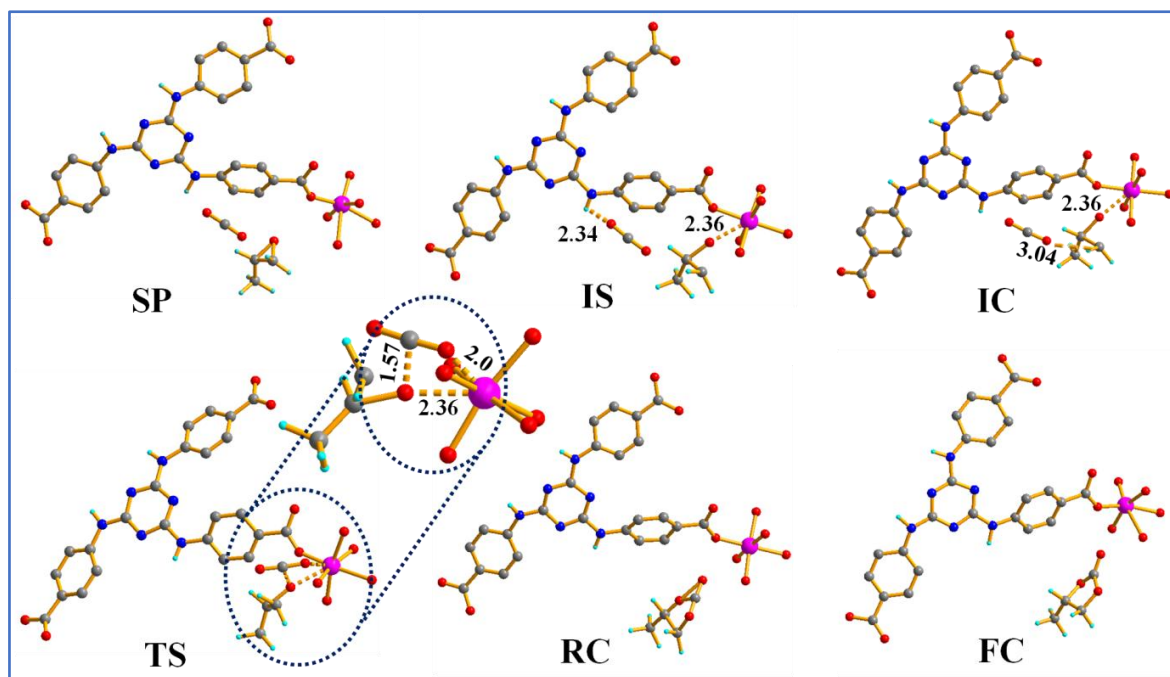


**Figure A49.** Mechanistic Pathways of the Intermediates and Transition States in the cycloaddition of propylene oxide and CO<sub>2</sub> using the Mg-MOF catalyst (bond distances are in Å).

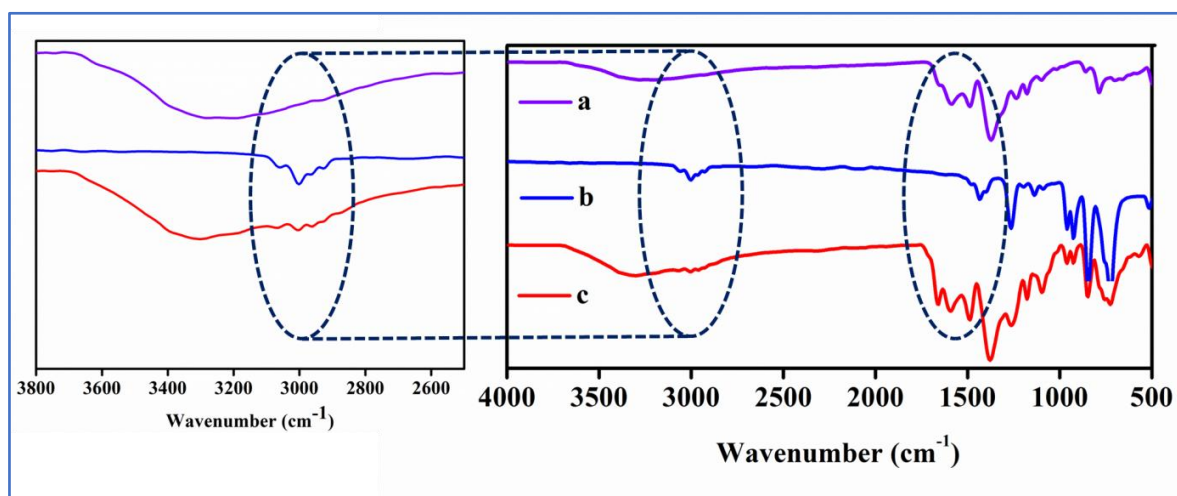


**Figure A50.** FT-IR spectra of (a) Mg-MOF, (b) Epichlorohydrin, and (c) Mg-MOF treated with epichlorohydrin.

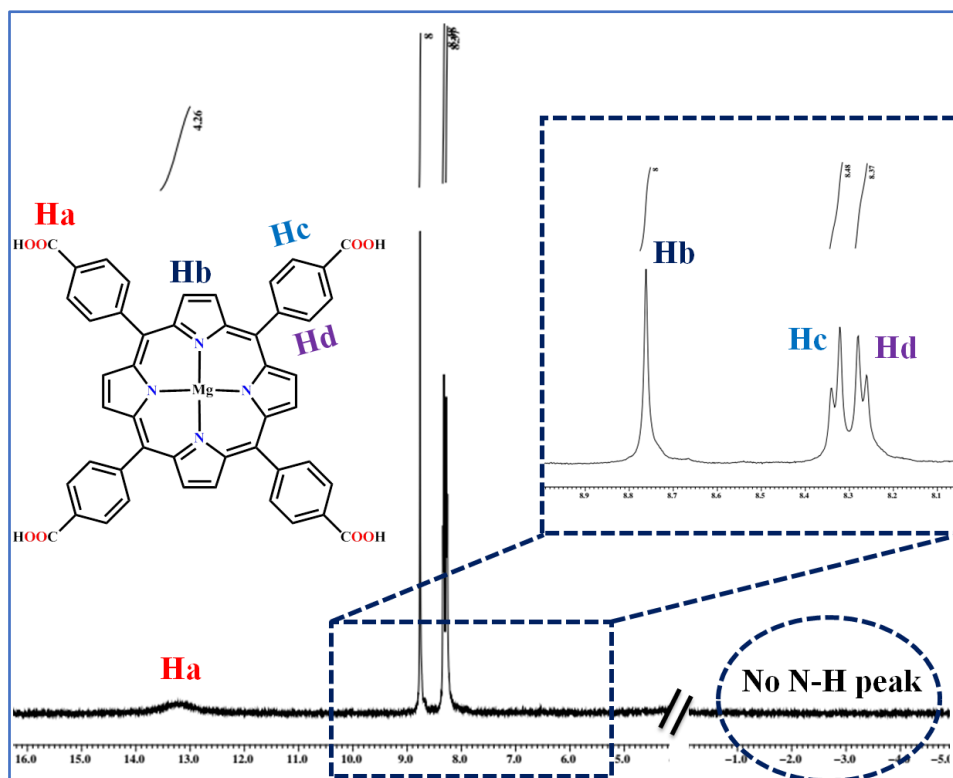


**Figure A51.** <sup>1</sup>H NMR spectrum of [5, 10, 15, 20-Tetrakis (4-carboxyphenyl) Mg(II) porphyrin] (Mg-TCPPH<sub>4</sub>) ligand.

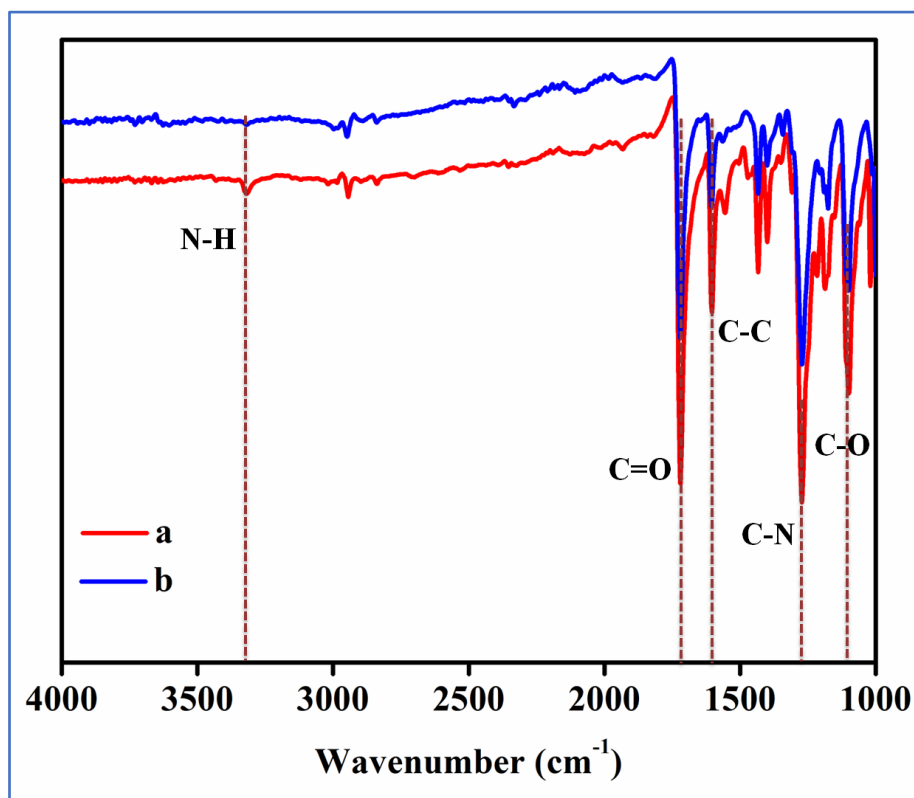


**Figure A52.** FT-IR spectra of (a) H<sub>4</sub>TCPP(H<sub>2</sub>) and (b) Mg-TCPPH<sub>4</sub> complex ligand.

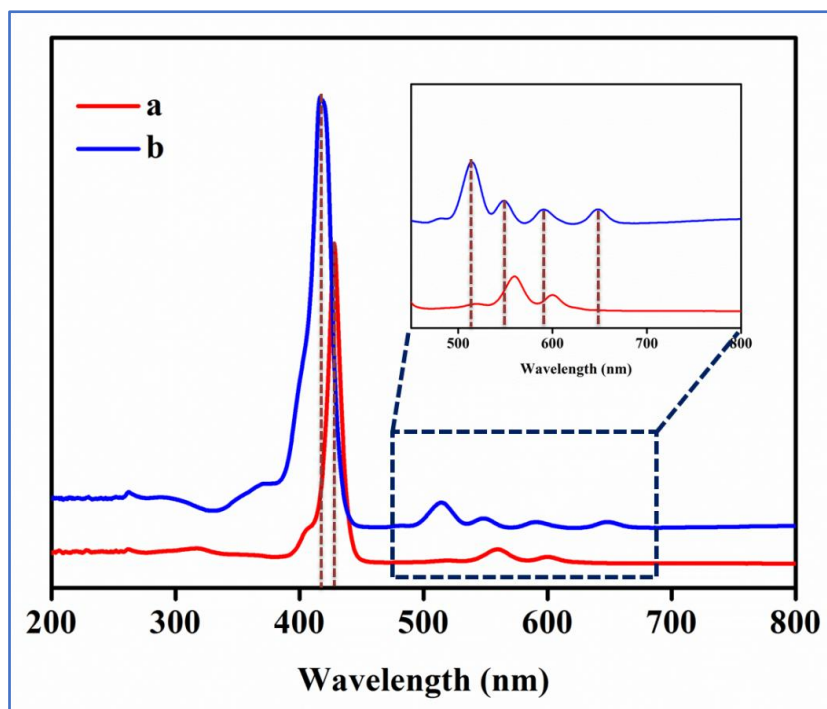


Figure A53. UV-Vis absorption spectra of (a) Mg-TCPPH<sub>4</sub>, and (b) H<sub>4</sub>TCPP(H<sub>2</sub>).

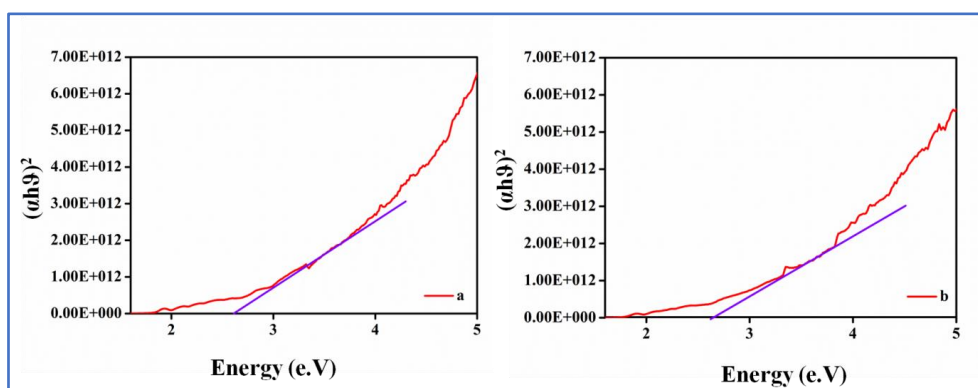


Figure A54. Bandgap plots for PCN-224 and PCN-224(Mg) MOF.

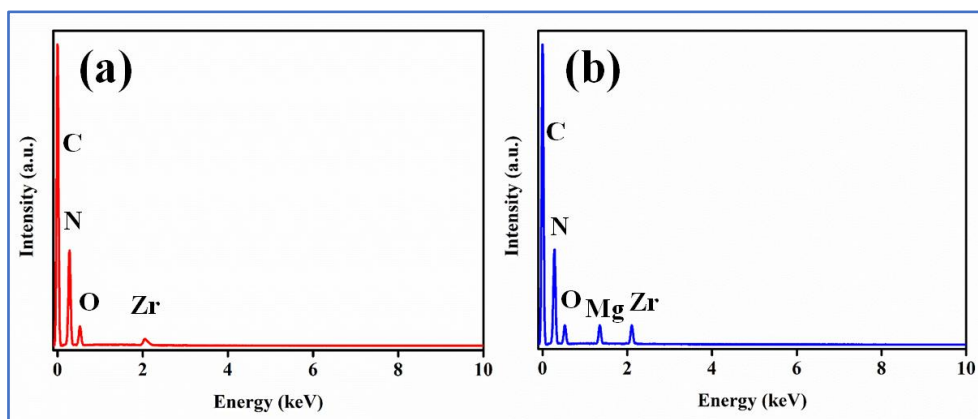
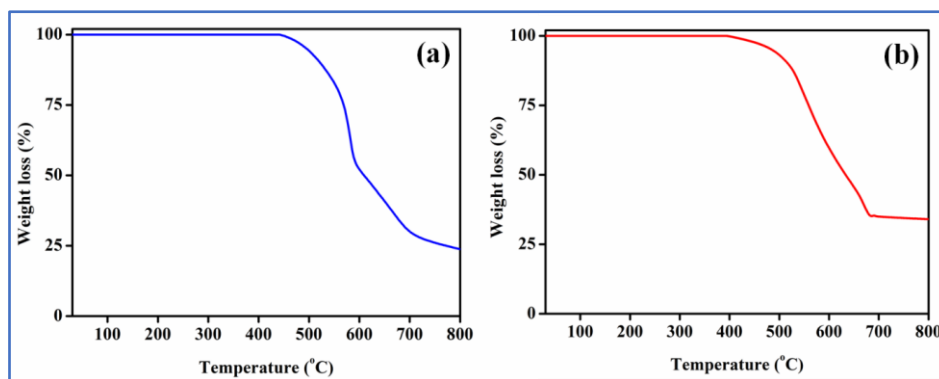
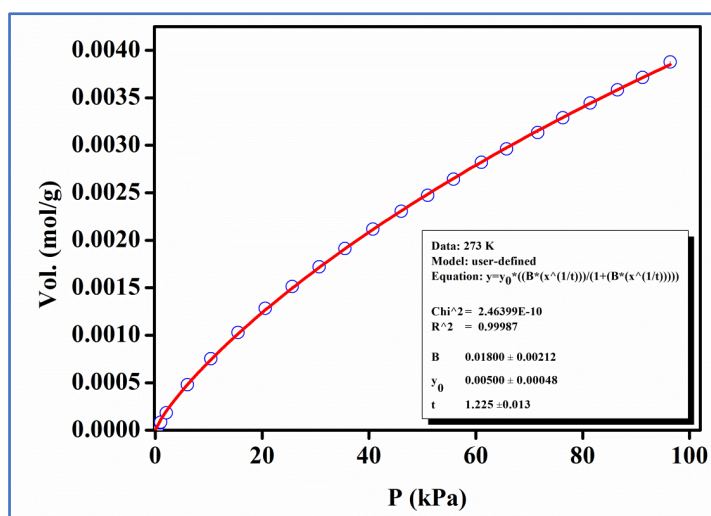


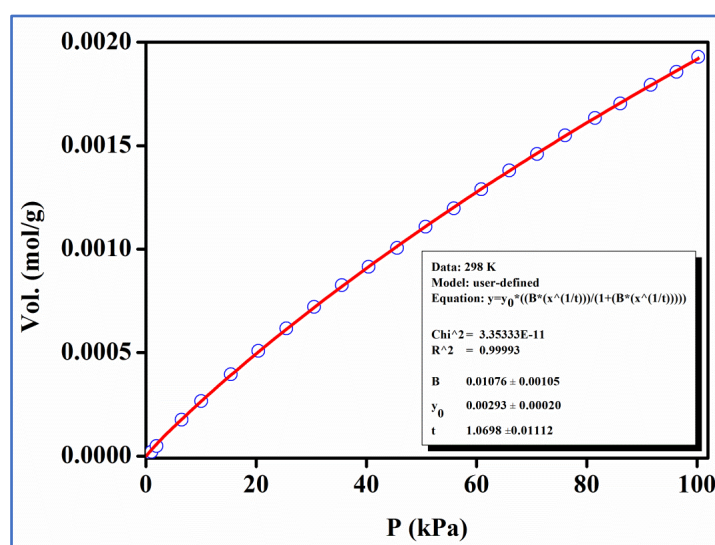
Figure A55. EDS plot of (a) PCN-224, and (b) PCN-224(Mg) MOF.



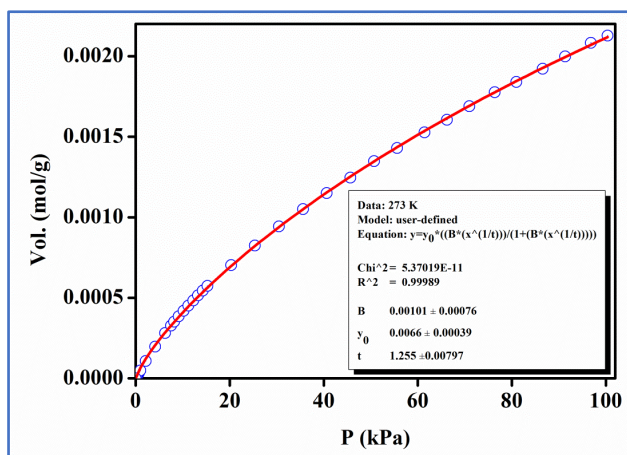
**Figure A56.** TGA plot of (a) PCN-224, and (b) PCN-224(Mg) MOF.



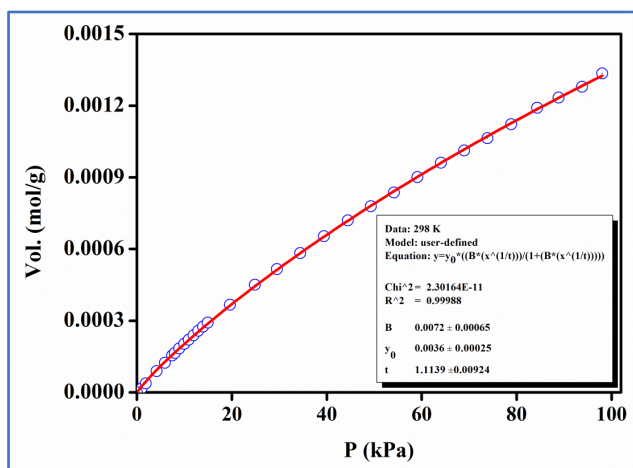
**Figure A57.** Carbon dioxide adsorption isotherm of PCN-224(Mg) carried out at 273 K. The solid line shows the best fit to the data using the Langmuir-Freundlich equation.



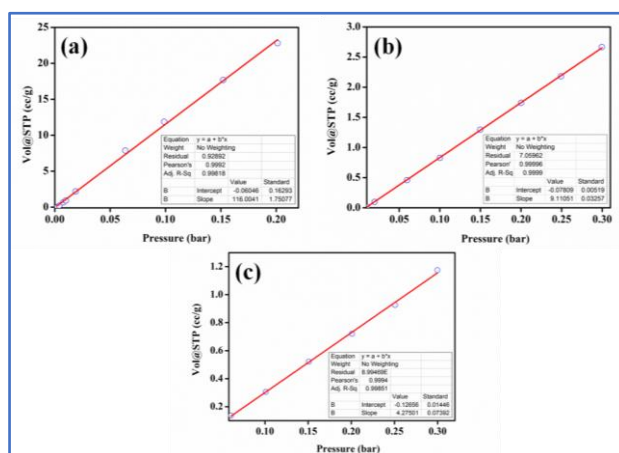
**Figure A58.** Carbon dioxide adsorption isotherm of PCN-224(Mg) carried out at 298 K. The solid line shows the best fit to the data using the Langmuir-Freundlich equation.



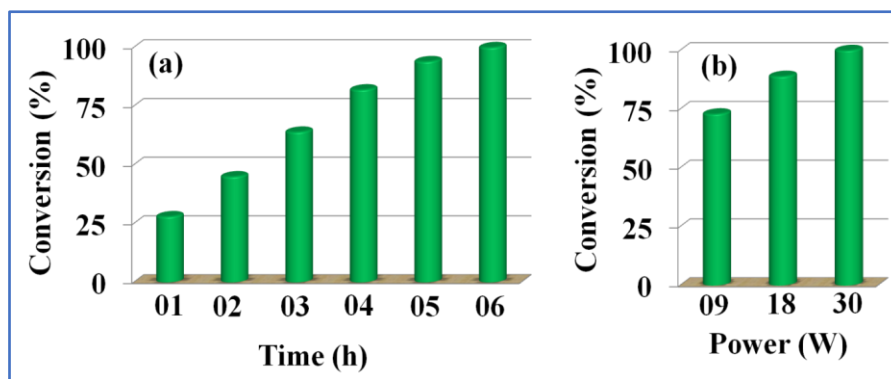
**Figure A59.** Carbon dioxide adsorption isotherm of PCN-224 carried out at 273 K. The solid line shows the best fit to the data using the Langmuir-Freundlich equation.



**Figure A60.** Carbon dioxide adsorption isotherm of PCN-224 carried out at 298 K. The solid line shows the best fit to the data using the Langmuir-Freundlich equation.

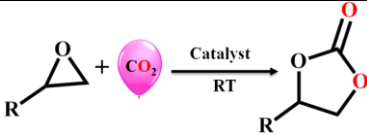


**Figure S61.** Calculation of Henry gas selectivity constants for gases (a)  $\text{CO}_2$ , (b)  $\text{CH}_4$ , and (c)  $\text{N}_2$ .



**Figure A62.** Optimization of photocatalytic cycloaddition of CO<sub>2</sub> with ECH by varying (a) reaction time, and (b) power of LED bulb.

**Table A18.** Catalytic optimization table using ECH as model substrate under mild conditions.<sup>a</sup>

					
Sl. No.	Catalyst	Co-catalyst	Time (h)	Light Source (LED light)	Conversion (%)
1	PCN-224(Mg)	-	6	Light (30 w)	-
2	-	Bu <sub>4</sub> NBr	6	Light (30 w)	17
3	PCN-224(Mg)	NaCl	6	Light (30 w)	11
4	PCN-224(Mg)	KBr	6	Light (30 w)	13
5	PCN-224(Mg)	KI	6	Light (30 w)	21
6	PCN-224(Mg)	Et <sub>3</sub> NH <sub>2</sub>	6	Light (30 w)	10
7	PCN-224(Mg)	NH <sub>4</sub> Br	6	Light (30 w)	32
8	PCN-224(Mg)	Bu <sub>4</sub> NBr	2	Light (30 w)	44
9	PCN-224(Mg)	Bu <sub>4</sub> NBr	4	Light (30 w)	77
10	PCN-224(Mg)	Bu <sub>4</sub> NBr	6	Light (09 w)	72
11	PCN-224(Mg)	Bu <sub>4</sub> NBr	6	Light (18 w)	87
12	PCN-224(Mg)	Bu <sub>4</sub> NBr	6	Light (30 w)	>99
13	PCN-224(Mg)	Bu <sub>4</sub> NBr	6	RT	18
14	PCN-224(Mg)	Bu <sub>4</sub> NBr	6	80 °C	>99

<sup>a</sup>Reaction condition: epichlorohydrin (20 mmol), catalyst (0.025 mol%), co-catalyst (1 mol%) and 1 atm CO<sub>2</sub> (balloon).

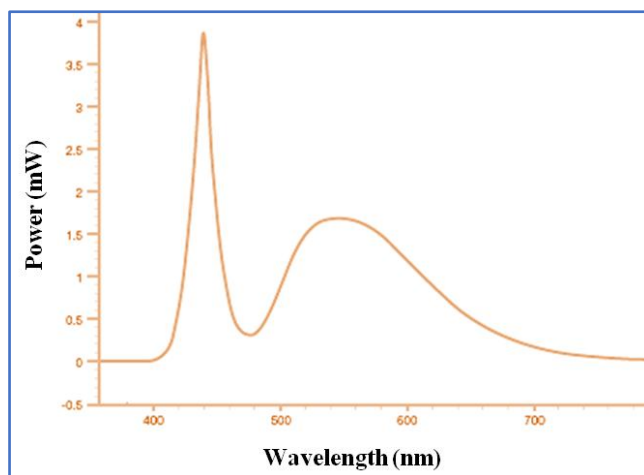


**Figure A63.** Emission spectrum of a commercial white LED light.

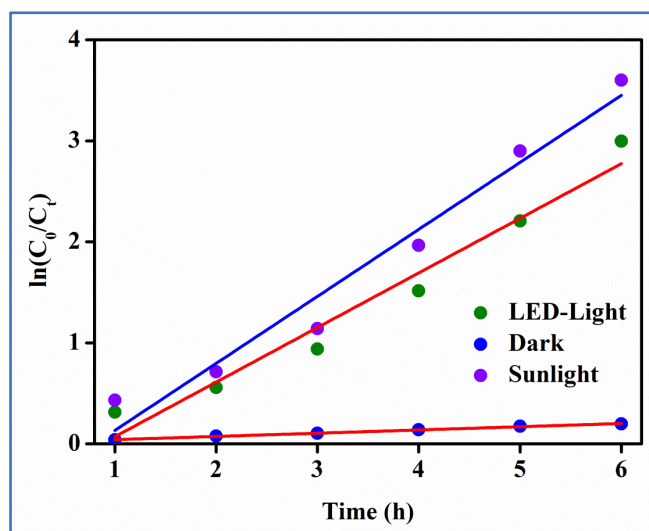
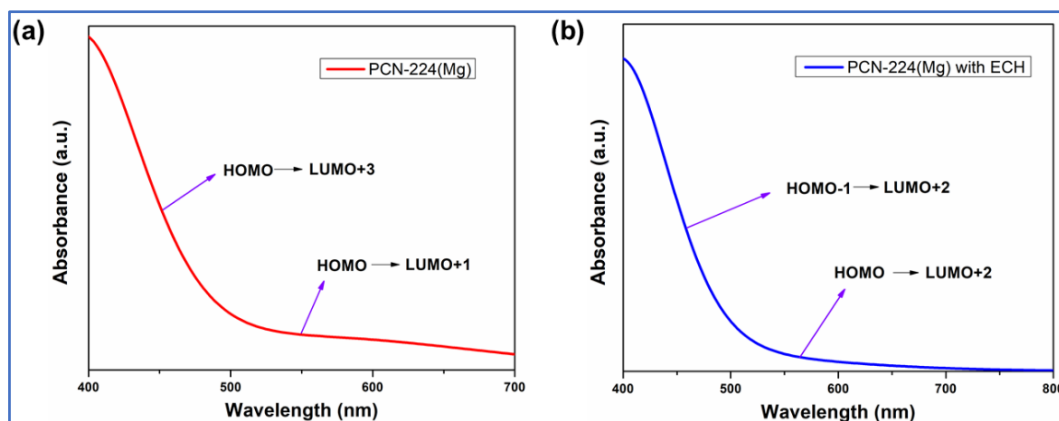


**Figure A64.** Kinetics of CO<sub>2</sub> utilization with ECH under sunlight, LED-light, and dark conditions.

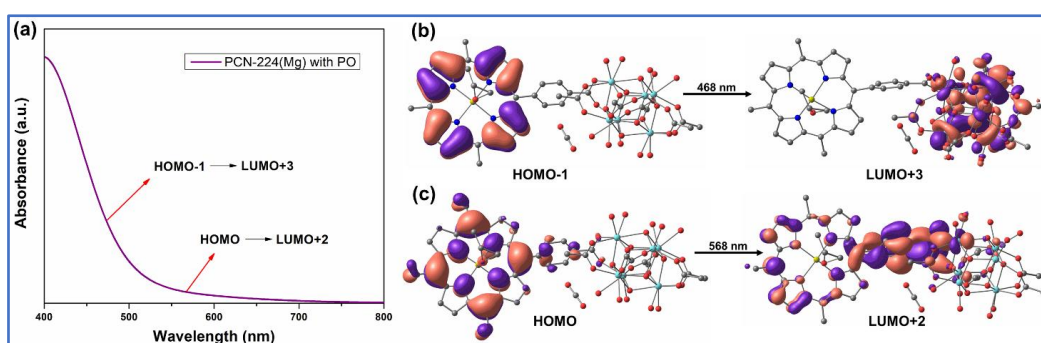
**Table A19.** Catalytic optimization table using ECH as model substrate under mild conditions.<sup>a</sup>

Sl. No.	Catalyst (Mol%)	Time (h)	Conversion (%)
1	PCN-224(Mg) (0.025 mol%)	6	19
2	PCN-224(Mg) (0.050 mol%)	6	31
3	PCN-224(Mg) (0.075 mol%)	6	39
4	PCN-224(Mg) (0.075 mol%)	12	68
5	PCN-224(Mg) (0.075 mol%)	24	97

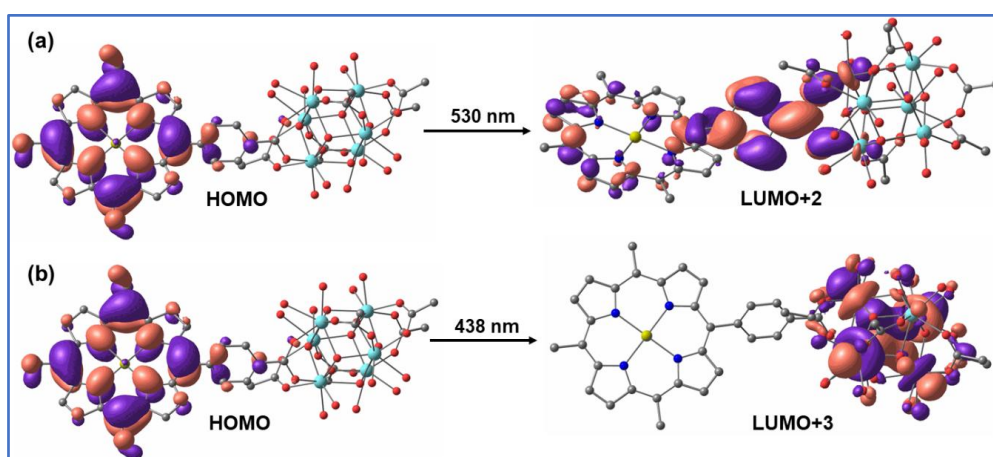
<sup>a</sup>Reaction condition: epichlorohydrin (20 mmol), TBAB (1 mol%) and continuous bubbling of laboratory air.



**Figure A65.** Simulated absorption spectra of PCN-224(Mg) (a) and with ECH epoxide (b).



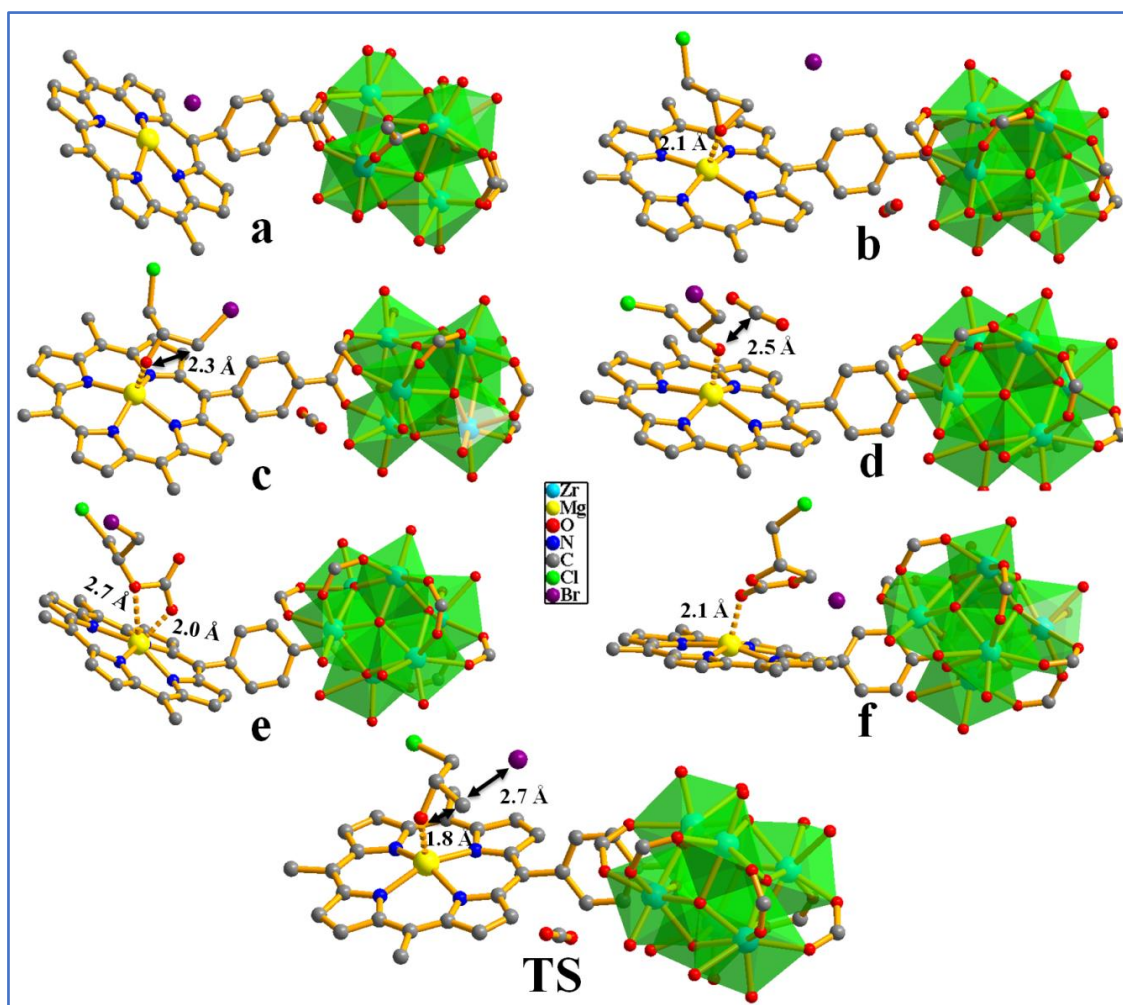
**Figure A66.** (a) Simulated absorption spectra of PCN-224(Mg) in PO epoxide. The frontier molecular orbital of high (b) and low (c) intense absorption spectra of PCN-224(Mg) in PO epoxide. Colour code: Zr, cyan; Cl, green; Mg, yellow; O, red; N, blue; C, grey. For clarity, we have removed the hydrogen atoms.



**Figure A67.** The frontier molecular orbitals involved in the optical transitions of PCN-224(Mg) without epoxide are low intense (a) and high intense peaks (b). Colour code: Zr, cyan; Cl, green; Mg, yellow; O, red; N, blue; C, grey. For clarity, we have removed the hydrogen atoms.

**Table A20.** HOMO/LUMO energy values of with and without ECH epoxide in PCN-224(Mg).

PCN-224(Mg)	With ECH epoxide	Without ECH epoxide
HOMO (eV)	-4.789	-4.937
LUMO (eV)	-2.198	-2.277

**Figure A68.** Optimized geometries of intermediates and transition state in the cycloaddition of ECH and CO<sub>2</sub> using the PCN-224(Mg) catalyst.

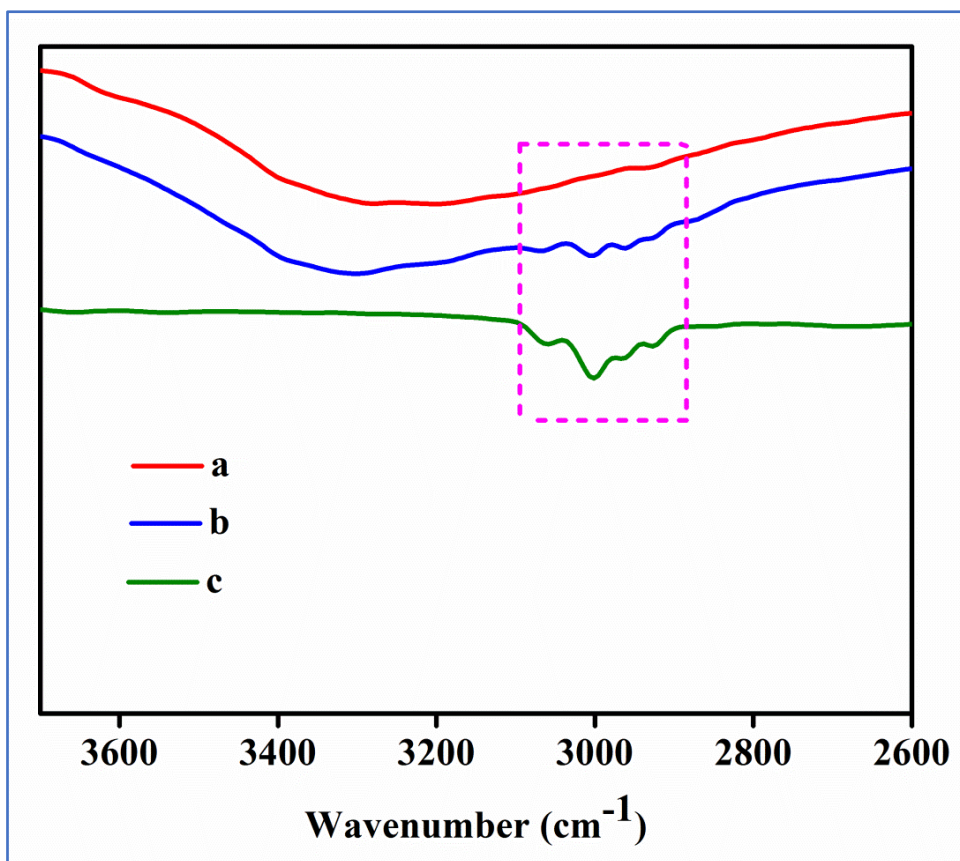


**Figure A69.** FT-IR spectra of (a) pristine PCN-224(Mg), (b) PCN-224(Mg) treated with epichlorohydrin, and (c) Epichlorohydrin.

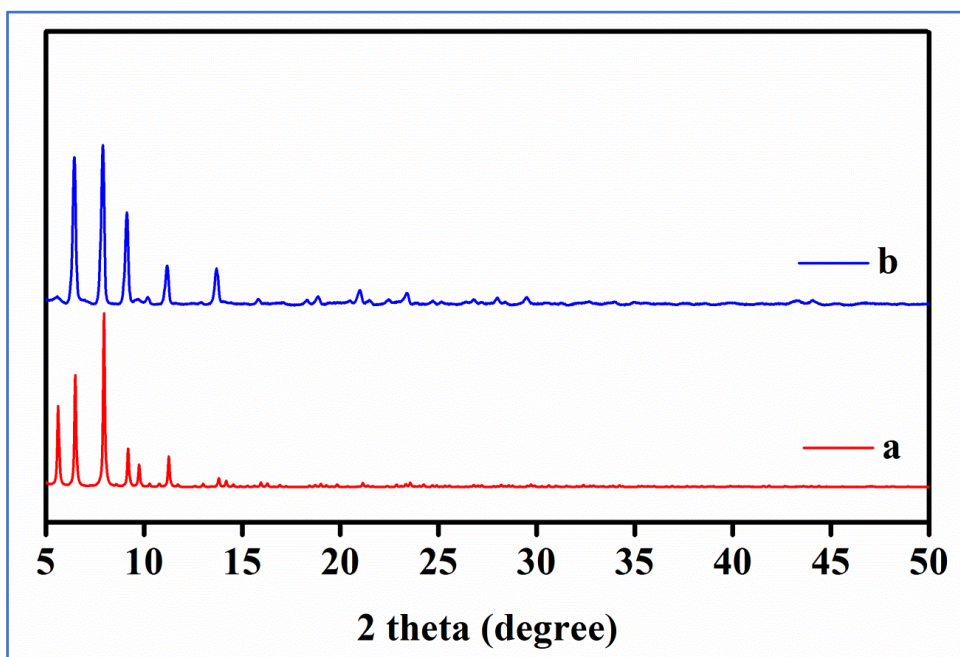


**Figure A70.** PXRD pattern of (a) PCN-224(Mg), and (b) recycled PCN-224(Mg).

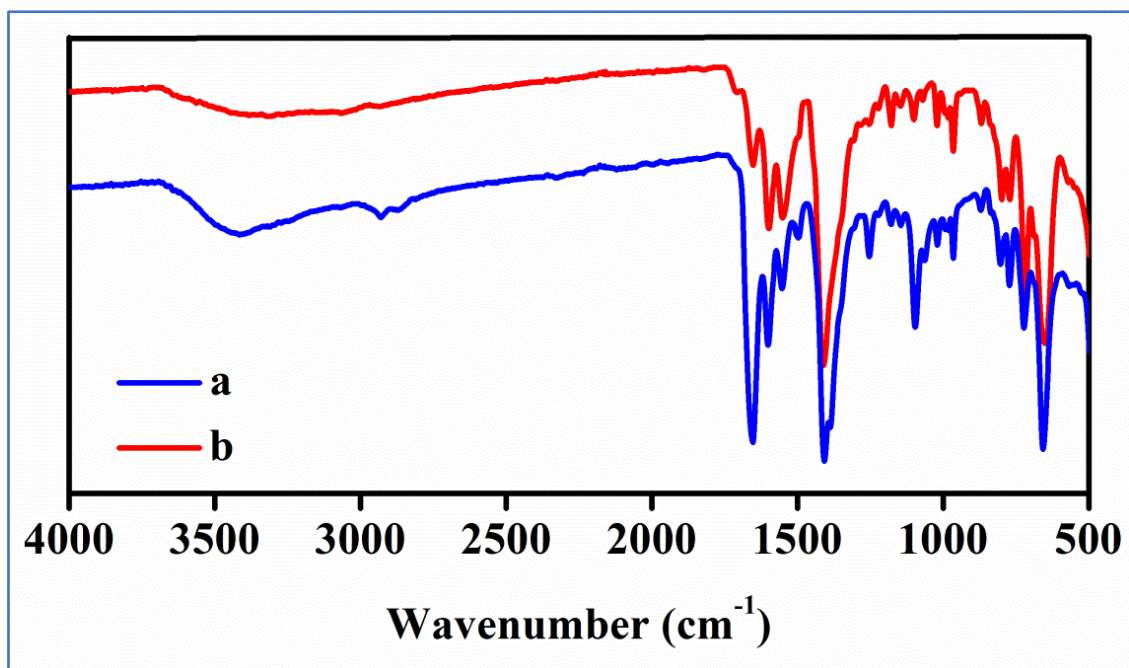


**Figure A71.** FTIR spectra of (a) PCN-224(Mg), and (b) recycled PCN-224(Mg).

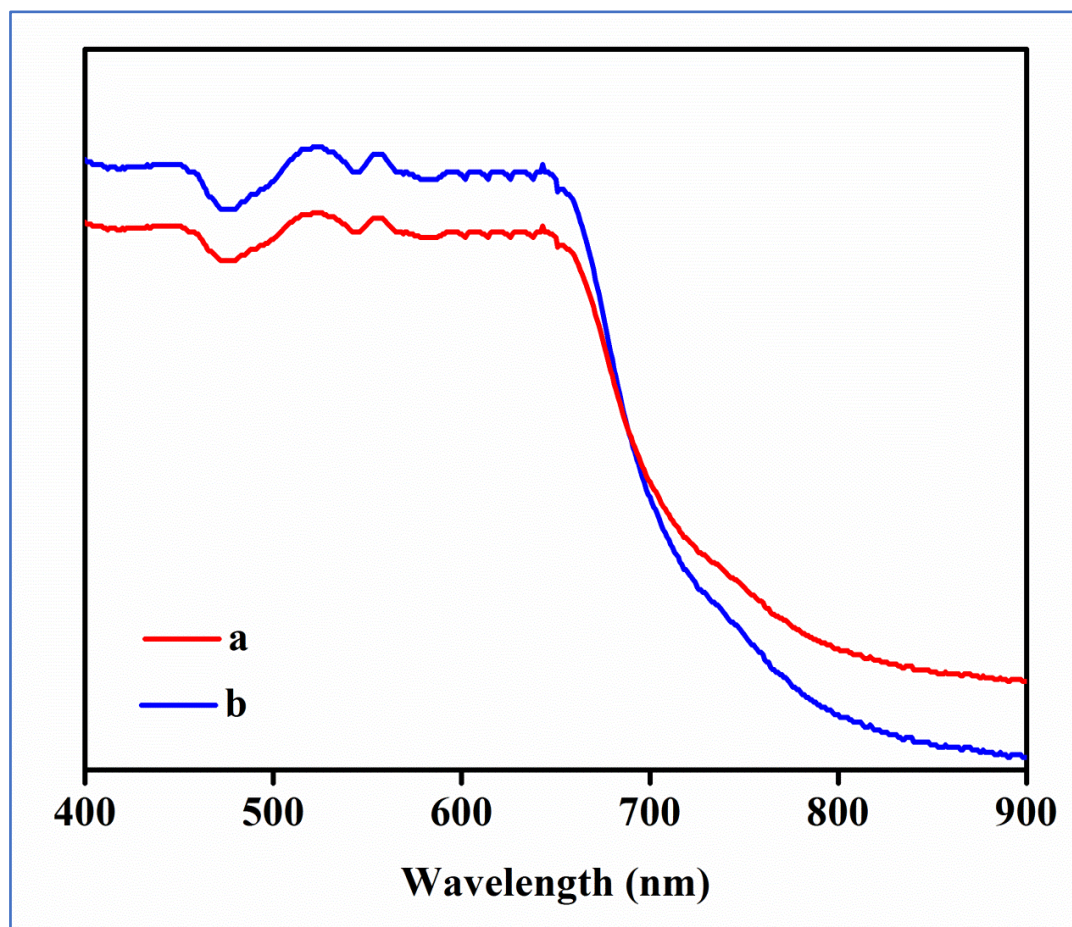


**Figure A72.** UV-Vis diffuse reflectance spectra (DRS) of (a) PCN-224(Mg), and (b) recycled PCN-224(Mg) after catalysis.

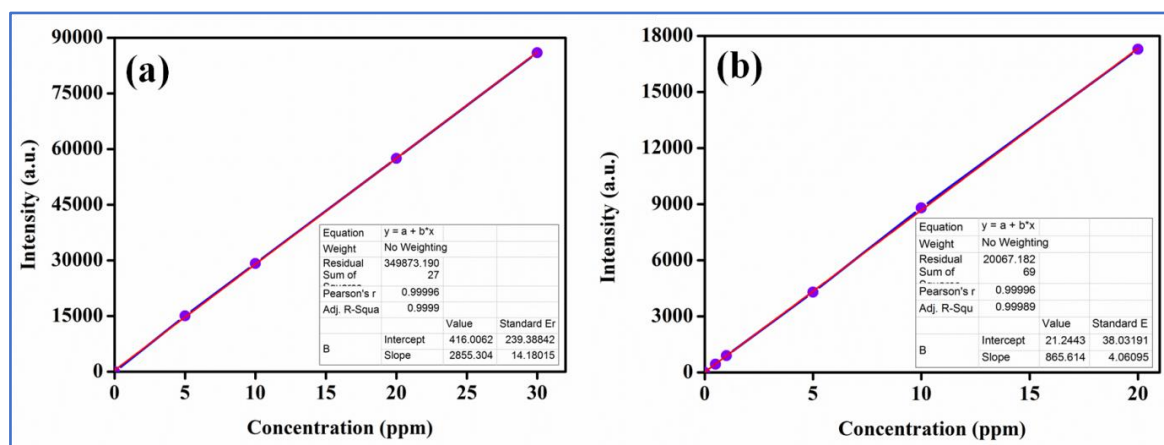


**Figure 73.** Calibration curve of MP-AES analysis for (a) Zr-metal, and (b) Mg-metal of PCN-224(Mg).

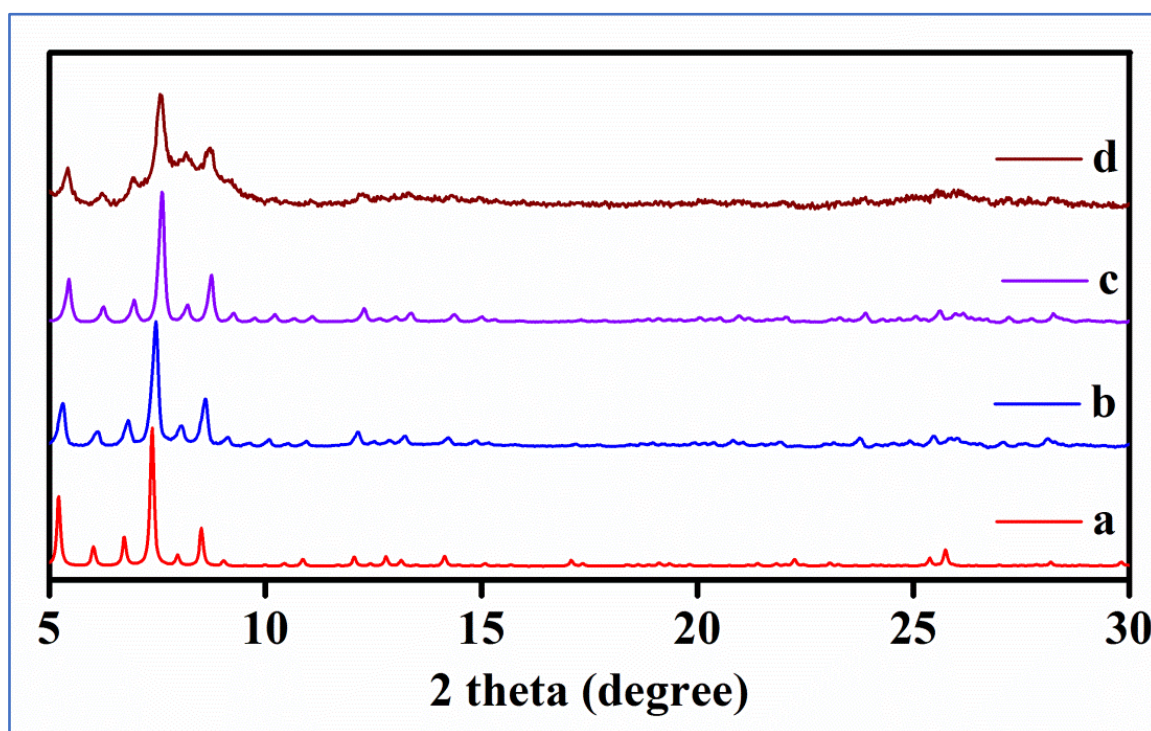


**Figure A74.** PXRD patterns of MOF-SO<sub>3</sub>H (a) simulated pattern (b) as-synthesized (c) for MOF-SO<sub>3</sub>Ag and (d) recycled sample of MOF-SO<sub>3</sub>Ag after five catalytic cycles.

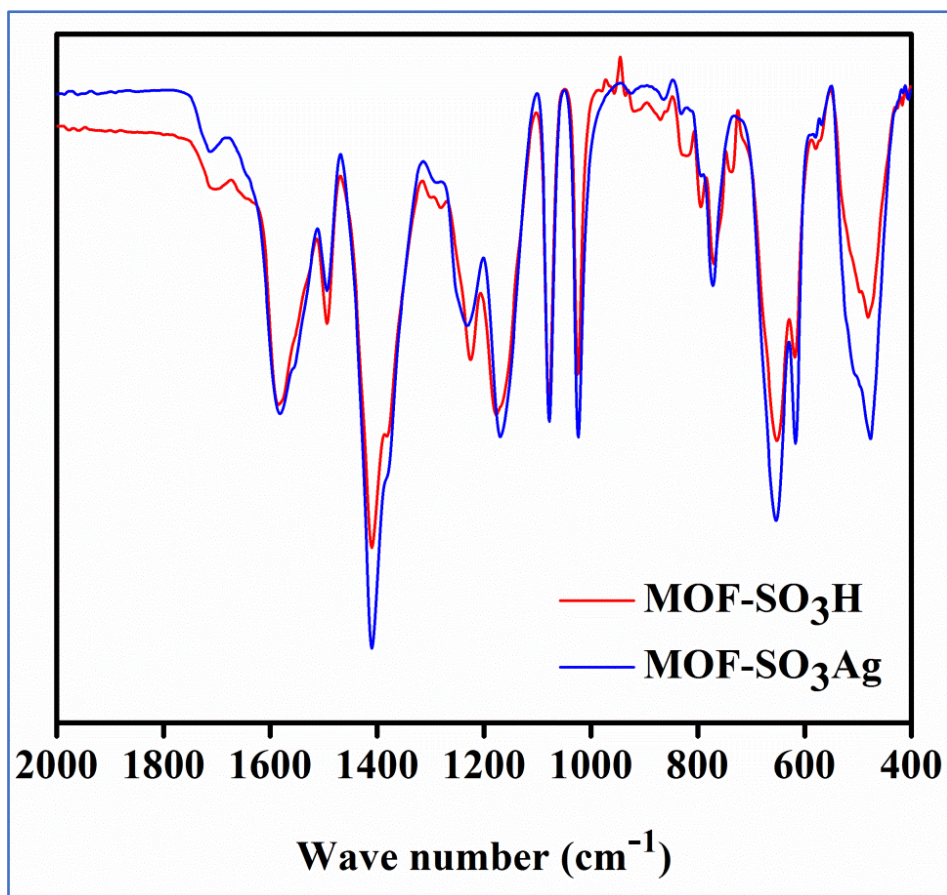


Figure A75. FT-IR spectra of MOF-SO<sub>3</sub>H and MOF-SO<sub>3</sub>Ag.

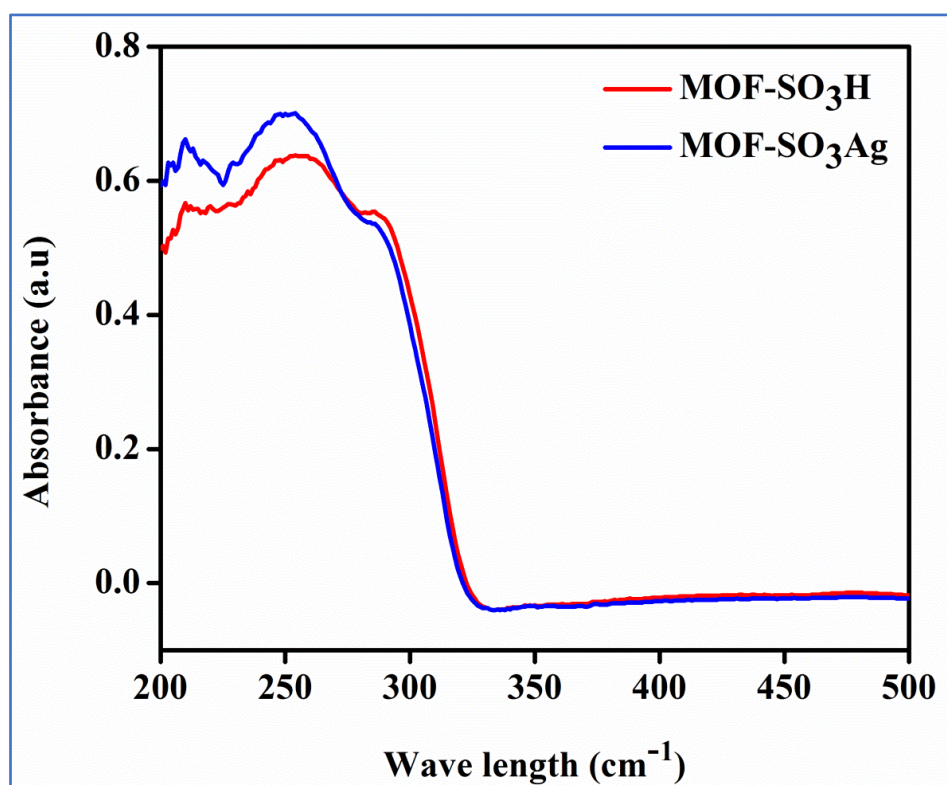
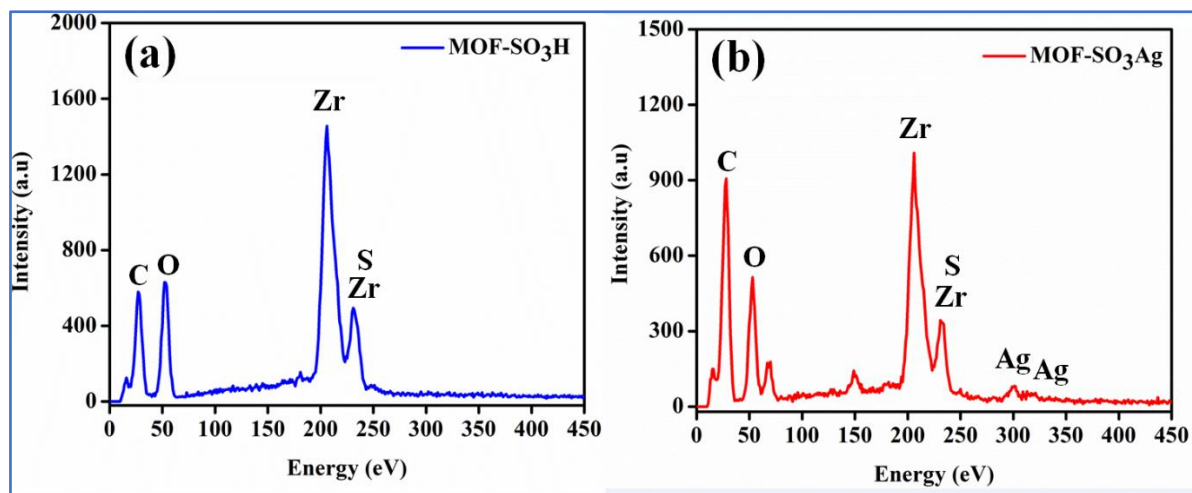
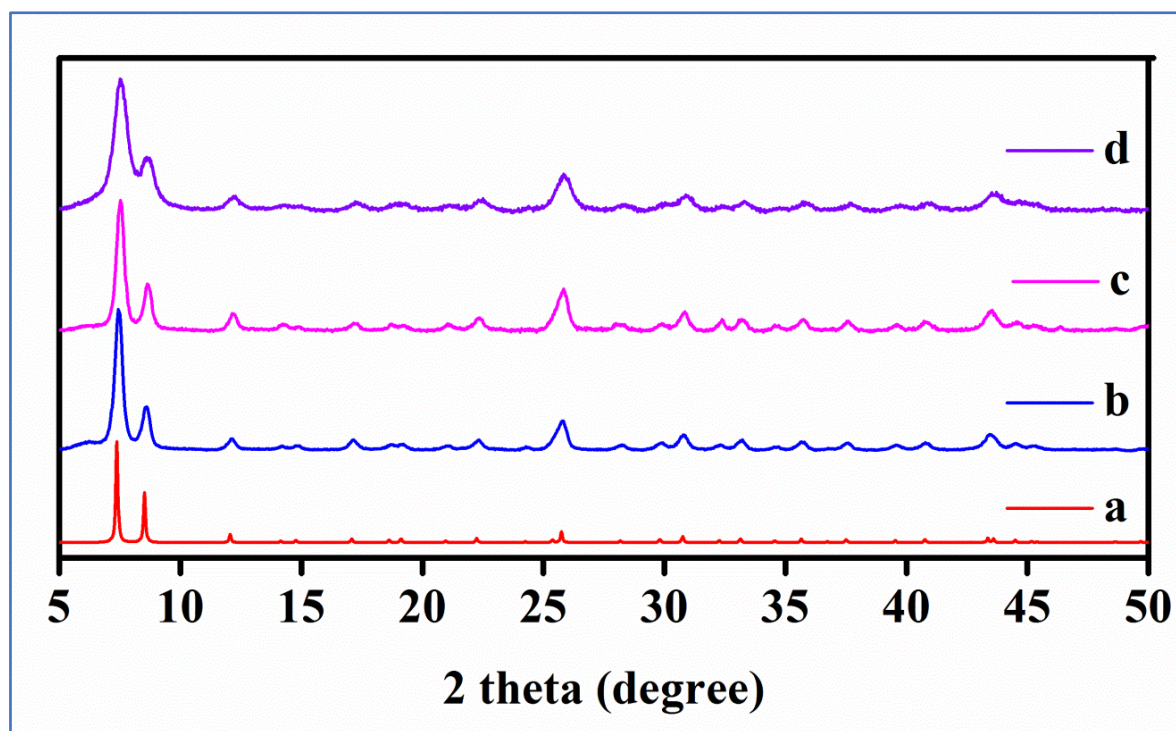


Figure A76. UV-Vis spectra of MOF-SO<sub>3</sub>H and MOF-SO<sub>3</sub>Ag.



**Figure A77.** EDS spectra of (a) MOF-SO<sub>3</sub>H and (b) MOF-SO<sub>3</sub>Ag.



**Figure A78.** PXRD patterns of UiO-66 (a) simulated pattern (b) as-synthesized (c) Ag(I)@UiO-66 and (d) recycled sample of Ag(I)@UiO-66 after reaction.

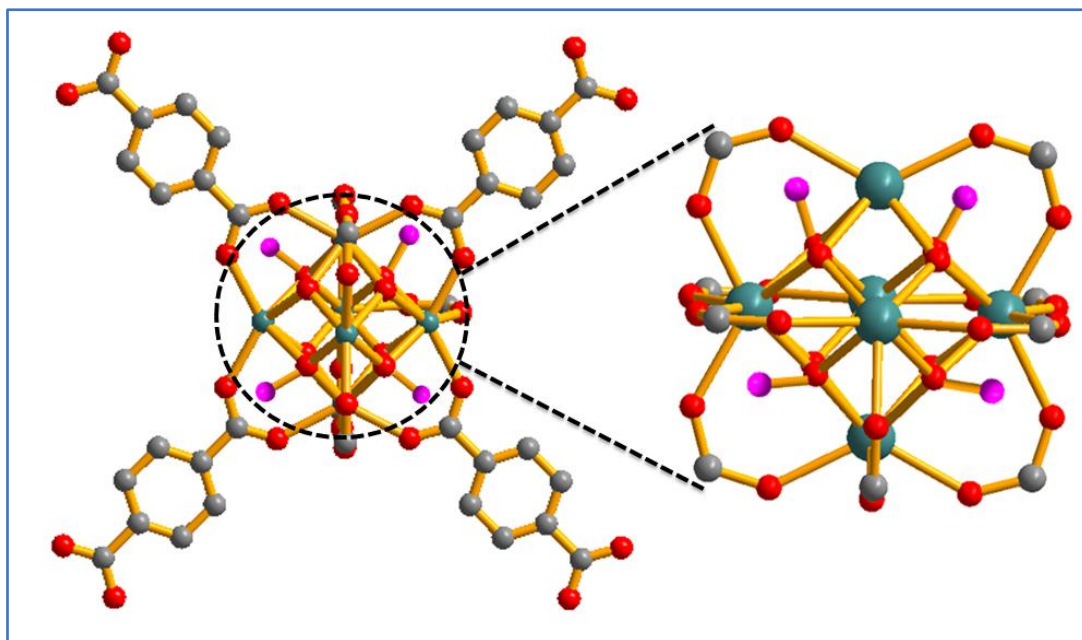


**Figure A79.** View of Zr-O cluster/SBU of UiO-66 MOF showing the presence of hydroxide groups.

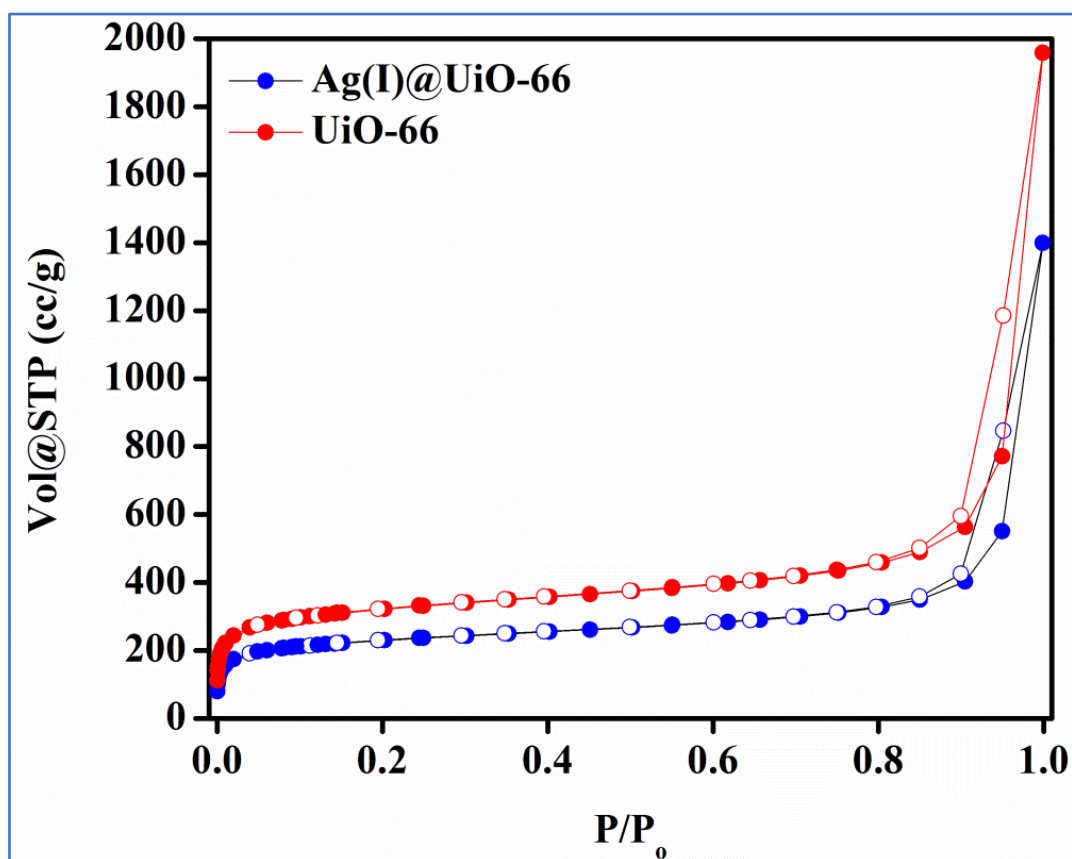


**Figure A80.** N<sub>2</sub> adsorption-desorption isotherms for UiO-66 and Ag(I)@UiO-66 MOF carried out at 77K.

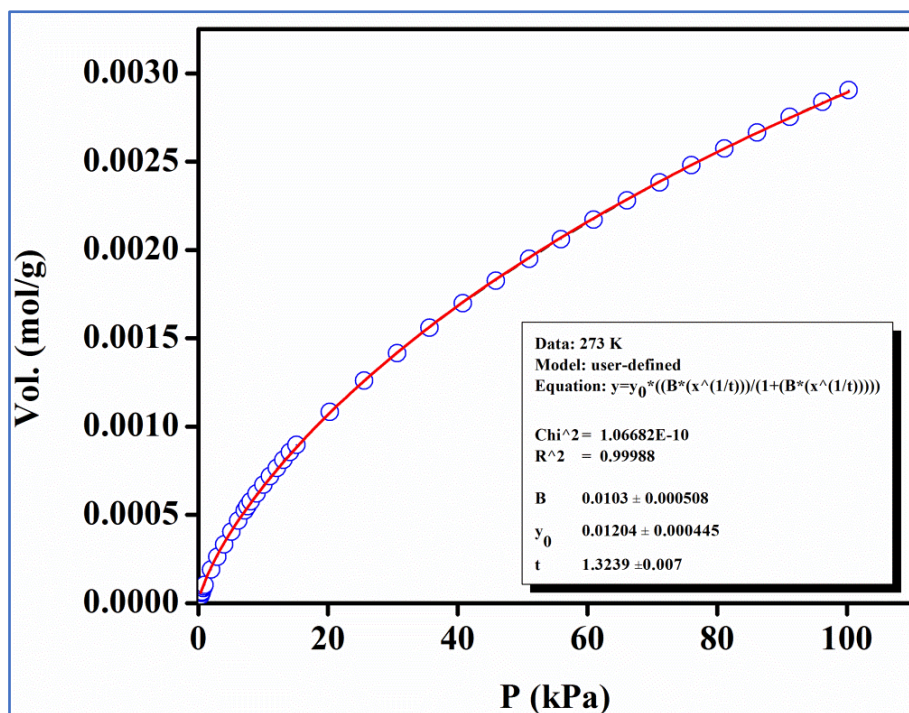


**Figure A81.** Carbon dioxide adsorption isotherm of MOF-SO<sub>3</sub>H carried out at 273 K. The solid line shows the best fit to the data using the Langmuir-Freundlich equation.

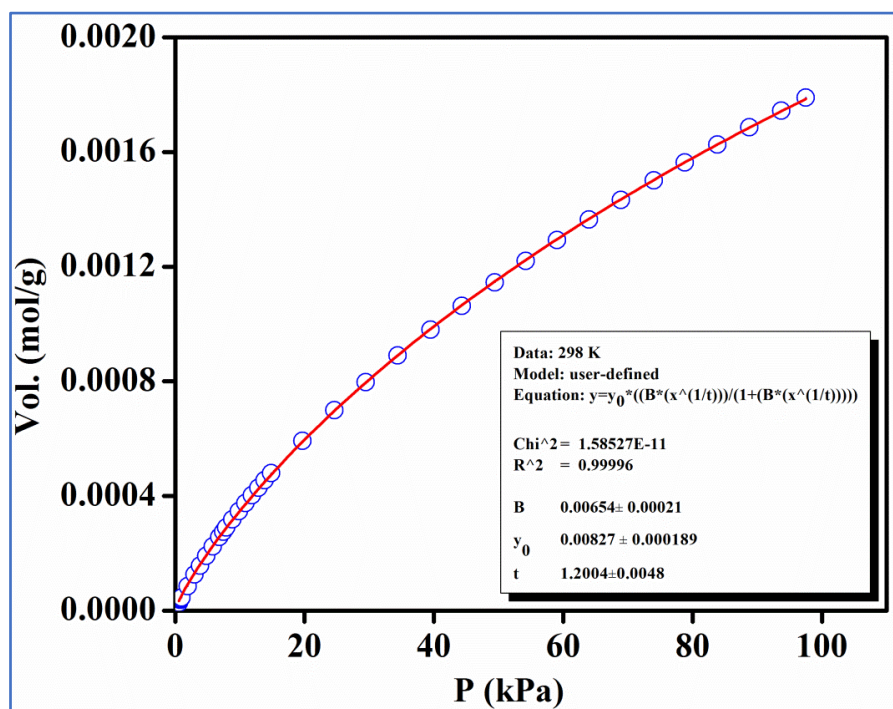


**Figure A82.** Carbon dioxide adsorption isotherm of MOF-SO<sub>3</sub>H carried out at 298 K. The solid line shows the best fit to the data using the Langmuir-Freundlich equation.

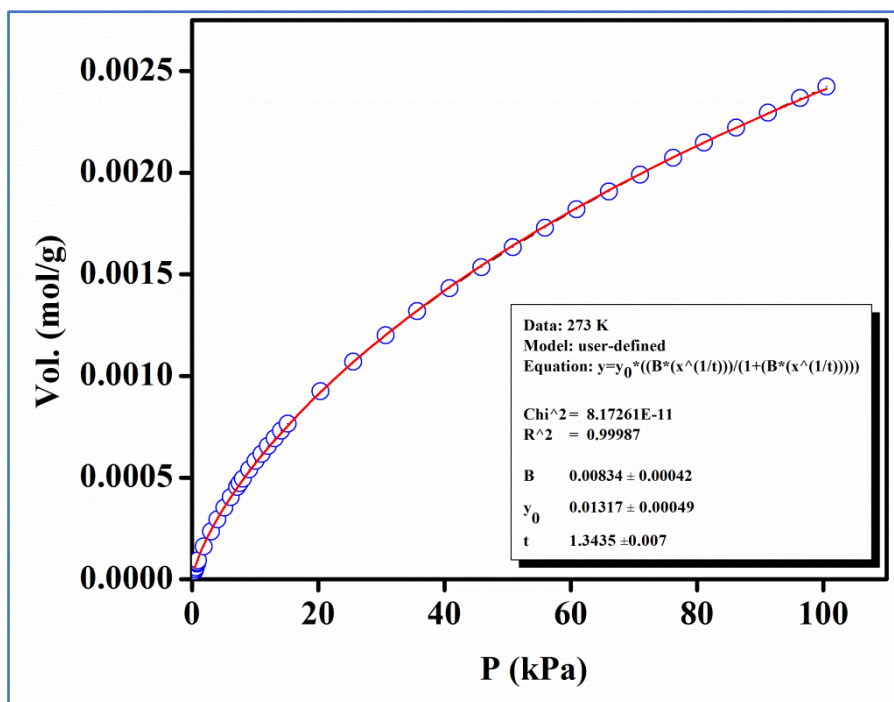


**Figure A83.** Carbon dioxide adsorption isotherm of MOF-SO<sub>3</sub>Ag carried out at 273 K. The solid line shows the best fit to the data using the Langmuir-Freundlich equation.

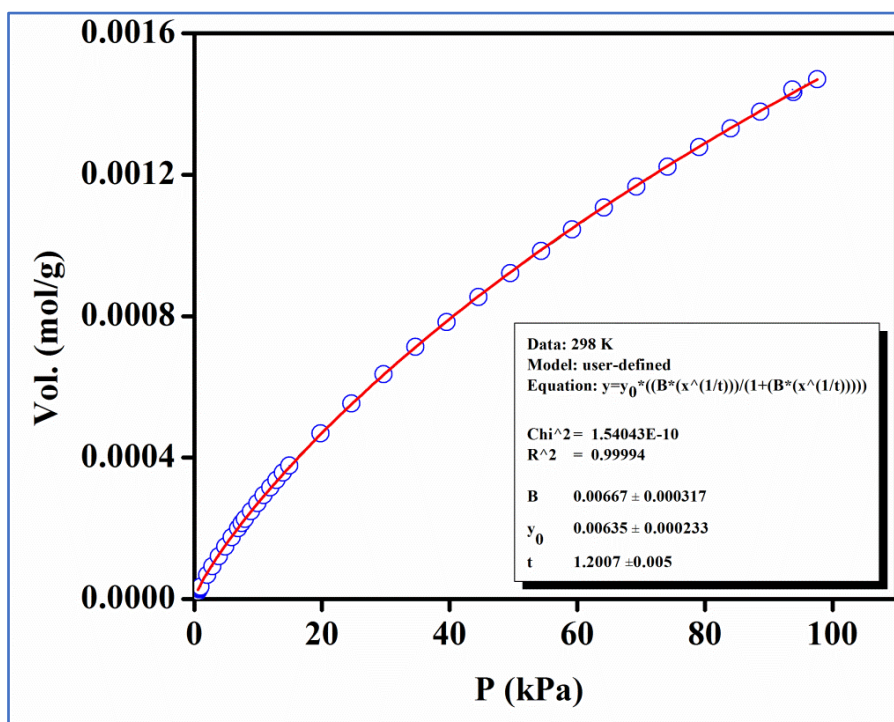


**Figure A84.** Carbon dioxide adsorption isotherm of MOF-SO<sub>3</sub>Ag carried out at 298 K. The solid line shows the best fit to the data using the Langmuir-Freundlich equation.

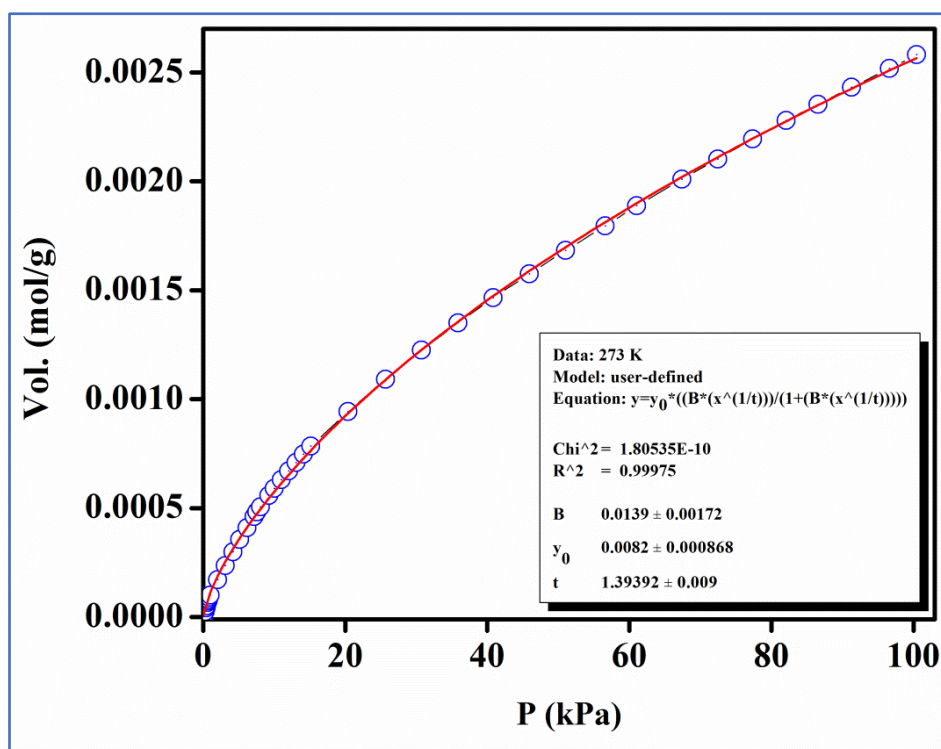


**Figure A85.** Carbon dioxide adsorption isotherm of Ag(I)@UiO-66 carried out at 273 K. The solid line shows the best fit to the data using the Langmuir-Freundlich equation.

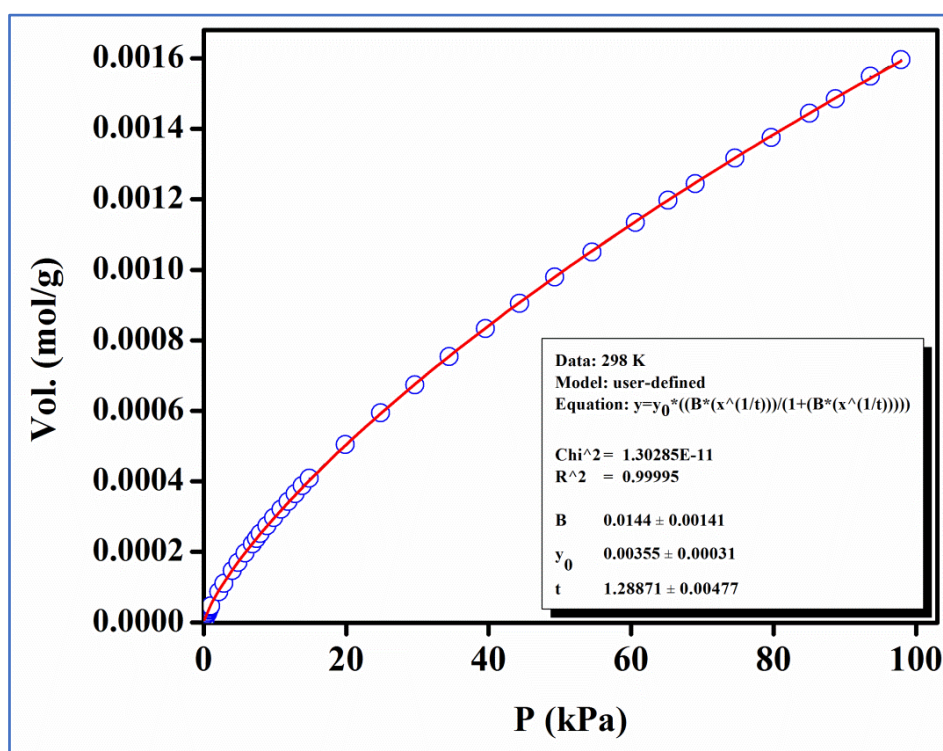


**Figure A86.** Carbon dioxide adsorption isotherm of Ag(I)@UiO-66 carried out at 298 K. The solid line shows the best fit to the data using the Langmuir-Freundlich equation.

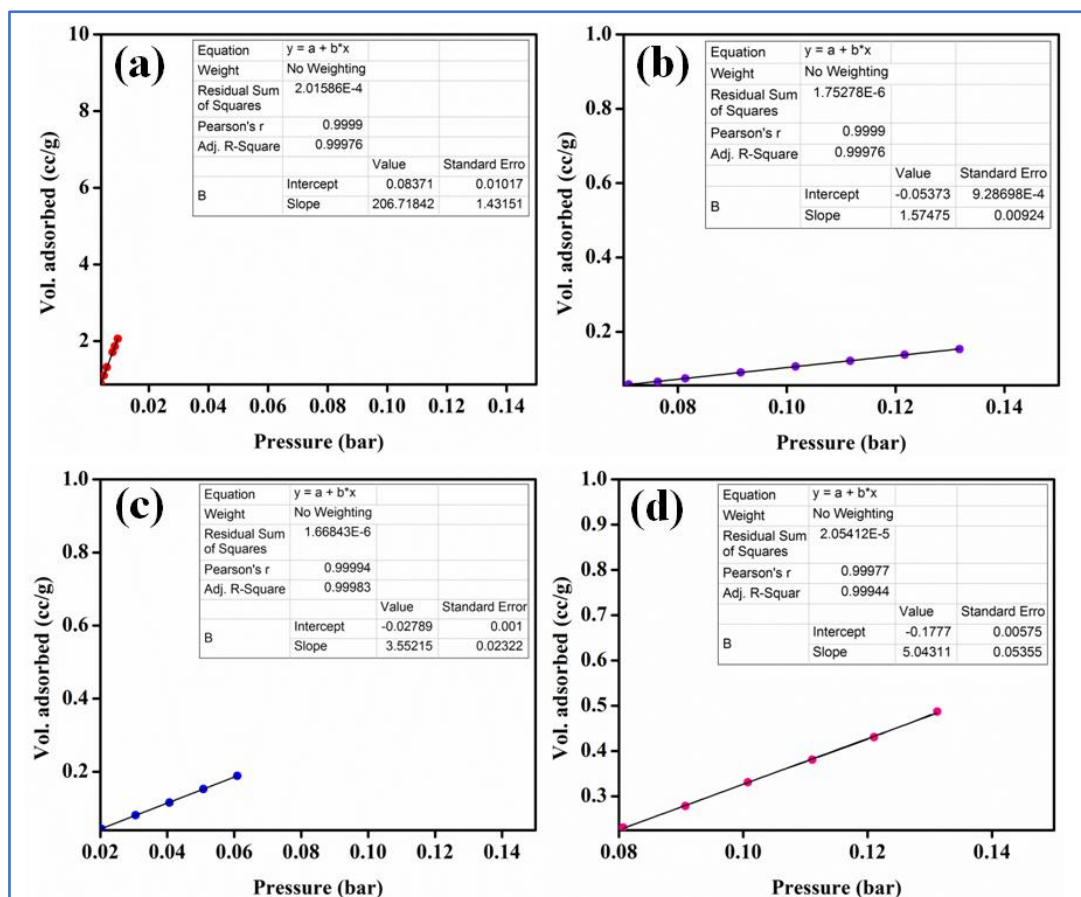


Figure A87. Calculation of Henry gas selectivity constants for gases CO<sub>2</sub>, Ar, H<sub>2</sub> and N<sub>2</sub>.

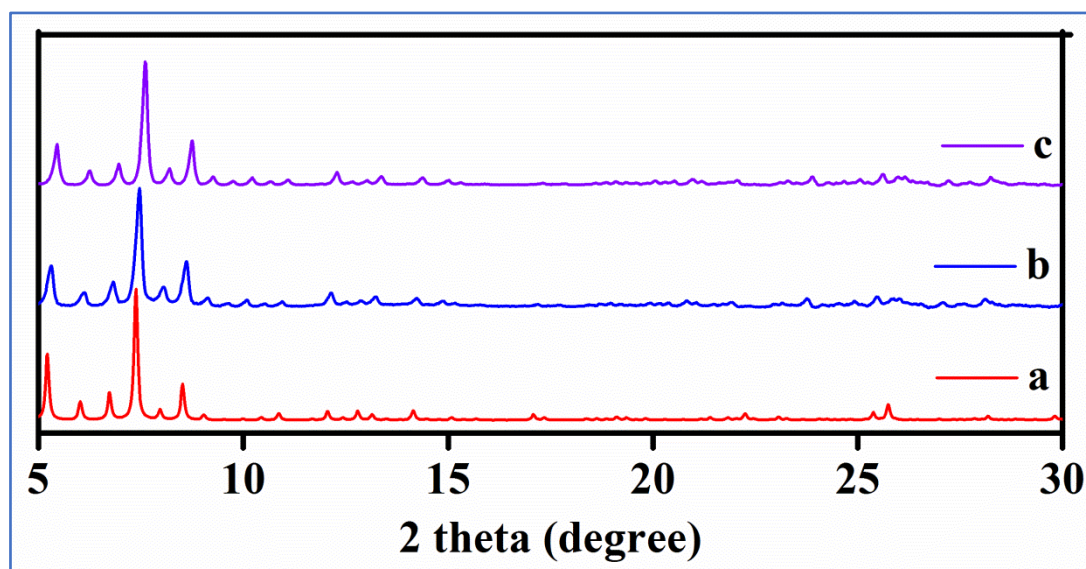
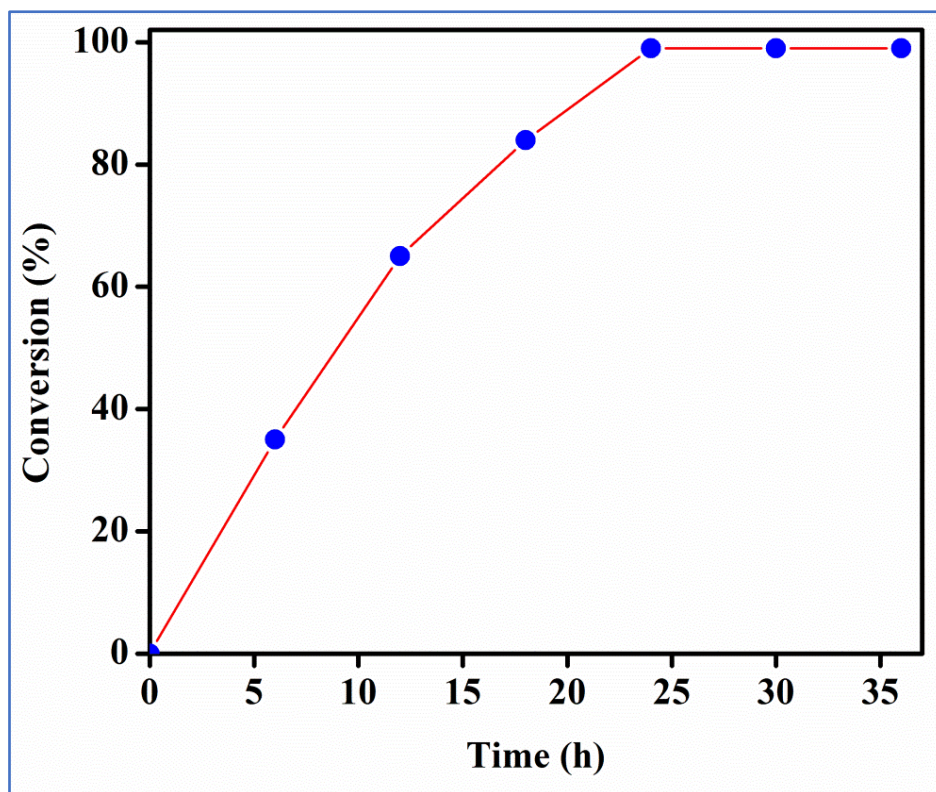
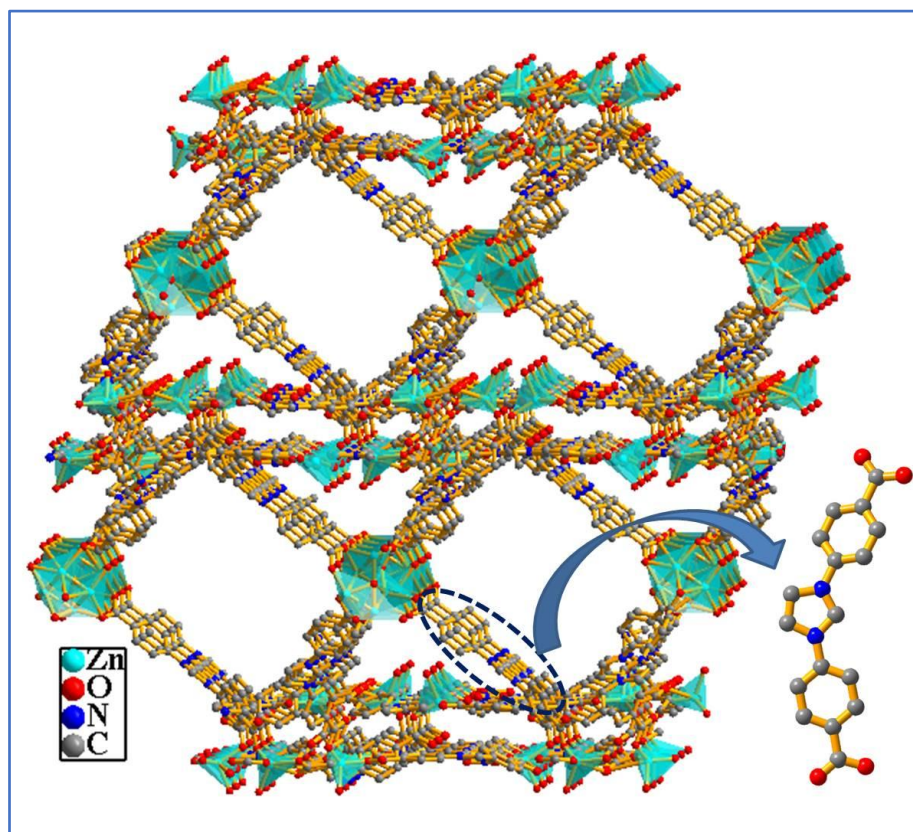


Figure A88. PXRD patterns of MOF-SO<sub>3</sub>Ag (a) simulated pattern, (b) Activated MOF-SO<sub>3</sub>Ag (c) After five cycles of CO<sub>2</sub> adsorption.



**Figure A89.** Reaction progress for cyclic carboxylation of 2-Methyl-3-butyn-2-ol with CO<sub>2</sub> catalysed by MOF-SO<sub>3</sub>Ag.



**Figure A90.** View of one-dimensional pore along *b*-axis containing NHC sites.

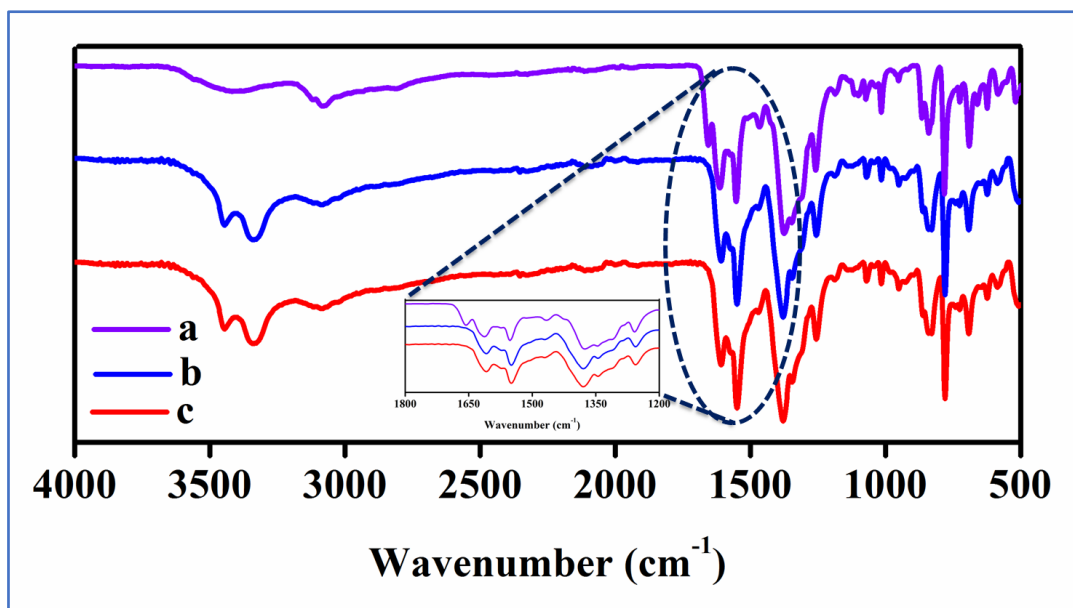


**Figure A91.** FT-IR spectra of (a) NHC-MOF, (b) Cu(I)@NHC-MOF and (c) recycled sample of Cu(I)@NHC-MOF after ten catalytic cycles.

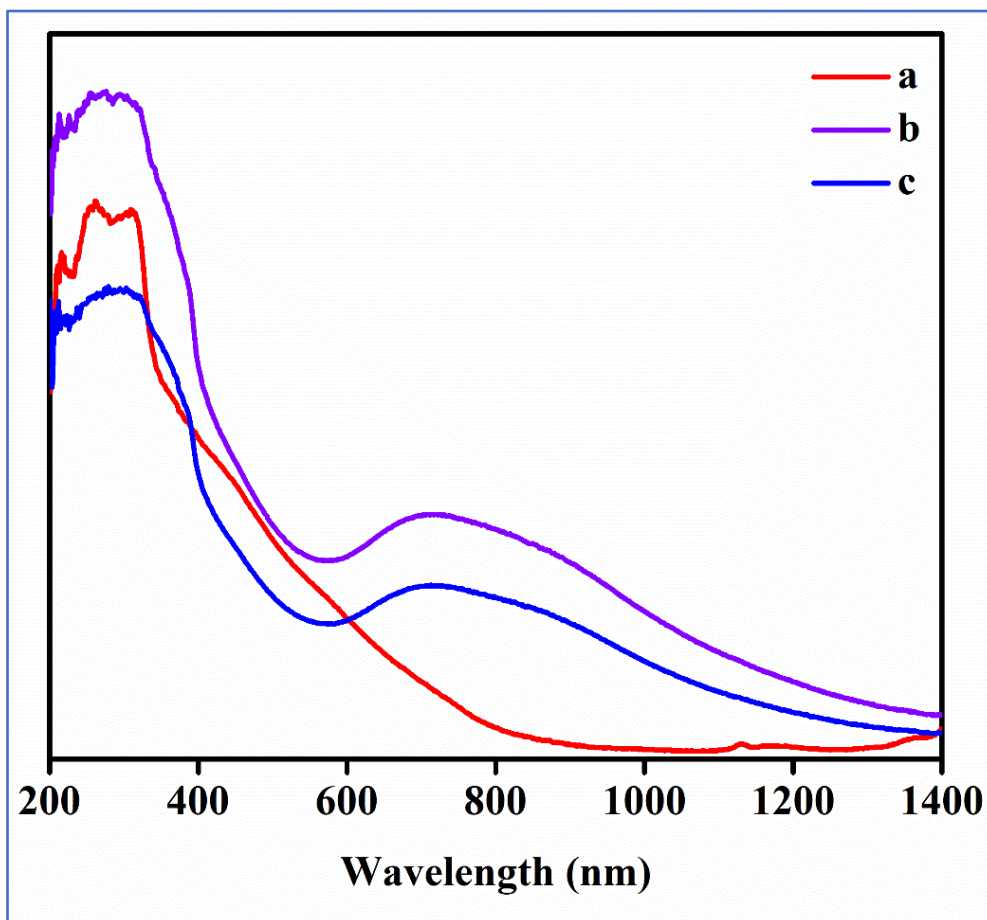


**Figure A92.** UV-Vis absorption spectra of (a) NHC-MOF, (b) Cu(I)@NHC-MOF and (c) recycled sample of Cu(I)@NHC-MOF after ten catalytic cycles.

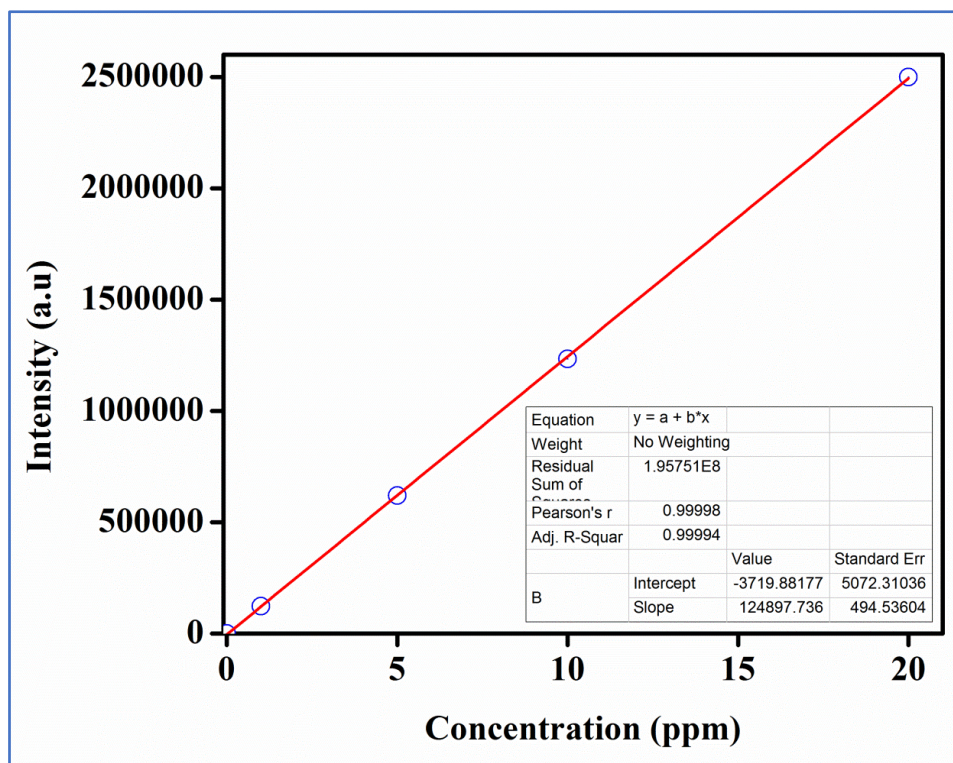


**Figure A93.** Calibration curve of MP-AES analysis for Cu(I)@NHC-MOF.

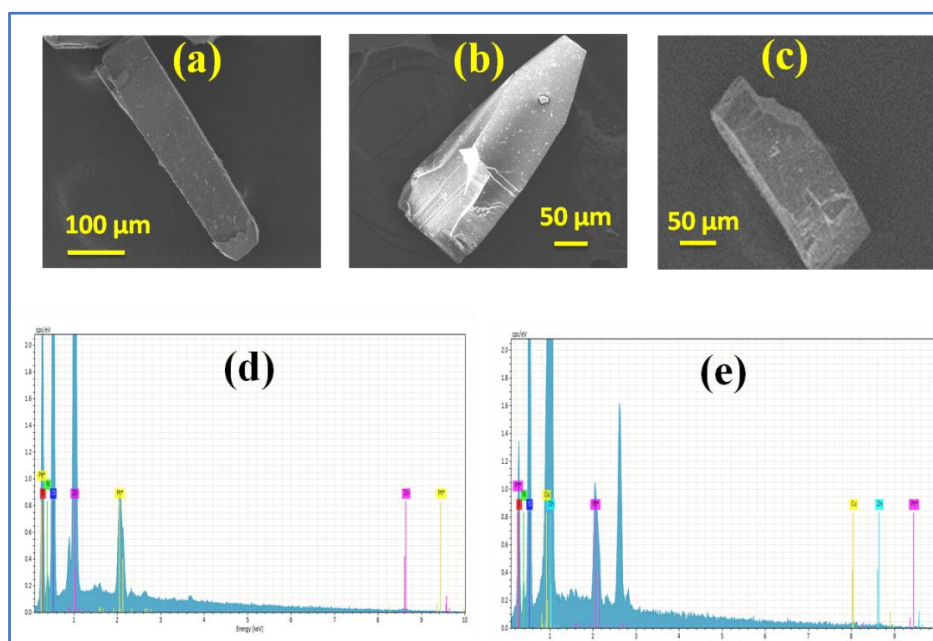


**Figure A94.** SEM image of (a) NHC-MOF, (b) Cu(I)@NHC-MOF, (c) recycled sample of Cu(I)@NHC-MOF after ten catalytic cycles, EDS plot of (d) NHC-MOF and (e) Cu(I)@NHC-MOF.

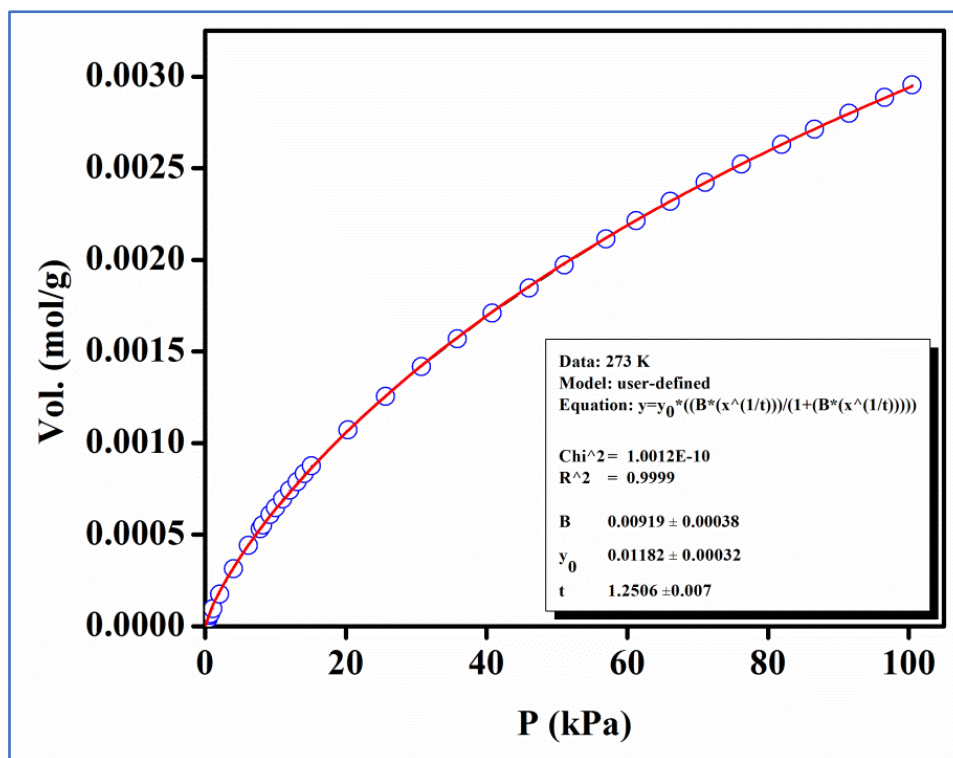


**Figure A95.** Carbon dioxide adsorption isotherm of Cu(I)@NHC-MOF carried out at 273 K. The solid line shows the best fit to the data using the Langmuir-Freundlich equation.

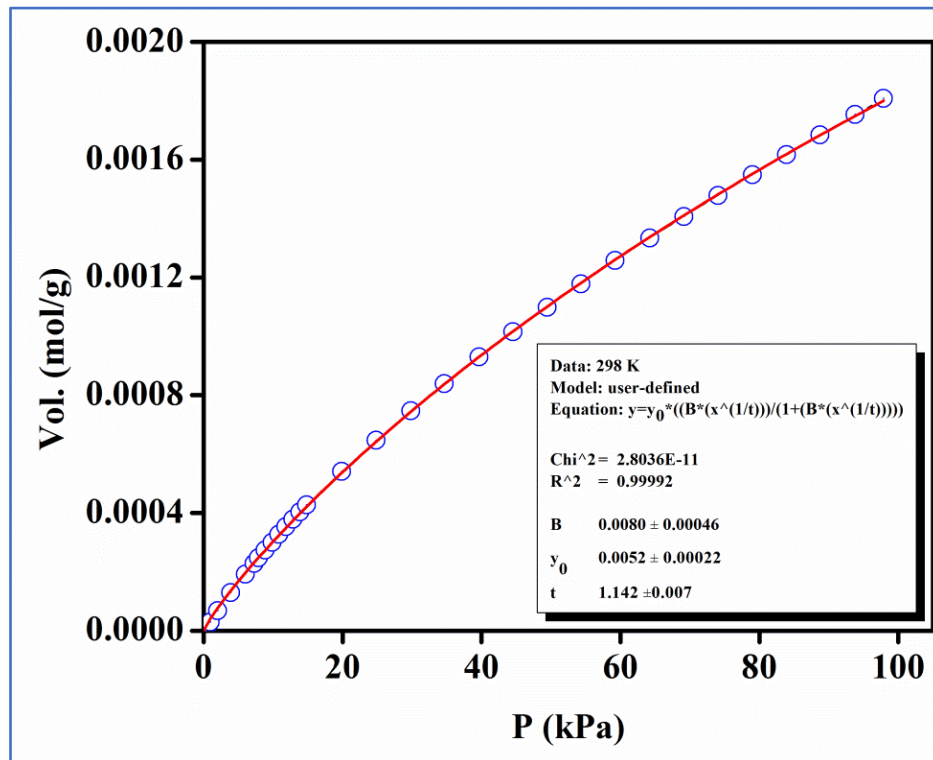


**Figure A96.** Carbon dioxide adsorption isotherm of Cu(I)@NHC-MOF carried out at 298 K. The solid line shows the best fit to the data using the Langmuir-Freundlich equation.

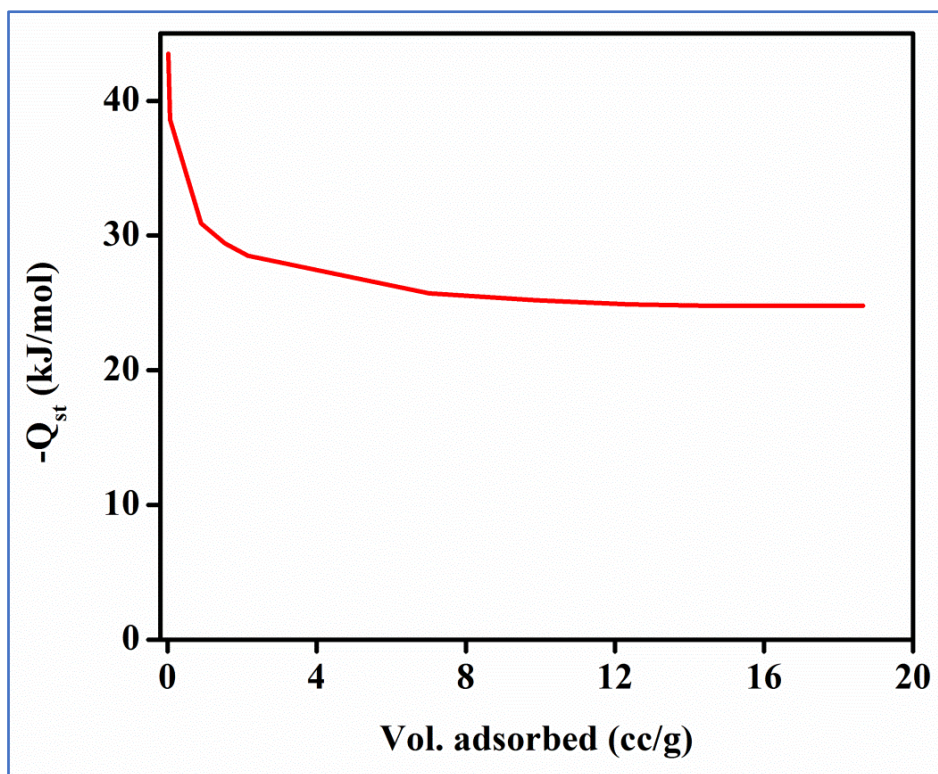


**Figure A97.** Enthalpy of carbon dioxide adsorption for Cu(I)@NHC-MOF determined using the Clausius-Clapeyron equation.

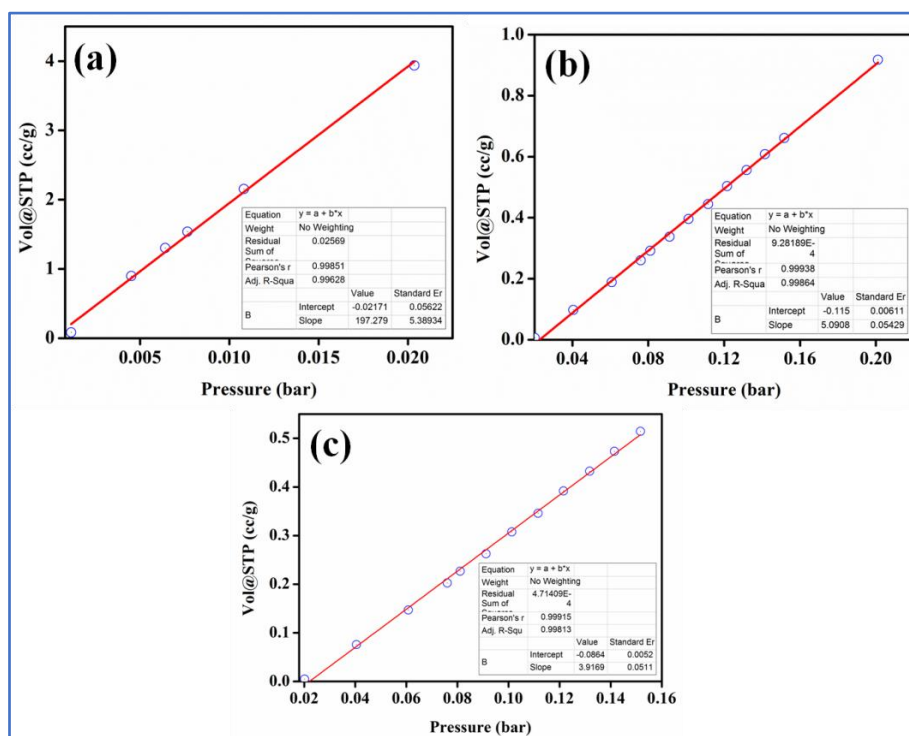


**Figure A98.** Calculation of Henry gas selectivity constants for gases (a) CO<sub>2</sub>, (b) N<sub>2</sub> and (c) O<sub>2</sub>.

**Table A21.** Catalyst optimization towards carboxylation of 2-methyl-3-butyn-2-ol.<sup>a</sup>

Sl. No.	Catalyst	Pressure	Conversion (%) <sup>c</sup>
1	-	1 atm CO <sub>2</sub>	-
2	NHC-MOF	1 atm CO <sub>2</sub>	-
3	Cu(NO <sub>3</sub> ) <sub>2</sub> .6H <sub>2</sub> O	1 atm CO <sub>2</sub>	-
4	CuCl	1 atm CO <sub>2</sub>	78
5	Cu(I)@NHC-MOF	Bubbling of laboratory air	21
6	Cu(I)@NHC-MOF	1 atm (CO <sub>2</sub> :N <sub>2</sub> = 13:87)	67
7	Cu(I)@NHC-MOF	1 atm CO <sub>2</sub>	88 <sup>b</sup>
8	Cu(I)@NHC-MOF	1 atm CO <sub>2</sub>	99

Reaction Conditions, a: 2-methyl-3-butyn-2-ol (4 mmol), catalyst (0.005 mmol), DBU (0.05 equivalent), DMF (2 mL), temperature (RT), time (12 h), b: time (10h) and c: The percentage of conversion was determined by <sup>1</sup>H NMR analysis.

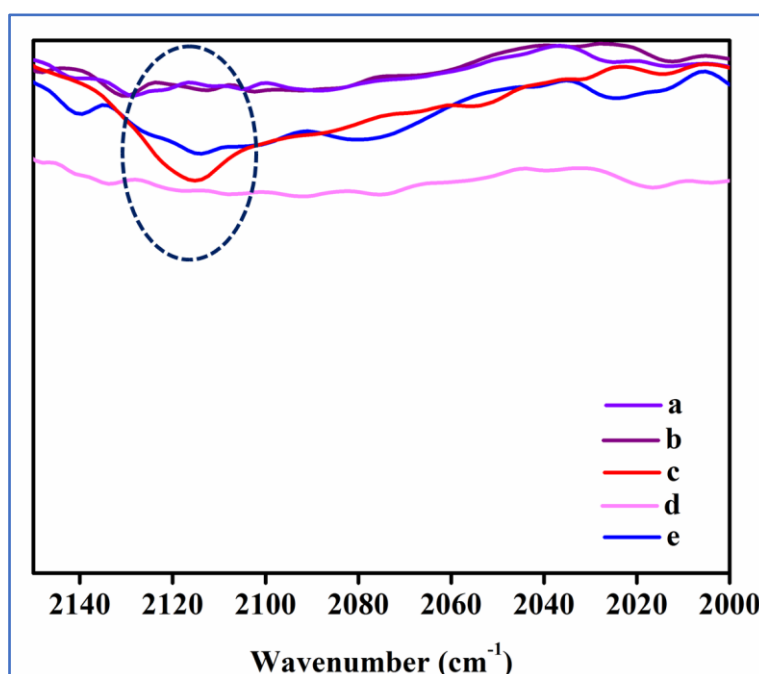
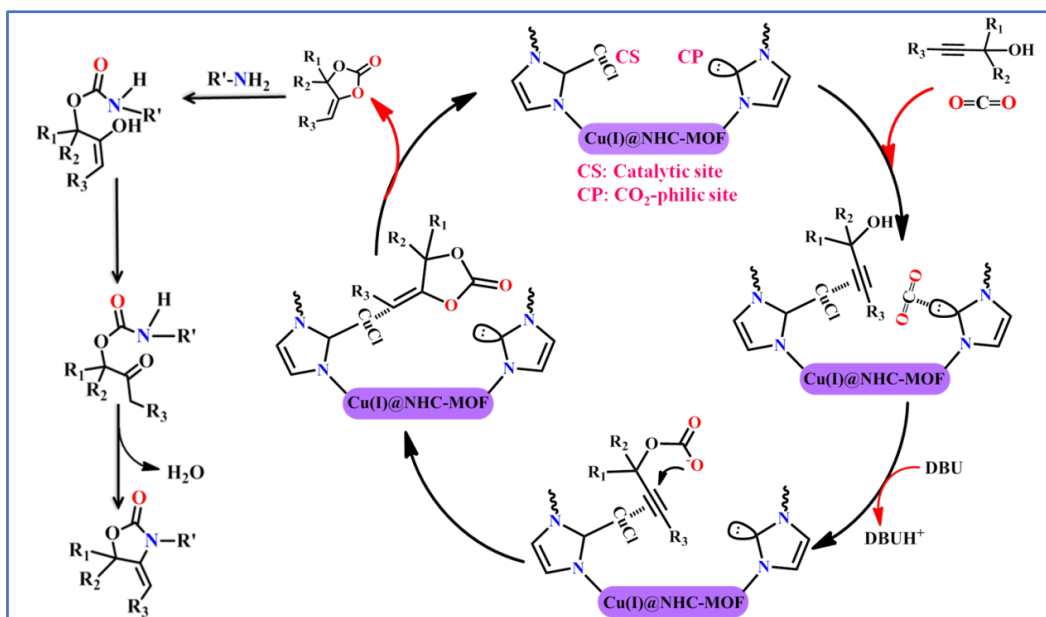


**Figure A99.** FT-IR spectra of (a) NHC-MOF, (b) Cu(I)@NHC-MOF, (c) 2-methyl-3-butyn-2-ol, (d) NHC-MOF treated with 2-methyl-3-butyn-2-ol, and (e) Cu(I)@NHC-MOF treated with 2-methyl-3-butyn-2-ol.



**Scheme A1.** A plausible mechanism for the three-component reaction between CO<sub>2</sub>, propargylic alcohol and primary amine catalysed by Cu(I)@NHC-MOF.

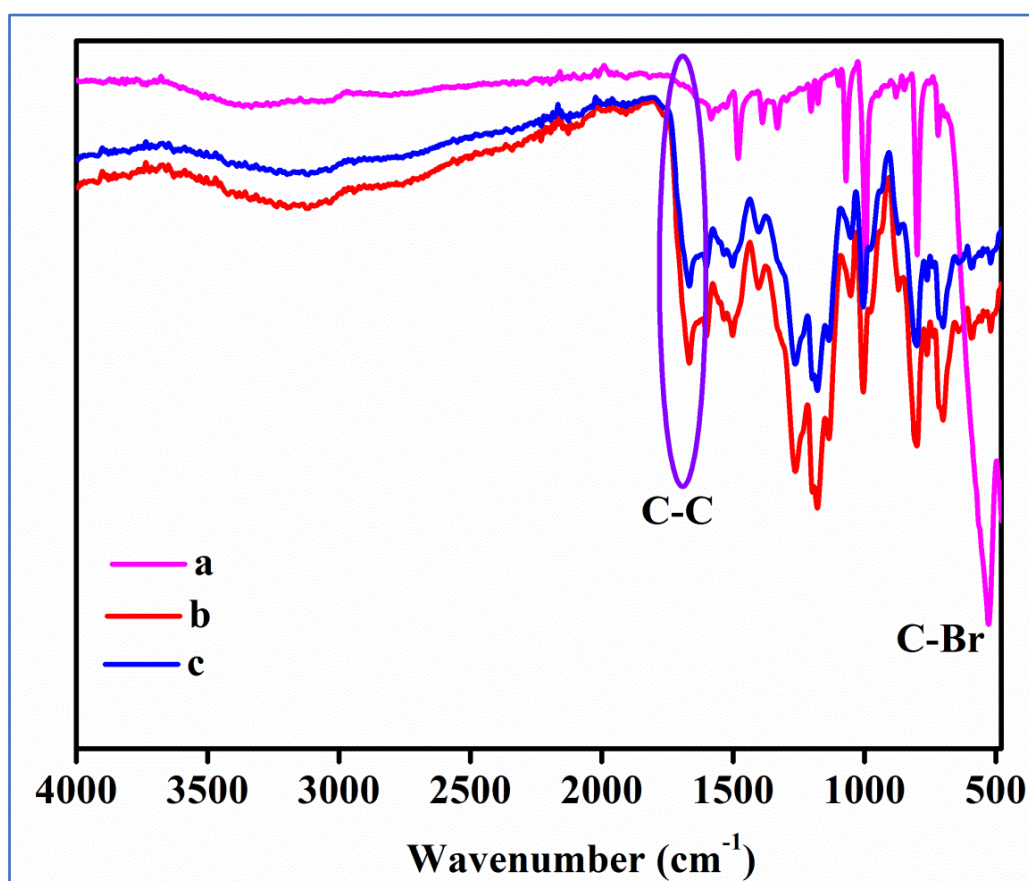


**Figure A100.** FTIR spectra of (a) TBPP(M), (b) POFCo, and (c) POF(Zn).

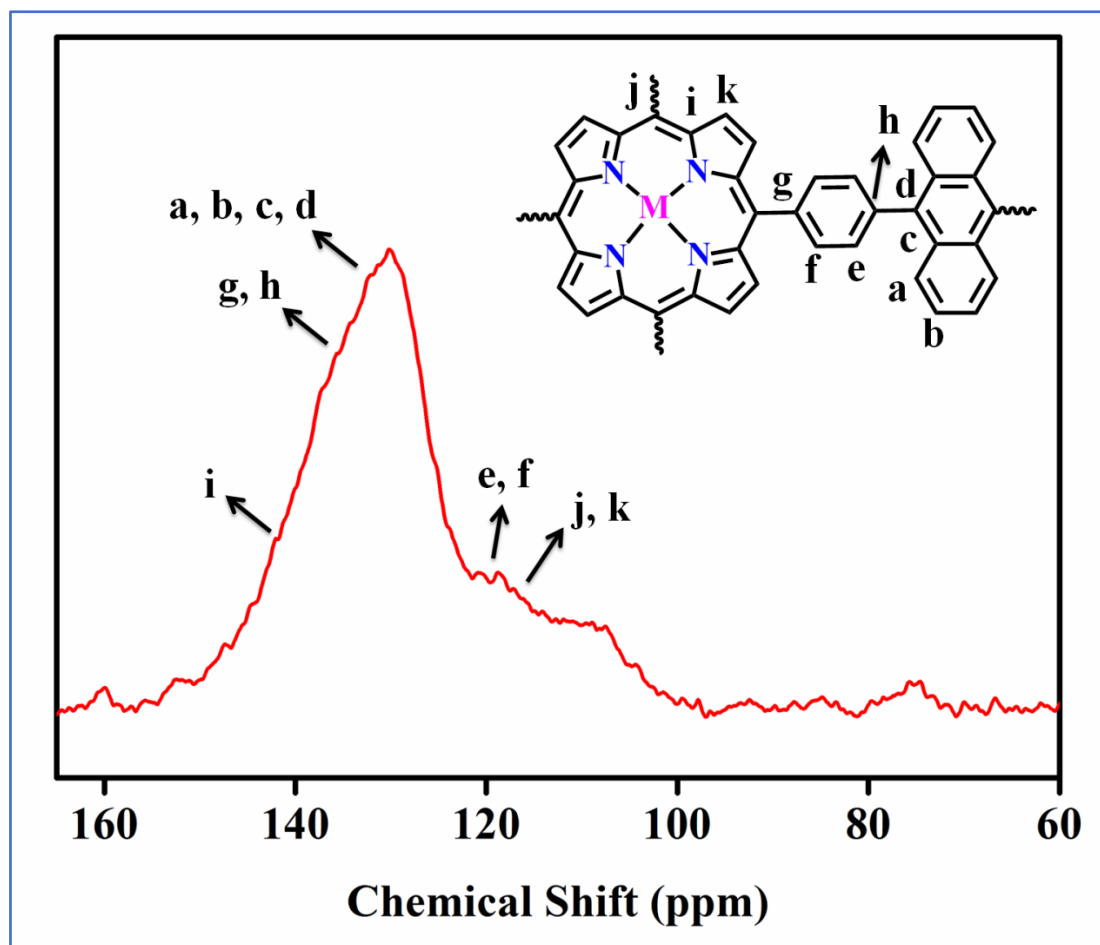


**Figure A101.**  $^{13}\text{C}$  CP-MAS (cross-polarized magic angle spinning) NMR spectra of POF(Zn).

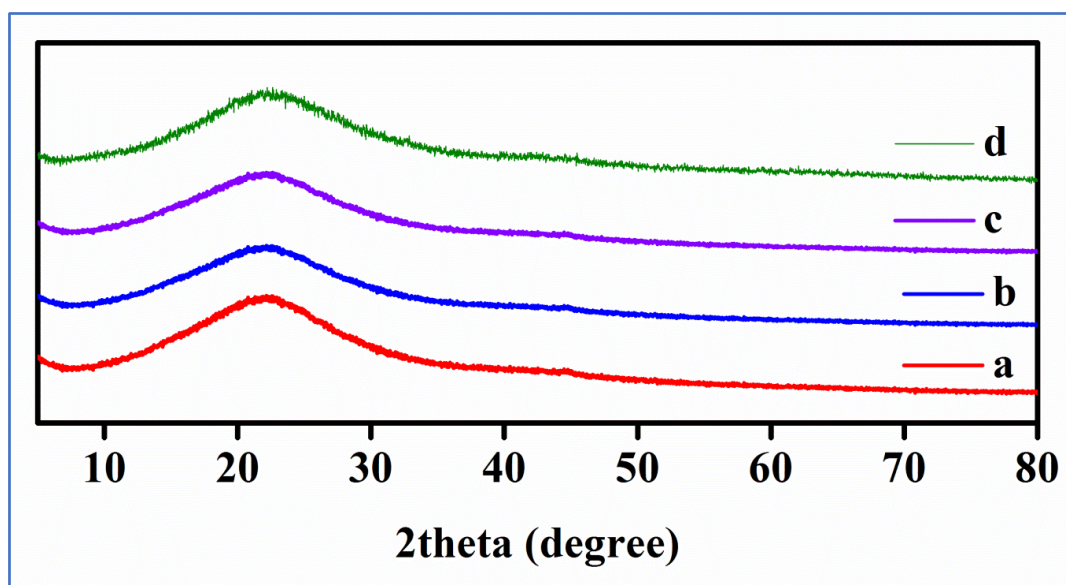


**Figure A102.** PXRD plot of (a) POF(Co), (b) POF(Zn), (c) activated POF(Co), and (d) recycled POF(Co) after catalysis.

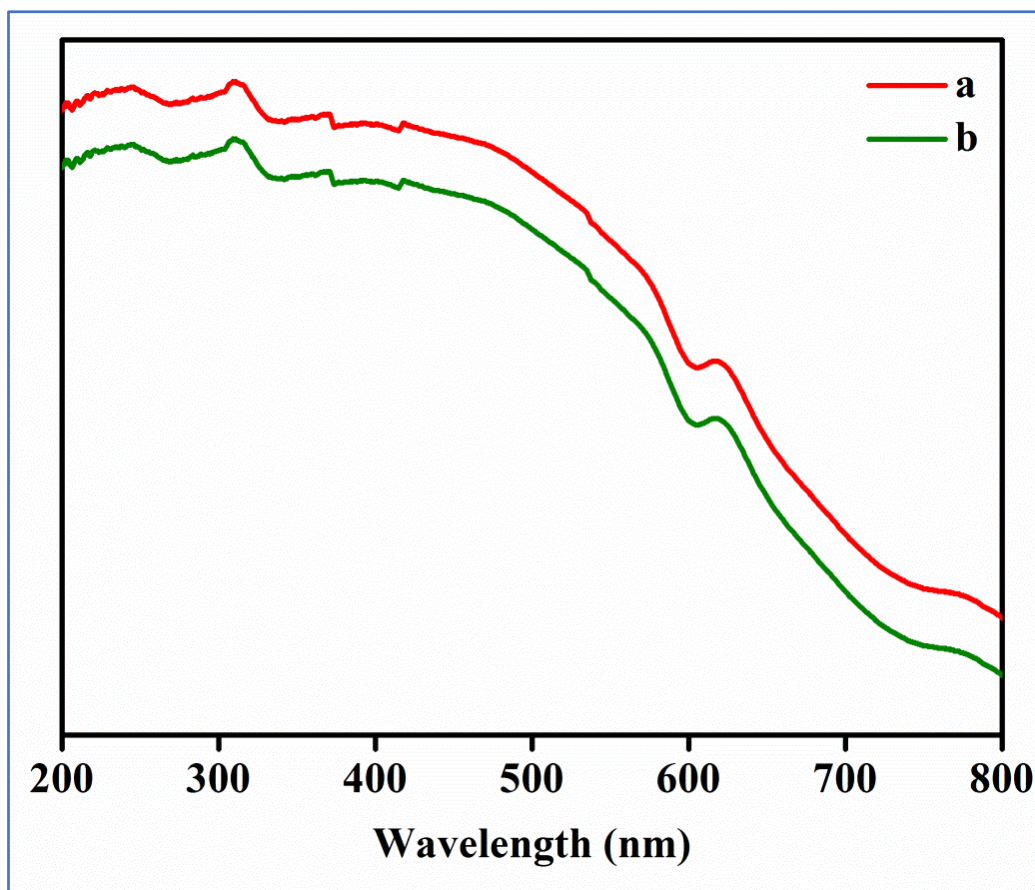


**Figure A103.** UV-Vis absorption spectra of (a) POF(Co), and (b) POF(Zn).

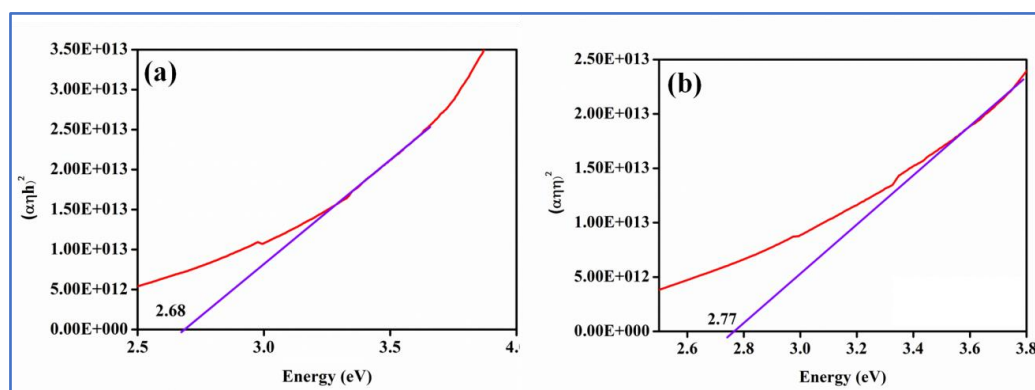


**Figure A104.** Bandgap plots for (a) POF(Co), and (b) POF(Zn).

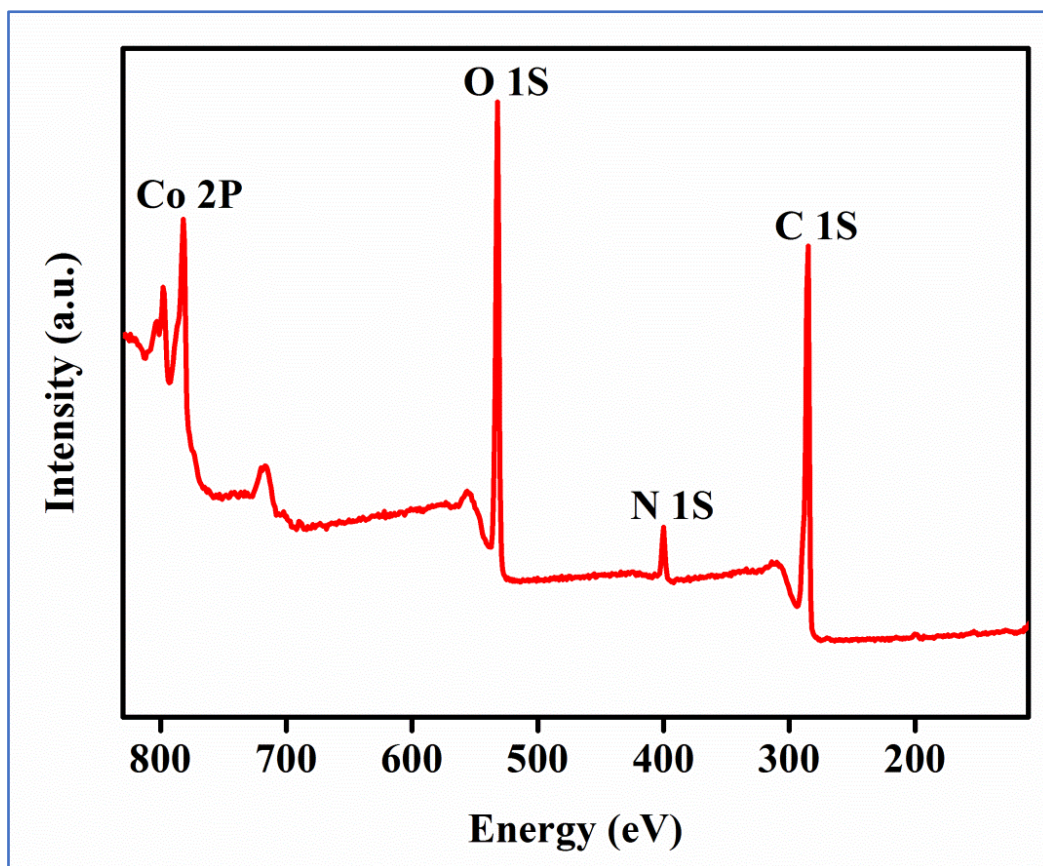


**Figure A105.** XPS survey scan for POF(Co).

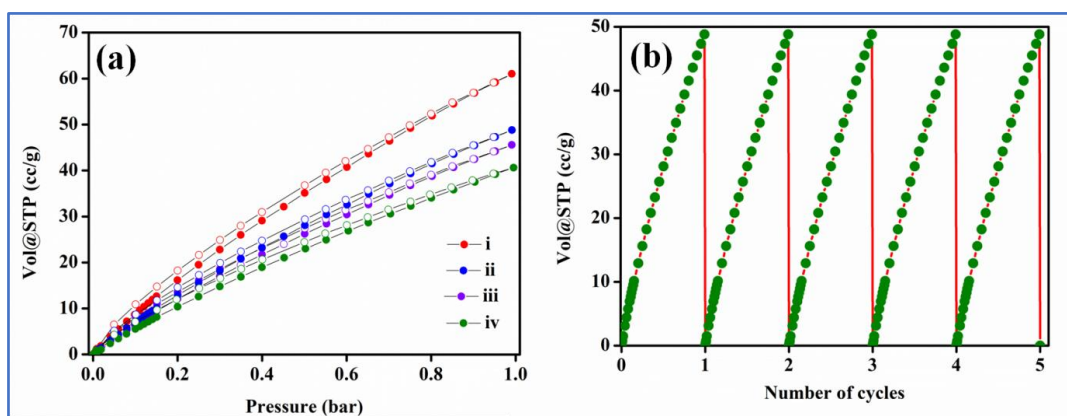


**Figure A106.** (a) CO<sub>2</sub> adsorption isotherms of POF(Co) (i and iii), POF(Zn) (ii and iv) carried out at 273 and 298 K, respectively, and (b) recyclable CO<sub>2</sub> adsorption carried out at 298 K.

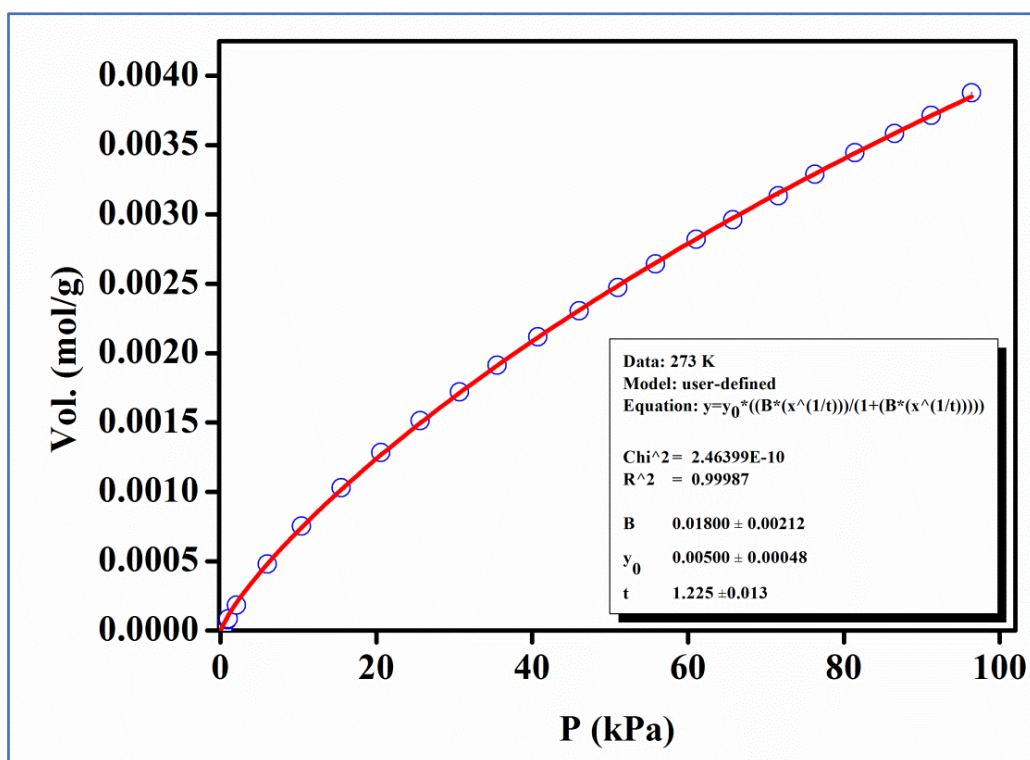


**Figure A107.** Carbon dioxide adsorption isotherm of POF(Co) carried out at 273 K. The solid line shows the best fit to the data using the Langmuir-Freundlich equation.

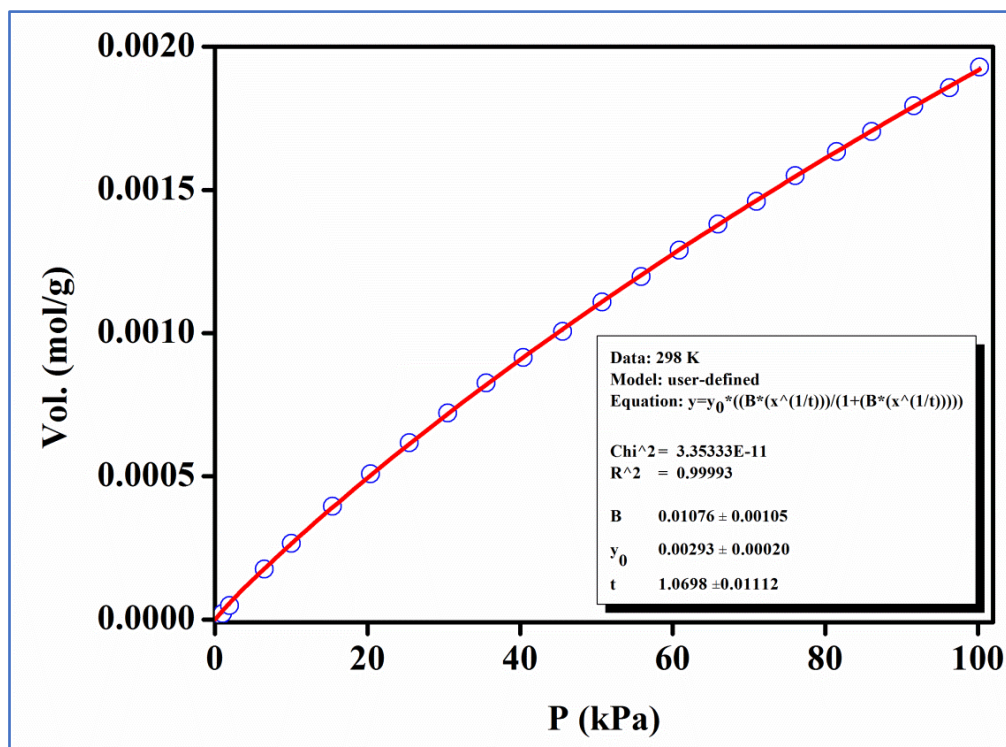


**Figure A108.** Carbon dioxide adsorption isotherm of POF(Co) carried out at 298 K. The solid line shows the best fit to the data using the Langmuir-Freundlich equation.

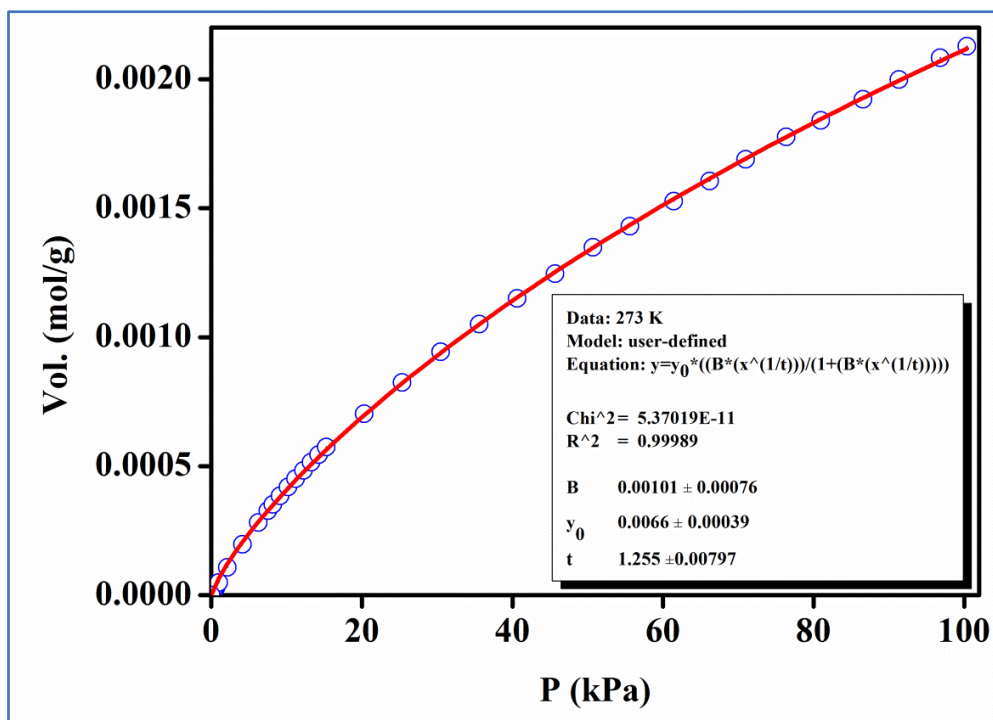


**Figure A109.** Carbon dioxide adsorption isotherm of POF(Zn) carried out at 273 K. The solid line shows the best fit to the data using the Langmuir-Freundlich equation.

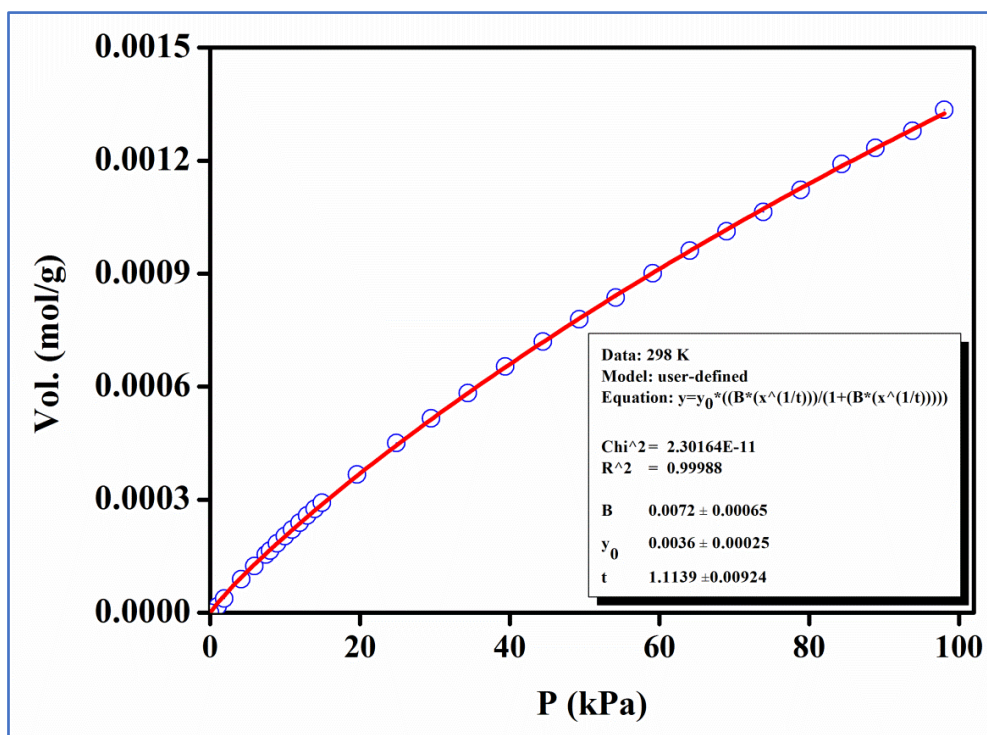


**Figure A110.** Carbon dioxide adsorption isotherm of POF(Zn) carried out at 298 K. The solid line shows the best fit to the data using the Langmuir-Freundlich equation.

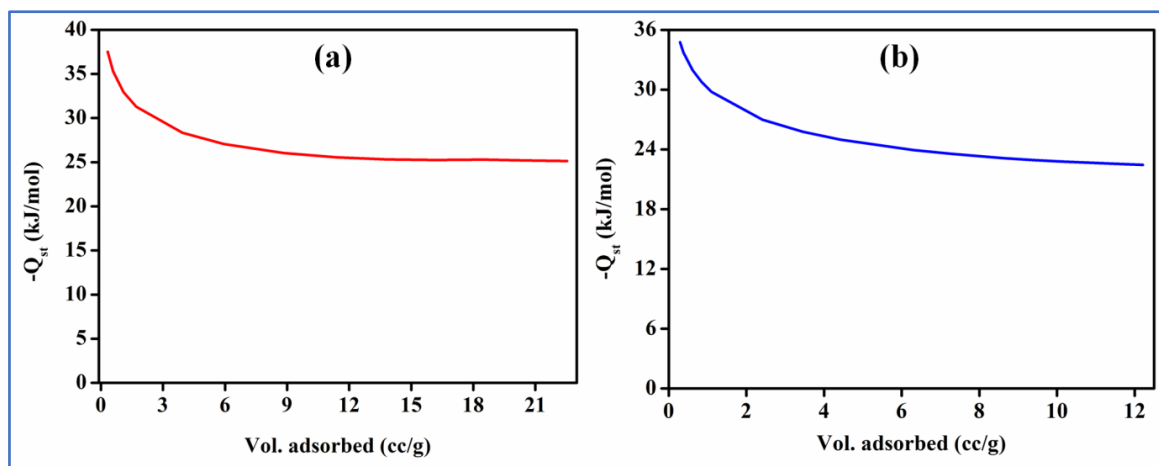


**Figure A111.** Enthalpy of carbon dioxide adsorption for (a) POF(Co), and (b) POF(Zn) determined using the Clausius-Clapeyron equation.

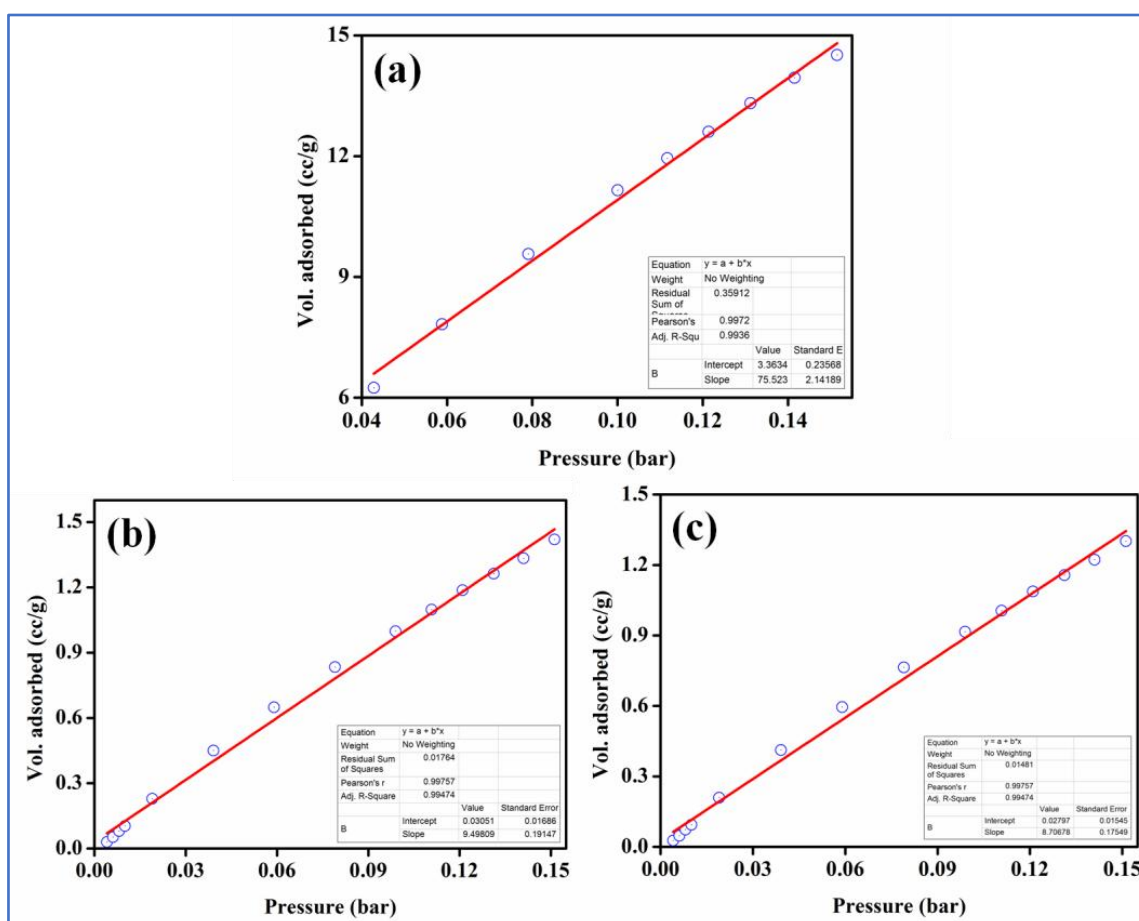


**Figure A112.** Calculation of Henry gas selectivity constants for gases (a) CO<sub>2</sub>, (b) CH<sub>4</sub>, and (c) N<sub>2</sub>.

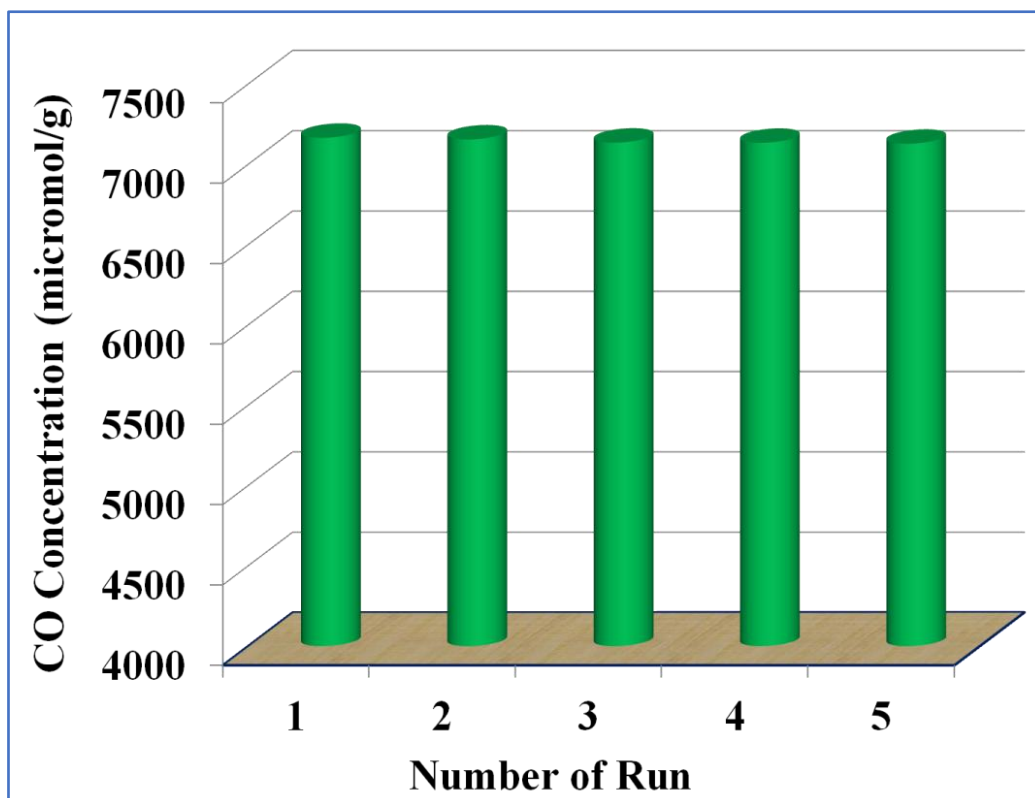


Figure A113. Recyclability of photocatalytic CO<sub>2</sub> reduction.

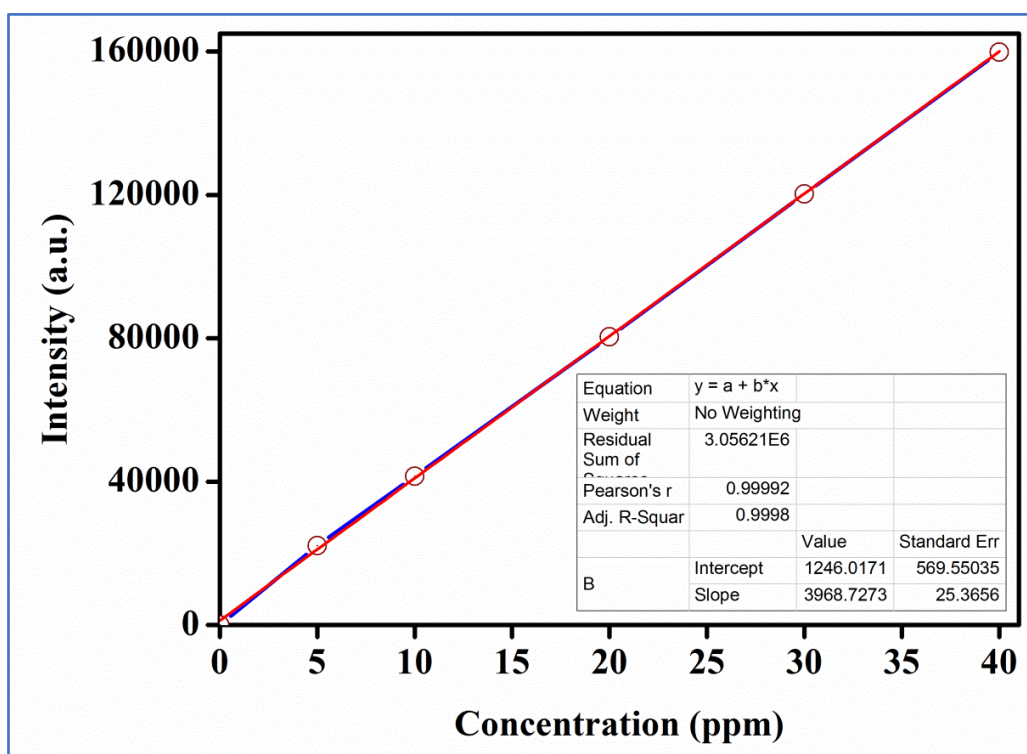
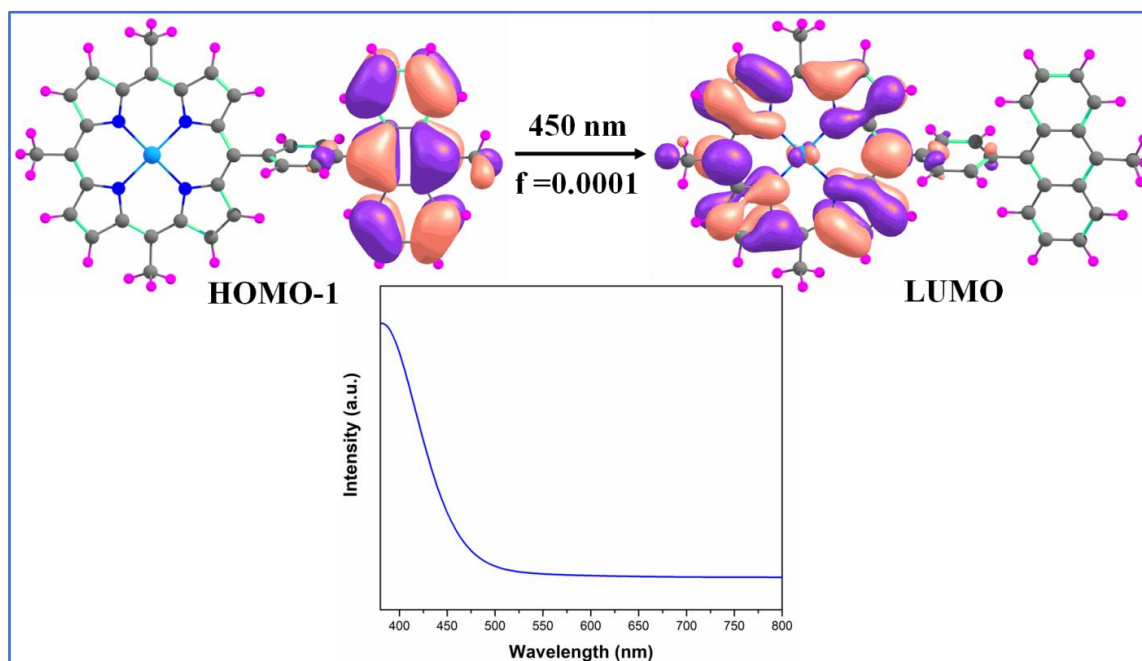


Figure A114. Calibration curve of MP-AES analysis for detection of Co metal.

## Theoretical section

The geometry optimization of the primitive structure of metal-containing POF unit, HOMO, and LUMO energies was carried out using Density Functional Theory (DFT) with gradient exchange-correlational functional of B3LYP. The Pople basis of 6-31G\* has been used for all main group elements of H, C, N, and the LANL2DZ basis set was implemented for the Co and Zn transition metals.<sup>21</sup> Acetonitrile and water mixed solvent is used under the conductor-like polarizable continuum solvation model (CPCM). The electronic absorption spectra (ligand to metal charge transfer, LMCT) have been performed by the time-dependent density functional theory (TD-DFT) method, scanning across 300 excited states. All calculations were performed using Gaussian 09 software. The reaction-free energy change ( $\Delta G$ ) has been calculated from the reaction-free energy difference between the final and initial intermediates. The Zero-point vibrational energy (ZPVE) and thermal correction have been considered in total electronic energy to obtain the reaction-free energy at 298 K temperature and 1 atm pressure. The Natural bond orbital (NBO) calculations have also been considered on some intermediates to investigate the natural charges.<sup>22</sup>



**Figure A115.** The frontier molecular orbital and simulated absorption spectra of POF(Co).

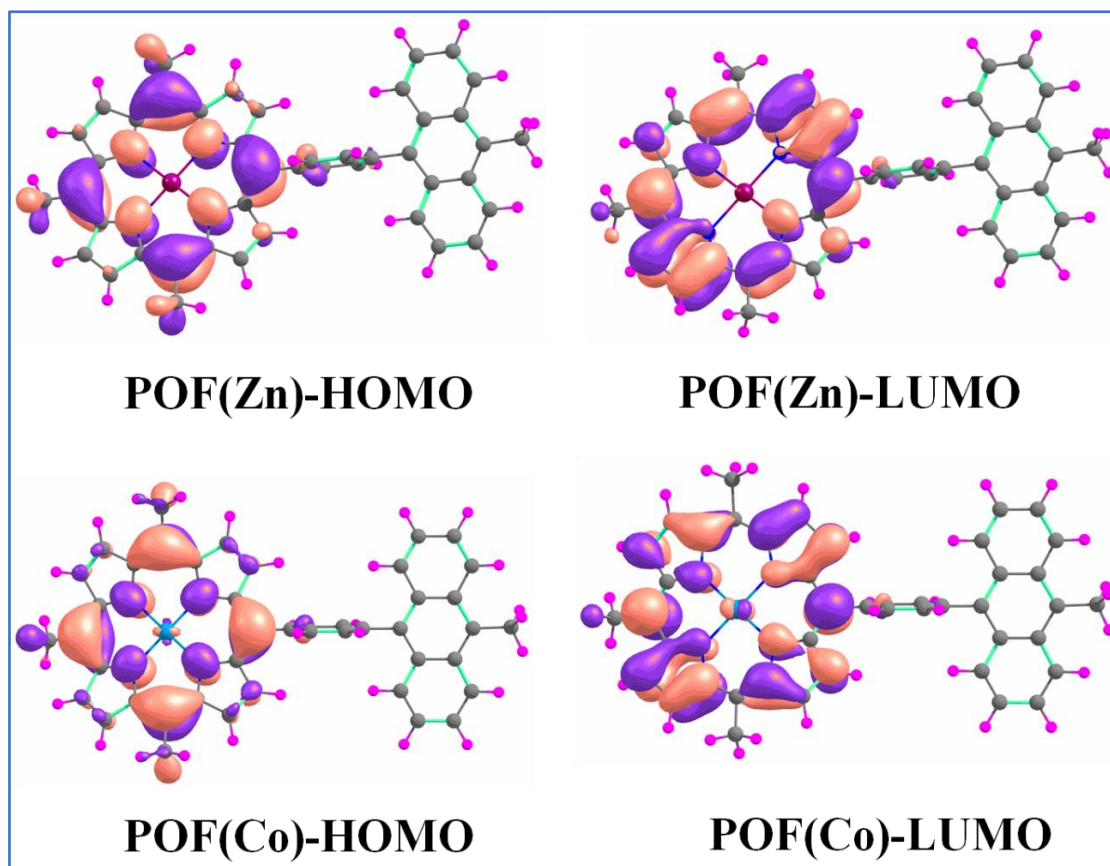


**Figure A116.** The frontier HOMO-LUMO molecular orbital of POF(Zn/Co).

### References

- (1) Pan, H.; Ritter, J. A.; Balbuena, P. B. Examination of the approximations used in determining the isosteric heat of adsorption from the Clausius-Clapeyron equation. *Langmuir* **1998**, *14*, 6323–6327.
- (2) Yang, R. T. Gas Separation by Adsorption Processes, Butterworth, Boston, **1997**.
- (3) Frisch, M. J.; Trucks, G. W.; Schlegel, H. B.; Scuseria, G. E.; Robb, M. A.; Cheeseman, J. R.; Scalmani, G.; Barone, V.; Mennucci, B.; Petersson, G. A. *Gaussian 09, Revision D.01,;Revision B.01,; Gaussian, Inc.: Wallingford CT, 2010*.
- (4) Gao, W. Y.; Chen, Y.; Niu, Y.; Williams, K.; Cash, L.; Perez, P. J.; Wojtas, L.; Cai, J.; Chen, Y. S.; Ma, S. Crystal Engineering of an nbo Topology Metal-Organic Framework for Chemical Fixation of CO<sub>2</sub> under Ambient Conditions. *Angew. Chem. Int. Ed.* **2014**, *53*, 2615–2619.
- (5) Wei, L.-Q.; Ye, B.-H. Efficient Conversion of CO<sub>2</sub> via Grafting Urea Group into a [Cu<sub>2</sub>(COO)<sub>4</sub>]-Based Metal–Organic Framework with Hierarchical Porosity. *Inorg. Chem.* **2019**, *58*, 4385-4393.

- (6) He, H.; Sun, Q.; Gao, W.; Perman, J. A.; Sun, F.; Zhu, G.; Aguila, B.; Forrest, K.; Space, B.; Ma, S. A stable metal-organic framework featuring a local buffer environment for carbon dioxide fixation. *Angew. Chem., Int. Ed.* **2018**, *57*, 4657-4662.
- (7) Song, J.; Zhang, Z. f.; Hu, S.; Wu, T.; Jiang, T.; Han, B. MOF-5/n-Bu<sub>4</sub> NBr: an efficient catalyst system for the synthesis of cyclic carbonates from epoxides and CO<sub>2</sub> under mild conditions. *Green Chem.* **2009**, *11*, 1031-1036.
- (8) Kathalikkattil, A. C.; Roshan, R.; Tharun, J.; Babu, R.; Jeong, G. S.; Kim, D. W.; Cho, S. J.; Park, D. W. A sustainable protocol for the facile synthesis of zinc-glutamate MOF: an efficient catalyst for room temperature CO<sub>2</sub> fixation reactions under wet conditions. *Chem. Commun.* **2016**, *52*, 280.
- (9) Gao, W. Y.; Wojtas, L.; Ma, S. A porous metal–metalloporphyrin framework featuring high-density active sites for chemical fixation of CO<sub>2</sub> under ambient conditions. *Chem. Commun.* **2014**, *50*, 5316-5318.
- (10) Zalomaeva, O. V.; Chibiryaev, A. M.; Kovalenko, K. A.; Kholdeeva, O. A.; Balzhinimaev, B. S.; Fedin, V. P. Cyclic carbonates synthesis from epoxides and CO<sub>2</sub> over metal–organic framework Cr-MIL-101. *J. Catal.* **2013**, *298*, 179-185.
- (11) Babu, R.; Kathalikkattil, A. C.; Roshan, R.; Tharun, J.; Kim, D. W.; Park, D. W. Dual-porous metal organic framework for room temperature CO<sub>2</sub> fixation via cyclic carbonate synthesis. *Green Chem.* **2016**, *18*, 232-242.
- (12) Sun, X.; Gu, J.; Yuan, Y.; Yu, C.; Li, J.; Shan, H.; Li, G.; Liu, Y. A Stable Mesoporous Zr-Based Metal Organic Framework for Highly Efficient CO<sub>2</sub> Conversion. *Inorg. Chem.* **2019**, *58*, 7480–7487.
- (13) Lan, J.; Liu, M.; Lu, X.; Zhang, X.; Sun, J. Novel 3D Nitrogen-Rich Metal Organic Framework for Highly Efficient CO<sub>2</sub> Adsorption and Catalytic Conversion to Cyclic Carbonates under Ambient Temperature. *ACS Sustainable Chem. Eng.* **2018**, *6*, 8727-8735.
- (14) Das, R.; Dhankhar, S. S.; Nagaraja, C. M. Construction of a bifunctional Zn(II)–organic framework containing a basic amine functionality for selective capture and room temperature fixation of CO<sub>2</sub>. *Inorg. Chem. Front.* **2020**, *7*, 72-81
- (15) Yang, D.-A.; Cho, H.-Y.; Kim, J.; Yang, S.-T.; Ahn, W.-S. CO<sub>2</sub> capture and conversion using Mg-MOF-74 prepared by a sonochemical method. *Energy Environ. Sci.* **2012**, *5*, 6465–6473.
- (16) Tran, Y. B. N.; Nguyen, P. T. K.; Khoi, Q. T. L.; Nguyen, D. Series of M-MOF-184 (M = Mg, Co, Ni, Zn, Cu, Fe) Metal–Organic Frameworks for Catalysis Cycloaddition of CO<sub>2</sub>. *Inorg. Chem.* **2020**, *59*, 16747-16759

- (17) Kim, H.; Sohail, M.; Yim, K.; Park, Y. C.; Chun, D. H.; Kim, H. J.; Han, O. S.; Moon, J.-H. *ACS Appl. Mater. Interfaces* **2019**, *11*, 7014-702.
- (18) Nguyen, P. T. K.; Nguyen, H. T. D.; Pham, H. Q.; Kim, J.; Cordova, K. E.; Furukawa, H. Synthesis and Selective CO<sub>2</sub> Capture Properties of a Series of Hexatopic Linker-Based Metal–Organic Frameworks. *Inorg. Chem.* **2015**, *54*, 10065-10072.
- (19) Dietzel, P. D. C.; Besikiotis, V.; Blom, R. Application of metal–organic frameworks with coordinatively unsaturated metal sites in storage and separation of methane and carbon dioxide. *J. Mater. Chem.* **2009**, *19*, 7362-7370.
- (20) Remy, T.; Peter, S. A.; Perre, S. V.; Valvekens, P.; Vos, D. E. D.; Baron, G. V.; Joeri, F.; Denayer, M. Selective Dynamic CO<sub>2</sub> Separations on Mg-MOF-74 at Low Pressures: A Detailed Comparison with 13X. *J. Phys. Chem. C* **2013**, *117*, 9301-9310.
- (21) Frisch, M. J.; Pople, J. A.; Binkley, J. S. Self-consistent molecular orbital methods 25. Supplementary functions for Gaussian basis sets. *J. Chem. Phys.* **1984**, *80*, 3265-3269.
- (22) Grimme, S.; Antony, J.; Ehrlich, S.; Krieg, H. A consistent and accurate ab initio parametrization of density functional dispersion correction (DFT-D) for the 94 elements H-Pu. *J. Chem. Phys.* **2010**, *132*, 154104-154119.

## BIO DATA

1. Name: Rajesh Das

Ph.D. Scholar,

Contact no. 9658973016

Email: 2018cyz@iitrpr.ac.in and dasrajesh3016@gmail.com

Department of Chemistry,

Indian Institute of Technology,

Ropar, Punjab – 140001.

2. Date of Birth: 26<sup>th</sup> July 1996

3. Permanent Address:

Name- Rajesh Das, S/o Sh. Pramod K. Das,

At- Salijanga, PO- Kuradha, Jagatsingpur,

Odisha-754136.

4. Educational Qualifications:

Sl. No.	Qualification	School/College/ Department	University/Institute	Passing Year	Class
1	Matric (10 <sup>th</sup> )	IBVM, Kostimallikapur	CHS Board, Odisha, India	2011	First
2	HSCE (10+2)	A.S.D. Jr. College, Tritol	HSC Board, Odisha, India	2013	First
3	B.Sc	A.S.D. College, Tritol	Utkal University, Odisha, India	2016	First
4	M.Sc (Inorganic Chemistry)	School of Chemistry	Sambalpur University, Odisha, India	2018	First
5	Ph.D in Chemistry	Department of Chemistry	Indian Institute of Technology Ropar, Punjab, India	2023	NA

## Publications based on thesis work

- (1) **Das, R.;** Dhankhar, S. S.; Nagaraja, C. M. Construction of a bifunctional Zn(II)-organic framework containing basic amine functionality for selective capture and room temperature fixation of CO<sub>2</sub>. *Inorg. Chem. Front.* **2020**, *7*, 72-81.
- (2) **Das, R.;** Muthukumar, D.; Pillai, R. S.; Nagaraja, C. M. Rational design of a Zn(II)-MOF with multiple functional sites for highly efficient fixation of CO<sub>2</sub> at mild conditions: combined experimental and theoretical investigation. *Chem. Eur. J.* **2020**, *26*, 17445-17454.
- (3) **Das, R.;** Ezhil, T.; Palakkal, A. S.; Muthukumar, D.; Pillai, R. S.; Nagaraja, C. M. Efficient chemical fixation of CO<sub>2</sub> from direct air under environment-friendly co-catalyst and solvent-free ambient conditions. *J. Mater. Chem. A* **2021**, *9*, 23127-23139.
- (4) **Das, R.;** Nagaraja, C. M. Highly Efficient Fixation of Carbon Dioxide at RT and Atmospheric Pressure Conditions: Influence of Polar Functionality on Selective Capture and Conversion of CO<sub>2</sub>. *Inorg. Chem.* **2020**, *59*, 9765-9773.
- (5) **Das, R.;** Nagaraja, C. M. Noble metal-free Cu(I)-anchored NHC-based MOF for highly recyclable fixation of CO<sub>2</sub> under RT and atmospheric pressure conditions. *Green Chem.* **2021**, *23*, 5195-5204.
- (6) **Das, R.;** Manna, S. S.; Pathak, B.; Nagaraja, C. M. Strategic Design of Mg-Centered Porphyrin MOF for Efficient Visible Light-Promoted Fixation of CO<sub>2</sub> at Ambient Conditions: Combined Experimental and Theoretical Investigation. *ACS Appl. Mater. Interfaces* **2022**, *14*, 33285-33296.
- (7) **Das, R.;** Parihar, V.; Nagaraja, C. M. Strategic design of a bifunctional Ag(I)-grafted NHC-MOF for efficient chemical fixation of CO<sub>2</sub> from dilute gas at ambient conditions. *Inorg. Chem. Front.* **2022**, *9*, 2583–2593.
- (8) **Das, R.;** Nagaraja, C. M. Rational design of porphyrin-based porous organic framework having single active Co(II) site for the photocatalytic reduction of CO<sub>2</sub> to syngas (Manuscript submitted).

## Publications based on other research work

- (1) **Das, R.;** Kamra, S.; Nagaraja, C. M. Ionic Fe(III)-porphyrin frameworks for the one-pot synthesis of cyclic carbonates from olefins and CO<sub>2</sub>, *Inorg. Chem. Front.* **2023** 10, 2088-2099.
- (2) **Das, R.;** Parihar, V.; Nagaraja, C. M. Strategic design of a bifunctional Ag(I)-grafted NHC-MOF for efficient chemical fixation of CO<sub>2</sub> from dilute gas at ambient conditions, *Inorg. Chem. Front.* **2022**, 9, 2583-2593.
- (3) **Das, R.;** Ezhil, T.; Nagaraja, C. M. Design of Bifunctional Zinc(II)-Organic Framework for Efficient Coupling of CO<sub>2</sub> with Terminal/Internal Epoxides under Mild Conditions, *Crystal Growth & Design*, **2022**, 22, 598-607.
- (4) Dhankhar, S. S.; **Das, R.;** Ugale, B.; Pillai, R. S.; Nagaraja, C. M. Chemical Fixation of CO<sub>2</sub> Under Solvent and Co-Catalyst-free Conditions Using a Highly Porous Two-fold Interpenetrated Cu(II)-Metal–Organic Framework, *Cryst. Growth Des.* **2021**, 21, 1233-1241.

## Oral/Poster presentations at conferences

- (1) Presented poster at International Conference on Modern Trends in Inorganic Chemistry (MTIC-XVII), organized by the Department of Chemistry, IITG December-2019.
- (2) Presented poster at CRIKC Chemistry symposium (CCS-2019) organized by the Department of Chemistry, IISER Mohali, 2019 (**Won a best poster award**).
- (3) Presented poster at International Conference on Main-group molecules to material-II (MMM), organized by the Department of Chemistry, NISER, BBSR 2021 (**Won ACS catalysis best poster award**).
- (4) Presented oral at 58th International Conference on Recent Trends in Chemical Sciences-Environmental Chemistry” (RTCS-ENV 2021) hosted by the Department of Chemistry, IIT Ropar.
- (5) Presented poster at ‘Conference on Advances in Catalysis for Energy and Environment (CACEE-2022)’, & CO<sub>2</sub> India Network 1st Annual Meet, TIFR, Mumbai, India.
- (6) Presented poster at Chemical Research Society of India (CRSI) national symposium in Chemistry organized by Department of Chemistry, IISER Mohali, 2022.
- (7) Presented poster in MOF-2022 8th International Conference on Metal-Organic Frameworks and Open Framework Compounds held at the international congress center Dresden, Germany.
- (8) Presented oral at Chem Fest-2023, Department of Chemistry, IIT Ropar.

